



**HAL**  
open science

# Experiment based development of a non-isothermal pore network model with secondary capillary invasion

Nicole Vorhauer

► **To cite this version:**

Nicole Vorhauer. Experiment based development of a non-isothermal pore network model with secondary capillary invasion. Chemical and Process Engineering. Institut National Polytechnique de Toulouse - INPT; Otto-von-Guericke-Universität Magdeburg, 2018. English. NNT : 2018INPT0082 . tel-04220157

**HAL Id: tel-04220157**

**<https://theses.hal.science/tel-04220157v1>**

Submitted on 27 Sep 2023

**HAL** is a multi-disciplinary open access archive for the deposit and dissemination of scientific research documents, whether they are published or not. The documents may come from teaching and research institutions in France or abroad, or from public or private research centers.

L'archive ouverte pluridisciplinaire **HAL**, est destinée au dépôt et à la diffusion de documents scientifiques de niveau recherche, publiés ou non, émanant des établissements d'enseignement et de recherche français ou étrangers, des laboratoires publics ou privés.



Université  
de Toulouse

# THÈSE

En vue de l'obtention du

## DOCTORAT DE L'UNIVERSITÉ DE TOULOUSE

**Délivré par :**

Institut National Polytechnique de Toulouse (Toulouse INP)

**Discipline ou spécialité :**

Génie des Procédés et de l'Environnement

---

**Présentée et soutenue par :**

Mme NICOLE VORHAUER

le mardi 18 septembre 2018

**Titre :**

Experiment based development of a non-isothermal pore network model  
with secondary capillary invasion

---

**Ecole doctorale :**

Mécanique, Energétique, Génie civil, Procédés (MEGeP)

**Unité de recherche :**

Institut de Mécanique des Fluides de Toulouse (I.M.F.T.)

**Directeur(s) de Thèse :**

M. MARC PRAT

M. EVANGELOS TSOTSAS

**Rapporteurs :**

M. ANDREAS BUCK, UNIVERSITE D'ERLANGEN-NUREMBERG

M. FABRICE GOLFIER, UNIVERSITÉ LORRAINE

**Membre(s) du jury :**

Mme FRANZISKA SCHEFFLER, UNIVERSITE OTTO VON GUERICKE MAGDEBURG, Président

M. EVANGELOS TSOTSAS, UNIVERSITE OTTO VON GUERICKE MAGDEBURG, Membre

M. MARC PRAT, CNRS TOULOUSE, Membre

Mme PETRA FORST, TECHNISCHE UNIVERSITAT MUNICH, Membre

# Declaration

I hereby declare that I prepared the work submitted without inadmissible assistance and without the use of any aids other than those indicated. Facts or ideas taken from other sources, either directly or indirectly have been marked as such.

In particular, I did not use the services of a commercial graduation consultation. Further I have not made payments to third parties either directly or indirectly for any work connected with the contents of the submitted dissertation.

The work has not been submitted as a dissertation either in Germany or abroad in the same or similar form and has also not been published as a whole.

Magdeburg, June 19, 2018

Nicole Vorhauer



# Acknowledgements

First of all, I would like to express my deepest gratitude for Dr.-Ing. habil. Thomas Metzger, Dr. Marc Prat and Prof. Dr.-Ing. habil. Evangelos Tsotsas, for their guidance, advice and inspiration. It was and still is a great privilege to work with you, which I appreciate more than you might imagine.

Dear Thomas, thank you for your trust in me, when you offered me to work in the pore network group in Magdeburg and thank you for the uncomplicated and very efficient teamwork. You helped me to get started with pore network modeling and also allowed me to change my direction more towards experimental investigations after we had realized the importance of the validation of the pore network models before continuing to work on parameterization of macroscopic models.

Dear Marc, thank you for giving me the chance to work with one of the greatest experts in pore network modeling. Thank you for taking your time for (sometimes very long) discussions and for sharing your insider knowledge with me. The research stays in Toulouse were always a boost for my work and of course a lot of fun. I hope that we can continue our collaboration in future.

Dear Prof. Tsotsas, thank you for your support, for your clear advices and for giving me the freedom to follow my own ideas. You forced me to try more than my best: 'You're still young, that's your fault. There's so much you have to know.' (to cite Cat Stevens). During the years under your supervision I learned many practical things, which will be useful for a lifetime. I wish that I could pay back some of the things.

I would like to thank everybody who helped me to build the experimental set-up: Manuel Marcoux for giving me an insight into the experimental work in Toulouse, Marc-Peter Schmidt for producing the very accurate microfluidic pore network, Diethard Kürschner for being readily available in the lab and helping me to build up experimental set-ups and the people from the workshop of our institute, namely Ernst-Albert Gehrke, Hans-Jürgen Ritzmann, Mike Rusche and Dirk Blanke for their ideas and very precise work.

I would like to thank all my colleagues who accompanied me through the years and became very good friends, especially Lothar Mörl, Nicolle Degen, Andreas Bück, Fabian Weigler, Antje Rossau/Stresing, Thi Thu Hang Tran, Muhammad Usman Farid and many more.

I would like to thank the students who did their research work under my supervision and who contributed in discussions and forced me to recapitulate my ideas and concepts with different perspectives: Quoc Tiep Tran, Nguyen Xuan Duong, Yasen Trayanov, Jeanine Benecke, Sebastian Graner, Adnan Shabbir Najmi, Pan Yue, Shuai Huang, Sheshadri Eswar Iyer, Unaiz Ahmed Khan, Faez Ahmad, Bilal Zulfiqar, Niloofar Mirsadraee, Christin Velten, Markus Vondran, Debraj Ghosh, Aiham Adi, Alaa Zwaid.

I would like to thank Benoît Fond for helping me with the translation of the abstract into French.

**Last but not least, I would like to thank my beloved family, Nico, Mathilda and Julius**, who forced me to find a very efficient work-life-balance and who gave me the freedom to study, travel and work late or on weekends. Thank you Opa, for putting pressure on me. You and Oma always gave me the feeling that nothing else matters but family and that every little thing that we can achieve apart from this must be done with love and passion. I also thank my very good friends for keeping in contact, although I did not very often take the time, Maria Schmidt, Daniela Adolf, Anika Schlünz, Wiebke Süthoff and Katrin Zscheppang.

# Prolegomenon

This PhD thesis was written in the frame of a cotutelle de thèse in cooperation of the Otto-von-Guericke University Magdeburg and the Institut National Polytechnique de Toulouse, starting in November 2010. The presented experimental and simulation results were obtained by studies at both institutes. Structure and contents of this PhD thesis are based on the standards of the two institutes.

The main objective of this work is the experiment based development of a pore network model for drying in presence of imposed thermal gradients. This problem did arise from the study and development of macroscopic drying models based on parameter extraction from pore network simulation. It was one of the main questions, if the pore network models applied for estimation of effective parameters used in macroscopic continuum models, can realistically reproduce the drying behavior of microfluidic pore networks. This central question initiated the development of a quasi 2-dimensional microfluidic pore network and experimental set-up with which the mathematical pore network model could be validated. The presentation and discussion of this work is one of the main parts of this thesis. It shows that drying of the microfluidic pore network, although seemingly simple in structure, is influenced by several pore scale processes which occur simultaneously, overlap or counteract each other. The capillary film effect is highlighted as one prominent example, where the governing pore scale effects are usually overseen with macroscopic continuum models. It is shown and discussed that the consideration of structural peculiarities can lead to a significantly better agreement of the overall comparison of simulations and experiments. In addition to that, the situation drastically changes if temperature gradients are imposed on the pore network. Exemplarily, vapor can diffuse through partially liquid saturated zones and lead to the re-saturation of the pore network. Consideration of this effect in the pore network model leads to the disclosure of the dependency of liquid phase distribution and drying performance on the interrelation of thermal gradient, pore size distribution and overall drying rate in presence of liquid films which are usually also anticipated in drying of porous media.

# Abstract

Drying of capillary porous media is a process of gradual receding of the liquid phase inside the porous medium and simultaneous invasion of the void space with gas. The phase patterns that evolve during the drying process depend on the capillary number, Bond number as well as the temperature profile along the porous medium. If the drying process is slow and capillarity controlled, invasion of the pore space by the gas phase can be assumed as quasi-steady. The evolving distributions of gas and liquid phase resemble invasion percolation patterns, with penetrating gas branches and numerous disconnected liquid clusters. Understandably, the discrete pore-level events that can lead to such ramified phase distributions cannot be captured by macroscopic continuum models that average the volume elements of the porous medium. Instead, due to the conformity of drying and invasion percolation patterns, pore network models (PNMs) are applied to model capillarity driven drying of porous media. PNMs are discrete mathematical models that originate from hydrology and the oil-recovery related research. In this, the void space of the porous medium is represented by a network of interconnected pores and pore throats. Liquid and gas phase mass transfer equations are expressed in each pore throat and the boundary conditions are given by the state of neighboring pores. Consequently, the number of mass balances to be solved is consistent with the number of pores inside the pore network (PN), usually restricting the computable size of PNs. Current studies cover a wide range of drying processes from drying of inorganic matrices to drying of biological materials, from drying regular 2-dimensional PNs to drying of irregular particle packings, from removal of non-viscous liquid to salt solutions and particle suspensions, i.a.; further application of PN modelling aims at the estimation of parameters to be used in continuous drying models. Common strength of all PNMs is the discrete character which allows study of temporally and spatially discretized pore-level phenomena, such as the simultaneous evaporation and condensation, local structure of liquid films or crystallization. This is useful for the investigation of the relation between pore level events and macroscopic drying behavior.



In this thesis, PN simulations of drying are compared with experimentally obtained data from drying of a representative 2D microfluidic network in SiO<sub>2</sub> under varying thermal conditions with the aim to identify governing physical pore scale effects. Gravity and viscous effects are disregarded in this thesis. Instead drying with slight local temperature variation and drying with imposed thermal gradients are studied. Based on this investigation, a powerful non-isothermal PNM is developed. This model incorporates i) the phenomena associated with the temperature dependency of pore scale invasion, namely thermally affected capillary invasion and vapor flow as well as ii) the secondary effects induced by wetting liquid films of different morphology.

This study clearly evidences that the macroscopic drying behavior is fundamentally dictated by the temperature gradient imposed on the PN and moreover by the secondary capillary invasion as well. In agreement with literature, invasion patterns as in invasion percolation with progressive evaporation of single clusters are observed in drying with negligible local temperature variation; gradients with temperature decreasing from the surface (negative temperature gradient) can stabilize the drying front, evolving between the invading gas phase and the receding liquid phase, whereas temperature increasing from the surface (positive temperature gradient) leads to destabilization of the liquid phase with early breakthrough of a gas branch and initiation of a second invasion front migrating in opposite direction to the evaporation front receding from the open surface of the PN. Special attention is paid on the distinct drying regimes found in the situation of a positive gradient because they are associated with different pore scale invasion processes. More precisely, temperature dependency of surface tension dictates the order of invasion as long as the liquid phase is connected in a main liquid cluster (usually found during the first period of drying). In contrast to this, detailed study of the vapor transfer mechanisms emphasizes that vapor diffusion through the partially saturated region can control the pore level distributions of liquid and gas phase during the period of drying when the liquid phase is disconnected into small clusters. This is also related to the cluster growth induced by partial condensation of vapor. It is shown and discussed in detail in this thesis that this effect not only depends on direction and height of the temperature gradient for a given pore size distribution but that moreover the overall evaporation rate influences the cluster growth mechanism. This indicates that liquid migration during drying of porous media might be controlled by the interplay of thermal gradients and drying rate.

In summary, the study of thermally affected drying of the 2-dimensional PN reveals complex pore scale mechanisms, usually also expected in drying of real porous media. This leads to the development of a strong mathematical pore scale model based on experimental findings. It is demonstrated how this model might be applied to understand and develop modern drying processes based on the simulation of thermally affected pore scale mass transfer.

# Kurzzusammenfassung

Die Trocknung von kapillarporösen Medien kann als Prozess des sukzessiven Zurückweichens der Flüssigphase und des gleichzeitigen Eindringens der Gasphase in den Porenhohlraum beschrieben werden. Die Phasenverteilungen, welche sich während dieses Prozesses ergeben, werden von der Kapillarzahl, der Bond-Zahl sowie der Temperaturverteilung innerhalb des porösen Mediums diktiert. Wenn der Trocknungsprozess langsam und kapillarkontrolliert stattfindet, kann das Eindringen der Gasphase in den Porenraum als quasistationär angenommen werden. Die entstehenden Phasenverteilungen sind mit der Perkolationstheorie beschreibbar. Sie sind charakterisiert durch vordringende Gaszweige und zahlreiche voneinander getrennt vorliegende Flüssigkeitscluster. Diese charakteristischen Flüssigkeitsmuster als auch die porenskaligen Effekte, welche zu diesen Mustern führen, sind nicht mit makroskopischen Kontinuumsmodellen vorhersagbar, da sie die Eigenschaften des porösen Mediums über Volumenelemente mitteln. Anstelle dessen werden auf Grund der Konformität der Flüssigkeitsmuster der Trocknung und der Perkolationstheorie Porenetzwerkmodelle (PNM) für die Modellierung kapillarkontrollierter Trocknung poröser Medien angewendet. PNM sind diskrete mathematische Modelle, die ihren Ursprung in der Hydrologie und der Forschung in Bezug auf die Erdölgewinnung haben. In diesen Modellen wird der Porenhohlraum durch ein Netzwerk von miteinander verbundenen Poren und Porenhälsen (engl. Throats) repräsentiert. Die Transportgleichungen für Flüssigkeit und Gasphase werden den Porenhälsen zugewiesen, während die Poren die Informationen zu den Randbedingungen des Stofftransportes enthalten. Daraus folgt, dass die Anzahl der zu lösenden Bilanzgleichungen direkt von der Anzahl der Poren abhängt. In aktuellen Studien werden PNM für die Untersuchung der Trocknung einer Vielzahl von unterschiedlichen Materialien, Flüssigkeiten und Trocknungsbedingungen angewendet; zum Beispiel für die Trocknung von anorganischen Matrizen, biologischen Materialien, regulären 2-dimensionalen Netzwerken, unregelmäßigen Partikelschüttungen, nicht-viskosen Flüssigkeiten sowie Salzlösungen, Suspensionen, usw. In weiteren Studien werden PNM für die Bestimmung effektiver Parameter, welche in Kontinuumsmodellen Anwendung finden sollen, verwendet. Die

gemeinsame Stärke der diesen Studien zugrundeliegenden PNM basiert auf dem diskreten Charakter der Modelle, denn dieser erlaubt die Untersuchung zeitlich und örtlich diskreter Ereignisse, wie beispielsweise die gleichzeitige Verdunstung und Kondensation, lokale Strukturen von Flüssigkeitsfilmen oder Kristallisation. Dies ist nützlich in Bezug auf die Untersuchung des Zusammenhangs zwischen diskreten porenskaligen Ereignissen und dem makroskopisch zu beobachtenden Trocknungsverhalten.

In der vorliegenden Arbeit wird die Trocknung eines repräsentativen 2-dimensionalen mikrofluidischen Porennetzwerks (PNs) in  $\text{SiO}_2$  unter verschiedenen aufgeprägten thermischen Bedingungen mit dem Ziel untersucht, die treibenden Effekte der Trocknung zu ermitteln und darauf basierend ein leistungsfähiges PNM zu entwickeln. Für die Simulation werden die experimentell bestimmten Temperaturprofile berücksichtigt, jedoch Gravitations- und Reibungseffekte vernachlässigt. Das neue PNM berücksichtigt i) die thermisch beeinflussten Mechanismen während der Entleerung des PNs als auch ii) den Einfluss benetzender Flüssigkeitsfilme mit unterschiedlichen Strukturen.

Diese Arbeit zeigt deutlich den Einfluss aufgeprägter Temperaturgradienten sowie sekundärer Mechanismen auf das makroskopisch beobachtbare Trocknungsverhalten: bei vernachlässigbaren örtlichen Temperaturänderungen entsprechen die Phasenverteilungen den in der Literatur als ‚Invasion Percolation Patterns mit progressiver Verdunstung von Einzelclustern‘ beschriebenen Verteilungen; aufgeprägte Temperaturgradienten hingegen verändern die Flüssigkeitsmuster grundlegend. Die Trocknungsfront, welche sich zwischen der eindringenden Gasphase und der zurückweichenden Flüssigkeit herausbildet, wird stabilisiert, wenn die Temperatur von der Oberfläche ausgehend abnimmt (negativer Temperaturgradient). Der entgegengesetzte Temperaturgradient (positiver Temperaturgradient) löst jedoch die Destabilisierung der Trocknungsfront aus. Diese ist gekennzeichnet durch den frühen Durchbruch eines Gaszweigs und der Initiierung einer zweiten Trocknungsfront, welche der ursprünglichen Front entgegenläuft. Diese beiden Phasen der Trocknung (mit positivem Gradienten) können unterschiedlichen porenskaligen Effekten zugeschrieben werden: während der ersten Trocknungsperiode bestimmt die Temperaturabhängigkeit der Oberflächenspannung die Reihenfolge der Entleerung solange die Flüssigphase in einem Hauptcluster verbunden ist, während der späteren Trocknungsperiode bestimmt jedoch die Dampfdiffusion durch das entstehende 2-Phasengebiet die Verteilung der Flüssigkeit auf der Porenebene. Letzteres kann zu Kondensation und einem Clusterwachstum führen. Es wird in der vorliegenden Arbeit gezeigt und diskutiert, dass dieser Effekt bei gegebener Porenradialverteilung nicht allein von der Richtung und der Höhe des Temperaturgradienten abhängt, sondern dass das Clusterwachstum auch von der Trocknungsgeschwindigkeit beeinflusst wird. Hieraus kann geschlossen werden, dass die Flüssigkeitsverteilung während der Trocknung durch Kombination von geeigneten Temperaturgradienten und Trocknungsgeschwindigkeiten kontrolliert werden kann.

Zusammenfassend, zeigt diese Studie der thermisch beeinflussten Trocknung eines 2-dimensionalen PNs komplexe porenskalige Mechanismen auf, welche auch unter realen Trocknungsbedingungen von realen porösen Medien erwartet werden können. In der Konsequenz wird, basierend auf den experimentellen Ergebnissen, ein leistungsfähiges mathematisches Porenskalenmodell für die Simulation von thermisch beeinflusstem Stofftransport entwickelt und es wird gezeigt, wie dieses Modell angewendet werden kann um moderne Trocknungsprozesse zu verstehen und weiterzuentwickeln.

# Résumé de la thèse

Le séchage de milieux poreux capillaires est un processus de recul progressif de la phase liquide dans le milieu poreux et l'invasion simultanée de l'espace vide par le gaz. Les schémas de phases qui évoluent pendant le processus de séchage dépendent du nombre capillaire, du nombre de Bond, ainsi que du profil de température le long du milieu poreux. Si le processus est long, et contrôlé par la capillarité, l'invasion de l'espace à l'intérieur des pores par la phase gazeuse, peut être considéré comme quasi-stationnaire. L'évolution des distributions de la phase gazeuse et de la phase solide ressemble aux schémas que l'on trouve dans l'invasion percolatrice avec des branches de phase gazeuse qui pénètrent dans le milieu, et de nombreuses poches de liquides déconnectées les unes des autres. Il est évident que les événements discrets au niveau des pores qui aboutissent à de telles distributions de phase ramifiées ne peuvent pas être capturés par des modèles macroscopiques de continuum qui font la moyenne des éléments volumiques du milieu poreux. À la place, du fait de la similitude entre les schémas de séchage et de ceux de l'invasion percolatrice, des modèles de réseaux de pores (Pore network models ou PNMs en anglais) sont utilisés pour modéliser le séchage par capillarité des milieux poreux. Les PNMs sont des modèles mathématiques discrets qui proviennent de l'hydrologie, et de la recherche liée à la récupération de pétrole. Dans ces modèles, l'espace vide dans le milieu poreux est représenté par un réseau de pores interconnectés et de tuyères. Les équations de transfert de masse de la phase liquide et de la phase gazeuse sont exprimées dans chaque tuyère et les conditions limites sont données par l'état des pores avoisinantes. En conséquence, le nombre de bilans de masse à résoudre est lié au nombre de pores dans le réseau de pores (PN pour pore network). Les études récentes couvrent une large gamme de procédés de séchage allant des matières inorganiques aux matières biologiques, des réseaux réguliers en deux dimensions, aux séchages d'assemblages de particules irrégulières, de l'élimination de liquide non-visqueux à des sels en solution et des particules en suspensions, i.a. ; l'autre application de la modélisation PN est dans l'estimation de paramètres à utiliser dans les modèles de séchage continu. Le point fort que tous les modèles PNMs partagent est leur caractère discret qui permet d'étudier des phénomènes temporellement ou

spatialement discrets au niveau des pores, tels que l'évaporation et condensation simultanées, les films liquides, ou la cristallisation. Cela est utile dans l'étude de la relation entre événements à l'échelle des pores, et le comportement de séchage à l'échelle macroscopique.

Dans cette thèse, des simulations PN de séchage sont comparées à des données expérimentales obtenues dans le séchage d'un réseau de micro-fluidique 2D représentatif dans du SiO<sub>2</sub> soumis à des conditions thermiques variables dans le but d'identifier les phénomènes physiques à l'échelle des pores qui sont les plus influents. A partir de cette étude, un PN efficace non-isotherme est développé. Ce modèle incorpore i) les phénomènes associés à la dépendance en température de l'invasion à l'échelle des pores, c'est à dire l'invasion capillaire sous effet thermique et le flux de vapeur ainsi que ii) le transport secondaire induit par d'épais films liquides observé dans les expériences de microfluidique.

Cette étude prouve clairement que le comportement macroscopique du séchage est fondamentalement dirigé par le gradient de température imposé sur le PN ainsi que par le transport capillaire secondaire. En accord avec la littérature, les schémas d'invasion que l'on trouve dans l'invasion percolatrice avec l'évaporation progressive d'amas individuels sont observés dans le séchage à variation de température locale négligeable; des gradients où la température diminue à partir de la surface (gradient de température négatif) peut stabiliser le front de séchage, qui évolue entre la phase gazeuse invasive et la phase liquide qui recule, alors qu'une température qui augmente à partir de la surface (gradient de température positif) amène à la déstabilisation de la phase liquide avec une percée prématurée de la branche gazeuse et l'initiation d'un deuxième front de séchage qui migre dans la direction opposé de celle du front de séchage original. Une attention particulière est prêtée aux régimes distincts que l'on trouve dans le second cas (gradient positif) parce qu'ils sont associés à différents procédés d'invasion à l'échelle des pores. Plus précisément, la dépendance en température de la tension de surface établit l'ordre d'invasion tant que la phase liquide est connectée au groupe liquide principal (que l'on trouve généralement pendant la première période de séchage). En revanche, l'étude détaillée des mécanismes de transfert de la vapeur met l'accent sur le fait que la diffusion de la vapeur à travers la région partiellement saturée peut contrôler les distributions des phases gazeuses et liquides à l'échelle des pores pendant la période de séchage lorsque la phase liquide est déconnectée en petits groupes. Cela est aussi lié à la croissance des amas induite par la condensation partielle de la vapeur. Cette thèse montre et discute en détail que cet effet ne dépend pas seulement de la direction et magnitude du gradient de température pour une distribution de tailles de pores donnée mais qu'en plus le taux d'évaporation influence le mécanisme de croissances des amas.

Cela indique que la migration du liquide pendant la phase de séchage de milieux poreux peut être contrôlé par l'interaction des gradients thermiques et du taux de séchage. En somme, l'étude du séchage sous effet thermique des réseaux de pores 2D révèle des phénomènes complexes à l'échelle des pores, généralement aussi anticipés dans le séchage des milieux poreux réels. Cela mène au développement d'un modèle mathématique efficace au niveau des pores basés sur des découvertes expérimentales. Cette thèse démontre la manière dont ce modèle peut être appliqué afin de comprendre et développer des procédés de séchage modernes basés sur la simulation du transfert de masse sous effet thermique à l'échelle des pores.

# Contents

<b>Acknowledgements</b>	i
<b>Prolegomenon</b>	iii
<b>Abstract</b>	iv
<b>Kurzzusammenfassung</b>	vi
<b>Résumé de la these</b>	viii
<b>Contents</b>	x
<b>Notation</b>	xiv
<b>1 Introduction</b>	1
1.1 Motivation and scope of the thesis	1
1.2 Previous works	7
1.2.1 Pore network models of isothermal drying	8
1.2.2 Pore network models of non-isothermal drying	10
1.2.3 Experimental evaluation of pore network models	15
1.3 Outline of the thesis	20
<b>2 Fundamentals</b>	21
2.1 Introduction	21
2.2 Percolation	22
2.2.1 Pore networks	22
2.2.2 Drainage and imbibition	23
2.2.3 Drying	25
2.3 Drying of porous media	27
2.3.1 Phase equilibrium	27
2.3.2 Vapor diffusion	29
2.3.3 Boundary layer	31

2.3.4 Capillary invasion	32
2.3.4.1 Emptying as a consequence of evaporation	33
2.3.4.2 Refilling as a consequence of condensation	36
2.3.5 Liquid transport	38
2.3.6 Wetting liquid films	40
2.4 Temperature dependency of vapor diffusion and capillary invasion	42
2.4.1 Gas side	42
2.4.1.1 Saturation vapor pressure	42
2.4.1.2 Diffusion coefficient	43
2.4.2 Liquid side	44
2.4.2.1 Surface tension	44
2.4.2.2 Dynamic liquid viscosity and liquid density	45
2.5 Micro-Macro coupling of non-isothermal drying	46
2.5.1 Drying front structure	46
2.5.2 Drying curve and drying rate curve	47
2.5.3 Impact of liquid films	48
2.5.4 Impact of thermal gradients	49
2.5.5 Drying periods	51
<b>3 Experimental Principles</b>	<b>53</b>
3.1 Introduction	53
3.2 The microfluidic device	55
3.2.1 Production process	56
3.2.2 Limitations of the production process	58
3.2.3 Physical parameters of the microfluidic device	60
3.3 Experimental design and procedure	63
3.3.1 Experimental set-up	63
3.3.2 Temperature gradients	66
3.3.3 Experimental procedure	67
3.4 Image processing of optical data	69
3.4.1 Computation of phase distributions	69
3.4.2 Remarks on the accuracy of image analysis	73
3.4.3 Computation of drying curves and drying rate curves	76
3.4.4 Estimation of characteristic parameters of the travelling 2-phase zone	78
3.5 Summary	80
<b>4 Drying experiments with the microfluidic pore network</b>	<b>82</b>
4.1 Introduction	82
4.2 Pore scale analysis of pore network invasion	84
4.2.1 Primary invasion	84
4.2.2 Secondary invasion	86
4.2.2.1 Liquid film rings	87
4.2.2.2 Edge effect	89
4.3 Drying with spatially quasi-constant temperature	90
4.3.1 Phase distributions	90
4.3.2 Drying curve and drying rate curve	93
4.3.3 Capillary number	95
4.4 Drying in presence of imposed thermal gradients	96
4.4.1 Drying with stabilizing thermal gradient	97

4.4.1.1 Phase distributions	98
4.4.1.2 Drying curve and drying rate curve	101
4.4.2 Drying with destabilizing thermal gradient	103
4.4.2.1 Phase distributions	104
4.4.2.2 Variance of the travelling 2-phase zone	110
4.4.2.3 Drying curve and drying rate	112
4.5 Summary and discussion	113
<b>5 Experiment based development of the pore network model</b>	<b>115</b>
5.1 Introduction	115
5.1.1 Non-isothermal pore network model with secondary capillary invasion	116
5.1.2 Non-isothermal pore network model with cluster growth mechanism	118
5.2 Pore network structure	119
5.2.1 Primary pore network structure	121
5.2.2 Secondary pore network structure	122
5.2.2.1 Capillary liquid rings	122
5.2.2.2 Edge effect	124
5.2.3 Structure of the computational boundary layer	125
5.2.4 Neighbor relations	126
5.3 Gas side moisture transfer	126
5.3.1 Vapor pressure field	127
5.3.2 Evaporation and condensation rates of pores and throats	133
5.3.3 Evaporation and condensation rates of liquid clusters	137
5.3.4 Overall evaporation rate from the pore network surface	137
5.4 Quasi-steady invasion of the pore network	138
5.4.1 Invasion by the gas phase (evaporation)	138
5.4.2 Invasion by the liquid phase (condensation)	141
5.4.3 Cluster dynamics	141
5.4.3.1 Progressive invasion of evaporating liquid clusters	142
5.4.3.2 Cluster growth and cooperative invasion	143
5.4.4 Cluster labeling	145
5.4.4.1 Cluster labeling based on pore liquid saturation	145
5.4.4.2 Cluster labeling based on liquid rings	145
5.4.4.3 Cluster labeling in presence of cluster growth	146
5.5 Pore network drying algorithm incorporating capillary liquid rings	148
5.6 Pore network drying algorithm incorporating cluster growth	150
Summary	152
<b>6 Experiment based evaluation of the pore network model</b>	<b>155</b>
6.1 Introduction	155
6.2 Quasi-isothermal drying	156
6.2.1 Estimation of the boundary layer thickness	158
6.2.2 Impact of liquid viscosity	161
6.2.3 Impact of competitive pore and throat invasion	164
6.2.4 Impact of local temperature variation	165
6.2.5 Impact of secondary capillary invasion	168
6.2.5.1 Lateral pinning of liquid	169
6.2.5.2 Simulation with the continuous liquid film pore network model	170
6.2.5.3 Simulation with the capillary ring pore network model	175



6.2.6 Quasi-isothermal pore network simulation with secondary capillary invasion	177
6.2.6.1 Phase distributions	178
6.2.6.2 Drying curves and drying rate curves	181
6.2.6.3 Structural analysis of pore scale liquid distribution	182
6.2.7 Summary	183
6.3 Drying with imposed thermal gradients	184
6.3.1 Pore network drying with stabilizing thermal gradient	184
6.3.1.1 Phase distributions	187
6.3.1.2 Drying curves and drying rate curves	188
6.3.1.3 Structural analysis of pore scale liquid distribution	192
6.3.1.4 Summary	193
6.3.2 The heat pipe effect	195
6.3.3 Pore network drying with destabilizing thermal gradient	198
6.3.3.1 Phase distributions	199
6.3.3.2 Drying curves and drying rate curves	201
6.3.3.3 Structural analysis of pore scale liquid distribution	202
6.3.3.4 Analysis of the impact of cluster labeling	203
6.3.3.5 Summary	210
6.4 Phase diagram of thermally affected drying	211
6.5 Comparison of pore network drying with different heating modes	212
6.6 Summary and discussion	214
<b>7 Summary and Outlook</b>	<b>217</b>
7.1 Summary	217
7.2 Outlook	220
<b>References</b>	<b>222</b>
<b>Appendix</b>	<b>232</b>
A Experimental Data	232
A.1 Equipment	232
A.2 Experiments with quasi-constant temperature in time and space	233
A.3 Experiments with a negative temperature gradient	240
A.4 Experiments with a positive temperature gradient	247
B Pore network simulations	255
B.1 Study of the vapor transport equation and diffusion coefficient	255
B.2 Study of the effect of capillary pore invasion during drying	257
B.3 Study of the condensation effect in a pore network with positive thermal gradient	262
B.4 Details of the continuous film pore network model with remarks on the implementation C	280
Summary of simulations	288
<b>Student theses</b>	<b>297</b>
<b>List of publications</b>	<b>298</b>
<b>Curriculum Vitae</b>	<b>300</b>

# Notation

$a$	accuracy	mm
$A$	cross sectional area	$m^2$
$\mathbf{A}$	conductance matrix	-
$b$	vector of boundary conditions	-
$c_{0,1}$	binarization threshold	-
$c_h$	scaling parameter for height	-
$c_p$	heat capacity	$J\ kg^{-1}\ K^{-1}$
$c_{w,h}$	scaling parameter for width and height	-
$Ca$	capillary number	-
$D$	diffusion coefficient	$m^2\ s^{-1}$
$e_{cl}$	cluster size	-
$f^{red}$	size reduction factor (edge effect)	-
$g_v$	vapor conductance	$m\ s$
$g^\infty$	vapor conductance in bulk air	$m\ s$
$h$	height	$m$
$h$	specific enthalpy	$J\ kg^{-1}$
$I_{1,2,3}$	image matrices 1,2,3	-
$k$	correction factor (continuous film model)	-
$K$	permeability	$m^2$
$k_{rel}$	relative permeability	-
$lb$	coordinate of left boundary of PN (image processing)	-
$l$	label	-
$L$	length, lattice spacing	$m$
$L_{air}$	flow length of air	$m$
$L_{Ca}$	capillary length	$m$
$L_d$	network depth	$m$
$L_g$	gravitational length	$m$
$L_r$	ring width	$m$

$m$	number of PN rows	-
$\tilde{M}$	molar mass	kg kmol <sup>-1</sup>
$\dot{M}$	mass flow rate	kg s <sup>-1</sup>
$\vec{M}$	vapor diffusion rate	kg s <sup>-1</sup>
$n$	number of PN columns	-
$n$	window size (in image processing)	-
$N$	number	-
$N^{S=0}$	number of empty pore neighbors	-
$\dot{N}$	molar flow rate	mol s <sup>-1</sup>
$\vec{N}$	molar vapor diffusion rate	mol s <sup>-1</sup>
$pnp$	matrix of pore neighbor relations	-
$pnr$	matrix of pore and ring neighbor relations	-
$pnt$	matrix of pore and throat neighbor relations	-
$P$	total pressure	Pa
$P_v$	vapor pressure	Pa
$\dot{Q}$	heat flow rate	J s <sup>-1</sup>
$r$	radius	m
$rnp$	matrix of ring and pore neighbor relations	-
$rnr$	matrix of ring neighbor relations	-
$rnt$	matrix of ring and throat neighbor relations	-
$r_0$	radius of throat corner (film model)	m
$r_1$	radius of curvature 1 of a capillary	m
$r_2$	radius of curvature 2 of a capillary	m
$Re$	Reynolds number	-
$\tilde{R}$	universal gas constant	J mol <sup>-1</sup> K <sup>-1</sup>
$s_{BL}$	boundary layer thickness	m
$S$	saturation	-
$t$	time	s
$tnp$	matrix of throat and pore neighbor relations	-
$tnr$	matrix of throat and ring neighbor relations	-
$tnt$	matrix of throat neighbor relations	-
$t_{comp}$	computational time	s
$T$	temperature	°C, K
$T_{glas}$	glas transition temperature	°C
$T_M$	temperature of fusion	°C
$ub$	coordinate of upper boundary of PN (image processing)	-
$v$	velocity	m s <sup>-1</sup>
$v_c^+$	ratio of condensed liquid volume	-
$v_c^-$	neglected ratio of condensed liquid volume	-
$v_e$	Abbe number	-
$V$	volume	m <sup>3</sup>
$\dot{V}$	volume flow rate	m <sup>3</sup> s <sup>-1</sup>
$\tilde{V}_l$	liquid molar volume	m <sup>3</sup> mol <sup>-1</sup>
$w$	width	m
$Y$	mass loading of air	-
$z$	position, coordinate	m

$z^{pin}$	coordinate of liquid pinning	m
-----------	------------------------------	---

### Greek symbols

$\alpha$	ratio of ring evaporation interface (ring model)	-
$\alpha$	half angle of corner (film model)	°
$\alpha_1$	coefficient of thermal expansion	K <sup>-1</sup>
$\beta$	mass transfer coefficient	m s <sup>-1</sup>
$\eta$	dynamic liquid viscosity	Pa s
$\theta$	contact angle	°
$t_{1,2}$	frame index (image processing)	-
$\lambda$	thermal conductivity	W m <sup>-1</sup> K <sup>-1</sup>
$\mu$	chemical potential	J mol <sup>-1</sup>
$\nu$	kinematic liquid viscosity	m <sup>2</sup> s <sup>-1</sup>
$o$	pre-factor defining vapor flow direction	-
$\rho$	density	kg m <sup>-3</sup>
$\sigma$	surface tension	N m <sup>-1</sup>
$\varphi$	relative humidity	-

### Subscripts

0	initial
1-4	indices
2pz	2-phase zone
air	air phase
back	denotes the water flow through heat conducting plate
bottom	bottom side of PN (in images)
BL	boundary layer
c	capillary
cl	cluster
cond	condensation
crit	threshold value in image segmentation
crit1,2	threshold values in image segmentation
dew	dew point
eff	effective
edge	denotes the PN side walls
evap	evaporation
film	liquid film
front	drying front
g	gas
high	high (temperature side)
hor	horizontal throats
H <sub>2</sub> O	water
i,j,k,l	pore indices
ij,ik,kl	throat indices
in	inlet

<i>l</i>	liquid
<i>low</i>	low (temperature side)
<i>L</i>	liquid water from thermal baths
<i>LAP</i>	least advanced point
<i>m</i>	meniscus
<i>mask</i>	photomask
<i>MAP</i>	most advanced point
<i>p</i>	pore
<i>pix</i>	pixel
<i>PN</i>	pore network
<i>r</i>	ring
<i>slice</i>	denotes a PN slice
<i>si</i>	single (pore, throat)
<i>steps</i>	invasion steps
<i>Si</i>	silicon
<i>SiO<sub>2</sub></i>	silicon dioxide
<i>t</i>	throat
<i>top</i>	top side of PN (in images)
<i>tot</i>	total
<i>v</i>	vapor
<i>ver</i>	vertical throats
<i>void</i>	void space

### Superscripts

0	reference value
*	saturation, threshold
-	average
∞	bulk phase
<i>est</i>	experimentally estimated
<i>exp</i>	experiment
<i>i</i>	index of time step
<i>max</i>	maximum value
<i>min</i>	minimum value
<i>std</i>	standard deviation
<i>t</i>	time index

### Abbreviations

BL	boundary layer
CCD	charge-coupled device (camera)
CLO	cluster labeling option
CLSM	confocal laser scanning microscopy
CMA	central moving average
CRP	constant rate period
EGP	etched glass plate
ER	empty ring
FRP	falling rate period

GDL	gas diffusion layer
HSC	Hele-Shaw cell
IR	infrared
LAP	least advanced point
LED	light-emitting diode
MAP	most advanced point
max	maximum
PDMS	Polydimethylsiloxane
PN	pore network
PNM	pore network model
PMMA	Poly methyl methacrylate
PSD	pore size distribution
RFP	receding front period
RGB	red-green-blue (image)
RLO	ring labeling option
SiO <sub>2</sub>	silicon dioxide
SE	southeast
SM	single meniscus
SR	single ring
SW	southwest
TPR	transparent polyester resin

„Allgemein in der menschlichen Natur liegt der Trieb nach Erkenntnis.“

Aristoteles 'Metaphysik'

\* 384 B.C. in Stageira

† 322 B.C. in Chalkis

## Chapter 1

# Introduction

### 1.1 Motivation and scope of the thesis

At least since the beginning of agriculture more than 13 thousand years ago, drying is intensively used to preserve food and natural products. With the onset of industrialization at the beginning of the 18<sup>th</sup> century more and more technical applications emerged that involved drying of capillary porous media, ranging from porous materials with a more or less rigid solid matrix (e.g. paper, catalysts) to particulate materials or powders (e.g. coal, bricks, ceramic, granules, food pellets) (Plumb 2000). However, compared to the long history of drying of porous media, the history of understanding the underlying physical effects that are incorporated in the drying process is relatively young and may have started with Leonardo DaVinci<sup>1</sup>, famous painter, sculptor and also a diligent engineer and natural philosopher who found already around 1500 that liquid rises into a wettable capillary dipped into a liquid source without any exterior driving force (Westphal 1970). More than 100 years later, French, English and Italian scientists could demonstrate that the height of liquid rise is inversely proportional to the radius of the capillary (de Gennes 2004) from which it is concluded that a very high tree must essentially contain very small capillaries at the treetop in order to supply it with water (Fig. 1-1). In a system of interconnected capillaries, such as a porous medium, liquid usually fills the pores in the order of increasing pore radius and when the process is reversed and the overall saturation of the porous medium is again reduced, as in drying, it is the smallest pore that maintains full saturation until the end of the drying process. The physical cause of this phenomenon was found by Thomas Young<sup>2</sup> and Pierre-Simon Laplace<sup>3</sup> in 1805 who ascribed, independently of each other, the liquid rise in a capillary to surface tension of the liquid (Smiles 1914) and proposed a relation between capillary radius, surface tension, contact angle and the pressure inside the capillary. At that time, both, Young and Laplace were neglecting the effects counteracting capillary pumping,

---

<sup>1</sup> Leonardo DaVinci (1452-1519)

<sup>2</sup> Thomas Young (1773-1829)

<sup>3</sup> Pierre Simon Laplace (1749-1827)

namely gravity forces acting on the liquid column and friction forces inside the liquid phase. Unfortunately, both scientists died before the German engineer Hagen<sup>4</sup> (1839) and the French physicist Poiseuille<sup>5</sup> (1840) could present a theory that considers friction in laminar fluid flow through a cylindrical capillary (Bird, Stewart and Lightfoot 1960), finding that flow rate is inversely proportional to viscosity. Again more than 100 years later Richard Lucas (1918) and Edward W. Washburn<sup>6</sup> (1921) combined the equations of Young-Laplace and Hagen-Poiseuille to describe the dependency of capillary rise on viscosity.



**Figure 1-1** Schematic illustration of capillary transport on the example of tree capillaries: large trees need very small capillaries to supply the treetop with liquid.

Based on these achievements, scientists started to intensively study and model the transport phenomena in porous media mainly in the second half of the 20<sup>th</sup> century (parallel to the development of computational techniques). Examples are found in a wide range of technical applications. These are, besides the drying of porous media studied in this thesis, also e.g. oil recovery, chromatography, membrane technologies (e.g. in fuel cells or electrolyzers, Vidakovic-Koch 2016), thin film technologies (e.g. in production of batteries, Baesch et al. 2017) or energy storage, to name only a few. Medical applications are e.g. biomedical porous coatings used as a bone-implant interface (Prat and Agaesse 2015). Beyond this, especially space applications profit from capillary action as it can overcome the problem of absent gravity (e.g. in heat pipes and fuel cells). A general overview of transport in porous media can be obtained from e.g. Krischer and Rohnhalter (1940), Phillip and De Vries (1957), Luikov (1966), Suzuki and Maeda (1967), Whitaker (1977), de Boer (1988), Bories (1991), Plumb (2000), Kowalski 2007 (literature related to drying of porous media) or in van Brakel (1975), Celia et al. (1995), Berkowitz and Ewing (1998), Dullien (2012) (literature related to transport through porous media in general). This shows, although the underlying physical phenomena have already been known since the early 19<sup>th</sup> century, advancing measuring techniques (such as cameras, tomographs or spectrometers) as well as computational power and capacities allowed for an extensive experimental and numerical study of transport in porous media within the past 40 years. Seemingly most of the published books and scientific articles from this period refer to geophysics applications (e.g. Wilkinson (1986), Lenormand (1989), Selyakov and Kadet (1996), Berkowitz and Ewing (1998) and references therein); also the publication of Tsimpanogiannis et al. (1999) about scaling theory of drying porous media is essentially inspired by oil recovery related problems. This is quite comprehensible since the soil forms the largest porous medium of

---

<sup>4</sup> Gotthilf Heinrich Ludwig Hagen (1797-1884)

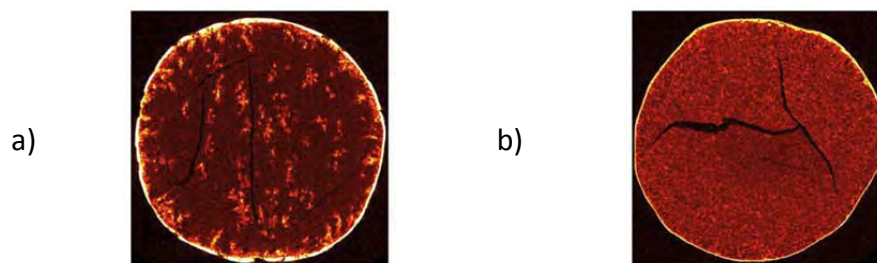
<sup>5</sup> Jean Léonard Marie Poiseuille (1797-1869)

<sup>6</sup> Edward Wight Washburn (1881-1934)



the world and moreover the exploration of oil from sedimentary rock was worldwide one of the economically and ecologically most important processes in the 20<sup>th</sup> century. Independent of this, drying is at least equally important because almost every solid product must be dried before its final application (including thin films, solid fuels, catalysts, membranes, paper and processed food) and moreover the process of drying is always accompanied by considerable energy expenses and costs (refer e.g. to Plumb (2000) and references therein).

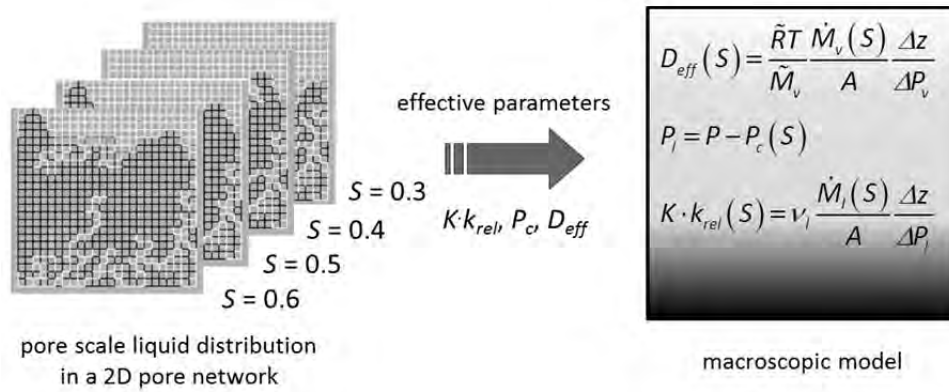
Traditionally, drying focused on agricultural (herbes, crop, hay) and construction materials (clay, brick, reed). But from a contemporary point of view drying increasingly plays an important role in product formulation. This means, that not just the removal of liquid (path independent drying result) is of interest but that moreover the pore level processes or more clearly the evolution of the drying front inside the porous medium is a key parameter for product formulation (path dependent drying result). Exemplarily, Boernhorst et al. (2016) show that the drying velocity can control the impregnation of a porous medium with salt (Fig. 1-2); this finding is based on the different structures of the drying front evolving during drying as will be explained below. The use of drying as a process step in product formulation finally leads more and more to the application of alternative drying processes which complete or replace the rather traditional drying methods, which are namely convective drying, contact drying and infrared drying (sun light). Examples are freeze drying, microwave drying (i.e. electromagnetic drying) or supercritical drying (Plumb 2000). Other examples are combined processes such as e.g. combined convective and contact drying in the production of thin films (e.g. for batteries, Baesch et al. 2017) or inductive energy supply in fluidized beds (Idakiev et al. 2017).



**Figure 1-2** Drying as a process step in product formulation. The example from Boernhorst et al. (2016) shows that the distribution of salt can be controlled by the drying rate. Slow drying leads to a heterogeneous distribution of salt inside the porous medium (a), while fast drying leads to a rather homogeneous distribution of salt (b). (In these figures salt is represented by the light red areas, the white patches and the white surface layer. Regions without salt appear in dark red).

However, choice of an appropriate drying process is still usually based on experience and macroscopic observations of drying curves, shrinking behavior, flow behavior or sensory properties (in food process engineering). Additionally to that, the majority of drying models, applied to study and predict drying processes, are macroscopic continuum models (e.g. Krischer and Kast (1992), Luikov (1966), Whitaker (1977), Scherer (1990), Perré and Turner (1999), Plumb (2000), Schluender (2004), Tsotsas et al. (2012), Mujumdar (2015)). The essential underlying pore scale effects and processes, however, are rarely taken into account to choose the drying method, because they are relatively difficult (or costly) to obtain. This appears quite surprising because e.g. according to Tsimpanogiannis et al. (1999)

the ,phenomenological approaches [...] consider the medium as a structureless continuum' ignoring ,the pore microstructure and the underlying phenomena, which are key to the quantitative understanding of the process'. As a consequence structure of the drying front is usually blurred when continuous models are applied (Fig. 1-3). Macroscopic models are thus commonly used to determine drying behavior (e.g. the overall energy consumption, overall drying time, saturation curve and drying rate) *on the sample scale* or process scale.

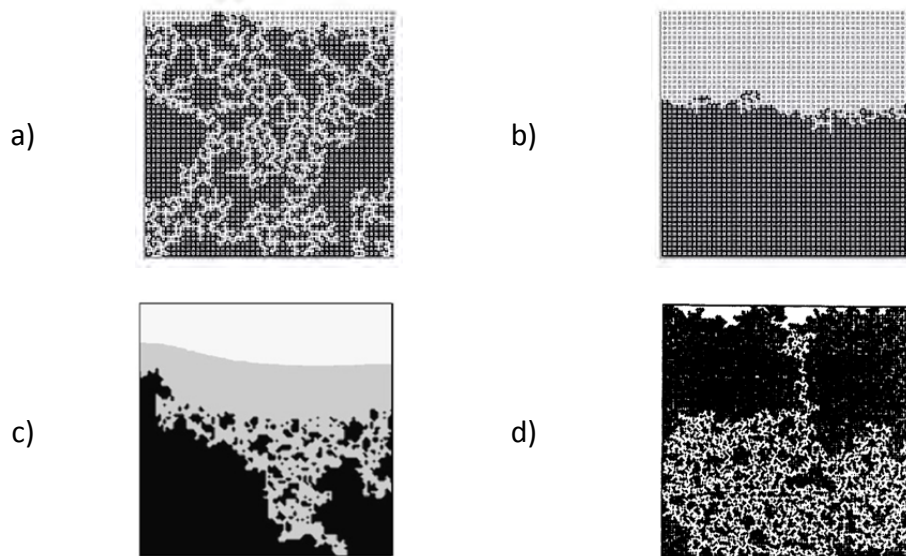


**Figure 1-3** Illustration of macroscopic volume-averaged continuous models of drying (related to the use of effective parameters) (right) and comparison to the pore scale liquid distribution during drying (from pore network simulation) (left). The liquid is shown in black and dry regions are shown in white; the solid appears in gray (in the image on the left). The evaporation front is located along the gas-liquid interface in the pore network. Contrary, the drying front is marked by the transient gray region in the continuous representation of the pore network.

A number of mathematical tools have been developed to investigate and describe the impact of pore scale effects on drying. Besides the pore network models (PNMs) studied in this thesis, molecular dynamics simulation (e.g. Defraeye et al. 2016), discrete element models (e.g. Peron et al. 2009), Lattice-Boltzman models (Sukop et al. 2004, Yiotis et al. 2007) and bundle of tubes models (e.g. Metzger 2005a, Irawan 2006) shall be mentioned here to name some prominent examples.

Pore network models (PNMs) are discrete pore scale models used to compute mass and energy transfer between the individual elementary components of a porous medium in order to understand and describe the transfer phenomena *on the microscale*. In this sense, PNMs can complement continuous macroscopic models (see also Geoffroy and Prat (2014) for a comparison of continuum models and PNMs). Additionally, pore network (PN) computations, although limited by pore number as well as the number of physical effects to be taken into account, represent a mathematical tool with the potential to parameterize macroscopic continuous models, either by Monte Carlo simulation (Nowicki et al. 1992, Prat 2002, Vu 2006) or by application of percolation theory (for the latter see e.g. Tsimpanogiannis et al. (1999), Selyakov and Kadet (1996) or Berkowitz and Ewing (1998) and references therein). Reviews on PNMs can be found in Celia et al. (1995), Sahimi (1995), Dullien (2012) and Berkowitz and Ewing (1998). In the field of drying, PNMs received particular attention since the early nineties of the past century as they could readily be adapted from soil physics (Shaw 1987, Daian and Saliba 1991, Nowicki et al. 1992, Prat 1993). Since then, PNMs could give a great insight and consolidate the understanding of

mass transfer processes in porous media. Exemplarily, PNMs could illuminate the dependence of drying front structure on capillary number (Shaw 1987, Metzger et al. 2007a, Metzger and Tsotsas 2008) and Bond number (Prat 1993, Laurindo and Prat 1996, Yiotis et al. 2012a, Yiotis et al. 2012b) as well as on thermal gradients (Hunink et al. 2002, Plourde and Prat 2003, Surasani 2009), the impact of wetting phenomena (Yiotis et al. 2004, Prat 2011), the transport of particles and efflorescence (Veran-Tissoires and Prat 2014), etc. It could be shown that the width of the drying front can be reduced by increase of viscous effects, i.e. increased drag forces, reduced variance of the pore size distribution or increased drying rates (Metzger et al. 2007c) (Fig. 1-4a,b). The relevance of this effect, which is also known as the drying front stabilization, is shown in the example of Fig. 1-2.

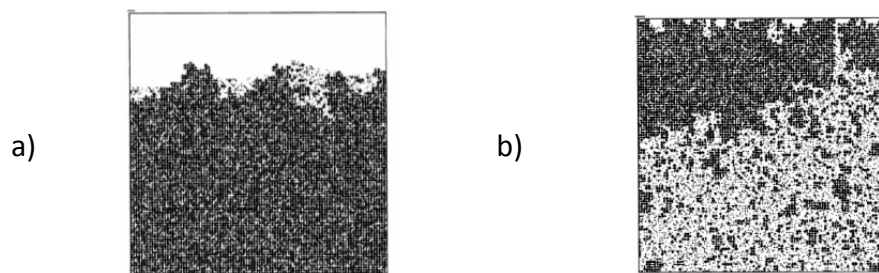


**Figure 1-4** Distinct drying phenomena that can be related to the underlying pore scale effects: a) Capillarity controlled drying process with front widening and capillary fingering (from Metzger et al. 2007b), b) viscous stabilization of the drying front (from Metzger et al. 2007b), c) drying in presence of wetting liquid films (from Prat 2007), d) gravitational destabilization of the liquid phase (from Laurindo and Prat 1996). (Drying from the top. Liquid phase in black, gas phase in white, solid (a,b) and liquid films (c) in gray).

Following up on this, PN simulations revealed that the extent of wetting capillary films, which can form a secondary capillary transport system, is limited by viscosity of the liquid phase wherefore liquid films rather develop in case of small capillary numbers (Prat 2007) (Fig. 1-4c). Study of gravitational effects showed that gravitation, similarly to viscous effects, stabilizes the drying front and thus counteracts capillary forces (Prat 1993, Yiotis et al. 2012a, Yiotis et al. 2012b), if the hydrostatic pressure decreases in the same direction as the migration of the drying front (similar as in Fig. 1-4b). Contrarily, a destabilizing effect, characterized by ramification of the liquid phase and early breakthrough of the gas phase, can be found in case of the opposite direction of the imposed hydrostatic pressure gradient (Laurindo and Prat 1996) (Fig. 1-4d). To complete this list, it is noted that a destabilizing effect is also obtained in presence of a bi- or multimodal pore size distribution with interpenetration of the various porous domains, thus allowing the displaced fluid (water) and the displacing fluid (air) to span the 2D PN (similar as in Fig. 1-4a).

In summary, these examples illustrate that the choice of the parameter setting (either in PN computations or in drying of real porous media) dictates the formation of different drying front structures (Fig. 1-4). From this can be concluded that a wise selection of parameters can promote drying time as well as product quality. In this sense, PNMs are applied especially in those investigations in which knowledge of the evolution of the drying front structure is essential to understand and predict the macroscopic drying behavior. This is exemplarily useful in the study of salt distribution shown in Fig. 1-2. Moreover, the list of examples shows that the multiple interactions of the physics of transport processes in porous media together with material, liquid and gas properties can lead to the application of complex PNMs. The associated increase in computational effort indeed limits the use of the complex models. Though, PNMs are usually applied to simulate the prominent effects on a much smaller scale with the aim of quantification and to understand the interaction of micro- and macroscale effects, usually realized in the frame of Monte Carlo simulations.

In this thesis, the effect of imposed thermal gradients on drying of porous media is studied by PNMs. Similarly as the effects discussed above, change of the macroscopic thermal conditions has a direct impact on the pore scale transport mechanisms. Specifically, thermal gradients can lead to similar stabilizing and destabilizing effects as viscosity and gravity (Huinink et al 2002, Plourde and Prat 2003, Surasani 2009) (Fig. 1-5).



**Figure 1-5** Impact of thermal gradients on pore level liquid distribution. a) Stabilization of the drying front by a negative thermal gradient and b) destabilization of the liquid phase by a positive thermal gradient (from Plourde and Prat 2003). (Drying from the top. Liquid phase in dark gray, gas phase and solid in white).

Precisely, a temperature gradient with temperature decreasing in the direction of the advancing drying front (referred to as a negative temperature gradient throughout the thesis) can lead to stabilization of the drying front with a gradually increasing vapor diffusion zone between evaporation front and product surface (Fig. 1-5a). Contrarily, the opposed thermal gradient (i.e. a positive temperature gradient) destabilizes the penetration front resulting in long term capillary pumping to the network surface (Fig. 1-5b). These temperature gradients can be linked to contact drying (positive temperature gradient) and convective drying (negative temperature gradient). Similar gradients are also expected in microwave drying, freeze drying and inductive drying (Idakiev et al. 2017). Besides this, thermal gradients also naturally evolve in building rocks and the soil under daily and annual temperature fluctuations with the result of thermally affected moisture migration and drying. Examples are heat and mass transfer processes in the vicinity of buried nuclear waste (Gu et al. 1998) and related contamination problems (Celia et al. 1995). Another example is the thermally affected transport in GDLs during operation of fuel cells and electrolyzers. Moreover, similar as the distribution of dissolved particles or salt crystals (as shown in

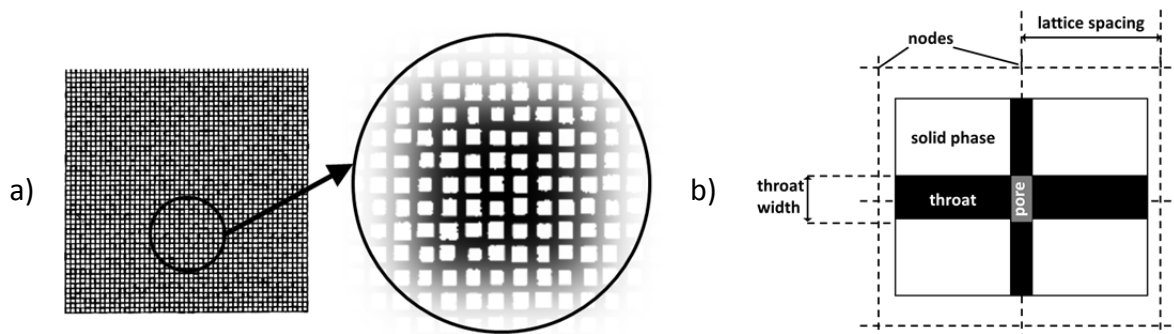
Fig. 1-2), the surface covering hydrophobicity of GDLs depends on the pore scale migration of liquid during the drying step in the production of the GDLs. Following the argumentation above, this process might be controlled by imposed thermal gradients.

It is thus the aim of this thesis to study pore scale liquid and vapor transfer in presence of imposed thermal gradients in order to understand and describe the coupling of microscale effects and macroscale drying behavior. It will be shown that the variation of the thermal gradient offers indeed a tool to control drying and product quality of porous media especially in situations in which the variation of other parameters (pore size distribution of the porous medium, viscosity, surface tension and wettability) is not possible because of physical constraints or for cost reasons.

## 1.2 Previous works

PN modeling may have started in the field of hydrology and oil recovery, namely with Fatt in 1956 (Fatt 1956a) when he presented the first network of tubes, facing the inability of available models, namely the bundle of tubes and pack of spheres, to describe flow through porous media sufficiently. While the first kind of models strongly simplified the porous medium under investigation, the second kind of models, at this time, was too complex and incorporated questionable empirical parameters (Fatt 1956a). For his computations, Fatt used an analog computer of interconnected electrical resistors. He found similar capillary pressure curves as from sandstone and glass bead packs. However, from today's point of view, a drawback of his model is the assumption of an interconnected liquid phase until complete desaturation, which means that he excluded trapping and computed the order of emptying independently of the position of the gas-liquid interface. To prove the validity of his model and its advantage over a simple bundle of tubes he also investigated flow properties by means of the permeability or rather electrical conductivity of the network. (The problem was adapted by a network of electrical resistors and the resistance was measured by Wheatstone-bridges) (Fatt 1956b, Fatt 1956c).

The first publications in the frame of PN modeling of drying of porous media and percolation theory are the ones of Shaw (1987), Daian and Saliba (1991), Nowicki et al. (1992) and Prat (1993). Since then, various PN drying models were developed for various applications (a brief overview is given below, reviews can e.g. be found in Segura (2007), Prat (2002) or Metzger et al. (2007b)). In these models the void space of the porous medium is represented by a quadratic or cubic network of interconnected pores and pore throats that can either contain liquid (saturated) or gas (empty) or both (then the phase boundary of gas and liquid is found inside the partially saturated pore or pore throat) (Fig. 1-6). Usually, two kinds of models are distinguished. These are the models that assign the void space entirely to the pores (or sites/nodes) and the models that assign the void space entirely to the throats (or bonds). This is related to the rather traditional use of PNMs in the frame of percolation theory (Stauffer and Aharony 1994). In drying, models of the second type are usually applied. However, there are also PN drying models incorporating pore *and* throat volume (as e.g. in this thesis); this can be advantageous if the physics of simultaneous drying and imbibition are studied in the same PN. Independently of the kind of PNM, emptying of the void space, due to the combined action of evaporation of water at the gas-liquid interface and capillary invasion, can be followed pore by pore (or throat by throat), which gives a great insight in the leading effects in drying of porous media.



**Figure 1-6** Illustration of a PN (from Prat 1993). a) Complete network of interconnected pores and throats which form the void space of the PN. (Note that contrary to the networks generally presented throughout the thesis the void space is in black and the solid in white in this figure.) b) Representative part of the network, indicating a pore, throats, nodes, the solid phase as well as the lattice spacing.

### 1.2.1 PNMs of isothermal drying

The earliest publication usually cited in the context of drying of PNs, is the one by Shaw (1987), although his work was only experimental (in the Hele-Shaw cell) and did not incorporate any PNM. Anyways, Shaw (1987) presented the idea of applying percolation theory to drying of porous media based on the finding of the similarity of the fractal structure of a drying front and a percolating system. In this (and also other publications of that time) drying is described as a process of immiscible displacement with a fractal structure of the drying front identical to the fractal structure found in the classical percolation process of drainage. (Exemplarily, Prat (1993) used the term ‘percolation model’ in his first publication on this subject, whereas the term ‘pore network model’ can be found in later publications (e.g. Laurindo and Prat 1996)).

In his work, Shaw (1987) discussed the experimental determination of the scaling exponent of a drying front developing in a porous packed bed of silica spheres. He found that the drying front, although of fractal character on the microscale, gets stabilized (i.e. exhibits a limited width) if the porous medium is sufficiently large, even if the capillary number and the viscosity ratio of liquid to gas phase are in favor of capillary fingering (see also Lenormand 1989). This was also confirmed by Tsimpanogiannis et al. (1999): ‘Near the leading front, the displacement will be of the percolation type [...] as the width of the front increases, viscous forces become increasingly important, leading to a displacement described by IPSG’ (invasion percolation in a stabilizing gradient). They emphasized that a macroscopic model, incorporating an effective porous medium and neglecting capillarity, would misinterpret this effect which could only be explained by limited diffusion-driven vapor transport in such a model. Accordingly, protruding drying front sections (also referred to as the least advanced point of the front) would be subject to high evaporation rates and thus naturally disappear. PN simulation instead, can shed light on this effect as it demonstrates that stabilization is caused by viscous friction forces counteracting capillary pumping. This seems to be reasonable in the face of the large porous system and the involved small pores in Shaw’s porous network (see Section 1.2.3 below for details of the network). Consequently, Shaw (1987) ascribed the stabilizing effect to the counter flow of gas and liquid phase. Prat (1993) again hypothesized that drying of disconnected clusters in

the front region might have an additional stabilizing effect since these clusters are screening the main liquid cluster from the evaporation front. For obvious reasons, disconnected clusters are not representable with a continuum model, however, they might have a comparable effect as the protuberance described by Tsimpanogiannis et al. (1999). In addition to these works, Schluender (2004) ascribed the drying front stabilization to the slight temperature variations inside the front assuming circulation of moisture. Later, besides Shaw (1987) also several other authors tried to determine drying front scaling exponents (e.g. Tsimpanogiannis et al. 1999), usually facing the limitation of network size (too small to allow stabilization of the front (Prat 1993)) and problems from the confinement effect of network edges (Nowicki et al. 1992) or pore sizes in the nanometer range (Vorhauer et al. 2010). Though, in general it is found that width of the drying front scales with the capillary number. Namely the frontwidth decreases as the capillary number increases, i.e. at higher drying rate or in presence of smaller disorder (e.g. Tsimpanogiannis et al. 1999).

After Shaw (1987), the first application of a PNM to drying was described by Nowicki and co-authors in 1992. Nowicki et al. (1992) followed another concept of upscaling of pore level phenomena to the macroscale, namely using a 2D PNM of 30x30 pores for Monte Carlo simulations with the aim to determine effective transport parameters of a continuous drying model under isothermal but viscous conditions. These authors may have been the first who found that the individual evolution of the phase patterns has a direct impact on effective transport parameters (such as relative and absolute permeability of liquid and effective diffusivity of vapor), challenging the determination of those parameters by the introduced method. In the same spirit, Daian and Saliba (1991) proposed a PNM to compute effective parameters (namely saturation curves for gas invasion, sorption and desorption isotherms, vapor diffusivity and combined liquid-vapor diffusivity) for liquid sorption/desorption and moisture migration (liquid/gas) in a piece of cement (containing 20x20x20 and 50x50x50 pores).

A first fundamental description of a PN drying model combined with a discussion of pore scale phenomena and their comparison to the classical percolation process of drainage can be found in Prat (1993) (Fig. 1-6). Similarity of the fractal structure of drying and drainage fronts is highlighted in this work (and also later in Laurindo and Prat 1996). Prat (1993) emphasized that the classical percolation model without trapping cannot be used for the study of drying, due to the interaction of capillary pumping, vapor diffusion and evaporation. He showed that simulation neglecting trapping leads to a completely different phase distribution, contradicting experimental findings. Moreover, Prat (1993) showed that a 2D pore network with 5000 throats is still too small to study the stabilizing effects as described by Shaw (1987). But if a hydrostatic pressure gradient is imposed on the pore network, the drying front sharpens significantly. Comparison of his simulation results to experiments (incorporating an equivalent PN) finally revealed certain differences in the structure of gas-liquid phase distributions, namely a high number of surviving disconnected liquid clusters, which he assigned to the effect of wetting liquid films (observed in his experimental PN) (Prat 2007, Prat 2011).

Tsimpanogiannis et al. (1999) experimentally investigated the effect of evaporation (of volatile components) as observed during oil recovery (i.e. a process of drainage followed by drying due to the injection of gas at low flow rates). They found that in presence of viscous friction forces, counteracting capillary pumping, the displacement process is much more complex than simple percolation due to the spatial variance of liquid pressure which

basically allows for more than one cluster invasion event at a time (also denoted as invasion percolation (Wilkinson and Willemsen 1983)). As a result of this study, drying could only be regarded as a form of percolation in the limit of capillarity controlled emptying.

Laurindo and Prat (1998), Yiotis et al. (2004), Prat (2007) and Chauvet et al. (2009) shed light on the role of liquid films during isothermal drying. These works were essentially motivated by the significant underestimation of experimental drying rates as for example documented in Laurindo and Prat (1998). At first, Yiotis et al. (2004) proposed an isothermal PN drying model including film flow and discovered a major impact of film flow in a capillarity controlled drying situation. These authors could nicely prove the assumption of elevated drying rates in presence of thick wetting films. Moreover, they found that the effect of film transport is favored by high surface tension, film thickness at the percolation front and low values of liquid viscosity. More precisely, they showed that the extent of the film region is approximately proportional to surface tension (Yiotis et al. 2004). The impact of the wetting angle as well as of the pore structure is discussed in Prat (2007). Chauvet et al. (2009) promoted the understanding of the role of surface roughness as they investigated the development of liquid films in a single capillary with square cross section and varying corner roundness. In general it is found that a good agreement of experimental and simulated drying behavior can either be obtained by adjusting the contact angle (Prat 2007) or the corner roundness (Chauvet et al. 2009).

Finally, recent work on drying of porous media considered discrete effects directly linked to the evolving pore level liquid and gas phase distribution, such as the transport of ions and salt crystallization (Veran-Tissoires et al. 2014) or drying of biological (Gueven and Hicsasmaz 2013) or cellular material (Huang et al. 2014), as well as combined evaporation and imbibition (Rahimi et al. 2016).

At the Otto von Guericke University Magdeburg the study of (isothermal) PN drying models started in the year 2003 with the works of Thomas Metzger (Metzger et al. 2005a), Thai Hong Vu (Vu 2006) and Anton Irawan (Irawan 2006). Metzger et al. (2007c) presented 2D and 3D PNMs for viscous affected drying. Vu (2006) parameterized a macroscopic (continuous) drying model based on the works of Whitaker (1977) and P erre and Turner (1999) by two discrete approaches, namely the bundle of tubes and the PNM developed by Irawan (2006). Sun (2014), Wang et al. (2013), Rahimi et al. (2016) and Moghaddam et al. (2017) further developed the PNM as originally proposed by Irawan (2006) and Metzger et al. (2005b) for an application to imbibition in wet wipes (Sun 2014), drying of heterogeneous particle packings (Wang et al. 2013), transport of dissolved species (Boernhorst et al. 2016) and PNM based parameter estimation for macroscopic modeling (Moghaddam et al. 2017).

### 1.2.2 PNMs of non-isothermal drying

One of the first studies and model proposals for moisture transfer through porous media under thermal gradients is the one of Phillip and de Vries (1957), who already separated the overall moisture transfer into vapor and liquid transport and furthermore separated the underlying driving forces into moisture dependent (liquid and vapor), temperature dependent (liquid and vapor) and gravity dependent (liquid) transfer. Moreover, they described the simultaneous evaporation and condensation of isolated liquid pockets, accompanied by capillary mass transfer from the condensation front to the evaporation front and by re-equalization of the gas-liquid interfaces (related to the so-called Haines



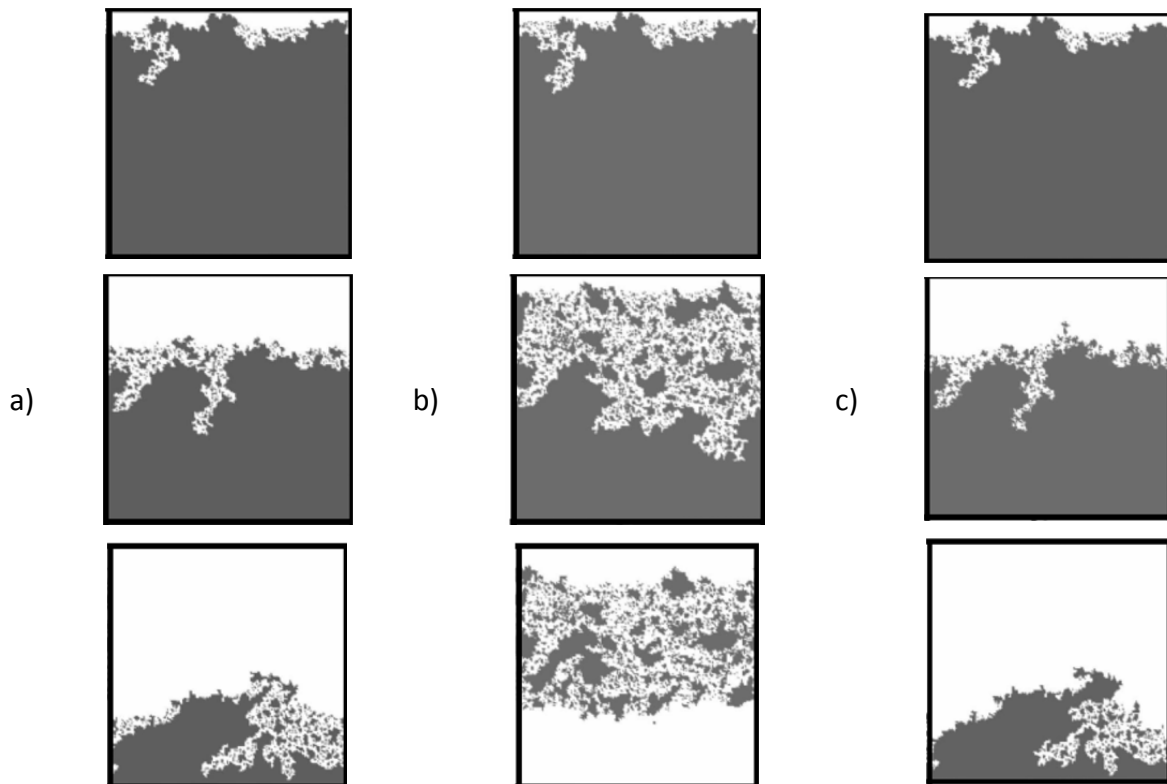
jumps (Haines 1930). This was also confirmed by Huang (1979), who pointed out that besides vapor diffusion drying is vitally controlled by the interaction of vapor transport and capillary liquid transport accompanied by evaporation-condensation mechanisms. However, Phillip and de Vries (1957) and also Huang (1979) finally presented continuum approaches to this problem incorporating average effective diffusivities and neglecting the aforementioned pore scale effects.

Pore scale effects in drying related mass transfer under non-isothermal conditions were first studied by Huinink et al. (2002), Plourde and Prat (2003) and Surasani et al. (2008a) in the frame of PNM. Huinink et al. (2002) assumed a linear temperature gradient and neglected heat transfer, comparable to what will be presented in this thesis. However, the authors focused on the impact of equilibrium vapor pressure on phase patterns as they found this parameter to be most sensitive on temperature gradients and thus controlling the structure of the drying front (Fig. 1-7). They argued that thermal gradients have an impact on capillarity only if the pressure difference induced by the variation of surface tension is greater than the pressure difference induced by the pore size distribution over a length comparable to the size of the sample. Thus, they concluded that temperature affects capillarity only in case of a relatively narrow pore size distribution (Huinink et al. 2002). This assumption was confirmed by Plourde and Prat (2003), who presented results from drying of 2D PNs with different disorder in the pore space. However, Huinink et al. (2002) could show that the order of emptying and thus the drying front structure is affected not only by the pore size distribution (as in a classical percolation process) but that it is moreover additionally controlled by evaporation and vapor diffusion. They showed that stabilization of the drying front occurs if the disconnected clusters in the two-phase zone above the front are at a higher temperature level than the front (i.e. in case of a negative temperature gradient) because the higher equilibrium vapor pressures allow for evaporation of the isolated clusters before the drying front further recedes (Fig. 1-7a). In addition to that, the vapor pressure gradient internal of the evaporation front can induce a heat pipe effect and lead to further stabilization (Fig. 1-8) (e.g. Plourde and Prat 2003, Schluender 2004, Surasani 2009). Udell (1984) has shown that the temperature can be macroscopically constant in the two-phase zone (or that only very small temperature gradients occur here) because of the countercurrent flow of hot vapor and cold liquid. However, as the temperature gradient smooths with progressive penetration of the drying front, the stabilizing effect diminishes with decreasing network saturation (Surasani 2009, p. 97). As discussed below, considering the temperature dependency of capillary pressure additionally supports stabilization of the drying front as shown in Fig. 1-8.

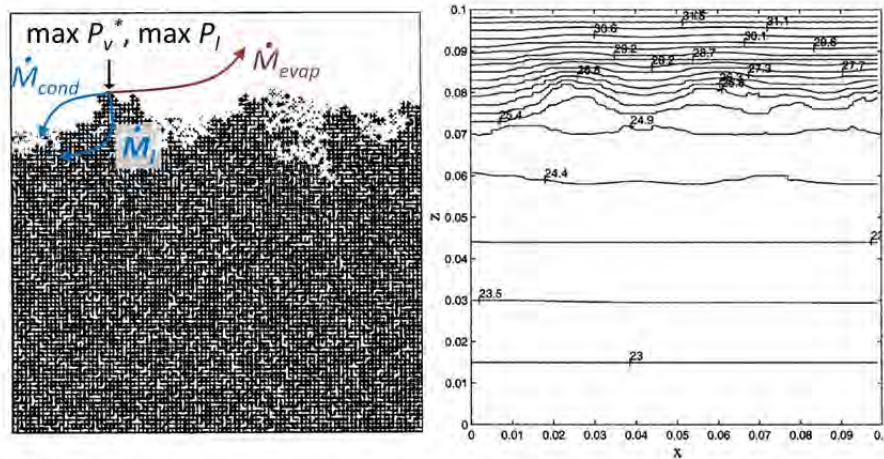
Contrarily, if a positive temperature gradient is imposed on the pore network, the disconnected clusters are colder than the main cluster front and thus survive for a significantly longer time period (Fig. 1-7b). In this case, the vapor pressure gradient facilitates diffusion through the partially saturated zone. Thus, disconnected single clusters can survive due to the reduced evaporation rate on the one hand and due to the vapor flow towards these clusters on the other hand. This results in a phase distribution characterized by a high number of single clusters over most of the drying process and the development of a second front at the hot network side (Fig. 1-7b). Plourde and Prat (2003) expanded the research of non-isothermal drying of porous media by introducing quasi-steady heat conduction into their PNM. They assumed a connected solid phase, negligible convective heat transfer and a saturation depending effective conductivity. The authors additionally included the interplay of capillarity and vapor diffusion in their investigation by taking the

temperature dependency of surface tension into account. The simulations were realized with temperature gradients in the range of  $dT/dz = \pm 1 \text{ K cm}^{-1}$ . Four remarkable outcomes shall be mentioned here: i) stabilizing and destabilizing effects are reinforced in networks with small disorder due to the impact of the temperature dependent liquid pressure; ii) the temperature gradients are almost linear in both, the saturated and the unsaturated zones; iii) if the effective thermal conductivity of the empty network is assumed to be much lower than the one of the saturated network, comparably higher thermal gradients are found in the dried network regions in case of the negative thermal gradient (Fig. 1-8), however, the thermal gradient smooths in case of the positive thermal gradient (in agreement with Udell 1984); iv) drying can be much faster in case of the positive temperature gradient if connectivity of the liquid phase to the entry of the PN can be sustained over most of the drying period.

Surasani (2009) validated these observations for convective and contact drying using a transient heat transfer model and incorporating much broader pore size distributions and bimodal PNs of different structure. The free evolution of temperature in the model proposed by Surasani (2009) is based on the computation of heat conduction. Convective heat transfer is neglected in this PNM and local thermal equilibrium inside control volumes, which are formed by the solid island and throats adjacent to a pore node (very similar to the illustration in Fig. 1-6b), is postulated (Surasani et al. 2008a). A semi-implicit scheme is proposed in Surasani (2009) to overcome the computational time limitation of solving the



**Figure 1-7** Phase distributions reported by Huinink et al. (2002) for vapor diffusion controlled non-isothermal drying: a) drying front penetration in case of a negative temperature gradient and b) breakthrough of the gas phase and initiation of a second front (similar to invasion percolation with destabilizing gradient) in case of a positive temperature gradient. c) Patterns obtained for isothermal simulation. Liquid in dark gray and vapor in white. Simulations with  $\Delta T = 50 \text{ K}$  (Huinink et al. 2002).



**Figure 1-8** Left: Stabilizing effect as e.g. also described by Schluender (2004) (adopted from Plourde and Prat (2003)). Right: Temperature profile.

heat transfer equation (explicitly implemented in earlier versions of the Surasani model, e.g. Surasani et al. (2008b)). Furthermore Surasani et al. (2008a,b) considered the heat sources related to the condensation of vapor as well as the reduction of drying rates in presence of condensation. However, cluster growth (i.e. the refilling of the already empty void space with the condensate) was disregarded, leading to a certain amount of neglected liquid volume. (Following up on this, it is one of the main objectives of this work to investigate the impact of condensation on the overall drying process). In summary, the simulation results from the transient heat transfer model proposed in Surasani (2009) reveal the coupling of pore scale liquid distribution and temperature. In drying with positive thermal gradient almost linear temperature gradients are computed for the complete drying process (Surasani 2009, pp. 126-127). The drying simulation with negative thermal gradient instead shows that the linear temperature profile, found at the start of drying when the PN has still a high saturation, alters with the development of a dry zone at the PN surface. Then, temperature decreases with a higher gradient in the dry zone on top of the PN while inside the liquid zone almost uniform temperature is observed ( $\Delta T \rightarrow 0$  at the end of drying). This observation is partly in contrast to Plourde and Prat (2003) who computed slight linear temperature gradients inside the liquid zone also after detachment of the drying front from the PN surface (Fig. 1-8). This difference implies that the drying front stabilization predicted by Plourde and Prat (2003) as a result of the variation of surface tension with temperature is only simulated at the start of drying in Surasani (2009). This is explained with the uniform temperature in the liquid saturated zone and the related diminishing impact on surface tension variation at later stages of drying. The quasi-steady PN simulation presented in Plourde and Prat (2003) can thus be seen as an example for limited heat transfer through the liquid zone. Such a situation could be expected if exemplarily the solid content with  $\lambda_s \ll \lambda_l$  is high (i.e. at low porosity). A similar drying behavior as shown by Plourde and Prat (2003) would be obtained if the thermal conductivity or the porosity in the simulations of Surasani (2009) were adapted. Finally, Surasani (2009) showed that the distinct drying periods, usually observed in drying of porous media, can be simulated with the transient model also for 2D PNs. These are the warming up period, the constant rate period (CRP) and the receding front period (RFP). In addition to that, very similar drying behavior was presented for 3D PNs.

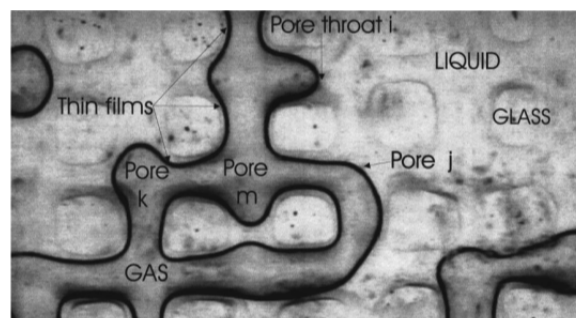
It is summarized that in general negative thermal gradients, comparable to convective drying, lead to stabilization of the drying front, mainly depending on the disorder of the pore space, the height of the temperature gradient and vapor diffusion inside the partially saturated zone (also referred to the drying front). The reverse (positive) temperature gradient, as e.g. found in contact drying, destabilizes the liquid phase resulting in an early breakthrough of the gas phase and numerous disconnections of single clusters, again depending on the disorder, the height of the temperature gradient and the vapor diffusion through the 2-phase zone. Nevertheless, although recognizing that condensation of vapor must occur in presence of thermal gradients, previous authors totally ignored (Huinink et al. 2002, Plourde and Prat 2003) or partially neglected (Surasani 2009) the effect of condensation on the liquid structure or discussed temperature gradients which do not allow for significant condensation effects. However, in a process of fluid counter-flow vapor condensation is expected to reduce local evaporation rates or to lead to the refilling of already empty or partially filled pores and pore throats (Schluender 2004). It should be remarked that the condensation related refilling of the pore space must be distinguished from the processes described in Masoodi and Pillai (2012) or Beyhaghi et al. (2014) referring to combined evaporation and wicking from a connected liquid source. Such a situation of simultaneous evaporation and imbibition has also been studied by Rahimi et al. (2016) in the frame of droplet deposition. It should also be distinguished from the process of capillary condensation as e.g. studied in Kainourgiakis et al. (1995) and from the process of imbibition as e.g. described in Mogensen and Stenby (1998). However, very similar transport mechanisms occur in the different situations. In general, invasion of a porous medium by imbibition requires application of more complex invasion rules than drainage or drying. Exemplarily, the invasion of pores and throats must be differentiated, which finally leads to a hysteresis of capillary pressure curves of drainage and imbibition (e.g. Morrow 1970). Furthermore, several authors have shown that prominent effects naturally accompany and control the imbibition process. These are the mechanism of snap-off of wall covering liquid films (Li and Wardlaw 1986a,b, Mogensen and Stenby 1998, Bustos and Toledo 2003, Patzek 2000) and Haines jumps (e.g. Morrow 1970, Xu et al 2008, Moebius and Or 2012). Following Mogensen and Stenby (1998), Mohanty et al. (1980) or Wu et al. (2016), for example, the situation becomes even more complex in the presence of large pore volumes and small throat volumes.

However, none of these authors has yet studied imbibition as a result of vapor condensation in a non-isothermal PN. Furthermore, an experimental study of thermal pore scale effects related to drying is missing (except of already published own results). Experimental studies of vapor and liquid transport through porous media under non-isothermal conditions yet usually addressed the determination of effective transport parameters (such as vapor diffusivity, e.g. by Krischer and Rohnhalter (1940), Mujumdar (2015)) or macroscopic phenomena. Exemplarily, Crausse (1983), Udell (1985) and Gu et al. (1998) investigated moisture migration under thermal gradients. More specifically, Crausse (1983) experimentally and numerically studied coupled heat and mass transfer in particle packings (quartz sand was used in these experiments). Udell (1985) studied the temperature profiles in sand packs evolving from countercurrent flow of liquid and vapor (similar as in a heat pipe). Gu et al. (1998) studied the macroscopic effect of enhanced vapor transport due to coupled evaporation and condensation in a glass bead packing. However, no PN study of simultaneous evaporation and condensation has yet been presented in literature.

### 1.2.3 Experimental evaluation of pore network models

Development of mathematical PNMs requires several intermediate steps incorporating validation by experiments (Lenormand et al. 1988). For obvious reasons, it is very difficult to directly compare a drying simulation result with experimental drying of a real sample, at least if the individual governing microscale drying effects are regarded. For this reason, commonly model experiments are applied to assess the mathematical model. These can involve single droplets, single particles or single capillaries in the simplest cases. Purpose of single capillary experiments, for example, is the study of fluid/fluid or fluid/solid interactions as wetting by liquid films (Buckley 1991). Also the capillary pressure associated with the pendular liquid rings at the contact point between two spheres before and after disconnection from the bulk liquid phase can be measured with single particle experiments (Morrow 1970). A bundle of capillaries can be used to study capillary effects such as Haines jumps (Buckley 1991). Interaction of a system of particles or tubes is usually investigated in particle beds (usually glass beads), Hele-Shaw cells or rigid 2-dimensional PN structures (Fig. 1-9), depending on the kind of system to be modeled. Microfluidic PNs offer the advantage of readily accessible data (e.g. by a simple CCD camera) and the feasibility of a pore-by-pore comparison of experiment and simulation. The simulated behavior can then easily be transferred to an equivalent 3D system (Prat 1993). Literature specifies several different types of transparent 2D micromodels applied for the investigation of various capillarity controlled displacement processes, of which some relevant examples are summarized in Table 1-1. A review of PNMs and accompanying experimental studies can for example be found in Buckley (1991) and Segura et al. (2005).

In summary, the PN micromodels can be classified into high surface energy micromodels (glass micromodels) and low surface energy micromodels (polymers) (Diaz et al. 2011). The latter offer generally advantages in pore structure and mechanical strength but lack in thermal properties. Pore sizes in resin based micromodels are usually in the range of 1 mm in depth and at least 0.1 mm in width (Oyarzun and Segura 2009). The glass micromodels instead offer the advantage of very high thermal conductivity (which was e.g. also required for the present work) and comparably higher wettability but compromise concerning the pore structure, which usually deviates from strictly rectangular or circular due to the wet etching technique (Vorhauer et al. 2010) or fusion (Lenormand et al. 1983). The etched glass micromodels usually contain pores of minimum size of 10  $\mu\text{m}$  (Oyarzun and Segura 2009). They were first introduced by Mattax and Kyte in 1961 (Buckley 1991). Table 1-2 addresses the main advantages and disadvantages of the different types of PN micromodels.



**Figure 1-9** Top view image of a 2D microfluidic PN from Tsimpanogiannis et al. (1999). The snapshot indicates the liquid phase and the solid (glass) in light gray, the gas phase in dark gray as well as the location of the gas-liquid interface e.g. within pore *j*. The empty pores are indicated by *k* and *m*; furthermore, the liquid films evolving at the solid surface are highlighted.

**Table 1-1** 2D experimental microfluidic PNs from literature.

Reference	Type of network	Remarks
Bonnet and Lenormand (1977), Lenormand et al. (1983)	<b>transparent polyester resin (TPR)</b> , photographically etched mould, $w_t = 0.2-1.4$ mm, $L_d = 1$ mm, 135 nodes	<b>rectangular cross-sections</b> , wetting liquid films, $a = \pm 0.1$ mm
Chatzis and Dullien (1983)	<b>pore doublet</b> , etched mirror images in window glass using hydrofluoric acid, fusion in furnace at $T = 720^\circ\text{C}$ for 30 min	<b>elliptical cross sections</b> , aspect ratios of 2:1 and 10:1 depending on etching time, used for drainage and imbibition
Chatzis et al. (1983)	<b>glass mirror plate</b> , photofabrication and etching, fusion to cover plate (with mirrored pore structure)	<b>eye-shaped cross sections</b> after fusion
Shaw (1987)	<b>Hele-Shaw cell (HSC)</b> (15-20 $\mu\text{m}$ x 2.5 cm x 4 cm) <b>with silica spheres</b> (0.5 $\mu\text{m}$ )	<b>quasi 2D network</b> , different liquid transfer mechanisms in the particle-particle contact and particle-wall voids
Lenormand et al. (1988)	<b>TPR</b> (135 x 150 $\text{mm}^2$ ), photolithographically etched mould, $w_t = [0.1:0.1:0.6]$ mm, $L_d = 1$ mm, 42000 throats	<b>rectangular cross-sections</b> , wetting liquid films, $a = \pm 0.1$ mm
Prat (1993)	adapted from Lenormand et al. (1988), $w_t = 0.1-0.6$ mm, 5000 throats	wetting liquid films
Li and Yortsos (1995)	<b>etched glass plate (EGP)</b> fused <b>with glass cover plate</b> , Rayleigh distributed, $w_t \leq 1000$ $\mu\text{m}$ , $w_p \leq 1500$ $\mu\text{m}$	comparison of bubble growth in 2D lattice structure (more fractal) and Hele-Shaw cell (more compact bubbles)
Laurindo and Prat (1996)	adapted from Lenormand et al. (1988), size 140x140 pores, $w_t = 0.1-0.6$ mm, $L_d = 1$ mm, $L = 1$ mm, 39000 throats	evaporation and drainage experiments with inclined PN
Xu et al. (1998)	<b>vertical HSC</b> (30x4x2 $\text{cm}^3$ ) <b>with glass beads</b> (100 $\mu\text{m}$ ), porosity $\cong 40\%$ , $K \cong 40 \cdot 10^{-12}$ $\text{m}^2$	gravitational effects avoided by using liquids of similar density

Table 1-1 Continued.

Reference	Type of network	Remarks
Tsimpanogiannis et al. (1999)	<b>EGP</b> , injection and exit ports, cover plate fused (25 x 10 cm <sup>2</sup> ), Rayleigh distributed, $\bar{w}_t = 450 \mu\text{m}$ , $\bar{w}_p = 900 \mu\text{m}$ , $L_d = 100 \mu\text{m}$	<b>eye-shaped cross section</b> after fusion, drainage and drying by low flow rate gas injection ( $\dot{V} = 0.052 \text{ ml min}^{-1}$ ), liquid films
Tsakiroglou and Avraam (2002)	<b>Poly methyl methacrylate (PMMA)</b> , combination of etching (excimer laser ablation) and LIGA techniques	<b>rectangular cross sections</b> , reproducible network structures at low price
Amyot et al. (2007)	<b>rough polymeric material with PMMA cover</b> , roughness by digital drilling (maximum height 55 $\mu\text{m}$ )	drainage flow between rough surfaces, $a = \pm 10 \mu\text{m}$
Oyarzun and Segura (2009)	<b>photoetched glass plate fused with glass cover plate</b> , normal distribution, $\bar{r}_p = 11.35 \pm 1.85 \mu\text{m}$ , $L_p = 3.12 \pm 0.55 \text{ mm}$	generation of pore morphology of softwoods in glass micromodel, visualization of liquid films and Haines jumps
Tran (2011)	<b>PMMA</b> , 25x25 pores, normal distribution, $w_t = [300:50:800] \mu\text{m}$ , $L_d = 1 \text{ mm}$ , $L = 2 \text{ mm}$	<b>rectangular cross sections</b> , high surface roughness due to milling, no chemical bonding, $a \geq \pm 25 \mu\text{m}$
Diaz et al. (2011)	<b>TPR</b> , printing by flexography, 100x100 pores, log-normal distribution, $w_p^{min} = 100 \mu\text{m}$ , $L_d = 0.1 \text{ mm}$ , $L = 1.5 \text{ mm}$	<b>rectangular cross sections</b> , mimicking the bimodal structure of carrots
Segura et al. (2014)	<b>Polydimethylsiloxane (PDMS)</b> , $r_p = 150\text{-}300 \mu\text{m}$	deformable structure used to investigate shrinkage effects
Sun (2014)	<b>silicon dioxide (SiO<sub>2</sub>)</b> , adapted from Vorhauer et al. (2013), 45x49 pores	<b>non-cylindrical cross section</b> (see Chapter 3 for further specifications)
Yiotis et al. (2012b)	<b>HSC with glass beads</b> (100-850 $\mu\text{m}$ ), cross section 15x1 mm <sup>2</sup> and 20x2 mm <sup>2</sup> with round corners, height 60-300 mm	visualization of gravity stabilized drying fronts and film region (in dependence of corner roundness)
Wu et al. (2016)	<b>PDMS</b> , 4x4 pores, $L_p = 1 \text{ mm}$ , $L_t = [0.14:0.02:0.94] \text{ mm}$ , $L_d = 0.1 \text{ mm}$ , $L = 2 \text{ mm}$	<b>square cross section</b> , temporally hydrophobic, visualization of pore invasion from throat neighbors, $a = \pm 0.01 \text{ mm}$

**Table 1-2** Comparison of 2D experimental microfluidic PNs.

Type of network	Treatment	Advantages	Disadvantages	Reference
PMMA (Poly methyl methacrylate)	- milling - sealing by tape	- inexpensive - mechanically robust	- sensitive to chemicals (stress corrosion cracking) - low thermal conductivity (liquid condensation) - maximum working temperature < 100°C - relatively large pores - high surface roughness - high inaccuracies - undesired loss of liquid due to taping	Tran (2010)
	- etching by excimer laser ablation (and LIGA) - moulding (hot embossing) - sealing by PMMA foil (glued)	- mechanically robust - highly reproducible structure due to moulding - small pore width ( $w_p^{min}=10\mu\text{m}$ )	- sensitive to chemicals (stress corrosion cracking) - low thermal conductivity - maximum working temperature < 100°C	Arnold et al. (1995), Tsakiroglou and Avraam (2002)
transparent etched-glass micromodels	- combined photo lithography and chemical wet etching - sealing by fusion with glass wafer or - chemical bonding to Si-wafer	- small production inaccuracies - low surface roughness - clear observation - one-by-one comparison of experiment and PN simulation	- pore structure not well defined - pore structure production sensitive - correlation of pore width and depth - non-rectangular cross section	Tsimpanogiannis et al. (1999), Vorhauer et al. (2013)



Table 1-2 Continued.

Type of network	Treatment	Advantages	Disadvantages	Reference
glass bead layer in Hele-Shaw cell	- glass beads of different size inside narrow transparent chamber (glass or synthetics)	- inexpensive - robust - good visibility of the displacement process - visibility of liquid films	- only quasi 2D - different mass transfer phenomena inside bulk structure and wall covering liquid films - usually heterogeneous pore structures - usually no direct comparison to PN simulation	Shaw (1987), Li and Yortsos (1995), Yiotis et al. (2012b)
polyester resin	- moulding technique using resin and photolithographically etched mould	- well defined pore structure - rectangular cross section - production of very large networks ( $\cong 10^6$ pores) - heat resistant	- relatively large throats - limited network depth - limited lattice spacing (deformation if lattice spacing too small) - low thermal conductivity	Lenormand et al. (1983) Lenormand et al. (1988), Diaz et al. (2011)
SU-8 (photoresist)	- UV lithography	- well defined pore structure - straight pore walls - very high aspect ratios	- low working temperatures - comparably low thermal conductivity	
PDMS (Polydimethylsiloxane)	- moulding technique	- hydrophobic surface properties	- permeation of water - water permeation might lead to a gradual change of wettability	Wu et al. (2016)

### 1.3 Outline of the thesis

Focus of the thesis is the development of a powerful PNM of drying affected by imposed thermal gradients and secondary capillary invasion. The model will be developed by adapting PN drying simulations to experimental results gained by drying of a 2-dimensional microfluidic PN inside a glass ( $\text{SiO}_2$ ) wafer. Strength of the PNM will be evaluated for different drying regimes, namely drying with spatially almost constant temperature and drying with imposed negative and positive thermal gradients, which are temporally constant. Furthermore, conclusions concerning the phenomena that control thermally affected drying in PNs will be drawn from the presented experimental and simulation results. It will be discussed how variation of temperature gradients imposed on the PN can impact on microscale transport mechanisms and drying curves. For this, drying under quasi isothermal conditions will be compared with drying in presence of imposed temperature gradients. The applied heating modes will be discussed in the face of characteristic liquid and gas distributions during drying, drying rates and the overall drying time taking the phenomenon of secondary capillary invasion into account. It will also be discussed how locally limited structural peculiarities, such as the formation of pendular rings around the solid islands of the 2D PN structure or the liquid pinning to the lateral edges of the PN, impact on the macroscopic drying behavior. Special attention will be paid on the cluster growth mechanism induced by vapor condensation in presence of high thermal gradients. Both effects are key aspects of the proposed PNM.

The thesis is structured as follows. At first the relevant fundamentals of drying and mass transfer in rigid capillary porous media are recalled in Chapter 2. Then, the experimental design and procedure of drying experiments is summarized in Chapter 3. In this chapter, precise information about the designed microfluidic PN, experimental set-up and procedure as well as analysis by image processing and numerical evaluation of drying experiments can be found. The experimental results of quasi isothermal and non-isothermal PN drying experiments are presented and discussed in Chapter 4. In this chapter the experimental study of wetting liquid films by Confocal Laser Scanning Microscopy (CLSM) is also presented. Development of the mathematical non-isothermal PNM with secondary capillary invasion and cluster growth mechanism, based on experimental observations, is described in Chapter 5. The proof of concept is examined in Chapter 6 on the base of an objective numerical comparison of experimental results and the results obtained from PN simulations. Validation of the PNM in this chapter reveals the governing pore scale phenomena that control non-isothermal drying of the PN. Finally, Chapter 7 summarizes and discusses the outcomes of the thesis, with regard of practical applications, and gives an outlook on future works. A summary of conducted experiments, simulations as well as additional information and remarks concerning PN drying simulations are provided in Appendices A-C.

„Ich möchte die Natur verstehen, ich möchte wissen, wie es dazu gekommen ist, dass etwas so ist, und zwar genau und nachprüfbar und nicht geglaubt oder kulturell eingeprägt.“

Christiane Nüsslein-Volhard, first female German Nobel price winner  
\* October 20, 1942 in Heyrothsberge/Magdeburg, Germany

## Chapter 2

# Fundamentals

### 2.1 Introduction

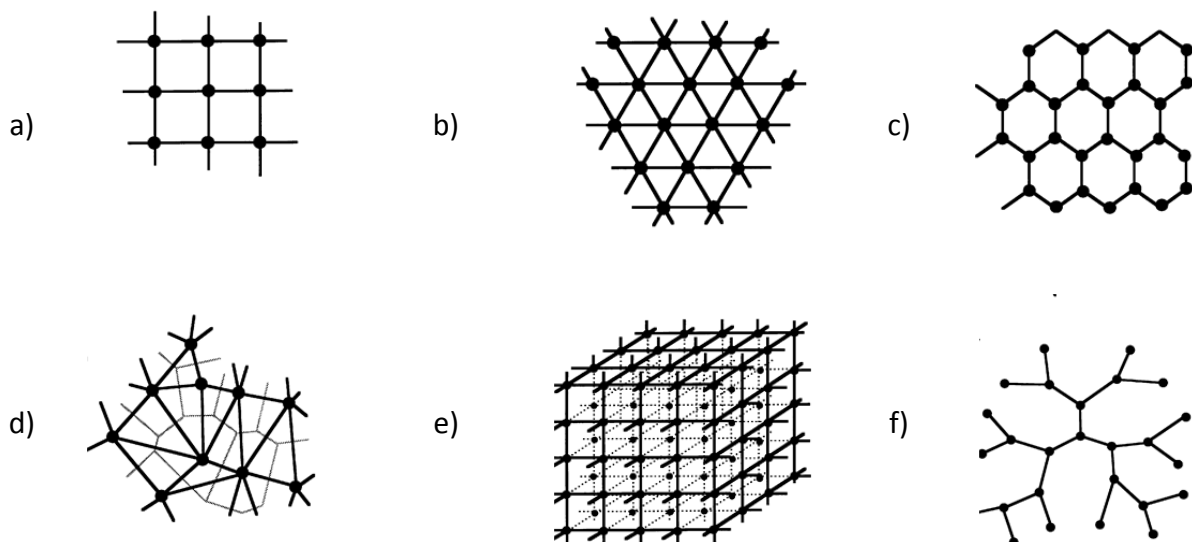
Objective of this work is the investigation and description of drying of porous media under imposed non-isothermal conditions based on a pore scale study that incorporates pore networks (PNs). The purpose is to show the relevance of different thermally affected mass transfer mechanisms (on the micro level) for the macroscopically observable drying behavior (as e.g. drying rate and drying time); heat transfer is disregarded in this thesis. This chapter therefore gives an introduction to PNMs and temperature controlled mass transfer. It summarizes the fundamentals of PNs and the classical invasion processes typically studied with PNMs in the frame of percolation theory in Section 2.2. The summary focusses on drying as a percolation process (Section 2.2.3) in comparison to drainage and imbibition. The physical basics of coupled diffusive mass transfer and capillary invasion in the framework of non-isothermal drying as well as condensation induced imbibition of liquid are given in Sections 2.3 and 2.4. It is shown in Section 2.3.2 and Section 2.4.1 how the direction of vapor diffusion is dictated by the saturation vapor pressure gradient evolving in a non-isothermal environment. The prominent invasion mechanisms linked to the direction of vapor transport are presented in association with the temperature affected capillary invasion (Section 2.3.4 and Section 2.4.2). In this context, the invasion of the pore space by the gas phase in situations where the vapor pressure gradient allows for evaporation and reinvasion by the liquid phase when the vapor pressure gradient allows for condensation are discussed (in Sections 2.3.4.1 and 2.3.4.2). Special attention is paid on the secondary liquid invasion in capillary liquid films (Section 2.3.6) since this effect significantly influences pore level transport mechanisms and thus the overall drying rate and drying time. Relevance of the pore scale mechanisms on the macroscopic drying behavior is presented in Section 2.5 with the focus on phase patterns (Section 2.5.1), drying rates, overall drying time (Section 2.5.2) and the relation to drying periods typically observed during drying of porous media. Here again the role of liquid films (Section 2.5.3) as well as of the effects leading to a macroscopic stabilization and destabilization of the liquid phase are highlighted.

## 2.2 Percolation

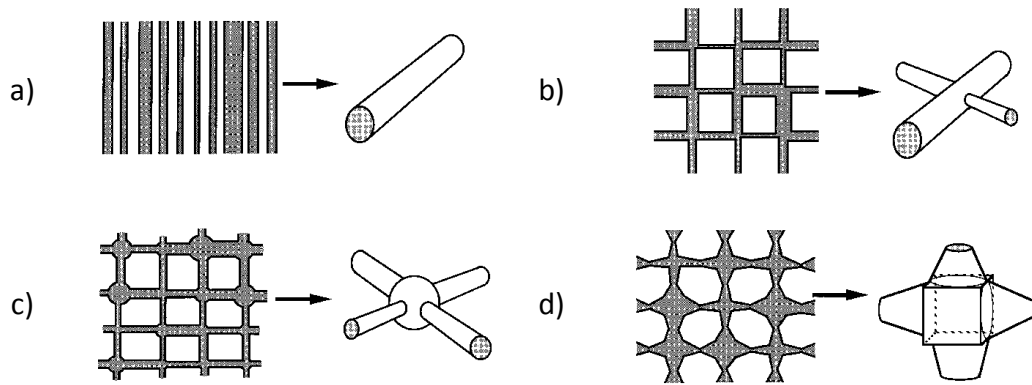
Drying of porous media is usually a kinetically controlled process, because the transport of heat to the evaporation front and the transport of vapor from the evaporation front to the bulk air phase is limited due to the heat and mass transfer resistances occurring in the (partially saturated) porous medium. Nevertheless, displacement of liquid by the gas phase can be regarded as a quasi-static invasion process, if capillary number is low; i.e. in the case of slow drying and negligible viscosity of the liquid phase or relatively large variance in the pore size distribution. In detail, the invasion of the liquid filled porous medium by the gas phase occurs in discrete steps in which the pores and throats are emptied successively. On this base, percolation concepts could originally be adopted from classical percolation processes (drainage/imbibition) to drying of porous media (Shaw 1987, Prat 1993, Nowicki et al. 1992) initiating the use of PNMs.

### 2.2.1 Pore networks

Pore networks (PNs) are idealized geometrical structures of the pore space of porous media. They are applied to study and to predict invasion processes on the pore level. Consequently, care is taken to adapt pore size distribution, interconnectivity of the void space and porosity of the PN to the situation under study. Figure 2-1 illustrates PNs from the literature (Berkowitz and Ewing 1998). As can be seen, the void space is usually either totally subscribed to the throats (or bonds) (i.e. the lines in Fig. 2-1) or to the pores (or sites) of the PN (i.e. the circles in Fig. 2-1). Depending on the structure of the PN, different invasion patterns are expected (Stauffer and Aharony 1992). In more complex representations, the void space can be distributed among the pores and the throats (Fig. 2-2). This is useful especially for the simulation of imbibition processes because pores and throats are typically assigned with different invasion rules (see Section 2.3.4.2).



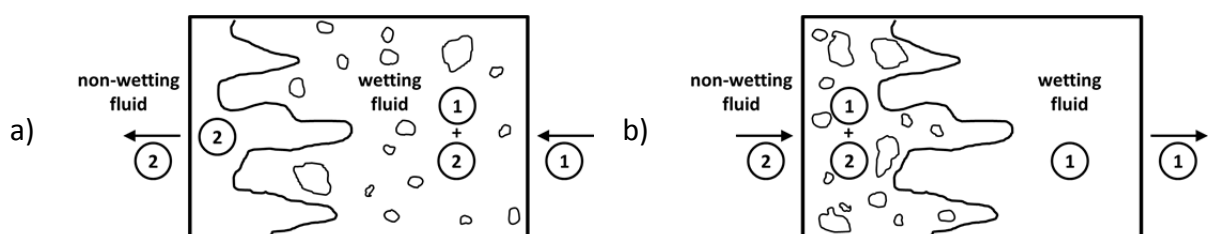
**Figure 2-1** Typical examples of PNs (from Berkowitz and Ewing 1998): a) 2D square lattice of pores (circles) and throats (lines), b) 2D triangular lattice, c) 2D honeycomb lattice, d) Voronoi structure, e) 3D square lattice, f) irregular 2D lattice. Notice that the width of pores/throats is distributed in a given range.



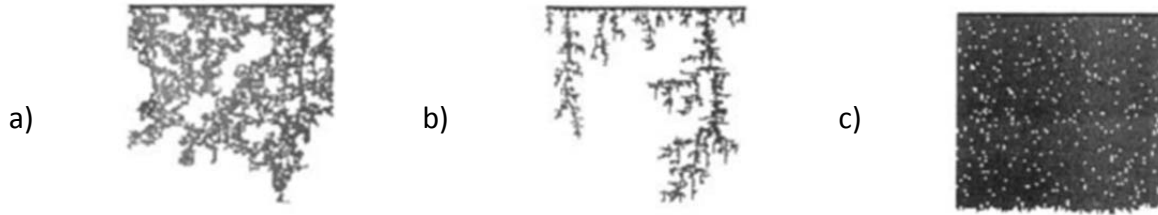
**Figure 2-2** Illustration of various pore and throat geometries (from Berkowitz and Ewing 1998). From a) to d): bundle of tubes, throat PN (from Fatt 1956), pore and throat PN, biconical PN.

### 2.2.2 Drainage and imbibition

In classical imbibition or wetting processes the wetting fluid is sucked into the porous medium from the side that is dipped into the source increasing the overall saturation in the sequence of decreasing capillary pressure, while the non-wetting fluid escapes from the opposite open side of the porous medium. One famous example is the displacement of oil from a porous medium by injection of water, where pressure of the wetting phase (water) is successively increased in order to displace the non-wetting phase (oil, at lower pressure) in the sequence of increasing pore radii (Blunt et al. 2002). In imbibition, wetting fluid and the non-wetting-fluid migrate into the same direction. This is illustrated in Fig. 2-3a by means of a 2D PN. Contrary, drainage, to some extent, can be seen as the reversed invasion process: the wetting fluid is displaced by the non-wetting fluid in the order of increasing capillary pressure with the result of decreasing overall saturation of the PN (Fig. 2-3b). Again, both fluids migrate in the same direction in this process. As will be discussed below, imbibition and drainage can follow different invasion paths leading to a hysteresis of the capillary pressure curves plotted against saturation. Typically, both processes stop when the invading fluid percolates the network and thus with the attained continuum flow path of the invading fluid to the outlet, leaving isolated islands of trapped oil (imbibition) and water (drainage) (Fig. 2-3a,b). This leads to the term *percolation with trapping*. Thus, the final saturation of the pore space with either wetting or non-wetting fluid is usually  $S > 0$  (if phase transition is neglected).

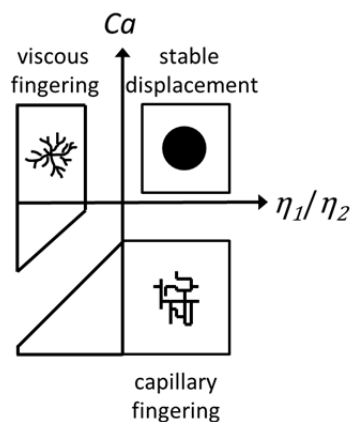


**Figure 2-3** Illustration of a) imbibition and b) drainage (adopted from Lenormand et al. 1988). 1 – wetting fluid, 2 – non-wetting fluid. A continuous 2-phase zone (presence of 1+2) emerges in drainage and imbibition. (Note that the pore structure is not shown).



**Figure 2-4** Illustration of a) capillary fingering, b) viscous fingering and c) stable displacement. (Displacing fluid in black, displaced fluid in white). (Lenormand et al. 1988)

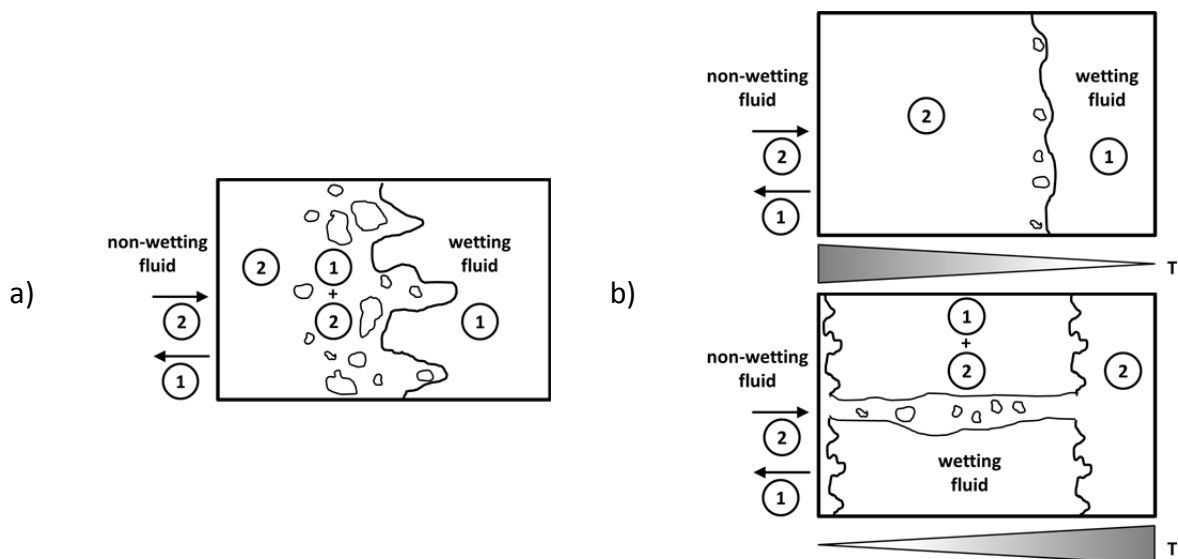
As highlighted in Fig. 2-4, various phase patterns can develop depending on the pore structure of the PN and the viscosity ratio of invading and displaced fluid  $\eta_1/\eta_2$  (Fig. 2-5). These are i) capillary fingering (Fig. 2-4a), ii) viscous fingering (Fig. 2-4b) and iii) stable displacement (Fig. 2-4c). According to Lenormand et al. (1988) capillary fingering occurs for low capillary number and negligible viscosity in the displaced fluid and the invading fluid as well. Thus, the fingering is based on capillary forces. The fingers span the PN at the end of the invasion process and the final saturation of the PN with displaced fluid is  $S > 0$ . In a process with viscous fingering instead, viscosity of the displaced fluid is the driving force for the evolving phase distributions; capillary effects in the invading fluid are negligible. The final saturation with displaced fluid is higher than in an invasion process with capillary fingering. Finally, stable displacement is associated with the viscosity of the invading fluid; capillary effects in the displaced fluid are negligible. A flat front evolves and travels through the PN. Only small clusters are trapped behind the front, leading to a significantly smaller final saturation of the PN. The boundaries of these displacement patterns are in general given by the phase diagram derived by Lenormand et al. 1988 (Fig. 2-5). They depend on the particular pore size distribution and must thus be adapted to the PN under study. The fraction of trapped fluid is an important measure for the permeability of the porous medium. Usually, a low fraction of trapped fluid is obtained at high permeability (Bustos and Toledo 2003). (This actually imposed one of the main challenges on oil and gas recovery from sedimentary rocks, one of the key processes in the 20<sup>th</sup> century, and established a growing interest in sustaining fluid continuity, e.g. by wall covering film flow).



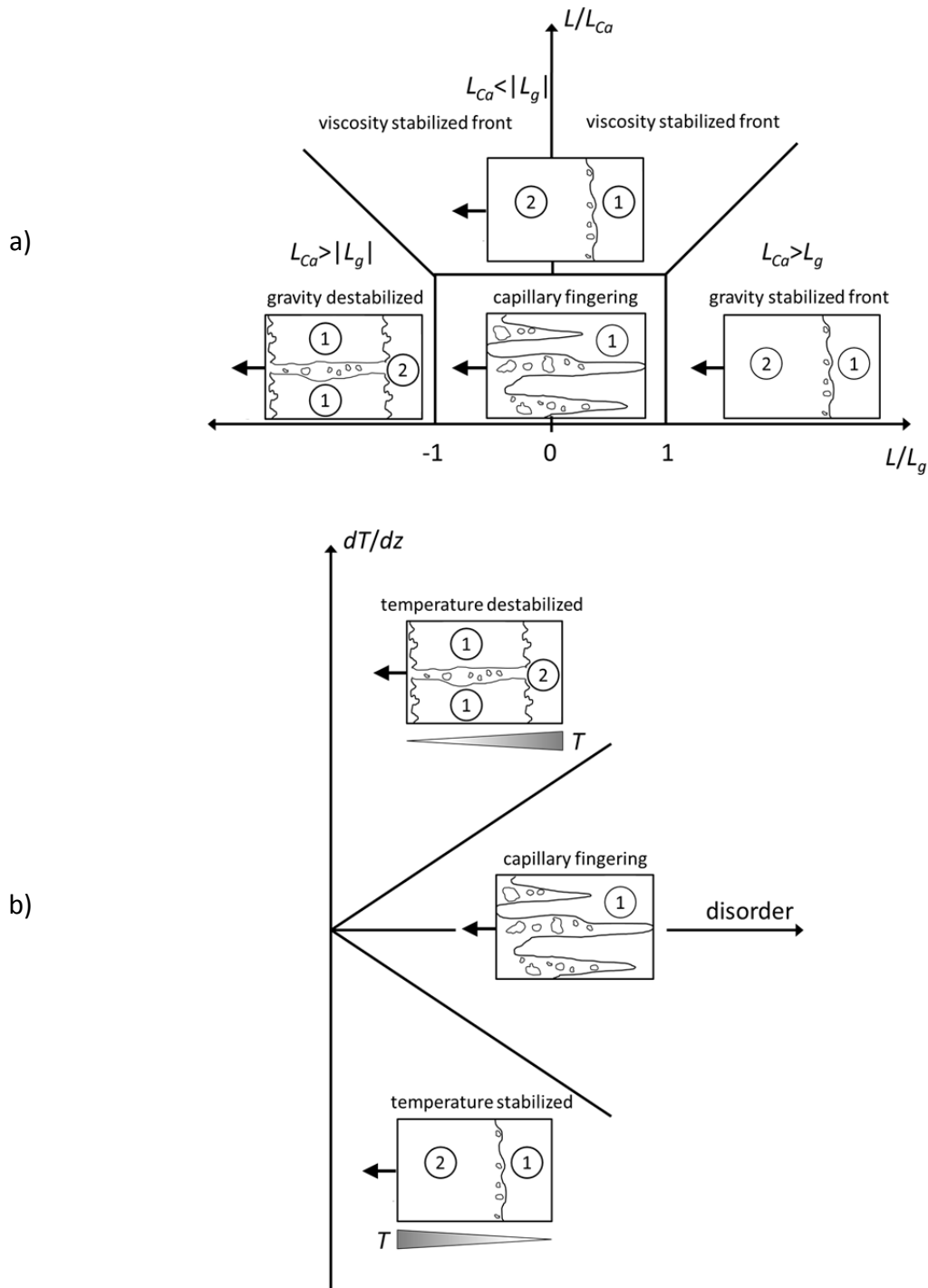
**Figure 2-5** Phase diagram adopted from Lenormand et al. (1990). The boundaries of the displacement regimes depend on the particular PN. (1 – wetting fluid, 2 – non-wetting fluid).

### 2.2.3 Drying

In drying, the invasion process is similar to drainage: the wetting fluid (in most cases water) is displaced by the non-wetting fluid (in most cases air). But, contrary to drainage, the wetting liquid must be evaporated before it can leave the porous medium in the vapor phase. Moreover, the directions of gas penetration and vapor removal are usually opposed. This is illustrated by means of a PN in Fig. 2-6a. The counterflow of invading gas and escaping vapor once led to the designation *immiscible displacement process with fluid counterflow* (Shaw 1987). In isothermal PNs, evaporation usually occurs at the tip of the evolving partially saturated zone. The tip of the 2-phase zone is thus also referred to as the evaporation front and the 2-phase zone is named the drying front. It is illustrated in Fig. 2-6a that this front can significantly widen during the drying process. As in drainage, the phase patterns evolving during isothermal drying of the PN depend on the pore structure and the viscosity ratio of wetting and non-wetting fluid. But the flow of vapor through the dry zone connected to the open side of the PN is kinetically controlled wherefore trapping of liquid islands is not observed in drying. This means, even in case of a discontinuity of the flow path the final saturation of the pore space with liquid is  $S = 0$ . Additionally, drying is usually a non-isothermal process, thus temperature gradients naturally evolve. This can lead to i) different travelling directions of the liquid phase (e.g. Huinink et al. 2002, Plourde and Prat 2003, Surasani 2009) (Fig. 2-6b) and ii) to condensation of vapor (Phillip and de Vries 1957) inside the 2-phase zone.



**Figure 2-6** Invasion related to drying of PNs. a) Isothermal drying (adopted from Prat and Bouleux 1999), b) non-isothermal drying with different temperature gradients as indicated by the triangles (low temperatures are associated with the tip of the triangles). The wetting fluid escapes through the open edge on the left in vapor phase. The liquid saturated zone is denoted by 1, the dry zone is denoted by 2 and the partially saturated zone is denoted by 1+2 (analog to Fig. 2-3). Note that the apparently dry zones contain air and water vapor as well. Contrary to drainage and imbibition, the extent of the 2-phase zone is limited due to evaporation of liquid.



**Figure 2-7** Phase diagrams classifying the invasion process of drying by means of 2D PNs. a) Isothermal drying under gravity and viscous stabilizing effects, b) non-isothermal drying.  $L$ - length of the PN,  $L_g$ - length of the gravity stabilized drying front,  $L_{Ca}$  - length of the viscous stabilized drying front. (1 - liquid zone, 2 – dry zone) (Adopted from Plourde and Prat 2003).

Phase diagrams for drying, analog to Lenormand et al. (1990), are provided by Plourde and Prat (2003) and given in Fig. 2-7. Additionally to viscosity, these diagrams take gravity and temperature effects on the distribution of liquid and gas phase into account. As can be seen, typical phase patterns can be distinguished for different drying regimes. Precisely, it is found that drying with stabilizing gravity effects (Fig. 2-7a) leads to similar phase patterns as drying



with negative thermal gradient (again, negative means that the highest temperature is found at the PN open side) (Fig. 2-7b). Akin invasion patterns are also expected in drying with viscous stabilized drying front. Analog, drying with destabilizing orientation of the PN leads to similar phase patterns as drying with positive thermal gradient (i.e. with lowest temperature at the PN open side). In summary, four different drying regimes can be distinguished in the phase diagram for isothermal drying of PNs (Fig. 2-7a): i) the stable displacement due to viscous friction forces counteracting capillary invasion (denoted as viscous stabilized front), ii) the stable displacement due to gravity (i.e. gravity stabilized front), iii) the gravity destabilized displacement and iv) capillary fingering. In the phase diagram for non-isothermal drying of PNs, two drying regimes are distinguished from isothermal drying (with capillary fingering). These are i) temperature stabilized displacement due to presence of a negative thermal gradient and ii) temperature destabilized displacement with breakthrough of a gas finger to the hot side of the PN under impact of a positive thermal gradient. The discrimination of different drying regimes in Fig. 2-7 is based on the capillarity of the PN and similar pressure gradients evolving due to the gravitational forces, friction forces and the thermal gradients. This is in agreement with the concept of Lenormand et al. (1988). The effect of vapor transport and condensation on the phase patterns, however, is not considered in these diagrams.

## 2.3 Drying of porous media

### 2.3.1 Phase equilibrium

Drying is a unit operation aiming at the separation of solid and liquid by evaporation of the liquid, based on the inequality of chemical potentials of the liquid (*l*) and gas (*g*) phase. Based on the constraint that the chemical potential in a system of two connected phases tends to its minimum value, liquid evaporates if

$$\mu_{l,H_2O} > \mu_{g,H_2O}, \quad (2-1)$$

(Fig. 2-8a) and vapor condenses if contrary

$$\mu_{l,H_2O} < \mu_{g,H_2O} \quad (2-2)$$

(Fig. 2-8b). In thermodynamic equilibrium of the two phases, the partial pressure of water vapor above the gas-liquid interface becomes equal to its saturation vapor pressure at saturation temperature  $T^*$ ,

$$P_{v,H_2O} = P_{v,H_2O}^*(T^*). \quad (2-3)$$

The relation  $P_{v,H_2O}^*(T^*)$  can e.g. be determined from the partly empirical Antoine<sup>7</sup> equation (with constants *A*, *B*, *C*), which is a result of the Clausius-Clapeyron<sup>8</sup> equation:

$$\log P_{v,H_2O}^* = A - \frac{B}{T + C}. \quad (2-4)$$

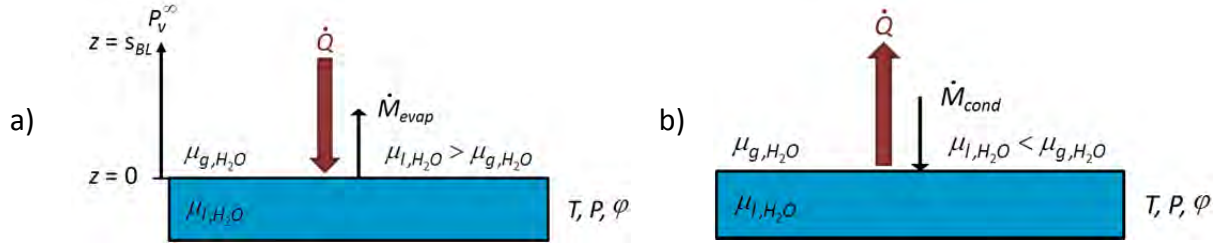
<sup>7</sup> Louis Charles Antoine (1825–1897)

<sup>8</sup> Rudolf Clausius (1822-1888) and Émil Clapeyron (1799-1864)

The Antoine equation is available for a broad range of pure substances and acceptably precise in a wide temperature range below the critical temperature. For water it reads:

$$\log \frac{P_{v,H_2O}^*}{P^0} = 8.07131 - \frac{1730.63}{T[^\circ\text{C}] + 233.426}, \quad (2-5)$$

(Perry's Chemical Engineers' Handbook 1997) with  $P^0 = 133.322$  Pa (for  $T = 1-100^\circ\text{C}$  under atmospheric pressure). If not otherwise mentioned, Eq. 2-5 is used to define thermodynamic phase equilibrium (Fig. 2-9a).



**Figure 2-8** Illustration of a) evaporation and b) condensation. Phase change is realized by heat transfer to and from the interface and vapor transfer away from the interface or towards the interface.

It is remarked that Eq. 2-5 provides the vapor pressure over a planar surface. Denoted by  $P_{v,H_2O}^{*,\infty}$ , this saturation vapor pressure is reduced above a curved surface (such as a liquid meniscus confined in the pore space of a PN):

$$P_{v,H_2O}^*(r) = \exp\left(-\frac{2\sigma(T)\cos\theta\tilde{V}_{l,H_2O}}{r}\frac{1}{\tilde{R}T}\right)P_{v,H_2O}^{*,\infty}, \quad (2-6)$$

according to W. T. Kelvin<sup>9</sup>. In Eq. 2-6,  $\tilde{V}_{l,H_2O} = \tilde{M}_{H_2O} / \rho_{l,H_2O}(T)$  is the molar volume of water (VDI Heat Atlas 2010). Figure 2-9b illustrates the dependency of  $P_{v,H_2O}^*(r)$  at constant temperature levels. It is found that the decrease of saturation vapor pressure is negligible in the range of pore sizes studied in this work, i.e.  $r \geq 1 \mu\text{m}$ ; but it is not negligible in nanoporous media ( $r < 1 \mu\text{m}$ ).

The change in the state of air from dry air ( $P_{v,H_2O} = 0$ ) to wet air ( $P_{v,H_2O} = P_{v,H_2O}^*$ ) is commonly illustrated by the Mollier<sup>10</sup> diagram (Fig. 2-10). In this

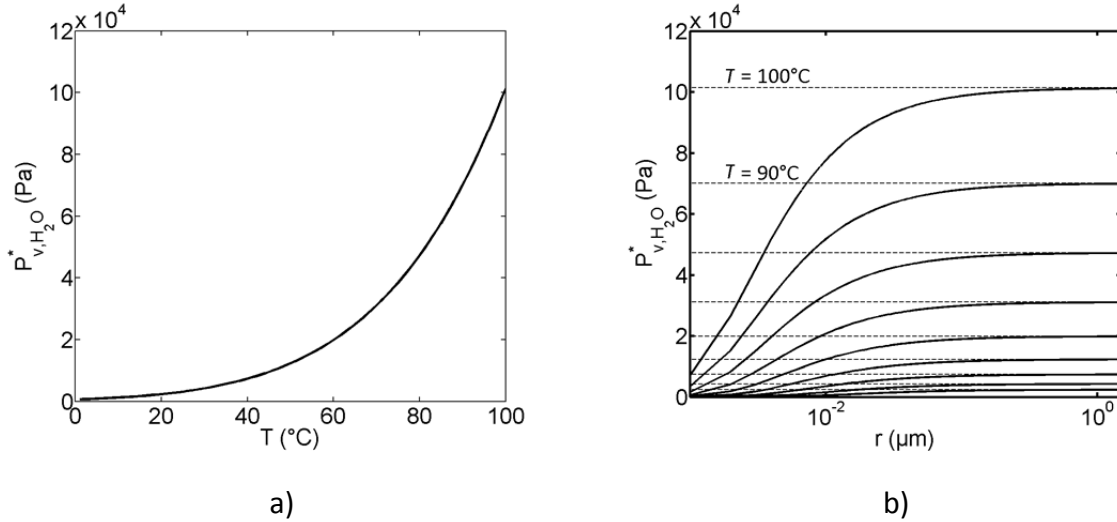
$$\varphi = \frac{P_{v,H_2O}}{P_{v,H_2O}^*}, \quad (2-7)$$

denotes the relative humidity and the mass loading of the gas phase with water is denoted:

$$Y_{H_2O} = \frac{\tilde{M}_{H_2O}}{\tilde{M}_{air}} \frac{P_{v,H_2O}}{P - P_{v,H_2O}} \sim 0.6215 \frac{P_{v,H_2O}}{P - P_{v,H_2O}} \quad (2-8)$$

<sup>9</sup> William Thompson Kelvin (1824-1907)

<sup>10</sup> Richard Mollier (1863-1935)



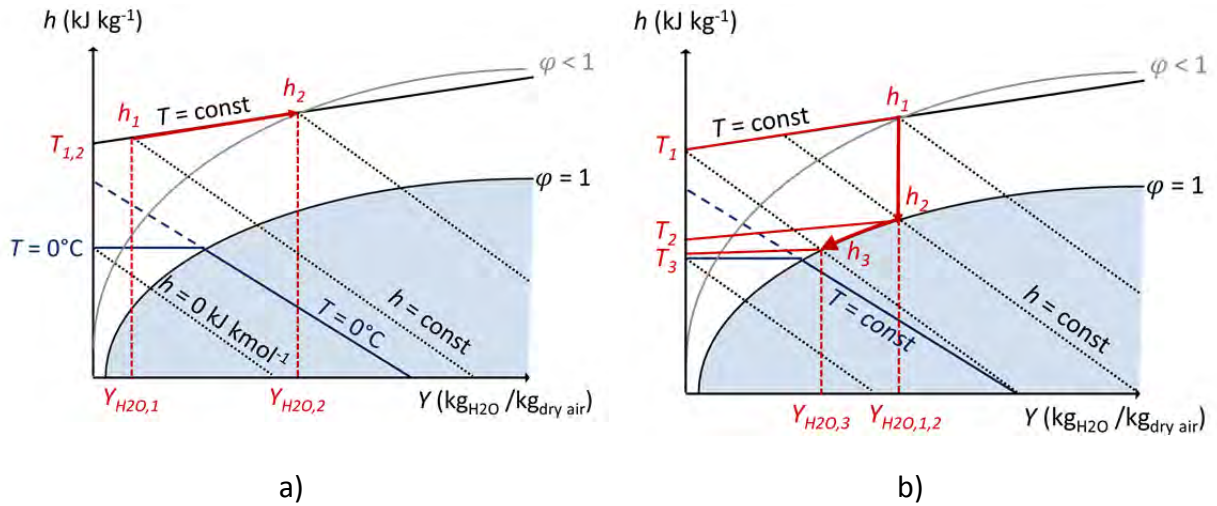
**Figure 2-9** a) Saturation vapor pressure curve of water. b) Semi-logarithmic plot of  $P_{v,H_2O}^*(r)$  for  $T = [20:10:100]^\circ\text{C}$ ,  $\tilde{R} = 8314.5 \text{ J kmol}^{-1} \text{ K}^{-1}$ ,  $\tilde{M}_{H_2O} = 18 \text{ kg kmol}^{-1}$ ,  $\cos\theta = 1$ ,  $\sigma(T)$  from Eq. 2-53,  $\rho_{l,H_2O}(T)$  from Eq. 2-55 and  $P_{v,H_2O}^{*,\infty}(T)$  from Eq. 2-5. The dashed lines indicate the saturation vapor pressure for  $r \rightarrow \infty$ , i.e. over a planar surface (Eq. 2.5).

From Eq. 2-7 follows that  $\varphi = 1$  in case of phase equilibrium with  $P_{v,H_2O} = P_{v,H_2O}^*$ , i.e. when air is saturated with water vapor.

In the situations discussed throughout this thesis, the phase change of air occurs at temporally constant temperatures. This is shown in the sketch of the Mollier diagram in Fig. 2-10a. Starting from  $T_1$ ,  $h_1$  and  $Y_{H_2O,1}$ , increase in the gas loading with water leads to an increase in air enthalpy at slightly increasing relative humidity and constant temperature, i.e.  $T_2 = T_1$  and  $Y_{H_2O,2} > Y_{H_2O,1}$  as well as  $h_2 > h_1$ . According to Fig. 2-10a the potential of air to take up water vapor is increased with increasing air temperature at constant initial absolute loading of air with water vapor. Figure 2-10b highlights the phase change associated with the condensation of water. Condensation occurs if the air temperature is decreased (i.e. from  $T_1$  to  $T_2$ ). This is especially observed in the case of vapor diffusion in the direction of decreasing temperature, i.e. in presence of local temperature gradients. Then, the air finally reaches the saturation state, i.e.  $\varphi = 1$ , and any further reduction of the air temperature from  $T_2$  to  $T_3$  leads to the decrease in  $Y_{H_2O}$ , which is indicated by the arrow along the line with  $\varphi = 1$  in Fig. 2-10b. The resulting  $\Delta Y_{H_2O} = Y_{H_2O,1,2} - Y_{H_2O,3}$  reflects the amount of water condensed from the wet air for the given temperature drop.

### 2.3.2 Vapor diffusion

In the situations discussed here, diffusion processes are a result of the partial pressure gradients of water vapor in air (Figs. 2-8a, 2-10). At low saturation vapor pressures, i.e. at low temperatures, and in presence of nearly equalized air partial pressure, diffusion can usually be described with the linear diffusion approach, according to Adolf Fick (1855) and



**Figure 2-10** Schematic illustration of the Mollier diagram of wet air. a) Increase in air saturation at constant temperature, b) decrease in air saturation as a consequence of condensation. The blue region marks the saturated zone (with  $\varphi \geq 1$ ).

Albert Einstein (1905)<sup>11</sup>,

$$\vec{M}_v = -A \frac{D\tilde{M}_v}{\tilde{R}T} \frac{dP_v}{dz}. \quad (2-9)$$

Integration within the boundaries of  $[P_v]_{P_v^*}^{P_v^\infty}$  and  $[z]_0^{s_{BL}}$  yields

$$\vec{M}_v = A\beta^0 \frac{\tilde{M}_v}{\tilde{R}T} (P_v^*(T) - P_v^\infty), \quad (2-10)$$

with  $\beta^0 = D/s_{BL}$  according to the film theory (Prandtl 1904, Bird, Stewart and Lightfoot 1960) (see below). It is emphasized that this applies in cases where the mean free path of the vapor molecules is much smaller than the pore size, thus if  $Kn \ll 1$ , which is assumed to apply in all the cases regarded in this work ( $Kn_{H_2O} = 0.099$  for  $T = 80^\circ\text{C}$  and  $d = 1 \mu\text{m}$ ).

However, the vapor pressure gradient between the phase boundary, with  $P_v = P_v^*(T)$  at position  $z = 0$ , and the bulk air phase, with  $P_v = P_v^\infty$  at  $z = s_{BL}$  (see Fig. 2-8a), induces a partial pressure gradient of air opposite to the vapor pressure gradient. This opposed partial pressure gradient forces the air to diffuse towards the gas liquid interface with the same rate as the countercurrent vapor diffusion,

$$\vec{M}_{air} \Big|_{z=0} = -\vec{M}_v, \quad (2-11)$$

in the case of binary diffusion. But since air is assumed to not be solved in the already saturated liquid phase, the mass flow rate of air must disappear at the phase boundary, which gives the boundary condition

$$\dot{M}_{air} = 0. \quad (2-12)$$

<sup>11</sup> Adolf Fick (1829-1901), Albert Einstein (1879-1955)

Consequently, an additional convective stream occurs co-currently to the vapor mass transfer. The flow rate of this drag stream follows from the condition given in Eq. 2-11, thus:

$$\dot{N}_v = \vec{N}_v + \frac{P_v}{P} \dot{N}. \quad (2-13)$$

with  $\dot{N} = \dot{N}_v$ . Thus, in contrast to Eq. 2-10 the mass transfer coefficient is in fact depending on the vapor partial pressure, and the mass flow rate of evaporation reads

$$\dot{M}_v = A \frac{D \tilde{M}_v}{\tilde{R} T} \frac{P}{P - P_v} \frac{dP_v}{dz}. \quad (2-14)$$

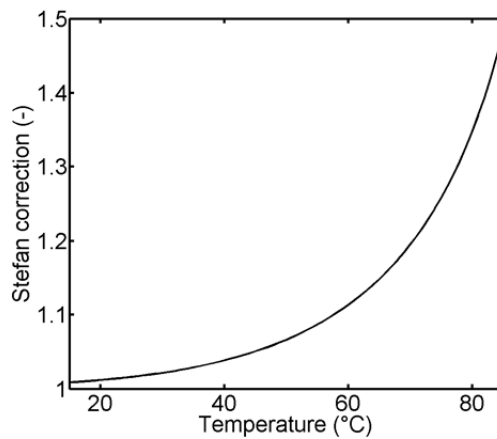
Equation 2-14 was first derived by Josef Stefan<sup>12</sup> in 1889 (Stefan 1889, Schirmer 1938). Integration within the given boundaries yields:

$$\dot{M}_v = A \frac{D}{s_{BL}} \frac{P \tilde{M}_v}{\tilde{R} T} \ln \frac{P - P_v^\infty}{P - P_v^*(T)}. \quad (2-15)$$

Comparison of Eq. 2-15 and Eq. 2-10 evidences the dependency of the mass transfer coefficient on the partial vapor pressure:

$$\beta = \beta^0 \frac{P}{P_v^*(T) - P_v^\infty} \ln \frac{P - P_v^\infty}{P - P_v^*(T)}. \quad (2-16)$$

This is illustrated in Fig. 2-11, which shows that the correction factor increases significantly with increasing temperature. Consequently, if not other mentioned, Eq. 2-15 is applied to compute vapor diffusion through empty PN pores and throats throughout the thesis.



**Figure 2-11** Temperature dependency of  $\left( \frac{P}{P_v^*(T) - P_v^\infty} \right) \ln \left( \frac{P - P_v^\infty}{P - P_v^*(T)} \right)$ .

### 2.3.3 Boundary layer

The term boundary layer (BL) denotes the gaseous viscous zone above a surface (Schluender 2004) (Fig. 2-8a). Based on the no-slip condition of the laminar convective air flow the BL can be assumed as a diffusive BL in which the above defined equations can be applied (Bird, Stewart and Lightfoot 1960). According to the BL theory first proposed by

<sup>12</sup> Joseph Stefan (1835-1893)

Ludwig Prandtl<sup>13</sup> in 1904 (Prandtl 1904), thickness  $s_{BL}$  of the diffusive BL developing along a horizontal straight wall as a result of the laminar flow of a fluid above the wall can be computed from:

$$\frac{s_{BL}}{L} \sim \frac{1}{\sqrt{Re}} = \sqrt{\frac{\nu}{Lv_{air}}}, \quad (2-17)$$

with  $L$  length of the wall,  $v_{air}$  velocity of the air flow and kinematic viscosity  $\nu$ . Blasius<sup>14</sup> proposed a proportional factor of 5 (Schlichting 1942, Perry's Chemical Engineers' Handbook 1997):

$$s_{BL} = 5 \sqrt{\frac{Lv}{v_{air}}}. \quad (2-18)$$

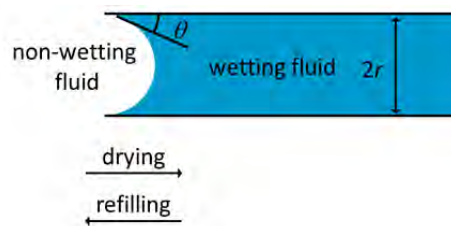
Accurate thickness of the BL cannot be computed since it increases asymptotically with increasing length of the wall (Schlichting 1942). Application of proportionality factor 5 gives the BL thickness, measured at a distance to the plate where

$$v_{air} = 0.99v_{air}^0, \quad (2-19)$$

with  $v_{air}^0$  maximum flow velocity of air.

### 2.3.4 Capillary invasion

Emptying of the pore space occurs due to combined evaporation of the liquid and capillary invasion of the gas phase, while refilling of the pore space is a result of condensation and invasion of the liquid phase (Fig. 2-12). Thus, the saturation is decreased in presence of evaporation and increased in presence of condensation. Due to this, invasion associated with drying can be related to drainage of the pore space, while refilling is related to imbibition.



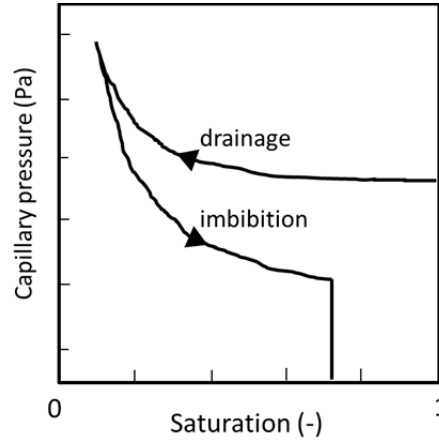
**Figure 2-12** Invasion mechanisms at pore level: piston-type propagation of the wetting phase (based on Fenwick and Blunt 1998).

Drainage and imbibition can usually not be regarded as reversible processes, because usually different capillary pressure thresholds must be assigned to the pores and the throats in drainage and imbibition processes (e.g. Mani and Mohanty 1999). Consequently, a hysteresis between the two processes is naturally observed (Fig. 2-13). From this follows that other invasion rules must apply for the refilling of the PN than for drying. Apart from that, both processes are assumed as piston-type invasions. (Although exceptions might be expected in

<sup>13</sup> Ludwig Prandtl (1875-1953)

<sup>14</sup> Heinrich Blasius (1883-1970)

presence of liquid films). According to Lenormand and Zarcone (1984) the piston-type displacement is very fast because the driving force, namely the pressure difference between the equilibrium capillary pressure and the liquid pressure, is very high. In contrast to this, the dynamic invasion of the pore space as a result of liquid pressure gradients within the liquid phase is rather slow. This is discussed in Section 2.3.5.



**Figure 2-13** Drainage-imbibition hysteresis curve based on Fenwick and Blunt (1998). Water is drained by a non-wetting liquid phase. Drainage stops at the minimum saturation with water ( $S > 0$ ). Re-invasion of the pore structure with water follows a different capillary pressure curve. The final saturation of the porous medium with water after imbibition is significantly lower than the initial saturation with water (which was  $S = 1$ ).

### 2.3.4.1 Emptying as a consequence of evaporation

Progressive evaporation of liquid is a result of vapor transport from the gas-liquid interface to the bulk air phase according to Eq. 2-15. This leads principally to the decrease of liquid volume:

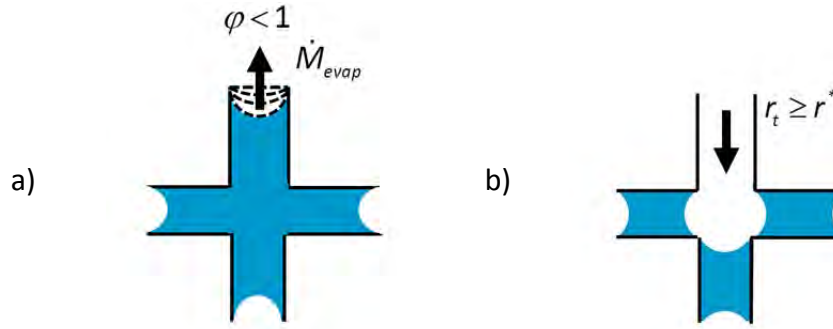
$$\dot{M}_{evap} = \dot{M}_v = \frac{\rho_l dV_l}{dt}, \quad (2-20)$$

and thus the invasion of the PN by the gas phase. The order of invasion thereby depends on the pore size distribution of the PN or more clearly on the invasion pressure thresholds associated with the curvatures of the gas-liquid interface in individual pores or pore throats. Based on Scherer (2004), the radius of curvature of interconnected menisci confined in a capillary porous medium is identical with constant liquid pressure inside the continuum liquid phase. Its dependency on relative humidity (Eqs. 2-6, 2-7, Fig. 2-9) is given by:

$$r = \frac{2\sigma(T)\cos\theta\tilde{V}_l}{\tilde{R}T\ln\phi} \quad (2-21)$$

Scherer (2004). The curvature decreases with progressive evaporation (Fig. 2-14). The entry pressure threshold at which the invasion of a meniscus can occur depends on its curvature. It is computed from the Young-Laplace equation:

$$P_c \approx P_c^* = \frac{2\cos\theta\sigma(T)}{r^*}. \quad (2-22)$$



**Figure 2-14** a) Decrease of meniscus curvature as a consequence of evaporation. Notice that all menisci connected in the liquid cluster have the same curvature if  $P_l = \text{const}$ . This is a basic assumption of the PNM presented in this thesis. b) If  $r = r^* = r_t$ , the throat is rapidly invaded by the gas phase. During this event, the overall saturation remains constant, i.e. no evaporation occurs. After invasion of the throat the liquid is re-distributed which is associated with a change in interface curvature and a change in liquid pressure as well.

In this,  $r^*$  denotes the radius of curvature of the meniscus confined in a pore throat with identical radius, i.e.  $r = r^* = r_t$ . Note the temperature dependency of the surface tension  $\sigma(T)$  in Eq. 2-22.

More generally, the curvature of a meniscus confined in a non-cylindrical capillary is given by:

$$\frac{1}{r} = \frac{1}{2} \left( \frac{1}{r_1} + \frac{1}{r_2} \right) \quad (2-23)$$

(VDI Heat-Atlas 2010) or rather

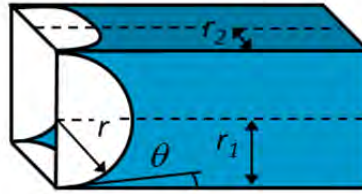
$$r_m = \frac{2r_1r_2}{r_1 + r_2}, \quad (2-24)$$

with mean meniscus radius  $r_m$  and  $r_1$  and  $r_2$  the main radii of curvature of the capillary (Fig. 2-15). Thus, in general it applies (e.g. Morrow 1970):

$$P_c = \sigma(T) \cos \theta \left( \frac{1}{r_1} + \frac{1}{r_2} \right). \quad (2-25)$$

Additionally to geometry dependence, the radius of curvature  $r$  is also a function of the wetting properties of the capillary wall, expressed by the contact angle  $\theta$  of the liquid phase with the capillary wall (see Fig. 2-15). Note that the wetting angle  $\theta$  also depends on temperature, surface roughness and contaminations as well (e.g. Palzer et al. 2001). From Eq. 2-25 follows that a fully developed (circular) liquid meniscus can be found for  $\cos \theta = 1$  or  $\theta \cong 0^\circ$  (i.e. in a hydrophilic medium); however, the curvature decreases with increasing  $\theta$  and reverses in the case of a hydrophobic capillary (i.e.  $\theta \geq 90^\circ$ ). In this thesis, perfect wettability of the PN is generally assumed, thus  $\theta = 0^\circ$  and  $\cos \theta = 1$ . An exception is made for the application of the continuous film model in Section 6.2.5.2 and Appendix B.4.





**Figure 2-15** Liquid meniscus confined in a rectangular capillary.

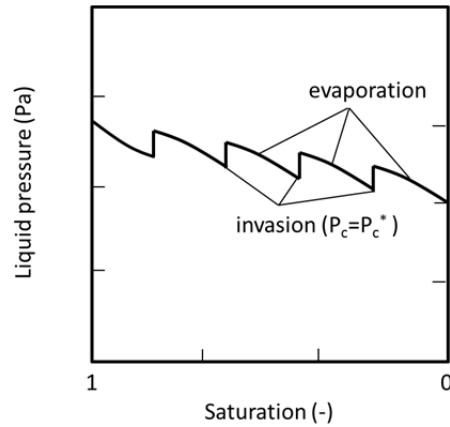
As a consequence of Eq. 2-22 or Eq. 2-25, the liquid pressure  $P_l$  inside the wetting liquid cluster to which the invading meniscus is connected is reduced compared to the surrounding pressure:

$$P_l = P - P_c \quad (2-26)$$

with atmospheric pressure  $P$ . This is in principle the cause of capillary ascension. Contrary, the liquid pressure would be increased in case of a non-wetting liquid with  $\theta > 90^\circ$  and thus reversed curvature of the gas-liquid interface resulting in capillary depression.

It is a basic assumption of the PNM presented in this thesis, that the liquid pressure inside pores and throats connected in a wetting liquid cluster is constant and thus that the radii of curvature of interface menisci belonging to this cluster are identical. From this can be concluded that all menisci are stationary during evaporation. This is based on the assumption of a no flow condition (Haines 1930). From this follows that the invasion of the PN must occur in discrete events (Fig. 2-14). More clearly, the pore space is gradually invaded in the order of increasing invasion pressure threshold  $P_c^*$ . These invasions are piston-type invasions and take place in significantly shorter time intervals than evaporation. The pressure measured in the liquid cluster is re-equilibrated during each invasion event, which is associated with a change of liquid curvature. The liquid pressure decreases if the curvature of the interconnected liquid menisci decreases compared to the situation before the invasion.

The sudden change of liquid pressure was first described by William B. Haines (Haines 1930); Morrow (1970) distinguishes the liquid pressure decrease associated with the decrease of interface curvature of liquid menisci (i.e. the isons in the publication of Morrow 1970) from the liquid pressure increase associated with the sudden invasion of a meniscus pore or throat (i.e. the rheons) (Fig. 2-16). It is highlighted that the change of saturation is negligible during the invasion of the pore or throat. From this follows that the liquid contained right before invasion of the particular candidate must be redistributed to the connected liquid menisci (Fig. 2-14). This can also lead to the phenomenon in which already empty pores and throats adjacent to the liquid cluster are suddenly refilled with liquid. This phenomenon is also called Haines jump (Haines 1930, Xu 2008, Moebius 2012, Berg et al. 2012). It is possible because the invasion pressure threshold of imbibition (see below) is lower than the pressure of the liquid cluster connected to the empty pore or throat. Such an event occurs without external work on the system but considerable energy is dissipated by the liquid redistribution (Berg et al. 2012). More clearly, after the redistribution the liquid must be removed from pores and throats with smaller width.



**Figure 2-16** Liquid pressure curve of drying of hydrophilic capillary porous media (based on Morrow 1970). As can be seen, evaporation and invasion occur subsequently. The change in saturation of the PN is associated with the evaporation period whereas during the invasion the saturation remains constant.

### 2.3.4.2 Refilling as a consequence of condensation

Condensation of vapor is a result of vapor transport through the partially saturated zone as shown in Fig. 2-6. This leads principally to the increase of liquid volume:

$$|\dot{M}_{cond}| = \frac{\rho_l dV_l}{dt} \quad (2-27)$$

The invasion pressure threshold for *piston-type invasion of throats* expressed in its general form is given by Eq. 2-25. From this follows that the empty throat is invaded by the liquid phase when the capillary pressure becomes equal or slightly smaller than the entry pressure threshold of the throat (Lenormand and Zarcone 1984, Mani and Mohanty 1999). It is remarked that this invasion event is based on the connectivity of the empty throat to any liquid filled pore or throat. This can also explain the Haines jumps over several pore rows as mentioned earlier in this chapter. As illustrated in Fig. 2-17, the imbibition of liquid can occur if the capillary pressure in a liquid cluster connected to an empty throat is similar as the invasion pressure threshold of this throat. In detail, in Fig. 2-17 the throat with the smallest entry pressure threshold for gas invasion is initially invaded. This is throat *k*. It is

$$P_{c,k}^* = \frac{2\sigma(T)}{r_k} \leq P_{c,j}^* = \frac{2\sigma(T)}{r_j}, \quad (2-28)$$

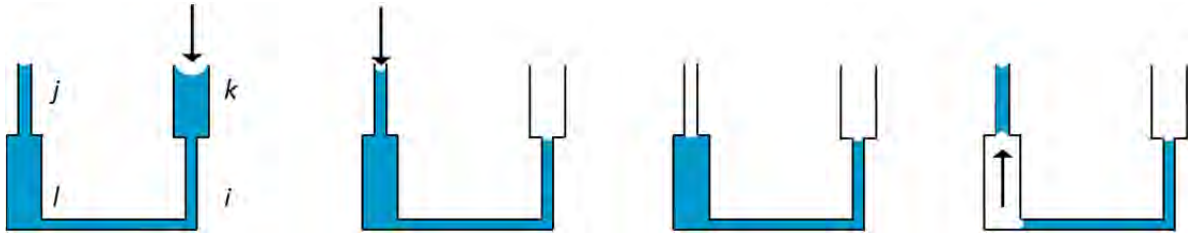
as  $r_k > r_j$ . The second invasion occurs in throat *j*, because

$$P_{c,j}^* = \frac{2\sigma(T)}{r_j} \leq P_{c,i}^* = \frac{2\sigma(T)}{r_i} \quad (2-29)$$

and  $r_j > r_i$ . But then, an instability occurs because the liquid meniscus position in throat *i* is unstable. More clearly,

$$P_{c,j}^* = \frac{2\sigma(T)}{r_j} > P_{c,i}^* = \frac{2\sigma(T)}{r_i} \quad (2-30)$$

as  $r_j < r_i$ . Consequently, invasion of throat *i* must be accompanied by liquid invasion in throat *j*. During this invasion the total saturation of the PN shown in Fig. 2-17 remains constant.



**Figure 2-17** Illustration of Haines jumps (based on Irawan 2006). ( $r_i < r_j < r_k < r_l$ )

*Piston-type invasion of pores*, however, depends on the number of saturated throat neighbors (Fig. 2-18). Thus, pore invasion is usually a process of cooperative invasion from several adjacent throats. As can be seen in Fig. 2-18, four different mechanisms ( $l_0$  to  $l_3$ ) are in principal distinguished (Lenormand and Zarccone 1984, Mogensen and Stenby 1998, Fenwick and Blunt 1998, Chapuis and Prat 2007). Mechanism  $l_0$  describes a situation, where a pore filled with the non-wetting fluid (this can be a mixture of air and vapor in PN drying processes) is invaded from the four adjacent liquid saturated throats. This situation can only occur if the non-wetting phase is compressible (Chapuis and Prat 2007) or if air and water vapor are solved in the liquid phase. Mechanism  $l_1$  describes a situation, where the empty pore is connected to one empty and three saturated throats. The pore is invaded when the capillary pressure is equal or greater than the threshold pressure

$$P_c \approx P_c^* = C \frac{\sigma(T)}{r^*} \quad (2-31)$$

with constant  $C$  depending on geometry, wetting properties and the number of adjacent throats (Fenwick and Blunt 1998). Exemplarily,

$$\frac{P_c^*}{\sigma(T)} = \frac{\sqrt{2}}{r_1} + \frac{2 \cos \theta}{r_2} \quad (2-32)$$

in a rectangular cross section (Lenormand and Zarccone 1984) (refer to Fig. 2-15 for a definition of  $r_1$  and  $r_2$ ). According to Fenwick and Blunt (1998) or Chapuis and Prat (2007) the displacement is most favored for mechanism  $l_1$ . Regarding mechanism  $l_2$ , two different situations can be distinguished: invasion of the pore from two neighboring throats forming a connected liquid wing inside the pore, i.e.  $l_{2,1}$ , and invasion of the pore from two opposite liquid throats, i.e.  $l_{2,2}$ . The constant  $C$  in Eq. 2-31 is slightly smaller for mechanism  $l_2$  than for  $l_1$  (Fenwick and Blunt 1998). In the rectangular cross section studied in Lenormand and Zarccone (1984) the threshold pressure of the  $l_{2,1}$  invasion event is:

$$\frac{P_c^*}{\sigma(T)} = \frac{\cos \theta}{r_1} - \frac{1}{\sqrt{2}r_1} + \frac{2 \cos \theta}{r_2}. \quad (2-33)$$

Invasion occurs when the liquid meniscus reaches the opposite side of the pore. Finally, mechanism  $l_3$  is characterized by invasion of the pore from a single liquid throat. According to Lenormand and Zarccone (1984),  $l_3$  is a very stable configuration wherefore invasion is assumed by snap-off (see below). (As shown by Chapuis and Prat (2007) the situation differs if the displacement of air by water occurs in a hydrophobic PN. Then  $l_3$  is most favorable and  $l_1$  never occurs).

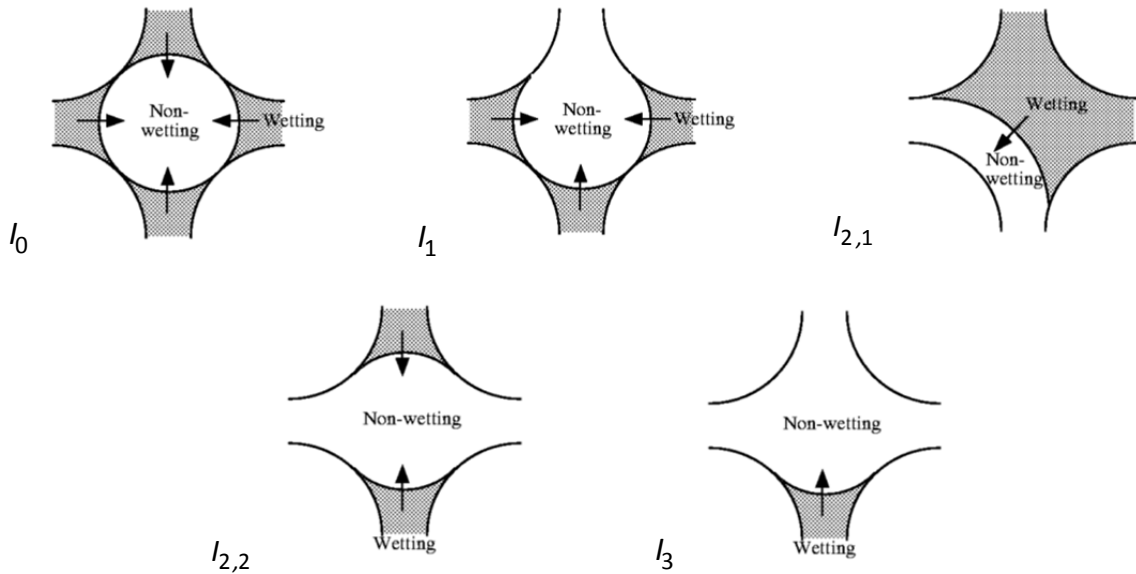
Mani and Mohanty (1999) provide a simple approach for cooperative pore invasion by piston-type advancing of the gas-liquid interface. This is:

$$P_c^* = \sigma(T) \left( \frac{1}{r^{eff}} + \frac{1}{r_2} \right), \quad (2-34)$$

with

$$r^{eff} = \frac{r_1}{1 + 0.25(N^{S=0} - 1)}. \quad (2-35)$$

In Eq. 2-35  $N^{S=0}$  represents the number of empty neighbor throats of the pore;  $r_1$  and  $r_2$  are the half width of the pore in consistence with Fig. 2-15.



**Figure 2-18** Basic invasion mechanisms of refilling of an empty pore as described by Lenormand and Zarcone (1984) and Mogensen and Stenby (1998). (Images are from Mogensen and Stenby 1998).

### 2.3.5 Liquid transport

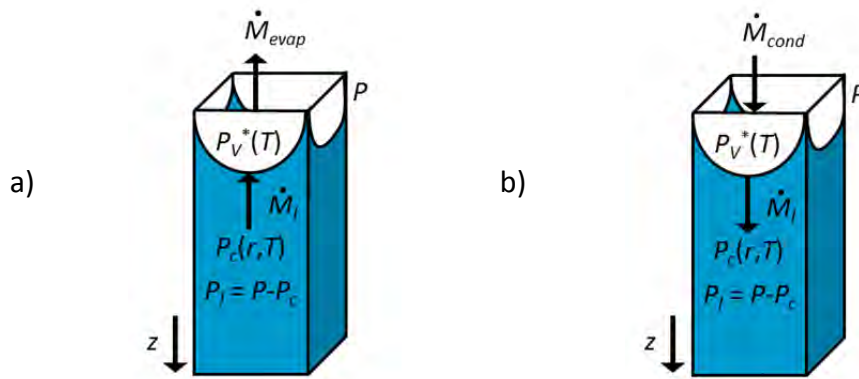
Liquid flow between pores and throats is computed based on the pressure difference between the fully developed liquid menisci which slowly recede as a consequence of evaporation and the stationary menisci to which the receding menisci are connected (as an invasion percolation process). The basics of dynamic invasion of PNs are briefly recalled in the following. Note that in most cases discussed in this thesis invasion of the PN is computed as a quasi-stationary process with discrete invasion events as described before. An exception is the discussion of experimental observations related to viscous effects presented in Chapter 4.

Starting from the two situations illustrated in Fig. 2-19, namely evaporation from an initially fully saturated capillary (Fig. 2-19a) and condensation in an initially fully empty capillary (Fig. 2-19b) the following equations are defined:

$$\dot{M}_l = \dot{M}_{evap} \quad (2-36)$$

in the capillary with net evaporation and

$$\dot{M}_{cond} = -\dot{M}_l \quad (2-37)$$



**Figure 2-19** Coupling of liquid and vapor transport at the gas liquid interface: a) evaporation of liquid and emptying of the capillary if  $\dot{M}_l < \dot{M}_{evap}$ , b) condensation and refilling of the capillary if  $\dot{M}_l < \dot{M}_{cond}$ .

in the capillary with net condensation. If these conditions are fulfilled, the liquid meniscus remains pinned at the entry of the capillary in both situations. The liquid flow  $\dot{M}_l$  is dictated by the liquid pressure difference between the meniscus confined in the capillary shown in Fig. 2-19 and any connected capillary containing a meniscus with significantly different radius of curvature. It is

$$\dot{M}_l = \frac{\rho_l \pi r^4}{8\eta L} \Delta P_l \quad (2-38)$$

(Hagen-Poiseuille equation). In this  $r$  denotes the mean radius of the capillary according to Fig. 2-15. From Eq. 2-38 follows that the liquid flow rate is proportional to the pressure difference  $\Delta P_l$ . In detail, if  $\Delta P_l$  is positive, liquid is transported towards the meniscus interface in Fig. 2-19; otherwise the transport is vice versa. According to Metzger et al. (2007b), liquid transport in a PN of interconnected liquid filled pores/throats is dictated by the pressure difference between menisci confined in pores/throats of significantly different widths, as

$$P_l = P - \sigma(T) \cos\theta \left( \frac{1}{r_1} + \frac{1}{r_2} \right), \quad (2-39)$$

with  $r_1$  and  $r_2$  according to Fig. 2-15. If the difference in the interface curvature is not high enough, invasion occurs simultaneously in several pores/throats meeting the mass balances given in Eqs. 2-36 and 2-37. Velocity of the moving menisci follows from:

$$\frac{dz}{dt} = \frac{\pm \dot{M}_l}{\rho_l A} = \frac{D}{L} \frac{\rho_v}{\rho_l} \ln \frac{P - P_v^\infty}{P - P_v^*} \quad (2-40)$$

according to Eq. 2-15 with  $\dot{M}_l = \dot{M}_{evap} = \dot{M}_v$  and with

$$\frac{dz}{dt} = \pm v = \frac{\pm \dot{V}_l}{A}, \quad (2-41)$$

$$\dot{V}_l = \frac{\dot{M}_l}{\rho_l} \quad (2-42)$$

and

$$\rho_v = \frac{P\tilde{M}_v}{\tilde{R}T}. \quad (2-43)$$

The time required to completely empty an initially full or refill an initially empty pore/throat of volume  $V$  can be computed from:

$$t = \frac{M_l}{\dot{M}_{evap}} = \frac{V\rho_l}{\dot{M}_{evap}} \quad (2-44)$$

or

$$t = \frac{V\rho_l}{|\dot{M}_{cond}|}. \quad (2-45)$$

### 2.3.6 Wetting liquid films

Liquid films are likely to be found in wettable porous systems with geometrical singularities such as crevices, corners and surface roughness. They are usually observed if  $\theta \ll 45^\circ$ . Figure 2-20a illustrates corner film flow in a square capillary. As can be seen, capillarity of the corners allows for capillary ascension and thus liquid transport from the meniscus to the tip of the capillary (Chauvet et al. 2009). This effect is promoted by corners with smaller radius (or smaller degree of roundness) (Chauvet et al. 2010) wherefore exemplarily triangular pore structures can sustain longer film regions than e.g. hexagonal pore structures at else identical conditions (Prat 2007). Contrarily, vapor diffusion from the meniscus to the tip is interrupted (if the drying process is isothermal) due to the presence of constant saturation vapor pressure inside the film region. It must be noted that the situation illustrated in Fig. 2-20a changes if a temperature gradient is applied. Then moisture is transferred by both, the wetting liquid film and vapor diffusion. This can induce a heat pipe effect, if the temperature is lower at the meniscus surface (Fig. 2-20b).

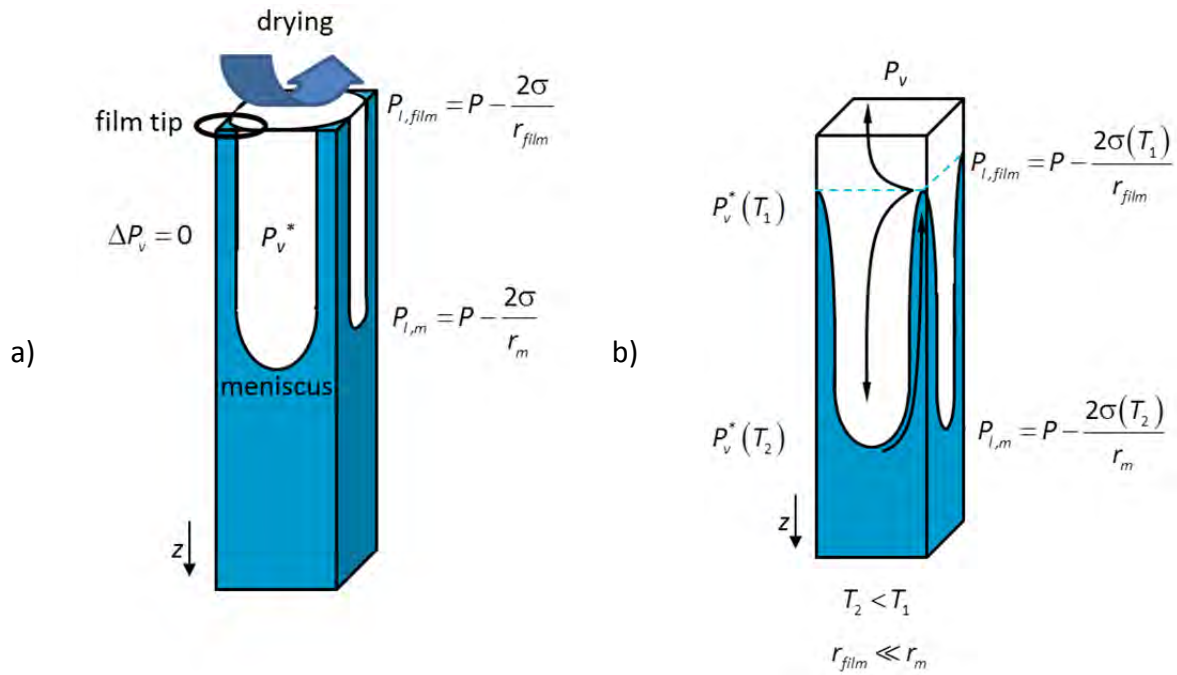
Modeling of liquid flow through corners is usually based on the work of Ransohoff and Radke (1988) and Zhou et al. (1997) (e.g. Mogensen and Stenby 1998, Bustos and Toledo 2003, Yiotis et al. 2005, Prat 2007) (see Appendix B.4 for more details). From these works follows that  $r_{film} \ll r_m$  to sustain liquid transport towards the film tip. If this is not fulfilled, the film tip must recede (in agreement with discussions referred to Eq. 2-38 above). According to Prat (2007) maximum extension of the film length depends on capillary number,

$$Ca = \frac{\Delta P_l}{\Delta P_c}, \quad (2-46)$$

with  $\Delta P_l$  from Eq. 2-38 and

$$\Delta P_c = 2\sigma \left( \frac{1}{r_{film}} - \frac{1}{r_m} \right) \quad (2-47)$$

(with  $\cos \theta = 1$ ) and the geometry of the corners.



**Figure 2-20** a) Illustration of film flow in isothermal drying (based on Metzger et al. 2007b); b) moisture transport in non-isothermal drying with  $T_1 > T_2$  (as exemplarily in convective drying). The heat pipe effect is highlighted for this situation.

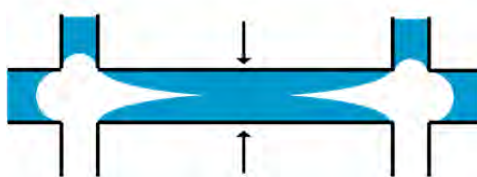
Obviously, the corner flow and the roughness flow can lead to a different order of invasion. Moreover, in contrast to the piston-type invasion in the absence of liquid films as described above, snap-off can occur if the pore (or throat) wall is wetted with liquid, both, due to surface roughness or due to the capillarity of the geometrical singularities of the pore space (Fig. 2-21). The term ‘snap-off’ describes the interruption of the continuity of the gas phase due to accumulation of liquid in the pore/throat center. The critical pressure for snap-off to take place in a square capillary is defined as

$$P_c^* = \frac{\sigma(\cos\theta - \sin\theta)}{r_1} \quad (2-48)$$

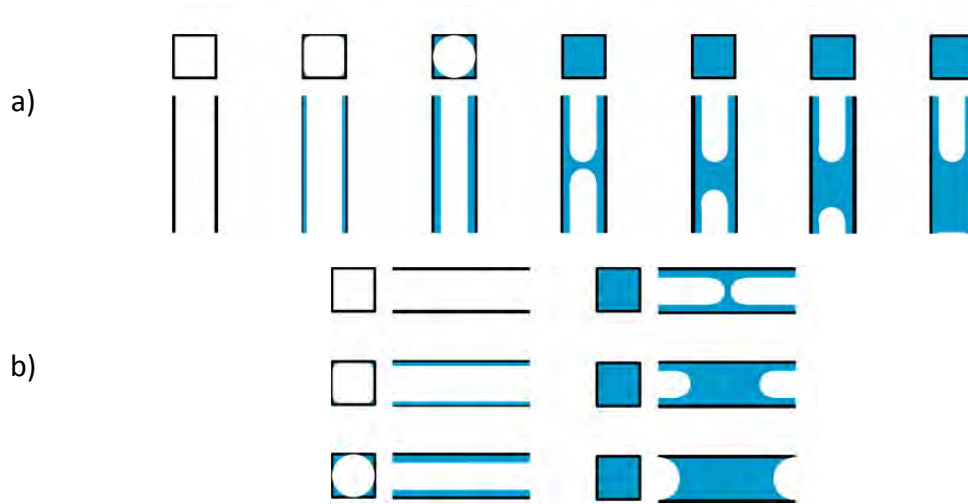
with  $r_1$  half width of the square capillary (Lenormand and Zarcone 1984, Fenwick and Blunt 1998) or as

$$P_c^* = \frac{\sigma \cos(\alpha + \theta)}{r \cos\alpha}, \quad (2-49)$$

with half angle of the throat corner  $\alpha$  and contact angle  $\theta$  (Bustos and Toledo 2003) (see Appendix B.4).



**Figure 2-21** Snap-off of the liquid phase. (Adopted from Lenormand and Zarcone 1984).



**Figure 2-22** Pore invasion in presence of wetting liquid films. a) vertical capillary, b) horizontal capillary. The images illustrate thickening of the liquid film until formation of a liquid bridge (i.e. the snap-off), which successively grows if liquid is added. The invasion process shown here is related to capillary condensation; similar patterns are expected in imbibition in presence of liquid films. (Images adopted from Bustos and Toledo 2003).

Contrary to the piston-type invasion, snap-off is a very slow displacement process (Lenormand and Zarcone 1984). Refilling of a throat based on the snap-off mechanism is shown in Fig. 2-22 (Bustos and Toledo 2003).

## 2.4 Temperature dependency of vapor diffusion and capillary invasion

Temperature gradients arise in drying processes since the evaporation of liquid is an endothermic process (and the inverse process of condensation is exothermic). Moreover, temperature gradients are usually externally imposed to supply energy for evaporation (Fig. 2-8) and to reduce drying time. However, transport and equilibrium equations involve physical parameters which are temperature depending. These temperature dependencies are summarized in the following. Based on them, this work discusses the specific pore level phenomena resulting from temperature variation in non-isothermal drying processes (Chapters 4 and 6).

### 2.4.1 Gas side

#### 2.4.1.1 Saturation vapor pressure

Temperature dependency of saturation vapor pressure was given in Section 2.3.1 and Fig. 2-9. Variance of saturation vapor pressure in a non-isothermal PN with local temperature distribution induces a diffusive vapor flow from menisci with high saturation vapor pressure  $P_V^*(T_2)$  to menisci with lower saturation vapor pressure  $P_V^*(T_1)$ , according to



$$\dot{M}_v = A \frac{D}{L} \frac{P \tilde{M}_v}{\tilde{R} T} \ln \frac{P - P_v^*(T_1)}{P - P_v^*(T_2)}. \quad (2-50)$$

From this follows that vapor can diffuse through the non-isothermal partially saturated zone of the PN (refer to Fig. 2-6b). This is in contrast to isothermal drying, where vapor diffusion through the partially saturated zone is usually neglected.

#### 2.4.1.2 Diffusion coefficient

Diffusion coefficients of water vapor-air mixtures have intensively been studied. The relevant works generally propose an empirical relation of diffusivity, temperature and pressure of the form (Luikov 1958):

$$D = D^0 \left( \frac{T}{T^0} \right)^c \frac{P}{P^0}. \quad (2-51)$$

In this,  $T^0$  denotes the reference temperature (usually  $T^0 = 273$  K),  $P^0$  the reference pressure and  $D^0$  the experimentally determined diffusion coefficient under the reference conditions. Parameters estimated by various authors are given in Table 2-1. A comparison of the results is provided by Fig. 2-23. Additionally, the curve from Fuller (1969),

$$D \left[ \text{cm}^2 \text{s}^{-1} \right] = \frac{0.00143 (T[\text{K}])^{1.75} \left( \tilde{M}_{\text{H}_2\text{O}}^{-1} + \tilde{M}_{\text{air}}^{-1} \right)^{1/2}}{P \sqrt{2} \left( \left( \sum V_{\text{H}_2\text{O}} \right)^{1/3} + \left( \sum V_{\text{air}} \right)^{1/3} \right)^2}, \quad (2-52)$$

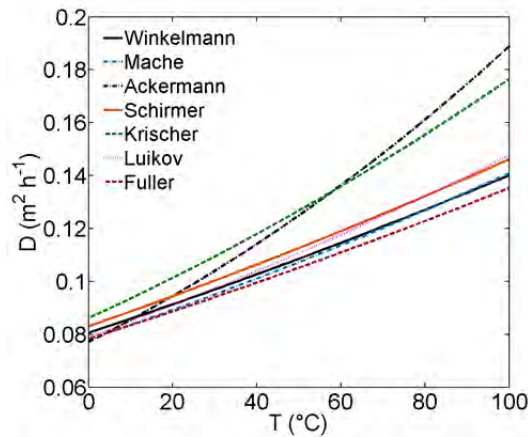
(VDI Heat Atlas 2010) is plotted in Fig. 2-23 (with  $\sum V_{\text{H}_2\text{O}} = 13.1$  and  $\sum V_{\text{air}} = 19.7$ ,  $\tilde{M}_{\text{H}_2\text{O}} = 18 \text{ g mol}^{-1}$ ,  $\tilde{M}_{\text{air}} = 28.95 \text{ g mol}^{-1}$  and  $P = 1 \text{ bar}$ ).

From Eq. 2-52 follows  $D^0 = 0.0784 \text{ m}^2 \text{ h}^{-1}$  for  $T^0 = 273 \text{ K}$  and  $P^0 = 1 \text{ bar}$ .

Surasani (2009) proposes the diffusion coefficient by Schirmer (1938) in his study of non-isothermal drying. Schirmer, however, conducted his experiments under isothermal conditions with temperatures varying between 29.9°C and 93.6 °C. He used a classical diffusion pipe but considered also the heat loss due to evaporation and the resulting lowering of saturation vapor pressure for the definition of his parameters. However, Philip and De Vries (1957) postulated that the water vapor diffusivity estimated under isothermal conditions differs significantly from the diffusivity in a temperature gradient. They applied the correlation from Krischer and Rohnlalter (1940) in their model. Krischer and Rohnlalter (1940) performed their experiment using two differently tempered heating plates separated by a rubber ring. The diffusion coefficient was estimated from the transferred liquid volume and the saturation pressure difference between the two plates (Luikov 1958, Krischer 1992). Diffusivities according to Krischer and Rohnlalter (1940) are generally higher than the values obtained from the other models (except that by Ackermann (1934) which gives even higher values at temperatures above 58°C, Fig. 2-23) (also refer to Appendix B.1). If not other mentioned, this thesis follows the proposal of Surasani (2009), wherefore the correlation of Schirmer (1938) is applied. For the study of vapor transfer through the partially saturated zone of a PN with imposed positive thermal gradient also the correlation of Krischer and Rohnlalter (1940) is applied with the purpose to show the impact of higher diffusivities on condensation.

**Table 2-1** Experimentally estimated parameters of Eq. 2-51. ( $P^0 = 1 \text{ at}^{15}$ ,  $T^0 = 273 \text{ K}$ ).

Author(s)	$D^0 [m^2 h^{-1}]$	$C$
Winkelman (1889)	0.0805	1.774
Mache (1910)	0.078	1.890
Ackermann (1934)	0.077	2.87
Schirmer (1938)	0.083	1.81
Krischer, Rohralter (1940)	0.086	2.3
Luikov (1958)	0.079	2



**Figure 2-23** Temperature dependent diffusivity of water-vapor in air at atmospheric pressure ( $P = 1 \text{ bar}$ ), computed from the correlations given in Eqs. 2-51 and 2-52 and the coefficients in Table 2-1.

## 2.4.2 Liquid side

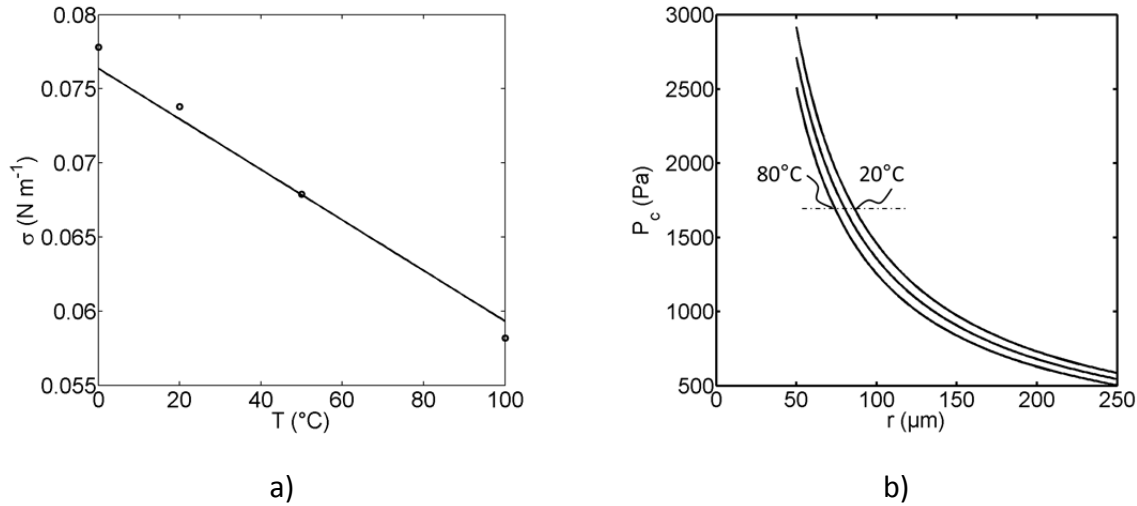
### 2.4.2.1 Surface tension

The temperature dependent surface tension of water is obtained following the proposal of Surasani et al. (2008b):

$$\sigma(T) [Nm^{-1}] = A - BT [^{\circ}C], \quad (2-53)$$

with  $A = 7.636 \cdot 10^{-2} \text{ N m}^{-1}$  and  $B = 1.704 \cdot 10^{-4} \text{ N m}^{-1} \text{ }^{\circ}C^{-1}$  (also refer to Perry's Chemical Engineers' Handbook 1997). This relation is plotted in Fig. 2-24a. The zero point of the function is at around  $448^{\circ}C$  (Eq. 2-53). It is found that the function computed with Eq. 2-53 slightly differs

<sup>15</sup> The unit *at* refers to the technical atmosphere.  $P^0 = 1 \text{ at} = 1 \text{ kg cm}^{-2} = 0.98067 \text{ bar}$ . This unit is not applied (in Germany) since January 1<sup>st</sup> 1978.



**Figure 2-24** a) Temperature dependency of surface tension. The solid line represents the result of Eq. 2-53. Points are from VDI Heat Atlas (2010). b) Capillary pressure dependency on capillary radius  $r$  for  $T = 20^\circ\text{C}$ ,  $60^\circ\text{C}$  and  $80^\circ\text{C}$ . The capillaries are perfectly wetting with water ( $\cos \theta = 1$ ). The curves are computed with Eq. 2-53 and Eq. 2-25 for varying  $r$ .

from the values given in VDI Heat Atlas (2010). However, good agreement is found in the interesting temperature range ( $T = 20 - 80^\circ\text{C}$ ).

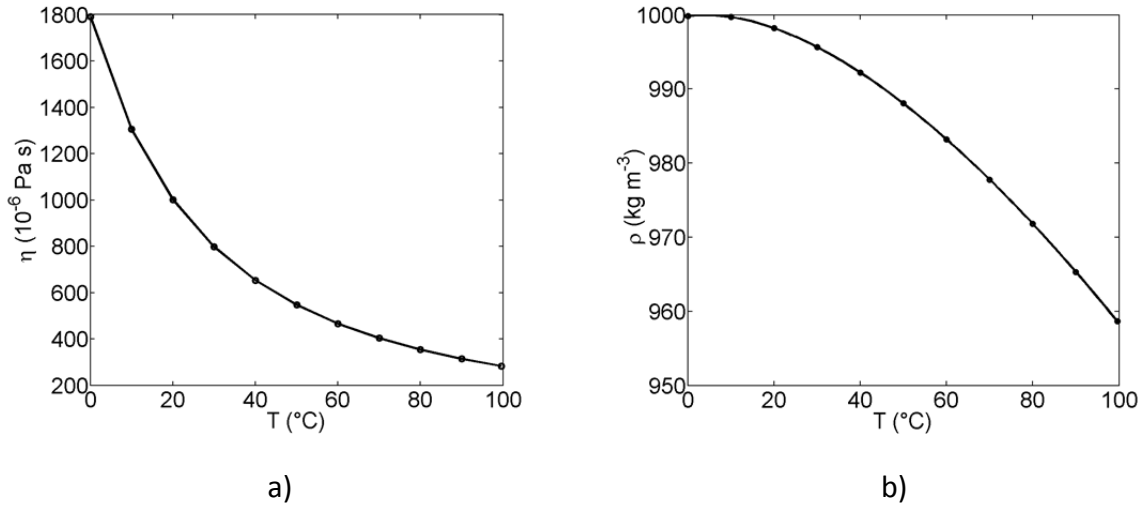
According to Fig. 2-24a, surface tension decreases with increasing temperature. As will be discussed in this thesis, this has a direct impact on capillary pressure in Eq. 2-25 if  $\theta = \text{const}$ . This can affect the order of emptying if temperature variation throughout the PN is high enough, namely, if the thermally affected smaller pores/throats produce a lower capillary pressure than the thermally affected larger pores/throats. This is illustrated in Fig. 2-24b, where capillary pressure is plotted against the radius of cylindrical capillaries at different temperature levels. As can be seen, the capillary with radius  $r = 85.9 \mu\text{m}$  and  $T = 80^\circ\text{C}$  can produce identical capillary pressure as the colder capillary ( $T = 20^\circ\text{C}$ ) of size  $r = 100 \mu\text{m}$ . This means, that both capillaries would compete in the invasion process of a PN. This is in contrast to isothermal capillary invasion, discussed in Section 2.3.4, where the order of invasion is always with decreasing capillary radius.

#### 2.4.2.2 Dynamic liquid viscosity and liquid density

Dynamic invasion of the PN computed with Eq. 2-38 requires knowledge about the temperature dependency of the dynamic liquid viscosity. The following equation is given in VDI Heat Atlas (2010):

$$\eta_l(T) [\text{Pa s}] = E \exp \left( A \left( \frac{C-T}{T-D} \right)^{1/3} + B \left( \frac{C-T}{T-D} \right)^{4/3} \right). \quad (2-54)$$

with  $A = 0.45047$ ,  $B = 1.39753$ ,  $C = 613.181^\circ\text{C}$ ,  $D = 63.697^\circ\text{C}$  and  $E = 6.896 \cdot 10^{-5} \text{ Pa s}$  for liquid water. As can be seen in Fig. 2-25a, dynamic viscosity of liquid water drastically decreases with increasing temperature. From this follows that dynamic invasion of the PN might be facilitated in warmer pores/throats.



**Figure 2-25** a) Temperature dependency of dynamic viscosity of liquid water according to VDI Heat Atlas (2010). b) Temperature dependency of liquid density (VDI Heat Atlas 2010).

Temperature dependency of liquid density is e.g. given by the virial equation,

$$\rho_l(T) \left[ \text{kgm}^{-3} \right] = \frac{A + BT + CT^2 + DT^3 + ET^4 + FT^5}{1 + GT}, \quad (2-55)$$

(VDI Heat Atlas 2010) with virial coefficients  $A = 999.83952^{\circ}\text{C}$ ,  $B = 16.952577^{\circ}\text{C}^{-1}$ ,  $C = -7.9905127 \cdot 10^{-3}^{\circ}\text{C}^{-2}$ ,  $D = -4.6241757 \cdot 10^{-5}^{\circ}\text{C}^{-3}$ ,  $E = 1.0584601 \cdot 10^{-7}^{\circ}\text{C}^{-4}$ ,  $F = -2.8103006 \cdot 10^{-10}^{\circ}\text{C}^{-5}$  and  $G = 0.0168872^{\circ}\text{C}^{-1}$  and  $T$  in  $^{\circ}\text{C}$ . This relation is illustrated in Fig. 2-25b. As can be seen, local liquid density differences can evolve in a non-isothermal PN.

## 2.5 Micro-macro coupling of non-isothermal drying

This section summarizes the pore scale effects with their relevance for macroscale drying. Knowledge about the coupling of the pore level transport and the macroscopically observed drying behavior can be essential for control of drying processes. Moreover, the internal structure of the drying front is vitally important for the overall drying process, as it dictates not only evaporation rate and drying time but also product quality after drying. Exemplarily, the distribution of salt or catalyst particles or the wetting properties of membranes used in fuel cells depend on the evolution of the gas-liquid interface(s) during drying.

### 2.5.1 Drying front structure

Invasion of a liquid saturated PN (or any porous medium) by the gas phase leads to the formation of a partially saturated zone, in which liquid filled pores/throats and gas filled pores/throats coexist, as already presented in Section 2.2.3. The gradual invasion leads to a fractal appearance of the drying front on the pore scale. As discussed before, several mechanisms provoke stabilization of the drying front on the macroscale. Correlations of the

drying front width can be found in theoretical physics (Jurin's<sup>16</sup> height, Hagen-Poiseuille equation) or statistical physics (i.e. percolation theory). Figure 2-26 shows the evolution of drying fronts in PNs under non-stabilized (Fig. 2-26a) and stabilized (Fig. 2-26b) conditions. As can be seen the 2-phase zone is significantly smaller in the stabilizing regime which leads to the formation of a long dry zone, in which vapor diffusion controls mass transfer.

### 2.5.2 Drying curve and drying rate curve

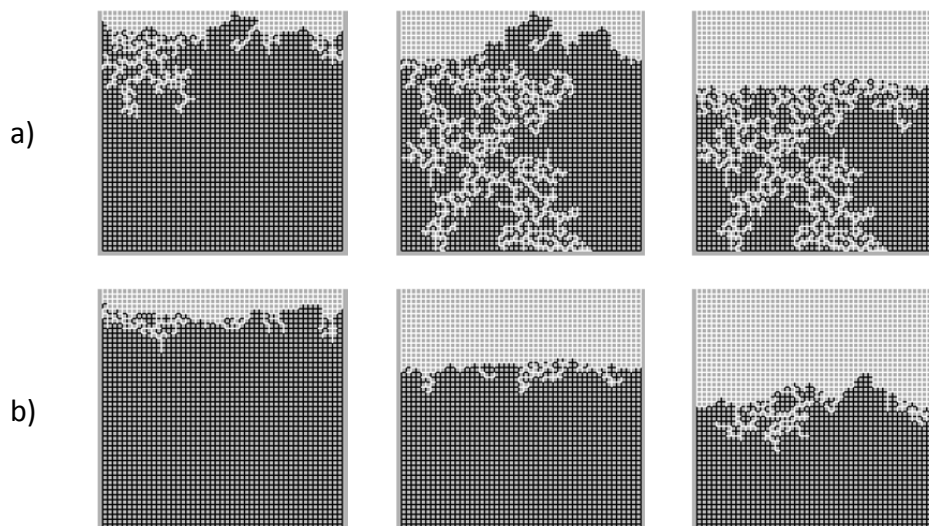
The drying curve and the drying rate curve macroscopically describe evolution of the drying process. They illustrate the decrease in liquid saturation over time (drying curve) as well as the drying rate as a function of liquid saturation (drying rate curve). With this, it is possible to predict overall drying time as well as the drying periods (see below). Usually, typical forms of both curves can be associated with different pore scale phenomena controlling the drying process.

#### *Drying curve*

The drying curve represents the time dependent liquid saturation of the PN:

$$s(t) = \frac{V_l(t)}{V_{tot}}. \quad (2-56)$$

In this  $V_{tot}$  represents the total void volume of the PN. Figure 2-27a shows the two drying curves corresponding to Fig. 2-26. From this, the overall drying time  $t(S = 0)$  as well as the drying rate  $dS/dt$  can be derived (see below). It can be seen that the overall drying time is significantly shorter if the viscous effects are disregarded.



**Figure 2-26** Phase distributions in isothermal PNs: a) Drying front evolution if stabilizing due to gravity and viscosity is disregarded (also referred to as non-viscous drying); computed from the invasion rules discussed in Section 2.3.4. b) Viscous stabilized drying front; computed from the concept discussed in Section 2.3.5. Drying from top; all other sides impermeable for mass transfer. (Liquid in black, gas phase in white and solid in gray).

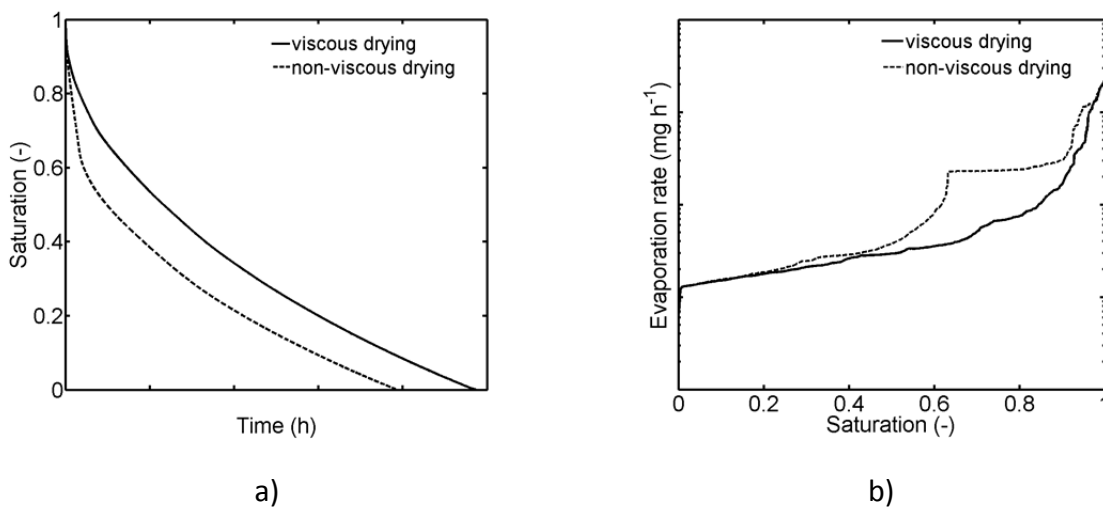
<sup>16</sup> James Jurin (1684-1715)

*Drying rate curve*

Slope of the drying curve in Fig. 2-27a represents the overall drying rate, i.e.

$$\dot{M}_{evap} = V_{tot} \rho_l \frac{dS}{dt}, \quad (2-57)$$

or the per unit time removed amount of liquid. Figure 2-27b shows the two drying rate curves referring to Fig. 2-26. As can be seen, slope of the curves is governed by the specific pore level effects. A longer period of initially high drying rates is obtained if the drying front is not stabilized by viscous effects. This is explained with the longer period of liquid supply to the PN surface, whereas in the stabilized regime, liquid connectivity to the surface is rapidly interrupted leading to the limitation of mass transfer by vapor transport resistances associated with the increasing dry zone.



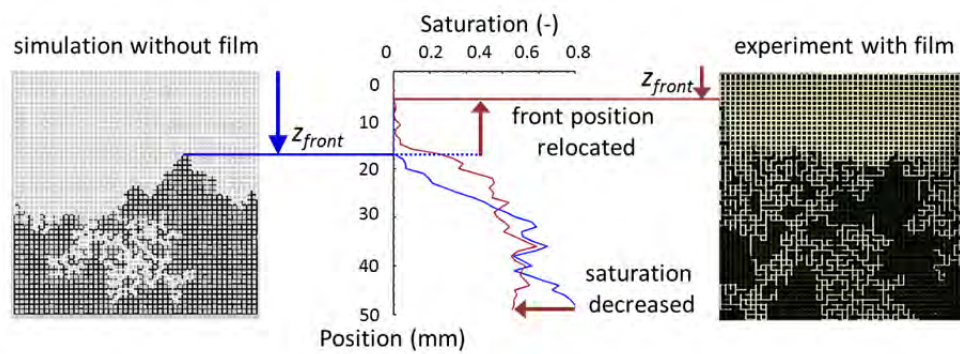
**Figure 2-27** a) Drying curves, b) drying rate curves from the situations shown in Fig. 2-26.

**2.5.3 Impact of liquid films**

Presence of wetting liquid films significantly impacts on the structure of the distribution of liquid and vapor phase. As illustrated in Fig. 2-28, position of the evaporation front profits from the formation of liquid films. From this follows that the extent of the dry region, in which vapor diffusion controls mass transfer, is reduced. Additionally, in presence of liquid films, saturation at the bottom of the PN can in general be decreased compared to drying without liquid films. This is based on the interconnectivity of liquid clusters in presence of liquid films and on sustained liquid transport from clusters at the bottom to the evaporation front. Both effects allow for a significant decrease in drying time. Extent of the film region and thus impact on the drying rate and overall drying time depends on capillary number and Bond number. The impact of capillary number is studied e.g. in Lenormand and Zarcone (1984), the impact of gravity is studied in Chauvet et al. (2009). For this thesis, especially the work of Lenormand and Zarcone (1984) is of interest, while gravity effects are disregarded in this study.

Lenormand and Zarcone (1984) investigated the role of roughness and edges during imbibition in 2-dimensional etched microfluidic networks with rectangular throats. In their article, the authors highlight the impact of capillary number on moisture transfer: at high

flow rates ( $Ca > 10^{-4}$ ) liquid flow is only through the bulk phase of throats, at low flow rates ( $10^{-6} > Ca > 10^{-9}$ ) the wetting fluid flows along corners and ducts and at very low flow rates ( $Ca < 10^{-9}$ ) the wetting fluid flows along the surface roughness. Dependency of capillary number on the drying kinetics (Eq. 2-46) implies that capillary number must decrease with progressive desaturation of the PN since the evaporation rate naturally decreases during the drying process (also refer to Fig. 2-27). From this follows that the impact of viscous forces decreases. Consequently, phase distributions show a widening of the front with decreasing drying rates (also refer to Fig. 2-26). Impact of the film transport in a wettable PN grows analogously. Long liquid film regions can be found in case of low viscosity, high variance between width of the bulk pores and throats and geometric singularities as well as low evaporation rates (i.e. especially at the end of drying). Contrarily, the drying front sharpens for higher capillary numbers (situation of a stabilized drying front discussed above) and the distance over which liquid films can support liquid is also decreased.



**Figure 2-28** Schematic illustration of the film effect. The evaporation front position is relocated closer to the open PN side and additionally the saturation at the bottom of the PN is decreased in presence of liquid films. (Liquid in black and gas phase in white. The solid appears in gray on the simulated image and in black on the experimental image).

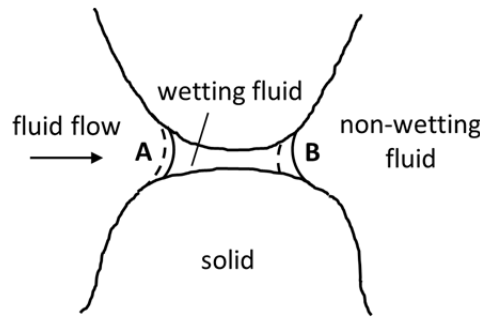
#### 2.5.4 Impact of thermal gradients

Temperature dependency of thermodynamic equilibrium and drying kinetics induces several interesting pore level phenomena. On the gas side, increase of saturation vapor pressure at higher temperature levels (Eq. 2-5) positively affects the driving force of evaporation. Furthermore, a vapor pressure gradient develops between menisci at different temperature levels (Eq. 2-50) which allows for mass transfer inside the partially saturated zone. Additionally, the transferred vapor condenses at the colder menisci due to the decreased saturation vapor pressure (also refer to Fig. 2-10b for an explanation of the condensation effect). On the liquid side, invasion is temperature affected due to the temperature dependency of surface tension (Eqs. 2-25 and 2-53) (Fig. 2-29).

A more detailed description of the thermally affected transport phenomena is given in Fig. 2-30 which exemplarily illustrates two connected capillaries at different temperatures. If the capillaries have identical radii (Fig. 2-30a), the capillary with higher temperature is first invaded, because

$$P_{c,2} = \frac{2\sigma(T_2)}{r} = P_c^* < P_{c,1} = \frac{2\sigma(T_1)}{r}, \quad (2-58)$$

as  $\sigma(T_2) < \sigma(T_1)$ .



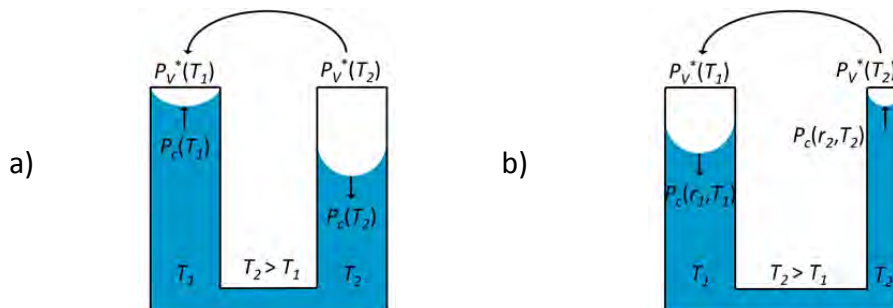
**Figure 2-29** Coupled pore level vapor and liquid transport in a non-isothermal porous medium (adopted from Phillip and De Vries 1957). The vapor diffusing towards the meniscus at position A condenses, leading to an increase of meniscus curvature. At the same time, liquid evaporates at position B, leading to a decrease of meniscus curvature and receding of this meniscus. Liquid pumping is expected from the meniscus with the smaller curvature (fully developed) at position B to the meniscus with the flat curvature (at position A). This coupled moisture transfer can lead to an increased effective diffusivity (if liquid and vapor migrate into the same direction).

If, contrary, the connected capillaries have different radii (Fig. 2-30b) a situation can occur where the smaller capillary can produce a higher capillary pressure than the larger capillary, so that the liquid transport is reversed:

$$P_{c,2} = \frac{2\sigma(T_2)}{r_2} > P_{c,1} = \frac{2\sigma(T_1)}{r_1}, \quad (2-59)$$

as  $\sigma(T_2)/r_2 > \sigma(T_1)/r_1$  and  $r_2 \ll r_1$ . This situation is also known as the heat pipe effect and it can be found in presence of capillary liquid films (which have usually a significantly smaller radius than the bulk menisci).

From the macroscopic point of view, the combined liquid and vapor transport in the direction of decreasing temperature (as shown in Fig. 2-30a) can have a stabilizing effect similar as in Fig. 2-26b, if a negative temperature gradient is imposed on the PN. Contrary, a positive temperature gradient leads to destabilization of the liquid phase (also refer to Fig. 1-5).



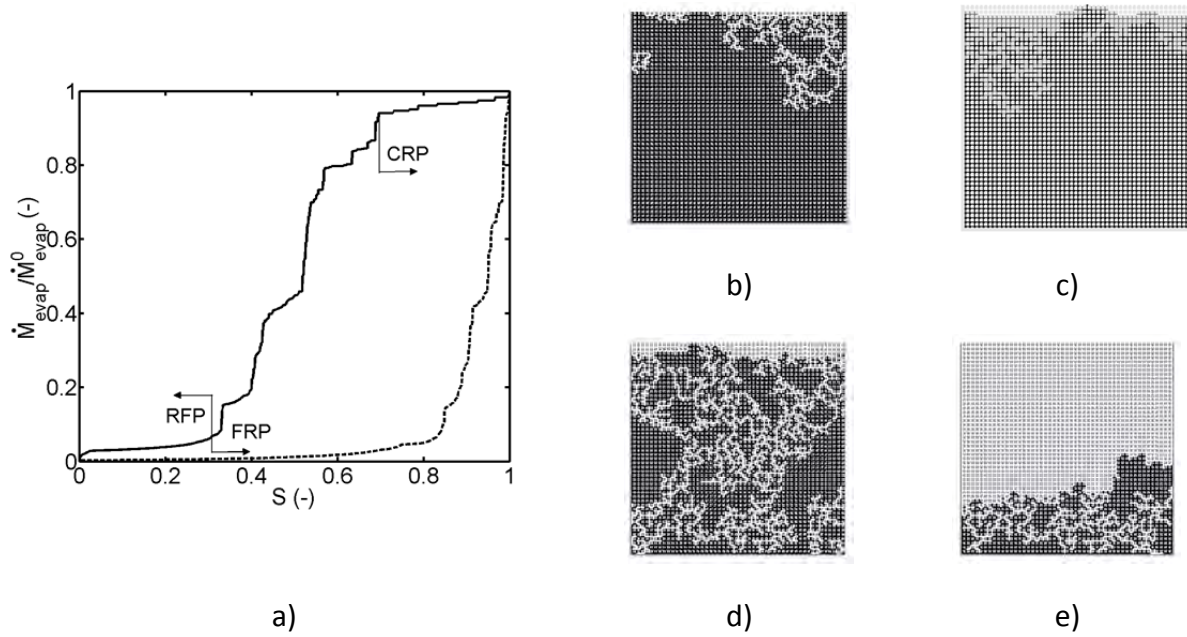
**Figure 2-30** Illustration of the heat pipe effect. a) If two connected capillaries have identical radius, both, liquid and gas transport are directed towards the capillary with lower temperature. This is the situation at a stabilized drying front. b) If, however, the warmer capillary is significantly smaller (as is the case in capillary liquid films) a heat pipe effect is induced at the drying front.



### 2.5.5 Drying periods

The drying process usually occurs in several drying periods (e.g. Huang 1979, Laurindo and Prat 1998). The discrimination of different periods of drying is traditionally based on the form of the drying rate curve, as e.g. shown in Fig. 2-31a. However, occurrence and duration of these periods depend on the governing pore level mass transfer phenomena during the individual drying periods, because these affect the pore scale liquid distribution and thus the drying rate curves. This is in detail discussed in Chapters 4 and 6 of this thesis.

The first drying period classically marks drying of the PN like a free liquid surface, thus with almost constant drying rate at the initial high level (solid line in Fig. 2-31a). Therefore, this period is also denoted the 'constant rate period' (CRP). In this period the PN is at wet-bulb temperature if the enthalpy of vaporization is supplied by convective dry air. As demonstrated by Metzger et al. (2007b), Surasani et al. (2010) and Prat (2007) a long CRP benefits from relatively small capillary numbers, film flow, and a favorable temperature field. Additionally, a bimodal pore size distribution with interpenetration of large and small pores/throats contributes to the existence of a CRP. This is explained with the long duration of liquid connectivity to the PN surface (Fig. 2-31b,c). It is remarked that in 2D PN simulations the drying rate naturally starts decreasing with the invasion of the first surface pores and throats (Fig. 2-31b). This is in contrast to experimental observations of drying of porous media. Exemplarily, according to Suzuki and Maeda (1967) or Schluender (2004) the drying rate can remain constant as long as the surface is partially wet. The consideration of this effect thus currently imposes one of the key issues in PNM (e.g. Talbi and Prat 2019). Independent of this, no CRP is found in a drying situation with planar liquid front (dashed line in Fig. 2-31), i.e. in the case of low wettability and high liquid viscosity (Metzger et al. 2007b) because then the top pore layers are initially invaded before widening of the drying front is observed (also refer to Fig. 2-26b). When the connectivity of the liquid phase to the PN surface is reduced, i.e. when pores and throats at the PN surface gradually dry out, the falling rate period (FRP) is initiated (e.g. Chauvet et al. 2009). Then, the evaporation front, i.e. the gas liquid interface, recedes from the surface of the PN and drying rates drop with increasing distance between the evaporation front and the surface. In this period, the liquid phase is though still connected, thus forming a continuum over the pore space (leading to the term 'funicular saturation stage' in Huang (1979)). This means, coupled moisture transfer by capillary invasion (towards the receding front) and vapor diffusion (from the front to the surface) occurs (Fig. 2-31d). The FRP is a transient drying period continuously passing into the receding front period (RFP) (Chauvet et al. (2009). The RFP is initiated with the complete split up of the liquid phase into isolated clusters (also referred to as the start of the 'pendular saturation stage' in Huang (1979)) (Fig. 2-31e). In this stage, capillary invasion occurs only over short distances and thus vapor diffusion controls moisture transfer. Accordingly, this is the period with the lowest drying rates. Duration of this period depends, besides on vapor transfer rates, mainly on the PN saturation at the point when the liquid phase is completely split up. This again depends on the pore structure and wettability of the PN as well as viscous, gravity and thermal effects. The latter are investigated in this thesis.



**Figure 2-31** a) Standardized drying rate curves for drying with relatively long first drying period (solid line) and no first drying period (dashed line). b-e) Pore scale liquid distribution associated with distinct drying periods: b) Purely capillary invasion in the CRP, c) sustained CRP due to the presence of liquid films interconnecting the bulk liquid phase with the PN surface, d) coupled capillary invasion and vapor diffusion during the FRP (and transition to RFP), e) purely diffusive moisture transfer after split up of the liquid phase (RFP). Gas phase in white, liquid phase in black and liquid films and the solid in gray. (Images in b,d,e from Metzger 2007b).

„Entia non sunt multiplicanda sine necessitate.“

Wilhelm von Ockham

\* 1288 in Ockham, Surrey, England

† April 9, 1347 in Munich, Germany

## Chapter 3

# Experimental principles

### 3.1 Introduction

Mathematical pore network models (PNMs) can well reproduce the phenomena that are usually observed during drying of porous media, provided that they are founded on a strong physical base. Such a strong base requires knowledge about the leading pore level phenomena and these are usually experimentally evaluated (Lenormand et al. 1988). In general, respective experiments should be designed with constraints concerning a defined pore network (PN) geometry and the possibility to identify the leading physical phenomena while excluding or reducing any experimental uncertainty. These constraints induce a simplification of the experiment and thus a reduction of unwanted side effects. This allows to fundamentally investigate, e.g., the impact of capillarity or wettability on the drying behavior.

In this sense, a complex porous system might be reduced to a bundle of capillaries (Metzger and Tsotsas 2005a) or 2 or 3-dimensional PNs (Prat 1993) to study capillarity controlled quasi-steady invasion as presented in this work. The fundamental physical phenomena of drying are generally independent of the PN; however, impact of PN size, coordination number, interconnectivity and irregularities of the pore structure on the macroscopic distribution of gas and liquid phase are studied with complex PNs (2D or 3D). For obvious reasons, emphasized below, experimental validation of the leading pore scale phenomena to be implemented in the mathematical model preferably involves 2D PNs because of the convenience of the analyzing methods. Once the mathematical model has been validated, pore scale mechanisms can easily be transferred from the 2D model to a 3D PN which may then be applied to predict drying of real porous media.

Table 3-1 summarizes the requirements on which the conception of the experimental set-up presented in this chapter is basically founded. The list in Table 3-1 takes into account the objectivity of the (image) analysis method as well as propagated errors; the latter must be kept small if discussion of the differences between experiment and simulation shall be based

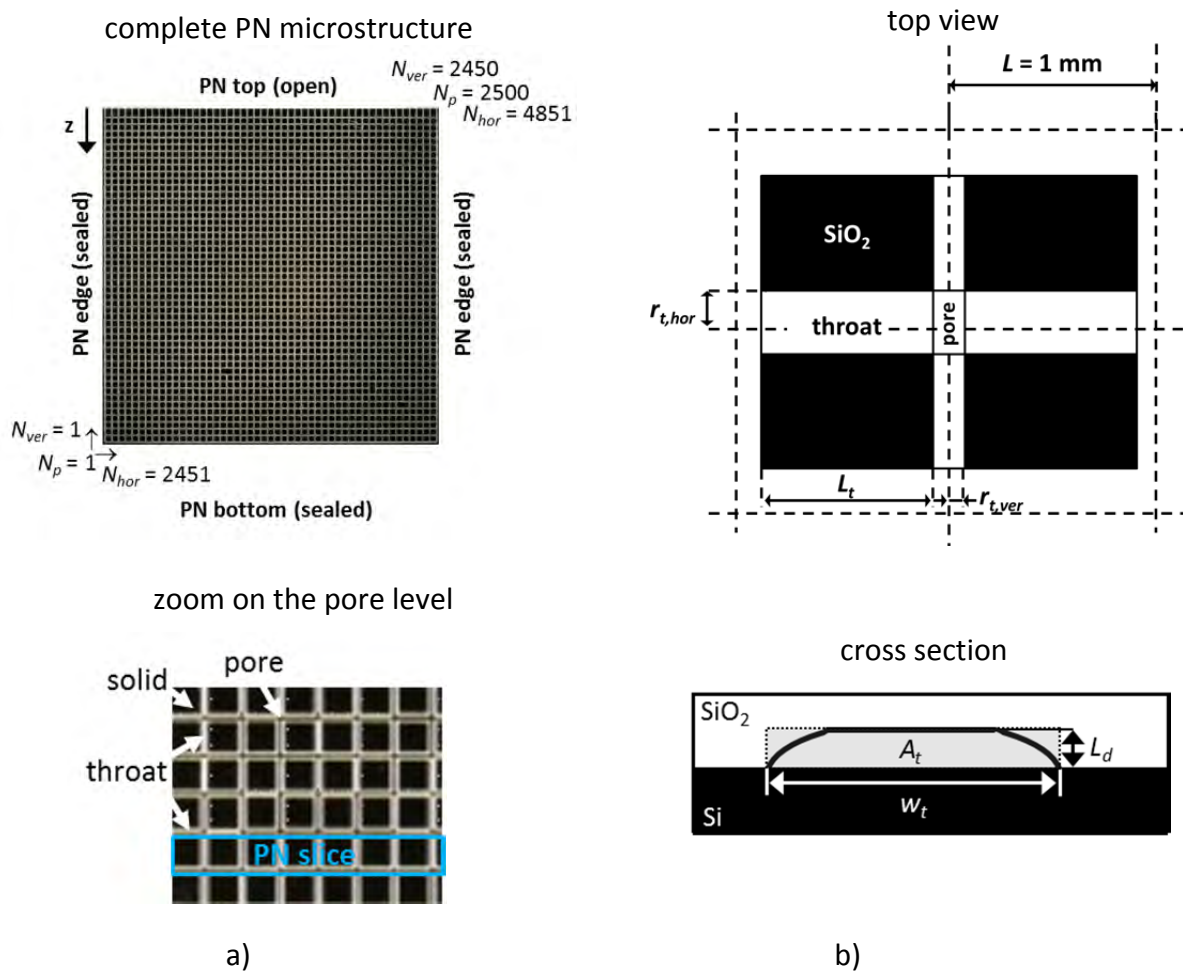
on underlying physical differences rather than on failure of the analysis method. If these constraints are fulfilled, the experimental design of the PN itself as well as its periphery allows to follow the discrete emptying of pores and pore throats during the drying process using an optical CCD camera - a comparably simple, nondestructive and inexpensive method (Sections 3.2 and 3.3). It will be explained in detail in Section 3.4 how the optical data can be transferred into numerical data, such as phase distributions and saturation profiles as well as drying curve, drying rate curve and relevant statistical parameters. From the discussion of these in Chapter 4 the dominating effects that control drying of the microfluidic PN will be discriminated.

**Table 3-1** Basic requirements on drying experiments with the 2D microfluidic PN in the frame of model development for thermally affected invasion.

Constraint	Motivation	Background
exact PN structure / known production errors	crucial to avoid differences in simulated and experimental phase distributions	capillarity controlled order of emptying → deviations affect phase distribution and drying rate
constant PN position	direct comparison of pore/throat saturation	computation of saturation from image pixels → misinterpretation affects phase distribution and drying rate
controlled illumination (homogenous, constant, without reflections)	correct evaluation of pore/throat saturation	computation of saturation from image pixels → misinterpretation affects phase distribution and drying rate
	visualization of liquid films	capillary film flow → affects drying rate
known surface structure	estimation of film flow conditions	capillary film flow → affects drying rate
controlled temperature field for $t \geq 48$ h	implementation in PN drying model	temperature dependent surface tension affects order of emptying
controlled drying conditions	avoidance of impact on PN emptying	diffusive boundary layer transport in PN simulations

### 3.2 The microfluidic device

The development of a production method for microfluidic PNs was a cooperative project with the Institute of Micro and Sensor Technique (OVGU) started in August 2009. As the result of this cooperation, the first micromodel with a 2D quadratic PN structure of size 50x50 was available for drying experiments in January 2011 (Fig. 3-1). This microfluidic device basically consists of a transparent glass wafer (silicon dioxide,  $\text{SiO}_2$ ) which contains the PN microstructure and a black silicon wafer (Si) chemically bonded to the glass wafer for sealing purposes. As can be seen in Fig. 3-1, the PN structure is of kind b) in Fig. 2-2; the void space is thus distributed among pores and throats. The details of this micromodel are given in this chapter together with a discussion of its quality related to the involved materials and production method. This *one* microfluidic PN was used for all experiments summarized in Chapter 4 and Appendix A. The successful application of the  $\text{SiO}_2$  micromodel in this study opened the way for applications also in other studies (e.g. in imbibition (Sun 2014)).



**Figure 3-1** a) Presentation of the microfluidic PN model with  $m = 50$  pore rows and  $n = 50$  pore columns (numbering of pores and throats starting from the left corner at the bottom). The top of the PN is located at  $z = 0$  and the bottom at  $z = (m - 1)L$  with  $L = 1 \text{ mm}$ . The void space etched into the  $\text{SiO}_2$  wafer appears in white and the solid ( $\text{SiO}_2$ ) appears in black due to the Si-wafer connected at the bottom. Additionally a zoom of the pore structure is given, indicating part of a horizontal PN slice. b) Geometric parameters. The cross section is approximated by  $A_t = L_d w_t$  (rectangular) which is apparently slightly greater than the true cross section. The half width of pores is  $r_p = \sqrt{r_{t,ver} r_{t,hor}}$ .

### 3.2.1 Production process

The production process is summarized in the flow chart in Fig. 3-2 (refer to Schmidt et al. 2011 and Sun (2014) for additional information). It can basically be separated into three main parts.

The first part includes the conception of the PN geometry with Matlab and the preparation of the data for the production of the photomask using AutoCad. Principally, the PN structure was produced by stochastic (Gaussian) distribution of throat sizes with  $\bar{r}^0 = 75 \mu\text{m}$  (mean of the half width of throats) and  $r^{std,0} = 7.5 \mu\text{m}$  (standard deviation of the half width of throats) distributed among the 4851 throats of a 50x50 PN (blue line in Fig. 3-3a). The throat sizes were classified into 22 classes with stepsize  $2.5 \mu\text{m}$  (referred to the half width of throats) and the generated distributions were tested by PN simulations of drying to ensure that percolation patterns are obtained. (Note that the term *pore size distribution* (PSD) refers to the distribution of throat sizes inside the PN microstructure). The data were then prepared for the production of the photomask used in the wet chemical production of the microfluidic

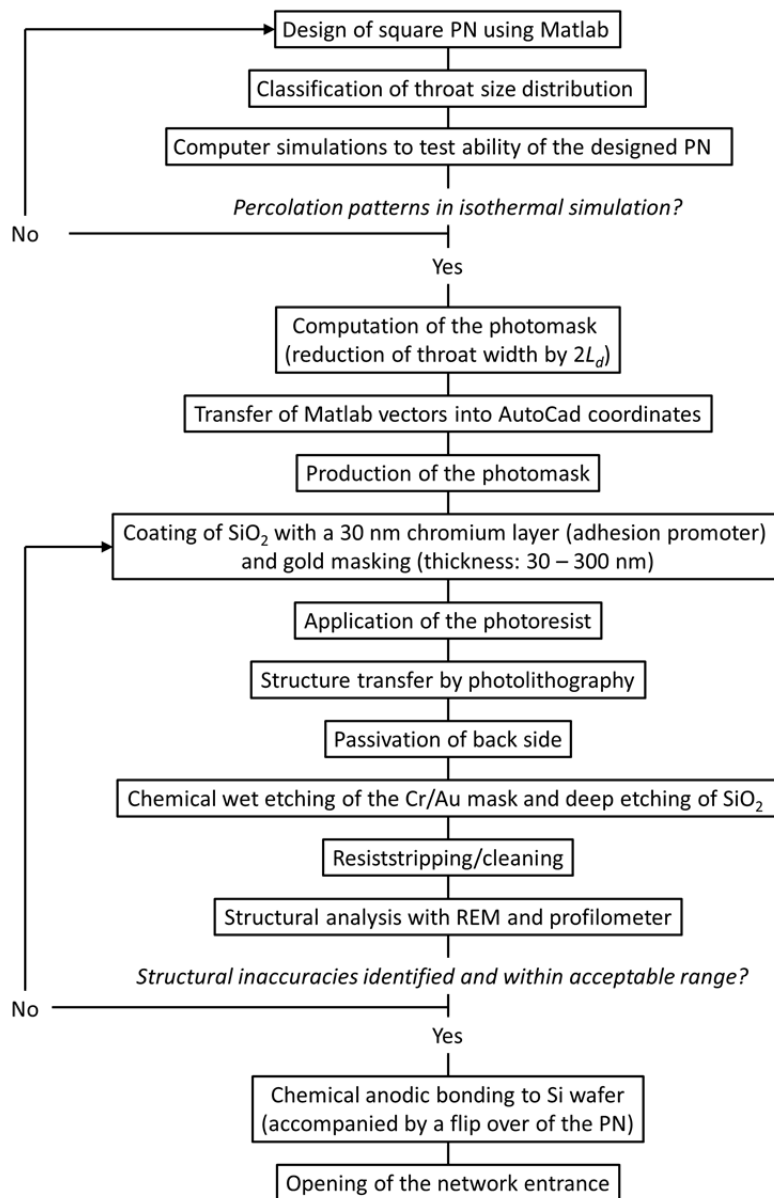
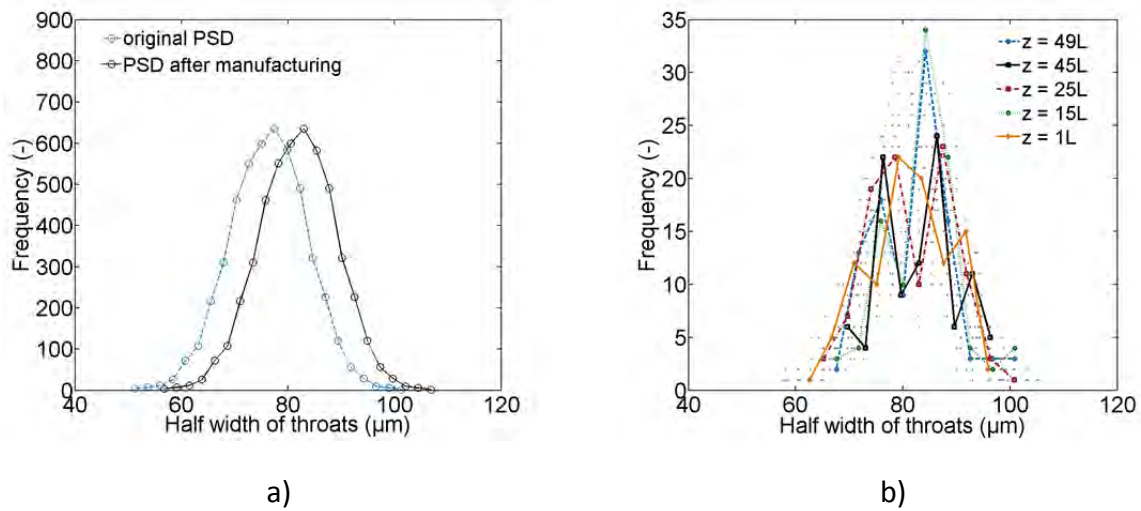


Figure 3-2 Flow chart of the production steps.



**Figure 3-3** a) PSD of the PN which was used as the base for the production (blue line) and PSD of the manufactured micromodel (black line) (discussion in Section 3.2.2). b) Slice resolved PSD; slices for vertical slice positions  $z = [1, 15, 25, 45, 49]L$  are highlighted. As indicated in Fig. 3-1a, the slices are made up by the pores of a row at position  $z$  together with the horizontal throats inside that row connected with the upper row of vertical throats.

PN. Additionally, the PN structure was conserved for the later application in drying simulations, thus allowing for a direct comparison of simulation and experiment. (It is noted that the conserved PSD was adapted later on so as to take into account the production inaccuracies discussed below (black line in Fig. 3-3a)). For the photomask, the throat width was reduced by factor  $2L_q^0$  ( $L_q^0$  = height of throats and pores of the designed network, i.e. the network depth) (also refer to Fig. 3-5). This is necessary when the wet chemical etching is assumed isotropic with direction independent etching rate.

The second part of the production process includes the wet chemical etching process, thus the transfer of the PN structure (originally generated with Matlab) to the SiO<sub>2</sub> wafer. This was a crucial step because it controlled the final quality of the microfluidic PN. It is characterized by the application of adhesive agents, passivation agents and the photoresist mask, as well as by photolithography and the chemical etching in a continuously stirred reactor containing the SiO<sub>2</sub> wafer and the etching solution (Fig. 3-2). The used etching solution was a mixture of HF (49 % diluted in water), HNO<sub>3</sub> (69 % diluted in water) and DI-H<sub>2</sub>O. A volume of 1.5 l of this solution was prepared and filled into a continuously stirred reactor working at 21°C with a stirring velocity of 250 rpm. The following constraints controlled the production process in this step: i) corrosion of the wafer aside the channel structure by the etching solution (mostly avoided by passivation), ii) width of the PN structure in the photomask (must be wide enough to allow the etching solution to penetrate into the SiO<sub>2</sub> wafer;  $r^{min,0} \geq 50 \mu\text{m}$ ) and iii) limitation of the vertical mass transfer of the etching solution inside the throats/pores (partly overcome by stirring). After an etching time of 138 min the wafer was removed from the etching solution, cleaned and analyzed by REM and profilometer. A discussion of the outcomes of these measurements is given in the following section.

In the third part, the transparent glass wafer was chemically bonded to a (black) silicon (Si) wafer at temperatures above 300°C. With this step, complete sealing of the PN structure was achieved. Bonding of the transparent SiO<sub>2</sub> wafer to the black (not transparent) Si wafer induces a flip over of the microfluidic device for the purpose of optical detection of drying. More clearly, the PN structure is horizontally mirrored compared to the PN originally computed with Matlab. This needs to be taken into account when comparing the experimentally obtained gas-liquid distributions with the simulated phase patterns.

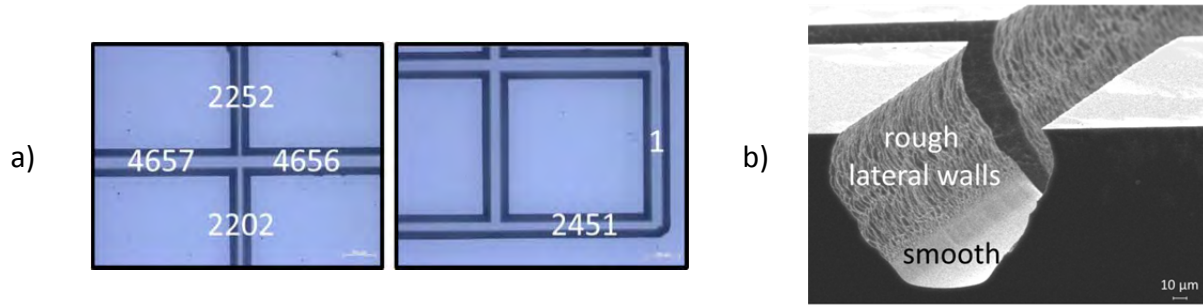
The PN was then opened at one edge by dicing. This edge is referred to as the top edge of the PN, the surface of the PN or the PN entrance throughout the thesis and it is the only edge open for mass transfer between the pore structure and its surrounding. The opposite (closed) edge is referred to as the PN bottom.

It must be remarked that the failure rate of the PN production was 75 %, i.e. only one out of 4 micromodels could be used for the experimental investigation. This is based on production inaccuracies already addressed before and in detailed discussed in the following section. However, deviations found in the one micromodel used for studies presented in this thesis lie within an acceptable range. This is also reflected by Fig. 3-3b which indicates that the throat sizes are not correlated with position.

#### 3.2.2 Limitations of the production process

The production process was basically limited by the technical feasibility on the one hand and the accuracy of the production method on the other hand. First of all it is noted that the size of the PN was generally limited by the wafer size (i.e.  $d = 150$  mm). At second, geometry of the channels was essentially confined by the isotropic etching technique (see also Fig. 3-5a). Furthermore, the aspect ratio of pores and throats was limited by the PN depth as well as the properties of the photomask. The limitation by PN depth is explained with the isotropic etching behavior; basically a smaller aspect ratio would have implied a smaller depth of the PN. In addition to that, realization of the photomask did not allow throat sizes of  $r^0 \leq 50$  μm because smaller throats could not be transferred to the wafer. Although taking this limitation into account when conceptual designing the PN structure for the microfluidic device, Fig. 3-1a reveals two positions where throats are missing. Apart from that, the photomask showed no serious defects. Pinholes and notches (as e.g. described in Sun 2014) are rarely found (Fig. 3-4a). At third, classification of the throat widths was based on the a-priori expected production inaccuracies (assumed with  $r < 2.5$  μm). This was important so as to avoid an impact of production inaccuracies on the order of invasion during drying experiments. But in fact, it was found that the throats were on average 11.67 μm wider and 10.64 μm less deep than originally stipulated, thus greater than the a-priori estimated production inaccuracies (Table 3-2 and Fig. 3-3a). This finding is based on the microscopic measurement of the 6 throats shown Fig. 3-4a as well as the profilometer measurement of the complete PN. It was somehow surprising, because the etching process was basically assumed isotropic (i.e. independent of the crystallographic direction of SiO<sub>2</sub>) with direction independent etching rate expected to lead to the channel geometry illustrated in Fig. 3-5a. However, the measurement with the profilometer revealed that the channels have a geometry as shown in Fig. 3-5b and a ratio of anisotropy of  $(1-w/L_d) > 0.8$ , thus significantly different from the ideal isotropic etching profile. This leads to the assumption that the lateral etching rate must have been higher than the vertical etching rate which is explained



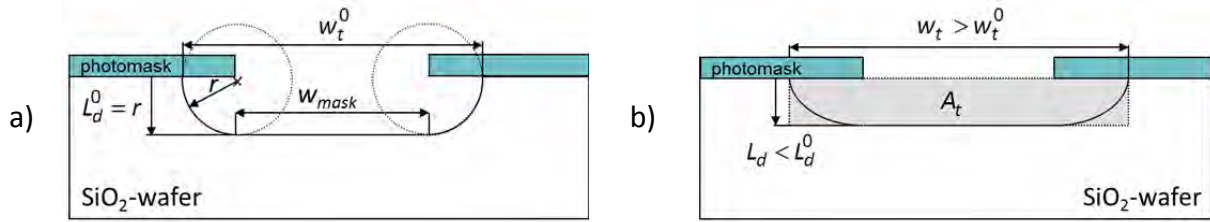


**Figure 3-4** a) Microscopic image of the PN in the open SiO<sub>2</sub> wafer. The numbers are based on the numbering of throats in the PN: at first the vertical throats (1-2450) are numbered starting in the left corner at the bottom of the PN and then the horizontal throats (2451-4851) are numbered consecutively starting at the same position (see also Fig. 3-1). Notice that the numbering is flipped in this image due to the flip of the PN structure. Details of the throats shown here are listed in Table 3-2. b) Cross section of a channel in SiO<sub>2</sub> (Vorhauer et al. 2015). The electron microscopic image reveals that the sidewalls are significantly rougher than the bottom of the channel. Notice that this image was obtained from another microfluidic PN than studied in this thesis; however, similar surface roughness is expected in the investigated PN. (Images from Institute of Micro and Sensor Technique, OVGU).

**Table 3-2** Examples of production variances (provided by the Institute of Micro and Sensor Technique, OVGU). Refer to Fig. 3-4a for a designation of the numbering. ( $w_t^0$ ,  $L_d^0$  width and height of throats in the designed PN;  $w_t$ ,  $L_d$  width and height in the microfluidic PN).

Throat	$w_t^0$ ( $\mu\text{m}$ )	$w_t$ ( $\mu\text{m}$ )	$w_t - w_t^0$ ( $\mu\text{m}$ )	$L_d^0$ ( $\mu\text{m}$ )	$L_d$ ( $\mu\text{m}$ )	$L_d - L_d^0$ ( $\mu\text{m}$ )
1	155	167.26	12.258	50	39.538	-10.462
2202	120	131.36	11.359	50	39.303	-10.697
2252	105	116.35	11.351	50	38.911	-11.089
2451	140	151.65	11.645	50	39.515	-10.485
4656	160	171.88	11.875	50	39.425	-10.575
4657	160	171.55	11.551	50	39.480	-10.520

with technical limits associated with the vertical heterogeneous distribution of the etching solution inside the pores/throats during the production process (e.g. Tsakiroglou et al. 2002). As a result, the throats are relatively wide and shallow and approximated with a rectangular geometry (Fig. 3-5b). As a consequence, the order of emptying is expected to be partly controlled by the network depth  $L_d$ . Though, since it is assumed that the deviations are



**Figure 3-5** a) Theoretically assumed cross section for isotropic wet etching of SiO<sub>2</sub>-wafer. This cross section might be approximated by  $A_t = w_{mask}L_d^0 + \pi/2(L_d^0)^2$ . The image additionally reveals why the throat width of the photomask is by factor  $2L_d^0$  smaller than the etched structure. b) Schematic representation of the practically obtained cross section. The half width of throats corresponds to  $r_t = w_t/2$ . The cross sectional area is approximated with  $A_t = L_d w_t$ , i.e. rectangular. Note that the wafer is bonded to a Si-wafer on the top edge in this representation; thus the SiO<sub>2</sub>-wafer is upside-down in experiments (and images presented in this thesis).

constant and uncorrelated throughout the PN, as also reflected by Fig. 3-3b, it is still expected that the order of invasion is not influenced by the production inaccuracies. Thus the PSD of the microfluidic PN (black line in Fig. 3-3a) is transferred to the PNM (as will be explained in Chapter 5). In addition to that, REM measurements revealed a significant roughness of the channel walls, while the bottom of the channels appeared comparably very smooth (Fig. 3-4b). This is an inherent problem of the production process and it appears that the height of the roughness correlates with the time that the material is exposed to the etching solution. The roughness is also known as the sidewall effect, e.g. Liu et al. (2003), Iliescu et al. (2005) and references therein. As will be explained in what follows, the sidewall roughness particularly plays a role for the development and identification of wall covering thick liquid films.

### 3.2.3 Physical parameters of the microfluidic device

The detailed parameters and characteristics of the one micromodel used in the studies in the frame of this thesis are summarized in Table 3-3 (material parameters) and Table 3-4 (PN parameters). A designation of the PN parameters can be found in Fig. 3-1. The PSD of the microstructure is given in Fig. 3-3 (black curve) and it is referred to the distribution of the throat width; the pore widths, however, result from the configuration of adjacent throats (Fig. 3-1). It is noted again that the geometry of the throats is approximated with a rectangular cross section based on the observations discussed in the previous section.

Advantages of the microfluidic model are basically the optical accessibility of the drying process, the chemical and thermal stability as well as the high thermal conductivity (Tables 3-3 and 3-4). These advantages are mainly linked to the material properties of SiO<sub>2</sub> and Si. Exemplarily, the different light reflection of SiO<sub>2</sub> and Si is essential for optical tracking of the drying process. While light is strongly reflected from the relatively rough etched sidewalls of the PN channels, the untreated glass is translucent and Si absorbs most of the light. Thus, the void space can clearly be distinguished from the solid in Fig. 3-1, as it appears

**Table 3-3** Material parameters.

Material parameter	Numerical value
Borofloat® 33 Borosilicate glass wafer (with PN structure) <sup>17</sup>	
water-resistant, acid-resistant, alkali-resistant	
SiO <sub>2</sub> content	81 % (13 % B <sub>2</sub> O <sub>3</sub> , 4 % Na <sub>2</sub> O/K <sub>2</sub> O, 2 % Al <sub>2</sub> O <sub>3</sub> )
Thickness	$L_{d, SiO_2} = 700 \mu\text{m}$
Heat capacity	$c_p = 0.83 \text{ kJ kg}^{-1} \text{ K}^{-1}$
Thermal conductivity	$\lambda_{SiO_2} = 1.2 \text{ W m}^{-1} \text{ K}^{-1} (90^\circ\text{C})$
Coefficient of thermal expansion	$\alpha_l = 3.25 \cdot 10^{-6} \text{ K}^{-1} (20\text{-}300^\circ\text{C})$
Glass transition	$T_{glas} = 525^\circ\text{C}$
Abbe number	$\nu_e = 65.41$
Silicon wafer (for sealing of PN structure)	
Thickness	$L_{d, Si} = 600 \mu\text{m}$
Heat capacity	$c_p = 0.703 \text{ kJ kg}^{-1} \text{ K}^{-1} (25^\circ\text{C})$
Thermal conductivity	$\lambda_{Si} = 170 \text{ W m}^{-1} \text{ K}^{-1} (0^\circ\text{C})$
Coefficient of thermal expansion	$\alpha_l = 2.6 \cdot 10^{-6} \text{ K}^{-1} (20^\circ\text{C})$
Melting point	$T_m = 1412^\circ\text{C}$

in white while the solid appears in black (due to the connection of the Si-wafer at the bottom). Water attenuates the reflection effect due to light refraction wherefore liquid filled channels can easily be distinguished from empty channels, on the one hand, and wall covering liquid films are identifiable along the rough lateral channel walls on the other hand. As will be explained below, the separation of empty and liquid filled throats and pores and the solid is essential for the image processing of experimental data.

In addition to that the Si-wafer permits a very effective thermal conduction ( $\lambda_{Si} = 170 \text{ W m}^{-1} \text{ K}^{-1} (0^\circ\text{C})$ ) (VDI Heat-Atlas 2010) to the SiO<sub>2</sub> PN. Additionally, both wafers show a very low coefficient of thermal expansion ( $\alpha_{l, SiO_2} = 3.25 \cdot 10^{-6} \text{ K}^{-1} (20 - 300^\circ\text{C})$ ,  $\alpha_{l, Si} = 2.6 \cdot 10^{-6} \text{ K}^{-1} (20^\circ\text{C})$ ) (Okada 1984)) as well as a very high glass transition and melting

<sup>17</sup> DIN ISO 3585, EN 1748 T1

**Table 3-4** Parameters of the 2D quadratic SiO<sub>2</sub> PN used in the studies presented in Chapter 4.

Network parameter	Numerical value
$n \times m$	50x50
Number of pores	$N_p = 2500$
Number of throats	$N_t = 4851$
Lattice spacing	$L = 1000 \mu\text{m}$
Depth	$L_d = 39 \mu\text{m}$
Mean throat length	$\bar{L}_t = 829 \mu\text{m}$
Half width of throats	$r_t = 55.5 - 108 \mu\text{m}$
Mean half width of throats	$\bar{r}_t = 81.8 \mu\text{m}$
Standard deviation of the half width of throats	$r_t^{std} = 7.6 \mu\text{m}$
Total throat volume	$V_{t,tot} = 25.7 \mu\text{l}$
Pore radius (from throat configuration)	$r_p = 71.2 - 98.9 \mu\text{m}$
Mean pore radius	$\bar{r}_p = 85.8 \mu\text{m}$
Standard dev. of pore radius	$r_p^{std} = 4.4 \mu\text{m}$
Total pore volume	$V_{p,tot} = 2.8 \mu\text{l}$
Percentage ratio of pore volume	9.82 %
Capillary pressure range of throats (based on PSD)	$(4.4063 - 5.0438) \cdot 10^3 \text{ (21}^\circ\text{C)}$
Capillary pressure range of pores (based on PSD)	$(4.4686 - 4.7544) \cdot 10^3 \text{ (21}^\circ\text{C)}$
Total void volume	$V_{tot} = 28.5 \mu\text{l}$

point ( $T_{glas,SiO_2} = 525^\circ\text{C}$ ,  $T_{m,Si} = 1412^\circ\text{C}$  (VDI Heat-Atlas 2010)). As the bonding of Si and SiO<sub>2</sub> is additionally heat resistant, experiments at higher temperature levels (up to the boiling temperature of water) appear unproblematic.

Besides this, the good wettability with water shall be mentioned. Depending on the degree of fouling (as a result of experimentation) the measured wettability varied between

$\theta = 10^\circ - 40^\circ$  (static contact angle measured with sessile drop method using the device Dataphysics OCA 15 Pro), which is in good agreement with literature (e.g. Sghaier et al. 2006).

Disadvantages of the microfluidic model are mainly connected with the production process from which certain geometrical constraints and several uncertainties arise (Section 3.2.2). The main complaint is surely associated with the formation of liquid films inside the microfluidic PN during drying. It was originally intended to reduce the pore scale effects to a minimum with the aim to validate existing PNMs. However, the non-cylindrical shape of the throats as well as the surface roughness did not allow this. Instead, application of the microfluidic device revealed the importance of liquid films in drying of PNs. Additionally to that, the final structure of throats deviates from the intended isotropic structure. The final geometry resembles the structure of a rectangle with rounded corners. It can be expected that the small height of the throats significantly impacts on the order of invasion. This is in the following accounted for by application of the half width of the mean meniscus radius  $r_m$  from Eq. 2-24 for the computation of capillary and liquid pressures. Note that the ratio of the throat depth  $L_d$  to mean throat radius  $\bar{r}_t$  is  $L_d/\bar{r}_t = 0.48$  in the microfluidic PN. From this results that  $\bar{r}_m \cong 31.5 \mu\text{m}$  with a standard deviation of  $r_m^{std} = 0.58 \mu\text{m}$ .

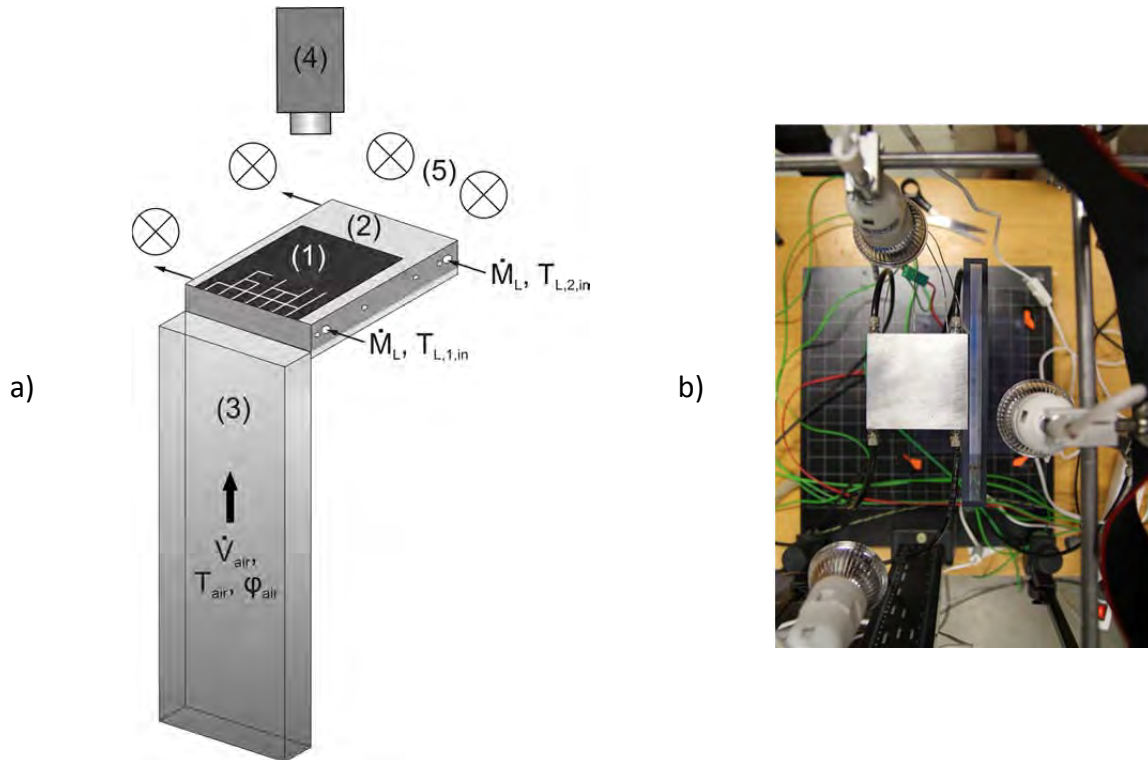
### 3.3 Experimental design and procedure

#### 3.3.1 Experimental set-up

Experimental design follows the ideas and constraints as summarized in Table 3-1. Arbitrative is the recording of the drying experiment by CCD camera and the potential of imposing controlled temperature gradients on the PN. The experimental set-up is schematically sketched in Fig. 3-6a; the photo in Fig. 3-6b shows the set-up from the point of view of the CCD camera. The technical data of the experimental equipment is summarized in Table A-1 in Appendix A. Technical details of the set-up are given in Fig. 3-7.

The heart of the experimental set-up is the PN at position 1. It was positioned on a horizontal heat conducting plate (2) with the (black) Si wafer in contact with the plate and the (transparent) SiO<sub>2</sub> wafer at the top side and with the open side facing the air flow channel (3). The metal plate is an aluminum plate of size 80x85x10 mm<sup>3</sup> (width x height x depth). It was tempered by two separated water circuits at temporally constant inlet temperatures  $T_{L,1,in}$  and  $T_{L,2,in}$ . The exact positions of the water connections are given in the technical illustration in Fig. 3-7a. The evolving constant temperature gradients between the two water circuits depended on the thermal conductivity and geometry of the heat conducting plate, the heat losses from the plate surface and the height of the temperature difference as well. Temperature of the water circuits was controlled by two circulating heating baths operating at different temperatures depending on the temperature setting under study. Notice that due to the high temperatures of the heating baths in certain experiments, the water evaporated from the baths requiring several refills in the interval of several hours. This could lead to a very short drop of temperature (Appendix A). Apart from that, the temperature gradients were reproducible very well. The temperature profiles were continuously detected and recorded by thermocouples located inside the heat conducting plate (2 mm below the surface) and the temperature of the PN surface was additionally

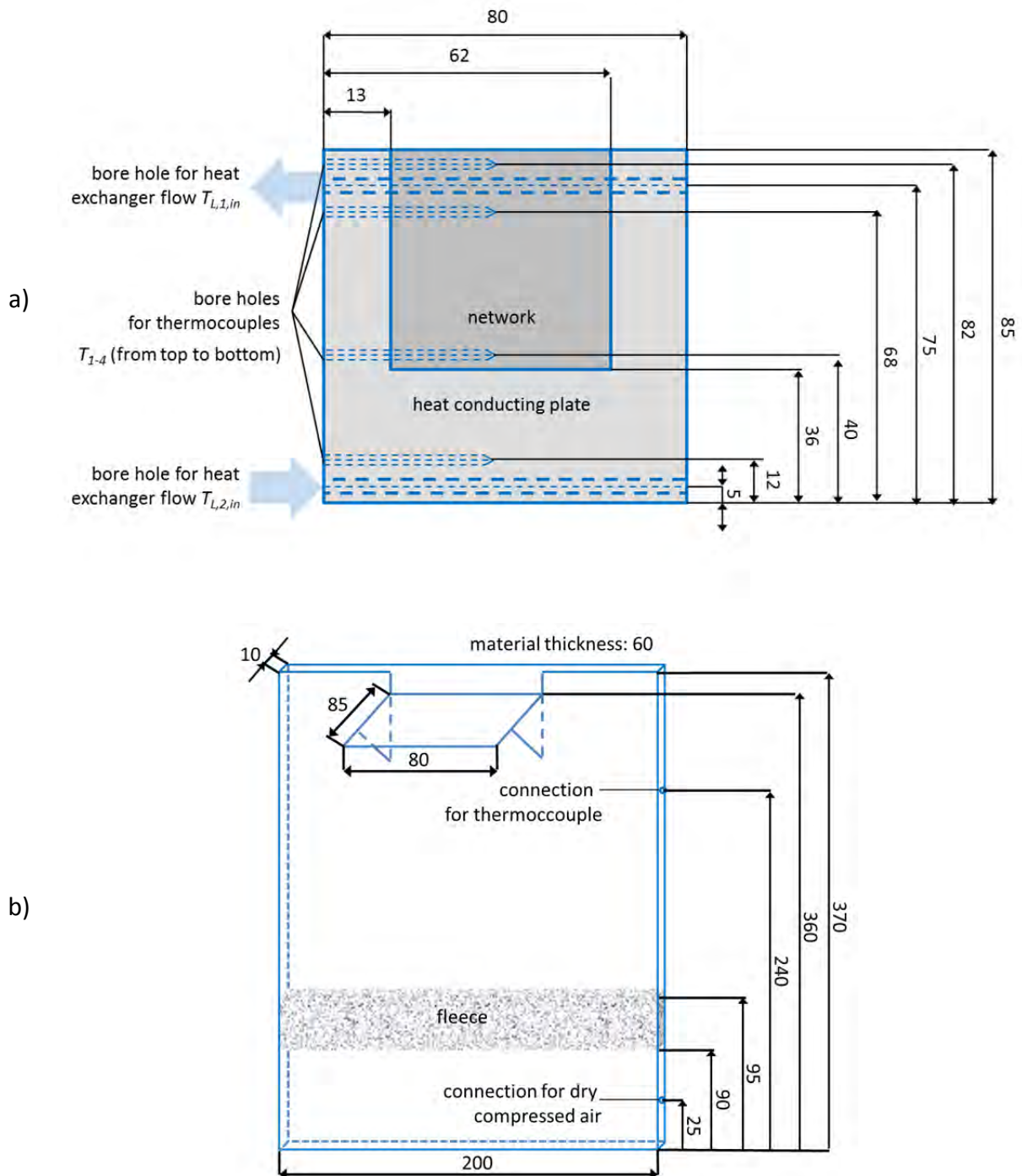
recorded by infrared (IR) measuring technique in separate experiments. While thermocouples allow continuous monitoring of the temperature profiles at distinct positions, the IR measurement can complete this information giving the snapshot of the temporally constant temperature distribution of the SiO<sub>2</sub> wafer (which contains the PN structure). The bore holes for the connection of thermocouples are sketched in Fig. 3-6a; the exact position of these bore holes is given in the technical illustration in Fig. 3-7a. For the IR measurement an infrared camera was installed perpendicularly above the PN, i.e. at the position of the CCD camera shown in Fig. 3-6, while the temperature setting was kept as in the drying experiment.



**Figure 3-6** a) Graphical representation of the set-up: (1) PN, (2) heat conducting plate, (3) air flow channel, (4) CCD camera/IR camera, (5) LED lightning (Vorhauer et al. 2013). b) Top view showing the heat conducting plate in the center, cross section of the air flow channel east of the heat conducting plate, connections of the heat exchanger (black tubes north and south of the plate), connected thermocouples (in the north of the plate) and 3/4 LED lights (north, east and south).

As mentioned before, the CCD camera (4) was installed perpendicularly above the PN with the purpose to record the invasion of the PN during drying. Four LED lights (5) distributed among the 4 sides of the PN illuminated the microfluidic device. Notice that the invasion can be followed very well because the top side of the PN is transparent with very good contrast characteristics discussed above. The air flow channel (3) connected to the open side of the PN allowed to impose vapor pressure gradients between the PN and the bulk air phase, slowly passing the PN surface (at the PN top edge in images presented throughout the thesis). The material of the air flow channel was PMMA with a material thickness of 60 mm. The channel was 370 mm long with rectangular cross section  $A = 200 \times 10 \text{ mm}^2$ . The channel was partially filled with nonwoven polyester fabric of  $50 \times 200 \times 10 \text{ mm}^3$  in order to reduce

possible contamination with residual oil from the fan. The fabric additionally served as a homogenizer for the air flow with the aim to achieve fully developed laminar flow (and diffusive boundary layer). Compressed dry air ( $T_{dew} = -15^{\circ}\text{C}$ ) at room temperature was supplied to the channel at a height of 25 mm; the PN was located at the upper side of the air flow channel (at a height of 360 mm).



**Figure 3-7** a) Illustration of the heat conducting plate with specification of technical dimensions. The thermocouples are installed 2 mm below the surface of the metal plate. b) Technical dimensions of the air flow channel.

### 3.3.2 Temperature gradients

Table 3-5 gives an overview of the temperature settings realized with the above described set-up. In this  $T_{top}$  refers to the temperature at the open side of the PN which is exposed to the air flow and which appears as the top edge in figures presented throughout the thesis. The temperature  $T_{bottom}$  instead refers to the temperature of the PN opposite to the open side, i.e. at the bottom side in the figures below. As can be seen, three different temperature settings are investigated: drying with spatially almost constant temperature, drying with high top and low bottom temperature (also referred to as negative gradient) and drying with low top and high bottom temperature (also referred to as positive gradient).

**Table 3-5** Overview of investigated heating modes. The values refer to the temperatures measured at the bottom and the top side of the PN with infrared technique. Temperatures of the water circuits and the metal plate are provided in Appendix A.

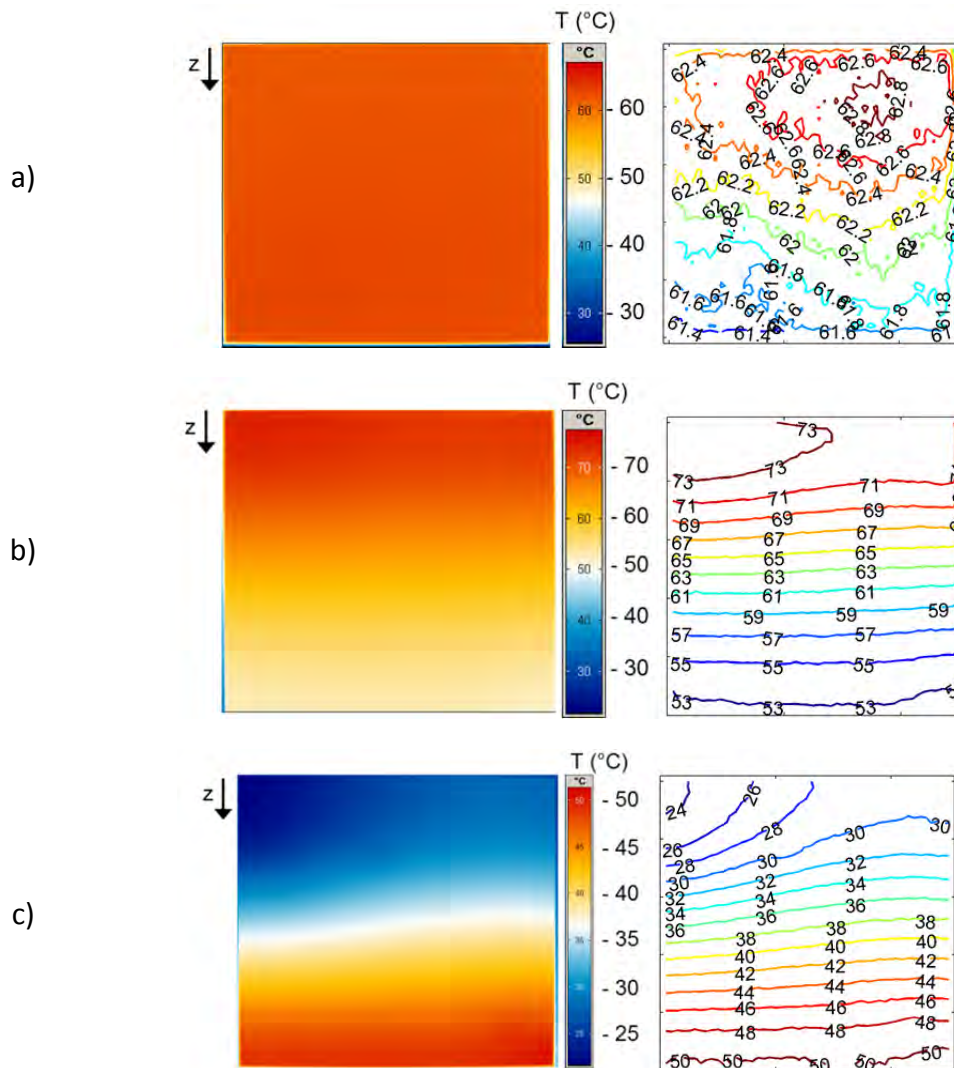
Quasi-isothermal	Negative gradient		Positive gradient	
$\bar{T} \cong 63^\circ\text{C} = \text{const.}$	$\bar{T}_{top} \cong 76^\circ\text{C}$	$\bar{T}_{bottom} \cong 52^\circ\text{C}$	$\bar{T}_{top} \cong 27^\circ\text{C}$	$\bar{T}_{bottom} \cong 50^\circ\text{C}$

Note that these temperature gradients were temporally constant. The temperatures of the water circuits, with which these temperature profiles were achieved, are referred to as  $T_{back}$  and  $T_{front}$  and are specified for each experiment in Appendix A. It is noted and discussed below, that a spatially constant temperature could not be achieved with this set-up wherefore the experiment with almost constant temperature is also denoted by quasi-isothermal experiment.

The thermograms recorded for the different temperature settings studied in the frame of this thesis are given in Fig. 3-8; the temperature profiles detected with the thermocouples are given in Appendix A. The IR measurement of the PN surface is generally in good agreement with the thermocouple measurement (inside the metal plate). The contacting measurement method with thermocouples shows overall steady temperature fields; however very short drops of the temperature were detected when the thermal baths were refilled. Nevertheless, it can be assumed that a snapshot of the temperature distribution with the IR camera can very well represent the temperature profile of the specific drying experiment. Moreover, due to the high thermal conductivity of the silicon wafer in contact with the heat exchanger plate and the microfluidic structure, its small thickness of 600  $\mu\text{m}$  and the very small liquid volume ( $V_{tot} = 28.5 \mu\text{l}$ ) a temperature decrease at the evaporation front could not be observed. Consequently, the snapshots of the thermograms are used for the later comparison of experiments and non-isothermal PN drying simulations (Chapter 6).

It is noted that the thermograms reveal vertical *and* horizontal variation of temperature. The temperature gradient in vertical direction is a result of the temperature difference between the two water circuits; the horizontal temperature variation is a result of heat losses of the water circuits over the length of 80 mm between the inlets of the heat conducting plate and the outlets (Fig. 3-7).



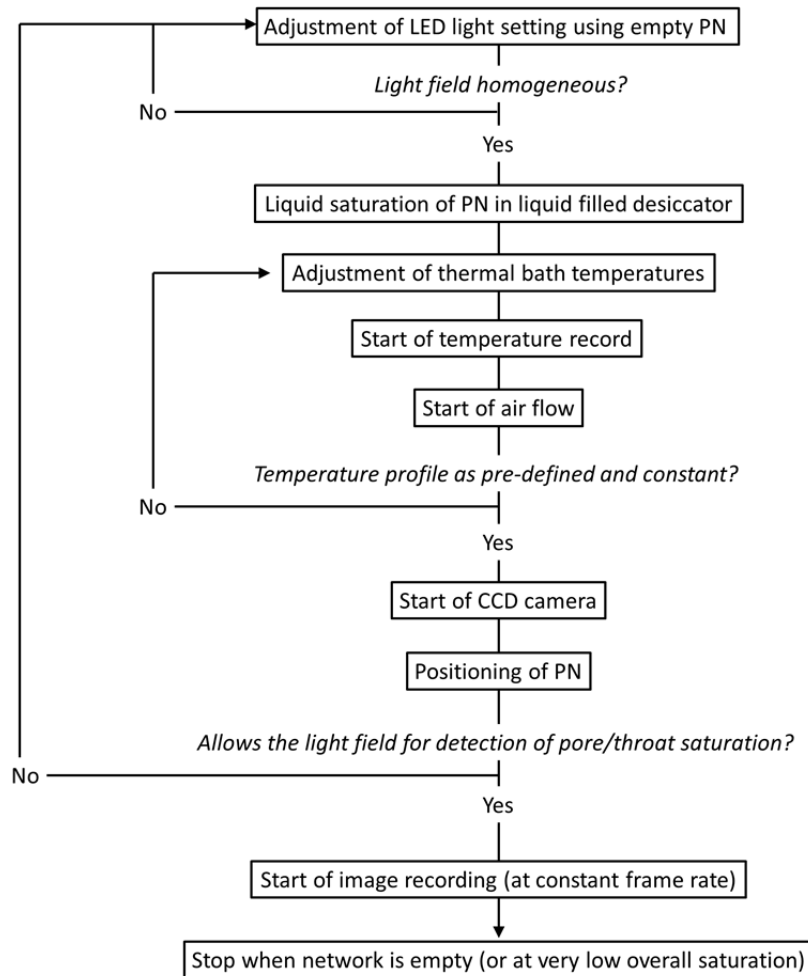


**Figure 3-8** Temperature fields as imposed on the PN in case of a) quasi-isothermal drying (with  $\bar{T} \cong 63.5^\circ\text{C}$ ), b) non-isothermal drying with stabilizing temperature gradient ( $\bar{T}_{\text{bottom}} \cong 52^\circ\text{C}$  and  $\bar{T}_{\text{top}} \cong 76^\circ\text{C}$ ) and c) drying with a destabilizing gradient ( $\bar{T}_{\text{top}} \cong 27^\circ\text{C}$  and  $\bar{T}_{\text{bottom}} \cong 50^\circ\text{C}$ ). Left: Images from IR thermography. Right: Isotherms.

### 3.3.3 Experimental procedure

Drying experiments were performed following a fixed scheme, which is summarized by the flowchart given in Fig. 3-9. Initially, the light setting was adjusted so as to allow for an optimal illumination of pores and throats in purpose of the precise image processing after the experiment. A desiccator, filled with liquid water, was used to saturate the PN with degassed, deionized water. With this method, usually more than 99.5 % of the void space could be saturated with liquid water. In certain cases some throats and pores could not be invaded by the liquid phase with this procedure. This is exemplarily visible in Fig. 3-10 below. Here, in total 19 throats close to the bottom of the PN, i.e. aside of the drying front, are obviously filled with air. This must especially be taken into account when analyzing the structural details of phase distributions with the purpose of model validation. After filling of the microfluidic device temperatures of the heating baths were adjusted and the pneumatic valve for the drying air was opened. The convective flow of pressurized dry air had a

constant flow rate of  $\dot{V}_{air} = 20 \text{ l min}^{-1}$ , a dew point of  $T_{dew} = -15^\circ\text{C}$  (i.e. a relative humidity  $\varphi < 0.01$ ) and room temperature in all experiments. The air temperature was constantly recorded. With positioning of the liquid saturated microfluidic device at the surface of the metal plate, the light setting was fine-tuned and recording of the experiment was started with constant frame rate. Care was taken to avoid invasion of the PN during this step; however, as will be discussed below, this constraint could not be fulfilled in most of the drying experiments. (Especially in experiments with high surface temperature, the top rows of the PN dried out before image recording could be started). The experiment was stopped when the PN was empty or at very low saturation. This could take several days depending on the temperature setting. Afterwards the image data was analyzed by the image processing method explained in detail below.

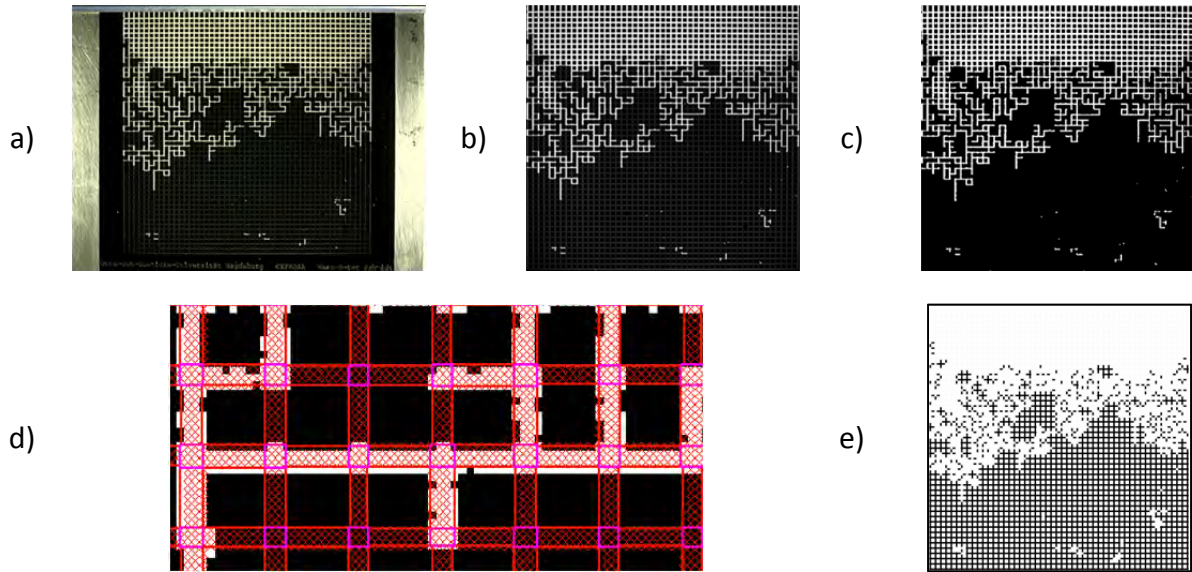


**Figure 3-9** Flow chart of experimental procedure.

A list of experiments can be found in Appendix A. It is noted that 55 % of the experiments failed because of several factors; exemplarily, the light setting changed, the PN slightly moved or the camera failed during experiments. The unsuccessful experiments are not listed in Appendix A. Nevertheless, for each temperature setting 3 experiments are evaluated in Chapter 4. These are experiments 17, 19, 20 for quasi-isothermal drying, experiments 8, 13, 15 for drying with imposed negative temperature gradient and experiments 10, 11, 18 for drying with imposed positive temperature gradient.

### 3.4 Image processing of optical data

If the drying experiment was successful and if the recorded images had a very high and constant quality, the image data was analyzed using an image processing algorithm in Matlab R2014a with the purpose to identify the pore scale liquid distribution and to derive from this the drying curves as well as statistical parameters. The algorithm includes binarization of the image, segmentation of the image and liquid screening (Fig. 3-10) and basically applies the Image Processing Toolbox with the Matlab functions *imread*, *rgb2gray* and *im2bw*. In total, 5 steps are necessary for the conversion of the photo into numerical data. These steps will be explained in detail in what follows.



**Figure 3-10** Image processing: (a) RGB image recorded during the drying experiment (experiment 17). b) Computed gray level image. c) Binarized image with black pixels where  $I_3 = 0$  and white pixels where  $I_3 = 1$ . d) Image section of a partially saturated PN region that illustrates image segmentation aiming at an identification of pore and throat saturation; gas in white, liquid in throats/pores and the solid in black. The red crosses show the positions of image pixels. Throat and pore saturations are computed from the ratio of black and white pixels inside the plotted rectangles. e) Resulting phase distribution stored for subsequent computation of e.g. drying curve and drying rate curve.

#### 3.4.1 Computation of phase distributions

The digital data from experiments are truecolor RGB-images of width  $w = 768$  pixel and height  $h = 576$  pixel (Fig. 3-10a and Fig. 3-11). Information about the red (R), green (G) and blue (B) color portions in an image point (pixel) are stored in a 3D matrix of size  $I_1 = w \times h \times RGB = 768 \times 576 \times 3$  (Fig. 3-11a). Generally, solid and liquid filled pores and throats appear in black and empty pores and throats appear in white.

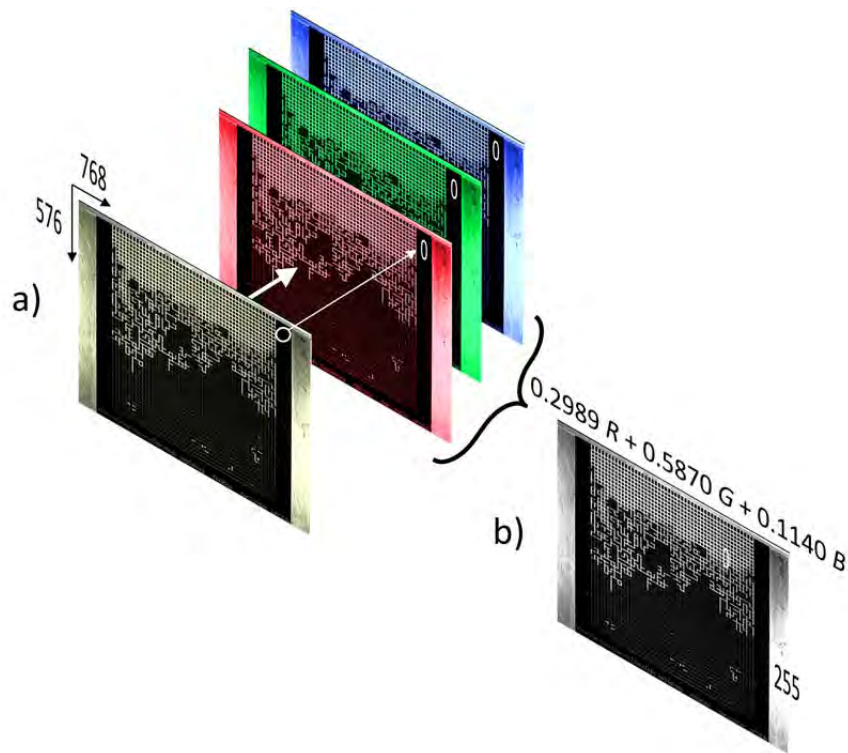
In *step 1*, images are converted from the truecolor images into graylevel images (Figs. 3-10b and 3-11b) using the Matlab function *rgb2gray*. In this, the red, green and blue portions of any image pixel are converted into a 2D matrix  $I_2$  with integer values in the range of  $[0:1:255]$  by application of a weighted sum of the red, green, and blue portions:

$$I_2 = 0.2989R + 0.5870G + 0.1140B. \quad (3-1)$$

Afterwards, matrix  $I_2$  is binarized in *step 2* using the Matlab function *im2bw*. More precisely, the gray value of each image pixel in matrix  $I_2$  is compared to the threshold  $c_{0,1}$  and then either rounded towards 0 (and thus appears as a black pixel in the binary image) or towards 1 (and thus appears as a white pixel) (Fig. 3-10c):

$$I_3 = \begin{cases} 0 & I_2 \leq 255c_{0,1} \\ 1 & I_2 > 255c_{0,1} \end{cases} \quad (3-2)$$

Then, the PN mesh is computed and imposed on the image in *step 3*. For this, the true network dimensions of the microfluidic PN are multiplied with the scaling coefficients  $c_{w,h}$  (scaling of the mesh width and height) and  $c_h$  (additional scaling of the mesh height<sup>18</sup>). Figure 3-10d shows how the mesh fits onto the image and helps to segment pores, throats and solid blocks. Each throat contains on average 2-3x8 pixels of size 0.0904x0.0933 mm<sup>2</sup> (represented by the red crosses in Fig. 3-10d and Fig. 3-12).



**Figure 3-11** a) Graphical representation of the composition of the 3D matrix  $I_1$ . Each image point (pixel) has a dimension of around 0.0933x0.0904 mm<sup>2</sup> ( $w \times h$ ) and contains information about the portion of red (R), blue (B) and green (G). The color bars have a spectrum of [0:255]; a black pixel is the result of 3x0 and a white pixel is the result of 3x255. b) The gray level image results from weighting of the RGB color portions in the 2D matrix  $I_2$ .

<sup>18</sup> Owing to the properties of the recorded digital image, width and height of the PN image is approximately 540x525 pixels, which is related to the true width and height of the microfluidic PN by application of the scaling parameters. The distortion of images must be attributed to the lens properties of the CCD camera. It results in a vertical compression of the PN image which requires an additional correction of the mesh positions by correction factor  $c_h$ . Another correction could be achieved by a linear correlation of scaling factor  $c_{w,h}$  (applied in cases of very significant horizontal or vertical distortion).

The throat saturation is computed from the ratio of black pixels (with  $l_3 = 0$ ) to total pixels within the fragments:

$$S_t^0(1:N_t) = \frac{N_{pix} - N_{pix, l_3=1}}{N_{pix}}. \quad (3-3)$$

The pore saturation  $S_p^0$  is computed analogously.

However, shadows or a mesh shift<sup>19</sup> could lead to misinterpretation of pore and throat saturation. In such a case, a black pixel, assigned to the liquid inside pores and throats, would for instance originally be a part of the solid or a shadow. Thus, it is useful to filter or binarize the data in  $S_t^0$ . This is done in *step 4*, where the data set is compared to either  $S_{crit}$  (in the case of application of only one threshold, i.e.  $S_t \in [0,1]$ ) or  $S_{crit,1}$  and  $S_{crit,2}$  (in the case of two thresholds, i.e.  $S_t \in [0,0.5,1]$ ):

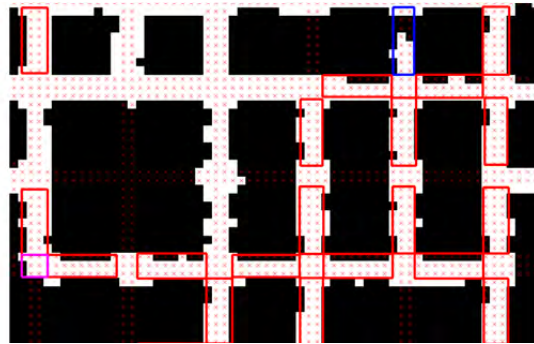
$$S_t = \begin{cases} 0 & S_t^0 < S_{crit} \\ 1 & S_t^0 \geq S_{crit} \end{cases} \quad (3-4)$$

or

$$S_t = \begin{cases} 0 & S_t^0 < S_{crit,1} \\ 0.5 & S_t^0 \geq S_{crit,1} \ \& \ S_t^0 < S_{crit,2} \\ 1 & S_t^0 \geq S_{crit,2} \end{cases} \quad (3-5)$$

The pore saturation  $S_p$  is computed analogously.

For example, it was  $S_{crit} = 0.8$  in most experiments, which means that around 12-19 black pixels in a throat with else white pixels could still result in  $S_t = 0$ . This was e.g. advantageous for the kind of throats as emphasized in red in Fig. 3-12, i.e. in the case of a mesh shift towards the channel wall.



**Figure 3-12** Pixels that are accounted for the computation of throat/pore saturation are shown by red crosses. The red rectangles represent throats that are assigned with  $S_{t,p} = 0$  for  $S_{crit} = 0.8$ . The blue rectangle represents one example where an obviously partially saturated throat is also assigned with  $S_t = 0$  (rare). This misinterpretation could partially be overcome by introduction of two thresholds,  $S_{crit,1}$  and  $S_{crit,2}$ .

<sup>19</sup> A mesh shift can generally result from the PN compression in the stored images as well as (minimal) rotation of the network during experiment.

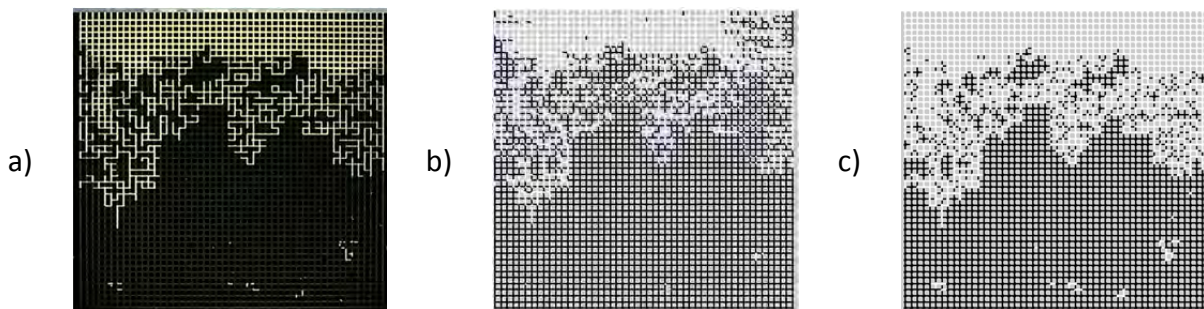
Figure 3-13 shows how the binarization of  $S_t^0$  can contribute to an improvement of the output distribution of gas and liquid phase after image processing. Nevertheless, partially saturated throats (blue throat in Fig. 3-12) might erroneously be interpreted as empty throats resulting in an overall decrease of network saturation or even in a fluctuation of individual throat saturations from consecutive images. Moreover, due to the data filter in step 4 liquid films, evolving along the rough lateral walls during drying, completely disappear from the computed phase distribution.

The computed phase distribution, resulting from the image processing steps 1-4, is shown in Fig. 3-10e. It is generated from the vectors  $S_t$  and  $S_p$ . In step 5 the overall network saturation is then computed as

$$S = \frac{\sum S_p \cdot V_p + \sum S_t \cdot V_t}{\sum V_p + \sum V_t}. \quad (3-6)$$

Steps 1-5 are repeated for each RGB image of the drying experiment (in total up to around 3000 images were evaluated for each experiment depending on the overall drying time and the frame rate of image record). The resulting phase distributions are stored for the following computation of drying curve and drying rate curve as well as for comparison of the drying experiment to PN simulations. It must be emphasized that the organization of the vectors  $S_t$  and  $S_p$  is especially important for the comparison with simulation results. Coordinate origin of the experimental images is located in the upper left corner. This is in contrast to the computed phase distributions, which have their coordinate origin in the lower left corner (as shown in Fig. 3-1) and must be respected when organizing  $S_t$  and  $S_p$ .

It can be summarized that very good agreement between the original RGB images and computed phase distributions is obtainable with this relatively simple algorithm, provided a careful acquisition of image data during experiment. Further image processing (such as e.g. opening and closing methods as described in Sun (2014)) does not appear necessary in the face of this very good agreement. The impact of the choice of image processing parameters ( $C_{0,1}$ ,  $S_{crit}$ ,  $S_{crit,1,2}$ ,  $C_h$ ,  $C_{w,h}$ ) on the computed phase distributions and drying curves is discussed in the following section.



**Figure 3-13** Relevance of binarization for image analysis: a) original image (from experiment 17), b) totally empty throats (i.e. throats that contain *only* white pixels) in white and throats that contain at least one black pixel as black lines, c) artifacts are eliminated in the phase distribution after step 4, improving the image quality.

### 3.4.2 Remarks on the accuracy of image analysis

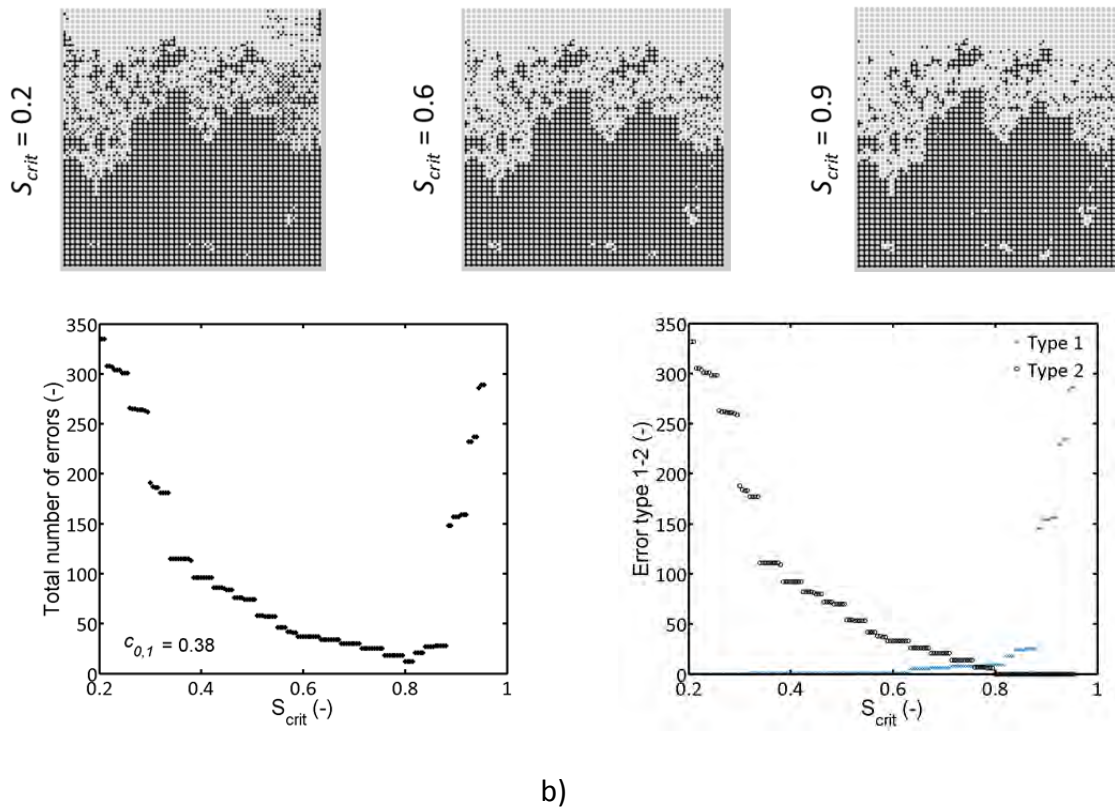
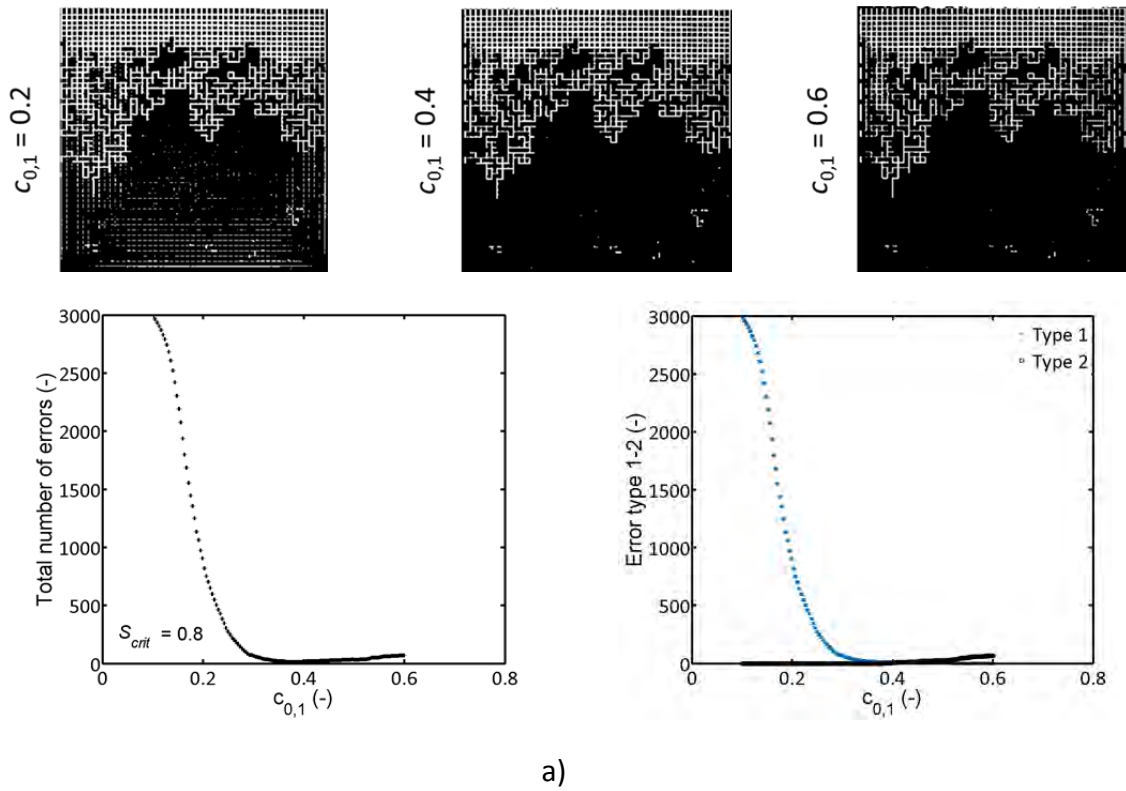
It must be remarked, that the threshold  $c_{0,1}$  as well as the scaling coefficients  $c_{w,h}$  and  $c_h$ , and furthermore the thresholds  $S_{crit}$  ( $S_{crit,1}$ ,  $S_{crit,2}$ ) are subjective parameters. The impact of the choice of these parameters is summarized in Table 3-6 with regard of specific image processing steps and the resulting estimated overall network saturation  $S$ . Figure 3-14 illustrates the impact of  $c_{0,1}$  (Fig. 3-14a) and  $S_{crit}$  (Fig. 3-14b) on the output phase distribution (also refer to Table 3-7). As expected, the binarization threshold  $c_{0,1}$  affects the ratio of white and black pixels while  $S_{crit}$  affects the ratio of detected empty and full throats.

**Table 3-6** Image processing steps and impact on overall PN saturation  $S$ .

Processing step	Parameter	Objective	Impact on $S$
Binarization (step 2)	threshold $c_{0,1}$	segmentation of gray pixels into black and white pixels	$c_{0,1} \uparrow : S \uparrow$ (more black pixels)
			$c_{0,1} \downarrow : S \downarrow$ (more white pixels)
Mesh generation (step 3)	scaling coefficients $c_{w,h}$ and $c_h$	segmentation of void pores, throats and solid	$c_{w,h}, c_h \uparrow : S \uparrow$ (inclusion of channel walls)
			$c_{w,h}, c_h \downarrow : S \downarrow$ (reduction of dataset)
Binarization of throat/pore saturation (step 4)	threshold $S_{crit}$ (or $S_{crit,1}, S_{crit,2}$ )	segmentation of the full range of throat and pore saturation into $S = [0, 0.5, 1]$	$S_{crit}, S_{crit,2} \downarrow : S \uparrow$ (more full throats)
			$S_{crit}, S_{crit,1} \uparrow : S \downarrow$ (more empty throats)

**Table 3-7** Definition of error types.

Type	True saturation (RGB image)	Estimated saturation (phase distribution)	Difference
1	1	0	1
2	0	1	-1

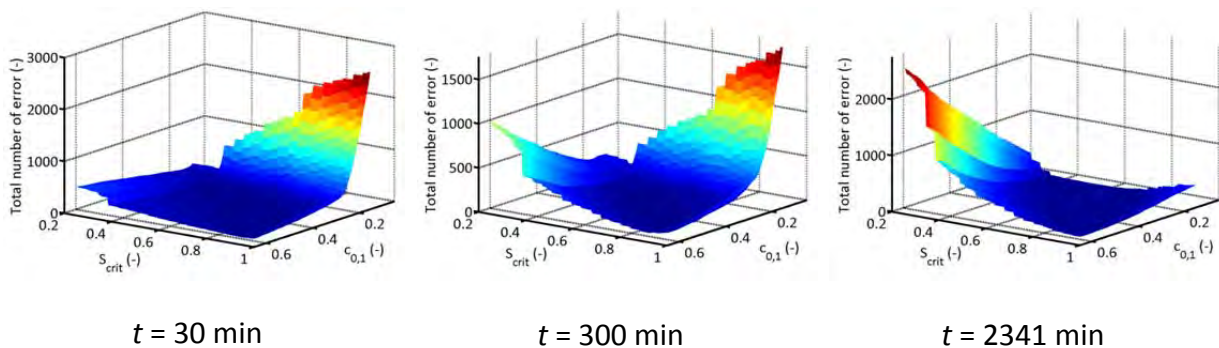


**Figure 3-14** Impact of  $c_{0,1}$  and  $S_{crit}$  on the total number of misinterpreted throats. a) Gray-level threshold variation at  $S_{crit} = 0.8 = const.$  and b) variation of  $S_{crit}$  at  $c_{0,1} = 0.38 = const.$  on the example of experiment 17. Additionally the types of errors are discriminated (refer to Table 3-7 above).



The 2D configuration has the advantage that the deviation between the original image and the output phase distribution can easily be quantified. For this, the number of falsely interpreted throats/pores must be visually identified for a chosen set of parameters. The variation of  $S_{crit}$  and  $c_{0,1}$  results in various different phase distributions which are compared to the true (visually estimated) distribution. The surface plot in Fig. 3-15 quantifies the impact of a variation of the two thresholds,  $c_{0,1}$  and  $S_{crit}$ , on the total number of misinterpreted throat saturations on 3 experimental images from experiment 19. As can be seen, the total number of errors is small and constant in a wide range of these parameters. It can then be supposed that the variation of these parameters in this range has a negligible impact on the estimated overall PN saturation  $S$ . Moreover, Fig. 3-15 evidences that the maximum of the surface plots (i.e. the maximum total number of misinterpreted throats) changes during image recording. This can be explained as follows.

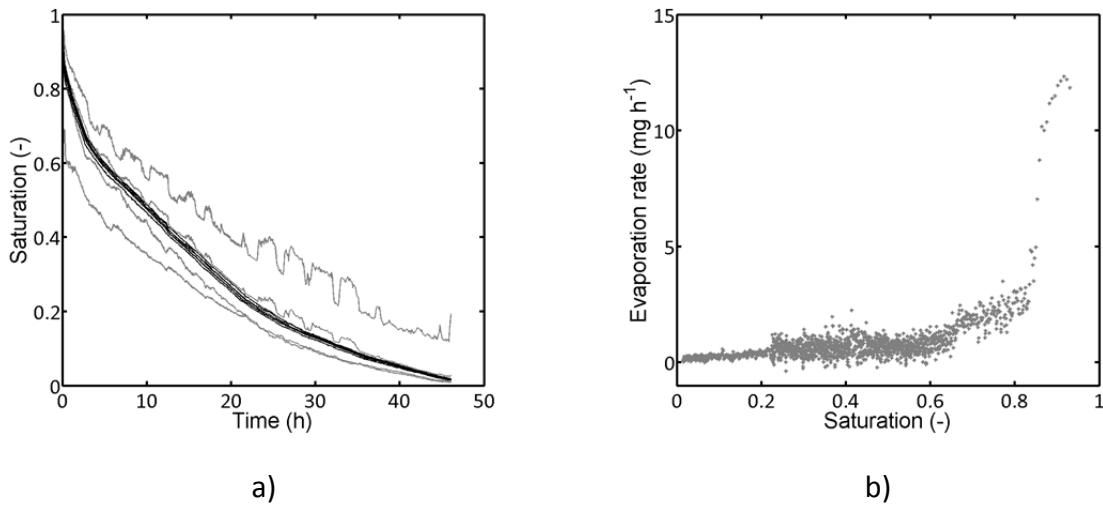
When drying starts (at  $t = 30$  min in Fig. 3-15) most of the throats are saturated with liquid and appear in black on the binary image. An excessive amount of white, resulting from the choice of a small binarization threshold  $c_{0,1}$ , produces the error of type 1 (Table 3-7, Fig. 3-14). Error of type 1 occurs if a saturated throat is erroneously interpreted as an empty throat, which is favored by the high proportion of white image pixels. If additionally the critical saturation is high (e.g.  $S_{crit} = 0.8$ ) only the throats with a high saturation are identified as full. In summary, the information about the partially filled and totally saturated throats is lost, increasing the maximum number of total errors. During drying, more and more throats empty and thus appear white in the binary image naturally increasing the proportion of white pixels. At the end of drying more than 4500 throats are already empty ( $t = 2341$  min in Fig. 3-15). But the choice of a high binarization threshold increases the proportion of black pixels. The additional decrease of  $S_{crit}$  leads to the misinterpretation of image artifacts (reinforced by the choice of a high  $c_{0,1}$ ) as full throats. This corresponds to the error of type 2 in Table 3-7 and Fig. 3-14. Hence, the maximum number of errors is shifted towards high binarization thresholds  $c_{0,1}$  and low critical saturations  $S_{crit}$ . Nevertheless, again, the optimum remains obviously unaffected in a wide range of both parameters. It is found for  $c_{0,1} \cong 0.26 - 0.52$  and  $S_{crit} \cong 0.8$  for all experiments. A summary of the used image processing parameters as well as the according error quantification is given together with the summary of experiments in Appendix A.



**Figure 3-15** Temporal evolution of the dependency of the total number of misinterpreted throats on  $c_{0,1}$  and  $S_{crit}$  on the example of experiment 19.

### 3.4.3 Computation of drying curves and drying rate curves

The drying curve is the time dependent function of the overall PN saturation  $S(t)$ . It can easily be derived with the knowledge about the camera frame rate and the PN saturations  $S$  (computed from Eq. 3-6). As an example, Fig. 3-16a shows the decrease of overall network saturation  $S$  with the progress of drying time (on the example of experiment 17). It is also shown that the function of PN saturation versus time  $S(t)$  is almost unaffected in a relatively wide range of image processing parameters. Furthermore, it indicates that the frame rate is high enough to allow for a constant decrease of PN saturation (i.e. the number of dried throats between the record of two consecutive images is higher than the total number of eventually misinterpreted throats). This is favorable in regard of the later comparison of experiment with simulation.



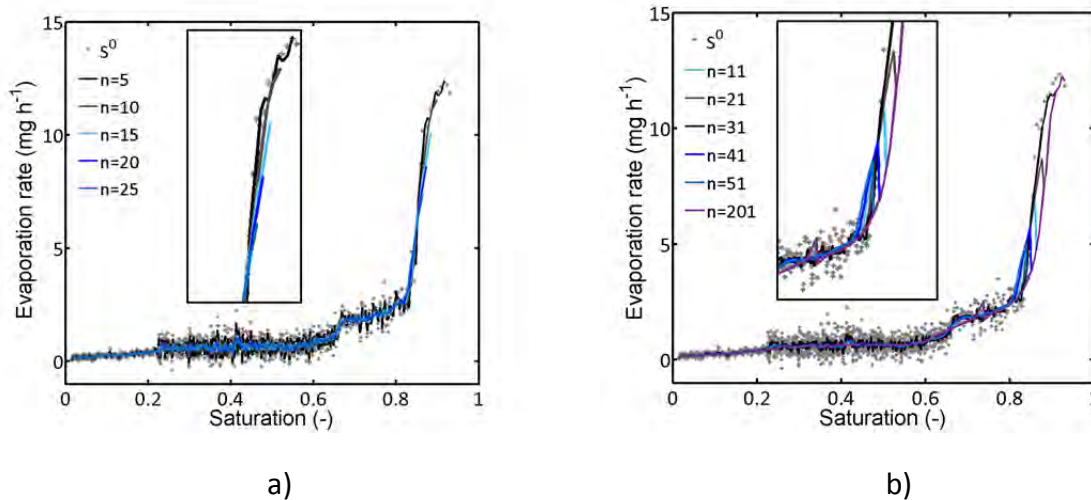
**Figure 3-16** a) Saturation curves computed for varying  $c_{0,1}$  and  $S_{crit}$ . Black lines show the results for  $c_{0,1} = [0.3:0.1:0.6]$  (and  $S_{crit} = 0.8$ ) and  $S_{crit} = [0.6, 0.8]$  (and  $c_{0,1} = 0.38$ ) (these curves are almost overlapping), gray lines represent  $c_{0,1} = 0.2$  and  $S_{crit} = 0.8$  (lower limit),  $S_{crit} = 0.2$  (with  $c_{0,1} = 0.38$ ) (upper limit) and  $S_{crit} = [0.4, 0.9]$  (with  $c_{0,1} = 0.38$ ). b) Drying rates as computed from Eq. 3-7 (and with  $S_{crit} = 0.8$ ,  $c_{0,1} = 0.38$ ). (Data from experiment 17).

It must be noted that the liquid content of wall covering liquid films is not taken into account for the computation of PN saturation because basically the films are eliminated with the algorithm described above. Additionally, partially saturated pores and throats are vanished. This leads to an overall reduction of the computed PN saturation compared to the real saturation of the  $\text{SiO}_2$  network during experiments. A better agreement of the liquid saturation would be obtained with a camera of higher resolution because this would allow for a more precise image analysis. (Principally larger matrices are obtained with higher resolution leading to a more precise interpretation of the liquid content in pores and throats).

The drying rate curve  $\dot{M}_{evap}(S)$  is computed from the difference of PN saturation between two subsequent images recorded at time  $t^{i-1}$  and  $t^i$ ,

$$\dot{M}_{evap} = \frac{(S(t^{i-1}) - S(t^i)) \rho_l (\sum V_t + \sum V_p)}{t^i - t^{i-1}}, \quad (3-7)$$

and plotted against the PN saturation  $S$  in Fig. 3-16b. Based on the assumption that the gas side mass transfer resistances increase during the drying process (with the result of an overall decrease of evaporation rates at the gas liquid interface), one would expect that the difference of the PN saturation,  $S(t^{i-1}) - S(t^i)$ , would generally also decrease. However, the point cloud of the drying rate in Fig. 3-16b demonstrates that  $S(t^{i-1}) - S(t^i)$  underlies a considerable fluctuation. This is a result of several effects. One effect is surely the misinterpretation of throat saturation during the preceding image processing step, for example due to neglecting partially saturated throats. Another effect might be the temporal advance and retreat of the drying front in certain pores and throats. For this reason, it is useful to smooth the data for a better graphical representation of the drying rate curve, with the criterion of not distorting the information (mainly at the beginning of drying). This criterion is fulfilled by the moving average filter (i.e. a low pass filter), which is commonly applied for time series and which suppresses the high-frequency components of a signal while the low-frequency components are almost not attenuated. Regarding the drying rate curve, application of a low pass filter eliminates the high frequency fluctuations of the drying rate while the main trend is unaffected.



**Figure 3-17** a) Drying curves obtained by application of the simple moving average filter with different window sizes  $n$ . The inset shows that information of the start of drying is lost; the effect grows with growing window size  $n$ . b) Drying curves obtained by application of the moving average filter with different window sizes  $n$  indicate a jump of the function independent of the size of the window. The jump is increased for growing  $n$ .  $S^0$  denotes the original data from experiment 17.

The moving average filter computes the moving mean value of a previously defined data window. The width  $n$  of the window determines the number of input values that are accounted for the computation of the current mean value (or output value) and thus it determines the extent of the suppression of the high frequency component. The simple moving average filter computes the mean value at  $t_1$  (frame index) from the  $n-1$  previous values:

$$S(t_1) = \frac{1}{n} \sum_{t_2=0}^{n-1} S^0(t_1 - t_2) \quad (3-8)$$

and

$$t(t_1) = \frac{1}{n} \sum_{t_2=0}^{n-1} t^0(t_1 - t_2). \quad (3-9)$$

As revealed by Fig. 3-17a, this filter has the disadvantage of a lag of  $n-1$ , which means that the information from the start of drying is lost. A remedy can be found using the central moving average filter. In this, the window size  $n$  has an odd number and the window is shifted by  $n/2$  to take values from both sides of the present value  $t_1$  into account, e.g. for  $n = 5$ :

$$s(t_1 - 2) = \frac{1}{n} (s^0(t_1) + s^0(t_1 - 1) + s^0(t_1 - 2) + s^0(t_1 - 3) + s^0(t_1 - 4)) \quad (3-10)$$

and

$$t(t_1 - 2) = \frac{1}{n} (t^0(t_1) + t^0(t_1 - 1) + t^0(t_1 - 2) + t^0(t_1 - 3) + t^0(t_1 - 4)). \quad (3-11)$$

Boundaries of the input data can be treated with an increasing/decreasing window size, e.g. for  $n = 7$ :

$$s(t_1 = 1) = s^0(1), \quad (3-12)$$

$$s(t_1 = 2) = \frac{1}{3} (s^0(1) + s^0(2) + s^0(3)), \quad (3-13)$$

$$s(t_1 = 3) = \frac{1}{5} (s^0(1) + s^0(2) + s^0(3) + s^0(4) + s^0(5)), \quad (3-14)$$

$$s(t_1 = 4) = \frac{1}{7} (s^0(1) + s^0(2) + s^0(3) + s^0(4) + s^0(5) + s^0(6) + s^0(7)), \quad (3-15)$$

$$s(t_1 = 5) = \frac{1}{7} (s^0(2) + s^0(3) + s^0(4) + s^0(5) + s^0(6) + s^0(7) + s^0(8)). \quad (3-16)$$

This results in an overall smaller weighting of the first three values of the output saturation, which inevitably induces a jump when reaching to the final window size and shift of the window in step  $t_1 = 5$ . Consequently, higher jumps are likely to occur for larger window sizes (Fig. 3-17b). Nevertheless, the central moving average filter has a certain advantage compared to the simple moving average filter, namely the good representation of the start of the drying process, which could not be captured with the simple moving average filter. This is confirmed by Fig. 3-17. For the analysis of experiments presented throughout the thesis the central moving average filter with  $n = 51$  is applied.

#### 3.4.4 Estimation of characteristic parameters of the travelling 2-phase zone

Analysis of the travelling 2-phase zone, i.e. the evolving partially saturated zone (also referred to as the drying front), has a significant relevance for the discussion of the characteristic drying behavior at different temperature settings. This is because of the impact of temperature on the invasion of the PN. A main tool to characterize the drying behavior is the analysis of the saturation profiles. From this, width of the travelling 2-phase zone as well as its most advanced point (MAP), least advanced point (LAP) and mean

position can be derived with the aim to be compared to other experimental data or simulations. In addition to that, conclusions regarding interconnectivity of the liquid phase by liquid films as well as condensation effects can be drawn from the number and size of clusters or the number of displacement events as well as the locations of emptying and refilling (especially relevant in the context of condensation).

### *Saturation profiles, position and width of the travelling zone*

Saturation profiles are estimated from the network slice saturations related to the total slice volume (Fig. 3-1),

$$S_{slice} = \frac{V_{l,slice}}{\sum V_{t,slice} + \sum V_{p,slice}}, \quad (3-17)$$

with

$$V_{l,slice} = \sum V_{ver} S_{t,ver} + \sum V_{hor} S_{t,hor} + \sum V_p S_p. \quad (3-18)$$

From this, detachment of the liquid phase from the network top (at  $z = 0$ ) and bottom ( $z = (m - 1)L$ ) can be numerically derived. The LAP of the 2-phase zone represents the upper position of the 2-phase zone, i.e. closest to the network top (at  $z = 0$ ). It is derived from the saturation profile by:

$$z_{LAP} = z^{min}(S_{slice} > S_{crit}). \quad (3-19)$$

In most cases  $S_{crit} = 10^{-3}$ .

The MAP of the 2-phase zone represents the most advanced position of the gas phase. This is the position furthest away from the PN top (at  $z = 0$ ). It is computed from:

$$z_{MAP} = z^{max}(S_{slice} > S_{crit}). \quad (3-20)$$

In most cases  $S_{crit} = 0.98$ . It is noted that throats and pores that could initially not be saturated with liquid with the procedure described in Section 3.3.3 can lead to a misinterpretation of the MAP of the 2-phase zone.

The distance between the LAP and the MAP of the 2-phase zone is denoted as the frontwidth:

$$W_{front} = z_{MAP} - z_{LAP}. \quad (3-21)$$

From this follows, that the maximum frontwidth is found, if both, liquid and gas phase, penetrate the PN from the open top surface to the opposite side, i.e. the bottom of the PN. The mean position of the 2-phase zone results from the mean distance between both points:

$$\bar{z} = \frac{z_{LAP} + z_{MAP}}{2}. \quad (3-22)$$

A more advanced statistic could weight the position of the 2-phase zone with the saturation.

### Number and location of displacement events

The number of displacement events (i.e. liquid/gas or gas/liquid) can simply be derived from a comparison of the saturation state of pores and throats on two subsequent images:

$$\Delta S_{t,p} = S_{t,p}^{t^{i-1}} - S_{t,p}^{t^i}. \quad (3-23)$$

Emptying occurs if

$$\Delta S_{t,p} > 0, \quad (3-24)$$

contrarily, refilling of a pore or throat is given by:

$$\Delta S_{t,p} < 0. \quad (3-25)$$

The number of respective events can then be counted for each network element. It is remarked that any misinterpretation of liquid saturation of pores and throats by image processing impacts on the estimation of phase change events.

### Cluster number and cluster size

The number of clusters is derived from the number of different cluster labels  $l_{cl}$  identified for a given PN saturation (based on the Hoshen-Kopelman algorithm (Al-Futaisi and Patzek 2003, Metzger et al. 2003) as will be explained in Section 5.4.4):

$$N_{cl} = \sum l_{cl}. \quad (3-26)$$

In this  $l_{cl}$  represents the cluster label. Size of a cluster with label  $l_{cl}$  is computed from the sum of liquid filled throats that are connected within this cluster:

$$e_{cl} = \sum (l_t \in l_{cl}) \quad (3-27)$$

The cluster dynamics, i.e. the growth and shrinkage of clusters, is defined from comparison of the cluster size on two consecutive images. For this purpose, the current size of any cluster  $e_{cl}$  at time  $t^j$  is compared to the size of this cluster at time  $t^{j-1}$ :

$$\Delta e = e_{cl}^{t^{j-1}} - e_{cl}^{t^j}, \quad (3-28)$$

From this follows that the cluster is shrinking (or drying) if  $\Delta e$  is positive and contrarily it is growing (due to condensation and refilling) if  $\Delta e$  is negative. It must be noted that the frame rate has an impact on the evaluation of cluster dynamics. Precisely, if the frame rate is too high, even small misinterpretation in the image processing step impacts on the identification of growing and shrinking clusters.

## 3.5 Summary

In order to develop and to experimentally validate the mathematical PN model to be presented in Chapter 5, as discussed a 2D microfluidic PN was produced by photolithography and chemical wet etching and evaluated in this chapter. In addition to that, an experimental set-up was presented which allows to impose defined temperature gradients of different direction on the microfluidic device. This is an innovation in the field of the study of drying in porous media by PNs. The suitability of this set-up for drying experiments with different

imposed temperature settings was shown, and, its advantages and disadvantages were discussed in detail. As a main advantage, high quality images can be obtained with this set-up and allow to follow the discrete invasion of the PN with an optical CCD camera - a comparably simple, nondestructive and inexpensive method. Disadvantages are linked to the undefined shape of the channels as well as the undefined surface roughness, both a result of the production process, which are relevant for the development of liquid films during drying experiments (as will be discussed in Chapter 4). It was discussed that such films are optically detected with the experimental set-up. The impossibility to avoid liquid films in the microfluidic PN shows their basic importance for drying of porous media.

Furthermore, dependency of the analysis of drying experiments by the image processing method on the experimental design was explained. It was discussed how deterioration of the images can affect the analysis of pore scale liquid saturation and how the estimated PN saturation depends on the choice of image processing parameters, namely the binarization threshold and the critical saturation. It was proven that the drying curves and drying rate curves can be accurately determined for a wide range of these parameters. However, the image filters vanish liquid films as well as partially saturated pores and throats. This can lead to a slight reduction of the estimated PN saturation compared to the true saturation. Furthermore, the location of the film region cannot be numerically investigated with this method. As a consequence, alternative methods are explained in Chapter 4.

It can be summarized that the developed experimental design and microfluidic PN provides a very strong base for the investigation of mass transfer under non-isothermal conditions in PNs. For this purpose, the numerical data obtained from the optical record of drying experiments is accurately and reliably prepared with the aim of model development and validation (Chapters 5 and 6). It is noted that such a detailed study of the pore scale liquid distribution in microfluidic PNs has never been presented before.

„I am a firm believer that without speculation there is no good and original observation.“

Charles Darwin

\* February 12, 1809 in Shrewsbury/Shropshire, UK

† April 19, 1882 in Downe/Kent, UK

## Chapter 4

# Drying experiments with the microfluidic pore network

### 4.1 Introduction

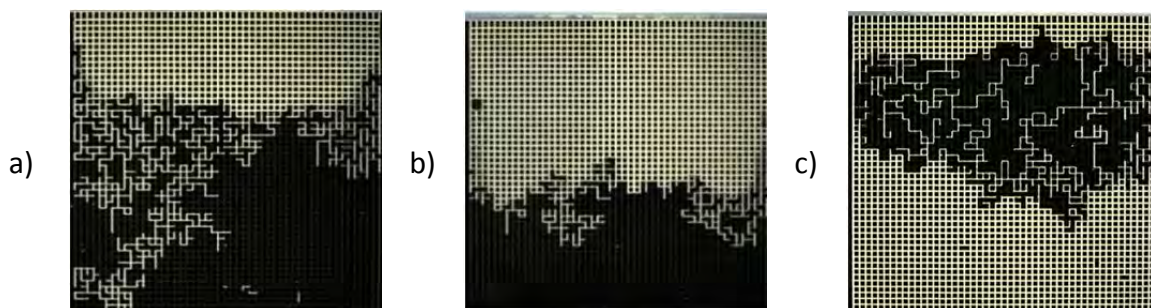
The distribution of liquid and gas phase inside a drying porous medium depends on the inner pore structure and the physical properties of liquid and solid, which are usually fixed. Despite of this, it is possible to externally influence the drying process by either imposing gravity forces on the porous medium or thermal gradients. The impact of thermal gradients on drying of the microfluidic 2D SiO<sub>2</sub> PN shall be discussed in what follows. Gravity effects are disregarded as they are excluded with the experimental setup.

The chapter initially provides an overview on the relevant invasion processes observed during non-isothermal drying of the microfluidic PN. These are basically the primary invasion of the bulk pore space (Section 4.2.1) and the secondary invasion of the sub-structure of the PN with high capillarity, namely crevices and corners (Section 4.2.2). It is shown that wetting liquid films control drying of the PN independently of the temperature field as they remain in geometrical singularities when the bulk menisci recede. Consequently, the secondary network essentially contributes to the sustainment of a significantly higher connectivity of the liquid phase as well as an evaporation front position closer to the PN open side. In agreement with literature, e.g. Yiotis et al. (2004), Prat (2007) and Chauvet et al. (2009), drying rates are increased and the overall drying time is reduced in presence of liquid films. Due to this, the secondary invasion is seen as a major process in the microfluidic device. Morphology and extent of the liquid films, besides material wettability, strongly depend on the structure of the local geometrical singularities and the surface roughness. It will be shown and discussed in Section 4.2.2 (by images from Confocal Laser Scanning Microscopy) that the secondary capillary structures in the center of the 2D PN have the shape of liquid film rings, i.e. markedly different from the classical conception of a continuous liquid film region of much greater extent upstream of the drying front (Yiotis et al. 2004, Prat 2007),



whereas the wall covering liquid films along the PN lateral side walls are in good agreement with literature.

The main focus of this chapter is the presentation and analysis of experiments with different heating modes. Section 4.3 therefore summarizes the experimental study of quasi-isothermal drying at an elevated temperature level, with temporally constant temperature of around  $\bar{T} \cong 63^\circ\text{C}$ , with the aim to i) validate reproducibility of experiments (under constant conditions) and ii) develop further the PNM of drying (as will be presented in Chapter 5) in the face of prominent pore scale effects, such as the liquid films. The relevant experiments are designated by numbers 17, 19, 20. Subsequently, focus of Section 4.4 is on the experimental study of drying with imposed, temporally constant temperature gradients with the aim to experimentally prove trends deduced from simulations in literature (Huinink et al. 2002, Plourde and Prat 2003 and Surasani et al. 2008a) and moreover to investigate more precisely the prominent impact of the two different thermal gradients on the observable physical effects and the overall drying behavior. The relevant experiments are # 8, 13, 15 for drying with imposed negative temperature gradient and # 10, 11, 18 for drying with imposed positive temperature gradient. It is clearly demonstrated that the temperature settings deeply influence the drying process of the microfluidic device (Fig. 4-1). As also predicted by simulations (Plourde and Prat 2003, Surasani et al. 2008a) stabilization of drying front occurs in case of a negative temperature gradient ( $dT/dz < 0$ ) whereas destabilization with early breakthrough and initiation of a second invasion front is observed in case of a positive temperature gradient ( $dT/dz > 0$ ). The presented experiments are in very good agreement with these literature observations and therefore reveal and illustrate that the drying process can be fundamentally affected by externally imposed temperature gradients. It is additionally emphasized that experiments with positive gradient show strong condensation effects as a result of vapor diffusion opposite to the temperature gradient. Condensation was yet either totally ignored or underestimated in literature. However, experiments clearly show that condensation of vapor accompanied by refilling of partially saturated pores and throats and their empty neighbors significantly influences the phase distribution during drying and thus the overall drying process. These observations are the base for further model development in Chapter 5.



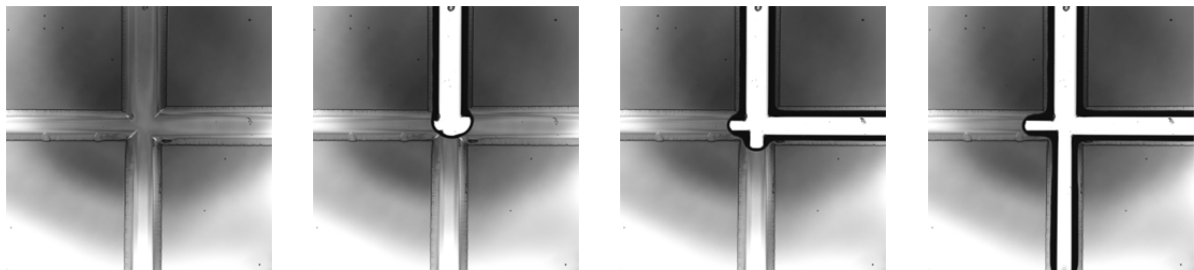
**Figure 4-1** Raw images from drying experiments with different heating modes: a) quasi-isothermal experiment (exp. 20), b) experiment with imposed negative thermal gradient (exp. 15), c) experiment with imposed positive thermal gradient (exp. 18). Liquid filled pores and throats and the solid appear in black, empty pores and throats appear in white. Liquid films can be identified through the intermediate gray regions in the partially saturated PN regions. Drying from the top edge.

## 4.2 Pore scale analysis of pore network invasion

Drying of the microfluidic PN is controlled by i) the primary invasion mechanisms, which are the capillary invasion of (bulk) pores and throats and the vapor diffusion through the empty bulk space as well as ii) secondary invasion mechanisms, i.e. in liquid films forming in the crevices of throats as well as along the side walls of the PN. The latter is denoted by lateral pinning of liquid or the edge effect. The relevance of both invasion mechanisms on drying was studied using Confocal Laser Scanning Microscopy (CLSM)<sup>20</sup>. With this, both, invasion of the bulk pore space as well as the structure and drying of liquid films could be visualized because distinct details on the pore scale could be magnified.

### 4.2.1 Primary invasion

Figure 4-2 shows the primary invasion of the PN in discrete steps on the example of a pore junction, i.e. one pore and the adjacent throats (similar to the representation on the right side in Fig. 3-1). The smooth surface (in the center of pores and throats) appears in white, the rough surface along the side walls appears in black due to multiple light refraction and absorption (Fig. 3-4b). Additionally, liquid films are identified as gray regions inside the black zone. In Fig. 4-2, the liquid saturated throat with the lowest capillary pressure threshold is spontaneously invaded by the gas phase (this is the throat in the north of the images) while the other throats remain liquid filled. The pore, to which the invading throat is connected, is invaded together with the throat. The remaining disconnected throats are then invaded independently of each other. The discrete invasion of throats is the basic assumption of the PN drying model proposed in Chapter 5.

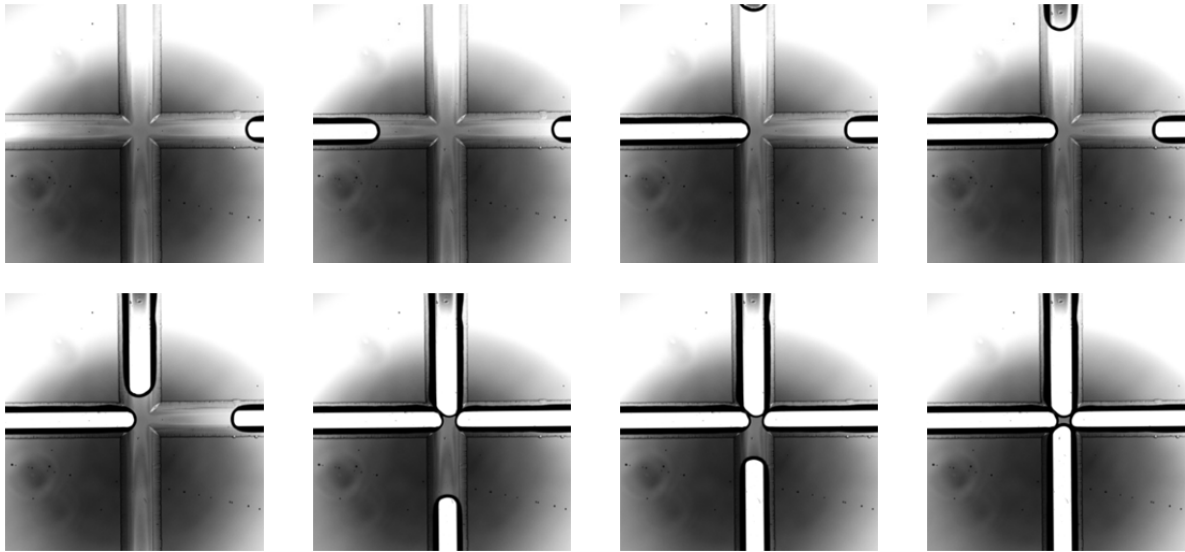


**Figure 4-2** Pore scale capillary invasion of a pore junction with 4 adjacent throats. Dry pore space in white, liquid and solid in gray and liquid films confined inside the black zone also in gray.

However, in most cases observed with the CLSM the gas-liquid interface did not invade the PN in discrete steps but moved continuously with low velocity (characteristic for invasion percolation processes (Wilkinson and Willemsen 1983)). This observation is explained with the relevance of liquid pumping as a consequence of liquid pressure gradients arising between the menisci that are interconnected in a liquid cluster (Tsimpanogiannis et al. 1999). This might be related to the relatively long throats and the small depth of the PN. As shown in Fig. 4-3, this leads to partially saturated throats with different positions of the gas-liquid interface inside the throats, the simultaneous invasion of liquid throats interconnected in one liquid cluster, liquid bridges as well as the pinning of

---

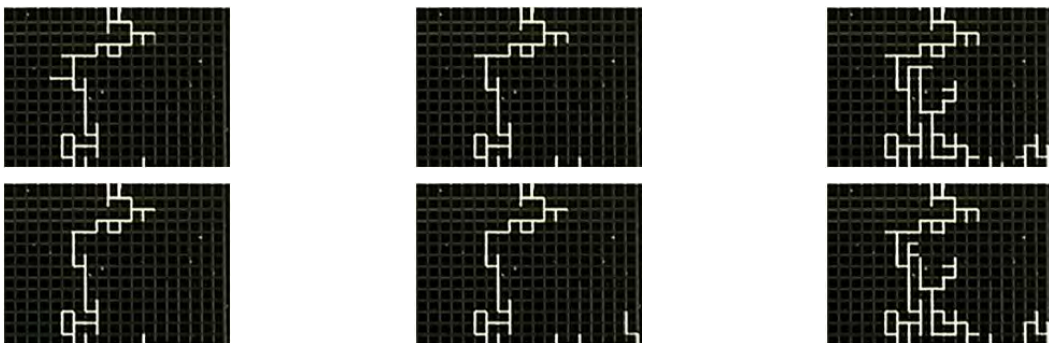
<sup>20</sup> Leica TCS SPE, 10x magnification, red laser 635 nm



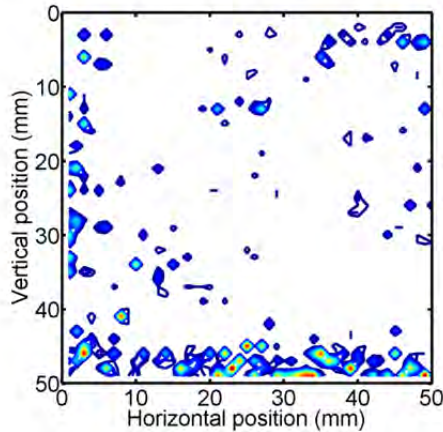
**Figure 4-3** Simultaneous invasion of adjacent throats and formation of a liquid bridge in the pore junction to which the throats are connected.

liquid inside pores. These observations clearly reveal the potential of a future study of pore scale gas invasion in the 2D microfluidic PN. Independent of this, the PNM presented in Chapter 5 is based on the assumption of capillary invasion in discrete steps. As will be shown in Chapter 6, this assumption already leads to very good agreement of the simulation results with experiments. This is partly explained with the temperature effects on physical parameters.

Figure 4-4 illustrates that the invasion process is affected by liquid re-distribution as already described in Section 2.3.4. It shows several examples from experiment 10. Comparison of each upper and lower image (taken at different drying times) reveals that the invasion of the selected liquid cluster by the gas phase is accompanied by liquid invasion at the same cluster boundary. This leads to a different order of emptying and refilling than compared to drying without redistribution of liquid along the cluster boundary. This effect is numerically analyzed in Fig. 4-5, which shows a map of the cluster boundary invasions as a contour plot for the complete microfluidic network and  $S \cong 0.4$ . The map indicates that redistribution occurs already at the start of drying when condensation effects, as will be explained in detail below, are expected to have a negligible impact on the phase distributions.



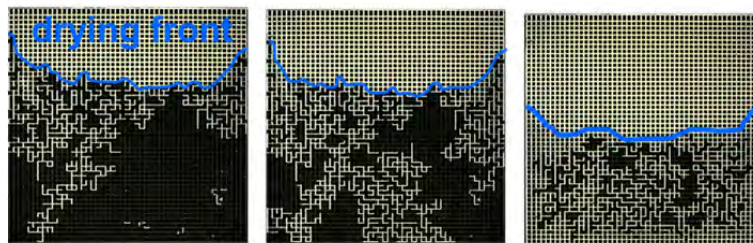
**Figure 4-4** Illustration of liquid redistribution along the cluster boundaries. The upper images show the situation before invasion and the lower images after invasion for varying network saturations. (Images from experiment 10).



**Figure 4-5** Map of the displacement events along cluster boundaries as a contour plot (exemplarily shown for experiment 10 after removal of 60 % of the liquid). The contours represent the position of cluster boundaries with more than 4 invasion events between 280 consecutive images (with  $\Delta t = 30$  s). The maximum number of local invasions is 29. (Minimum number of invasions as blue contour lines and peaks in red).

#### 4.2.2 Secondary invasion

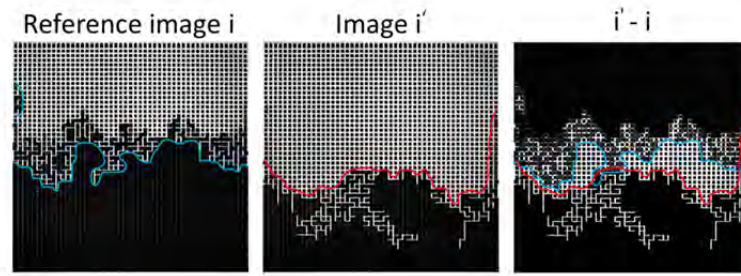
The liquid films can be distinguished from the raw data of the CCD camera as they appear as a gray region forming inside the partially saturated and dry zone of the PN. This is depicted in Fig. 4-6, where the desaturated pores and throats underneath the evaporation front contain liquid films and thus appear in gray. Contrarily the dry throats above the evaporation front appear in white.



**Figure 4-6** Raw images from experiment 17. Gas phase in white, liquid phase and solid islands in black and liquid films (underneath the evaporation front) in gray.

From the CCD images of the drying experiments, the extent of the film region is derived by image analysis based on the image processing algorithm presented in Section 3.4 (Fig. 4-7). Note that the gray level images are compared here, allowing for a discrimination of the liquid films from the different gray values of the image. The gray level difference between image  $i$  and image  $i'$  is obtained when subtracting image  $i'$  from image  $i$ . The difference is shown in the image at the right hand side of Fig. 4-7. In this, identical gray values appear in black (with value 0) and totally dried throats appear in white. Throats containing a liquid film either on image  $i$  or image  $i'$  appear in gray.

The situations illustrated in Figs. 4-6 and 4-7 are representative for drying of the microfluidic network. They indicate the confinement of liquid films to the 2-phase zone in the center of the PN; note that the edge effect is also observed above the 2-phase zone (Section 4.2.2.2).



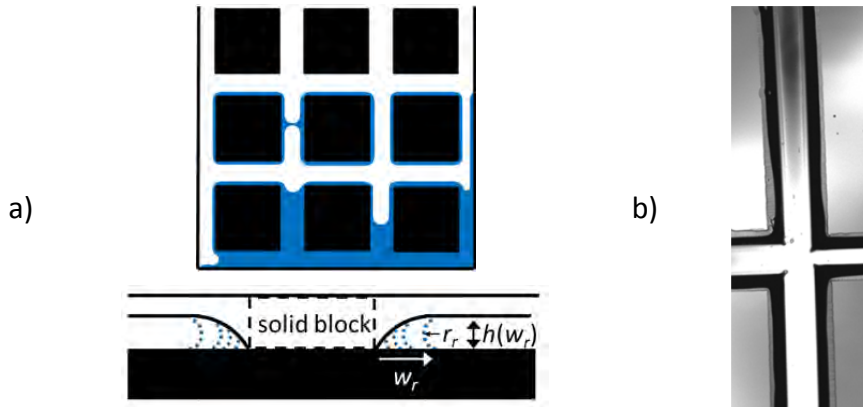
**Figure 4-7** Binary image from experiment 15. The blue line roughly indicates the lower boundary of the drying front in the reference image  $i$  and the red line roughly sets the upper boundary of the drying front in image  $i'$ . The zone between these two boundaries dries totally in this sequence, i.e. no films are found in this zone in image  $i' - i$ . Notice that the gray values of films disappearing above the red line and films developing below the blue line in image  $i' - i$  are different.

#### 4.2.2.1 Liquid film rings

Measurement with CLSM reveals the limited interconnection of liquid films in the 2D microfluidic network (if the edge effect is ignored) (Figs. 4-8 to 4-10). The microscopic study shows that liquid films form disconnected liquid wedges with an annular structure around the solid islands (similar to the anticlastic form of liquid films described by Haines (1930) or the liquid wedges described in Segura (2007)) (Fig. 4-8a). It appears that the film development is especially promoted by the non-cylindrical structure of the throats as well as the surface roughness along the side walls (Figs. 3-1 and 3-4b). Due to the annular structure of liquid wedges they are also referred to as liquid rings throughout the thesis.

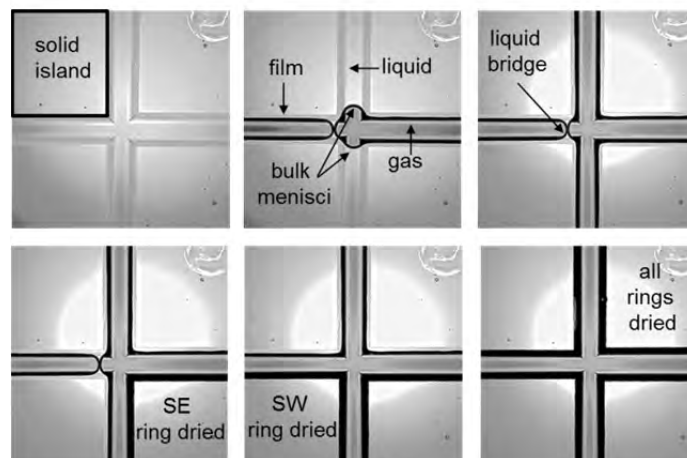
Figure 4-8b shows liquid films along a dried pore junction. Precisely, the liquid film rings appear in gray inside the black zone at the sides of the throats. Average width of the liquid film rings was determined in the range of  $21.4 \pm 2.4 \mu\text{m}$ . However, Fig. 4-8b reveals that the width can vary locally, which might be explained with the local variation of surface roughness and wettability and the pinning of films to the morphological inhomogeneities. Furthermore, CLSM measurements detected a temporal fluctuation of the ring width. This is assigned to variations in the capillary pressure threshold of the liquid cluster connected to a ring (Vorhauer et al. 2015). It is assumed that the temporal fluctuation of the ring width is also associated with the local PN structure. Figure 4-8a emphasizes that the height of the throat and thus the height of the ring increase from the lateral wall towards the throat center with  $h^{max}(w_r) = L_d$ . This affects the interface curvature of the ring as sketched in Fig. 4-8a. In consistency with Eq. 2-25, a smaller ring interface curvature  $r$  is referred to a higher capillary pressure. Thus, the capillary pressure is expected to increase with decreasing width  $w_r$  of the ring. Or, if the liquid pressure of the cluster to which the ring is connected increases, the ring can horizontally expand to a position with a greater height and interface curvature (Fig. 4-8a).

It is strongly assumed that, due to the ring structure of films, continuity of the film region can only be sustained if the film rings are connected by bulk menisci or liquid bridges (as exemplarily illustrated in Fig. 4-8a). This is revealed in Figs. 4-9 and 4-10. Notice the piston type displacement by the gas phase in these figures.



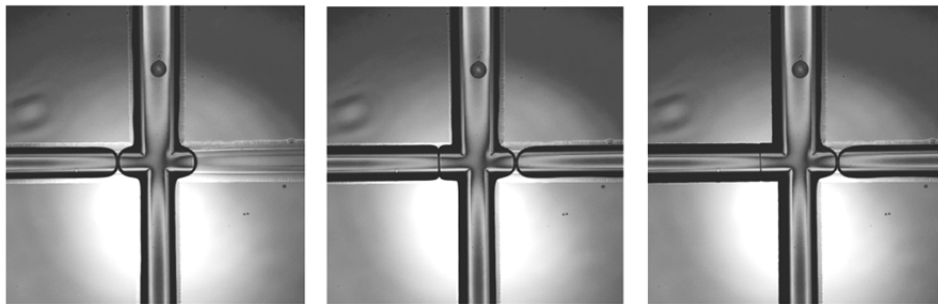
**Figure 4-8** Formation of liquid films along the throat side walls. a) Film geometry. The top view shows the formation of liquid rings (in blue) around the solid (in black) with dry out of the pore space (in white). The rings are connected by the bulk liquid phase (at the bottom) and liquid bridges (in the center). The cross sectional view shows the arrangement of one film around one solid block. The film height and interface curvature are a function of the film width due to the geometry of the pore space. b) Local variation of the film width due to surface defects from CLSM.

In Fig. 4-9 the pore junction as well as the adjacent throats are initially fully saturated with liquid. Then, the gas phase penetrates the pore node from the east and west as well as from the north and south, leaving a liquid bridge which connects the northwest liquid ring with the southwest liquid ring. The southeast (SE) ring then dries independently of the other liquid rings. The southwest (SW) ring dries after disconnection from the northwest ring, i.e. after disappearance of the connecting liquid bridge. This indicates that liquid rings must be isolated if liquid connectivity by either bulk menisci or liquid bridges vanishes. In contrast to this, the simultaneous drying of rings was observed in presence of sustained liquid bridges (Fig. 4-10), making worth a more precise investigation of the secondary invasion mechanisms in future.



**Figure 4-9** Development and drying of liquid film rings (SE: southeast, SW: southwest). Adopted from Vorhauer et al. (2015). Notice that the magnification of the microscope only allows to visualize the pore junction.

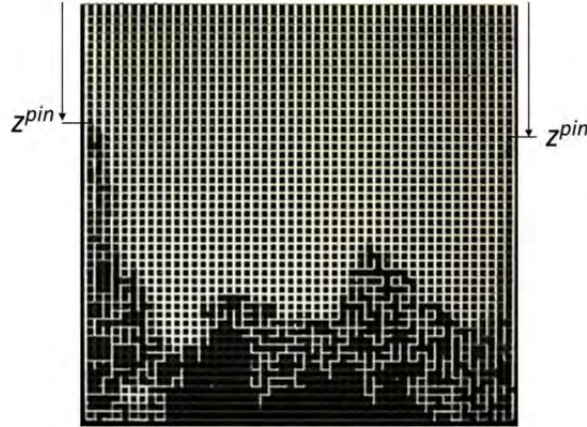
From Figs. 4-9 and Fig. 4-10 follows that the impact of liquid rings on the global moisture transfer is limited to the 2-phase zone, where the liquid phase is multiply connected by single bulk menisci and liquid bridges. Liquid rings can indeed increase the interconnectivity of the liquid phase within the 2-phase zone, but they cannot contribute to a favorable front position closer to the network opening, as associated with a continuous film region. Precisely, the evaporation front position in the center of the PN is only one or two pore rows closer to the network surface compared to the situation without liquid rings. From this follows that other effects need to be considered to explain the increase of overall drying rates observed in experiments (see Section 4.2.2.2). The higher interconnectivity in presence of liquid films can though positively affect liquid transfer within the 2-phase zone with the result that e.g. emptying of the network bottom occurs before detachment of the 2-phase zone from the network top side. This is obviously in favor for a shorter second drying period because less moisture has to be removed from the network bottom when diffusion resistances are high (see also Fig. 2-28).



**Figure 4-10** Simultaneous drying of liquid rings in presence of a connecting liquid bridge.

#### 4.2.2.2 Edge effect

Lateral pinning of liquid was experimentally observed along the PN edges (refer to Fig. 3-1). It is thus also referred to as the edge effect. More precisely, the edge effect was mainly observed in quasi-isothermal PN drying and drying with negative temperature gradient. It is depicted in Fig. 4-11 and explained by the capability of long and continuous liquid films to cover the lateral sides of the PN over several pore rows leading to liquid continuity from the bulk liquid phase at the PN bottom side to the laterally pinned tip of the evaporation front. Temperature distributions in Fig. 3-8 indicate that the temperature was slightly lower at the left side of the PN promoting stability of liquid films along this edge with the result that position of the film tip is generally at a more advanced position here. Based on this effect, the least advanced point (LAP) of the 2-phase zone is several pore rows closer to the network open side than the evaporation front in the center of the PN. This allows to significantly increase drying rates since the diffusive vapor transport can be accompanied by effective liquid transport along the lateral PN walls. (This is numerically investigated in Section 6.2.5). It is assumed that the specific structure of the microfluidic network, namely the straight lateral walls, supports the edge effect. As a consequence, it is recommended to avoid continuous walls inside microfluidic networks for future experimental investigations. Instead, the throat columns along the side boundaries should be removed or the respective throats should be made broader in order to avoid liquid connectivity along the network edges. Alternatively, irregular PN structures could be developed (e.g. Geistlinger et al. 2016).



**Figure 4-11** Lateral pinning of liquid in experiment 8 ( $S \cong 0.2$ ).

### 4.3 Drying with spatially quasi-constant temperature

The spatially constant temperature field was realized with the two water streams at almost identical temperature level ( $T_{back} \cong T_{front} \cong 64\text{-}65^\circ\text{C}$ ). Interestingly, infrared detection of the temperature field of the surface of the PN indicates heterogeneity with a slight temperature decrease in  $z$ -direction as well as a temperature drop along the lateral network edges (Fig. 3-8a). The latter can be explained with heat losses to the environment. In detail, the temperature gradient in  $z$ -direction is related to the geometrical construction of the heat exchanger plate and heat exchanger water circuits as well as heat exchange with the air flow channel (located at  $z = 0$ ). It is noted that the drying air was not pre-heated and had a temperature lower than the PN surface ( $\bar{T}_{air} \cong 25^\circ\text{C}$  in this study). According to Sections 2.3.4 and 2.4.2 the temperature distribution impacts on the order of emptying and the observable phase distributions. This was explained with the temperature dependency of surface tension in Section 2.4.2. Now, Fig. 4-12 shows the capillary pressure difference imposed due to the slight thermal gradient occurring in this setup. As can be found, the variance appears small in this case. Nevertheless, the small temperature gradients in penetration direction of the drying front can have a minor front stabilizing effect. This is reflected by the phase distributions as discussed in the following.

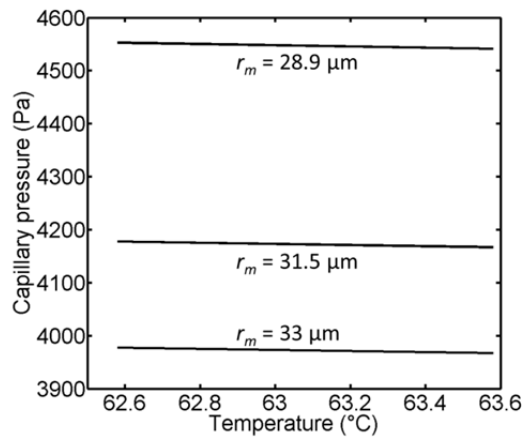
The phase distributions evolving from the imposed quasi-isothermal temperature field (Fig. 3-8a) are discussed in Section 4.3.1 (Fig. 4-13) on the example of experiment 17. It is noted that the repeatability of this drying experiment is excellent. (Refer to Appendix A.2 for further phase distributions, parameter specification of experiments and drying curves). The detailed structural analysis of the pore scale liquid distribution in Fig. 4-15 as well as the drying curves in Section 4.3.2 summarize all quasi-isothermal drying experiments. These are experiments 17, 19 and 20.

#### 4.3.1 Phase distributions

As illustrated in Fig. 4-13 the gas phase penetrates the microfluidic PN to position  $z_{MAP}$  (also referred to as the most advanced point of the 2-phase zone) while the network surface remains partially saturated at the start of drying (Fig. 4-13a); disconnection of the liquid



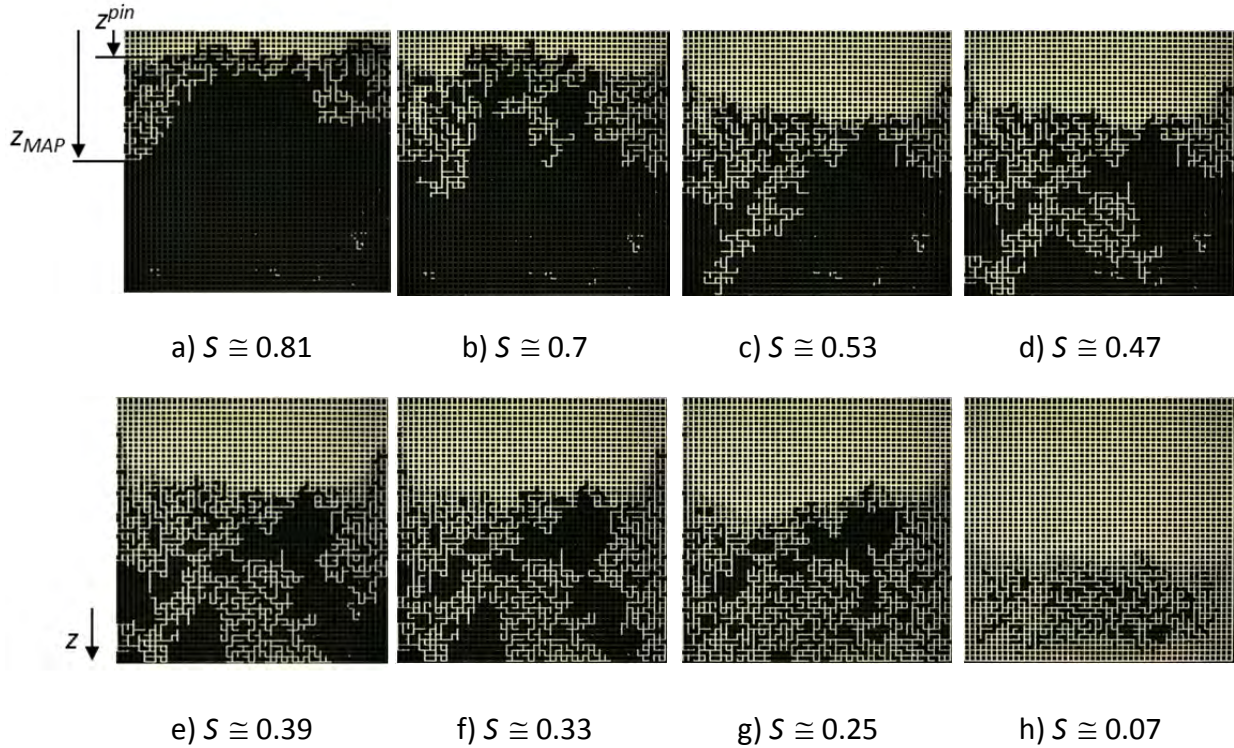
phase from the open network side occurs at overall network saturation of  $S \cong 0.81$ . Due to the edge effect, the LAP of the 2-phase zone remains pinned a few pore rows above position  $z_{MAP}$  ( $z^{pin} \cong (5-15)L$ ) while the liquid front is more and more split up into numerous disconnected single clusters (Fig. 4-13a-g). Pinning of the liquid front is also reflected by the saturation profiles in Fig. 4-14 and the structural analysis of the phase distribution in Fig. 4-15a, where the LAP is plotted. As can be seen the LAP remains close to the PN surface (in the center of the PN, compare also with Fig. 4-13a,b) until  $S \cong 0.65$  and then recedes to position  $z^{pin} \cong 6$  until  $S \cong 0.2$ . Notice that the position of liquid pinning is different on the left and right edges of the PN. More clearly, the position is slightly more advanced on the right side (due to the temperature profile, Fig. 3-8a).



**Figure 4-12** Temperature affected capillary pressure in the microfluidic PN computed in the range of the detected temperature field of quasi-isothermal drying. The three curves are plotted for varying half width of the mean menisci and  $\cos \theta = 1$  (Eq. 2-25).

Figure 4-13a,b reveals a minor stabilization of the main cluster, as numerous single clusters survive upstream of it while the width of the 2-phase zone remains temporally constant between  $S \cong 0.81$  and  $S \cong 0.55$  (not shown in Fig. 4-13). The stabilizing effect is explained with slight temperature variations and the high interconnectivity of the liquid phase due to liquid rings (Fig. 3-8a) and the possibly resulting moisture migration within the drying front: moisture evaporating at the LAP, at slightly higher network temperature, partly migrates towards the MAP, at slightly lower network temperature, and condenses. In the liquid phase, moisture migration is expected to occur also in the direction of decreasing temperature. Additionally, gas invasion might be promoted in the warmer regions (interconnected with colder zones by liquid filled pores and throats and liquid bridges). From this follows the stagnation of the broadening of the 2-phase zone in Fig. 4-15b. Notice that the stabilizing effect occurs only temporally and is additionally significantly less promoted than in drying with imposed negative thermal gradient. It might also be explained with viscous effects as detected by CLSM measurements. This issue is explored in Chapter 6 by PN simulations.

When the gas phase breaks through to the bottom of the network at  $S \cong 0.53$  (Fig. 4-13c), the phase distribution is characterized by a continuous dry zone connected to the top of the PN and a 2-phase zone with one main liquid cluster connected to the PN bottom. Afterwards the main liquid cluster shrinks, while the position of the evaporation front remains almost unaffected at the lateral edges and in the center of the PN as well. During this period, the

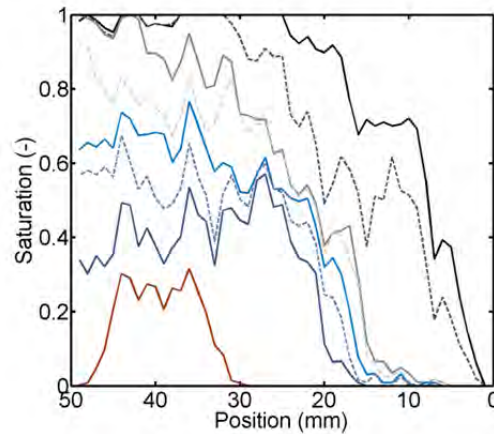


**Figure 4-13** Gas-liquid distributions in the quasi-isothermal PN. a) Disconnection of the liquid phase from the PN surface at  $S \cong 0.81$ . b) Thinning out of the drying front at almost constant most advanced point  $z_{MAP}$  ( $S \cong 0.7$ ). c) Breakthrough of a gas branch to the network bottom at  $S \cong 0.53$ . d-g) Further thinning out of the liquid phase at almost constant front position  $z^{pin}$  ( $S \cong 0.39$  to  $S \cong 0.25$ ). h) Residual liquid clusters and liquid films ( $S \cong 0.07$ ). Images from experiment 17. Gas phase in white, liquid phase and solid islands in black and liquid films in gray.

width of the 2-phase zone remains again constant between  $S \cong 0.53$  and  $S \cong 0.25$ . It is highlighted that the dry out of the two clusters connected to the bottom of the PN in Fig. 4-13f can only be explained with the existence of liquid films for the given temperature field in Fig. 3-8a, thus excluding evaporation at the bottom of the PN and vapor diffusion towards the bottom side. More clearly, invasion of these clusters is explained with a higher invasion probability (with mean half width of liquid menisci  $\bar{r}_m = 31.5 \mu\text{m}$ , Eq. 2-25) than compared to liquid film rings (interconnected by liquid filled pores and throats and liquid bridges) and liquid films associated with the edge effect at the evaporation front, which though have a higher temperature but significantly smaller width. The dry out of the two larger clusters leads to the formation of numerous smaller single clusters which are usually made up of only one or two liquid filled pores and throats. This is reflected by the plot of the maximum cluster size in Fig. 4-15d which shows a constantly decreasing trend. Following Section 4.2.2, these clusters are interconnected by liquid rings and liquid bridges. The maximum cluster number is found at a saturation of  $S \cong 0.3$  (Fig. 4-15c). The small drop of the cluster number at  $S \cong 0.6$  is explained with the stagnation of the MAP of the 2-phase zone and invasion of the clusters upstream of the drying front, i.e. with the stagnation of the expansion of the drying front width (see Appendix A.2, Table A-4 for phase distributions during this drying period).

At the end of drying (Fig. 4-13g,h) the liquid phase recedes from the PN center as well as from the lateral edges. Furthermore, it is observed that the liquid phase also detaches from the bottom of the network, which is indicated by overall higher saturation in the network center compared to the network bottom (Fig. 4-14). Residual liquid is found at a position between  $z \cong 32$  mm and  $z \cong 47$  mm. However, Fig. 4-13h indicates that the network bottom is not completely dried but covered by a zone of liquid films apparent by the intermediate gray image sections. This is though not detected by saturation profiles in Fig. 4-14 because of the applied image filters (see Sections 3.4.1 and 3.4.2 for a detailed discussion). Preferential drying of the network bottom is again explained with liquid transport through liquid films along the PN side walls.

In summary, these observations are generally in very good agreement with Tsimpanogiannis et al. (1999) who predicted i) a far-field regime of initial liquid phase, ii) a drying regime in which liquid and gas phase are macroscopically connected, iii) a regime in which the liquid phase is disconnected and individual liquid clusters show up, iv) a regime of pendular rings or films covering the solid surface and the v) totally dry PN.



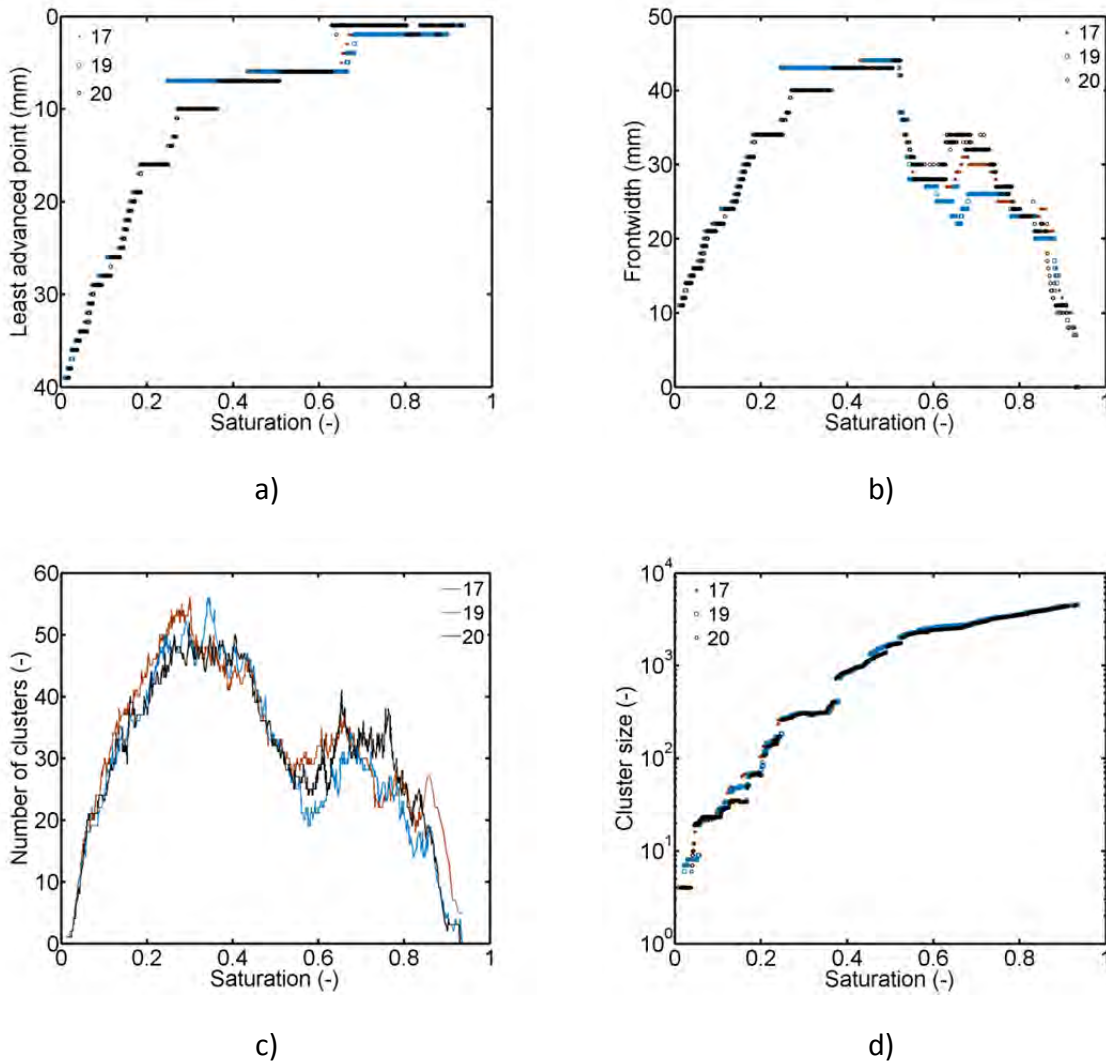
**Figure 4-14** Saturation profiles from experiment 17. The curves are plotted for overall network saturations  $S = [0.81, 0.7, 0.53, 0.47, 0.39, 0.33, 0.25, 0.07]$  (from right to left). Notice that the PN top is referred to position  $z = 0$ , i.e. on the right hand side of the figure.

### 4.3.2 Drying curve and drying rate curve

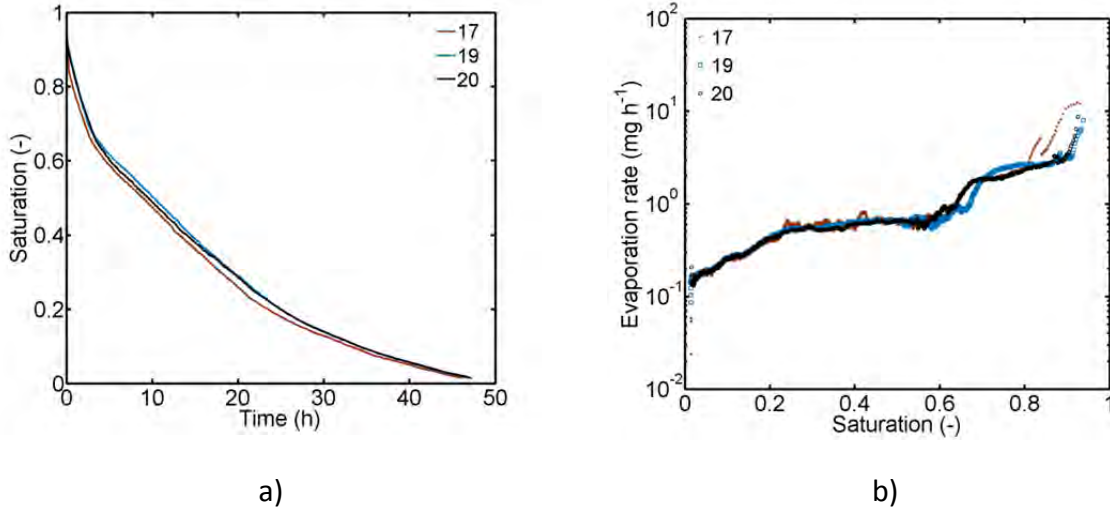
Drying curves and drying rate curves of experiments 17, 19, 20 are illustrated in Fig. 4-16 and reveal no distinct deviations. The average drying time to reach a residual network saturation of  $S \cong 0.015$  is  $t \cong 47$  h for a drying rate of  $\dot{M}_{evap,0} \cong 8 \text{ mg h}^{-1} - 12 \text{ mg h}^{-1}$  detected at the start of drying ( $S_0 \cong 0.94$ ).

In principal five drying periods are distinguished from the drying curves in Fig. 4-16 and phase distributions in Fig. 4-13; note that this is somehow different to the theory presented in Section 2.5.5. In each experiment the drying rate drops already at the beginning of the drying process, thus with the dry out of individual surface pores and the decrease of surface saturation (down to  $S \cong 0.81$ , compare with previous section). Ergo, a period of constant drying rate (Schluender 2004, Suzuki and Maeda 1967) is not observed at the very start of drying. This is mainly based on the 2-dimensional structure of the microfluidic network and the initially absent connectivity of the bulk liquid phase and network surface by liquid films (Prat 2002).

Then a period of nearly constant drying rate occurs until  $S \cong 0.7$  (exp. 19) and  $S \cong 0.65$  (exps. 17, 20). This is maintained by the constant LAP of the evaporation front in the center of the PN (Fig. 4-13a,b). When the liquid phase recedes from the open network side, especially in the center of the PN (Fig. 4-13b,c), the drying rate drops a second time. This drop is followed by another period of constant drying rate, which is favored by the pinning of the LAP of the evaporation front to the lateral edges of the PN as well as by the stable position of liquid clusters at the least advanced front position in the network center again promoted by liquid films (Fig. 4-13c-g). In the last period, drying rate decreases according to the receding of the evaporation front from the lateral edges and from the center (Fig. 4-13g,h).



**Figure 4-15** Characterization of the 2-phase zone and liquid cluster dynamics of experiments 17, 19, 20. a) LAP of the drying front (computed for  $S_{crit}(Z_{LAP}) = 10^{-3}$  in Eq. 3-19), b) frontwidth ( $S_{crit}(Z_{MAP}) = 0.98$  in Eq. 3-20), c) number of liquid clusters, d) maximum size of liquid clusters (in terms of interconnected cluster throats). Computation of the frontwidth in b) requires subtraction of the pore rows with initially non-saturated pores and throats according to Eq. 3-21. Note the good representation of the edge effect in a), b). The overall PN saturation decreases from right to left in these figures.



**Figure 4-16** a) Drying curves, b) semi-logarithmic plot of drying rate curves (from experiments 17, 19 and 20).  $\dot{M}_{evap,0}$  ( $S = 1$ ) is not available due to the experimental procedure, instead the drying rate curves start at a slightly lower saturation ( $S_0 \cong 0.94$ ).

### 4.3.3 Capillary Number

The capillary number is an indicator for the relevance of capillary invasion vs liquid pumping. From Eq. 2-46 follows that viscous friction forces are negligible if the capillary number is small. The capillary number is computed from (Metzger et al. 2007b):

$$Ca = 2 \frac{\eta(T) \dot{M}_{evap}}{\sigma(T) \rho_l(T) \bar{r}_t L_d r_t^{std}}, \quad (4-1)$$

assuming  $T = 63^\circ\text{C}$ , rectangular capillaries with average cross section  $A = 2\bar{r}_t L_d$  ( $\bar{r}_t$  denotes the average half width of throats) and standard deviation of the half width of throats  $r_t^{std}$ . From Eq. 4-1 follows that the capillary number decreases with decreasing evaporation rate  $\dot{M}_{evap}$ , thus with the progress of drying. The maximum capillary number is consequently found at the start of drying when  $\dot{M}_{evap}$  is maximum. The capillary number is plotted in Fig. 4-17a as a function of  $\dot{M}_{evap}$  adopted from experiment 17. A similar range of capillary number can be assumed for drying experiments with imposed thermal gradient and similar initial evaporation rates. But it is remarked that the capillary number is expected to vary due to the temperature dependency of surface tension  $\sigma$  (Fig. 2-24a) and dynamic liquid viscosity  $\eta_l$  (Fig. 2-25a). Thus, a lower capillary number (associated with a greater impact of capillary liquid transport) is expected in PNs affected by thermal gradients.

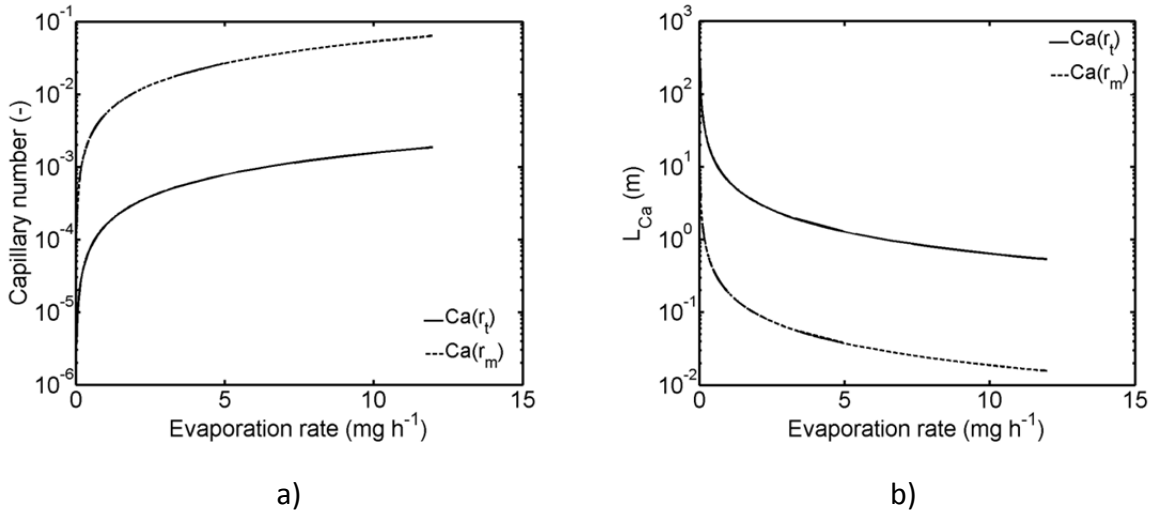
Figure 4-17a reveals overall low capillary number in the range between  $Ca \cong 10^{-3}$  to  $Ca \cong 10^{-6}$  (solid line). Following Lenormand et al. (1988), Shaw (1987) and Tsimpanogiannis et al. (1999) capillary fingering is expected for a viscosity ratio water/air of 50 and a capillary number of  $Ca \leq 10^{-4}$ . Additionally, in this range Lenormand and Zarccone (1984) predict corner flow.

According to Metzger et al. (2007b), the associated distance  $L_{Ca}$  over which liquid can be pumped without experiencing viscous friction forces is

$$L_{Ca} = \frac{\sigma \rho_l \bar{r}_t L_d r_t^{std}}{\eta \dot{M}_{evap} 2}. \quad (4-2)$$

It is  $L_{Ca}^{min} \cong 0.54$  m at the start of experiment 17 (solid line in Fig. 4-17b), which is in good agreement with Metzger et al. (2007b).

However, it is important to note that the ratio of the throat depth  $L_d$  to the mean of the throat half width  $\bar{r}_t$  is  $L_d/\bar{r}_t = 0.48$  in the microfluidic PN. The resulting mean half width of liquid menisci (using Eq. 2-24) is  $\bar{r}_m \cong 31.5$   $\mu\text{m}$  with a standard deviation of  $r_m^{std} \cong 0.576$   $\mu\text{m}$ . Thus, the capillary number associated with the initial evaporation rate of  $\dot{M}_{evap,0} = 12$   $\text{mg h}^{-1}$  is  $Ca \cong 0.06$  (dashed line in Fig. 4-17a) and the distance over which liquid can be pumped when mass transfer is controlled by the PN depth is reduced to  $L_{Ca}^{min} \leq 2$  cm (at the initial evaporation rate) (dashed line in Fig. 4-17b). This reflects control of the invasion process by the network depth. This result is in agreement with experimental observations in CLSM measurements, namely the limited distance of liquid pumping revealed by the receding of liquid menisci in adjacent throats. It might also partly explain the stabilized structure of the drying front at the start of drying (Fig. 4-13a,b), which is further studied in Section 6.2.2.



**Figure 4-17** a) Capillary number vs evaporation rate for drying experiment 17. b) Associated distance of capillary liquid transport. Computations for  $\dot{M}_{evap,0} = 12$   $\text{mg h}^{-1}$ ,  $\sigma = 0.0656$   $\text{N m}^{-1}$ ,  $\eta_l = 4.3291 \cdot 10^{-4}$   $\text{Pa s}$ ,  $\rho_l = 974.9840$   $\text{kg m}^{-3}$  and  $\bar{r}_t = 81.8$   $\mu\text{m}$  with  $r_t^{std} = 7.6$   $\mu\text{m}$  (solid lines) as well as  $\bar{r}_m \cong 31.5$   $\mu\text{m}$  with  $r_m^{std} \cong 0.576$   $\mu\text{m}$  (dashed lines).

#### 4.4 Drying in presence of imposed thermal gradients

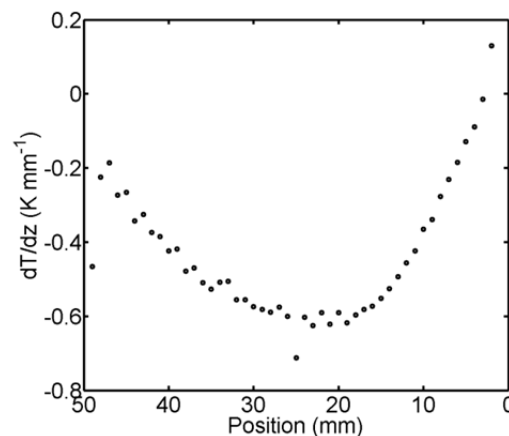
The study of thermally controlled capillary invasion and vapor diffusion in presence of imposed temperature gradients is one of the main aspects of this thesis. As already explained before, capillary invasion in PNs (and other porous systems) is dictated by the

temperature variation because capillary pressure basically depends on temperature via the surface tension (e.g. Huinink et al. 2002, Plourde and Prat 2003, Surasani et al. 2008). Additionally, the temperature gradient impacts on the direction of vapor diffusion and particularly allows for vapor diffusion through partially saturated regions of the PN.

In the following, thermally affected drying of the microfluidic PN is studied using imposed temperature gradients in two directions: a stabilizing thermal gradient with temperature decreasing in  $z$ -direction (also referred to as the negative thermal gradient) and a destabilizing gradient with temperature increasing in  $z$ -direction (also referred to as the positive thermal gradient). The relevant experiments are # 8, 13, 15 for drying with imposed negative temperature gradient and # 10, 11, 18 for drying with imposed positive temperature gradient. It is shown and discussed how the two distinct temperature gradients principally impact on the pore level invasion process and how knowledge about the temperature affected pore scale phenomena might help not only to predict drying but moreover to externally control drying with the purpose of process and product quality control.

#### 4.4.1 Drying with stabilizing thermal gradient

The temperature gradient illustrated in Fig. 3-8b was imposed on the microfluidic network for the study of the stabilizing thermal gradient. This gradient, with temperature decreasing in penetration direction of the drying front, is similar to a temperature gradient that would evolve in a convective drying process, i.e. when the heat supply is by a hot air flow. It was realized using the two heat exchanging baths operating at different temperatures. The water bath with lower temperature operated at  $T_{back} \cong 2^\circ\text{C}$  and the bath with higher temperature operated at  $T_{front} \cong 88^\circ\text{C}$ . Notice that temperature of the bath operating at the higher temperature temporally dropped when the bath was refilled (Appendix A.3). Apart from that, the temperature field was kept constant during the complete drying process. The obvious spatial inhomogeneity of the imposed temperature field (Fig. 3-8b) results from the experimental setup. On average, the temperature decreases with  $dT/dz -4.7 \text{ K cm}^{-1}$  in  $z$ -direction. But in detail, the temperature gradient is higher in the center of the PN and diminishes at both, the PN top and bottom side (Fig. 4-18). This is basically in contrast to literature where constant temperature gradients are imposed (e.g. Huinink et al. 2002).



**Figure 4-18** Slice average temperature decrease computed from Fig. 3-8b.

If, however, the nullification of the temperature gradient at the surface of the PN is disregarded, the tip of the evolving drying front always has a higher temperature than the MAP of the 2-phase zone. Thus, due to the impact of temperature on capillary invasion and vapor diffusion, the tip of the evaporation front is always preferentially invaded. More clearly, as long as the main cluster is connected to the tip of the front, invasion is controlled by capillary invasion in the order of decreasing temperature (and throat width). But when the liquid phase is disconnected into single clusters, vapor diffusion dominates moisture transport. According to Section 2.4.1.1 vapor is partly transported from the high temperature side of the front (i.e. the tip) to the surface and to the low temperature side of the front (i.e. the bottom), thus inducing a heat pipe effect. This effect is additionally promoted by the edge effect. As reflected by the phase distributions discussed on the example of experiment 15 in the following, the stabilizing effect is significant in this case.

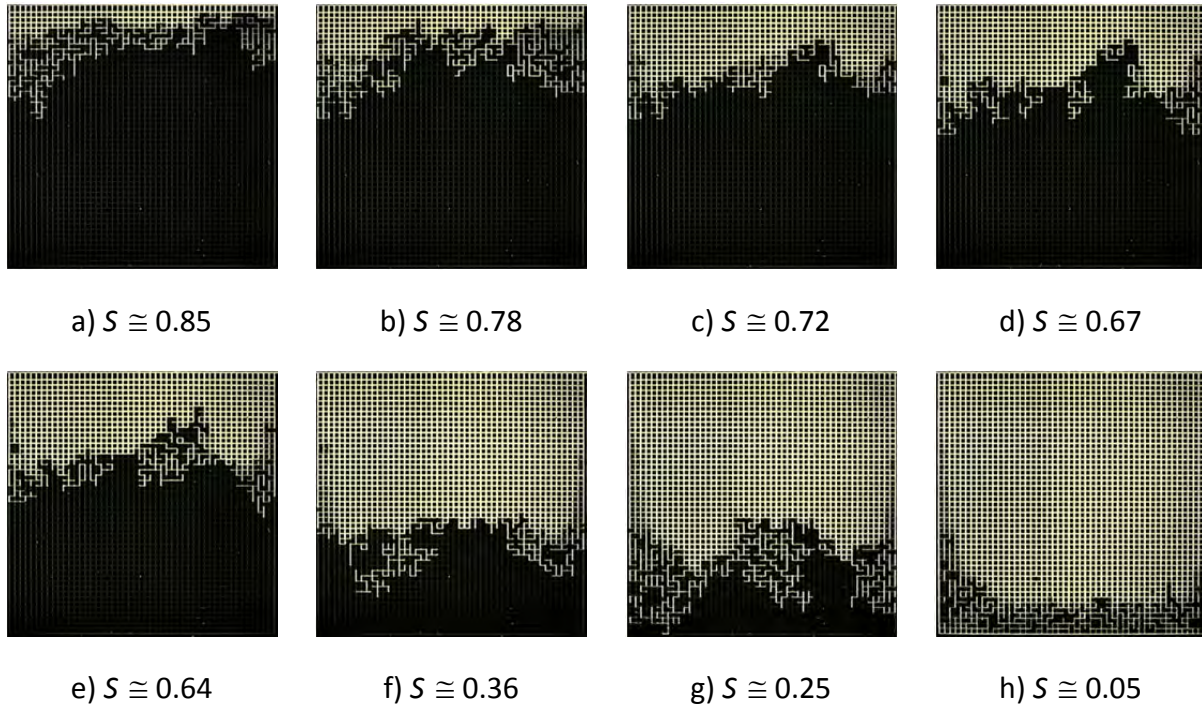
The phase distributions of experiments 8 and 13 are summarized in Appendix A.3. Here, also more details about the phase distributions of experiment 15 are given. The detailed structural analysis of the pore scale liquid distribution in Fig. 4-22 as well as the drying curves in Section 4.4.1.2 give an overview of all drying experiments with imposed negative thermal gradient.

#### **4.4.1.1 Phase distributions**

The phase distributions of drying experiment 15 are shown in Fig. 4-19. In comparison to the quasi-isothermal experiment discussed above, where disconnection of the liquid phase from the network surface occurred at  $S \cong 0.81$ , disconnection occurs already at a slightly higher network saturation of  $S \cong 0.85$  here. Additionally, the liquid phase appears less ramified and the MAP of the 2-phase zone is slightly less advanced in Fig. 4-19a than in the quasi-isothermal drying experiment (Fig. 4-13a). Figures 4-19b-g reveal a significantly more stabilized drying front. The protruding parts of the front as well as upstream liquid clusters dry out before further penetration of the front contributing to its apparently constant width. As will be explained below, the liquid films pinned along the lateral edges of the PN are excepted from this penetration as they can survive over the longest time. The stabilization of the front in the center of the PN, however, is the result of the imposed negative thermal gradient and in contrast to the isothermal experiment, where numerous small liquid clusters survived over most of the drying process. The breakthrough of the gas phase to the PN bottom occurs at  $S \cong 0.25$ , which is significantly lower than in the quasi-isothermal experiment ( $S \cong 0.53$ ).

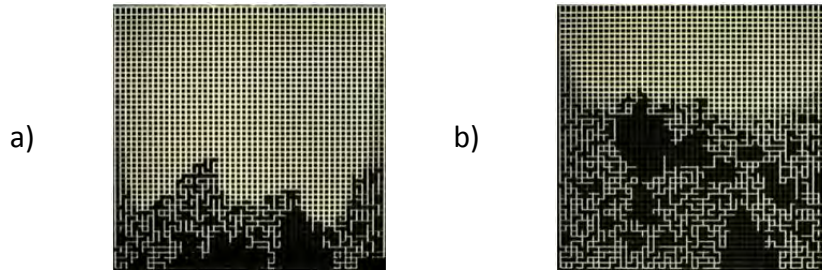
A comparison of the non-isothermal and the quasi-isothermal pore scale liquid distribution can be found in Fig. 4-20. Interestingly, identical cluster structures can be found in both situations. More precisely, a large dendritic liquid cluster develops at the network bottom in both cases. An explanation might involve the interplay of PSD and the temperature gradient in regard of the capillary controlled invasion process. If it is assumed that the effect of stabilization depends only on the temperature gradient (when viscous forces are ignored) than the similarities indicate that the temperature gradient spanning the dendritic cluster is not high enough at the given variation of throat sizes at the cluster boundary to provoke different structures. A similar explanation might be involved for the similarity of phase distributions at the start of drying (as discussed above phase distributions of experiment 17 appear temporally stabilized with constant front width).





**Figure 4-19** Gas-liquid phase distributions from experiment 15. a) Disconnection of the liquid phase from the PN entrance at  $S \cong 0.85$ . b) Thinning out of the drying front at almost constant MAP ( $S \cong 0.78$ ). c) Advancing of the LAP of the drying front at  $S \cong 0.72$ . d-f) Further penetration of the drying front at almost constant width ( $S \cong 0.67$  to  $S \cong 0.36$ ). g) Breakthrough of the gas phase at  $S \cong 0.25$ , i.e. significantly later than in the isothermal experiment. h) Residual liquid clusters, liquid films and pinning of the liquid to the lateral network edges ( $S \cong 0.05$ ).

The saturation profiles of experiment 15 are shown in Fig. 4-21. The profiles prove the early disconnection from the network surface as well as the limited width of the drying front (excluding the edge effect). This is also revealed in Fig. 4-22a,b where the LAP shows a constantly decreasing trend and the drying front an average constant width of around 17 pore rows. It is found, that the LAP of the drying front advances more steadily and that the frontwidth is more stable over most of the drying process than compared to the quasi-isothermal experiment if the edge effect is disregarded here. The red curve in Fig. 4-21 furthermore indicates a tendency of liquid phase disconnection from the network bottom, revealed by a peak at  $z = 49L$  which might again be explained with liquid transport through films along the lateral edges. Note that the visualization of the lateral pinning in the saturation profiles (Fig. 4-21) as well as in Fig. 4-22a,b strongly depends on the image processing parameters. As shown in Fig. 4-22a,b the edge effect can be diminished if a high critical saturation  $S_{crit}$  is selected in Eq. 3-19. In contrast to that, the lateral pinning of liquid can be shown by decreasing  $S_{crit}$  in Eq. 3-19 (Fig. 4-23). As indicated by Fig. 4-23 the position of liquid pinning is around 5-10 pore rows more advanced in the experiment with imposed negative thermal gradient than compared to the quasi-isothermal experiment. The additional phase distributions provided in Appendix A.3 reveal that the liquid phase recedes to the intermediate position already at high overall PN saturation ( $S \cong 0.75$ ). This is in contrast to the quasi-isothermal experiment where wetting of the lateral edges at  $z^{pin} \cong (6-7)L$  was observed until  $S \cong 0.25$ . It is expected that the earlier depinning is a result

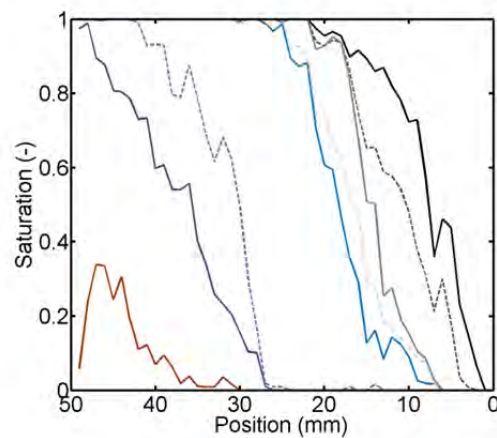


**Figure 4-20** Comparison of the gas-liquid phase distributions for a) negative thermal gradient (experiment 15,  $S \cong 0.16$ ) and b) quasi-isothermal conditions (experiment 17,  $S \cong 0.29$ ) right before drying of the large liquid cluster connected to the network bottom.

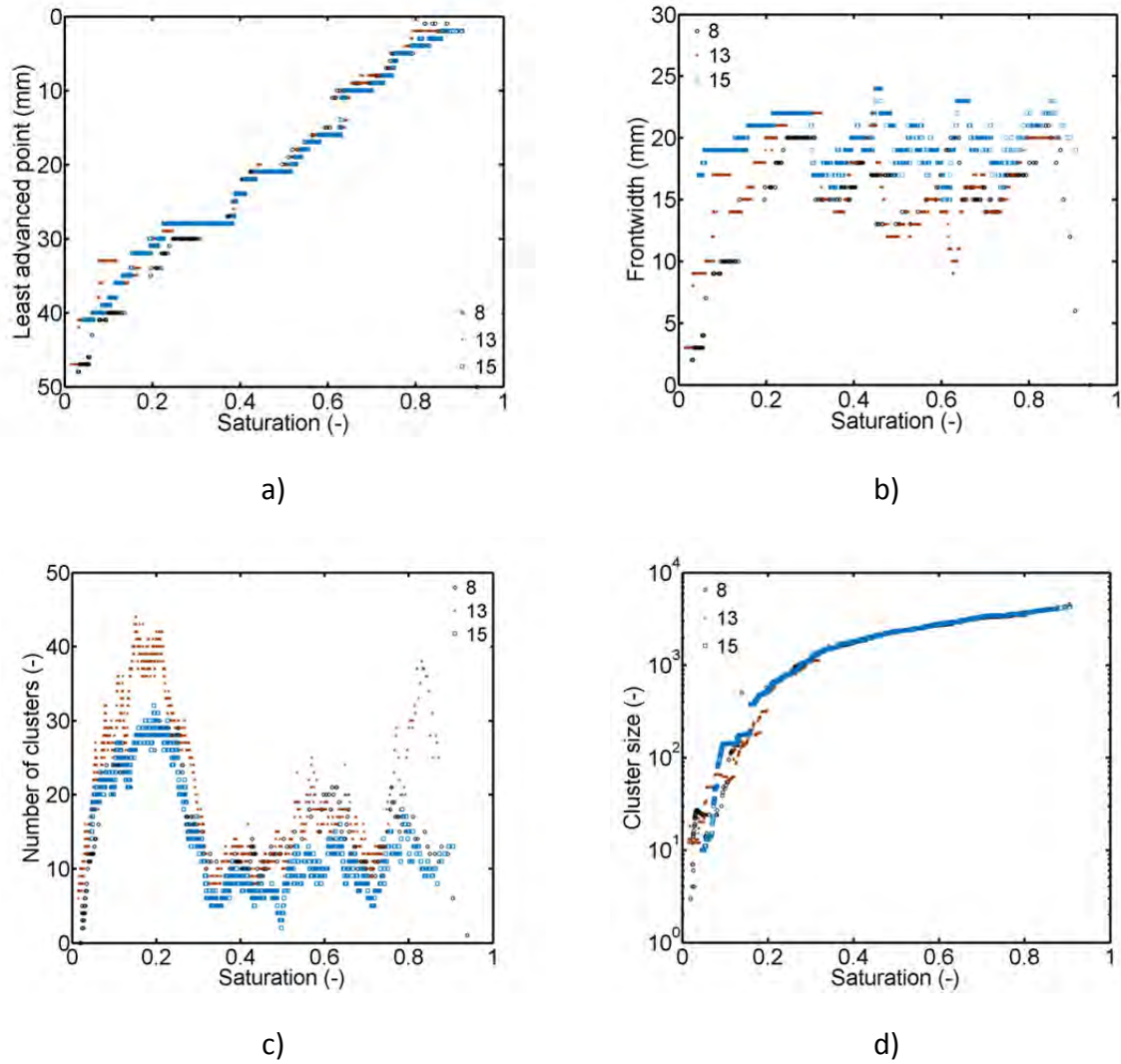
of the high temperature of  $T \cong 73^\circ\text{C} - 75^\circ\text{C}$  at the surface of the PN in this drying mode which counteracts the formation of liquid films along the straight walls. As a consequence, position of the evaporation front is lower over most of the drying experiment than comparably in the quasi-isothermal heating mode. Again, this is not reflected by the curves presented in Figs. 4-21 and 4-22, as the liquid films are suppressed by image processing.

Figure 4-22c shows that the cluster number is initially smaller than in quasi-isothermal drying. This is associated with a complex process of cluster disconnection from the main liquid cluster and evaporation of the disconnected clusters upstream of the main cluster front. Part of the evaporated liquid from these clusters might additionally diffuse towards the main cluster front at lower temperature. Consequently, the separated clusters screen the main cluster from the evaporation front. Further penetration of the latter therefore requires the dry out of the upstream single clusters. This effect contributes to the front stabilization; and it is additionally promoted by the edge effect. The total number of clusters increases significantly after breakthrough of the gas phase resulting in a similar peak as in Fig. 4-15c at the end of drying.

The maximum cluster size (Fig. 4-22d) decreases slower than in the quasi-isothermal experiment. This is a consequence of the stabilization of the main liquid cluster which remains compact and thus less ramified until breakthrough of the gas phase.



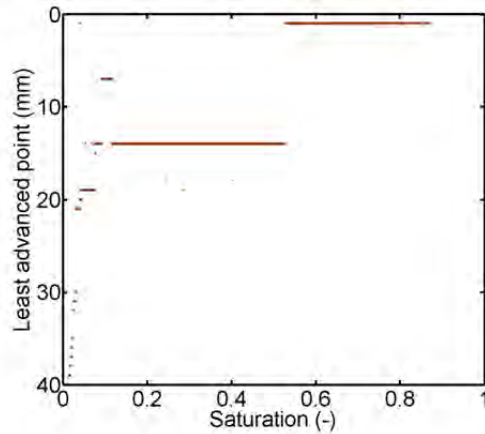
**Figure 4-21** Saturation profiles from experiment 15 for overall network saturations  $S = [0.85, 0.78, 0.72, 0.67, 0.64, 0.36, 0.25, 0.047]$  (from right to left).



**Figure 4-22** Drying front and liquid cluster dynamics. a) LAP of the drying front (computed for  $S_{crit}(z_{LAP}) = 10^{-1}$ ), b) drying front width (computed for  $S_{crit}(z_{MAP}) = 0.98$ ), c) number of liquid clusters, d) maximum size of liquid clusters in terms of interconnected liquid throats.

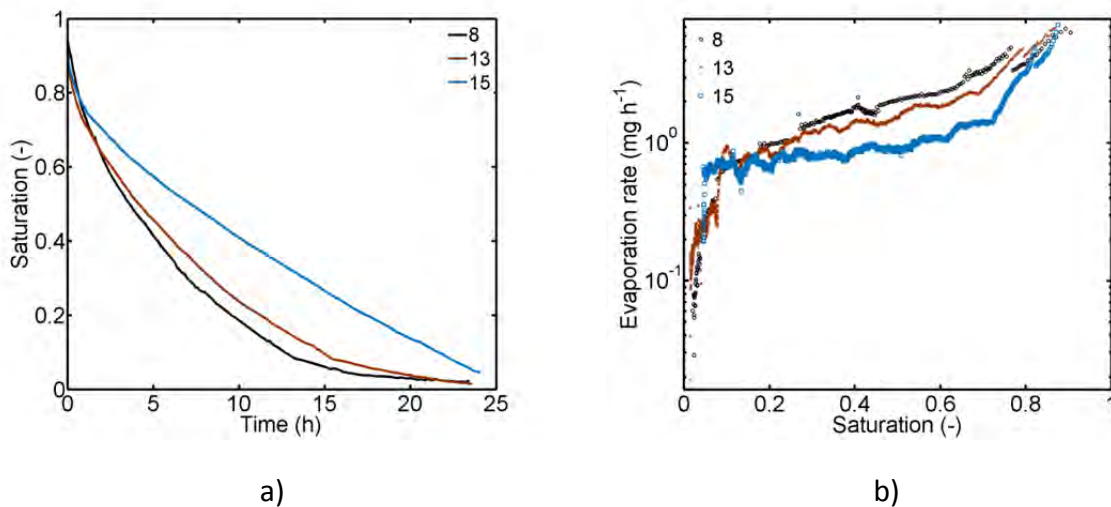
#### 4.4.1.2 Drying curve and drying rate curve

The drying curves and drying rate curves are summarized in Fig. 4-24. In summary, drying time is around factor 2 shorter than in the quasi-isothermal drying experiments (Fig. 4-24a). At the end of drying, liquid from the PN bottom side was removed at lower temperature ( $\bar{T}_{bottom} \cong 52^\circ\text{C}$ ) which results in overall lower drying rates at the end of drying compared to the situation shown in Fig. 4-16. However, at the start of drying the network surface temperature was higher ( $T \cong 75^\circ\text{C}$ ). Furthermore, the overall mean temperature was  $T \cong 64^\circ\text{C}$  and thus slightly greater than in the quasi-isothermal experiment. Interestingly, the evaporation rates at the start of drying are very similar and moreover they are in the range of experiments discussed in the previous section, namely  $\dot{M}_{evap,0} \cong 7 \text{ mg h}^{-1} - 20 \text{ mg h}^{-1}$  (Fig. 4-24b). (Note that  $\dot{M}_{evap,0}(S = 1)$  is not available due to the experimental procedure). But, over most of the drying process the evaporation rates are generally higher in the experiment with temperature gradient (Fig. 4-25).



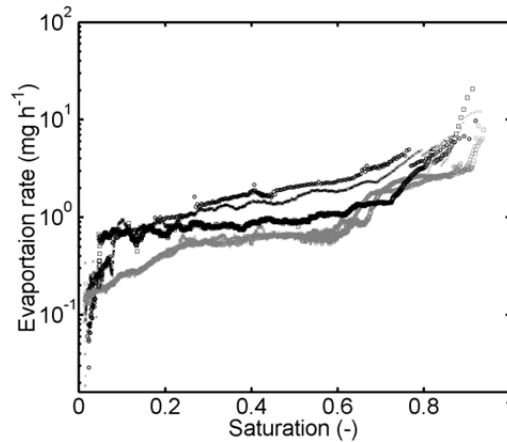
**Figure 4-23** Illumination of the edge effect on the example of experiment 13. If the image analysis parameters are adapted accordingly, the liquid pinning can be visualized. In this example this is realized by varying the critical saturation in Eq. 3-19. Here  $Z_{LAP} = z^{min}(S_{slice} > 10^{-2})$  is applied for the detection of the residual liquid along the lateral edges. Contrary, the plot in Fig. 4-22 is obtained for  $Z_{LAP} = z^{min}(S_{slice} > 10^{-1})$ . The constant position of the LAP reveals the importance of the edge effect on the drying process.

An exception is experiment 15, which reveals a lower evaporation rate than quasi-isothermal drying between  $S \cong 0.75$  and  $S \cong 0.65$  (Figs. 4-16, 4-24, 4-25). This observation is again ascribed to the lateral pinning of liquid along the PN edges which is less evolved in experiment 15. According to Table A-15, the position of the evaporation front at the PN edges is found at a more advanced position leading to a reduction of evaporation rate compared to experiment 8 and 13 as well as the quasi-isothermal experiments, where the position of liquid pinning is generally closer to the PN surface. Accordingly, the saturation decreases with a significantly smaller slope in experiment 15 (Fig. 4-24a). The residual moisture content is then  $S \cong 0.05$  after  $t \cong 24$  h while in experiments 13 and 8 it is  $S \cong 0.02$  after  $t \cong 23$  h. The drastic drop of drying rates at the end of drying is associated with the dry out of the PN edges. This reveals again the relevance of the edge effect for the overall drying performance.



**Figure 4-24** a) Drying curves, b) semi-logarithmic plot of drying rate curves (exps. 8, 13, 15).

In summary the evaporation rates can be higher in drying with negative thermal gradient although the drying front position is much more advanced in the center of the PN than in quasi-isothermal drying and the lateral pinning of the liquid phase is slightly less pronounced. Additionally, a heat pipe effect is associated with the combination of the thermal gradient and the edge effect. This allows for vapor diffusion from the film tip towards the drying front in the center of the PN, thus counter-current to the evaporation fluxes leaving the pore network. But this also enables the liquid transport along the edges of the pore network, which is expected to be much more efficient than vapor diffusion. This can positively affect the drying rates if the main liquid cluster remains compact over most of the drying experiment and furthermore if it remains connected to the liquid films associated with the edge effect. In contrast, the phase distributions from quasi-isothermal drying were very ramified but though connected by liquid rings and liquid bridges.



**Figure 4-25** Comparison of drying rates from the quasi-isothermal experiments (gray lines) and from experiments with imposed negative thermal gradient (black lines).

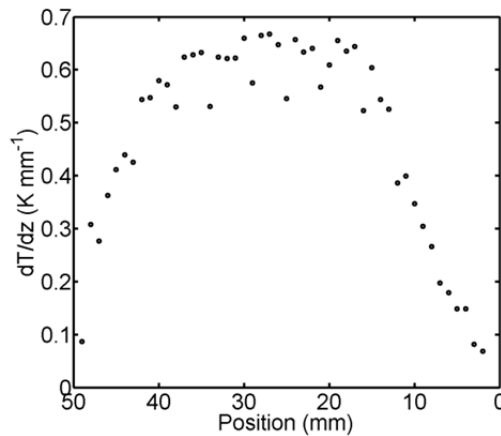
#### 4.4.2 Drying with destabilizing thermal gradient

The destabilizing temperature gradient (Fig. 3-8c) is realized with the experimental setup by selecting the temperatures of the thermal baths with  $T_{front} \cong 1.5^{\circ}\text{C} - 10^{\circ}\text{C}$  and  $T_{back} \cong 75^{\circ}\text{C} - 88^{\circ}\text{C}$  (refer to Table A-16). Notice that the temperature of the hot bath temporally dropped when the bath was refilled with water during the experiment (Fig. A-3). It is remarked that this could have a positive effect on condensation, although this could not be revealed by experiments. Local gradients extracted from the temperature field referred to experiment 10 are given in Fig. 4-26. It clearly reveals non-linearity of the temperature profile which is linked to the experimental setup and which is in distinct contrast to the reports on simulation results in literature (e.g. Huinink et al. 2002) where  $dT/dz$  was kept constant. Plotting  $dT/dz$  over position  $z$  in Fig. 4-26 indicates that the temperature decrease is indeed almost constant at  $dT/dz \cong 0.58 \text{ K mm}^{-1}$  between position  $z = 18 \text{ mm}$  and  $z = 41 \text{ mm}$ . However, Fig. 4-26 also indicates that the gradient drastically decreases towards the cold network surface at  $z = 0$ , reaching to a minimum of  $dT/dz \cong 0.05 \text{ K mm}^{-1}$  there.

Imposing of the positive thermal gradient on the liquid saturated PN results in the destabilization of the liquid phase because basically the pores and throats at the bottom of the PN (at higher temperature) are preferentially invaded. At the same time, liquid can evaporate at the high temperature side and then the evolving vapor can diffuse through the partially saturated region due to the temperature gradient. This phenomenon results in the

occurrence of two evaporation fronts. One evaporation front is found at the cold side of the PN and it is connected (close) to the network open side over most of the drying process. It is therefore also denoted as the cold (temperature) front. This front controls the overall evaporation rate of the PN. Emergence of a second evaporation front at the hot side of the PN is facilitated by the aforementioned breakthrough of the gas phase. The hot temperature front dominates the extent and mean position of the 2-phase zone as it detaches and recedes from the hot temperature side. Due to this, the 2-phase zone seemingly travels towards the network surface. According to Udell (1985) the length of the 2-phase zone depends on the temperature gradient.

The phase distributions of experiment 10 are discussed in detail in what follows. Apart from certain peculiarities emerging at the start of drying, repetition of experiments with imposed positive thermal gradient revealed overall similar drying phenomena. A summary of these drying experiments (# 10, 11, 18) can be found in Appendix A.4. Besides this, the detailed structural analysis of the pore scale liquid distribution in Figs. 4-32 and 4-33 as well as the drying curves in Section 4.4.2.3 give an overview of the three experiments.

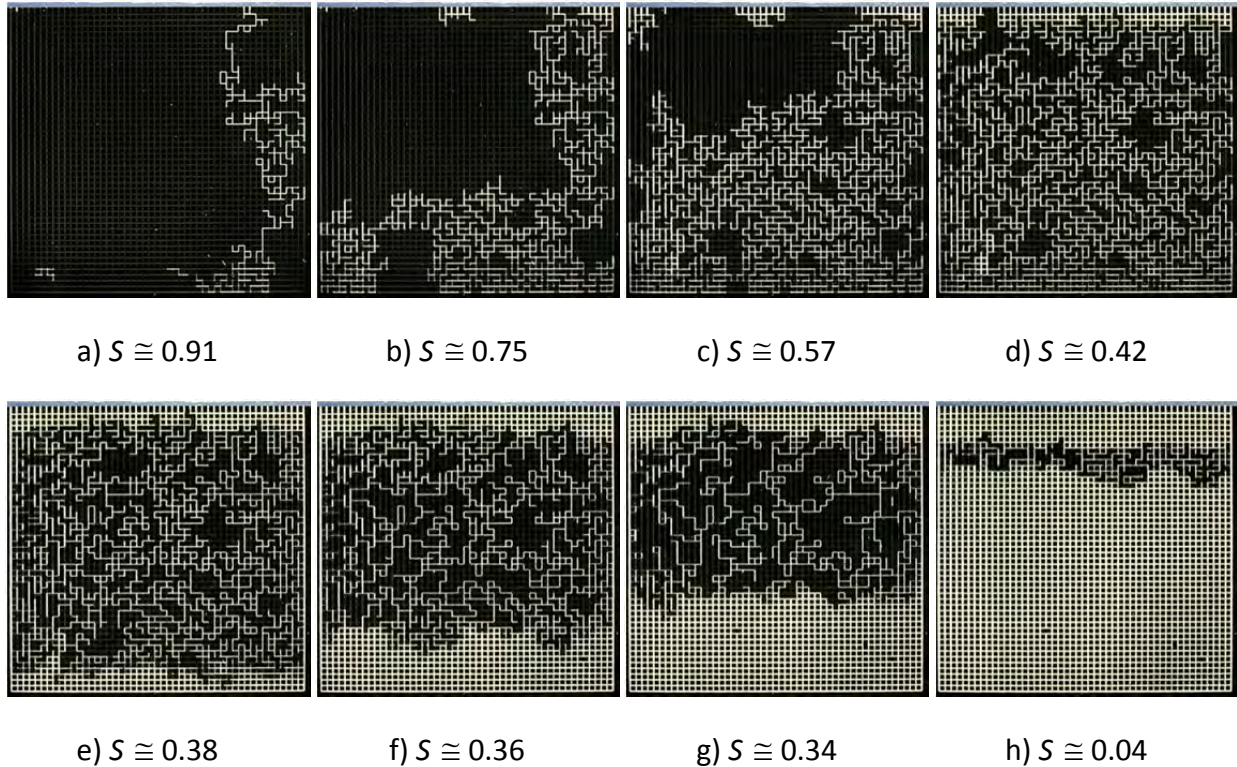


**Figure 4-26** Slice average temperature decrease computed from Fig. 3-8c.

#### 4.4.2.1 Phase distributions

The phase distributions in Fig. 4-27 clearly illustrate that distinct drying periods can be identified when drying with the positive temperature gradient. These drying periods are essentially different from the theory presented in Section 2.5.5.

In the *first drying period* evaporation occurs at the network surface and emptying of the network is controlled by capillary invasion. This leads to the formation of a tortuous gas branch which invades the PN from the open surface. The start of drying front destabilization depends on the PSD and the height of the temperature gradient when drying is capillarity controlled. This is illustrated in Fig. 4-28 which shows that different situations were observed in this study. As can be seen, start of destabilization occurs earlier in Fig. 4-28a (experiment 10) compared to Fig. 4-28b-c (experiments 11 and 18), where the evaporation front recedes from the network surface already before destabilization. This is explained with the different temperature settings in these experiments. In detail, flow direction of the water bath streams is reversed in experiments 11 and 18 (Fig. A-4). These experiments though are examples for the case where the temperature gradient is not sufficient to destabilize the phase distribution from the beginning of drying. Instead the initial phase distributions are rather very similar to quasi-isothermal drying and drying with negative temperature gradient

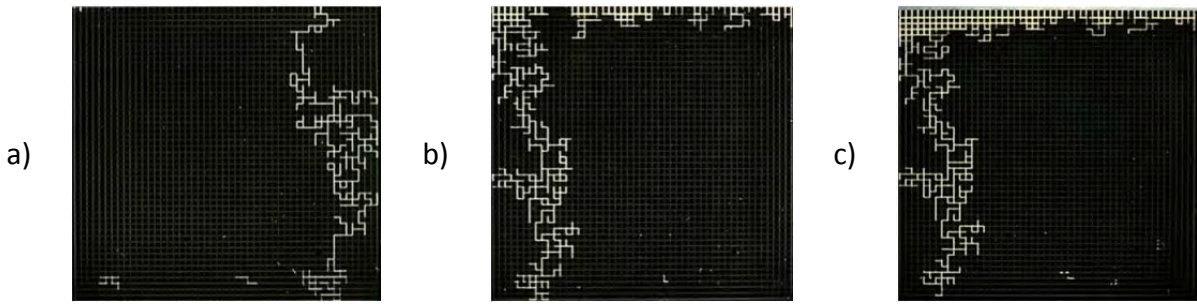


**Figure 4-27** Gas-liquid distributions from experiment 10. a) Destabilization of the liquid phase with fast breakthrough of the gas phase at  $S \cong 0.91$ . b-d) Ramification of the 2-phase zone ( $S \cong 0.75$  to  $0.42$ ). e) Initiation of a second evaporation front at the hot side at  $S \cong 0.38$ . f-g) Travelling of the 2-phase zone accompanied by growth and merging of clusters and formation of a faceted cluster connected to the pore rows slightly below the network open side, shown for  $S \cong 0.36$  to  $0.34$ . h) The faceted cluster dries out as travelling of the two-phase zone proceeds ( $S \cong 0.04$ ).

(Fig. 4-29). The different evaporation front structures have a direct impact on drying rates as will be discussed in Section 4.4.2.3. In other words, a pre-period occurs in drying processes in which the surface dries out before initiation of the gas branch, i.e. in experiments 11 and 18 in Fig. 4-28.

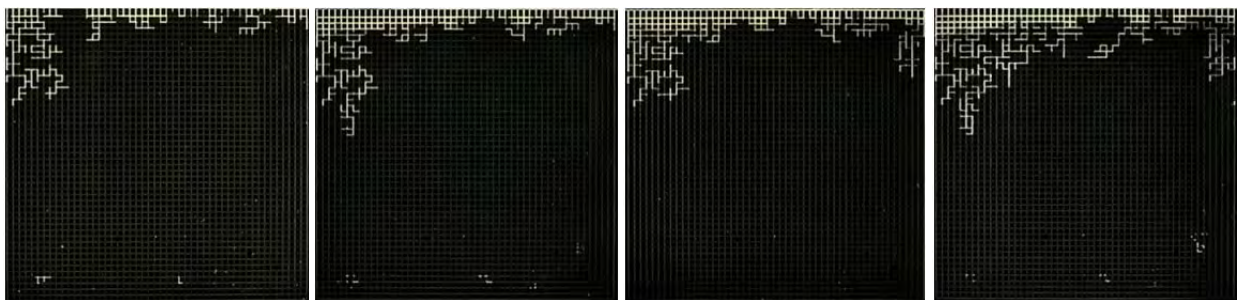
The *second drying period* starts with the breakthrough of the gas phase to the bottom of the PN (Fig. 4-27a). In this period the network surface remains saturated (Fig. 4-30). The second drying period is characterized by the ramification of the liquid phase starting from the PN bottom side (Fig. 4-27b,c). At the end of this drying period the liquid phase is nearly completely split up into significantly smaller liquid clusters (Fig. 4-27d) in experiment 10. This leads to the interruption of capillarity controlled invasion.

The transition to the *third period of drying* is designated by the invasion of the PN at the surface (Fig. 4-27e). This leads to the formation of a dry zone with significant diffusion resistances and a reduction of overall evaporation rates (see below). This is observed at  $S \cong 0.36$  to  $0.41$  in experiment 10 (also refer to Fig. 4-32 below); however a different situation is observed in experiments 11 and 18 because of the initial receding of the evaporation front (here the first and second drying period occur after dry out of the PN surface pores).



**Figure 4-28** Saturation of the PN surface at breakthrough: a) experiment 10 with temperature field as specified in Fig. 3-8c. b) experiment 11 and c) experiment 18, both with reversed flow direction through the heat conducting plate.  $S = [0.93, 0.87, 0.87]$  in a)-c).

In the third period, mass transfer is dominated by vapor diffusion and the drying of isolated liquid clusters. However, the evaporation front at the cold network surface only slightly recedes while a second evaporation front is initiated at the hot network bottom (Fig. 4-27e-g). This is based on the high saturation vapor pressures and the associated high evaporation rates at the hot side of the PN and moreover on vapor diffusion through the partially saturated zone. More precisely, the imposed temperature gradient allows for a gradient in saturation vapor pressures which again enables vapor diffusion from the hot to the cold side of the PN. But then, the direction of vapor diffusion provokes condensation if the vapor diffusion rate towards a cluster exceeds the evaporation rate from this cluster or if the saturation vapor pressure at position  $z$ , towards which the vapor diffuses, is lower than the partial vapor pressure of the origin of the vapor (Fig. 4-31). This leads to the interruption of the invasion at the PN surface. The condensation rate benefits from high temperature gradients (i.e. high saturation vapor pressure gradients) at low overall evaporation rates. (This interrelation is precisely studied by PN simulations in Appendix B.3). If the condensation rate is high enough, partially saturated pores and throats as well as their empty neighbors are refilled with liquid (at the local condensation rate) and significant cluster growth and merging of liquid clusters is observed. This phenomenon characterizes the third period of drying. It affects the saturation profiles in Fig. 4-30, which show an



a)  $S \cong 0.94$

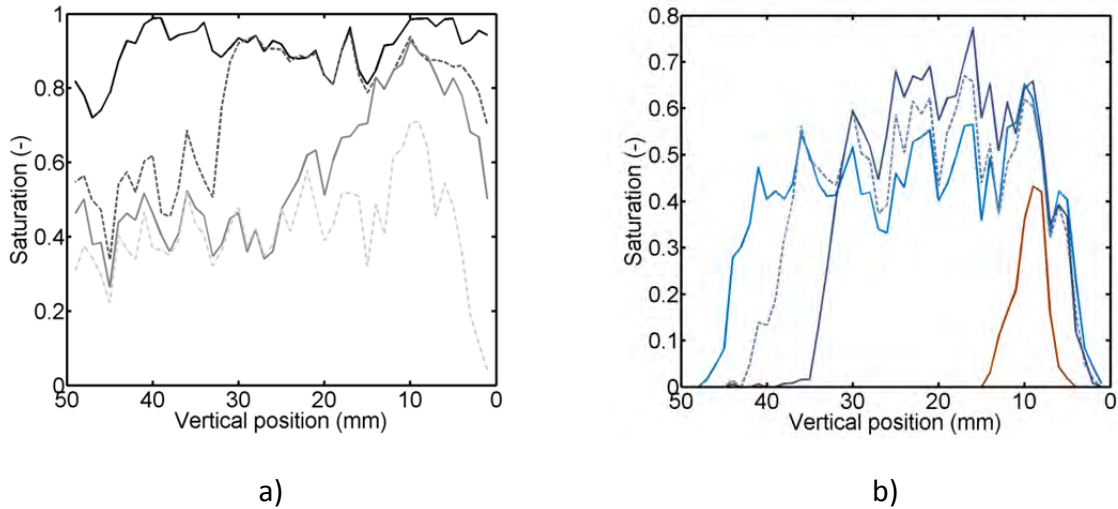
b)  $S \cong 0.92$

c)  $S \cong 0.92$

d)  $S \cong 0.89$

**Figure 4-29** Individual drying front structures at the start of drying. a-b) Examples for positive temperature gradient, c) negative temperature gradient and d) quasi constant temperature. (Images refer to experiments 11, 18, 15 and 17, from a) to d) respectively).

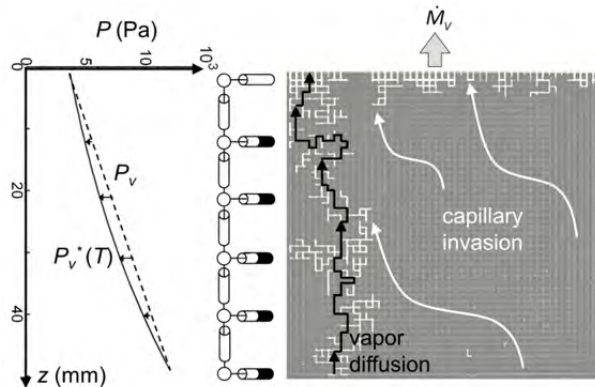




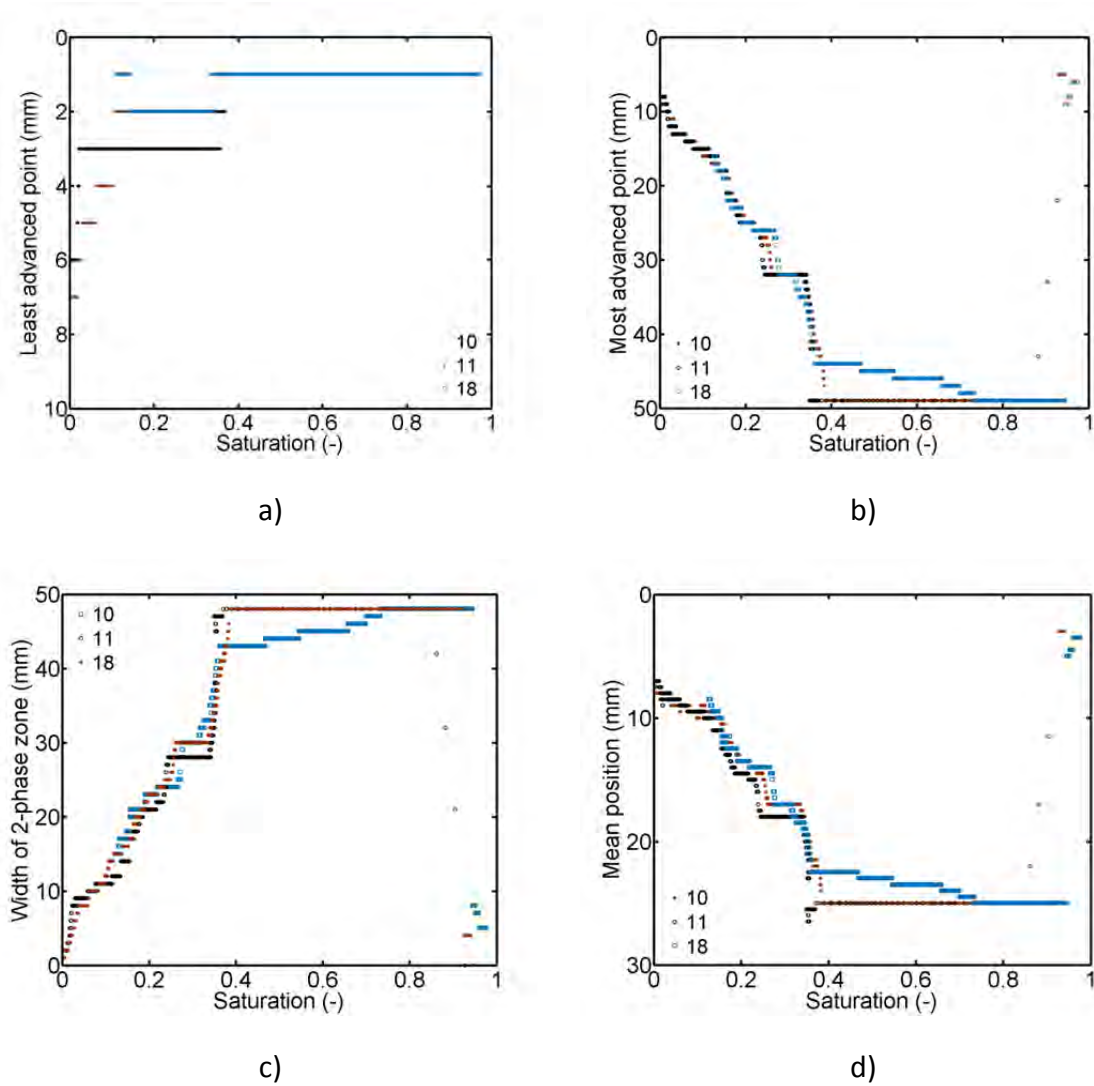
**Figure 4-30** Saturation profiles from experiment 10 reveal the initiation of a second evaporation front receding from the hot temperature side at  $z = 49$  mm, while the evaporation front at the cold temperature side,  $z = 0$ , remains at nearly constant position. The profiles indicate a temporal increase of slice saturation between vertical position  $z = 4$  mm and  $z = 31$  mm which is related to the condensation effect. Profiles for a)  $S \cong [0.91, 0.75, 0.57, 0.42]$  and b)  $S \cong [0.38, 0.36, 0.34, 0.04]$  (from right to left).

apparent increase of slice saturation (between  $z = 4$  mm and  $z = 31$  mm) with decreasing width of the 2-phase zone. More precisely, emptying and refilling of liquid clusters occur *simultaneously* during this drying period leading to the redistribution of liquid inside the PN. The saturation profiles in Fig. 4-30 indicate that due to this the 2-phase zone travels towards the network open side.

The third drying period ends with further receding of the cold temperature evaporation front and decrease of slice saturation (between  $z = 4$  mm and  $z = 31$  mm in Fig. 4-30b). This marks the decrease of condensation rates at constant overall drying rates because the liquid supply rate from the bottom side becomes lower than the evaporation rate at the top side of the 2-phase zone. In detail, the overall temperature gradient within the 2-phase zone is reduced with the contraction of this zone leading to a reduction of condensation rates.



**Figure 4-31** Graphical representation of the condensation effect resulting from vapor diffusion through the partially saturated zone.



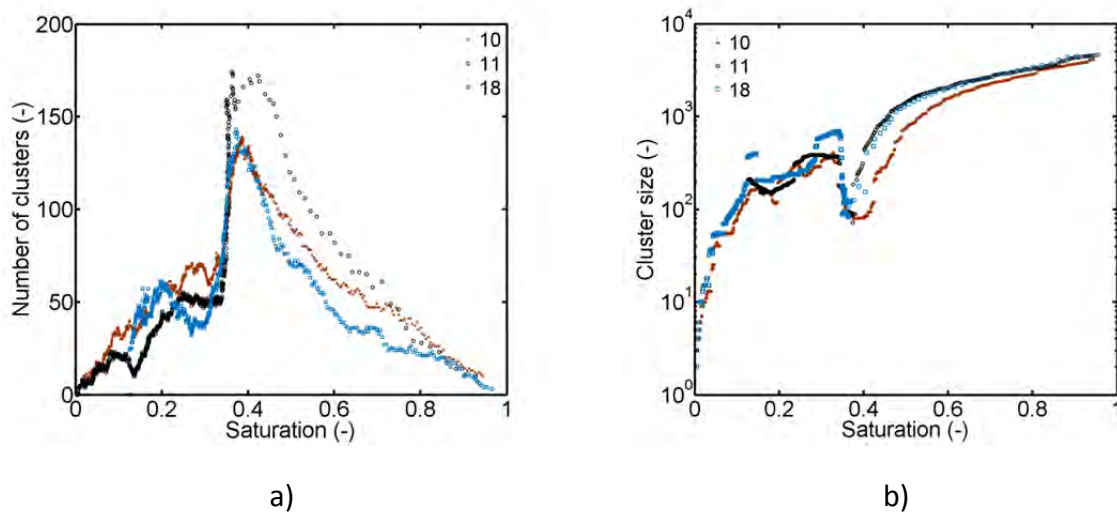
**Figure 4-32** a) LAP (computed for  $S_{crit}(Z_{LAP}) = 10^{-2}$  in experiment 10 and  $S_{crit}(Z_{LAP}) = 10^{-3}$  in experiments 11 and 18), b) MAP (computed for  $S_{crit}(Z_{MAP}) = [0.98, 10^{-1}]$ ), c) width and d) mean position of the travelling 2-phase zone of experiments 10, 11 and 18.

Then the third drying period passes into the *fourth period of drying* (Fig. 4-27h). In this last period, the separated clusters dry out, evidenced by receding of the 2-phase zone from both sides (Fig. 4-30b).

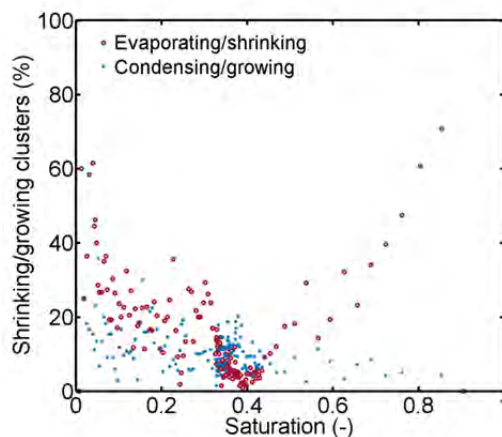
Figure 4-32 summarizes particular characteristics of the travelling 2-phase zone, namely least and most advanced points, width and mean position for experiments 10, 11 and 18 with good overall agreement among them. Notice that the position of the MAP of the travelling 2-phase zone is evaluated by two different critical thresholds  $S_{crit}$  in Eq. 3-20. This is necessary as the 2-phase zone recedes from two sides of the PN. In detail,  $S_{crit} = 0.98$  before disconnection of the second evaporation front from the PN bottom and  $S_{crit} = 10^{-1}$  after disconnection. The cold temperature evaporation front recedes only very slightly at low network saturation  $S < 0.1$  (Fig. 4-32a), which is associated with an increased ratio of evaporation to condensation rates. Contrarily, the MAP travels distinctly towards the network top (Fig. 4-32b), reaching its highest position at  $Z_{LAP}^{max} \cong Z_{MAP}^{min}$  when the PN dries out. Interestingly, extent of the 2-phase zone strictly decreases with decreasing saturation  $S$

(Fig. 4-32c). This evidences that the condensation related refilling of PN elements is limited to the interior of the 2-phase zone, so that the 2-phase zone cannot grow beyond its least and most advanced points. Therefore, the mean position of the travelling zone follows the upward movement of its MAP (Fig. 4-32d).

Figure 4-33a shows that the cluster number increases in the second drying period, revealing the progressive ramification of the liquid phase, and then reaches a maximum number at  $S \cong 0.36$  to  $0.41$  designating the transition from the second to the third period of drying. Afterwards the cluster number decreases rapidly, indicating drying and merging of clusters. This is confirmed by Fig. 4-33b which shows the evolving maximum cluster size in terms of interconnected liquid filled throats and which reveals an increase of cluster size at  $S \cong 0.36$  to  $0.41$ . The curves in Fig. 4-33a show another (slight) increase of the cluster number at the end of drying, i.e. when the merged clusters dry out and split off. Note that the condensation effect is apparently higher in experiment 18, where generally the cluster number is slightly smaller and where greater cluster sizes are obtained in the third drying period.



**Figure 4-33** a) Total number of clusters and b) maximum size of liquid clusters by means of interconnected liquid throats (shown for experiments 10, 11 and 18).

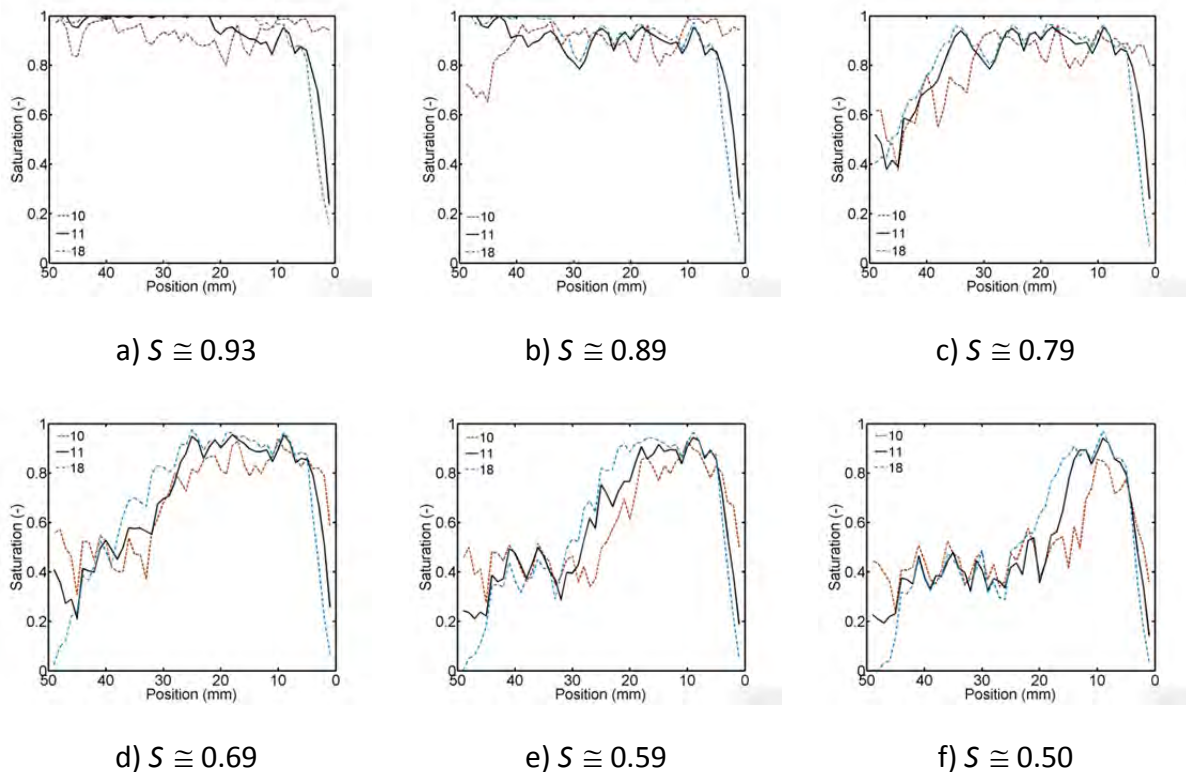


**Figure 4-34** Percentage ratio of shrinking and growing clusters related to the current total number of clusters (exemplarily shown for experiment 11) computed from Eq. (3-28).

The cluster dynamics, i.e. evaporation related shrinkage and condensation related growing of clusters, are shown in Fig. 4-34 based on Eq. 3-28. As the key message, the diagram indicates that the process is overall dominated by evaporation, because on average more clusters are shrinking than growing. (Notice that the majority of clusters is unaffected in the selected time interval  $t^{i-1} - t^j$ ). Furthermore, it reveals that massive cluster growth is observed at the transition between the second and the third drying period which again explains the drastic drop in drying rates in Fig. 4-37b below.

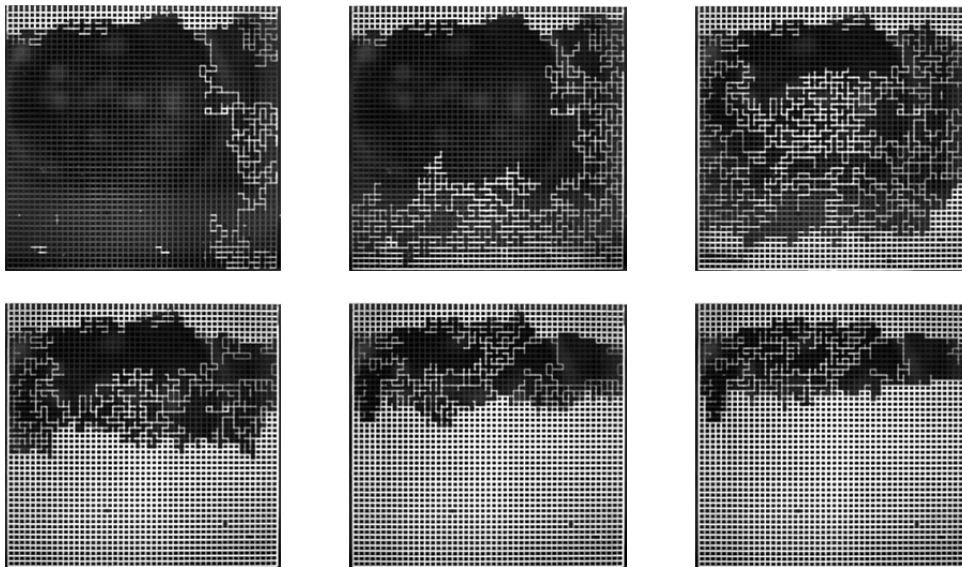
#### 4.4.2.2 Variance of the travelling 2-phase zone

The transition from the second to the third period of drying is found at an overall network saturation of  $S \cong 0.36$  to  $0.41$  in experiments 10, 11 and 18. From the phase distributions discussed above follows that this transition is characterized by passing from capillary dominated invasion to vapor diffusion dominated invasion (evidenced by the end of the split up of the liquid phase accompanied by initiation of the travelling 2-phase zone). Comparison of the saturation profiles of experiments 10, 11 and 18 in Fig. 4-35, however, reveals that different situations can occur. Exemplarily, in experiment 18 the travelling 2-phase zone is already initiated at higher PN saturations. This experiment shows slightly higher maximum saturations of the 2-phase zone and earlier disconnection of the second invasion front from the PN bottom in Fig. 4-35.



**Figure 4-35** Comparison of saturation profiles from experiments 10, 11 and 18 indicates that the transition from the second to the third period of drying is not necessarily dependent on the complete split up of the liquid phase because in experiment 18 larger clusters survive after the initiation of the second invasion front (also refer to Table A-22).

Figure 4-36 shows another example, where the transition from the second to the third period of drying occurs at different characteristic phase patterns. Note that this experiment was not numerically evaluated due to the low image quality. However, it shows i) that the PN surface is invaded before initiation of the gas branch and ii) initiation of the travelling 2-phase zone at a higher apparent saturation, i.e. when a large liquid cluster is still observed at the PN surface. This behavior might be explained with the lower temperature of the convective dry air ( $\bar{T}_{air} = 22.3^{\circ}\text{C}$ ) which might have led to greater heat losses and an overall lower surface temperature of the PN (including the upper pore rows). The resulting overall lower drying rates might have positively impacted on the condensation effect because the vapor diffusion rates towards the clusters confined inside the 2-phase zone, i.e. the large liquid cluster close to the surface, might have been greater than the local evaporation rates from these clusters. The large cluster disappears in the fourth drying period, when condensation rates are expected to decrease because of the reduced extent of the 2-phase zone. Duration of this drying process was  $t > 90$  h, and thus, as will be seen, considerably longer than in experiments 10, 11 and 18, although the cold front was approximately at similar position.



**Figure 4-36** Drying experiment with apparently higher saturation at the transition from the second to the third period of drying (numerical values are not given due to the low image quality). A large liquid cluster survives close to the network open side during the second and third period of drying. ( $T_1 \cong 28^{\circ}\text{C}$  and  $T_3 \cong 52^{\circ}\text{C}$  from thermocouple measurement).

In summary, it is strongly assumed that the transition from the second to the third drying period depends not only on the combination of PSD and temperature gradient (Plourde and Prat 2003) but that moreover the overall evaporation rate has an impact on the phase distributions. Repetition of this drying experiment would shed light on this phenomenon. This is of interest since the individual distribution of liquid during drying can be of great importance, especially in processes involving dissolved particles or crystallization, as the final distribution of these particles after drying and thus the product quality depend on the evolution of phase distributions during drying as already mentioned earlier. Moreover, liquid connectivity and drying front position affect drying time, wherefore it can be of a great importance to understand the effect of temperature distribution and condensation. Again,

the experimental results presented above indicate that the internal liquid distribution can be affected by the imposed temperature gradient on the one hand and by variation of the evaporation rate on the other hand (see also Fig. 4-37 below). The study of this phenomenon is provided by PN simulations in Chapter 6 and Appendix B.3.

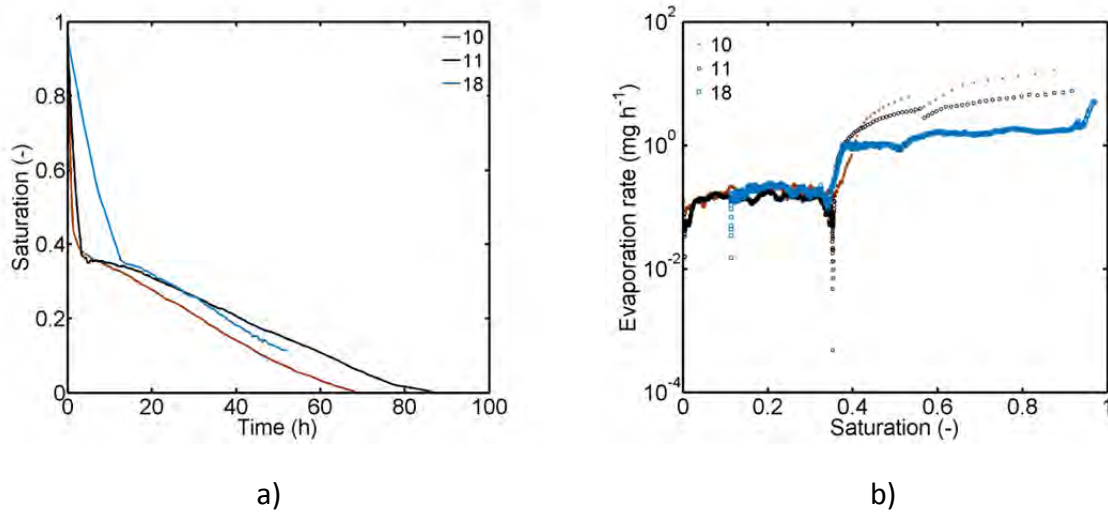
#### 4.4.2.3 Drying curve and drying rate curve

The drying curves and the drying rate curves of experiments 10, 11 and 18 are summarized in Fig. 4-37. In agreement with phase distributions depicted above and in Appendix A.4, drying is very reproducible. The semi-logarithmic plot in Fig. 4-37b reveals that drying rates can remain on a high and almost constant level in the first and second period of drying. This is explained with the interconnection of the 2-phase zone with the top pore rows at the network surface and the internal interconnectivity of the liquid phase (which is additionally promoted by liquid films). Differences in the level of the drying rates during the second period of drying as well as the duration of this period are related to local variations of network saturation, especially of the network top rows at the start of drying. Precisely, experiment 18 reveals a distinctly lower level of drying rates already from the very beginning. This might be explained with a slightly lower surface saturation than exemplarily compared to experiment 11. Additionally, the slightly lower air temperature might have influenced the temperature of the PN top rows, both effects leading to a decrease of the overall evaporation rate. This in turn leads to a greater impact of condensation, reflected by the large liquid cluster surviving close to the PN surface (see Appendix A.4 for more information). This finally impacts on the overall drying time, which is  $t \cong 68$  h in experiment 10 (with higher saturated top pore rows and slightly higher drying rates during the second period of drying) and  $t \cong 86$  h in experiment 11 (with initial dry out of the top pore rows). Duration of experiment 18, which was already stopped at  $S \cong 0.11$ , is expected between these results although the level of the drying rate was initially lower than comparably in experiment 11. This reveals the positive impact of the condensation effect on drying time.

A drop in drying rates occurs at the transition from the second to the third drying period, i.e. with the interruption of the connectivity of the liquid phase to the PN top pore rows and the emerging condensation within the 2-phase zone (at  $S \cong 0.36$  to  $0.41$ ). Then vapor diffusion becomes the dominant mass transfer mechanism with  $\dot{M}_v \propto 1/z$  (Eq. 2-15). The drop results from the increase in diffusion resistances with increasing distance of the LAP of the evaporation front from the network top and the growing impact of condensation. As a consequence network saturation decreases significantly slower with the initiation of the third period of drying (Fig. 4-37b). A further drop in drying rates is observed with the transition from the third to the fourth drying period which is associated with the disappearance of clusters at the cold front and further receding of the same (Figs. 4-27 and 4-30). This is again explained with the diminished relevance of condensation rates in this drying period. A more detailed discussion of this effect is given in Chapter 6, where PN simulations are applied to analyze the experimental drying behavior.

In summary, drying with imposed positive thermal gradient is approximately 40 % to 80 % longer than drying with  $\bar{T} \cong 63^\circ\text{C} \cong \text{const.}$  and 2 to 2.6 times longer than drying with the negative temperature gradient although similar drying rates were detected at the start of drying ( $\dot{M}_{\text{evap},0} \cong 5 \text{ mg h}^{-1} - 15 \text{ mg h}^{-1}$ ). Additionally, a more favorable drying front position was observed during most of the drying process resulting in longer constant drying rates at

the high initial level than compared to the other situations where drying rates dropped initially. More precisely,  $\dot{M}_{evap} \geq 1 \text{ mg h}^{-1}$  until  $S \cong 0.41$  in drying with positive gradient, while exemplarily  $\dot{M}_{evap} < 1 \text{ mg h}^{-1}$  below  $S \cong 0.68$  in the quasi-isothermal experiment. In drying with negative thermal gradient the drying rate constantly decreased with  $\dot{M}_{evap} < 1 \text{ mg h}^{-1}$  for  $S \leq 0.25$  (experiments 8 and 13). The deviations are partly based on the overall lower surface temperature ( $T_{top} \cong 24^\circ\text{C}$ ) and the overall significantly lower mean temperature of  $\bar{T} \cong 36^\circ\text{C}$  in drying with positive temperature gradient. It is expected, and demonstrated by simulations in Chapter 6 that the drying time would be decreased in the positive heating mode compared to the other experiments, if the mean temperature of the PN would be in the same range as selected in these experiments.



**Figure 4-37** a) Drying curves, b) drying rates in a semi-logarithmic plot (exps. 10, 11 and 18).

## 4.5 Summary and discussion

The 2-dimensional microfluidic device appears as an adequate base to study, interpret and demonstrate drying of porous media as well as to identify influential effects that must be taken into account for the development of strong mathematical models. The developed experimental setup thus provides an effective tool for an access to drying of porous media.

The presented and discussed experiments clearly reveal the governing role of different pore scale effects occurring during drying of the microfluidic PN. These effects are mainly associated with the impact of temperature gradients on the primary invasion of the PN and they are also expected in capillary porous media in general. Furthermore, the CLSM record of the pore scale primary invasion presented in Section 4.2 of this chapter showed that viscous effects might have affected the non-isothermal PN invasion. Exploration of this issue is further pursued in Chapter 6 where the experiments are evaluated by PN simulations. The CLSM measurement also elucidated the morphology of liquid films remaining along the rough side walls of the throats after primary invasion. It could be revealed that liquid films found inside the microfluidic device do not form a percolating or continuum film region (at least not in the center of the PN) but that they rather have a specific ring structure related to

the 2-dimensional structure of the PN. This is relevant for the secondary invasion as will also be shown by PN simulations in Chapter 6. In addition to that, it was found that the lateral pinning of liquid, enabled by the wall covering wetting of the lateral edges of the PN, plays a major role.

The structural analysis of the pore scale liquid distribution during drying of microfluidic networks has never been presented in such a detail before. It disclosed that the overall drying behavior can be dictated even by minor peculiarities. The different morphologies of liquid films in the center of the PN (liquid film rings) and along the PN edges (continuous films) demonstrate this very nicely. As discussed, the liquid film rings are disconnected in absence of bulk menisci or liquid bridges wherefore liquid communication is limited. Precisely, the discrete character of the liquid film rings does not allow for a favorable evaporation front position closer to the PN surface. However, the continuous liquid films forming along the side walls of the PN essentially controlled drying especially in quasi-isothermal experiments and experiments with imposed negative temperature gradient. In contrast to the discrete liquid rings, the lateral pinning of the liquid phase indeed allows for a favorable drying front position. This can positively affect drying rates as shown by comparison of experiment 15 with experiments 8 and 13.

In summary, experimental results are in very good agreement with literature predictions (e.g. Tsimpanogiannis et al. 1999, Surasani 2009). They reveal very clearly that the drying process can be controlled by imposing different thermal gradients. It could be shown that the drying front can be stabilized by a temperature gradient of the kind  $dT/dz < 0$ . Contrarily, a temperature gradient with  $dT/dz > 0$  can first destabilize the liquid phase and then provoke a second evaporation front travelling contrary to the initial evaporation front. This is additionally accompanied by condensation. A similar effect can otherwise only be obtained by gravity or rather hydrostatic pressure gradients imposed on the PN, which is difficult to manipulate. Based on these findings a powerful PNM will be developed in Chapter 5. This model will take the governing pore scale mechanisms into account. The developed model can be instrumental for control of product quality after drying, if one thinks of the impregnation of porous media with particulate matter, as well as for control of overall drying time.

Finally it is remarked that similar overall drying behavior is expected in 3D systems. Exemplarily, the particular drying phenomena presented here have also been indicated in simulations by Surasani (2009). Though gravity effects might play an additional role in a large 3D system. Additionally, heat transfer resistances are to be considered in larger 3D systems. Also, interconnectivity of the pore space is naturally higher in a 3D network, by what a period of constant drying rate is naturally promoted.



„You do not really understand something unless you can explain it to your grandmother.“

Albert Einstein

\* March 14, 1879 in Ulm, Germany

† April 18, 1955 in Princeton, USA

## Chapter 5

# Experiment based development of the pore network model

### 5.1 Introduction

In this chapter, the successive development of a PNM of non-isothermal drying is presented. The development is based on the structure of the microfluidic PN and the experimental findings presented in the previous chapters. This includes the implementation of temperature affected capillary invasion and vapor diffusion as also secondary capillary invasion.

Implementation of the thermal impact on drying can in principle be realized by three different approaches. In option 1 both, mass and heat transfer are simulated with the discrete PNM. An important step towards such a model was done by Surasani (2009). In option 2, the evolving temperature profile is either experimentally estimated or simulated (outside of the PNM), e.g. by a continuous model, and the estimated temperature profile is then implemented in the PNM using empirical equations. In option 3, the experimental data is directly used for the PN simulations. For this purpose, the pore scale temperature distribution is assigned to the individual pores and throats, similarly as the throat and pore width. The third option is chosen for the development of the non-isothermal PNM presented here. Choice of this method is based on the assumption that the heat transfer rate is high in comparison to the rate of vapor diffusion and thus temporal temperature variations do not evolve. In agreement with the drying experiments with imposed thermal gradients and assumptions of Huinink et al. (2002), Plourde and Prat (2003) and Surasani et al. (2008a) temporally constant temperature profiles over the complete drying process are anticipated. The assumption of constant temperature gradients is also consistent with temperature profiles in traditional drying processes (convective or contact drying of porous media), where the direction of the temperature gradient along the porous medium does usually also not change during drying.

Base of the model development is the isothermal drying model of Metzger et al. (2007c). The basics of this model are given below in Section 5.1.1 together with the modifications of the structure in regard of the consistency of model and microfluidic PN. From this benchmark model two routes are taken. These are principally sketched in Sections 5.1.1 and 5.1.2. The first route concerns the implementation of secondary capillary invasion as a major drying effect whereas condensation is disregarded. This model concept is the base for the simulation of situations in which local temperature variations are low enough to allow for a compensation of condensation rates, so that cluster growth due to the condensation of vapor does not occur. Temperature dependence of the physical parameters involved in this model as well as the directional dependence of the vapor pressure gradients are taken into account in this concept. The model is essentially applied for the simulation of quasi-isothermal drying; it is also applied for simulation of non-isothermal drying with imposed negative thermal gradient with the constraint of negligible condensation (i.e. when the edge effect is not prominent). For drying with imposed positive thermal gradient, where condensation of vapor is clearly visible in drying experiments, a second route is explored. It allows simulation of liquid invasion in presence of strong condensation effects. This model is also referred to the non-isothermal PNM with cluster growth mechanism and it has different levels of complexity (Section 5.1.2). Since liquid films arise independent of the heating mode, secondary capillary invasion is considered in this model by a variation of the labeling of liquid clusters emerging during drying. Liquid rings or capillary liquid films, instead, are not implemented in this model concept.

The structure of this chapter is as follows. At first Section 5.2 provides detailed information about the PN structure developed on the base of the microfluidic PN. Special attention is paid on the structural specifications that must be considered when implementing additional liquid elements such as pore volumes and liquid rings. Sections 5.3 and 5.4 address the transport equations with respect to the temperature dependency of involved physical parameters. Finally, Sections 5.5 and 5.6 summarize the PN algorithms. The result of the successive implementation of the experimentally identified governing pore scale effects is an advanced PNM with different concepts and levels. Validation of this model, in its different versions, can be found in Section 6.

### **5.1.1 Non-isothermal pore network model with secondary capillary invasion**

The isothermal PN drying model of Metzger et al. (2007c) serves as the benchmark for the model development of both, the non-isothermal PNM with secondary capillary invasion and the non-isothermal PNM with condensation effects presented in the following section. It is based on PNMs formulated in the early 80's (e.g. Wilkinson and Willemsen 1983) for the drainage of liquid from porous media. This is a percolation model with quasi-static displacement of the wetting liquid phase by the non-wetting gas phase enabled through the progressive evaporation of liquid. Viscosity of the liquid phase, temperature gradients and gravity as well as secondary capillary effects are disregarded in this benchmark PNM (Metzger et al. 2007c). Additionally, the pore space between adjacent throats is completely ignored in this PNM. Instead the complete void space of the PN is assigned to the pore throats which are directly connected to each other without overlapping. In agreement with classical PNMs for drainage, Irawan (2006) and Metzger et al. (2007c) implemented volumeless nodes (also named pores in their publications) to define the neighbor relations of the pore throats as well as to determine the boundary conditions for mass transfer between them. Then principally the gas side mass transfer equations (Eq. 2-15) are set up and solved

for each pore node of the network; on the liquid side the order of emptying of the throats is computed from the Young-Laplace equation (Eq. 2-25).

The benchmark model of Metzger et al. (2007c) can exemplarily be applied to predict the drying behavior depending on the pore (or throat) size distribution as well as spatial pore and throat configurations. The basic model assumptions of the benchmark model are summarized in Table 5-1. The main drawback of this model, in the face of experimental findings in Chapter 4, is the underestimation of mass transfer due to the negligence of secondary capillary effects (i.e. liquid films). Based on this, the model is further developed to take these effects into account. This is achieved by the implementation of additional *liquid* elements in the benchmark model. At first, the pore volumes are implemented (Section 5.2.1) leading to an advanced PNM with a pore structure very close to the microfluidic PN. Besides this, capillary liquid rings (Section 5.2.2.1) and the lateral pinning of liquid (also denoted by the edge effect) (Section 5.2.2.2) are implemented in this PNM. The additionally implemented liquid elements have in common that they significantly impact on the order of capillary invasion. Table 5-1 summarizes the main characteristics of the proposed non-isothermal PNM with secondary capillary invasion and compares the advanced features of this model with the benchmark model of Metzger et al. (2007c).

**Table 5-1** Comparison of the experiment based non-isothermal PNM with secondary capillary invasion with the benchmark PNM of Metzger et al. (2007c).

Benchmark PNM	Experiment based PNM
square network of throats and volumeless pores	square network of throats and pores with volume
rigid solid matrix	
quasi-static invasion of the throats by the gas phase	
temperature temporally and locally constant	temperature temporally constant with consideration of spatial temperature variations by temperature dependent physical parameters and directional vapor transfer
moderate drying rates at constant pressure	
diffusive boundary layer	
non-linear vapor diffusion	
neglected gravity and neglected viscous friction forces	
neglected secondary capillary transport	implementation of liquid rings and pinning of liquid by the edge effect

### **5.1.2 Non-isothermal pore network model with cluster growth mechanism**

The temperature affected drying experiments with different imposed thermal gradients, presented in Chapter 4, reveal very similar phase patterns as obtained by Huinink et al. (2002), Plourde and Prat (2003) and Surasani et al. (2008a) in case of drying with negative thermal gradient. From this can be concluded that these models can very well predict drying with stabilizing thermal gradient if secondary capillary invasion is negligible or, if this is not negligible, the above described PNM (Section 5.1.1) can be applied. Comparison of the experimental phase distributions with simulation results of these authors, predicted for drying with imposed positive thermal gradient, however, reveals obvious deviations associated with the refilling of the pore space as a consequence of condensation, which is neglected in their models. This finding is the starting point of the development of the non-isothermal drying model with simultaneous evaporation and condensation. Base of the development is again the benchmark model of Metzger et al. (2007c) expanded by the temperature dependency of the involved physical parameters (Table 5-2). The complexity of this model is successively increased to take into account the several levels of liquid invasion following from the condensation of vapor. This leads to the development of different versions of the non-isothermal PNM, also referred to PNM level 1-4 (also refer to Fig. 5-17). In detail, PNM level 1 designates the model with lowest level of complexity. In this, the structure of the mathematical PN is adapted to the structure of the microfluidic PN but any temperature dependence of vapor transport is disregarded. In PNM level 2, local evaporation rates are decreased by the local condensation rates. More precisely, the negative mass transfer rates (towards a liquid cluster) are taken into account by a reduction of cluster evaporation rates but any refilling of the PN is disregarded. This assumption particularly applies in the case of low temperature gradients, i.e. when the local saturation vapor pressure gradients are low. This version of the model is applicable to simulate drying with slight local temperature variations (in absence of secondary capillary effects). In presence of higher temperature gradients, however, this simple PNM leads to a significant underestimation of the condensation effect. In PNM level 3 the partially saturated elements at the cluster boundaries (which emerge from the cluster mass balances as will precisely be described below) are re-invaded by the liquid phase. This way, the amount of neglected condensed liquid can be reduced. However, fully saturated liquid clusters (i.e. without available partially saturated liquid elements at the cluster boundary) do not grow in PNM level 3. This is in contrast to experimental observations, where the clusters grew and merged, forming an intermediate dense liquid structure (Section 4.4.2). The refilling of adjacent empty throats or pores with the condensed liquid is thus incorporated in level 4 of the PNM. In the non-isothermal PNM level 3-4 the film effect is simplified by incorporation of the edge effect (developed on the base of the quasi-isothermal experiments) as well as different cluster labeling options (Section 5.4.4).

In summary, the developed non-isothermal PNM with cluster growth can be distinguished from the existing models (e.g. Huinink et al. (2002), Plourde and Prat (2003) and Surasani (2009)) in the following points:

- A constant temperature gradient is imposed on the PN and
- heat transfer is disregarded.
- Single pores with volume are introduced.
- Condensation with refilling of pores and throats is implemented.
- Different invasion rules are applied for pores and throats.
- Secondary capillary invasion is accounted for by the edge effect and cluster labeling.

**Table 5-2** Comparison of the experiment based non-isothermal PNM with cluster growth mechanism with the benchmark PNM of Metzger et al. (2007c).

Benchmark PNM	Experiment based PNM
square network of throats and volumeless pores	square network of throats and pores with volume
rigid solid matrix	
quasi-static invasion of the throats by the gas phase	quasi-static invasion by the gas phase (evaporation) and by the liquid phase (condensation); different invasion rules for pores and throats
temperature temporally and locally constant	temperature temporally constant with consideration of spatial temperature variations by temperature dependent physical parameters and directional vapor transfer
moderate drying rates at constant pressure	
diffusive boundary layer	
non-linear vapor diffusion	
neglected gravity and neglected viscous friction forces	
neglected secondary capillary transport	higher interconnectivity as in presence of liquid rings by different cluster labeling options

## 5.2 Pore network structure

The structure of the proposed PN is very close to the benchmark PN (also refer to Irawan 2006). Exceptions are the absence of periodic boundary conditions, which are deleted for a better representation of the experimental network, the introduction of pore volumes replacing the volumeless nodes in the model of Irawan (2006) and the introduction of both, liquid rings and the so called edge effect as a consequence of wall wetting phenomena.

The primary pore structure of the mathematical PN is adapted to the structure of the microfluidic PN presented in Section 3 so as to obtain a numerical PNM that has a similar geometry as the SiO<sub>2</sub> network presented in Table 3-4 and Figs. 3-1 and 3-3 (Fig. 5-1). This allows for a pore-by-pore or throat-by-throat comparison of drying experiments and simulations and thus evaluation of the governing pore scale phenomena in Chapter 6 and Appendix B. In the advanced PNM, the pores are typically distinguished from the throats as

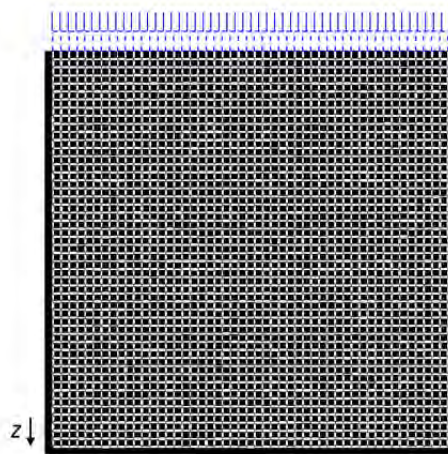
they have a significantly smaller aspect ratio and a smaller volume ( $\bar{V}_p \cong \bar{V}_t/5$ ). In the microfluidic SiO<sub>2</sub> network presented in Section 3 the throats have an aspect ratio of around 10:1 and the pores of around 1. Impact of the pore volumes on the drying behavior is described in detail in Appendix B.2. The most striking difference between the PNM taking pore volumes into account and the benchmark PNM is the different order of invasion. This is based on similar invasion pressure thresholds of pores and throats (also refer to Fig. 5.12 below). Notice that the implementation of pores with separate capillary entry pressure threshold can increase the number of invasions from 4851 to 7351 as these pores are invaded independently of the throats.

The crevices and corners of the throats as well as the lateral edges of the PN form a secondary PN structure. As will be discussed in what follows, significantly smaller invasion pressure thresholds are associated with the secondary PN (Fig. 5.12 below). This explained the formation of capillary liquid rings as well as the lateral pinning of the liquid phase along the PN edges in the microfluidic device. As will be elucidated in what follows, implementation of secondary capillary invasion in the PNM is realized by the introduction of additional liquid elements (namely liquid rings) and the increase of the invasion pressure threshold of the throats and pores along the straight lateral edges of the PN by a reduction of the width (edge effect). As a consequence, in the 2D square lattice of size 50x50, the implementation of liquid rings increases the number of invasions by 2401.

Additionally, a discretized boundary layer (BL) with similar structure as the PN lattice is incorporated and it connects the PN surface with the bulk air phase (Irawan et al. 2005) (Fig. 5-1). This is based on the assumption of a diffusive BL at the PN surface (Section 2.3.3). For this, the PN structure is extended in order to compute diffusive vapor transport from the PN surface to the bulk air phase analog to the vapor transport inside the PN. It is

$$s_{BL} = (N_{BL} + 1)L_{BL}, \quad (5-1)$$

the vertical width of the BL depending on the lattice spacing  $L_{BL}$  and the number of layers  $N_{BL}$ . In the simulations presented in Chapter 6, the BL thickness is adapted so as to fit the simulated initial evaporation rate to experiments.



**Figure 5-1** Structure of the primary PN with  $m = 50$  pore rows and  $n = 50$  pore columns (identical to the microfluidic PN in Fig. 3-1). Throats and pores in white, solid in black. The PN is open only at the top; the other sides are impermeable for mass transfer. The BL (in blue) on top of the PN has a similar structure as the PN lattice. In this example  $N_{BL} = 1$  and  $s_{BL} = 2L_{BL}$ .

### 5.2.1 Primary pore network structure

#### Throats

Based on the parameters of the microfluidic PN given in Table 3-4 and Fig. 3-1, geometry of the throats is assumed as cuboidal with significantly greater length than width and height (Fig. 5-2). This affects the cross section of throats (which is assumed as rectangular),

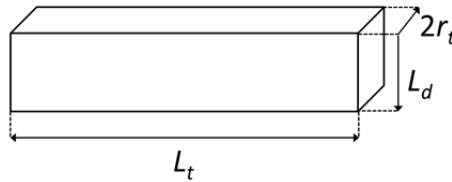
$$A_t = 2r_t L_d, \quad (5-2)$$

and the total volume as well,

$$V_t = A_t L_t. \quad (5-3)$$

Note that the estimated cross section and volume of throats is assumed to be slightly greater than the true values (Fig. 3-1).

As a consequence of the assumption of cuboidal structure a third dimension emerges, wherefore the PN is quasi 2D. The mean meniscus radius of the liquid phase confined inside throats is computed from Eq. 2-24.



**Figure 5-2** Cuboidal throat geometry as an approximation of the throat structure in the microfluidic PN shown in Fig. 3-1.

#### Pores

Based on the works of Lenormand et al. (1983) or Tsimpanogiannis et al. (1999) the pore volumes emerge from the throat arrangement (Fig. 5-3). Precisely, half width, volume and cross section of the pores are computed from the width and the arrangement of the neighboring throats:

$$r_p = \sqrt{r_{t,ver}^{max} \cdot r_{t,hor}^{max}}, \quad (5-4)$$

$$V_p = 4r_{t,ver}^{max} r_{t,hor}^{max} L_d - (r_{t,ver}^{max} - r_{t,ver}^{min}) (r_{t,hor}^{max} - r_{t,hor}^{min}) L_d \quad (5-5)$$

and

$$A_p \cong \frac{V_p}{2r_p}. \quad (5-6)$$

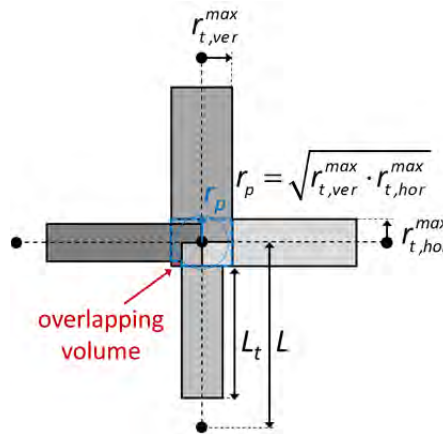
Following assumptions for the throats, the pores are also assumed with rectangular cross section. The mean meniscus radius of the liquid phase confined inside pores is computed from Eq. 2-24, analog to throats.

Note that the computational nodes are located in the pore center (see below for a further explanation) and the lattice spacing  $L$  of the PN is unaffected from the introduction of pores. More precisely, the diffusion length is  $L = 1000 \mu\text{m}$  in the PN under study. However, the throat length  $L_t$  is reduced in order to allow for the pore space, which results in a reduced

volume of pore throats when compared to a PN ignoring the pore volume (Fig. 5-3). Exemplarily, the length of a vertical throat is approximated by:

$$L_t \cong L - 2\bar{r}_{t,hor}^{max} \quad (5-7)$$

It is remarked that the resulting overlapping of throats (occurring if the half widths of the adjacent throats are significantly different), as illustrated by the small red rectangle in Fig. 5-3, is subtracted from the effective pore volume given in Eq. 5-5 (see also Prat (1993) or Segura (2007)).



**Figure 5-3** Sketch of pore implementation. The overlapping volume of throats is disposed to the pore volume (except of the red area). Lattice spacing  $L$  remains unaffected. (A different approach is presented by Chapuis (2006) who based the computation of  $r_p$  on the hypotenuse of the pore space).

Saturation of pores and throats is computed from

$$S_p = \frac{V_{p,l}}{V_p} \quad (5-8)$$

and

$$S_t = \frac{V_{t,l}}{V_t}, \quad (5-9)$$

whereas the overall network saturation in the presence of pore volumes is computed from

$$S = \frac{\sum S_t V_t + \sum S_p V_p}{\sum V_t + \sum V_p}. \quad (5-10)$$

## 5.2.2 Secondary pore network structure

### 5.2.2.1 Capillary liquid rings

Based on experimental observations and CLSM measurement it was concluded that the capillary film effect can be assigned to discontinuous liquid wedges forming around the solid islands in the microfluidic PN (Fig. 3-4b in Section 3.2.2 and Fig. 4-9 in Section 4.2.2.1). The structure of these liquid wedges is best represented by liquid rings (Fig. 4-8a). Implementation of capillary liquid rings is schematically illustrated in Fig. 5-4. The rings are



represented by gray rectangles in this figure. Notice that the gray rectangles represent fully and partly developed liquid rings with different liquid saturation: a partly developed liquid ring is still fully saturated ( $S_r = 1$ ) and connected to one or more liquid (bulk) menisci or liquid bridges and a fully developed ring is completely detached from the bulk liquid phase with a saturation  $0 < S_r \leq 1$ . These are the two rings in the top row of the sketch.

The simplified schematic illustration ignores the exact geometry of the liquid wedges. More precisely, according to the geometry illustrated in Fig. 4-8a, the total liquid volume of a ring is computed from the average length  $\bar{L}_t$  of the throats in the periphery of the ring at constant ring width  $w_r$  and throat depth  $L_d$ ,

$$V_r = \sum w_r L_d \bar{L}_t, \quad (5-11)$$

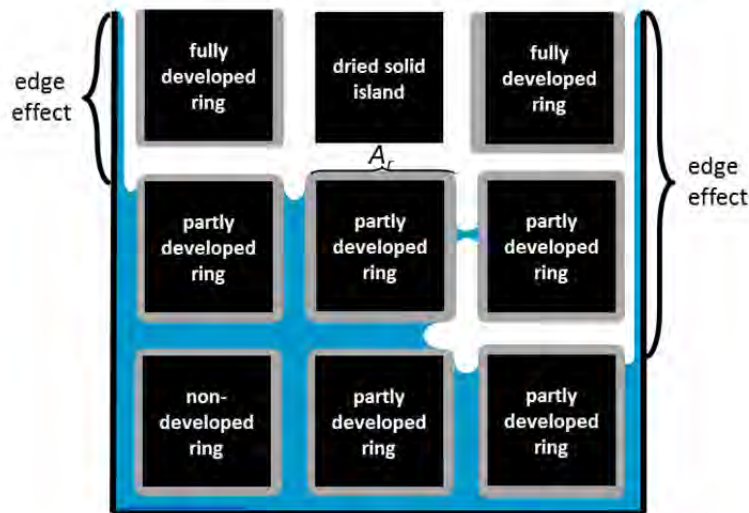
with

$$\bar{L}_t \cong L - 2\bar{r}_t. \quad (5-12)$$

(In a more exact formulation of the ring volume, the anticlastic geometry of the rings as well as the distribution of the throat length might be taken into account). The volume of liquid throats is reduced accordingly by

$$V_{t,l} = V_{t,l}^0 - N_r w_r L_d (L - 2\bar{r}_t). \quad (5-13)$$

In this  $V_{t,l}^0$  denotes the liquid volume in the throat if no ring is anticipated and  $N_r$  denotes the number of rings found inside the throat. The maximum number of rings in a throat is obviously  $N_r = 2$  (Fig. 5-4). The pore volume, instead, remains unaffected from the introduction of liquid rings. Moreover, invasion of single liquid pores is not computed in presence of liquid rings. Furthermore the cross sectional area of throats with gas-liquid interface is also not adapted.



**Figure 5-4** Simplified schematic representation of capillary liquid wedges in the form of liquid rings. Solid in black, empty rings, pores and throats in white and liquid in blue. Fully and partly developed liquid rings are indicated by gray rings surrounding the solid islands. Notice that the rings at the top row are constituted by only three wedges.

It is noted that the ring volume is adapted by variation of the ring width  $w_r$  which is a priori defined based on experimental and theoretical findings. In the majority of simulations with capillary liquid rings  $w_r = 22.4 \mu\text{m} = \text{const.}$  (based on measurements presented in Section 4.2.2.1). This leads to a slightly overestimated ring volume as regards the illustration in Fig. 4-8a because essentially the height of the ring is a function of  $w_r$  (in Eq. 5-11 instead constant height  $h = L_d = h^{\text{max}}$  is stipulated).

Notice that choice of the ring width impacts on the total liquid volume associated with the rings (Eq. 5-11). As discussed in Vorhauer et al. (2015) this can affect the drying time because more liquid remains in the throat corners after disconnection of the liquid rings, i.e when liquid communication of the ring with the bulk liquid phase is interrupted. The liquid contained inside the ring at the point of disconnection must be evaporated and transferred by vapor diffusion. Obviously, more liquid volume must be transported in the vapor phase when the initial ring volume is larger. This can lead to a longer drying time if the ring volume at detachment is larger.

The ring interface area is derived from the supposed geometric arrangement around the solid blocks. It is:

$$A_r = (L - 2\bar{r}_t)L_d, \quad (5-14)$$

the interface area of a ring covering one side of an else empty throat (Fig. 5-4). For the estimation of the total ring interface area, for instance of a ring that consists of four liquid wedges,  $A_r$  must be multiplied with factor 4 (the rings in the top row in Fig. 5-4 are ergo multiplied with factor 3).

The ring saturation is computed from

$$S_r = \frac{V_{l,r}}{V_r} \quad (5-15)$$

and the overall network saturation in the presence of liquid rings is computed from

$$S = \frac{\sum S_r V_r + \sum S_t V_t}{\sum V_r + \sum V_t}. \quad (5-16)$$

### 5.2.2.2 Edge effect

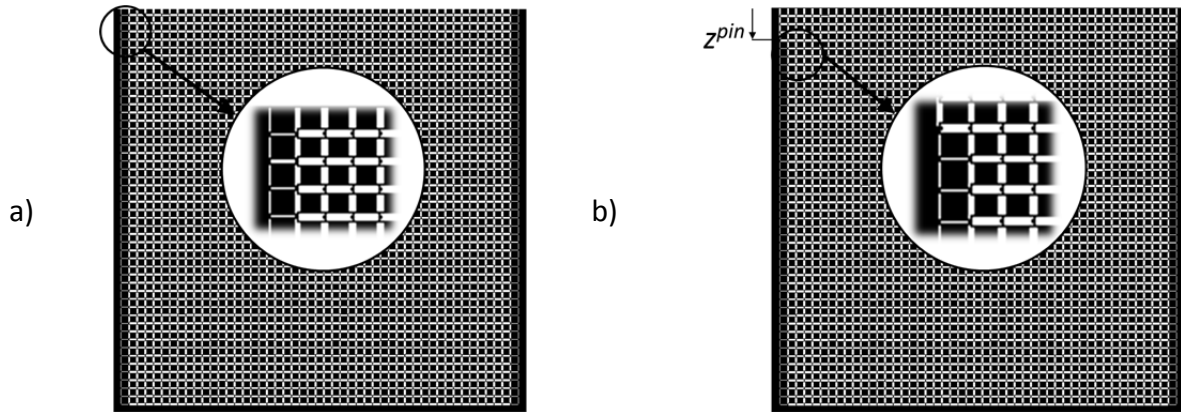
The experimentally observed pinning of the evaporation front along the lateral edges of the PN (Fig. 4-11) was explained with continuous liquid films evolving along the straight side walls (also highlighted in Fig. 5-4). As already discussed earlier in this thesis, liquid films generally produce higher invasion pressures due to the significantly smaller width compared to the primary PN pores and throats (e.g. Section 2.3.6). Based on this, the lateral pinning of liquid by continuous liquid films is taken into account in the PNM by implementation of the edge effect based on Eq. 2-25. This is realized simply by artificially reducing the meniscus curvatures of the edge pores and throats by a constant factor  $f^{\text{red}}$ :

$$r_{m,\text{edge}} = f^{\text{red}} r_m. \quad (5-17)$$

This is exemplarily illustrated in Fig. 5-5a. The reduction of meniscus curvatures aims at the increase of the capillary invasion pressure thresholds of these elements, similar as the increase of invasion pressure thresholds in liquid rings or continuous liquid films. As will be

discussed in detail in Section 5.4.1, the size reduction factor  $f^{red}$  depends on the capillarity of the PN. More clearly, to ensure that the lateral edges remain liquid filled when the bulk liquid phase recedes in the center of the PN, the capillary pressure threshold must be increased above a critical value. As will be shown below, this is  $p_{c,edge}^{min} (T = 63^\circ\text{C}) \cong 4674 \text{ Pa}$  in the PN discussed in this thesis. With this critical value a maximum radius of curvature of  $r_m^{max} \cong 28 \mu\text{m}$  can be associated (Eqs. 2-24 and 2-25). Consequently, the half width of the lateral pores and throats must artificially be virtually reduced to a value  $r_{t,p} \leq 50 \mu\text{m}$  (Eq. 2-24, assuming  $L_d = const.$ ) in order to capture the lateral pinning. Note, that the volume of the affected pores and throats is kept constant (Eqs. 5-3 and 5-5).

The impact on the lateral position of the evaporation front, i.e. the LAP of lateral pinning, and thus the impact on the overall evaporation rate can be adapted by the number of rows to which Eq. 5-17 is applied. Based on the experimental findings in Chapter 4 the position of liquid pinning is very close to the PN open side over the longest period of the drying process in most situations. This is taken into account in Fig. 5-5b where Eq. 5-17 is applied only to rows  $z = (5-49)L$ . This is applied in the majority of the simulations.



**Figure 5-5** Mathematical PN with identical pore and throat sizes as in the microfluidic pore network. a) Width of the lateral vertical and horizontal throats and the lateral pores is virtually reduced by factor  $f^{red}$  to take into account the lateral pinning of liquid. b) Application of Eq. 5-17 only to rows  $z^{pin} = (5-49)L$  with the aim to control the overall evaporation rate.

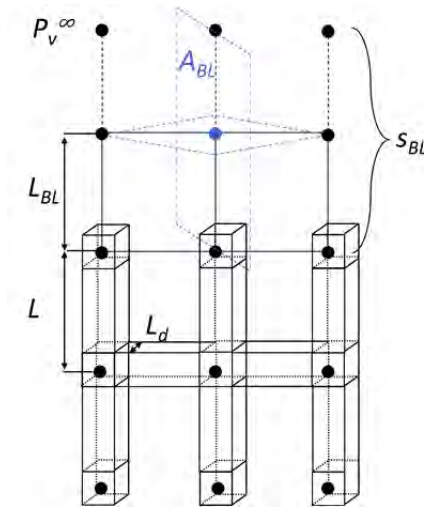
### 5.2.3 Structure of the computational boundary layer

The structure of the BL and its connection to the PN surface is shown in Fig. 5-6. As can be seen, the pores are replaced by computational nodes (dots in Fig. 5-6) without volume and the connections between these nodes have a significantly greater cross section than the throats in the PN. Otherwise, the arrangement of the computational nodes and their connections is very similar to the arrangement of pores and throats in the PN lattice. Precisely, the cross section of node connections inside the BL is given by

$$A_{BL} = L_d L_{BL} \quad (5-18)$$

and the cross section of horizontal BL connections to the network surface is defined as

$$A_{BL} = 0.5 L_d L_{BL} \cdot \quad (5-19)$$



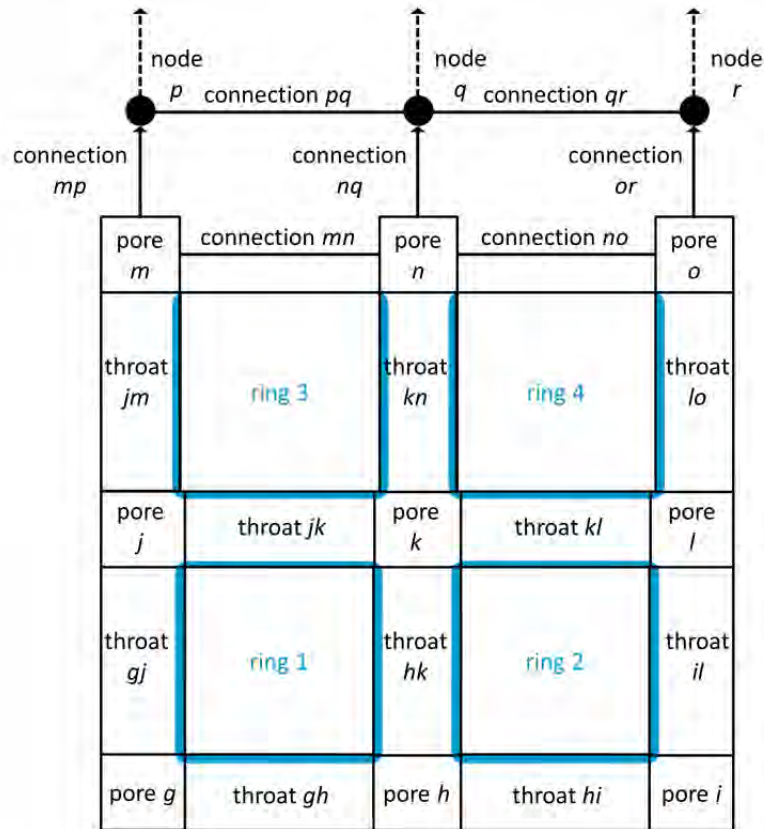
**Figure 5-6** Illustration of PN lattice and computational BL connected to the PN surface in purpose to model vapor transfer to the bulk air phase,  $L_{BL} = L$  and  $N_{BL} = 1$  in this example. The cross section of the connections between the computational nodes in the BL are enlarged so as to allow for higher vapor flow rates (Eq. 2-15) based on Schlunder (2004) and Talbi and Prat (2019).

### 5.2.4 Neighbor relations

The neighbor relations of pores/computational nodes and throats/node connections are defined according to Irawan (2006) who gives a precise overview on this in his PhD thesis. Notice that the computational nodes are located in the center of the pores inside the PN lattice (and inside the BL above the PN as already shown in Fig. 5-6). According to the proposal of Irawan (2006), basically the information about pore, throat and ring neighbor relations are stored in matrices. Figure 5-7 and Table 5-3 give an overview of the neighbor relations following the notation of Irawan (2006).

## 5.3 Gas side moisture transfer

Figure 5-8 illustrates vapor diffusion through the empty void space of the PN. The driving force of vapor diffusion is the vapor pressure difference (over constant distance  $L$ ) between the gas-liquid interface, with higher vapor pressure  $P_v = P_v^*(T)$  (with  $P_v^*(T)$  from Eq. 2-5), and the bulk air phase, with  $P_v = P_v^\infty = 0$ . As already explained before, the bulk air phase is connected by a discretized BL with lattice spacing  $L_{BL}$  (Irawan et al. 2005). The boundary conditions of vapor diffusion are determined by the state of the computational nodes located in the pore center (PN lattice) and in the BL lattice. Again, it is  $P_v = P_v^*(T)$  in pores connected to partially saturated throats as well as in partially saturated pores and  $P_v = P_v^\infty = 0$  in the bulk air phase connected to the upper pore row of the BL (Fig. 5-8). The vapor pressures inside empty pores and the pore nodes inside the BL are obtained from the mass balances. This is explained in detail in what follows. Special attention is paid on the implementation of directional vapor flow rates in presence of thermal gradients.



**Figure 5-7** Illustration of the neighbor relations of pores (or computational nodes), throats (or also the connections between the computational nodes) and rings.

### 5.3.1 Vapor pressure field

The computation of the vapor pressure in empty pores with  $P_v \neq P_v^*(T)$ , i.e. disconnected from the gas-liquid interface, is explained by the configuration exemplarily illustrated in Fig. 5-9. Precisely, Fig. 5-9 shows two empty pores located at the gas-liquid interface and one liquid filled pore with different temperatures (pore  $i$ , pore  $j$  and pore  $k$  with  $P_{v,i} = P_v^*(T_i)$ ,  $P_{v,j} = P_v^*(T_j)$  and  $P_{v,k} = P_v^*(T_k)$ ) and one empty pore which is not neighbored to the liquid phase (pore  $l$  with  $P_{v,l} \neq P_v^*(T_l)$ ). Additionally, the computational nodes in the BL are shown. For these it is assumed that  $P_{v,m} \neq P_v^*(T_{BL})$  and  $P_{v,n} \neq P_v^*(T_{BL})$ .

The gas side mass transfer is basically computed as a set of linear equations expressed for each computational node located in the center of the pores (PN lattice) as well as in the BL. In the linear diffusion approach it is:

$$\dot{M}_v \sim \frac{\Delta P_v}{L}, \quad (5-20)$$

and in the non-linear diffusion approach it is:

$$\dot{M}_v \sim \frac{1}{L} \ln \left( \frac{P - P_v^*(T_{low})}{P - P_v^*(T_{high})} \right). \quad (5-21)$$

**Table 5-3** Overview of the basic variables that store the neighbor relations in the PNM.

Explanation	Variable	Matrix formulation
neighboring computational nodes and pore neighbors with increasing node/pore index ( $k, l, m, n$ )	$pnp$	$\begin{bmatrix} \vdots & \vdots & \vdots & \vdots \\ n & l & j & h \\ o & k & i & 0 \\ p & n & j & 0 \\ q & o & m & k \\ \vdots & \vdots & \vdots & \vdots \end{bmatrix}$
neighboring node connections and throat neighbors starting with the vertical connections with increasing index, continuing with the horizontal connections with increasing index ( $kn, lo, gh, hi$ )	$tnt$	$\begin{bmatrix} \vdots & \vdots & \vdots & \vdots & \vdots & \vdots \\ nq & no & mn & kl & jk & hk \\ or & no & kl & il & 0 & 0 \\ gj & hk & hi & 0 & 0 & 0 \\ hk & gh & il & 0 & 0 & 0 \\ \vdots & \vdots & \vdots & \vdots & \vdots & \vdots \end{bmatrix}$
node/pore neighbors of a connection/throat ( $kn, lo, gh, hi$ )	$tnp$	$\begin{bmatrix} \vdots & \vdots \\ k & n \\ l & o \\ g & h \\ h & i \\ \vdots & \vdots \end{bmatrix}$
connections/throats neighboring a node/pore ( $k, l, m, n$ )	$pnt$	$\begin{bmatrix} \vdots & \vdots & \vdots & \vdots \\ kn & jk & kl & hk \\ lo & kl & il & 0 \\ mp & mn & jm & 0 \\ nq & no & mn & kn \\ \vdots & \vdots & \vdots & \vdots \end{bmatrix}$
ring neighbors in the order of increasing ring number (1, 2, 3, 4)	$rnr$	$\begin{bmatrix} 2 & 3 & 4 \\ 1 & 3 & 4 \\ 1 & 2 & 4 \\ 1 & 2 & 3 \end{bmatrix}$

**Table 5-3** Continued.

Explanation	Variable	Matrix formulation
nodes/pores neighboring a ring in the order of increasing ring number (1, 2, 3, 4)	$rnp$	$\begin{bmatrix} g & h & j & k \\ h & i & k & l \\ j & k & m & n \\ k & l & n & o \end{bmatrix}$
connections/throats neighboring a ring in the order of increasing ring number (1, 2, 3, 4)	$tnr$	$\begin{bmatrix} jk & hk & gj & gh \\ kl & il & hk & hi \\ kn & jm & jk & 0 \\ lo & kn & kl & 0 \end{bmatrix}$
ring neighbors of nodes/pores in the order of increasing index ( $k, l, m, n$ )	$pnr$	$\begin{bmatrix} \vdots & \vdots & \vdots & \vdots \\ 1 & 2 & 3 & 4 \\ 2 & 4 & 0 & 0 \\ 3 & 0 & 0 & 0 \\ 3 & 4 & 0 & 0 \\ \vdots & \vdots & \vdots & \vdots \end{bmatrix}$
ring neighbors of connections/throats in the order of increasing index ( $kn, lo, gh, hi$ )	$rnt$	$\begin{bmatrix} \vdots & \vdots \\ 3 & 4 \\ 4 & 0 \\ 1 & 0 \\ 2 & 0 \\ \vdots & \vdots \end{bmatrix}$

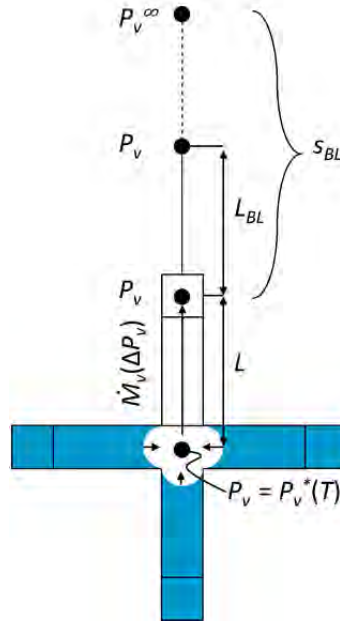
Consequently, if the temperature is spatially distributed, as in the example of Fig. 5-9, the vapor pressure gradient evolving from the variance of  $P_v = P_v^*(T)$  leads to the diffusion of vapor from pores with higher temperature to pores with lower temperature (according to the Antoine equation in Eq. 2-5 and Eq. 2-50).

The number of equations to be solved is identical to the number of empty pores at unknown vapor pressure inside the PN plus the computational nodes of the discretized BL. This means, for the PN shown in Fig. 5-9, *three* equations are to be solved.

Exemplarily, the mass balance of pore  $j$  is expressed as follows:

$$\dot{M}_{cond,j} = \dot{M}_{v,jl} - \dot{M}_{v,ij} \quad (5-22)$$

In this example, liquid is accumulating if  $\dot{M}_{v,ij} > \dot{M}_{v,jl}$ . (Contrary, evaporation would occur if  $\dot{M}_{v,ij} + \dot{M}_{v,jl} > 0$ ).



**Figure 5-8** Boundary conditions of vapor diffusion from the gas-liquid interface towards the gas bulk phase connected by a discretized BL of length  $s_{BL} = 2L_{BL}$ . The nodes at unknown vapor pressure are indicated with  $P_v$ .

The accumulation of liquid due to condensation of vapor is indicated by the arrows directed into the liquid phase while evaporation is represented by arrows directed into the gas phase. As represented by pore  $j$ , the condensation of vapor in presence of a temperature gradient principally leads to liquid saturated pores at the gas-liquid interface. The vapor pressure at the menisci confined in these pores is  $P_v = P_v^*(T)$ , as already mentioned before.

With the expression from Eq. 2-10, Eq. 5-22 can be written as:

$$\dot{M}_{cond,j} = \frac{\tilde{M}_v D(T_{jl}) A_{jl}}{\tilde{R} T_{jl} L} (P_{v,j} - P_{v,l}) - \frac{\tilde{M}_v D(T_{ij}) A_{ij}}{\tilde{R} T_{ij} L} (P_{v,i} - P_{v,j}) \quad (5-23)$$

or

$$\dot{M}_{cond,j} = -g_{v,jl} P_{v,l} - g_{v,ij} P_{v,i} + (g_{v,ij} + g_{v,jl}) P_{v,j} \quad (5-24)$$

substituting the conductances

$$g_{v,ij} = \frac{\tilde{M}_v D(T_{ij}) A_{ij}}{\tilde{R} T_{ij} L} \quad (5-25)$$

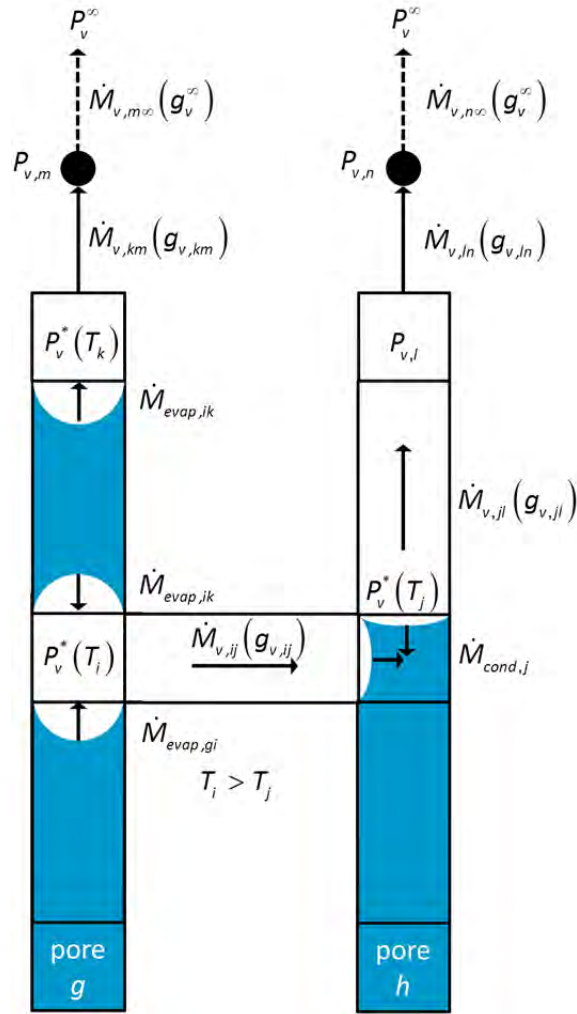
and

$$g_{v,jl} = \frac{\tilde{M}_v D(T_{jl}) A_{jl}}{\tilde{R} T_{jl} L}. \quad (5-26)$$

Assuming  $P_v = P_v^*(T)$  in pores  $i$  and  $j$ , Eq. 5-24 can also be expressed as follows:

$$\dot{M}_{cond,j} + g_{v,ij} P_v^*(T_i) - (g_{v,ij} + g_{v,jl}) P_v^*(T_j) = -g_{v,jl} P_{v,l}. \quad (5-27)$$





**Figure 5-9** Vapor diffusion from the gas-liquid interface to the bulk air phase connected by the BL on top of the PN. The sketch indicates pore and throat saturations, flow rates, conductances, evaporation and condensation rates and neighbor relations.

Analog equations are found for the expression from Eq. 2-15.

For the other empty pores and computational nodes in the BL (with index  $i, k, l, m, n$ ) follows accordingly:

$$\text{pore } i: \quad \dot{M}_{evap,i} = -g_{v,ij}P_{v,j} + g_{v,ij}P_{v,i}, \quad (5-28)$$

$$\text{pore } k: \quad \dot{M}_{evap,k} = -g_{v,km}P_{v,m} + g_{v,km}P_{v,k}, \quad (5-29)$$

$$\text{pore } l: \quad g_{v,jl}P_v^*(T_j) = -g_{v,ln}P_{v,n} + (g_{v,jl} + g_{v,ln})P_{v,l}, \quad (5-30)$$

$$\text{pore } m: \quad g_v^\infty P_v^\infty + g_{v,km}P_v^*(T_k) = (g_{v,km} + g_v^\infty)P_{v,m}, \quad (5-31)$$

$$\text{pore } n: \quad g_v^\infty P_v^\infty = -g_{v,ln}P_{v,l} + (g_{v,ln} + g_v^\infty)P_{v,n}, \quad (5-32)$$

with

$$g_{v,km} = g_{v,ln} = g_v^\infty = \frac{\tilde{M}_v D(T_{BL}) A_{BL}}{\tilde{R} T_{BL} L_{BL}}, \quad (5-33)$$

inside the BL, and at the top of the BL.

If these equations are transferred into the matrix notation,

$$\mathbf{A} P_v = b \quad (5-34)$$

(in the order  $g, h, i, j, k, l, m, n$ ) it follows:

$$\mathbf{A} = \begin{bmatrix} g_{v,gi} & 0 & -g_{v,gi} & 0 & 0 & 0 & 0 & 0 \\ 0 & g_{v,hj} & -g_{v,hj} & 0 & 0 & 0 & 0 & 0 \\ -g_{v,gi} & 0 & g_{v,gi} + g_{v,ij} + g_{v,ik} & -g_{v,ij} & -g_{v,ik} & 0 & 0 & 0 \\ 0 & -g_{v,hj} & -g_{v,ij} & g_{v,hj} + g_{v,ij} + g_{v,jl} & 0 & -g_{v,jl} & 0 & 0 \\ 0 & 0 & -g_{v,ik} & 0 & g_{v,ik} + g_{v,km} & 0 & -g_{v,km} & 0 \\ 0 & 0 & 0 & -g_{v,jl} & 0 & g_{v,jl} + g_{v,ln} & 0 & -g_{v,ln} \\ 0 & 0 & 0 & 0 & -g_{v,km} & 0 & g_{v,km} + g_v^\infty & 0 \\ 0 & 0 & 0 & 0 & 0 & -g_{v,ln} & 0 & g_{v,ln} + g_v^\infty \end{bmatrix}, \quad (5-35)$$

the matrix of coefficients,

$$P_v = \begin{bmatrix} P_{v,g} \\ P_{v,h} \\ P_{v,i} \\ P_{v,j} \\ P_{v,k} \\ P_{v,l} \\ P_{v,m} \\ P_{v,n} \end{bmatrix} = \begin{bmatrix} P_v^*(T_g) \\ P_v^*(T_h) \\ P_v^*(T_i) \\ P_v^*(T_j) \\ P_v^*(T_k) \\ P_{v,l} \\ P_{v,m} \\ P_{v,n} \end{bmatrix}, \quad (5-36)$$

and

$$b = \begin{bmatrix} 0 \\ 0 \\ \dot{M}_{evap,i} \\ \dot{M}_{cond,j} \\ \dot{M}_{evap,k} \\ g_{v,jl} P_v^*(T_j) \\ g_v^\infty P_v^\infty + g_{v,km} P_v^*(T_k) \\ g_v^\infty P_v^\infty \end{bmatrix}, \quad (5-37)$$

the vector of the known boundary conditions.

Note that in the matrix notation in Eq. 5-35  $\mathbf{A}$  represents the full matrix of all vapor conductances of the complete PN. As a consequence matrix  $\mathbf{A}$  is a symmetrical square matrix with  $\mathbf{A}^T = \mathbf{A}$ . In vector  $P_v$  the known vapor pressures of pores located at the gas liquid

interface with  $P_v = P_v^*(T)$  are stored. The unknowns are highlighted in red. Equations 5-35 to 5-37 can be simplified to

$$\begin{bmatrix} g_{v,jl} + g_{v,ln} & 0 & -g_{v,ln} \\ 0 & g_{v,km} + g_v^\infty & 0 \\ -g_{v,ln} & 0 & g_{v,ln} + g_v^\infty \end{bmatrix} \begin{bmatrix} P_{v,l} \\ P_{v,m} \\ P_{v,n} \end{bmatrix} = \begin{bmatrix} g_{v,jl} P_v^*(T_j) \\ g_v^\infty P_v^\infty + g_{v,km} P_v^*(T_k) \\ g_v^\infty P_v^\infty \end{bmatrix}, \quad (5-38)$$

because this basically contains the three unknown vapor pressures of the vapor pressure field in Fig. 5-9 whereas the other pores are at known vapor pressures.

More generally, it is:

$$\mathbf{A} = \begin{bmatrix} \vdots & \vdots \\ \cdots & \sum g_{ij} & \cdots & -g_{ik} & \cdots \\ \vdots & \vdots & \vdots & \vdots & \vdots \\ \cdots & -g_{ik} & \cdots & \sum g_{ki} & \cdots \\ \vdots & \vdots & \vdots & \vdots & \vdots \end{bmatrix} \quad (5-39)$$

and

$$b = \sum g_{v,ij} P_{v,i}, \quad (5-40)$$

in case of linear vapor diffusion with  $g_{v,ij}$  from Eq. 5-25 (e.g. applied in the PNM with continuous liquid films in Appendix B.4); in the situation with non-linear vapor diffusion (usually above  $T = 40^\circ\text{C}$ ) Eq. 5-40 reads

$$b = \sum g_{v,ij} \ln \left( 1 - \frac{P_{v,i}}{P} \right). \quad (5-41)$$

### 5.3.2 Evaporation and condensation rates of pores and throats

The evaporation and condensation rates of single pores and throats are based on the vapor flow rates between pores at the gas-liquid interface and the adjacent empty pores (Eq. 5-21 and Fig. 5-9). In general (isothermal drying), the sum of vapor flow rates leaving a pore or flowing into the pore is equal to the rate of evaporation if the sum is overall positive and equal to the rate of condensation, if the sum is overall negative, or

$$\sum \dot{M}_v \pm \dot{M}_{evap/cond} = 0. \quad (5-42)$$

Per definition, the vapor flow rate  $\dot{M}_v$  through any throat  $ij$  is computed from the pressure difference between neighbor pore 1 and neighbor pore 2 of that throat (Fig. 5-10a):

$$\dot{M}_{v,ij} = g_{v,ij} (P_{v,i} - P_{v,j}). \quad (5-43)$$

(linear diffusion approach) or

$$\dot{M}_{v,ij} = P g_{v,ij} \ln \left( \frac{P - P_{v,j}}{P - P_{v,i}} \right) \quad (5-44)$$

(non-linear diffusion approach). In the example liquid configuration in Fig. 5-9 neighbor pore 1 of throat  $ij$  is represented by pore  $i$  and neighbor pore 2 of this throat is represented by pore  $j$  (Fig. 5-10a).

It is noted that in isothermal conditions with  $T = const.$  diffusion is always assumed from the phase boundary towards the gas bulk phase. Per definition, the vapor flow rates are always positive in the isothermal PNM (Metzger et al. 2007b). However, in a situation of (even slight) temperature variations the direction of vapor flow can be reversed if local (saturation) vapor pressure gradients occur. This is indicated in Fig. 5-9 by the direction of the arrows representing the direction of vapor flow rates and this is also reflected by the mass balances of individual pores in Eqs. 5-27 to 5-32. The temperature dependence of the direction of vapor flow is taken into account in the non-isothermal PNM as described in the following. Staying with the example of Fig. 5-9, a positive vapor flow rate through throat  $ij$  follows from Eq. 5-43 because the pressure gradient

$$\Delta P_{v,ij} = P_{v,i} - P_{v,j}, \quad (5-45)$$

with  $P_{v,i} = P_v^*(T_i)$  and  $P_{v,j} = P_v^*(T_j)$ , is positive because  $T_i > T_j$ . This leads to the evaporation of liquid from the neighborhood of pore  $i$  with

$$\dot{M}_{evap,i} = g_{v,ij}(P_{v,i} - P_{v,j}), \quad (5-46)$$

according to Eqs. 5-42 and 5-43. However, in the mass balance of pore  $j$ , the same vapor stream must be accounted with a negative sign because of the direction of the vapor flow towards the gas-liquid interface (Eq. 5-22). This is realized by the introduction of the pre-factor  $o$ , which allows to reconcile the computation of the vapor flow rates from Eqs. 5-27 to 5-32 and the mass balances of the pores. The sign of the pre-factor depends on the definition of the neighbor relations of pores in the PN. This is given in Fig. 5-10b. Consequently,

$$o = [1 \ 1 \ -1 \ -1] \quad (5-47)$$

for  $ij = 1-4$ . From this follows for the mass balance of pore  $j$  in Fig. 5-9:

$$\dot{M}_{cond,j} = 1 \cdot \dot{M}_{v,jl} + 1 \cdot 0 - 1 \cdot \dot{M}_{v,ij} - 1 \cdot 0, \quad (5-48)$$

which is in agreement with Eq. 5-22. If, however, the temperature gradient between pores  $i$  and  $j$  would be reversed, the mass balances would read:

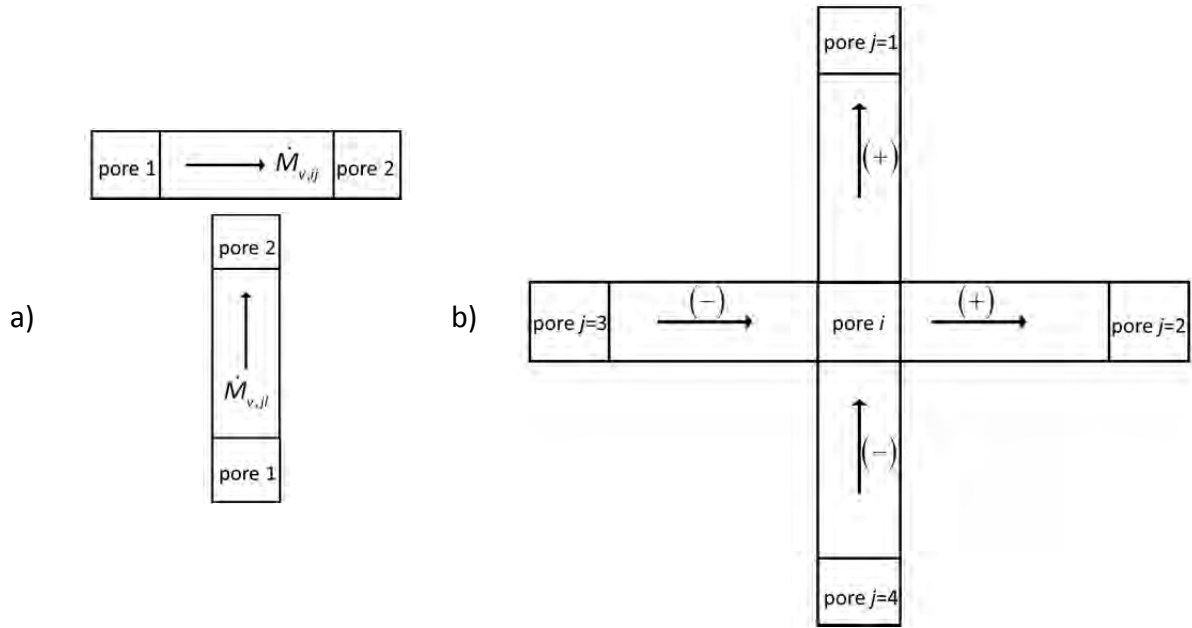
$$\text{pore } i: \quad \dot{M}_{cond,i} = 1 \cdot \dot{M}_{v,ij} = g_{v,ij}(P_{v,i} - P_{v,j}) < 0, \quad (5-49)$$

and

$$\begin{aligned} \text{pore } j: \quad \dot{M}_{evap,j} &= 1 \cdot \dot{M}_{v,jl} - 1 \cdot \dot{M}_{v,ij} \\ &= g_{v,jl}(P_{v,j} - P_{v,l}) - g_{v,ij}(P_{v,i} - P_{v,j}) > 0 \end{aligned} \quad (5-50)$$

with  $P_{v,i} = P_v^*(T_i) < P_{v,j} = P_v^*(T_j)$  and  $P_{v,j} > P_{v,l}$ .

This shows that implementation of the pre-factor  $o$  allows to compute direction dependent vapor flow rates in presence of temperature gradients, where the temperature depending saturation vapor pressures naturally vary along the phase boundary.



**Figure 5-10** Vapor diffusion through horizontal and vertical throats. a) Definition of neighbor pore 1 and 2 of throats  $ij$  and  $jl$  from Fig. 5-9. b) Impact of the definition of neighbor pore 1 and 2 on the mass balance of any pore  $i$  with neighbor pores  $j = 1,2,3,4$  (north, east, west and south of pore  $i$ ). The correction of the mass balance is achieved by multiplication of the vapor flow rates with pre-factor  $\phi$ .

In summary, evaporation and condensation rates of meniscus pores are computed from the sum of vapor diffusion flow rates through the adjacent dry neighbor throats (at least one) multiplied with  $\phi$ :

$$\dot{M}_{evap/cond,i} = \sum_{ij} \phi \dot{M}_{v,ij} \quad (5-51)$$

The evaporation rates of throat menisci  $ij$ , with empty neighbor pores  $i = 1,2$ , are computed accordingly:

$$\dot{M}_{evap/cond,ij} = \sum_{i=1}^2 \left( \frac{A_{ij}}{\sum_{ij} A_{ij}} \sum_{ij} \phi \dot{M}_{v,ij} \right), \quad (5-52)$$

Notice that the liquid menisci must be connected to at least one empty pore which has again at least one empty neighbor throat (e.g. throats  $gi$  and  $ik$  in Fig. 5-9). The term  $A_{ij} / \sum_{ij} A_{ij}$  distributes the evaporation rates of throat menisci with identical pore neighbors. Exemplarily,

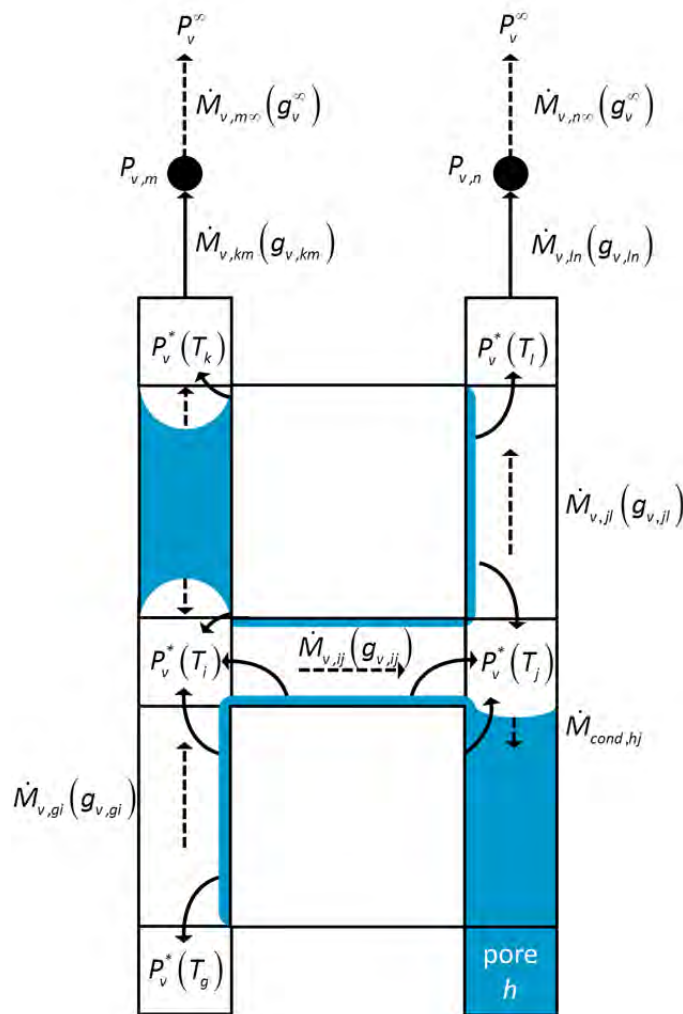
$$\dot{M}_{evap,ik} = \frac{A_{ik}}{A_{ik} + A_{gi}} \dot{M}_{v,ij} + \frac{A_{ik}}{A_{ik}} \dot{M}_{v,km} \quad (5-53)$$

(Fig. 5-9).

In the PNM with liquid ring elements, the equations are adapted accordingly. As will be shown in what follows, only slight modifications are necessary.

Figure 5-11 shows a similar liquid configuration as in Fig. 5-9 but in presence of liquid rings. The main deviation from Fig. 5-9 is the assumption of saturation vapor pressure in empty pores that are connected to liquid rings. As a consequence, all network pores are at  $P_v = P_v^*(T)$  in Fig. 5-11. Additionally, single liquid pore volumes are not stipulated here. Instead the pore volumes are emptied together with the largest neighbor throat (i.e. in the same time step). Independent of this, the vapor pressure field as well as the mass balances of the pores are computed identically to the above described method. The modification of the PNM concerns the distribution of evaporation rates, i.e. Eq. 5-52. Precisely, in the PNM with liquid rings the evaporation rates are distributed among the meniscus throats and the ring neighbors connected to an empty pore:

$$\dot{M}_{evap/cond,ij} = \sum_{i=1}^2 \left( \frac{A_{ij}}{\sum_{ij} A_{ij} + \sum_r \alpha A_r} \sum_{ij} \alpha \dot{M}_{v,ij} \right), \quad (5-54)$$



**Figure 5-11** Illustration of evaporating liquid rings. The arrows indicate that the evaporation rate following from the mass balances of the pores is distributed among the throats and the rings if the rings are partly developed, i.e. if they are connected to at least one empty pore.

for throat menisci, and

$$\dot{M}_{evap/cond,r} = \sum_{i=1}^4 \left( \frac{\alpha A_r}{\sum_{ij} A_{ij} + \sum_r \alpha A_r} \sum_{ij} o \dot{M}_{v,ij} \right) \quad (5-55)$$

for partly and fully developed liquid rings. The parameter  $\alpha$  in Eqs. 5-54 and 5-55 is introduced with the purpose to adjust the ratio of the ring interface area among which the evaporation rate is distributed (Vorhauer et al. 2015). If  $\alpha$  increases, the ratio  $A_{ij} / \sum_{ij} A_{ij} + \sum_r \alpha A_r$  decreases and more liquid is evaporated from the ring interface area while reducing the contribution of the meniscus throats. If  $\alpha = 1$ , 25 % of the ring interface area is activated and available for evaporation into one of the empty neighbor pores. In most simulations  $\alpha = 2$ , which means that half of the ring area is accessible for each empty pore. As will be discussed in Chapter 6, the variation of  $\alpha$  has almost no impact on the drying behavior. Instead very similar simulation results are obtained for different values of  $\alpha$ .

### 5.3.3 Evaporation and condensation rates of liquid clusters

The overall evaporation and condensation rates from pores and throats interconnected in liquid clusters are computed from the sum of evaporation and condensation rates at the interface of all cluster menisci:

$$\dot{M}_{evap/cond,cl} = \sum \dot{M}_{evap/cond,t} + \sum \dot{M}_{evap/cond,p} \quad (5-56)$$

in the drying algorithm taking into account the existence of single pores, and

$$\dot{M}_{evap/cond,cl} = \sum \dot{M}_{evap/cond,t} + \sum \dot{M}_{evap/cond,r} \quad (5-57)$$

in the drying algorithm incorporating wetting phenomena by liquid rings. In an isothermal PN drying simulation, the cluster evaporation rates are always positive. However, direction of diffusion flow is dictated by the vapor pressure gradient between two adjacent pores as already explained in detail above. If temperature variations (even only slightly) occur in the PN, diffusion flow can be directed towards the cluster boundary. This leads to a reduction of the overall cluster evaporation rate in Eqs. 5-56 and 5-57 or reversion of the invasion process. As will be discussed in Section 5.4.2, cluster growth occurs in presence of high temperature variations with overall negative cluster evaporation rates.

### 5.3.4 Overall evaporation rate from the pore network surface

The overall evaporation rate from the PN surface is computed from the sum of vapor flow rates from the top row of the BL connected to the gas bulk phase (computational nodes  $n$  and  $m$  in Fig. 5-9):

$$\dot{M}_{evap} = g_v^\infty \sum (P_{v,p} - P_v^\infty) \quad (5-58)$$

(linear diffusion approach), and

$$\dot{M}_{evap} = P g_v^{\infty} \sum \ln \left( \frac{P - P_v^{\infty}}{P - P_{v,p}} \right) \quad (5-59)$$

(non-linear vapor diffusion) with  $g_v^{\infty}$  from Eq. 5-33.

## 5.4 Quasi-steady invasion of the pore network

### 5.4.1 Invasion by the gas phase (evaporation)

The invasion of the PN is assumed as a quasi-steady invasion. The model is thus based on the assumption of constant liquid pressure in liquid clusters in equilibrium with the surrounding vapor phase i.e. with identical curvature of interface menisci. This is a basic model assumption following the concept of percolation with the result of discrete invasion of the single liquid elements in the order of increasing invasion pressure thresholds.

In contrast to the benchmark PNM, where only liquid throats were assigned to the capillary PN, the new model contains different liquid elements which are distinguished in terms of capillary pressures: i) the throats and pores as part of the primary PN structure with similar capillary invasion pressure thresholds and ii) rings and the edge effect as part of the secondary capillary PN with significantly higher capillary pressures than pores and throats (Fig. 5-12). The differences are explained with the different width of the network elements. As a consequence, a modified order of emptying of the PN can be computed compared to a PNM ignoring the additional liquid elements. This is explained in what follows.

The capillary pressure curves of pores and throats in Fig. 5-12 are computed based on Eq. 2-25 taking into account the non-cylindrical geometry. The capillary invasion pressure threshold of throats is:

$$P_{c,t}^* = \sigma \left( \frac{2r_t + L_d}{r_t L_d} \right) \quad (5-60)$$

and for pores with liquid menisci it reads:

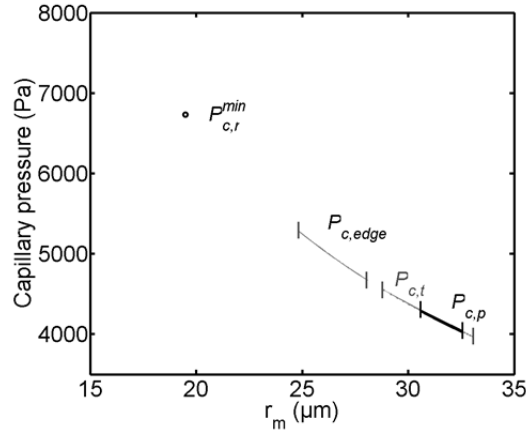
$$P_{c,p}^* = \sigma \left( \frac{2r_p + L_d}{r_p L_d} \right) \quad (5-61)$$

Due to the similar width and height of pores and throats, the capillary pressure curves overlap from which it is concluded that the primary PN elements compete in the order of invasion.

In contrast, liquid rings and the PN edges can produce higher capillary pressures (Fig. 5-12). The point denoted by  $P_{c,r}^{min}$  and the curve denoted by  $P_{c,edge}$  basically depend on the geometry of the secondary capillary elements. This is explained in detail in the following.

The minimum capillary pressure associated with liquid rings in Fig. 5-12 is computed from Eq. 2-22 assuming a maximum film height of  $h^{max}(w_r) = L_d/2$  according to Fig. 4-8a and related discussions:





**Figure 5-12** Capillary pressure curves of primary liquid elements and the edge effect computed for non-cylindrical cross sections based on Eq. 2-25 (for  $T = 63^\circ\text{C} = \text{const.}$  and  $\cos\theta = 1$ ). The minimum capillary pressure of rings,  $P_{c,r}^{\text{min}}$  is computed for the assumed maximum height of films,  $r_{m,r} = 2r_r = h^{\text{max}}(w_r) = L_d/2 = 19.5 \mu\text{m}$  (Eq. 2-22) and the pressure curve  $P_{c,\text{edge}}$  is computed for  $f^{\text{red}} = 0.85$ . Note that the illustrated relationships are shifted towards greater values of  $P_c$  for lower (constant) temperatures. The situation changes in PNs with temperature variation when overlapping can occur if the pressure difference induced by temperature is high enough.

$$P_{c,r} = \frac{4\sigma(T)}{L_d}. \quad (5-62)$$

If it is assumed that the maximum expansion of liquid rings is usually smaller than  $h^{\text{max}}$  (Fig. 4-8a), the capillary pressure threshold for ring invasion is naturally

$$P_{c,r}^* = \frac{2\sigma(T)}{r_{m,r}} \geq \frac{4\sigma(T)}{L_d}. \quad (5-63)$$

As discussed in Section 4.2.2.1, the width of the rings can vary depending on the local liquid pressure differences. This is also discussed in Vorhauer et al. (2015). Based on the assumption of liquid pressure continuity in a cluster formed by liquid filled pores, throats and rings, the radius of meniscus curvature of the liquid rings belonging to this cluster varies with the liquid pressure of this cluster:

$$P_j = P - \sigma(T) \left( \frac{1}{r} + \frac{2}{L_d} \right) = \text{const.} \quad (5-64)$$

In this  $r$  denotes the interface curvature of liquid menisci. This leads to the variation of the ring curvature (and also of the ring width  $w_r$  and ring volume  $V_r$ ) as already shown in Fig. 4-8a:

$$r_{m,r} = \frac{2\sigma(T)}{P - P_j} \leq \frac{L_d}{2} \quad (5-65)$$

(Vorhauer et al. 2015).

From Eq. 5-65 can be concluded that liquid rings do not affect the order of emptying of primary liquid elements as they do not compete with the invasion of these elements

because  $r_{m,r}^{max} = L_d/2 < r_{r,m}^{min}$ . Obviously, it is not necessary to compute the capillary pressure of liquid rings in the PNM. Instead the throat corners are assumed to remain liquid saturated during drying until detachment from the primary liquid elements. It is furthermore assumed that width of the liquid rings in the moment of disconnection from the bulk liquid phase is constant and independent of the liquid pressure in the cluster from which the rings are disconnected. The rings empty at the local evaporation rate once they are disconnected from the bulk liquid phase, i.e. fully developed. This leads to a higher liquid connectivity inside the PN.

A similar effect as referred to the liquid rings is associated with the lateral pinning of the drying front at the PN's lateral edges. As given in Fig. 5-12 the invasion pressure threshold of the virtually shrunken PN elements is overall higher than that of the primary PN. Thus, in the competition of invasion, the edges with virtually reduced pore/throat width remain liquid saturated until disconnection from the bulk liquid phase. This is obtained by reducing the mean meniscus radius of primary pores and throats (Eq. 5-17) by factor  $f^{red} = 0.85$ . Consequently,

$$P_{c,edge}^* = \frac{2\sigma}{f^{red} r_m} \quad (5-66)$$

with mean meniscus radius  $r_m$  computed from Eq. 2-24. As can be seen in Fig. 5-12 this increases the invasion pressure threshold of the virtually reduced lateral pores and throats by around 2.5 % compared to the maximum capillary pressure associated with throats. Competition of the edge elements and liquid rings is avoided if  $f^{red} = 0.85$  and thus if  $r_{m,edge}^{min}$  is still greater than  $r_r^{max} = L_d/2 = 19.5 \mu\text{m}$ . Precisely, if  $0.69 \leq f^{red} \leq 0.87$  the capillary pressure curve of the edge elements is not overlapping with the other curves or with  $P_{c,r}^{min}$ . These limits result from

$$f^{red,min} \geq \frac{r_r^{max}}{r_m^{min}} \quad (5-67)$$

and

$$f^{red,max} \leq \frac{r_m^{min}}{r_m^{max}} \quad (5-68)$$

with mean meniscus radius  $r_m$  computed from Eq. 2-24. A more sustained extension of liquid pinning would be expected if the capillary pressure curve of the edge effect would overlap with the capillary pressure curve of the rings.

In summary, the following order of emptying is expected in a PN taking the additional liquid elements into account:

1. throats and pores in the primary PN,
2. horizontal and vertical throats and pores along the PN side walls,
3. liquid rings.

It is highlighted that the temperature dependent surface tension computed from Eq. 2-53 affects the order of invasion if the temperature variation is high enough (e.g. Fig. 2-24b). In

more details, in PN drying simulations ignoring the thermally affected vapor transport, the order of invasion is dictated by the pore size distribution *and* the temperature distribution (also refer to Fig. 4-12). Thus, in case of thermal gradients, overlapping of the curves can occur if the pressure difference induced by temperature is high enough.

#### 5.4.2 Invasion by the liquid phase (condensation)

In the simulation of non-isothermal drying in presence of condensation and refilling of already empty pores and throats, the invasion by the liquid phase not only depends on the macroscopic pore and throat size distribution and temperature, but contrarily also the pore scale neighbor relations play a major role (Chapuis et al. 2007). Precisely, the invasion capillary pressure threshold of accessible empty pores adjacent to a liquid cluster with negative (condensation) rate is computed according to Mani and Mohanty (1999) assuming piston type displacement of the liquid phase in agreement with experimental observations:

$$P_{c,p}^* = \sigma(T) \left( \frac{1}{r_p^{eff}} + \frac{2}{L_d} \right), \quad (5-69)$$

with

$$r_p^{eff} = \frac{r_p}{1 + 0.25(N^{S=0} - 1)} \quad (5-70)$$

and  $N^{S=0}$  number of empty neighbor throats. Liquid invasion of throats, however, is computed from Eq. 5-60. The empty element with the greatest invasion potential (= highest capillary pressure) is selected for the invasion with liquid. According to Mani and Mohanty (1999) all throats adjacent to a liquid filled pore must be subsequently invaded. This implies that only one saturated pore can exist along the cluster boundary.

It is noted that in more complex situations (e.g. in the presence of snap-off) other rules than in Eq. 5-69 could apply (refer e.g. to the appendix in Chapuis et al. 2007 and Wu et al. 2016).

#### 5.4.3 Cluster dynamics

Progressive invasion of the gas phase naturally results in split up of the liquid phase and the formation of isolated single clusters (e.g Fig. 5-15 below) limiting the distance of liquid communication (Wilkinson and Willemsen 1983). This is in contrast to the assumption of a global percolation by e.g. Segura (2007), where it is assumed that liquid communication is not interrupted by the formation of single clusters (comparably to a continuum liquid phase). Contrary to drainage, the liquid clusters can be completely evaporated in a drying process. Additionally, simultaneous growing of the clusters is observed in situations where imposed temperature gradients lead to the condensation of vapor. It is thus essential to track invasion of the various clusters, due to evaporation and condensation, separately.

The vapor-air mixture (i.e. the non-wetting phase) though forms always a continuum in the drying PN and thus facilitates simultaneous drying of disconnected clusters throughout the network (at least in presence of a vapor pressure gradient). It must be noted that the situation might be different in case of condensation where refilling of the dry void space can lead to trapped gas pores or throats. The trapping of gas pores and throats, however, is disregarded throughout the thesis.

### 5.4.3.1 Progressive invasion of evaporating liquid clusters

The evaporation rate of clusters is computed from the sum of the evaporation rates of all pores and throats containing a liquid meniscus at the cluster boundary (Eq. 5-56). This leads to the shrinking of clusters with a rate that matches the overall evaporation rate of respective clusters. Precisely, in the drying model of quasi-steady invasion only one meniscus pore or throat located at the cluster boundary can be invaded at once. All other pores and throats remain stationary. For this purpose, all meniscus pores and throats along the cluster boundary are identified and the throat or pore with the lowest entry pressure threshold is invaded. The one pore or throat invaded during a time step is assigned as the local candidate. The time required to remove liquid from a cluster in order to allow for the full invasion of the local candidate at each cluster boundary is computed from:

$$\Delta t = \frac{S_p \rho_l (T_p) V_p}{\dot{M}_{evap,cl}}, \quad (5-71)$$

if the local candidate is a cluster pore, and

$$\Delta t = \frac{S_t \rho_l (T_t) V_t}{\dot{M}_{evap,cl}}, \quad (5-72)$$

if the local candidate is a cluster throat. Note that the invasion process is assumed as a percolation process as shown in Fig. 2-16. From all liquid clusters that are competitively invaded, the local candidate from the cluster with the minimum time associated with the invasion event is identified as the global candidate. The global candidate determines the length of the regarded invasion interval. All variables are updated after the invasion of the global candidate. In detail, this refers to the saturation of the local candidates (i.e. losing the competitive invasion), the cluster labeling, the vapor pressure field and the vapor flow rates and evaporation rates as well as the liquid pressures. Additionally, the new meniscus pores and throats emerging from the full invasion of the global candidate are identified.

It is remarked that in contrast to the basic assumptions of the percolation model, partially saturated liquid elements must evolve from the cluster mass balances as a consequence of the simultaneous invasion of several liquid clusters with different evaporation rates (e.g. because of different distances of the clusters from the PN open side or because of different cluster temperatures) and liquid volumes. It is

$$S_{p,t}^{t+1} = S_{p,t}^t - \Delta t \frac{\dot{M}_{evap,cl}}{\rho_l (T_{p,t}) V_{p,t}} \quad (5-73)$$

the transient saturation of the local candidates at all cluster boundaries. An analog formulation of Eq. 5-73 is also applied for single liquid elements disconnected from liquid clusters.

In the algorithm with formation of liquid rings, single pores are neglected, consequently  $\dot{M}_{evap,cl}$  is computed from Eq. 5-57. Furthermore, by definition, partially developed rings cannot be invaded, instead

$$\Delta t = \frac{S_r \rho_l (\bar{T}_r) V_r}{\dot{M}_{evap,r}} \quad (5-74)$$

is computed for the fully developed liquid rings. Analog to Eq. 5-73 the transient ring saturation follows from:

$$S_r^{t^{i+1}} = S_r^{t^i} - \Delta t \frac{\dot{M}_{evap,r}}{\rho_l(\bar{T}_r)V_r}. \quad (5-75)$$

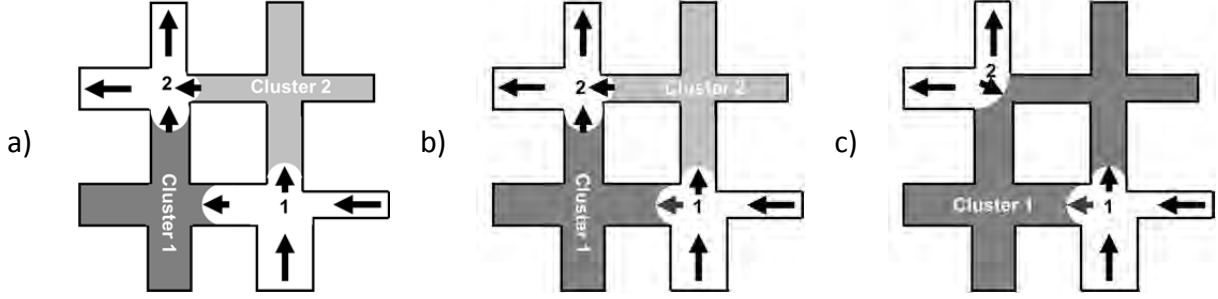
### 5.4.3.2 Cluster growth mechanism and cooperative invasion

As already explained above, cluster growth is based on vapor condensation with piston type invasion of the liquid phase (snap-off is neglected). Basically, three different levels of the invasion process are distinguished (Fig. 5-13): 1) reduction of the overall evaporation rate (Fig. 5-13a), 2) re-saturation of partially saturated elements (with transient saturation from Eq. 5-73) at the cluster boundary (Fig. 5-13b) and 3) re-invasion of empty pore and throat neighbors connected to the cluster boundary (also referred to the cluster growth) (Fig. 5-13c). The three levels of the invasion process are taken into account by different versions of the PNM as already explained before. Namely, the reduction of the overall evaporation rate is simulated with PNM level 2, the re-saturation of partially saturated elements is simulated with PNM level 3 and the cluster growth is taken into account with PNM level 4. The latter situation especially occurs in drying with positive temperature gradients, where vapor diffuses towards lower temperatures. As discussed before, the three versions of the PNM are applied in different situations depending on the height of the condensation rate. The reduction of the cluster evaporation rate in PNM level 2 as well as the re-saturation of the partially saturated cluster boundary in PNM level 3 are based on Eq. 5-56. (Note that liquid rings are disregarded in the model with cluster growth). If, however, the cluster boundary is liquid saturated and thus no partially saturated element is available, the cluster growth mechanism is activated in PNM level 4. Then the dry void space surrounding the liquid cluster (or the saturated single elements) is invaded with liquid. In this situation, the invasion capillary pressure threshold of accessible adjacent empty pores and throats is at first computed from Eqs. 5-60 and 5-69. The pore or throat with the highest entry pressure threshold (= highest capillary pressure) is selected for liquid invasion. This is pore 2 in Fig. 5-13c. It is highlighted that pores and throats can simultaneously be invaded from different clusters. This occurs if the empty candidate can be associated with the maximum entry pressure threshold at the boundary of several clusters. This situation is incorporated by computation of the overall condensation rate of the connected clusters, e.g. in the example in Fig. 5-13c:

$$\dot{M}_{cond,2} = \sum_{cl1-2} \dot{M}_{cond,cl} = \dot{M}_{cond,cl\ 1} + \dot{M}_{cond,cl\ 2}, \quad (5-76)$$

with  $\dot{M}_{cond,cl}$  from Eq. 5-56. However, simultaneous condensation *and* evaporation can be excluded in the drying algorithm by manipulation of the cluster labeling as will be explained below. The time required to condense enough liquid to completely re-saturate the respective local candidate follows from:

$$\Delta t = \frac{(1 - S_{p,t})\rho_l(T_{p,t})V_{p,t}}{\sum |\dot{M}_{cond,cl}|}. \quad (5-77)$$



**Figure 5-13** a) Reduction of the overall cluster evaporation rates of clusters 1 and 2, if the vapor diffusion rates into pore 1 are lower than the vapor streams leaving pore 2 (e.g. applied in Vorhauer et al. 2013). The temporary existence of a partially saturated throat at the cluster boundary of cluster 1 is a result of the different evaporation rates of both clusters and the definition of a global candidate (referred to cluster 2 in this example). b) Refilling of the intermediate partially saturated throat of cluster 1, while for cluster 2 the net evaporation rate is still greater than the net condensation rate. c) Invasion of the boundary pore of cluster 1 with the highest capillary pressure threshold. This is pore 2 in this configuration. Accordingly, clusters 1 and 2 merge.

The transient saturation of the local candidates is then updated by

$$S_{p,t}^{t^{i+1}} = S_{p,t}^{t^i} + \Delta t \frac{\sum |\dot{M}_{cond,cl}|}{\rho_l(T_{p,t})V_{p,t}}. \quad (5-78)$$

The total amount of condensed liquid volume (in refilling pores and throats) is computed from:

$$V_{cond} = \sum \left( \frac{|\dot{M}_{cond,cl}| \Delta t}{\rho_l} + \frac{|\dot{M}_{cond,p,t}| \Delta t}{\rho_l} \right), \quad (5-79)$$

taking into account condensing clusters with  $\dot{M}_{cond,cl}$  and condensing single pores and throats with  $\dot{M}_{cond,p,t}$ .

Furthermore, the overall condensation effect obtained from a drying simulation with PNM level 4 is defined by the ratio:

$$v_c^+ = \frac{V_{cond}}{\sum V_t + \sum V_p}, \quad (5-80)$$

with  $V_{cond}$  from Eq. 5-79, while the neglected condensed liquid volume (in non-refilling pores and throats from PNM level 2 and 3) is computed from:

$$v_c^- = \frac{\sum |\dot{M}_{cond,cl}| \Delta t + |\dot{M}_{cond,p,t}| \Delta t}{\bar{\rho}_l (\sum V_t + \sum V_p)} \quad (5-81)$$

with mean density  $\bar{\rho}_l$  in the given temperature range.

#### 5.4.4 Cluster labeling

The progressive invasion and growth of liquid clusters requires distinct computation of the individual cluster mass balances on the one hand and the identification of liquid cluster boundaries on the other hand. In the following, tracking of the liquid cluster boundaries, i.e. cluster labeling, shall be discussed in face of different model options: i) drying in presence of single pores, ii) drying in presence of liquid rings and iii) non-isothermal drying with cluster growth.

Cluster labeling is principally based on the Hoshen-Kopelman-algorithm used by Irawan (2006), Metzger et al. (2003) and Al-Futaisi and Patzek (2003). The main purpose of the cluster labeling is to identify different liquid clusters with their corresponding pores, throats and rings by different labels (greater than 0). In the algorithm ignoring liquid rings, cluster labeling is based on the saturation state of the pores (or the throats) while in the drying algorithm with liquid rings the labeling is based on the saturation state of the rings. Further options are involved in the latter case. These concern the implementation of different connectivity of the liquid phase according to Vorhauer et al. (2015) by manipulation of cluster connectivity with Ring Labeling Option 1 (RLO1) and Ring Labeling Option 2 (RLO2). For the same reason, different cluster labeling options (CLOs) are also developed in the frame of the cluster growth mechanism. These are denoted by CLO1, CLO2 and CLO3.

##### 5.4.4.1 Cluster labeling based on pore liquid saturation

As in Irawan (2006) the drying simulations usually start from a fully saturated network, where the liquid phase forms a continuum that completely covers the PN. In this situation all pores and throats are assigned with identical cluster label (label 1). After emptying of the first pore or any later, the network is scanned for new liquid clusters, starting from the neighbors of the just emptied pore (analog to the procedure precisely described in Irawan (2006) and Metzger et al. (2007b)). In order to save computational effort, scanning is limited to the liquid pores originating from the same cluster as the pore that has been invaded. Thus if pore  $i$  is invaded, all neighbor pores  $j$  are analyzed. These pores are named the *Children*. If their saturation is  $S_j \geq 0$  and if furthermore the throats connecting pore  $i$  with any of its liquid filled pore neighbors  $j$  have saturation  $S_{ij} \geq 0$ , these pores are assigned to different clusters, initiated by emptying of pore  $i$ . Then, all neighbor pores of pores  $j$ , i.e. the *Childrens' Children* are scanned consecutively. If their saturation is also  $S_j \geq 0$  and if the throats connecting the *Children* with their *Children* have  $S_{ij} \geq 0$ , these pores are assigned to the same cluster as their *Mother*. 'Cluster merging' numerically occurs if two or more *Childrens' Children* are assigned with the same cluster label. The scan stops at the cluster boundaries, i.e. where the liquid continuity is interrupted by gas pores with  $S_j = 0$  or gas throats with  $S_{ij} = 0$ . All liquid elements identified to belong to the original cluster are given the same label. Labels of liquid elements forming new clusters as well as the labels of all other clusters are updated accordingly (Irawan 2006).

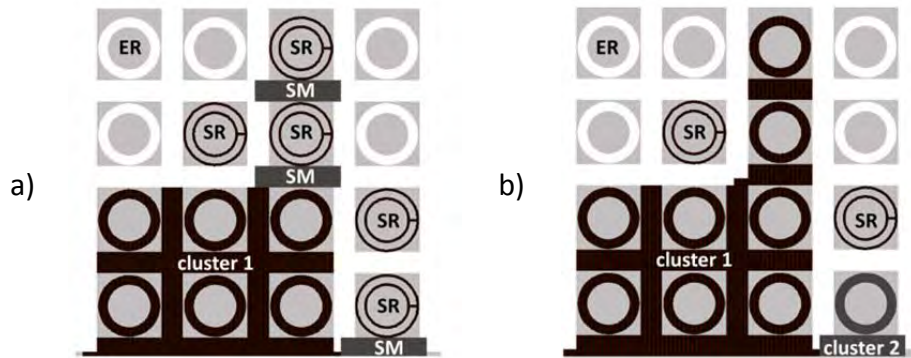
##### 5.4.4.2 Cluster labeling based on liquid rings

In the algorithm incorporating liquid trapping by capillary liquid rings, two situations are discriminated. The discrimination is based on the physical interpretation of liquid rings as capillary connectors. In situation 1 (RLO1), capillary connectivity of the liquid phase by liquid rings is ignored. In this situation, the liquid phase gets disconnected when the ring neighbor

pores dry out; i.e. all adjacent wet throats and liquid rings become disconnected. This means that the labeling algorithm can be based on the saturation state of the pores as described above (Section 5.4.4.1). In this, single liquid menisci and single rings are assigned with label 0 together with the empty elements. This situation is illustrated in Fig. 5-14a.

In situation 2 (RLO2) liquid filled rings are interpreted as capillary connectors, increasing liquid connectivity between else isolated liquid clusters or single menisci and single rings (Fig. 5-14b). In this situation, cluster labeling is based on the state of the ring, i.e. partly or fully developed. Analog to the labeling of pores, a label is assigned to each liquid filled ring integrated in a liquid cluster. Additionally, certain peculiarities are highlighted:

- Single pores are excluded in the algorithm with liquid rings. The pore volume is assigned to the largest neighbor throat that is first invaded.
- Initiation of re-labeling is based on the emptying of a throat.
- No re-labelling is required after a (fully developed) ring has emptied, as it is assumed to be isolated with label 0.



**Figure 5-14** Schematic illustration of the two different cluster labeling options. a) RLO1 based on the saturation of pores. b) RLO2 based on the state of rings, i.e. partly or fully developed. SM: single meniscus, SR: single ring, ER: empty ring. (Images from Vorhauer et al. 2014).

Once a throat has emptied, its former label is identified and the neighborhood of the throat is scanned for any liquid saturated rings with identical label similar as described in the previous section. In the 2-dimensional PN two liquid rings are usually connected to an emptied throat. These rings are named the *Children* (analog to Irawan (2006) and Metzger et al. (2007b)). Then, the neighborhood of the *Children* is scanned for liquid filled rings that are connected by either a liquid filled pore or a liquid filled throat, i.e. the *Childrens' Children*. All liquid elements that are identified to be connected within a cluster are assigned with the same cluster label.

#### 5.4.4.3 Cluster labeling in presence of cluster growth

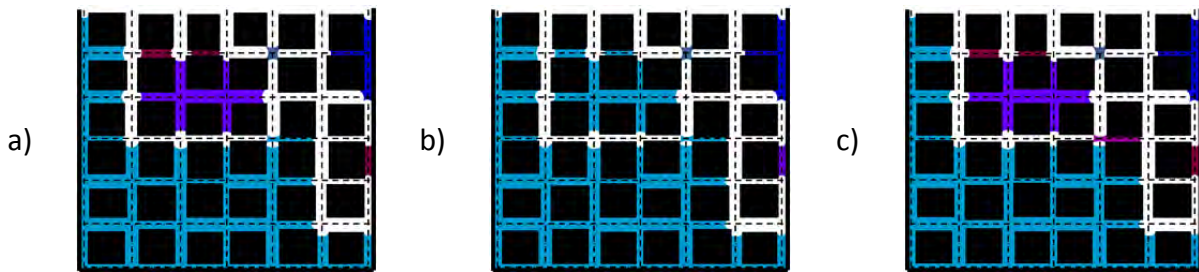
In the non-isothermal PNM liquid rings are disregarded. Cluster labeling is principally based on either the saturation state of the pores (CLO1 and CLO3) or the saturation state of throats (CLO2). In CLO2 increased connectivity of the liquid phase as anticipated with secondary capillary effects is considered by manipulation of the cluster connectivity. Thus, several



options are implemented depending on the drying situation. It is noted that single liquid pores are always treated as a cluster, meaning that all partially or fully saturated liquid pores are always assigned with a cluster label greater than zero in each of the CLOs.

*Cluster labelling based on pore liquid saturation*

In cluster labeling option 1 (CLO1) labeling is as presented in Section 5.4.4.1. In this, all liquid pores are assigned to a cluster if they are connected through a partially saturated or fully saturated throat (Fig. 5-15a). The liquid filled throats interconnected in the same liquid cluster are assigned with identical label. Single liquid pores are also assigned with a cluster number. In Fig. 5-15a, liquid throats and pores belonging to the same cluster are shown in identical color and the clusters are distinguished by different shades of blue. The single throats are shown in brown. Exemplarily, four separated clusters and three single throats co-exist in the PN. The clusters are separated by empty pores.



**Figure 5-15** Graphical presentation of the different cluster labeling options using a partially saturated PN with identical liquid saturation: a) CLO1, b) CLO2 and c) CLO3. Different clusters in different colors. The single menisci are shown in brown.

*Cluster labelling based on throat liquid saturation*

In cluster labeling option 2 (CLO2), increased connectivity, similar to the connectivity expected in presence of liquid rings, is assumed. In this, the cluster labeling is based on the saturation of throats. Single liquid throats are the basic element of a cluster in this option; additionally single liquid pores are interpreted as a cluster. In contrast to CLO1, all neighboring liquid throats are assumed to belong to the same liquid cluster (independent of the saturation of the connecting pore). Possibly existing single pores (only surrounded by empty neighbor throats) are labeled as follows:

$$I_{p,si} = N_{cl} + 1 \tag{5-82}$$

with  $I_{p,si}$  label of the single pore and  $N_{cl}$  number of clusters.

This way, the higher connectivity as found in the presence of liquid rings can be mimicked (Fig. 5-15b). Due to this, the two single throats as well as the smaller cluster in the center of the PN are merged with the large PN covering liquid cluster, although these clusters are separated by empty pores. Consequently, they appear in the same color in Fig. 5-15b. The single throat on the right and the empty pore, each, form separated clusters.

*Cluster labelling based on pore liquid saturation and proscribed pores and throats*

Another option is to track the history of refilled pores and throats and to prohibit cluster merging by partially saturated condensing pores or throats (also named the proscribed pores and throats). In cluster labeling option 3 (CLO3) pore labelling based on CLO1 is adapted so as to allow for two neighboring saturated pores or throats belonging to disconnected clusters (Fig. 5-15c). In this CLO the throats are labeled according to the label of their pore neighbors and the partially saturated condensing pores are labeled as their mother cluster, i.e. as the growing cluster from which they are emerging. Cluster labels of single pores are also computed from Eq. 5-82. With this it can be avoided that invasion of an empty element located at the boundary of a condensing cluster *and* at the boundary of an evaporating cluster leads to the intermittent shrinking and growing of the two clusters if interconnection by the invading element would be anticipated. In other words, this cluster labeling option allows to prevent fluctuation of merging condensing and evaporating clusters as would be expected with CLO1. As will be discussed below, the computational time drastically decreases when applying CLO3 instead.

In Fig. 5-15c, exemplarily the PN spanning large blue cluster and the pink cluster are disconnected although the pore between these clusters is partially saturated. The label of the pore is computed from Eq. 5-82 and the throat from which the pore is emerging is given the same label. Merging appears once the pore becomes fully saturated.

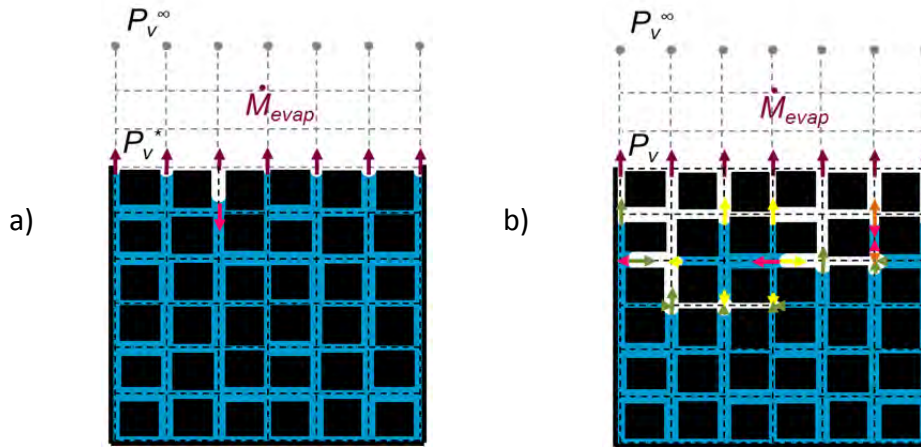
## **5.5 Pore network drying algorithm incorporating capillary liquid rings**

Simulation of drying usually starts from a fully liquid saturated PN (Fig. 5-16a). Emptying of the PN is dictated by the drying rate, imposed by the partial pressure difference between the wet network surface and the surrounding air phase. The liquid phase is initially connected in a main liquid cluster covering the complete PN. Progressive emptying of the PN leads to the split up of the liquid phase and the formation of single clusters (Fig. 5-16b). The order of invasion is computed from the different versions of the Young-Laplace Eq. 2-25 (with surface tension computed from Eq. 2-53). The time required to fully invade local candidates is coupled to the evaporation rate at the cluster boundaries which is again dictated by the vapor diffusion rate from the gas liquid interface to the network surface. In summary, computation can be specified as given below.

Steps 1-18 refer to the initiation of the drying simulation and are only computed once at the start of the drying simulation. Steps 19-36 are repeated until complete desaturation of the PN. The steps highlighted in *italics* are associated only to the simulation taking the trapping of liquid by liquid rings in throat corners into account.

*Initiation of the PN drying simulation*

1. Definition of network size, throat number and pore number.
2. Definition of lattice spacing  $L$ .
3. Definition of the number of layers in the BL and the vertical distance between the layers (i.e. the BL thickness  $s_{BL}$ ).
4. Generation of the PN neighbor relations (as proposed by Irawan 2006) (Table 5-3).
5. Definition of throat radii  $r_t$  and network depth  $L_d$  (adopted from the experiment).



**Figure 5-16** Schematic representation of the PN drying model. a) Evaporation from the initially fully saturated PN leads to the emptying of the largest throat at the gas liquid interface. All other liquid menisci remain stationary with identical interface curvature. b) Progressive invasion of the PN leads to the formation of several liquid clusters (of different size). The arrows mark the evaporating menisci in each cluster (green, yellow and orange) in case of non-isothermal drying. The bright red arrows indicate the (one) invading meniscus of each cluster and the invasion of a single liquid throat. Interconnection of the liquid phase (e.g. by liquid rings or cluster labeling manipulation) is disregarded in this sketch.

6. Computation of the mean meniscus radius  $r_m$  (Eq. 2-24).
7. Definition of ring width  $L_r$ .
8. Definition of the ratio of ring evaporation interface  $\alpha$  and computation of the ring evaporation interface  $A_r$  (Eq. 5-14) and the ring volume  $V_r$  (Eq. 5-11).
9. Computation of throat volumes  $V_t$  (Eq. 5-3 or Eq. 5-13 in the presence of rings) and computation of throat cross sectional areas  $A_t$  (Eq. 5-2).
10. Computation of pore volumes  $V_p$ , cross sectional areas  $A_p$  and pore radii  $r_p$  (Eqs. 5-4 to 5-6).
11. Definition of the air temperature in the BL and of the temperature inside the PN (temperature field uploaded from experimental data).
12. Definition of physical parameters  $P_v^*(T)$ ,  $D(T)$ ,  $\sigma(T)$ ,  $\rho_l(T)$  (see Section 2.4).
13. Computation of the vapor conductances  $g_{v,ij}$  (Eq. 5-25) and  $g_v^\infty$  (Eq. 5-33).
14. Identification of initial liquid saturation of network elements (pores, rings, throats).
15. Identification of initial liquid clusters and single liquid elements.
16. Set up of the matrix of vapor conductances  $\mathbf{A}$  (Eq. 5-39).
17. Computation of initial overall drying rate  $\dot{M}_{evap}$  from PN surface (Eqs. 5-58 or 5-59).
18. Computation of initial overall network saturation  $S$  (Eq. 2-56).

*Computation of discrete emptying (repetition of steps 19-36 until  $S = 0$ ).*

19. Identification of pores at known vapor pressure  $P_v^*(T)$ .
20. Set up of the vector of boundary conditions  $b$  (Eqs. 5-40 or 5-41).
21. Computation of the vapor pressure field inside empty network pores (Eq. 5-34).

22. Computation of the diffusion flow rates through empty network throats  $\dot{M}_v$  (Eqs. 5-43 or 5-44).
23. Identification of throat menisci and pore menisci and their active evaporation interface area.
24. *Identification of evaporating rings and their active evaporation interface area.*
25. Computation of invasion pressure thresholds of throat and pore menisci (Eqs. 5-60 and 5-61).
26. Computation of the evaporation rate from any meniscus throat (Eq. 5-51).
27. Computation of the evaporation rate from any meniscus pore (Eq. 5-52).
28. *Computation of the evaporation rate from any liquid ring (Eq. 5-55); then step 27 is omitted and in step 26 Eq. 5-54 is applied instead.*
29. Computation of the accumulated cluster evaporation rates (Eqs. 5-56 or 5-57 in presence of liquid rings). Clusters with overall negative flow rate are disregarded further, i.e.  $\dot{M}_{cond,cl} = 0$ .
30. Scan of each liquid cluster boundary for the meniscus throat or meniscus pore with the lowest capillary entry pressure threshold (= local candidate to be invaded). *(In the simulation with liquid rings, scan is (only) for the throat with the lowest capillary entry pressure threshold).*
31. Computation of the time required to fully invade the local candidate of each cluster at the current cluster evaporation rate (Eqs. 5-71 or 5-72).
32. Computation of the evaporation rate of single liquid elements and the time needed to completely invade these elements (e.g. Eq. 5-74).
33. Identification of the liquid element with the fastest invasion among all clusters and single liquid elements. This element is the global candidate (i.e. the only liquid element fully invaded during this time step) and it is assigned with  $S_{t,p} = 0$  (or  $S_r = 0$ ).
34. Determination of the time interval of this invasion event (i.e.  $\Delta t^{min}$ ).
35. Update of the saturation of all other liquid elements (Eqs. 5-73 and 5-75).
36. Update of cluster labeling (Section 5.4.4).
37. Repetition of steps 19-36 until  $S = 0$ .

## 5.6 Pore network drying algorithm incorporating cluster growth

The algorithm for the simulation of PN drying under non-isothermal conditions with refilling of already dried PN elements is summarized in the flowchart in Fig. 5-17. It illustrates the stepwise implementation of condensation and the different levels of the drying algorithm (refer to the flowchart in Fig. 5-17 for a recall of these levels). Labeling of clusters is adapted to the situation and liquid rings are not implemented in this PNM. It is emphasized that the computational effort is increased with increasing level of the algorithm because the liquid phase can multiply be re-evaporated in presence of strong condensation effects. This leads to more invasion steps and an increase of the computational loops in which the vapor pressure field and the cluster labeling as well are updated (in principle repetition of steps 1-15 in the algorithm given below). It should thus be recommended to use PNM level 2 or PNM level 3 in cases of negligible condensation effects (Fig. 5-17), as e.g. in the presented quasi-isothermal drying simulations.

In summary, set up of the algorithm (PNM level 4) is as follows. The *initiation of the PN drying simulation* is identical to the previous chapter (i.e. steps 1-18 but excluding the steps that refer to the liquid rings) and is therefore not repeated here. Steps 1-15 are repeated until complete desaturation of the PN. Notice that PNM level 2 is basically described in Section 5.5. In PNM level 3, steps 9.iii, 10.iii and 11 are omitted.

*Computation of discrete emptying (repetition of steps 1-15 until  $S = 0$ .)*

1. Identification of pores at known vapor pressure  $P_v^*(T)$ .
2. Set up of the vector of boundary conditions  $b$  (Eqs. 5-40 or 5-41).
3. Computation of the vapor pressure field inside empty network pores (Eq. 5-34).
4. Computation of the diffusion flow rates through empty network throats  $\dot{M}_v$  (Eqs. 5-43 or 5-44).
5. Identification of throat menisci and pore menisci and their active evaporation interface area.
6. Computation of invasion pressure thresholds of throat and pore menisci (Eqs. 5-60 and 5-61).
7. Computation of the evaporation/condensation rate from any meniscus throat (Eq. 5-51).
8. Computation of the evaporation/condensation rate from any meniscus pore (Eq. 5-52).
9. Computation of the accumulated cluster evaporation/condensation rates (Eqs. 5-56)
  - i. If the interfacial mass balance of the cluster is positive (i.e. the cluster is shrinking):
    - Scan of each liquid cluster boundary for the meniscus throat or meniscus pore with the lowest capillary entry pressure (= local candidate to be invaded by the gas phase) (Eqs. 5-60 and 5-61).
    - Computation of the time required to fully invade the local candidate at the current cluster evaporation rate (Eq. 5-71).
  - ii. If the interfacial mass balance of the cluster is negative and partially saturated elements are available at the cluster boundary (i.e. re-saturation of the cluster boundary) (as in PNM level 3):
    - Scan of each liquid cluster boundary for partially saturated meniscus throats or pores with the highest capillary entry pressure (= local candidate to be invaded by the liquid phase) (Eqs. 5-60 and 5-61).
    - Computation of the time required to fully invade the local candidate at the current cluster condensation rate (Eq. 5-77).
  - iii. If the interfacial mass balance of the cluster is negative and partially saturated elements are *not* available at the cluster boundary (i.e. the cluster is growing):
    - Scan of adjacent empty pores and throats for the local candidate with the highest entry pressure threshold (= local candidate to be invaded by the liquid phase) (Eqs. 5-60 and 5-69).
10. Computation of evaporation/condensation rates of single liquid throats (single liquid pores are always treated as a cluster).
  - i. If the interfacial mass balances of single liquid throats are positive (i.e. shrinking):

- Computation of the time required to fully invade the single liquid throats at the current evaporation rate (Eq. 5-71).
  - ii. If the interfacial mass balances of single liquid throats are negative and the single liquid throats are partially saturated (i.e. re-saturation of the single liquid element):
    - Computation of the time required to fully invade the single liquid throats at the current condensation rate (Eq. 5-77).
  - iii. If the interfacial mass balances of single liquid throats are negative and the single liquid throats are *totally* saturated (i.e. growing):
    - Scan of adjacent empty pores for the highest entry pressure threshold (= invaded by the liquid phase) (Eq. 5-69).
- 11. Computation of the time required to fully invade all empty candidates subjected to the cluster growth mechanism (Eq. 5-77).
- 12. Identification of the candidate with the fastest invasion among all clusters and single liquid elements. This element is the global candidate (i.e. the only element fully invaded during this time step) and it is assigned with either  $S_{t,p} = 0$  (evaporation) or  $S_{t,p} = 1$  (condensation).
- 13. Determination of the time interval of this invasion event (i.e.  $\Delta t^{min}$ ).
- 14. Update of the saturation of all other liquid elements (Eqs. 5-73 and 5-78).
- 15. Update of cluster labeling (Section 5.4.4).
- 16. Repetition of steps 11-15 until  $S = 0$ .

## **5.7 Summary**

In this chapter, the experiment based development of a non-isothermal PNM incorporating secondary capillary effects was presented. The proposed PNM is based on experimental findings from drying with the microfluidic SiO<sub>2</sub> PN presented in Chapters 3 and 4. In detail, experiments revealed a serious impact of secondary capillary invasion on the overall drying behavior, especially in drying under quasi-isothermal conditions, i.e. with local temperature varying only slightly. Furthermore, experiments with imposed positive temperature gradients revealed that pore scale distribution of liquid during the third period of drying, i.e. once the liquid phase is split up, is controlled by vapor diffusion through the partially saturated zone. Accordingly, both effects, namely secondary capillary invasion and temperature affected invasion and vapor transport, were independently implemented in the benchmark isothermal model based on Irawan (2006) and Metzger et al. (2007c). As the result, two different simulation routes are now available. These are the non-isothermal simulation with secondary capillary invasion and with negligible cluster growth (route 1) and the non-isothermal simulation with significant cluster growth – as a consequence of high condensation rates – and conversion of liquid interconnectivity (as achieved with liquid rings) into the cluster labeling (route 2).

The main characteristics of the developed non-isothermal model with secondary capillary effects (route 1) can be summarized as follows:

- Implementation of additional liquid elements (liquid pores with volume, capillary liquid rings).
- Artificial increase of the throat/pore invasion pressure thresholds along the lateral PN edges to capture secondary capillary invasion along these edges.

- Temperature dependency of vapor transport based on  $P_v^*(T)$ .
- Temperature dependency of gas invasion based on  $\sigma(T)$ .
- Computation of directional vapor flow rates.
- Interfacial mass balances based on directional vapor flow rates.
- Cluster labeling adjusted to liquid communication.

This model is applied to simulate drying under conditions, where the local temperature variations are small enough to allow for compensation of the condensation rates by evaporation rates, i.e. in situations where the condensation rates are not high enough to lead to the refilling of the already empty pore space. This is principally assumed in the simulations with spatially almost constant temperature (quasi-isothermal) and this assumption also applies in simulation with imposed negative thermal gradient, at least as long as the edge effect is not prominent as will be discussed in Chapter 6.

For the other situations, i.e. when the spatial temperature gradients lead to a significant increase of local condensation rates, an adapted PNM was proposed which incorporates cluster growth due to condensation and refilling of already empty pores and throats at the cluster boundaries. In this PNM a simplified representation of the secondary capillary effect is implemented, namely achieved by the artificial increase of invasion pressure thresholds of the throats/pores at the PN's lateral edges and the manipulated cluster labeling. This allows for liquid communication as expected in presence of liquid films. In summary, the proposed non-isothermal PNM with cluster growth mechanism (route 2) is characterized by:

- Implementation of additional liquid elements (single liquid pores with volume).
- Artificial increase of the throat/pore invasion pressure thresholds along the lateral PN edges to capture secondary capillary invasion along these edges.
- Temperature dependency of vapor transport based on  $P_v^*(T)$ .
- Temperature dependency of liquid and gas invasion based on  $\sigma(T)$ .
- Computation of directional vapor flow rates.
- Interfacial mass balances based on directional vapor flow rates.
- Cluster growth based on liquid invasion of cluster boundary gas pores and throats.
- Cluster labeling adjusted to liquid communication.

The different versions of this PNM are applied for the simulation of drying in situations where the imposed temperature gradients allow for high condensation rates (i.e.  $|\dot{M}_{cond}| > \dot{M}_{evap}$ ). This is mainly observed in drying with imposed positive thermal gradient and in drying with negative thermal gradient with pronounced edge effect, as will be presented in the following chapter.

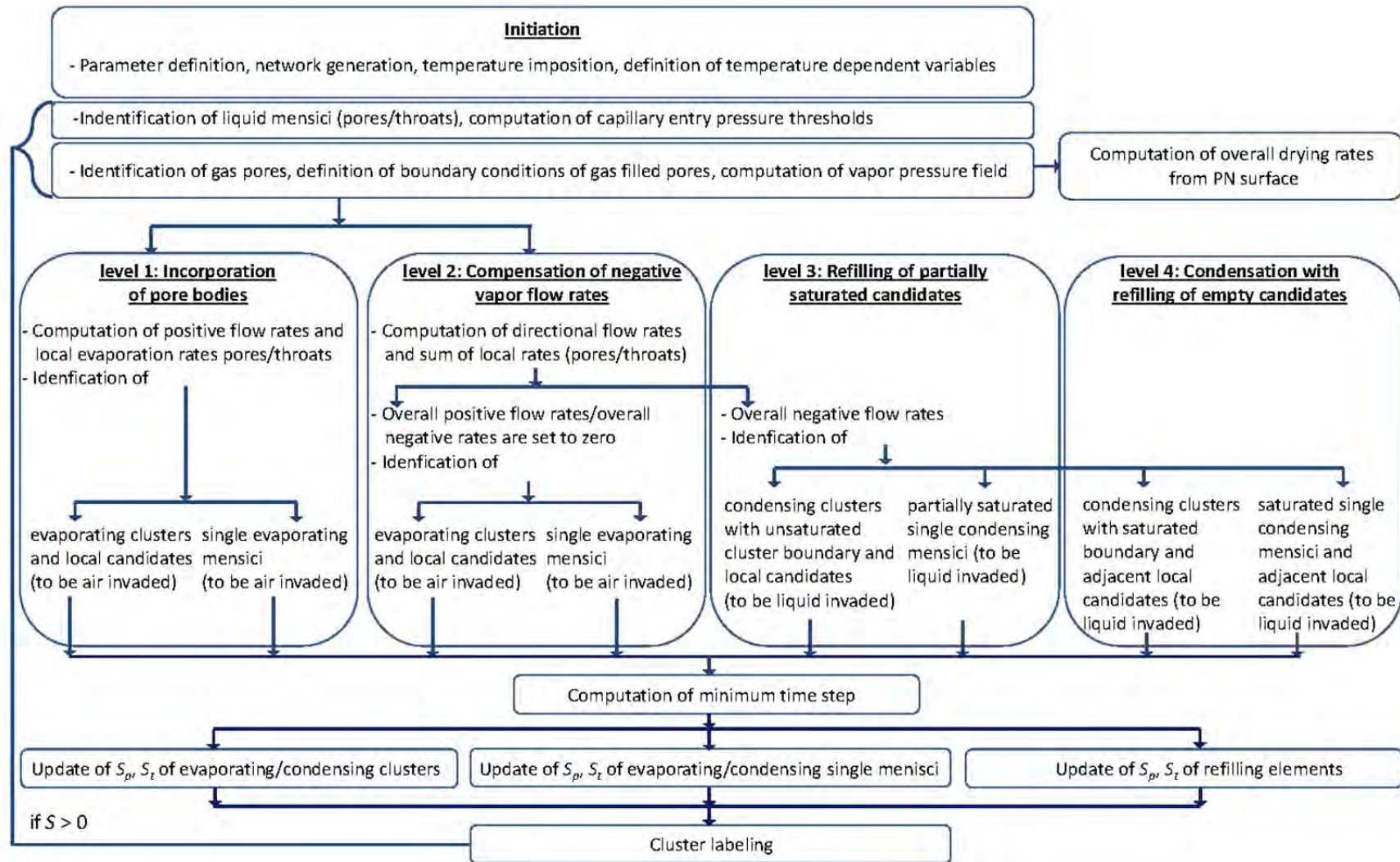


Figure 5-17 Flowchart of the non-isothermal drying algorithm with different levels of condensation related refilling.



„A theory is a good theory if it satisfies two requirements. It must accurately describe a large class of observations on the basis of a model that contains only a few arbitrary elements, and it must make definite predictions about the results of future observations.“

Stephen Hawking

\* January 8, 1942 in Oxford, Great Britain

† March 14, 2018 in Cambridge, Great Britain

## Chapter 6

# Experiment based evaluation of the pore network model

### 6.1 Introduction

Experiments with the microfluidic PN etched in a SiO<sub>2</sub> wafer, presented in Chapter 4, revealed significant differences in drying behavior depending on the temperature profile imposed on the PN. It was found that drying with spatially almost constant temperature of around 63°C leads to progressive invasion of the PN with increasing ramification of the liquid phase. The evolving drying front penetrated the PN from the open surface towards the bottom of the PN (notice that *bottom* designates the lower boundary in the images presented in Chapter 4 as well as below; the microfluidic PN, however, dried in horizontal position, thus in absence of gravity forces – this is also simulated with the model from Chapter 5). The phase patterns were characterized by a dry zone connected to the PN surface, a liquid zone connected to the PN bottom and an intermediate 2-phase zone with numerous disconnected single clusters. It was found that the invasion process was accompanied by secondary capillary invasion which controlled drying over the longest drying period. Precisely, formation of liquid film rings around the solid islands of the PN and wall covering liquid films at the side walls of the PN with temporally pinning of the liquid phase at these walls, were observed. Both effects were implemented in a PN drying model in Chapter 5.

Drying with imposed negative temperature gradient ( $dT/dz < 0$ ), i.e. a temperature gradient as evolving in a convective drying process, enforced the stabilization of the drying front. In contrast, in experiments with a positive temperature gradient ( $dT/dz > 0$ ), i.e. as evolving in a contact drying process, early breakthrough of the gas phase and initiation of a second invasion front was observed. It was additionally found that in case of  $dT/dz > 0$  vapor, evaporated at the hot network bottom, must diffuse from the hot region with high saturation vapor pressures towards the cold region with low saturation vapor pressures. Due to this, condensation of liquid and refilling with growing and merging of liquid clusters was

observed in experiments. As a result the previously ramified structure of the liquid phase appeared much more compact (Fig. 4-27). This revealed that the pore level liquid distribution evolving during drying of porous media is not only determined by the capillarity of the medium but also by temperature affected vapor diffusion. Consequently, the PNM was adapted so as to allow for temperature depending invasion of liquid clusters and vapor diffusion through the partially saturated zone accompanied by condensation induced cluster growth (Chapter 5).

In this chapter the experimental results from Chapter 4 are compared to simulation results obtained with the PNM proposed in Chapter 5 and implemented in Matlab R2014a. The structure of this chapter is as follows. At first, results of quasi-isothermal drying are discussed in Section 6.2. Validation of the respective PNM is based on a comparison to own experiments as well as to results from PNMs proposed by Metzger et al. (2007a) and Prat (2007). This involves discussion of the impact of boundary layer (BL) thickness, viscosity, slight temperature variations (in agreement with the ones resulting from the experimental realization of heat supply) as well as secondary capillary effects. It is shown that the competition of pore and throat invasion (resulting from the presence of single liquid pores with similar capillary invasion pressure thresholds as the throats) and viscous friction forces play a minor role in the investigated drying process because of the temperature dependence of capillary invasion. Instead overall good agreement of experimental results and simulated drying behavior is found, if the temperature variation and also the secondary capillary effects are taken into account. Especially the pinning of liquid to the network sides (edge effect) has a major impact on drying curves (see also Sections 4.3.1 and 4.3.2) as it can keep the drying front closer to the network entrance. It is also shown that the slight temperature variations detected during microfluidic drying experiments can lead to a temporal stabilization of the drying front if temperature is slightly decreasing with the penetration direction of the front (Fig. 3.8a). Drying with imposed thermal gradients is studied in Section 6.3 based on temperature fields recorded during microfluidic experiments (Fig. 3.8b,c). The impact of thermally affected transport equations on liquid distributions and macroscopic drying behavior is analyzed in detail. Special attention is paid on the role of liquid films. It is found that liquid films can induce a heat pipe effect inside the 2-phase zone of a drying PN with imposed negative thermal gradient. In addition to that, comparison of experimental and simulation results with imposed positive thermal gradient highlights the role of vapor diffusion through a partially saturated region. It is found that this mechanism can control the invasion process in thermally affected drying. This had not been studied before in such detail in the frame of PNM and may also deserve further attention in future works. A step towards such a future study is made in Appendix B.3, where the interrelation of thermal gradients, evaporation rate and pore size distribution of the 2D PN is discussed.

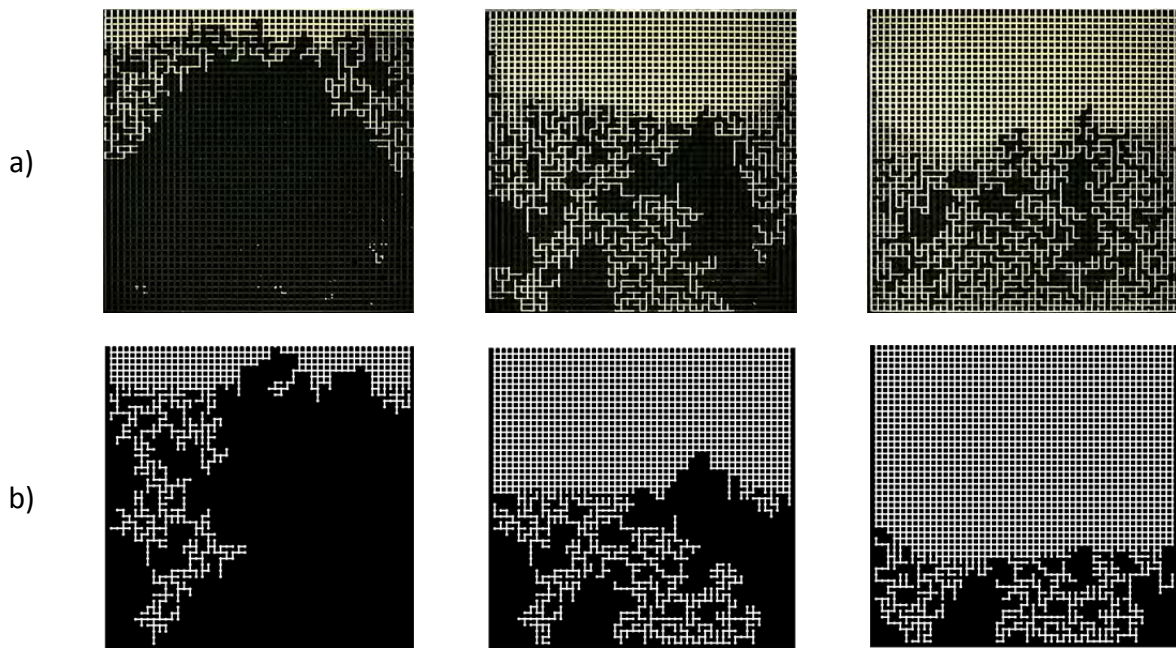
## **6.2 Quasi-isothermal drying**

In the following, different physical pore scale effects are investigated separately in order to objectively validate the leading pore scale phenomena of the drying process (Fig. 6-1). This includes the impact of the BL thickness on the initial overall evaporation rate, as well as the influences of viscosity, competitive invasion of pores and throats, slight local temperature variations and secondary capillary invasion (Sections 6.2.1 to 6.2.5). Apart from that, the impact of the variation of the void space (Section 5.2.1) and the wetting behavior of the PN (i.e. variation of contact angle  $\theta$ ) are subjects to future studies.

**Table 6-1** Summary of model parameters of quasi-isothermal drying.

$T_{BL}$	$P$	$P_v^\infty$	$L$	$L_d$	$S_{BL}$	$\cos\theta$
24.3°C	1 bar	0 bar	1000 $\mu\text{m}$	39 $\mu\text{m}$	1600 $\mu\text{m}$	1

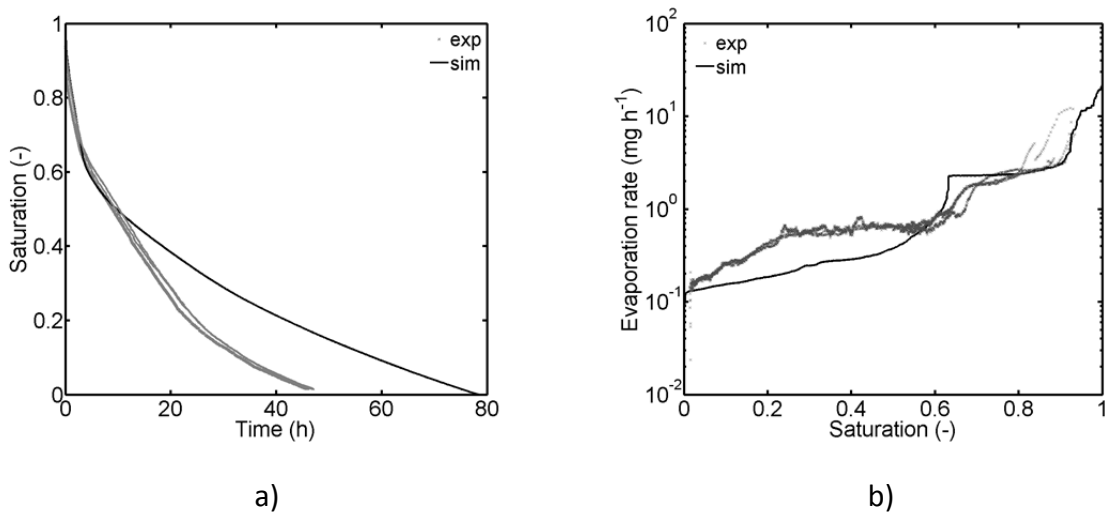
Since it is a priori anticipated that the different physical influences have a different impact on the drying front this study incorporates different versions of the non-isothermal PNM. Additionally, the PNMs of Metzger et al. (2007a) and Prat (2007) are used to validate the proposed PNM. Specifications of the applied models are given together with the simulation results below. The model parameters are adapted to the experiments and given in Table 6-1. If not other mentioned, this parameter set is applied in PN simulations presented below. Additionally, the pore size distribution from Fig. 3-3a (black line) is used. An overview of all simulations presented in this thesis is given in Appendix C. It is remarked that the spatial temperature variations in this study are small enough to neglect refilling of the void space due to condensation; this is shown in Section 6.2.4.



**Figure 6-1** a) Phase distributions from experiment 17. Breakthrough of the gas phase at  $S = 0.53$ . b) Phase distributions simulated with the benchmark PNM from Metzger et al. (2007c). Breakthrough of the gas phase at  $S = 0.79$  for  $T_{PN} = 63^\circ\text{C} = \text{const}$ . To adjust the total liquid volumes of the microfluidic PN and the PN in the benchmark model, the liquid volumes contained in pores in the microfluidic PN are dispensed to their largest throat neighbors in the benchmark model.  $S = [0.79, 0.4, 0.2]$ .

In total the results from 35 simulations are presented in the following and compared to experiments 17, 19, 20 and the simulation with the benchmark PNM (Section 5.1.1) as well (Figs. 6-1 and 6-2). Notice that the comparison of the very start of drying is not involved because due to the experimental procedure information for  $S > 0.95$  is not available. It is furthermore noted that the liquid saturation referred to the experimental images in Fig. 6-1a

is obtained from the analysis of the bulk liquid phase (in black); the liquid contained in liquid films, however, is not taken into account (Sections 3.4.1 and 3.4.3). This leads to a slight underestimation of the liquid saturation in the experimental images and drying curves. Exemplarily, if half of the PN would be assumed to be completely covered with liquid film rings, the according underestimation of liquid volume is around 5 % related to the total void volume of the PN assuming cylindrical films of width 21.4  $\mu\text{m}$ . Thus, the saturation corresponding to the image denoted with  $S = 0.2$  in Fig. 6-1a would have to be corrected: it is  $S = 0.25$  taking the liquid in films into account. This means that additionally around 25 % of the liquid would be contained in film rings in this case. Disregarding this, it is expected that the underestimation is lower in the presented results, because in all cases studied here much less than half of the PN is covered with liquid films.



**Figure 6-2** Drying curves (a) and drying rate curves (b) from experiments 17, 19, 20 (in gray) and the simulation with the benchmark model ( $T_{PN} = 63^\circ\text{C} = \text{const.}$ ) (in black). Note that the experimental curves are roughly overlapping. The drying time in a) is significantly overestimated because of the underestimation of drying rate (shown in a semi logarithmic plot) especially in the second period of drying (b). This is explained with the underestimation of single liquid clusters surviving upstream of the drying front in the microfluidic PN (Fig. 6-1). (Further discussion below).

### 6.2.1. Estimation of the boundary layer thickness

The BL thickness is estimated from Eq. 2-18 with air velocity

$$v_{air} = \frac{\dot{V}_{air} \rho_{air} \tilde{R} T_{air}}{\tilde{M}_{air} P A} \quad (6-1)$$

The variables in Eq. 6-1 are the volume flow rate of air  $\dot{V}_{air}$ , cross section of air flow  $A$ , air temperature  $T_{air}$ , air density  $\rho_{air}$ , the molar mass of air  $\tilde{M}_{air}$  and atmospheric pressure  $P$ . They are determined from the microfluidic drying experiments with  $\dot{V}_{air} = 20 \text{ l min}^{-1}$ ,  $A = 2 \cdot 10^{-3} \text{ m}^2$ ,  $T_{air} \cong 25^\circ\text{C}$ ,  $\rho_{air} = 1.1839 \text{ kg m}^{-3}$  and  $\tilde{M}_{air} = 28.949 \text{ kg kmol}^{-1}$ . Furthermore  $\nu \cong 158 \cdot 10^{-7} \text{ m}^2 \text{ s}^{-1}$  and  $L = 39 \mu\text{m}$  are the kinematic liquid viscosity and length of the incident flow. With this, the air velocity in drying experiments is estimated with around  $v_{air} \cong 0.17$

$\text{m s}^{-1}$ , corresponding to a BL thickness of around  $s_{BL}^{est} \cong 293 \mu\text{m}$  (BL thickness at  $v_{air} = 0.99 v_{air}^0$  (Schlichting 1942)).

This leads to a mass transfer coefficient of

$$\beta^{est} = \frac{D}{s_{BL}^{est}} \sim 0.1 \text{ m s}^{-1} \quad (6-2)$$

with  $D = 2.6484 \cdot 10^{-5} \text{ m}^2 \text{ s}^{-1}$  for  $T \cong 25^\circ\text{C}$  (Schirmer 1938).

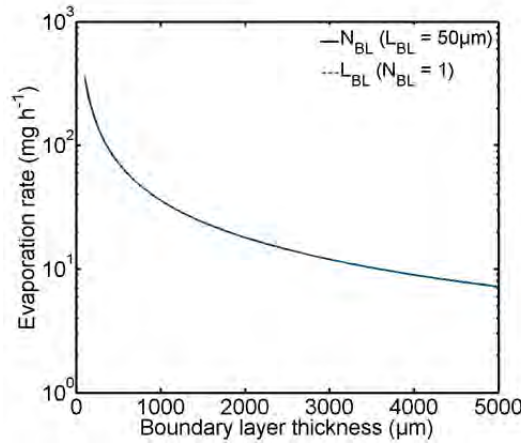
From quasi-isothermal experiments (Section 4.3) with an evaporation rate of  $\dot{M}_{evap} \cong 11 \text{ mg h}^{-1}$ ,  $\beta^{exp}$  is computed with

$$\beta^{exp} = \dot{M}_{evap} \frac{\tilde{R}T}{\tilde{M}_V P_V^*(T=25^\circ\text{C})A}, \quad (6-3)$$

with cross sectional area  $A = (n - 1)LL_d$  and assuming  $P_V^\infty = 0$ . This is based on the assumption that the initial evaporation rate is independent of the PN saturation at the surface and that furthermore the evaporation rates are locally constant (e.g. Schluender 2004, Suzuki and Maeda 1967). The result of Eq. 6-3 is  $\beta^{exp} = 0.07 \text{ m s}^{-1}$ . From this follows a BL thickness of  $s_{BL}^{exp} \cong 387 \mu\text{m}$ , i.e. in the range as predicted from the BL theory. If, however, the calculation is repeated taking into account that the saturation pressure at the surface of the PN is increased with temperature ( $T = 63^\circ\text{C}$ ), thus  $P_V^*(T = 63^\circ\text{C})$  and mean temperature  $\bar{T} \cong 44^\circ\text{C}$  is applied in Eq. 6-3, the BL thickness is increased to  $s_{BL}^{exp} \cong 2650 \mu\text{m}$ . Thus, the higher driving force associated with the higher temperature or rather the temperature gradient results in a significant increase of the BL thickness at the given experimentally estimated evaporation rate (in agreement with discussions in Philip and de Vries (1957)).

Note that the initial evaporation rate from the drying experiments was estimated for a PN saturation  $S < 1$ , thus after invasion of some pores and throats at the PN surface. It is furthermore noted that any increase in  $P_V^\infty$  can dramatically increase the BL thickness.

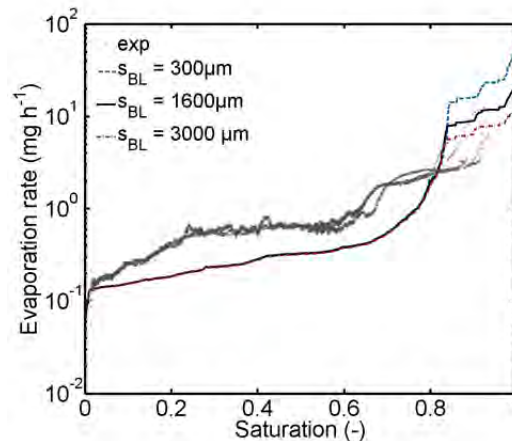
In the simulations presented below, the vapor transport from the surface of the PN to the bulk air phase is modeled with a discretized diffusive BL of thickness  $s_{BL}$  and with discretization  $N_{BL}$  (Fig. 5-6). The impact of the thickness of the BL on the initial PN drying rate is illustrated in Fig. 6-3 for  $P_V^*(T = 63^\circ\text{C})$ . As expected,  $\dot{M}_{evap}$  ( $S = 1$ ) decreases with growing BL thickness because of the decrease of the vapor pressure gradient  $dp/dz$ . It is remarked that the BL thickness is a fitting parameter in the presented model. It can basically be increased by two options: either by increase of the distance  $L_{BL}$  between the BL nodes or by increase of the number of computational nodes in terms of  $N_{BL}$  (Figs. 5-1 and 5-6). In most cases discussed in literature  $L_{BL} = L$ , i.e. identical lattice spacing in PN and BL is applied. Figure 6-3 reveals that almost identical results are obtained for any of the two options. The computed BL thickness for  $\dot{M}_{evap} \cong 11 \text{ mg h}^{-1}$  is  $s_{BL} \cong 3260 \mu\text{m}$ , thus in good agreement with the theoretically predicted value for  $P_V^*(T = 63^\circ\text{C})$ .



**Figure 6-3** Impact of thickness  $s_{BL}$  and discretization  $N_{BL}$  of the BL on the initial drying rate  $M_{evap}$  ( $S = 1$ ). The two curves are overlapping. Notice that the minimum number of  $N_{BL} = 1$  is referred to  $s_{BL} = 2 L_{BL}$  (Fig. 5-6).

In the simulations presented throughout this chapter, the BL thickness is adapted so as to allow similar initial evaporation rates as in the experiment. In the face of the optimization of the computational effort, this is achieved by variation of  $L_{BL}$  at  $N_{BL} = 1 = const$ . As will be shown, the consideration of different effects in the PNM can lead to a variation of  $s_{BL}$  for the same drying mode.

As expected from the discussions above and shown in Fig. 6-4 different initial evaporation rates are simulated for different BL thicknesses. The best agreement of experiments 17, 19 and 20 with simulation is obtained for  $s_{BL} \cong 1600 \mu\text{m}$  to  $s_{BL} \cong 3000 \mu\text{m}$ , thus as expected from the above discussions. Application of  $s_{BL} \cong 300 \mu\text{m}$  though results in an overestimation of the initial drying rate at  $S \cong 0.95$  (note that direct comparison at the start of drying, i.e. at  $S = 1$ , is not possible due to the experimental procedure). Independent of this, Fig. 6-4 reveals that very similar drying behavior over most of the drying process and thus similar drying times can be simulated independent of the BL; the impact of BL thickness essentially affects the initial evaporation rate and the initial level of the almost constant drying rates. In the limit of quasi-steady invasion, the discretization has negligible impact on the drying rate curves (and thus also on the predicted drying time).



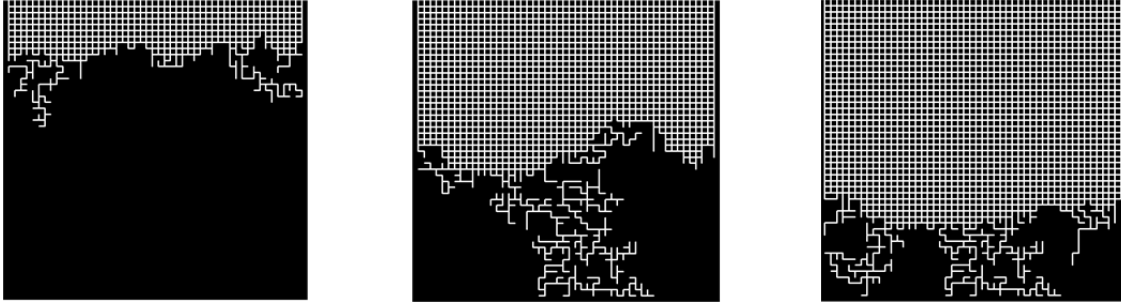
**Figure 6-4** Impact of BL thickness on the simulated drying behavior: drying rate curves in comparison to experimental data (in gray).

More clearly, this means that the drying process is mainly controlled by the pore scale processes during the FRP and RFP, not by the diffusion processes inside the BL during the initial period of drying. The decreasing trends at the very start of drying indicate that evaporation rate is not independent of the surface saturation (of the 2D PN) which is in contrast to literature (e.g. Talbi and Prat 2019). This shows that more details about the start of the drying process are required from future experiments.

### 6.2.2 Impact of liquid viscosity

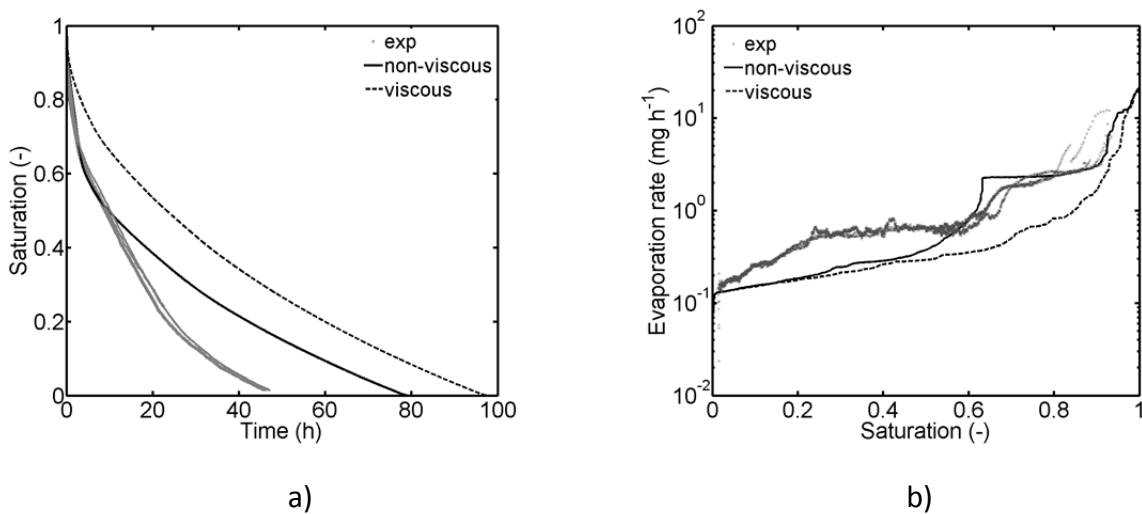
In the following, the results from the quasi-steady invasion computed with the benchmark model are compared to the results obtained from a PNM that allows for dynamic invasion of the pore space (from Metzger et al. (2007a)). This study is based on the CLSM measurement which showed continuous penetration of the gas-liquid interface in throats - a finding which is comprehensible in the face of the long throats and the small height of the PN controlling the capillary pressure curve in Fig. 5-12. It is also based on the finding of relatively high capillary numbers in Section 4.3.3 and the temporal stabilization of the drying front at the start of drying. Precisely, the variation of the mean meniscus radius (in pores and throats) is found to be only around 4  $\mu\text{m}$ . This might positively affect the role of viscosity of the liquid phase in the invasion process. More clearly, incorporation of liquid viscosity (analog to the transport equations formulated for the gas side in Section 5.3) has an effect on the pore scale gas-liquid phase distribution, such that the liquid phase appears more stabilized (i.e. less fractal) because of the limited distance of capillary liquid transport (compare with Eq. 2-38) (Tsimpanogiannis et al. 1999).

The two models under comparison are realized with the parameter setting in Table 6-1. In both models the pore volumes are assigned to their largest throat neighbor. The temperature dependency of parameters  $\sigma(T)$ ,  $D(T)$  and  $P_v^*(T)$  is taken into account and the invasion is computed for constant temperature  $T_{PN} = 63^\circ\text{C}$  (Figs. 6-1b, 6-5 and 6-6) as well as with the temperature variation from experiment (Figs. 6-7 and 6-8). In both studies, the direction of vapor diffusion is disregarded with the purpose to show the impact of thermally affected and viscous affected capillary invasion. Comparison of the phase patterns in Fig. 6-5 and Fig. 6-1 reveals overall similar drying behavior. The liquid phase (in black) recedes from the open PN side (on top) with the formation of an intermediate 2-phase zone between the dry zone (in white) connected to the open PN surface and the liquid saturated zone at the bottom. However, the simulated phase distributions in Fig. 6-5 show a stabilizing effect due to liquid viscosity principally by a smaller number of clusters ahead of the drying front and the limited width of the front. The breakthrough occurs at  $S = 0.45$  and thus significantly later than in the simulation neglecting stabilizing effects (Fig. 6-1b and related figures) and experiment 17 - as well as in experiments 19 and 20 as documented in Appendix A - where  $S = 0.53$ . Interestingly, the phase patterns are very similar to the stabilized patterns in Figs. 6-9 and 6-11 below, where stabilization is explained with the competitive invasion of pores and throats (Fig. 6-9) and temperature variation (Fig. 6-11). In addition to that, Fig. 6-6 reveals an early drop of drying rates and absence of a CRP. This is basically explained with the dry out of the pore rows at the PN surface already at the start of drying. As a consequence of this, the drying time is around 20 h longer than drying computed with the quasi-steady invasion model (Figs. 6-2 and 6-6). Independent of this, both models overestimate the drying time because basically they underestimate the drying rate during the RFP. Though, the underestimation is much greater using the PNM with dynamic invasion.



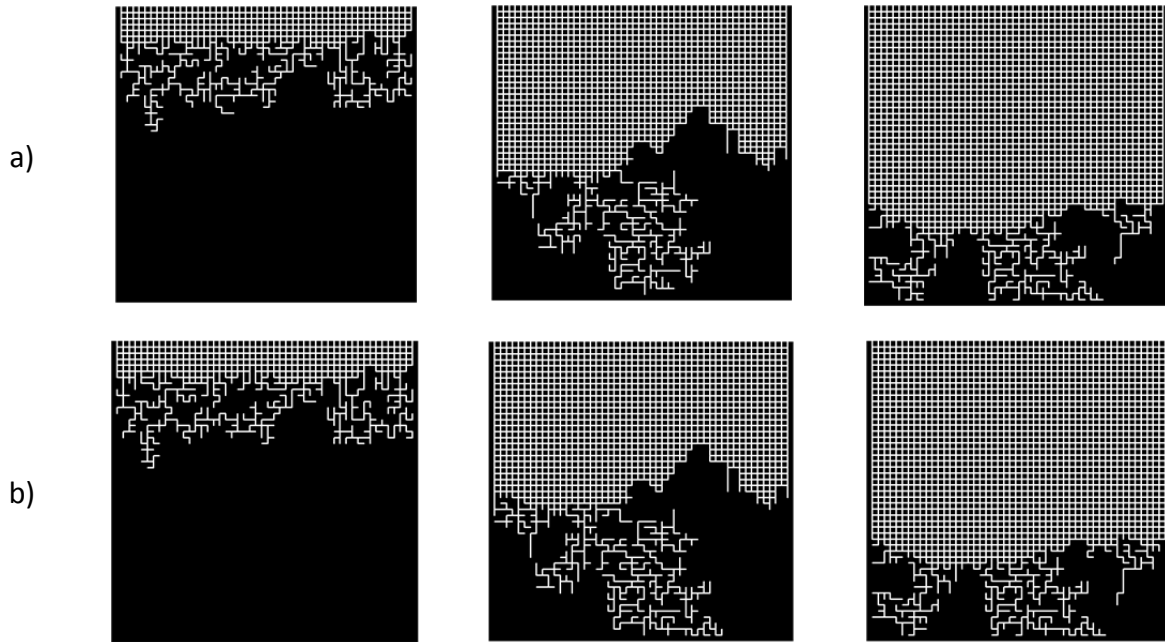
**Figure 6-5** Phase distributions obtained from the model of Metzger et al. (2007a) for dynamic throat invasion. Simulation with  $T_{PN} = 63^\circ\text{C} = \text{const.}$  and  $\eta = 466.59 \cdot 10^{-6} \text{ Pa s.}$   $S = [0.79, 0.4, 0.2]$ .

Repeating this simulation with respect to the local temperature variation for the computation of liquid pressure  $P_l = P - P_{c,t}(\sigma(T), r_{m,t})$  gives the results shown in Figs. 6-7 and 6-8. The temperature dependency of vapor transfer is disregarded here and any deviations between Figs. 6-5, 6-6 and Figs. 6-7, 6-8 are explained with the different invasion associated with  $P_l = P - P_{c,t}(\sigma(T), r_{m,t})$ . The comparison to the simulation with quasi-steady invasion and identical specifications and parameters generally reveals very similar drying behavior (Figs. 6-7 and 6-8). The phase distributions are almost identical and the drying curves are overlapping in Fig. 6-8. More liquid clusters are found upstream of the drying front than in Fig. 6-5. The breakthrough occurs at  $S \cong 0.41$  in both simulations. This indicates that a similar stabilizing effect as in the viscous drying simulation is obtained by implementation of the temperature field from experiment (and disregarding the viscous effect). However, in contrast to Fig. 6-6, an initial CRP (after a small drop of drying rates at the very start of drying) is simulated with the thermally affected viscous model, reflecting impact of temperature on the invasion process. This observation is explained with the variation of liquid pressure with temperature and the related increase of the distance of liquid transport in the dynamic PNM (also refer to Section 4.3.3).



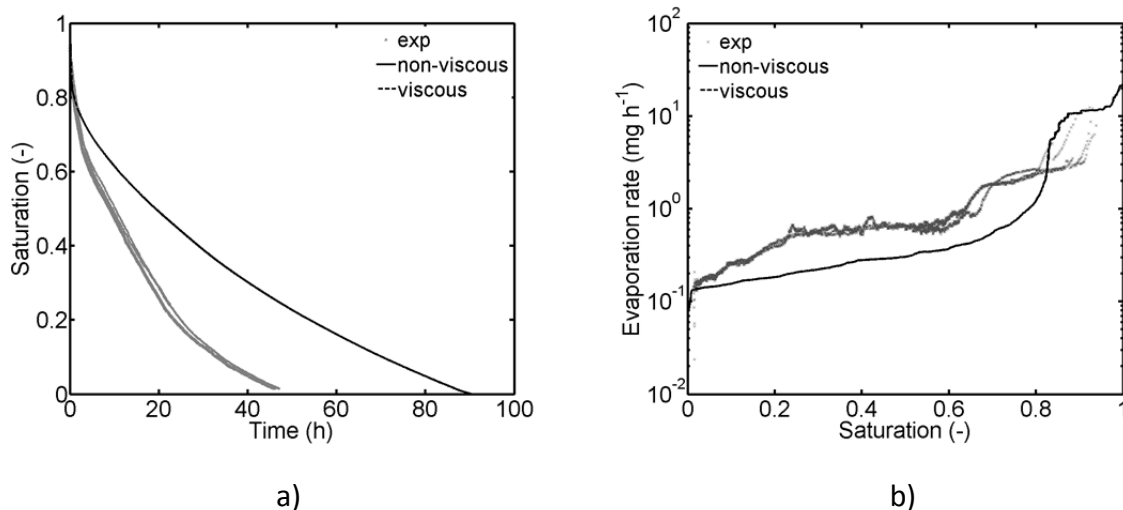
**Figure 6-6** Comparison of a) drying curves and b) drying rate curves from experiments 17, 19, 20 (in gray), simulation with quasi-steady invasion (from Fig. 6-2, denoted as non-viscous) and simulation with liquid pumping (Metzger et al. (2007a), denoted as viscous).





**Figure 6-7** Phase distributions from a) the benchmark model (pore volumes assigned to throats) and b) the model of Metzger et al. (2007a) for dynamic throat invasion. Simulation with temperature field from experiment and  $\eta = 466.59 \cdot 10^{-6}$  Pa s (in the viscous drying simulation). a) Quasi-steady invasion (non-viscous), b) dynamic invasion (viscous).  $S = [0.79, 0.4, 0.2]$ .

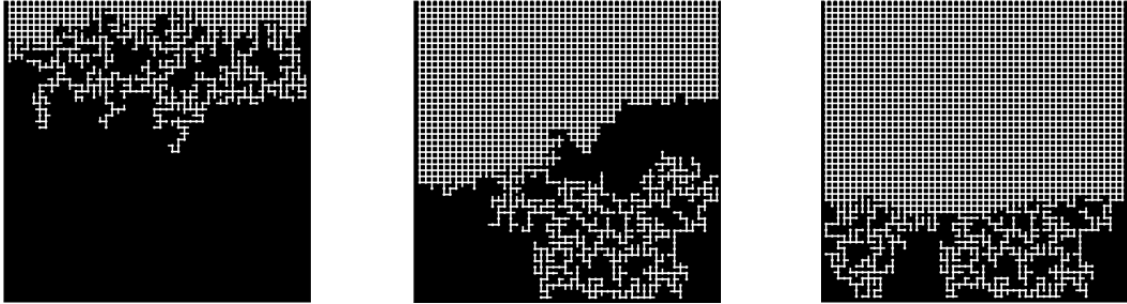
As a consequence, the dynamic tracking of the meniscus positions (Metzger et al. 2007a) may be disregarded and drying computed based on the assumption of quasi-steady invasion in the following. This can reduce the computational effort because the liquid pressure field, analog to Eq. 5-34, must not be computed.



**Figure 6-8** a) Drying curves and b) drying rate curves corresponding to Fig. 6-7 and experiments 17, 19, 20 (in gray). The curves denoted as viscous and non-viscous are overlapping.

### 6.2.3 Impact of competitive pore and throat invasion

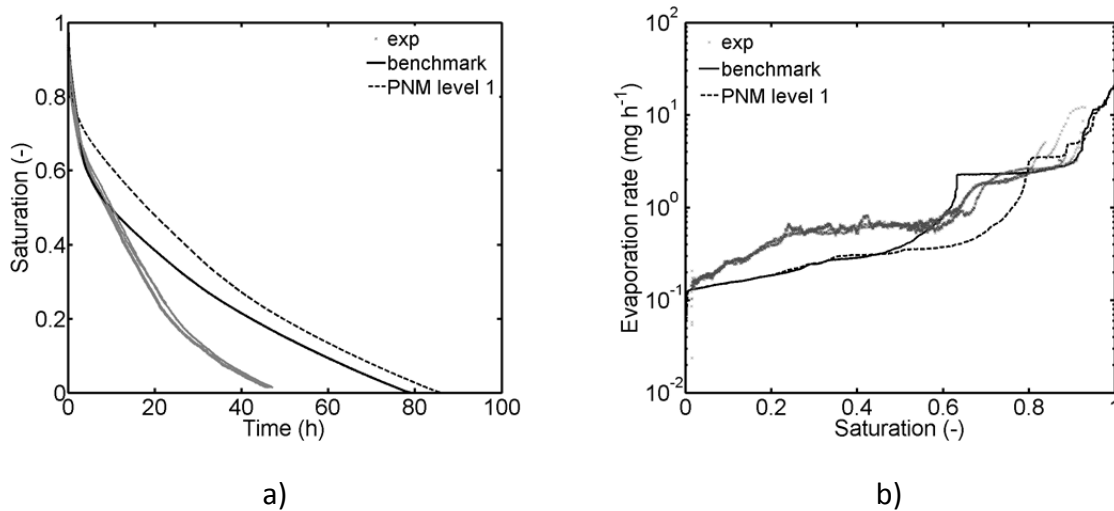
The introduction of pore volumes in the PN structure is realized by implementation of single liquid elements with capillary entry pressure  $P_{c,p}^*(\sigma(T_p), r_{m,p})$ . A general study of the impact of the implementation of single liquid pores in the PNM is given in Appendix B.1.



**Figure 6-9** Impact of pore invasion on phase distributions simulated with PNM level 1 and  $T_{PN} = 63^\circ\text{C} = \text{const.}$   $S = [0.79, 0.4, 0.2]$ .

The simulation results given in Figs. 6-9 and 6-10 indicate that implementation of single pore volumes slightly changes invasion of the PN compared to Fig. 6-1b and Fig. 6-2, where the liquid volume of the pores was simply dispensed to the largest throat neighbors with the purpose to adjust the liquid volume of the PN to the microfluidic device. This is explained with the competitive invasion of pores and throats and the shorter time steps associated with the pore invasion (also refer to Section 5.4.3). Both effects can allow for a different order of throat invasion.

It is found that the phase distributions are temporally stabilized in the simulation with competitive invasion of pores and throats. This leads to a later breakthrough of the gas phase (at  $S = 0.49$ ) than in the simulation that assigns pore volumes to throat neighbors ( $S = 0.79$ ), similarly as in the viscous stabilized simulation discussed in the previous section.



**Figure 6-10** Comparison of a) drying curves and b) drying rate curves corresponding to Figs. 6-9 (dashed lines), 6-1b (denoted as benchmark, solid lines) and experiments 17, 19, 20 (in gray).

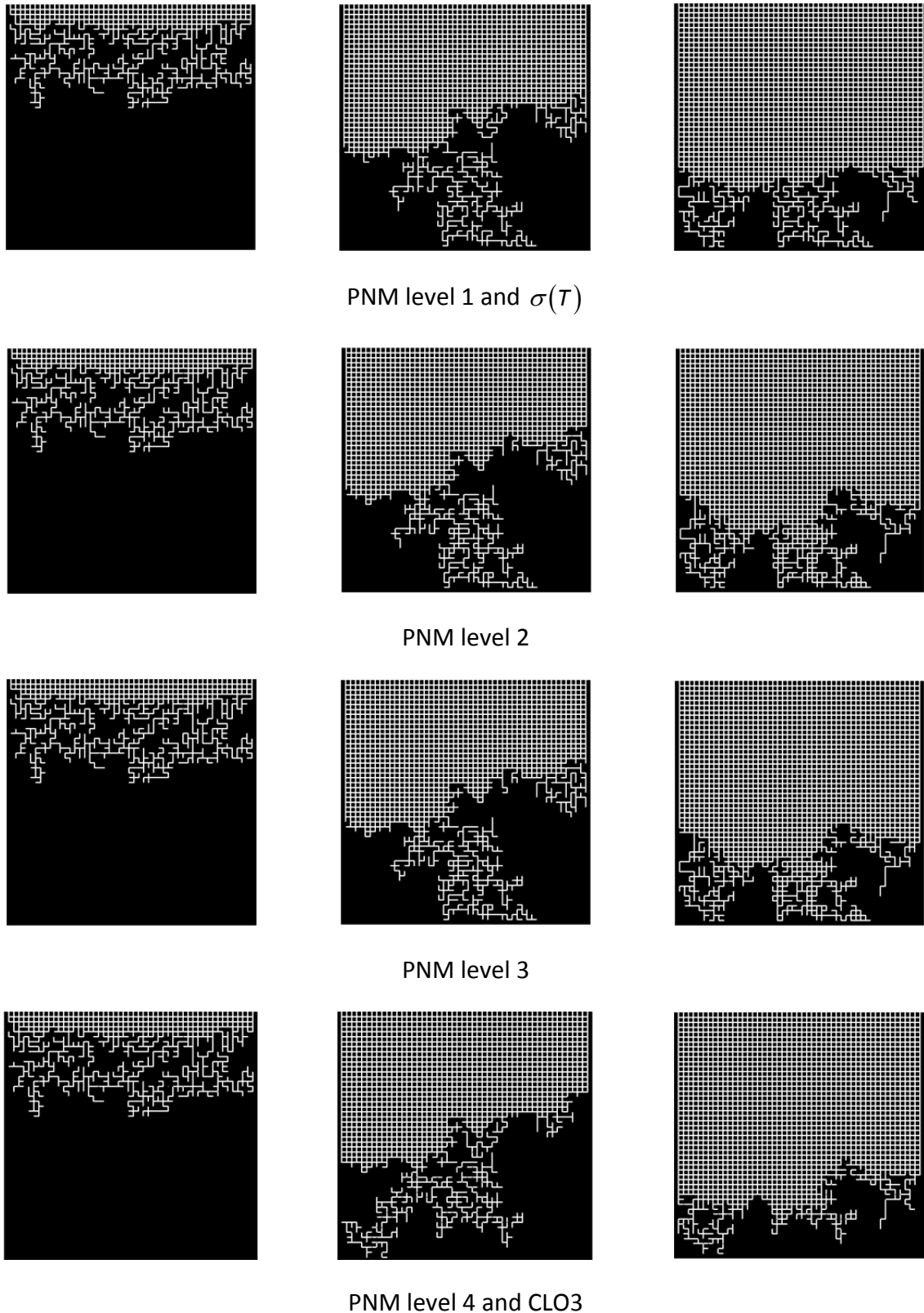
However, the structure of the liquid phase is more ramified than in Fig. 6-7, with a higher number of smaller liquid clusters upstream of the evaporation front. But still obvious differences from the experiment are to be mentioned: the number of clusters is apparently lower than in Fig. 6-1a and in addition to that wetting of the side walls of the PN (especially at the end of drying) is not captured. This can explain the significant overestimation of drying time and the related underestimation of overall evaporation rates in Fig. 6-10.

From the comparison of drying curves and drying rates in Fig. 6-10 it can be concluded that single liquid pores have an impact especially on the duration of the CRP shortly after the start of drying. It is found that the CRP is shorter when using PNM level 1. This is a consequence of the temporal stabilization of the drying front and passing of the CRP into the RFP at higher overall PN saturation accordingly. This leads to a slightly longer drying time. But, as will be shown in the following section, the role of competitive pore and throat invasion generally becomes unimportant in the regarded PN if the local temperature variation detected during the drying experiment is implemented in the PNM. This is explained with the small variation in  $r_m$  as will be discussed below.

#### 6.2.4 Impact of local temperature variation

If drying of the PN is assumed as a quasi-steady invasion process in the capillary controlled regime (and if furthermore the temperature dependency of vapor diffusion is disregarded), the order of pore and throat invasion is dictated by the entry pressure threshold of the competitive liquid elements, as already discussed above. As the invasion pressure of a liquid filled element is not only associated with its radius but also with its temperature, temperature variations affect the order of emptying if the pore or throat size distribution is narrow. More clearly, Fig. 5-12 reveals a very small distribution of  $r_m$  in the primary PN (induced by the small height of the PN). The impact of temperature can be revealed by PN simulations using the temperature field specified in Fig. 3-8a and else identical parameter setting as before. Simulations with PNM level 1 and temperature dependency of surface tension (thermal impact on vapor transport is neglected here) are compared to simulations with PNM level 2-4 (taking the dependence of vapor transport on temperature into account) in the following.

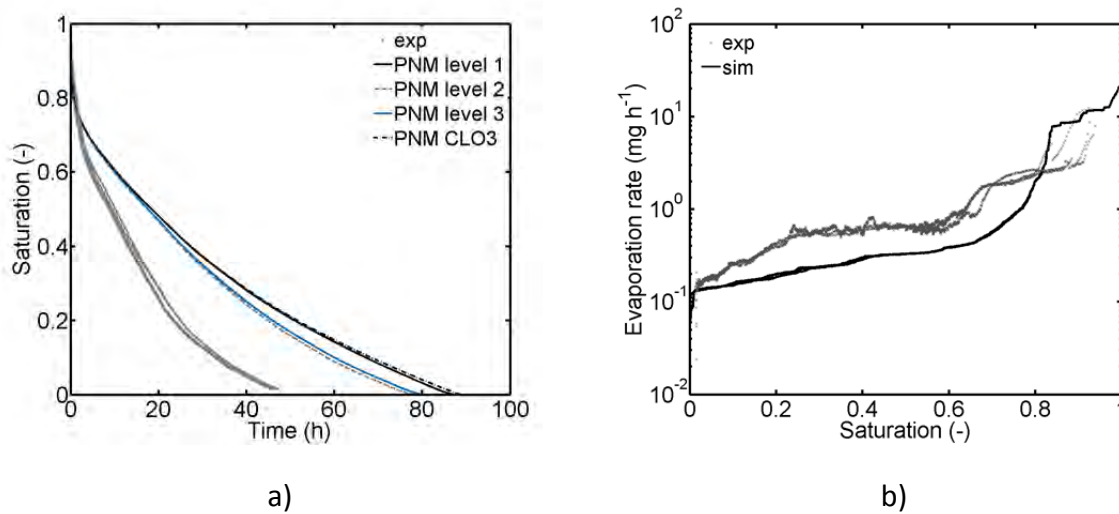
Figure 6-11 shows that independent of the model option a similar invasion behavior as shown before (Figs. 6-1b, 6-5, 6-7, 6-9) can be expected if temperature is assumed to vary locally as in the drying experiment. The good agreement of the phase patterns in Fig. 6-11 is explained with the negligible ratio of condensation, which is  $v_c^- \cong 0.06$  using PNM level 2,  $v_c^- \cong 0.08$  using PNM level 3 and  $v_c^+ \cong 0.06$  using PNM level 4 and CLO3 (i.e. the PNM in which the labeling is adjusted so as to prevent fluctuation of cluster merging). In general, the drying front appears more stabilized than in the isothermal drying simulation with the benchmark model (Fig. 6-1b), which is associated with the impact of the temperature variation on the order of invasion. The breakthrough occurs at  $S \cong 0.47$  (in PNM level 1-3) and  $S \cong 0.45$  (in PNM level 4, CLO3). It is furthermore evident that the effect of the temperature variation on the stabilization of the drying front is very similar to the effect of viscosity and single pore volumes. The drying rate curves presented in Fig. 6-12 reveal, independently of the PNM option, a quasi CRP at the start of drying (similarly as in Fig. 6-8). This period is on a higher level than found in Fig. 6-2b, but also much shorter (the drop occurs at  $S \cong 0.63$  in the benchmark model).



**Figure 6-11** Phase distributions from drying with temperature variation from experiment and separate invasion of liquid pores.  $S = [0.79, 0.4, 0.2]$ .

This shows that the impact of the slight spatial variation of temperature between  $T^{min} = 62.6^\circ\text{C}$  and  $T^{max} = 64.1^\circ\text{C}$  leads to i) different phase patterns than in drying with

constant temperature and ii) different initial drying behavior. Despite this, very similar drying times are predicted with the different versions of the model (Fig. 6-12). The deviations in Fig. 6-12a are explained as follows. With PNM level 1 the temperature dependency of the vapor pressure  $P_v^*(T)$  was neglected with the purpose to illustrate the impact of temperature on capillary invasion. This can affect vapor diffusion within the partially saturated zone and lead to an increase in drying time because of the slightly lower drying rates (indicated by the different slopes of the saturation curve for  $S \leq 0.6$ ). Deceleration of drying using PNM level 3 and PNM level 4 and CLO3 is explained with the condensation and refilling of the void space. More clearly, the condensed liquid volume must again be evaporated which slightly increases drying time.

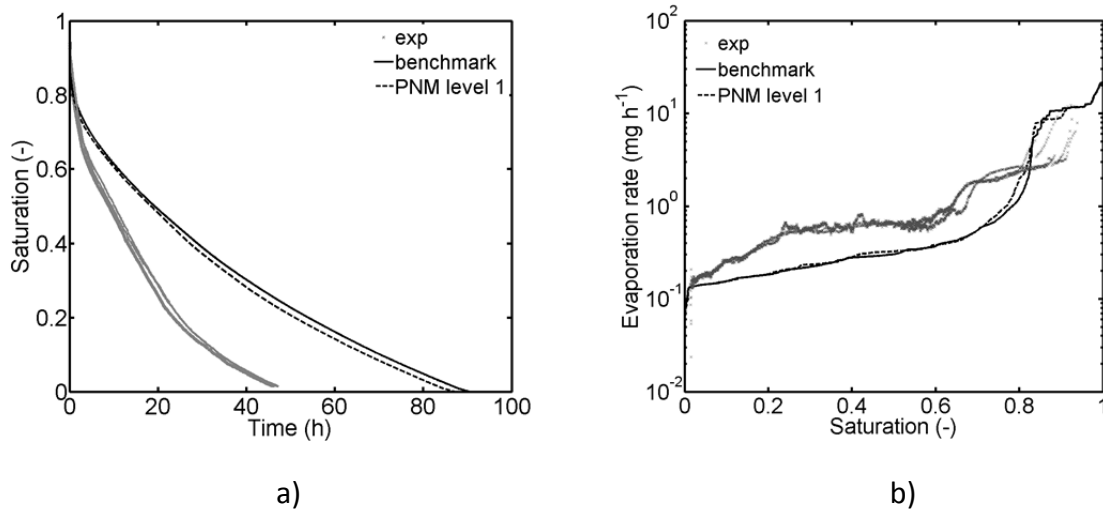


**Figure 6-12** a) Drying curves and b) drying rate curves corresponding to Fig. 6-11. Note that the drying rate curves of the four different simulations are almost overlapping. Experimental drying curves in gray.

Interestingly, comparison of the temperature affected drying of the PN with separate invasion of the pores (PNM level 1 with temperature dependent interface curvature) with the PN simulation in which the pore volumes are assigned to their largest throat neighbors (benchmark model with temperature dependent interface curvature of throats) reveals very similar drying behavior (upper rows in Figs. 6-7 and 6-11). The drying curves are almost overlapping in Fig. 6-13. This shows that in the PN under study the capillary pressure variation due to the existence of single pores plays a minor role for the order of invasion if  $\Delta T$  is high enough. This is because the capillary pressure distribution related to the pore radius variation is smaller than compared to the temperature variation. A different behavior is expected if either  $\Delta T$  is decreased or if the effective pore radii have greater variance.

From the above discussion it can be concluded that the separate invasion of liquid pores can alter the order of invasion if the impact of temperature is disregarded. If however, the temperature distribution is taken into account, the separate invasion of the pores has a minor impact for the given PN structure and temperature range (a similar finding was obtained for the comparison of viscous and non-viscous drying under the impact of temperature variation). This finding can be helpful to reduce the computational effort, namely if the separate invasion of pores is disregarded (because this reduces the invasion events from 7351 to 4851). It was also found, that the cluster growth mechanism can be

neglected in the further study of this temperature range as the amount of condensed liquid volume is very small. Apart from that, it must be concluded that none of the options of the PNM studied so far can reliably predict the drying time. This is explained with an underestimation of the duration of the CRP shortly after the start of drying as well as an underestimation of the drying rate during the period of drying in which the drying front recedes from the PN surface (RFP). This might be explained with the existence of liquid films in the crevices of pore throats in the microfluidic network, which is discussed in the following sections.



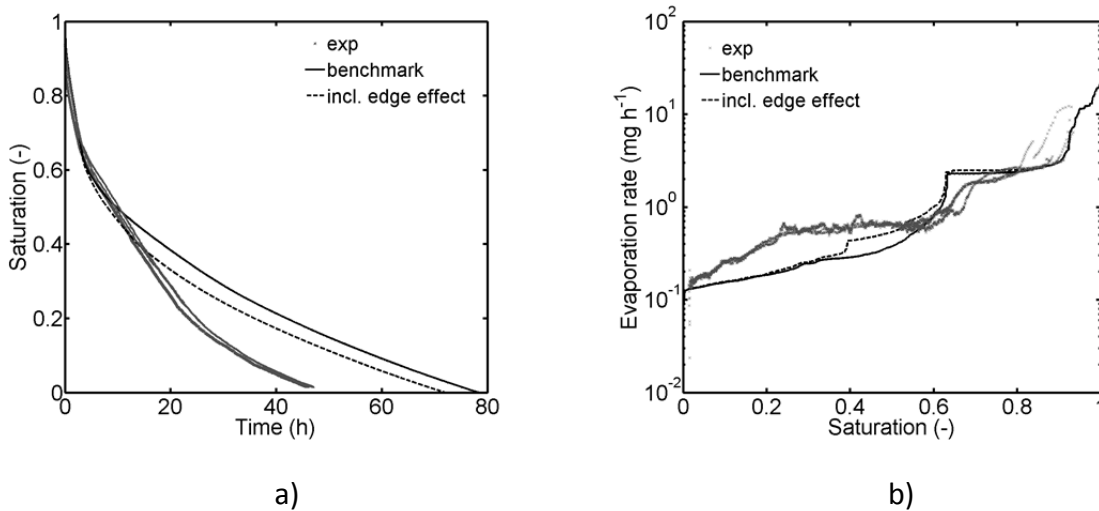
**Figure 6-13** Comparison of drying simulations with different assignment of pore volumes: a) drying curves and b) drying rate curves corresponding to the images in upper rows in Figs. 6-7 (denoted as benchmark) and 6-11 (denoted as PNM level 1). Experimental drying curves in gray.

### 6.2.5 Impact of secondary capillary invasion

As discussed in Section 4.2.2, wetting liquid films were observed in experiments with the microfluidic PN. As shown in Fig. 2-28, the presence of liquid films has a distinct relevance for the pore scale liquid structure and consequently for the position of the evaporation front and ergo also for the macroscopically observed drying rate. Based on this, the PNM was adjusted so as to take into account the role of wetting liquid films with the aim of a significantly better agreement with experiment. For this, two different model approaches were applied: i) the conventional film model based on the assumption of continuous liquid films as proposed by Prat (2007) or Yiotis et al. (2004) (Appendix B.4) and ii) the model of discrete liquid rings as introduced in Section 5. The second approach is based on the analysis of CLSM measurements according to which the liquid films have the form of ring structures surrounding the solid islands and are separately invaded. As will also be proven by the analysis of the simulation results in the following, this observation is contradictory to the continuous wall covering films assumed in the conventional model (approach i). Moreover, it will be shown that the different structure of liquid films underlying both model approaches leads to structural differences in the pore scale liquid distribution and thus the macroscopic drying behavior as well. The continuous film model (Prat 2007) though can predict the lateral pinning of liquid very well; however, it overestimates the drying front position in the center of the PN, as discussed in the following.

### 6.2.5.1 Lateral pinning of liquid

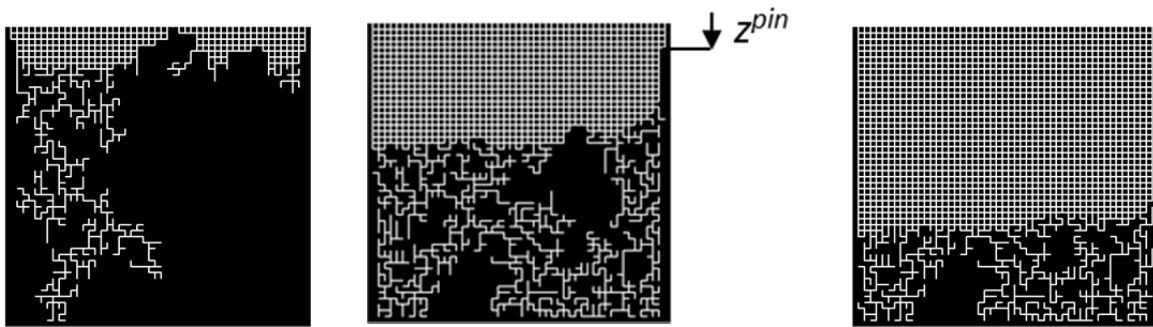
Experimental observations indicate that the vertical side walls of the microfluidic network are covered with a continuous liquid film which leads to the pinning of the liquid phase to the network edges. Based on this observation, this phenomenon has also been named the edge effect (Vorhauer et al. 2015). This lateral pinning contributes to a significantly higher position of the liquid front at the network boundaries than in the center of the microfluidic PN (e.g. Fig. 4-11). Thus, given liquid continuity, moisture transfer resistance is reduced in the microfluidic network with edge effect due to the elevated position of the evaporation front and, consequently, drying rates are elevated compared to drying without lateral pinning of liquid. This is confirmed by the drying rate curves and drying curves in Fig. 6-14 which evidence that incorporation of the edge effect in the PN simulation reduces overall drying time as it contributes to overall elevated drying rates. The curves are computed using the adjusted benchmark model with reduced width of the lateral throats (according to Section 5.2.2.2) (dotted line, denoted as *incl. edge effect*) and compared to the simulation without edge effect and else identical parameter setting (solid line, denoted as *benchmark* (from Fig. 6-2)). Note that a second route, i.e. different from the route sketched in Section 5.2.2.2, could be considered with a similar result. This route is based on the introduction of continuous liquid films that cover the PN up to the position of the tip of the lateral pinning and it is studied in Section 6.2.5.2 below.



**Figure 6-14** a) Drying curves and b) drying rate curves from PN simulation incorporating the edge effect by the approach given in Section 5.2.2.2 (denoted as *incl. edge effect*). Comparison with experiments (in gray) and benchmark simulation (from Fig. 6-2). Simulation with the adjusted benchmark model:  $r_{m,edge}$  from Eq. 5-17 with  $f^{red} = 0.85$  and  $z^{pin} = (5-49)L$ .  $T_{PN} = 63^{\circ}\text{C} = const.$

Figure 6-14 indicates that the reduction of throat sizes gives a slightly better agreement of drying curves and drying rate curves (than the benchmark model ignoring the edge effect) if the mean meniscus radius of the edge elements is reduced by factor  $f^{red} = 0.85$ . (Notice that size of the pores needs not to be reduced if the pore invasion is not treated separately from the throat invasion). The throat size reduction is applied to the lateral throats with position  $z^{pin} = (5-49)L$ . This is based on the experimental observation of liquid pinning in this range.

The phase distributions in Fig. 6-15 are similar to the isothermal simulation ignoring the edge effect (Fig. 6-1b), additionally, the overall PN saturation at breakthrough of the gas phase to the bottom of the PN occurs at a similar saturation ( $S = 0.8$ ). But in contrast to Fig. 6-1b, the liquid phase is temporally pinned at the PN sides due to the smaller invasion pressure threshold of the throats along the side walls. It is highlighted that the position of liquid pinning is not constant in the simulation (as also in the experiments) but rather migrates downwards with the progressive evaporation of the PN edges, starting from  $z^{pin} = 5L$ , which marks the upper limit of liquid pinning (in agreement with experiments). The agreement of the phase distributions with experiments is fair for  $S = 0.79$  and good for  $S = 0.4$  (Figs. 6-1a and 6-15). Apart from that, the position of the evaporation front is underestimated for  $S = 0.2$  due to the underestimation of the position of lateral pinning as well as the liquid film effect in the center of the PN (as will be in detail discussed below). The dynamic invasion of the PN edges might be adapted if the time-dependent position of the lateral pinning of the drying front would be estimated from the image data and used in the PN simulation. Another approach is the implementation of continuous liquid films studied below.



**Figure 6-15** Phase distributions referring to the simulation represented by the dashed lines in Fig. 6-14.  $S = [0.79, 0.4, 0.2]$ .

### 6.2.5.2 Simulation with the continuous liquid film pore network model

For the study presented in this section, the model of continuous liquid films as proposed by Prat (2007) or Yiotis et al. (2004) was implemented into the benchmark PNM (see Appendix B.4 for a detailed description). In difference to the other versions of the PNM discussed throughout the thesis, the main assumptions of the film model are:

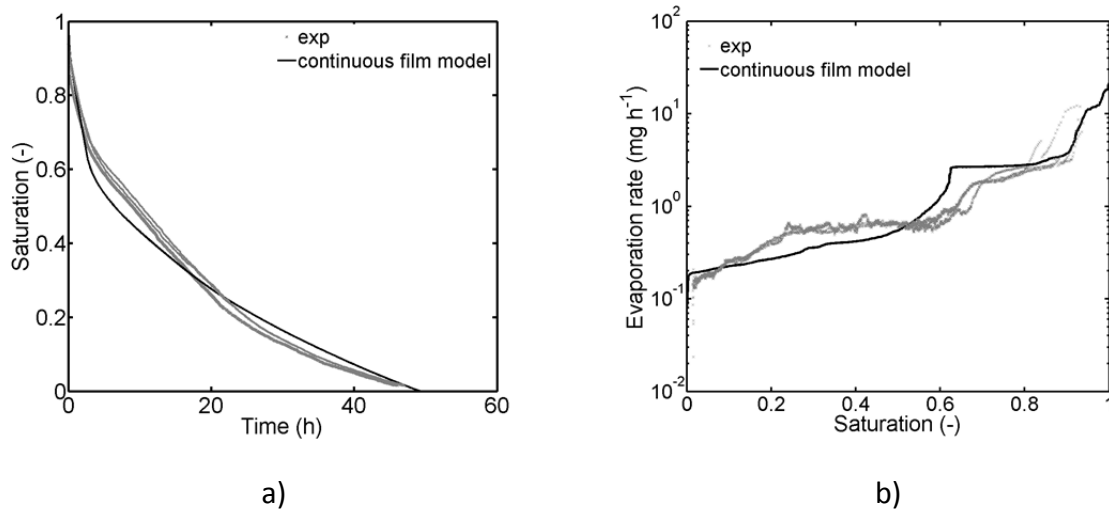
- linear diffusion through gas filled pores,
- no disorder of the width of gas filled pores (so as to allow for the same governing transport equations in the film region and the dry region),
- constant temperature ( $T_{PN} = T_{BL} = 63^\circ\text{C} = \text{const.}$ ),
- $k = 0.9$  (refer to Section B.4 for a discussion of this parameter),
- no discretization of the BL (i.e. an external mass diffusion layer of thickness  $s_{BL} = 225 \mu\text{m}$  was implemented),
- no cluster connectivity by liquid films.

In this model, the extent of the continuous film region is controlled by the choice of the wetting angle  $\theta$  and the choice of the number of corners  $N$  as well as the roundness of these corners  $r_0$ . Following Section 2.3.6, a longer film region is obtained if  $\theta$  is low ( $\theta \ll 45^\circ$ ), the



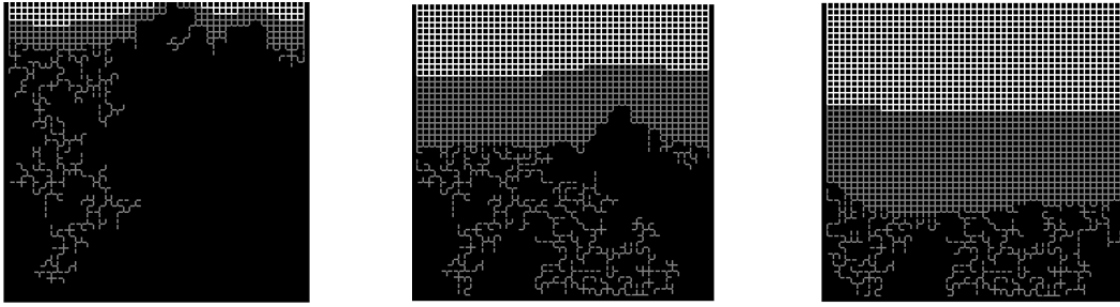
number of corners is small ( $N \leq 4$ ) and if furthermore the corners are sharp,  $r_0 = 0$  (Chauvet et al. 2010).

The BL thickness is adapted so as to allow identical initial evaporation rates as in the drying simulations studied above. This is achieved for  $s_{BL} = 225 \mu\text{m}$ . The small extent of the BL here is explained with the different structure of the BL (non-discretized) and the different temperatures inside the BL (here  $T_{BL} = 63^\circ\text{C}$ ). Notice that the assumption of linear diffusion in this model is in contrast to the assumption of non-linear diffusion in the simulations presented above which basically leads to overall lower vapor flow rates in the continuous film model. Additionally, different vapor flow rates are associated with the constant width of gas filled pores, which is also in contrast to the PNM presented in Chapter 5. An agreement of vapor flow rates and overall drying rates in both PNMs is obtained, when linear vapor diffusion is applied in the PNM from Chapter 5 and when furthermore the vapor flow rates in the continuous film model are multiplied with factor  $k = 0.9$  (this is explained in Appendix B.4).



**Figure 6-16** Comparison of the drying curves (a) and drying rate curves (b) from experiments 17, 19, 20 (in gray) and from the conventional continuous film model with  $\theta = 42.77^\circ$ ,  $r_0 = 0$ ,  $N = 4$ ,  $T_{PN} = T_{BL} = 63^\circ\text{C}$  and  $s_{BL} = 225 \mu\text{m}$ .

The simulation result from this model is shown in Figs. 6-16 and 6-17 in comparison to experiments 17, 19 and 20. A very good agreement of the predicted and the experimentally observed drying time was found for  $\theta \cong 43^\circ$  and  $r_0 = 0$ , i.e. for the assumption of sharp corners (Vorhauer et al. 2014, Vorhauer et al. 2015), given  $N = 4$  (Fig. 6-16a), because then the film region expanded over several pore rows (Fig. 6-14). The very good agreement is explained with the lateral pinning of liquid in the microfluidic PN, also referred to as the edge effect (Section 4.2.2.2). As already explained earlier, the pinning of the liquid phase is associated with wall covering continuous liquid films along the vertical side walls of the PN. This allows for a significantly higher position of the liquid phase at the lateral boundaries compared to the center of the PN. Consequently, the overall drying rate can be higher in the microfluidic PN. This elevation of drying rate associated with the edge effect is captured much better by the continuous film model, if the parameters (basically  $\theta$  for else constant parameters) are fitted so as to allow for an agreement of the overall drying time (compare Figs. 6-14 and 6-16).



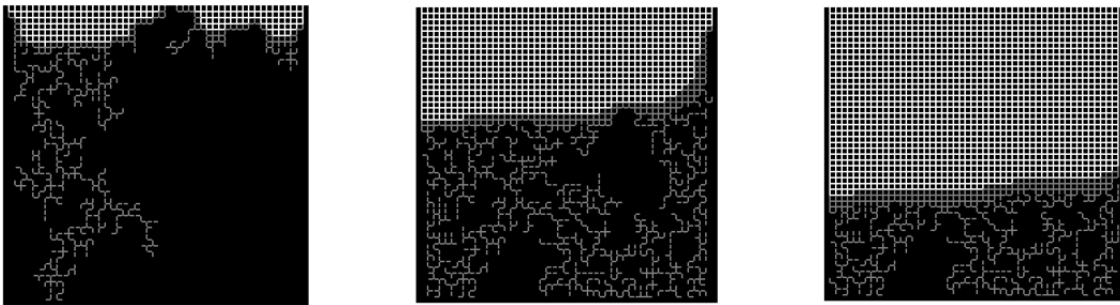
**Figure 6-17** Phase distributions referring to Fig. 6-16. Liquid films in gray and bulk liquid phase in black. The structure of clusters is identical to Fig. 6-1b. The position of the evaporation front refers to the LAP of the film region. Breakthrough at  $S = 0.79$ .  $S = [0.79, 0.4, 0.2]$ .

Then, position of the evaporation front, also denoted as the LAP of the film region, agrees with the position of the lateral pinning of liquid phase at the edges of the microfluidic PN (Figs. 6-1a, 6-15 and 6-17). This was already introduced as route 2 in Section 6.2.5.1. In addition to that, the experimentally observed position of the evaporation front in the center of the PN is also captured in this case.

The phase distributions in Fig. 6-17 reveal that the structure of the bulk liquid phase (in black) is identical with the isothermal PN simulation based on the benchmark model in Fig. 6-1b. The breakthrough is also computed for  $S = 0.79$  (if the liquid contained in liquid films is disregarded for the computation of  $S$ ). This exact agreement is based on the negligence of intercluster liquid communication in the continuous film model (Appendix B.4). In other words, the liquid films do not allow for liquid continuity in the wet region formed by the films and the liquid clusters. Instead, invasion of the clusters is computed as in the benchmark model. This feature of the continuous film model is especially relevant when comparing the simulated size and number of clusters with the experiment. It is found that a noticeably higher number of clusters occur in the experiment (Fig. 6-1a). Moreover, a high number of small clusters survive upstream of the drying front in the experiment. This is significantly highlighted by the image corresponding to  $S = 0.2$  where the position of the bulk liquid clusters (in black) is overestimated in the center of the PN (Fig. 6-17). The fit of  $\theta$  though allows to capture the evaporation front position (by adjustment of the width of the film region through the adjustment of wettability), because the film region spans the PN up to the position of the experimentally determined LAP of the drying front. But this leads to a certain inconvenience regarding the pore scale structure of the wet zone, especially concerning the size, number and position of liquid clusters. The disagreement is higher for  $S = 0.4$  and  $S = 0.2$ , thus in the period of drying when the simulated bulk liquid phase is found at an advanced position in the lower region of the PN. In addition to that, the simulated width of the film region (in gray) is incompatibly greater in this drying period than experimentally estimated, because it spans the PN from the front of the simulated bulk liquid phase to the experimentally determined position of the liquid clusters in the center of the PN and also to the experimentally determined position of lateral pinning of liquid phase (Figs. 6-1a and 6-17). The PNM with continuous liquid films can therefore very well account for the edge effect as it can predict the position of the evaporation front and based on this also the exact drying time (Fig. 6-16a). The inconvenient disagreement of the pore scale liquid structure though remains. This shows very clearly, that a macroscopic agreement of

the drying behavior (drying time and drying rate) does not necessarily induce an agreement on the pore scale. In other words, joint occurrence of several pore scale effects can lead to the same macroscopic drying behavior. This is an example for the potential use of PNMs in the pore-scale study of drying of porous media.

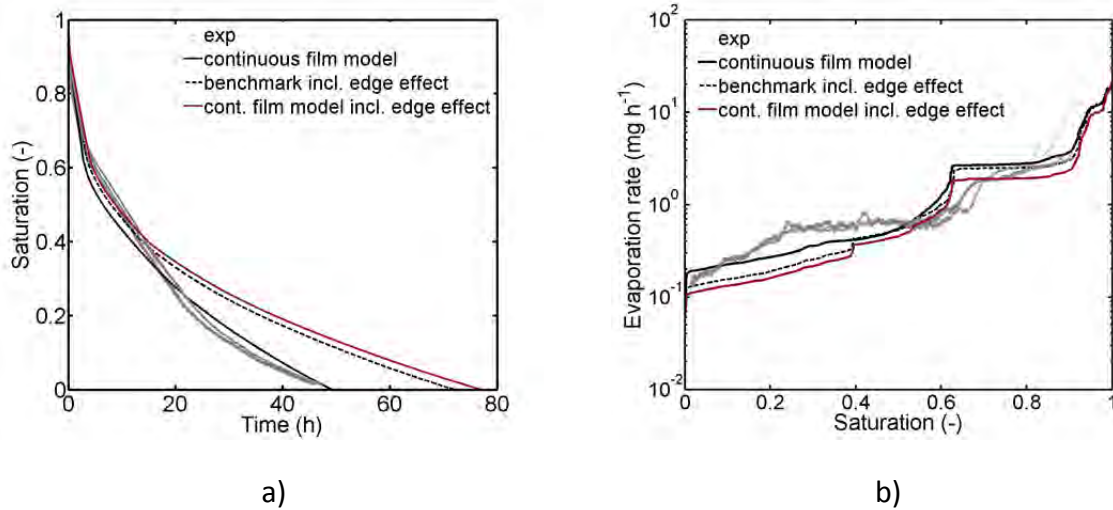
As shown in Fig. 6-18 a better agreement of the computed and the experimental pore scale liquid distribution is obtained, when the width of the film region is fitted instead of drying time. The good agreement of the extent of the film region is obtained for a slightly greater contact angle,  $\theta \cong 43.85^\circ$ , and else identical parameter setting as in Figs. 6-16 and 6-17. Additionally, the edge effect is taken into account in this approach by a combination of the benchmark model including the edge effect (according to Figs. 6-14, 6-15) and the continuous film model (according to Figs. 6-16, 6-17). Figure 6-18 indicates that the position of the liquid pinning can be partly captured for saturations of  $S \geq 0.4$ ; for  $S = 0.2$ , however, the position of the liquid phase, both in the center of the PN and at its sides, is again found to be lower than in experiments. Precisely, the most striking difference between Fig. 6-1a and Fig. 6-18 is the number, size and position of liquid clusters at  $S = 0.2$ . This leads to an overestimation of drying time as shown in Fig. 6-19.



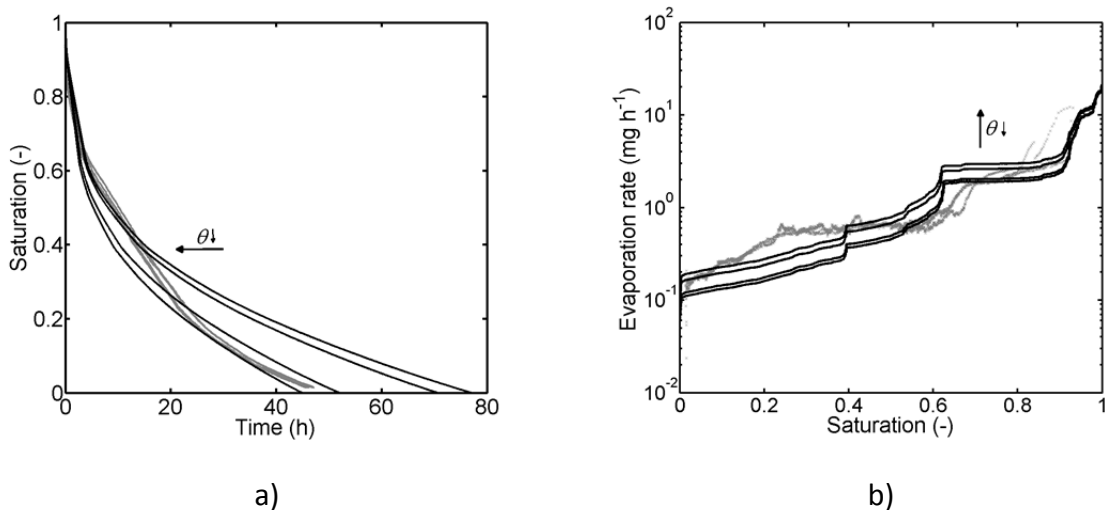
**Figure 6-18** Phase distributions from simulation with edge effect implemented in the continuous liquid film model. The wettability is adapted so as to allow for a similar extension of the film region as in the experiment ( $\theta = 43.85^\circ$ ). Breakthrough occurs at  $S = 0.8$ .  $S = [0.79, 0.4, 0.2]$ .

Interestingly, the drying curves computed from the simulations taking the edge effect into account show two distinct drops of the drying rate during the RFP (Fig. 6-19b). This is in contrast to drying with the continuous film model excluding the edge effect. It is explained with the dry out of the PN edges and advancing of the evaporation front along these edges at each of the drops. A more detailed analysis of Fig. 6-19 reveals that the edge effect can partly capture the film effect above a saturation of  $S = 0.62$  because the curves computed with the continuous film model and with the benchmark model including the edge effect are overlapping. After a transient period, the film effect controls drying at saturations lower than  $S = 0.39$ . In this period, the drying rate is underestimated with the model(s) including the edge effect (because of an overestimation of drying front position). Following the discussions above, it is obvious that fine-tuning of the wetting angle can be helpful to obtain a better agreement in this period of drying. (But again, this implies to tolerate a deviation between the predicted width of the film region and experimental observations). This is reflected by Fig. 6-20, which shows the drying curves and drying rate curves for different values of  $\theta$ . The curves are overlapping above  $S = 0.9$ , but at lower saturations ( $S \leq 0.6$ ) the different wettability of the PN affects the drying curves significantly. Most obvious are the two drops of drying rate, based on the dry out of the PN edges during the RFP, and the

different levels of the evaporation rate during the different drying periods. Interestingly, all curves overestimate duration of the CRP at the start of drying and later underestimate the drying rate. This shows that the structure of the liquid phase is still not predicted accurately with the continuous film model taking the edge effect into account. This is mainly referred to deviations in the center of the PN.



**Figure 6-19** Comparison of the drying curves (a) and drying rate curves (b) from experiments 17, 19, 20 (in gray) and the PNM corresponding to Fig. 6-18 (denoted as *cont. film model incl. edge effect*). Additionally the curves from Fig. 6-14 denoted as *incl. edge effect* and from Fig. 6-16 denoted as *continuous film model* are shown.

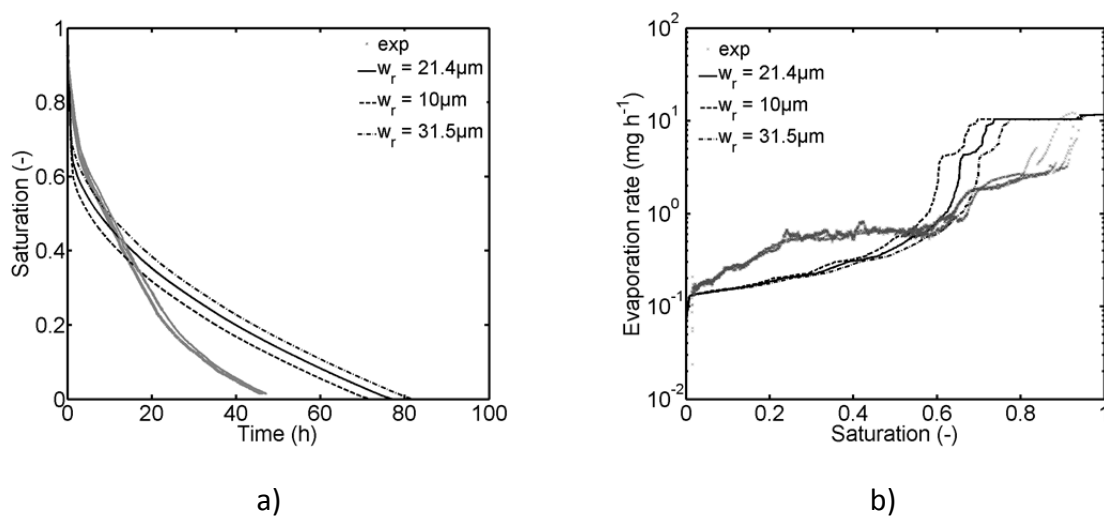


**Figure 6-20** Impact of wettability adjusted by variation of  $\theta$ . Higher wettability leads to a decrease of drying time (a) due to an increase of evaporation rate (b) based on the increasing extent of the film region and thus a position of the evaporation front closer to the PN surface. Simulations with  $\theta = [42.77, 42.97, 43.55, 43.85]^\circ$  and else identical parameter setting as in Fig. 6-18 (i.e. including the edge effect).

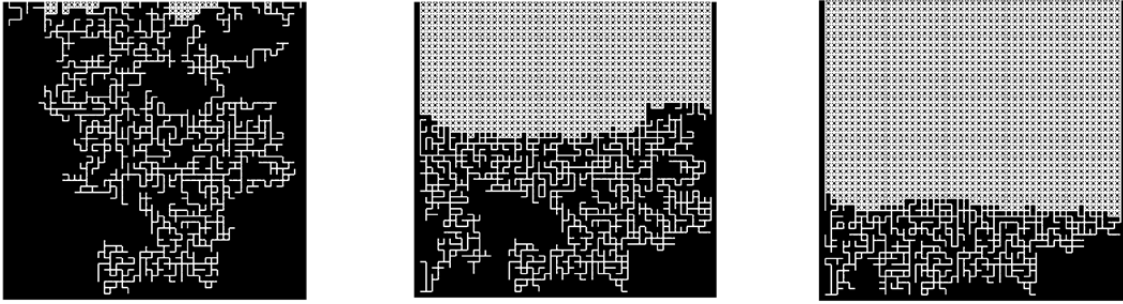
In summary, this reveals the inability of this version of the PNM to predict the structure of the liquid phase, because either the extent of the film region is overestimated or the predicted position of the evaporation front is much more advanced than in experiments. While in the first case a perfect match of the predicted drying time with the experimentally estimated drying time is obtained, in the second case the drying time is significantly overestimated. The main disagreement of the predicted pore scale liquid distributions with experiment is in the number, size and position of liquid clusters. Following this, it is assumed that a better representation of the film structure and the cluster connectivity by liquid films might lead to a better agreement of the results. This is studied in the following section.

### 6.2.5.3 Simulation with the capillary ring pore network model

Following the discussions in the previous section, the implementation of capillary liquid rings in the PNM aims at a more accurate representation of the pore scale liquid distribution. Precisely, the liquid film rings can better represent the real structure of films in the center of the PN (Section 4.2.2.1) and additionally the PNM with liquid film rings allows for a higher interconnectivity of the liquid phase. This is in contrast to the continuous film model, where the liquid clusters are not interconnected by the liquid films. As will be shown in the following, implementation of the liquid film rings with the adjusted cluster labeling allows for a better agreement of the liquid structure with experiments. Obviously, a continuous film region spanning a wide region of the PN cannot be simulated with the capillary ring model which is in contrast to the continuous film model (Prat 2007, Yiotis et al. 2004). Instead the film region is limited to the discrete film rings inside the 2-phase zone and maximum 2 pore rows above the drying front (Section 5.2.2.1). This is based on the drying of the liquid film rings as soon as they are disconnected from the main liquid phase and the screening effect of liquid rings (at least in an isothermal environment). In more detail, in isothermal drying the rings at the evaporation front must immediately dry out to fulfill the mass balance at the gas-liquid interface but pores/throats that are disconnected from the evaporation front (namely by these rings) cannot evaporate.



**Figure 6-21** Study of the PNM with capillary liquid rings. Impact of the variation of  $w_r$  and  $\alpha$  on drying curves (a) and drying rate curves (b). Comparison to experiments 17, 19, 20 (in gray). Note that the curves are overlapping for varying  $\alpha = [0.1, 2, 4]$ .

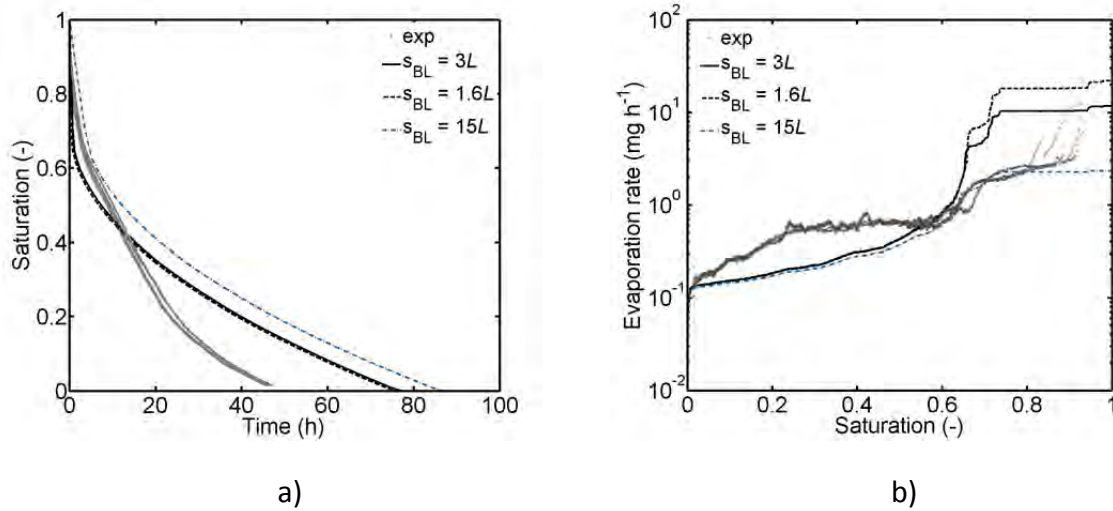


**Figure 6-22** Phase distributions from simulation with the capillary ring PNM. Simulation with  $T_{PN} = 63^\circ\text{C} = \text{const.}$ ,  $s_{BL} = 3L$ ,  $\alpha = 2$ ,  $w_r = 21.4 \mu\text{m}$ . Breakthrough occurs at  $S = 0.86$ .  $S = [0.79, 0.4, 0.2]$ .

The drying simulation presented here is realized using the benchmark model with constant temperature,  $T_{PN} = 63^\circ\text{C} = \text{const.}$  and the parameter setting in Table 6-1. The BL is adapted so as to allow interception of the experimental and the simulated curves at  $S = 0.94$ . The liquid rings as described in Section 5.2.2.1 are introduced in this model with adapted ring width  $w_r$  and evaporation interface of the rings  $\alpha$ . RLO2 (Section 5.4.4.2) is applied in the simulations presented here, thus allowing for a cluster interconnectivity by liquid rings. Figure 6-21 summarizes the results for different values of  $w_r$  and  $\alpha$ .

At first it is noted that  $\alpha$  has no impact on the drying curves since all curves are overlapping for varying  $\alpha$ . Variation of the width of the rings  $w_r$  reveals different drying behavior, namely an increasing duration of the CRP and thus decreasing drying time with decreasing  $w_r$ . This is explained as follows. Generally, larger liquid volumes can remain in the ring elements after disconnection from the bulk liquid phase if the ring width is larger because basically partially saturated liquid rings cannot be invaded (basic model assumption). As a consequence, more liquid must be removed from the larger ring elements after disconnection, thus by evaporation and vapor diffusion. As the vapor transport is by orders of magnitude slower than capillary invasion, drying decelerates for higher liquid volumes contained inside the ring elements at detachment from the bulk liquid phase. For the simulations presented here,  $w_r = 21.4 \mu\text{m}$  (as determined from the CLSM measurement) is applied. It is compared to results obtained for  $w_r = \bar{r}_{m,t} = 31.5 \mu\text{m}$ , thus ring radius identical to the mean meniscus radius in throats (Eq. 2-24), and  $w_r = 10 \mu\text{m}$ , which is an arbitrary lower limit of the film width. Note that according to Section 5.4.1 the capillary pressure of liquid rings is not computed wherefore the radius of meniscus curvature of liquid rings is not given here.

In the following the simulation results obtained for  $w_r = 21.4 \mu\text{m}$  and  $\alpha = 2$  are discussed. The phase distributions are shown in Fig. 6-22 while Fig. 6-23 shows the drying curve and drying rate curves for different BL thicknesses in comparison to experiments 17, 19 and 20. As can be seen, although structure of the liquid phase in Fig. 6-1a is well represented in the center of the PN with the ring PNM (Fig. 6-22) the drying time is strongly overestimated although a comparably long initial CRP can be simulated due to the interconnection of the liquid phase to the PN open side independently of the BL thickness (Fig. 6-23). As already mentioned earlier, the BL thickness mainly controls the initial level of the drying rate, though in the RFP the drying curves are overlapping (Fig. 6-23b) and finally the predicted drying time is almost independent of it (Fig. 6-23a).



**Figure 6-23** Comparison of the drying curves (a) and drying rate curves (b) from experiments 17, 19, 20 (in gray) and from the capillary ring PNM. The computed curves are shown for different BL thicknesses in order to demonstrate the impact of  $s_{BL}$  on  $\dot{M}_{evap}$  ( $S \geq 0.95$ ). In contrast to previous results, the persistent interconnectivity of the liquid phase leads to an overestimation of initial drying rates if  $s_{BL} = 1.6L$ , i.e. as before. Thus, the BL thickness must be increased to compensate the increased driving force at constant evaporation rates. The best agreement is obtained for  $s_{BL} = 3L$  here (thus in good agreement with the theoretical prediction).

A better agreement of drying time is expected if also the edge effect and the local variation of temperature are implemented. This is discussed in the following section.

### 6.2.6 Quasi-isothermal pore network simulation with secondary capillary invasion

Up to here it can be summarized that different pore scale effects impact on drying of the PN. The most relevant effects that control the pore scale liquid distribution and the macroscopic drying behavior, determined so far, are the local temperature variations, which control the order of invasion of the bulk liquid phase, and the secondary capillary invasion which controls the extent of the wet zone as well as the structure of the liquid phase. These effects are also referred to as the governing pore scale effects and they are jointly implemented in the PNM. The results of this implementation are presented in this section. They are obtained from PNM level 2 assigning the pore volumes to their largest throat neighbors and including the liquid rings as introduced in Section 5.2.2.1 with their specifications from Section 6.2.5.3 as well as the edge effect from Section 5.2.2.2 with specifications from Section 6.2.5.1.

The basic model parameters are again summarized as follows:

- pore size distribution from Fig. 3-3,
- temperature field from Fig. 3-8a,
- pore volumes assigned to the largest throat neighbor (no separate invasion of pores),
- liquid rings with  $w_r = 21.4 \mu\text{m}$  and  $\alpha = 2$ ,
- edge effect with  $f^{red} = 0.85$  and  $z^{pin} = (5-49)L$ ,

- temperature dependent saturation vapor pressure  $P_v^*(T)$ ,
- temperature dependent surface tension  $\sigma(T)$ ,
- directional vapor flow (vapor flow rates computed as in PNM level 2),
- BL thickness  $s_{BL} = 4.82L$  (adapted so as to fit the evaporation rates at  $S = 0.94$ ),
- no cluster growth,
- cluster labeling allowing for intercluster liquid connectivity (RLO2).

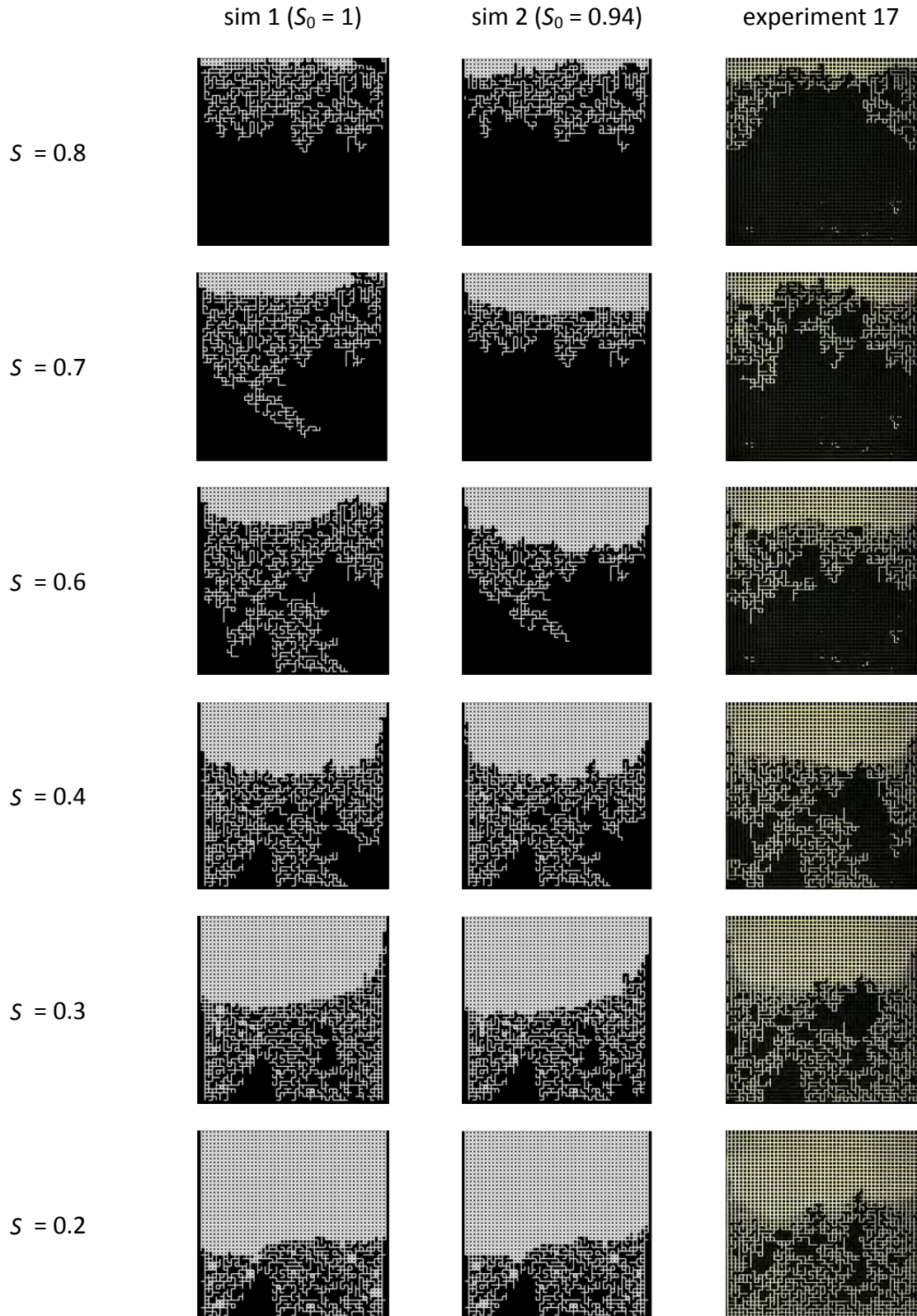
In the following, the results from two simulations are presented and discussed. In simulation 1, drying starts from the initially completely saturated PN, i.e. with  $S_0 = 1$ . In simulation 2, drying starts from the initial PN saturation determined from the drying experiments. This is  $S_0 = 0.94$  (Section 4.3). The total number of computed invasions in simulation 1 is 7252 with a computational time of 561 s (Intel i5\_4460, CPU 3.2 GHz, 8 GB RAM, 64 Bit, Matlab R2014a) and 6962 in simulation 2 ( $S_0 = 0.94$ ) with a computational time of 461 s. The neglected amount of condensed liquid volume is  $v_c^- \cong 0.02$  in both simulations. Figures 6-24 to 6-27 summarize the comparison of drying experiments 17, 19, 20 and simulations with the non-isothermal PN model incorporating the governing pore effects.

### 6.2.6.1 Phase distributions

Figure 6-24 reveals that very similar phase distributions as in experiment 17 are obtained with the PNM, almost independently of the initial saturation. However, breakthrough is predicted at  $S = 0.64$  in simulation 1 and at  $S = 0.55$  in simulation 2, thus for a slightly higher overall PN saturation than experimentally observed ( $S = 0.53$ ). In this context it is again noted, that saturation of the microfluidic PN might be effectively higher than estimated, because e.g. liquid films are not detected by image analysis. Furthermore, partially saturated pores and throats are ignored and only the liquid elements with a saturation of  $S_{p,t} \geq 0.8$  are identified as liquid saturated. These assumptions might lead to an apparently lower overall PN saturation in the microfluidic PN and thus to slight deviations of phase distributions in Fig. 6-24. However, the main features of the experimental invasion process are captured by the PNM, except at the end of the drying process ( $S = 0.2$  in Fig. 6-24). It is found that the LAP of the drying front in the microfluidic PN is closer to the network surface at  $S = 0.2$ . This is explained with a more pronounced edge effect than predicted with the model and a wider liquid film region in the center of the PN (interconnecting the small liquid clusters). The better agreement though is obtained when the simulation is started at  $S_0 = 0.94$ , because mainly the structure of the liquid phase is predicted with a higher similarity especially for  $S \geq 0.6$  and the predicted breakthrough ( $S = 0.55$ ) is much closer to the experimental result. However, the difference between the two drying simulations diminishes after the breakthrough.

The saturation profiles in Fig. 6-25 reveal that the position of the drying front in the first period of drying is very well predicted with both simulations (the saturation curves for  $S \geq 0.3$  are found at a position close to the PN surface). However, at lower saturations ( $S \leq 0.2$ ) the drying front position is less advanced in the experiment, as already shown in Fig. 6-24. The local increase of slice saturation close to the PN open side at the beginning of drying in simulation 1 is a result of the two larger surviving clusters close to the PN surface

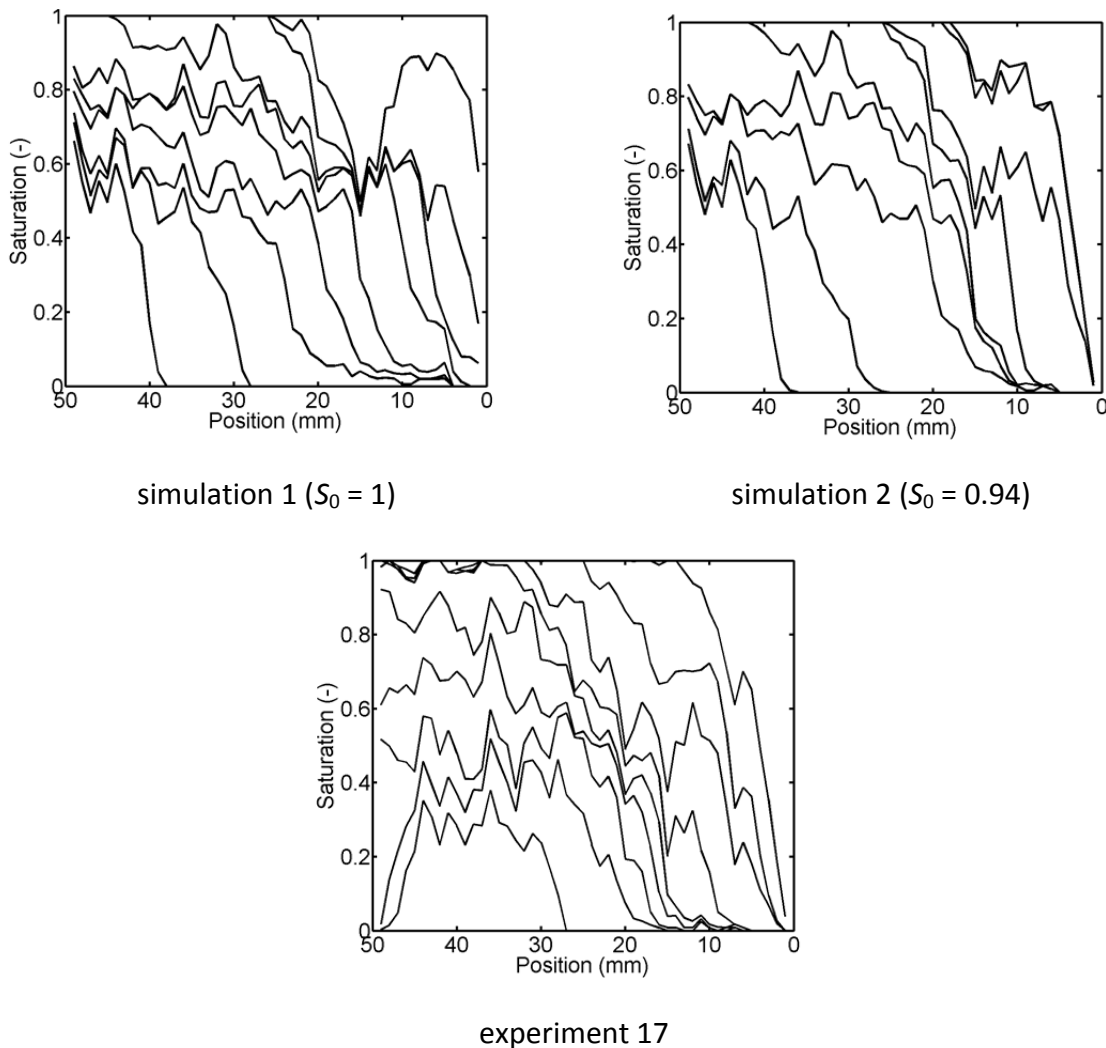




**Figure 6-24** Phase distributions from simulations with  $S_0 = 1$  and  $S_0 = 0.94$  and  $s_{BL} = 4.82L$ . Comparison to the quasi-isothermal experiment (right). Breakthrough at  $S_0 = 0.64$  in simulation 1 and at  $S_0 = 0.55$  in simulation 2.

(Fig. 6-25). This effect is partly diminished in drying simulation 2 (Fig. 6-25). At later drying stages, the saturation profiles are almost S-shaped with apparently homogeneously distributed liquid in the region of higher saturation level (Fig. 6-25). The structure of the saturation profiles is almost independent of the initial PN saturation (for  $S < 0.8$ ) and furthermore the simulated structures are in very good agreement with the experimental drying process (for  $S \geq 0.3$ ). However, at low saturations the liquid phase detaches from the PN bottom in the drying experiment. This is not predicted by the simulations. This might partly be explained by the underestimation of liquid connectivity in the PNM.

A still better agreement of simulation and experiment is expected if the image analysis would be improved based on a higher resolution of images (which could be obtained with a camera of higher resolution). Additionally, the exact pore structure, so far roughly approached by rectangular shape, could be experimentally analyzed (e.g. by CLSM or white light interferometry) and transferred to the PNM with the purpose to match liquid volumes in pores and throats. These measures could help to match the profiles for  $S \geq 0.3$ . Anyway, they will not basically affect the results for  $S \leq 0.2$ , because the disagreement of the curves is rather associated with an underestimation of liquid connectivity. It is thus proposed to verify experimentally the assumption of the structure of liquid films e.g. by Raman spectroscopy (using a microfluidic model sealed with a transparent glass plate) (e.g. Quino et al. 2016).

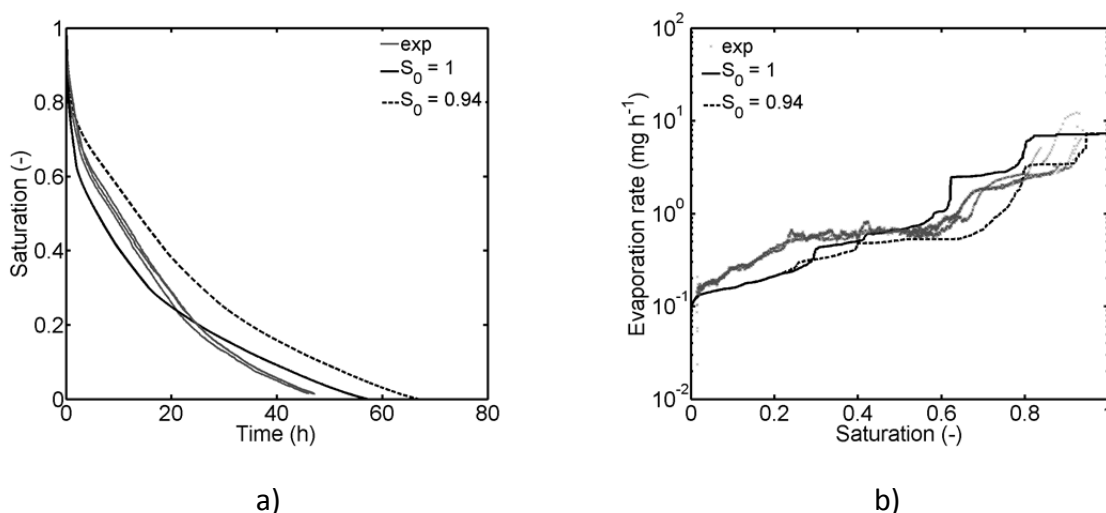


**Figure 6-25** Saturation profiles for  $S = [0.1:0.1:0.9]$  (from right to left).

### 6.2.6.2 Drying curves and drying rate curves

Figures 6-26a,b summarize the drying curves and drying rate curves corresponding to Figs. 6-24 and 6-25. Figure 6-26a indicates that the overall drying time can be well predicted with the proposed PNM (in simulation 1). Though, structure of the drying rate curve in Fig. 6-26b is better predicted with simulation 2. Independent of this, both simulations predict well the five drying periods as observed in experiments (Section 4.3.2), if the initial CRP in simulation 1 is disregarded.

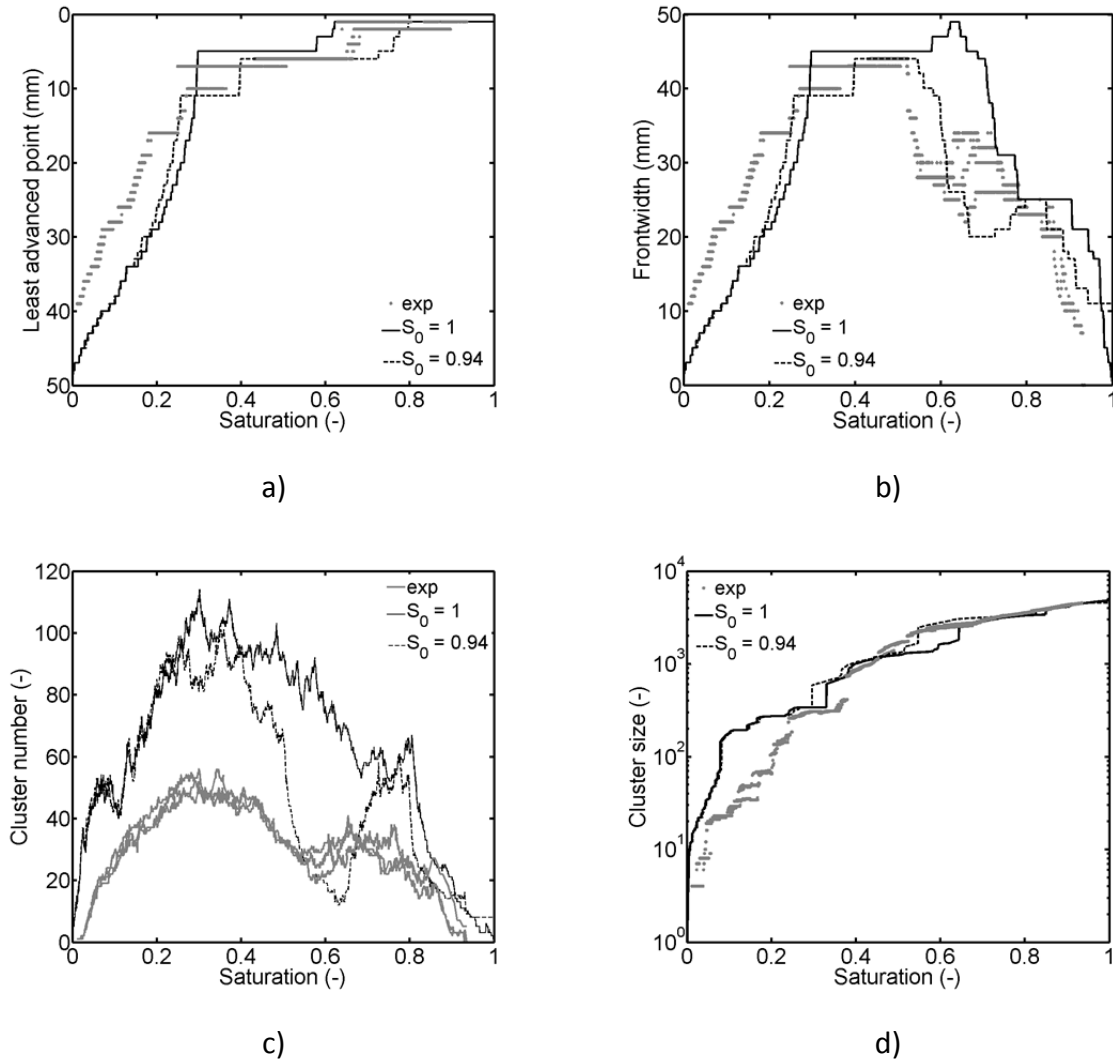
In detail, in simulation 2 the drying rate drops initially due to the partial dry out of the PN upper pore rows, followed by a CRP which is related to the initial interconnectivity of the liquid phase and the PN surface, and then followed by another drop of drying rate once this interconnectivity vanishes while the liquid phase remains pinned at position  $z^{pin} = 5L$  due to the edge effect. Then the drying rate is temporally constant due to the pinning of the liquid phase. The third drop of drying rate at  $S \cong 0.4$  is related to the dry out of the left PN side wall. This was not observed in the drying experiment, where the evaporation front remained on a higher level until low saturations and where the drying rate decreased with a smaller slope at low saturations (Fig. 6-25 and Section 4.3.2). With simulation 1, also three drops of drying rate are simulated. The disagreement to experiments is especially obvious at the start of drying, where a CRP is simulated and where the level of evaporation rate is overestimated. This is explained by the sustained liquid connectivity to the PN surface, which is obviously higher if  $S_0 = 1$ . The overestimation could partly be overcome by increase of the BL thickness as explained before. Again, at the later stages of drying (especially for  $S \leq 0.2$ ) the drying rates are underestimated (the curves from both simulations are overlapping in this stage). This is explained by the more advanced position of the evaporation front in simulations and causes the overestimation of the drying time. This effect is partly assigned to the simplification of the edge effect by increasing the invasion threshold pressure of the side throats (separate invasion of pores is not computed here). Additionally, the interconnectivity of the liquid clusters at low saturations might be underestimated with the ring PNM.



**Figure 6-26** a) Drying curves and b) drying rate curves corresponding to Figs. 6-24 and 6-25 and from experiments 17, 19, 20 (in gray).

### 6.2.6.3 Structural analysis of pore scale liquid distribution

Figure 6-27 summarizes the results of a statistical analysis of the structure of the liquid phase corresponding to Figs. 6-24 to 6-26. This includes analysis of the temporal evolution of the LAP of the drying front, the width of the partially saturated zone, the cluster number and cluster size. The figures reveal partly different trends in the two simulations (in Fig. 6-27a-c simulation 1 yields higher values), but the curves overlap for saturations of  $S \leq 0.2$ .



**Figure 6-27** Pore scale analysis of the simulation results. Comparison to experimental drying (in gray). a) Least advanced point of the drying front, b) frontwidth, c) number of clusters, d) maximum cluster size.

The main deviations between PN simulations and drying experiments can be summarized as follows. The drying front recedes earlier in the simulation (at  $S \cong 0.3$  and  $S \cong 0.25$  in Fig. 6-27a). In simulation 1, breakthrough of the gas phase occurs while the LAP of the drying front is still connected to the PN open side, leading to a drying front intermediately spanning the complete PN (Fig. 6-27b). The drying frontwidth is basically underestimated at high saturations and also at low saturations. The number of clusters is in general overestimated. At first sight, this appears surprising in the face of the higher interconnectivity of the liquid phase achieved with the applied RLO2, though this is in agreement with images in Fig. 6-24.

An explanation of the deviations is the expected underestimation of single liquid bridges (as in Fig. 4-3) interconnected with liquid rings by the image processing algorithm (Section 3.4). However the trends are very well represented by both simulations (Fig. 6-27c): the initial increase in the cluster number is followed by an intermediate drop and another increase before the cluster number decreases at low saturations. The drop of cluster number is significantly more evolved in simulation 2 related to the temporally narrower drying front (also refer to Figs. 6-24 and 6-25). Independent of this, the maximum cluster size is very well predicted with both simulations; though it is partly overestimated at the end of drying ( $S \leq 0.2$ ) (Fig. 6-27d). This might be explained with the underestimated liquid connectivity from image processing, because basically the liquid films are not identified with this method.

### 6.2.7 Summary

In summary it was proven that the proposed PNM can very well predict drying of the microfluidic PN if the physical mechanisms incorporated in this PNM are well adapted. These are the temporal stabilization of the liquid phase in presence of the slight temperature variation and the control of the internal liquid structure by secondary capillary invasion. Contrary, viscous effects and competitive pore and throat invasion are assumed to play a minor role in the given combination of PSD and temperature setting. In contrast to other studies, it could be shown that agreement of both, pore scale phase distributions *and* macroscopic drying rates as well, can be achieved if the distinct pore scale effects are considered. Exemplarily, the continuous film PN simulation showed very good agreement of drying curves but could not capture the position of the drying front in the center of the PN. This was explained with the pinning of liquid at the side walls of the PN. This effect is based on continuous liquid films covering the PN side walls, which was indeed captured by the continuous film model. But at the same time, the structure of the liquid phase in the center of the PN was very different from experiment. Namely, smaller liquid clusters could survive in the center of the microfluidic PN, almost at the same level as the liquid pinning. The continuous film model could not predict this behavior; instead a wide film region (without any liquid clusters) developed in the dry region upstream of the cluster front. The structure of the film region, spanning the PN over a wide space, was also contradictory to experimental observations which revealed that the liquid films in the PN center rather resemble discrete rings instead of the PN covering continuous film region. Consequently, the continuous film PNM overestimated the film region in the center of the PN. This drawback of the model is explained with the negligence of intercluster liquid communication. It was shown that this can lead to identical distribution of the bulk liquid clusters in the simulations without film and with film. At the same time, the pore scale morphology of the liquid distribution cannot be studied with this model.

In contrast to that, experiment based implementation of the ring structure in the PNM results in an overall better agreement if the edge effect is taken into account. This is, however, realized by a simplified method based on the reduction of invasion pressure thresholds of pores and throats along the side walls of the PN. A better agreement, especially at low saturations, is expected if the continuous film model and the ring model are combined. This could be achieved if the ring elements are implemented as additional liquid elements in the film model. However, the problem of the absent cluster connectivity would remain. This could be overcome by adaption of the cluster boundary conditions in the film model. (And this could also be seen as a step towards a non-isothermal continuous film

PNM). Another option would be the adaption of cluster labeling in the ring PNM so as to allow for liquid connectivity over a longer range.

In summary it was shown that the PNM with liquid rings and edge effect can provide very good agreement in terms of phase distributions *and* drying rate and drying time. Remaining differences in the pore scale liquid structure (revealed by the statistical study of the partially saturated zone) might be abolished by further improvement of the image analysis with the purpose to detect more carefully residual liquid in films (combined with the application of an optical camera with higher resolution) as well as a more complex implementation of the liquid films. Independent of this, position of the drying front could be predicted over the longest period of drying. The main deviations were determined for low saturations ( $S \leq 0.2$ ), i.e. when liquid films become increasingly important.

### **6.3 Drying with imposed thermal gradients**

If a temperature gradient is imposed on the PN during drying, significantly different drying behavior than in the quasi-isothermal situation is observed: stabilization of the drying front in presence of a negative thermal gradient and destabilization of the liquid phase with early breakthrough of the gas phase and initiation of a travelling 2-phase zone in presence of a positive thermal gradient. While in case of a negative thermal gradient both, impact of secondary capillary effects as well as condensation induced cluster growth are a priori expected to diminish (because vapor flows in the direction of temperature increase and the temperature gradient is expected to stabilize the drying front), these effects are supposed to dramatically affect drying in presence of the travelling 2-phase zone initiated in the second case (because vapor flows against the temperature increase and the secondary capillary structures can sustain liquid connectivity in the 2-phase zone). Consequently, in what follows, both drying modes are compared in face of these effects. Additionally, again the impact of the edge effect will be studied. It is found that the secondary invasion along the lateral edges of the PN controls drying in the stabilizing regime, thus contradicting the assumption of a stabilized drying front. Especially the sustained liquid interconnectivity with the tip of the drying front pinned at the PN side walls (at higher temperature) and the partial back-diffusion of vapor to the drying front in the center of the PN (at lower temperature) can induce a heat pipe effect leading to the growth of clusters. This is in contrast to the assumptions of PNMs ignoring the cluster growth mechanism and liquid films. In the destabilizing regime, however, the edge effect diminishes because position of the drying front is found close to the PN surface over the longest period of drying.

For this study, the two simulation routes sketched in Chapter 5 are applied: route 1, non-isothermal PNM with liquid rings and edge effects, is applied for the negative thermal gradient. Route 2, PNM with the cluster growth mechanism in its different versions, namely PNM level 2, level 3 and level 4 with CLO1, CLO2 and CLO3 (refer to Fig. 5-17 for a definition), is applied for both, positive and negative thermal gradient.

#### **6.3.1 Pore network drying with stabilizing thermal gradient**

In this section, the theoretically predicted drying behavior under non-isothermal conditions similar as in a drying process with hot convective air is compared to experimental drying of

the SiO<sub>2</sub> microfluidic network (presented in Section 4.4.1) based on the temperature profile in Fig. 3-8b. Table 6-2 summarizes the parameters of this study that are different from the study above (i.e. adapted to experiments). The BL thickness is again adapted so as to allow similar evaporation rates as in the experiment (at  $S_0 \cong 0.91$  here). Note that the BL thickness is significantly decreased compared to the situations discussed above according to the higher temperature at the PN open side (in agreement with discussions in Philip and de Vries (1957)). If not other mentioned, this parameter set is applied in PN simulations presented below. An overview of all simulations presented in this thesis is given in Appendix C.

**Table 6-2** Summary of model parameters.  $P, P_v^\infty, L, L_d, \cos\theta$  as in Table 6-1.

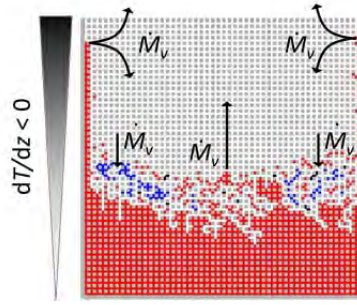
$T_{BL}$	$T^{min}$	$T^{max}$	$\bar{T}$	$S_{BL}$	$f^{red}$	$z^{pin}$
25.2°C	51.64°C	74.76°C	64.22°C	500 μm	0.85	(5-49)L

In this study, the two different routes introduced earlier are used. Again, in route 1 drying is simulated based on the assumption that the invasion process is controlled by capillary invasion, thus taking into account the secondary capillary invasion as well as the temperature dependence of the involved physical parameters. But cluster growth is disregarded in this route; due to this, the competitive invasion of pores and throats is not implemented. In route 2, the liquid ring elements are disregarded. Instead, the invasion process is assumed to be partly controlled by vapor diffusion (during the period of drying when the liquid phase has split up) and thus the various levels of the cluster growth mechanism are studied while the interconnectivity of the liquid phase is adjusted by the cluster labeling. The edge effect is accounted for in both routes with the purpose to study its impact on the drying rate and drying time as well as on the condensation effect. In summary, in the following the results from 7 different simulations are discussed and compared with the results from experiments 8, 13 and 15:

- simulation with the PNM already sketched in Section 6.2.6 (PNM level 2 assigning the pore volumes to their largest throat neighbors, including liquid rings and the edge effect),
- simulation with PNM level 2,
- simulation with PNM level 3,
- simulation with PNM level 4 and CLO1
- simulation with PNM level 4 and CLO2
- simulation with PNM level 4 and CLO3

Except of the first case, liquid rings are ignored and competitive pore and throat invasion as well as the edge effect are incorporated.

The most striking difference between the different options of the PNM is the consideration of the condensation effect and the different manipulation of the cluster labeling. This can affect the simulation results in presence of the edge effect as explained on the example of Fig. 6-28. Precisely, Fig. 6-28 illustrates that the lateral pinning of liquid phase allows for an



**Figure 6-28** Illustration of evaporating (red) and condensing (blue) clusters visualizes the elevated position of the evaporation front at the side walls of the PN (with higher temperature) and condensation in the center of the PN, where the temperature is lower. Notice that condensation occurs in the left and right wing of the central front whereas evaporation occurs at the axis. This reveals the screening effect of evaporation by the wetted side walls. Clusters without net condensation and evaporation are shown in black. Simulation with CLO2,  $S = 0.37$ .

elevated evaporation front because liquid from the large liquid cluster at the bottom side of the PN can be evaporated from the tip of the liquid phase interconnected along the PN edges. This cluster is shown in red. Consequently, liquid interconnectivity from the bottom of the PN with the regions close to the open side of the PN is sustained for a longer period than in a drying process without edge effect. Figure 6-28 also indicates that the vapor, evolving at the tip of the drying front pinned at the side walls of the PN (at higher temperature), partly migrates towards the drying front in the center of the PN (at lower temperature). This leads to the condensation of vapor at the cluster boundaries in this region (indicated by the smaller blue clusters). Exemplarily, the ratio of condensed liquid volume using PNM level 4 and CLO2 is only  $\cong 2\%$  ( $N_{steps} = 11497$  and  $t_{comp} = 0.64$  h) if the edge effect is ignored. Contrarily,  $\cong 5\%$  of the total liquid volume is condensed in the simulation with edge effect (Table 6-3). More precisely, the neglected volume ratio of condensed liquid, computed from Eq. 5-81 with  $\bar{\rho}_l = 981.13$  kg m<sup>-3</sup> (mean density in the given temperature range), varies depending on the model approach (Table 6-3). Surprisingly, the ratio of neglected condensed liquid is higher in PNM level 3, although refilling of partially filled throats and pores is allowed in this model (while no refilling occurs in the simulation with PNM level 2). This indicates that the computed (slight) structural differences allow for a higher condensation effect in PNM level 3.

**Table 6-3** Dependence of the condensation effect on the version of the PNM and its impact on the computational effort (Intel i5\_4460, CPU 3.2 GHz, 8 GB RAM, 64 Bit, Matlab R2014a).

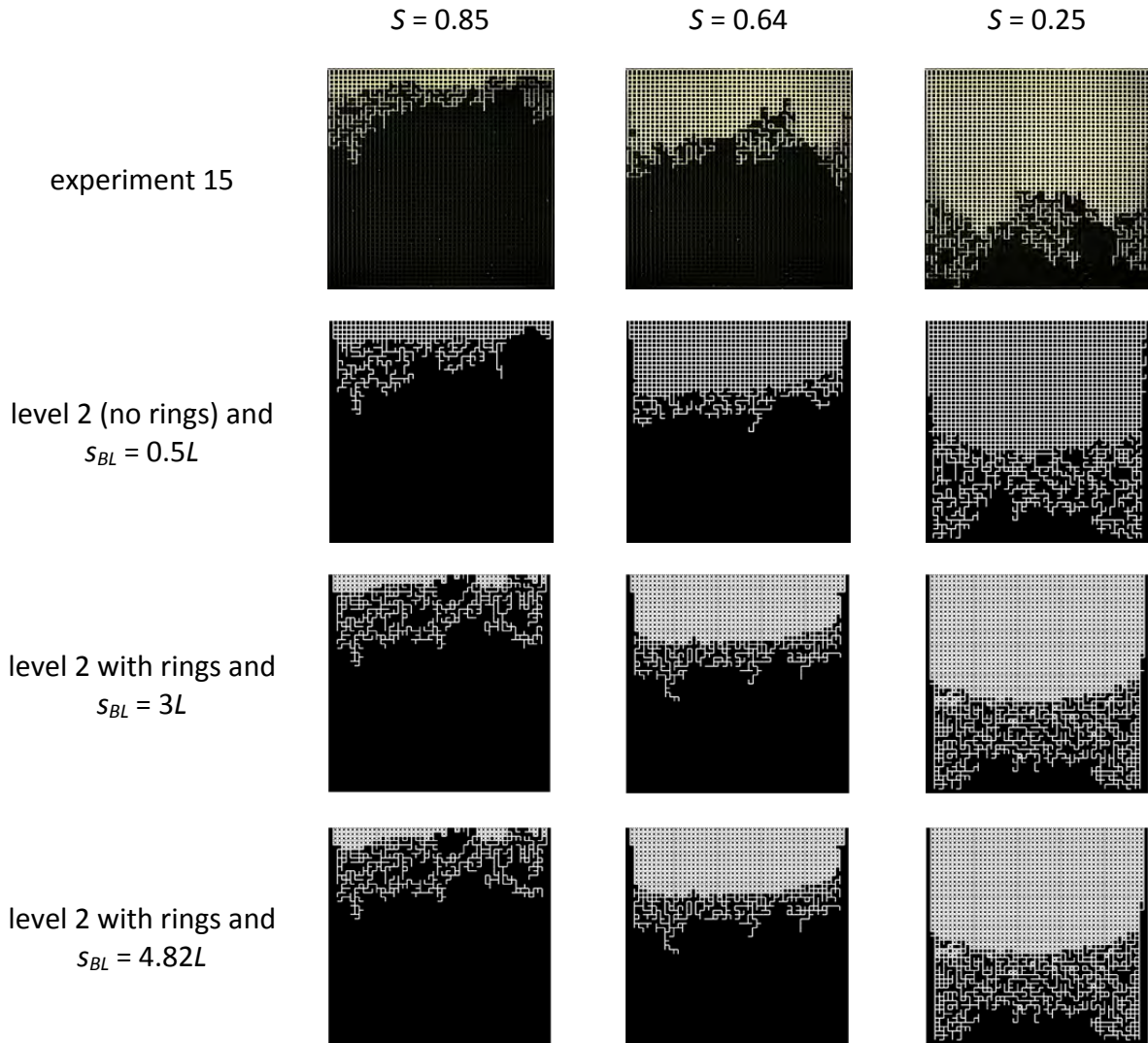
Parameter	Level 2	Level 2, incl. rings	Level 3	Level 4, CLO1	Level 4, CLO2	Level 4, CLO3
$v_c^{+,-}$	0.12 ( $v_c^-$ )	0.06 ( $v_c^-$ )	0.18 ( $v_c^-$ )	0.10 ( $v_c^+$ )	0.05 ( $v_c^+$ )	0.13 ( $v_c^+$ )
$N_{steps}$	7301	7252	7461	133156	13790	19200
$t_{comp}$	204 s	408 s	209 s	9.86 h	1 h	1.77 h



In comparison, the ratio of condensed liquid volume in PNM level 4, computed from Eq. 5-80 with density varying between  $\rho_l(T^{min}) = 974.98 \text{ kg m}^{-3}$  and  $\rho_l(T^{max}) = 987.28 \text{ kg m}^{-3}$ , is smallest for CLO2 (Table 6-3). The high ratio with CLO3 is explained with reduced oscillation of evaporating/condensing clusters and the resulting stabilization of cluster invasion. This allows for longer periods of refilling of partially saturated elements, while with CLO1 evaporating and condensing clusters are strongly oscillating (which is also reflected by the curves shown in Fig. 6-33 below). This shows that partially saturated pores/throats computed with the algorithm presented in Chapter 5 impact on the condensation effect. The different ratios of condensed liquid volume have an impact on the computational time because the liquid phase experiences several cycles of evaporation/condensation before it finally leaves the PN (Table 6-3). This is revealed by the remarkably high number of invasion steps using PNM level 4. (It is highlighted that the number of invasion steps can be reduced using PNM level 4 and CLO3). And it is also reflected by the drying curves in Fig. 6-32 below.

### 6.3.1.1 Phase distributions

Phase distributions of the non-isothermal drying experiment are compared with the simulated phase distributions for the 6 different model approaches in Fig. 6-29 (experiment and PNM level 2 in its different versions) and Fig. 6-30 (PNM level 3 and level 4 in its different versions). Almost identical overall liquid distributions are simulated with the different versions of the PN: the liquid phase recedes from the PN open side at the start of drying, resulting in the formation of a growing dry zone connected to the PN open side and a shrinking saturated zone connected to the PN bottom side. The intermediate 2-phase zone evolving between the totally dry and the totally wet zone is of finite width but growing while travelling downwards. It is highlighted that the lateral pinning of the liquid phase at the PN's left and right sides leads to temporally wetting of the PN edges at a constant position in each of the presented simulations, similar as observed on the images from experiment 15 (upper row in Fig. 6-29). In summary it is found that the predicted structures of the main liquid cluster as well as the intermediate 2-phase zone are very well predicted with each version of the drying model. In addition to that, the good agreement of the simulated phase distributions in Fig. 6-29 indicate that the initial level of the evaporation rate, controlled by  $s_{BL}$ , does not affect the internal liquid distribution as no differences are found between the images of row 3 and row 4 in Fig. 6-29. The agreement of phase distributions with experiment 15 is slightly better with PNMs ignoring the liquid rings. Additionally, the PNMs with cluster growth mechanism (PNM level 4 and CLO1, CLO2) predict slightly larger liquid clusters in the 2-phase zone as a result of the vapor diffusion from the elevated evaporation front at the PN side walls towards the colder liquid clusters in the center of the PN. Figures 6-29 and 6-30 also indicate that position of the LAP of the front is captured by all models if one regards the center of the PN. Position of the liquid front at the lateral edges of the PN, however, is rather overestimated (i.e. more advanced than in experiments) independently of the different consideration of liquid interconnectivity (by liquid rings and/or cluster labeling). The edge effect though appears stronger in the phase distributions obtained from PNM level 4 and CLO2 (especially at  $S = 0.25$ ) which is associated with the high liquid interconnectivity achieved by cluster labeling. This indicates that simplification of the wetting of the side walls (by artificially increasing the entry pressure thresholds) might not yet fully capture the physical phenomena of the edge effect but that rather the liquid connectivity should also be considered.

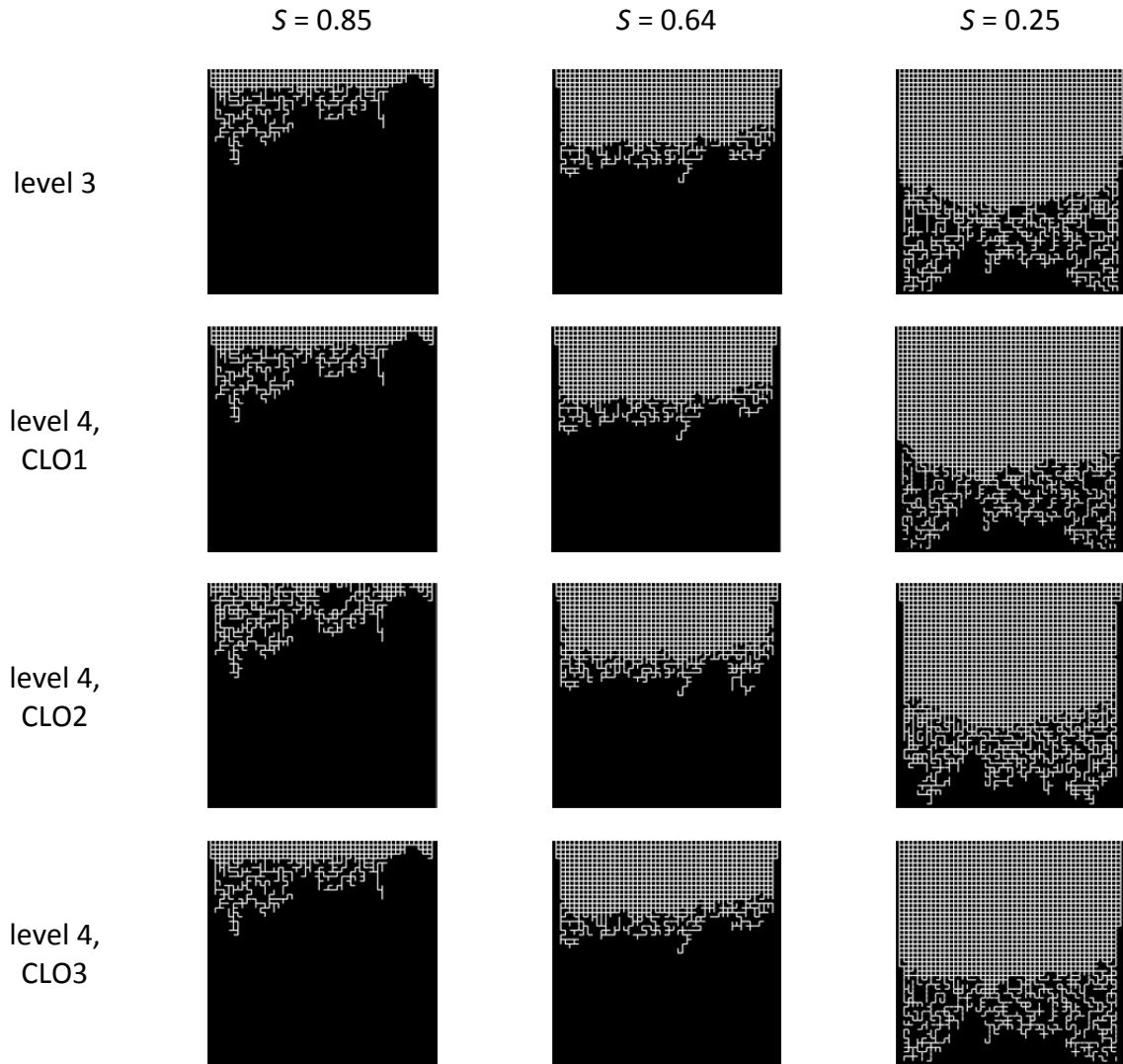


**Figure 6-29** Phase patterns from drying with imposed negative thermal gradient. The results obtained for different  $s_{BL}$  indicate that the drying behavior is not controlled by the initial value of the evaporation rate (resulting from the different BL thicknesses). Pores are shown in black for  $S_p > 0.8$  (in row 2; in rows 3 and 4 the pore volumes are assigned to their largest throat neighbors).

This is also reflected by the drying curves and drying rate curves presented in the following section. This problem might partly be overcome if the capillary entry pressure of the lateral pores and throats would be further reduced in order to allow sustained connectivity to liquid rings (Fig. 5-12). This would require revision of the current PNM regarding the invasion rules and the order of invasion (see Section 5.4.1).

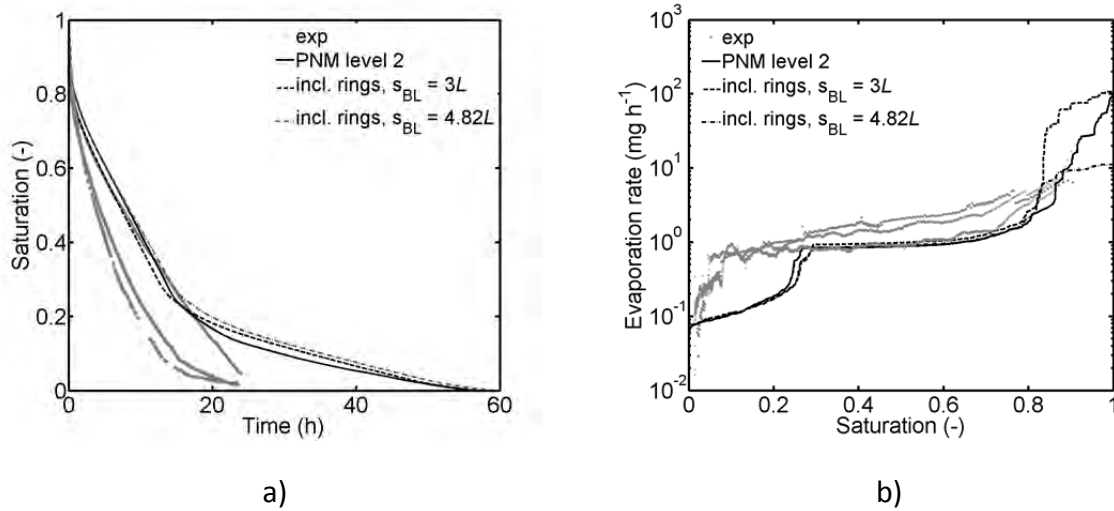
### 6.3.1.2 Drying curves and drying rate curves

Figures 6-31 and 6-32 summarize the drying curves and drying rate curves corresponding to the simulations and experiment 15 shown in Figs. 6-29 and 6-30. Additionally, the drying curves of experiments 8 and 13 are given.



**Figure 6-30** Phase patterns from simulation with refilling of only partially saturated liquid elements (PNM level 3) and simulation with cluster growth (PNM level 4). Pores are shown in black for  $S_p > 0.8$ . Simulation with  $s_{BL} = 0.5L$ .

Precisely, Fig. 6-31, comparing the simulation results from PNM level 2 in its different versions, reveals at first that the choice of the BL thickness has an impact only on the initial level of the evaporation rate (as already expected before and discussed in the context of quasi-isothermal drying in Section 6.2.1). Exemplarily, the initial drying rate period is significantly overestimated using  $s_{BL} = 3L$ ; a better agreement is found for  $s_{BL} = 4.82L$ . The deviation from the theoretically predicted value is explained with overall higher temperatures at the PN surface. Additionally, the BL thickness could not be exactly estimated for  $S = 1$  because essentially no experimental data is available. However, Fig. 6-31 also shows that the drying process is not controlled by the CRP because almost identical drying times are predicted independently of the initial drying rate period due to the overlapping of the curves in the later periods of drying. The simulated CRP is, however, in contradiction to drying experiments, where no CRP could be observed. Independently of this, two drops in the drying rates, as in experiments, are identified from the simulated curves. The first drop is related to the dry out of the PN surface pores and the second drop is related to the depinning of the liquid phase from the PN side walls. The intermediate long

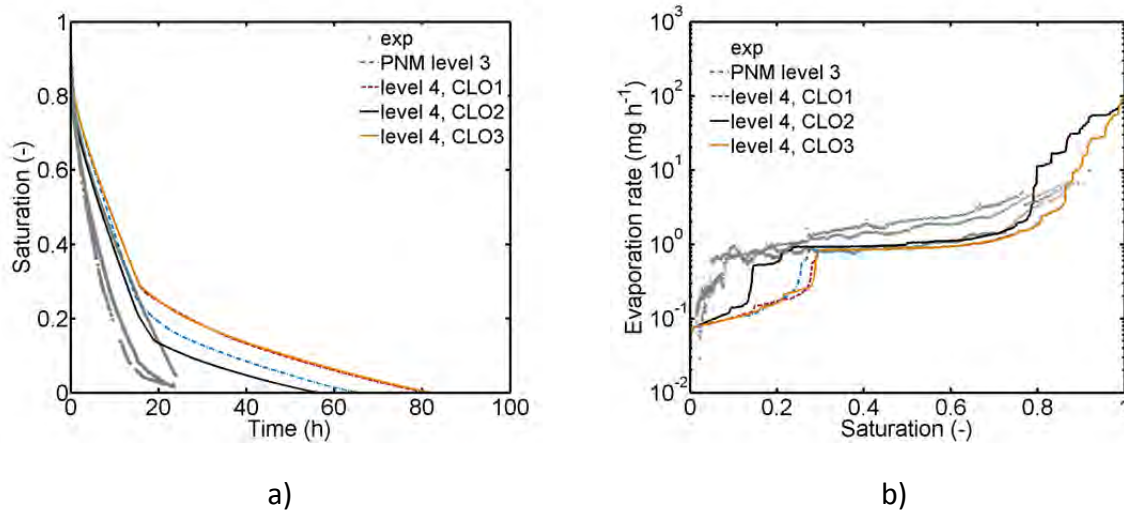


**Figure 6-31** Drying curves (a) and drying rate curves (b) corresponding to Fig. 6-29 and experiments 8, 13,15 (in gray).

period of relatively high and constant drying rates indicates that the liquid phase is interconnected along the lateral edges allowing for a constant elevated position of the evaporation front closer to the PN surface. This is very similar to the drying experiments. Though, the second drop of drying rates occurs obviously too early in every simulation in Fig. 6-31. The best agreement is achieved with experiment 15 (Fig. 4-24), where the edge effect is less evolved than in experiment 8 and 13 (see Section 4.4.1 for a further discussion). But obviously, the edge effect plays a major role at low saturations in experiment 15. This is not captured by the PNM.

Similar trends are also found in Fig. 6-32. In detail, the drying rate curves related to PNM level 3, PNM level 4 and CLO1 and CLO3 are very similar as the curve for PNM level 2 ignoring liquid rings in Fig. 6-31 (Fig. 6-32b). The drying rate curve simulated with PNM level 4 and CLO2 (highest cluster interconnectivity) instead is rather similar to the drying rate curves obtained for simulations with liquid rings in Fig. 6-31. The overestimation at the start of drying could be explained with absence of liquid films at the high initial evaporation rates in the microfluidic PN. Note that additionally, due to the late start of data recording in experiments, comparison of the curves at the very start of drying is not possible. Apart from that, the partial agreement of the two curves shows that the effect of liquid rings might be captured by simply adjusting the cluster labeling in PNM level 4 and CLO2. Also a later second drop of the drying rate is predicted with this model revealing a more prolonged connectivity of the liquid phase along the PN edges than obtained by the introduction of the edge effect and liquid rings. This version of the PNM though yields the best prediction of drying rate curves and drying time.

Deviations (of the predicted drying time) between PNM level 4 and CLO2 and PNM level 4 and CLO1, CLO3 also reveal the impact of vapor transport in the PN with imposed negative thermal gradient after disconnection of the liquid clusters. The predicted drying time can be around 60 % longer in the simulation taking the temperature dependency of vapor transport and the resulting condensation effect into account (PNM level 4 and CLO1, CLO3) (compared at  $S \cong 0.04$ ). This is not obtained from PNM level 4 and CLO2 because the liquid clusters are principally globally connected over the longest period of drying. The diffusion of vapor



**Figure 6-32** Drying curves (a) and drying rate curves (b) corresponding to Fig. 6-30 and experiments 8, 13, 15 (in gray). The best agreement is found for experiment 15 (see also Fig. 4-24) and PNM level 4, CLO2.

towards the colder region of the drying front (in the PN center) is thus compensated by the high drying rates at the tip of the front at the PN side walls. Consequently, condensation plays a minor role in this PNM. A similar result is found in the PNM with liquid rings (Table 6-3).

So far it is summarized that although the simulated phase distributions appear almost identical in Figs. 6-29, 6-30 comparison of drying curves and drying rate curves in Figs. 6-31, 6-32 reveals significant differences. The predicted drying time is overestimated at least by factor 3 in PNM level 4, CLO1 and CLO3 (also due to condensation) and by factor 2 in PNM level 2, level 3 and level 4, CLO2 (compared to the final saturation in experiments, i.e.  $S \cong 0.02$  to  $S \cong 0.04$ ). Overestimation of drying time is mainly related to the underestimation of drying rates over the longest period of drying, which is explained with the different evolution of the position of the LAP of the drying front at the lateral edges in simulations and experiment (see also Tables A-10 to A-15 in Appendix A). Though, comparison with experiment 15, where the edge effect was less pronounced, is very good over the longest time. But especially the early second drop of drying rates at  $S \cong 0.15$  to  $S \cong 0.3$  (associated with the dry out of the PN sides) leads to deceleration of drying in the PN simulation. From this follows, as already discussed above, that the simple manipulation of the throat and pore invasion pressure thresholds leads to phenomenological differences between the experimentally observed edge effect and the simulated edge effect. (Again, in the experiments, the edge effect is a result of wall covering continuous corner films wetting the straight side walls of the PN).

The overestimation of drying time is also related to the condensation induced cluster growth in PNM level 4 and CLO1, CLO3 because apparently more liquid must be evaporated if the empty void space of the PN is refilled with liquid (i.e. cyclic evaporation and condensation). The disagreement of the drying curves indicates that this effect is overestimated. In regard of the good agreement of PNM level 4 and CLO2, this finding can be explained with underestimated liquid connectivity in these PMNs. More precisely, the single liquid clusters evolving in PNM level 4 and CLO1, CLO3 cannot compensate the condensation flow rates

from the tip of the evaporation front towards the smaller clusters at the drying front in the center of the PN. From this follows that the smaller clusters are growing. Contrary, the global interconnectivity of the liquid phase in PNM level 4 and CLO2 allows for a compensation of condensation rates wherefore cluster growth is not observed over the longest period of drying in this PNM. These findings are further elucidated in the following section.

### **6.3.1.3 Structural analysis of pore scale liquid distribution**

The simulations in Figs. 6-29 to 6-32 are further analyzed in the following. Focus of this analysis is on the governing pore scale phenomena that allow for an elevated drying front position and also for a negligible cluster growth mechanism.

As expected, saturation profiles are very similar and in very good agreement with experiments (Fig. 6-33a). This is in accordance with phase distributions in Figs. 6-29 and 6-30. However, the simulated LAP of the drying front as well as the drying frontwidth in Fig. 6-33b,c differ from experimental findings. This is mainly explained with the inability of the image processing algorithm to reproduce the film region at the lateral edges (Figs. 4-22 and 4-23). More clearly, the regions with intermediate gray values are suppressed in the image processing algorithm (Section 3.4). As a consequence, the simulated LAP of the drying front is *apparently* closer to the PN open side than determined from the experimental image. But Figs. 4-22 and 4-23 as well as Tables A-10 to A-15 in Appendix A reveal that the film region evolving along the lateral edges of the PN is indeed temporally more stable than determined by image processing. This leads to a significant discrepancy. Precisely, the LAP of the front is *apparently* underestimated, i.e. computed at a less advanced position, by PN simulations (Fig. 6-33b). However, a more precise analysis of the images in Figs. 4-22 and 4.23 and Tables A-10 to A-15 in Appendix A reveals that the simulations overestimate the LAP instead. It is assumed that this discrepancy would diminish if the film region would be captured with an improved image processing algorithm based on the use of a camera with higher resolution (or a microscope).

The longest period of liquid pinning is simulated with PNM level 4, CLO2 which is explained with the high interconnectivity of the liquid phase in this model. This effect is also reflected by the frontwidth (Fig. 6-33c), showing an increase with receding liquid phase (in the center of the PN) while the LAP remains pinned close to the PN top side. For reasons explained before, the experimental curves instead reveal an *apparently* constant width of the drying front.

Interestingly, number (Fig. 6-33d-e) as well as the size (Fig. 6-33f) of liquid clusters (in terms of the maximum number of interconnected liquid filled throats) are partly overestimated with the different versions of the PNM. As expected, overestimation is lower when using CLO2 because this cluster labeling option allows for a higher interconnectivity of the liquid phase while in CLO1 and CLO3 the number of isolated clusters is higher. (The overestimation is greater using CLO3 because in this cluster labeling option adjacent liquid clusters connected by a condensing element can be detected as separate clusters). Also the PNM with liquid rings yields a comparably high cluster number, which is based on a different definition of liquid clusters in this model; here, namely, single liquid throats and pores connected to a liquid ring are defined as a cluster, while the single liquid throats in CLO1 and CLO2 as well as in PNM level 2 and level 3 (ignoring liquid rings) are not assigned with a cluster label. The drying models ignoring the cluster growth mechanism (denoted as PNM

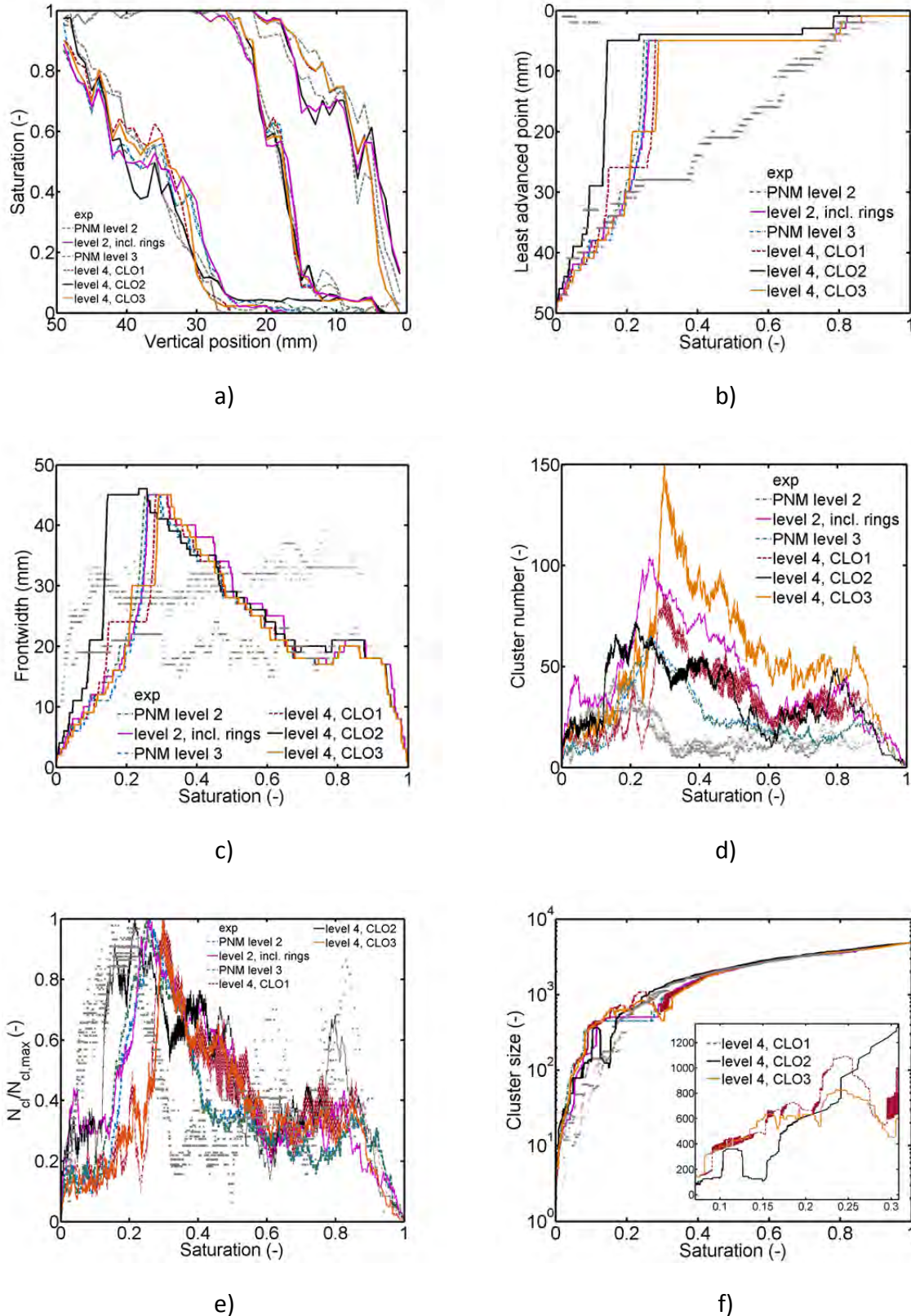
level 2 and PNM level 3) though predict an overall smaller number of clusters. This might also be based on the faster evaporation of isolated clusters compared to the situation with cluster growth. Apart from this, the same trend of cluster number and cluster size as in experiments is simulated with the different model options. In detail, the trend of cluster number shows an initial slight increase, then a slight decrease followed by a period of almost constant cluster number and another increase towards the end of drying. The very good agreement of experimental findings and CLO2 is clearly revealed in Fig. 6-33e where the total number of clusters is scaled with the maximum cluster number. As can be seen, trend of the curves and position of the peak is best predicted with CLO2. Notice that the oscillation of the curve computed with PNM level 4 and CLO1 in Fig. 6-33e is a result of the multiple disconnection and reconnection of clusters due to refilling elements at the cluster boundaries.

Figure 6-33f indicates that the computed maximum size of liquid clusters is also in very good agreement with the experimental data, especially in the range  $S \geq 0.44$ . From the six model approaches studied here, PNM level 4 and CLO2 shows again the best agreement over the longest period of drying, while especially PNM level 2 and PNM level 3 (ignoring liquid rings) underestimate the maximum cluster size. The PNM with liquid rings slightly underestimates the cluster size in the range  $0.2 \leq S \leq 0.54$  and overestimates the cluster size for  $S \leq 0.2$ . As a consequence of the different cluster definitions in CLO1, CLO2 and CLO3, the following is observed: a higher number of clusters (and smaller cluster sizes) is obtained from CLO3, while with CLO1 less clusters and larger cluster sizes are simulated. Contrary, a lower cluster number (and greater size of the clusters) is attained with CLO2 because of the higher interconnection of the liquid phase in this model. It is furthermore noted that independently of the CLO (and PNM level 4), increasing trends of the cluster size are found in Fig. 6-33f in the period when the process is controlled by vapor diffusion (detail highlighted in Fig. 6-33f). Since this effect is not observed in any of the other simulations, it is strongly expected that it can be assigned to the condensation effect and the growth of single liquid clusters as well as the reconnection of smaller single clusters. In detail, the cluster number is increased roughly by factor 2 in each of the three simulations, but the effect occurs at a significantly lower saturation when using CLO2 ( $S \cong 0.1$  to  $S \cong 0.13$ ). This indicates that the cluster connectivity is sustained until a low PN saturation. In the other two versions of the PN, vapor diffusion towards the disconnected liquid clusters is relevant already for  $S \leq 0.3$ .

It is finally concluded that the manipulation of cluster labeling offers a possibility to adjust liquid connectivity in PN drying simulations. Following discussions above, the drying algorithm denominated as PNM level 4, CLO2 can well represent experimental findings. Though, the position of lateral pinning (edge effect), cluster size and absolute cluster number are still not accurately predicted. This is also explained with remaining uncertainties from the processing of experimental data related to the structural details of liquid films.

#### 6.3.1.4 Summary

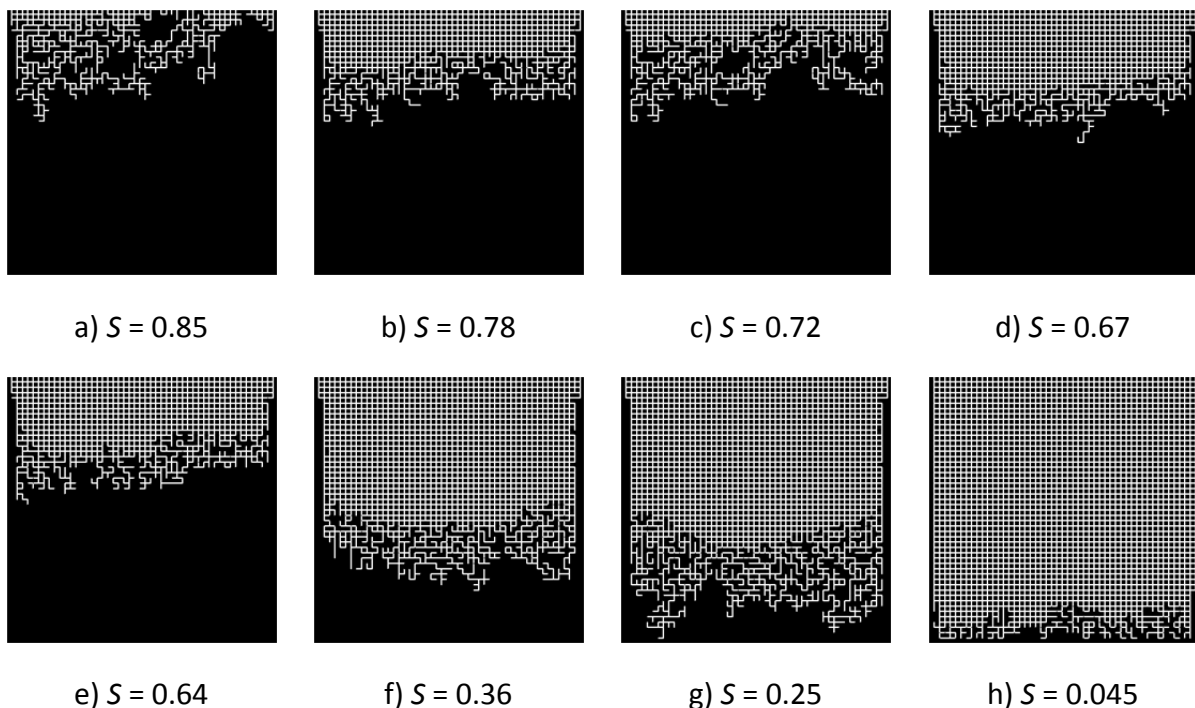
Drying with imposed negative thermal gradient was studied on the base of experimental findings taking two routes of PN modeling. The first route was based on the assumption that drying is rather controlled by secondary capillary invasion while the second route was exploited in regard of the condensation induced cluster growth (i.e. when invasion is controlled by vapor diffusion). The second route was associated with the assumption that the edge effect can induce a heat pipe effect.



**Figure 6-33** Comparison of simulated PN drying with experiments 8, 13, 15 (in gray): a) saturation profiles (plotted for overall network saturation  $S = [0.85, 0.64, 0.25]$ ), b) least advanced point of the drying front, c) width of the drying front, d) number of clusters, e) standardized number of clusters and f) maximum cluster size.



In summary, similar phase distributions, in very good agreement with the experimental images, were found with the different options of the non-isothermal drying model. The best agreement in regard of drying rate, drying time and pore scale structural analysis of the liquid distribution was obtained with PNM level 4, CLO2, which incorporates the edge effect, the cluster growth mechanism as well as a high interconnectivity of the liquid phase, similar as in presence of liquid films. This is also the model with the lowest computational effort among the PNMs with cluster growth. Details of the simulated phase distributions using PNM level 4 and CLO2 are summarized in Fig. 6-34. Comparison with Fig. 4-19 reveals very good agreement, both of the structure of the main liquid cluster as well as the position of the drying front in the center of the PN. Besides this, position of the lateral pinning of the liquid phase at the side walls is overestimated at low PN saturations (when the liquid phase has split up and invasion is controlled by vapor diffusion), leading to an overestimation of drying time by around factor 2 (compared to the final saturation in experiments, i.e.  $S \cong 0.02$  to  $S \cong 0.04$ ). This indicates that the details of the morphology of liquid films along the PN side walls as well as in the PN center and its impact on mass transfer in both, liquid and vapor phase, are not yet fully captured with this PNM. A further step towards a better understanding of this phenomenon is done in the following section, where drying in presence of a heat pipe effect, induced by the partial diffusion of vapor back to the colder region of the drying front, is studied.



**Figure 6-34** Phase distributions simulated with PNM level 4 and CLO2.

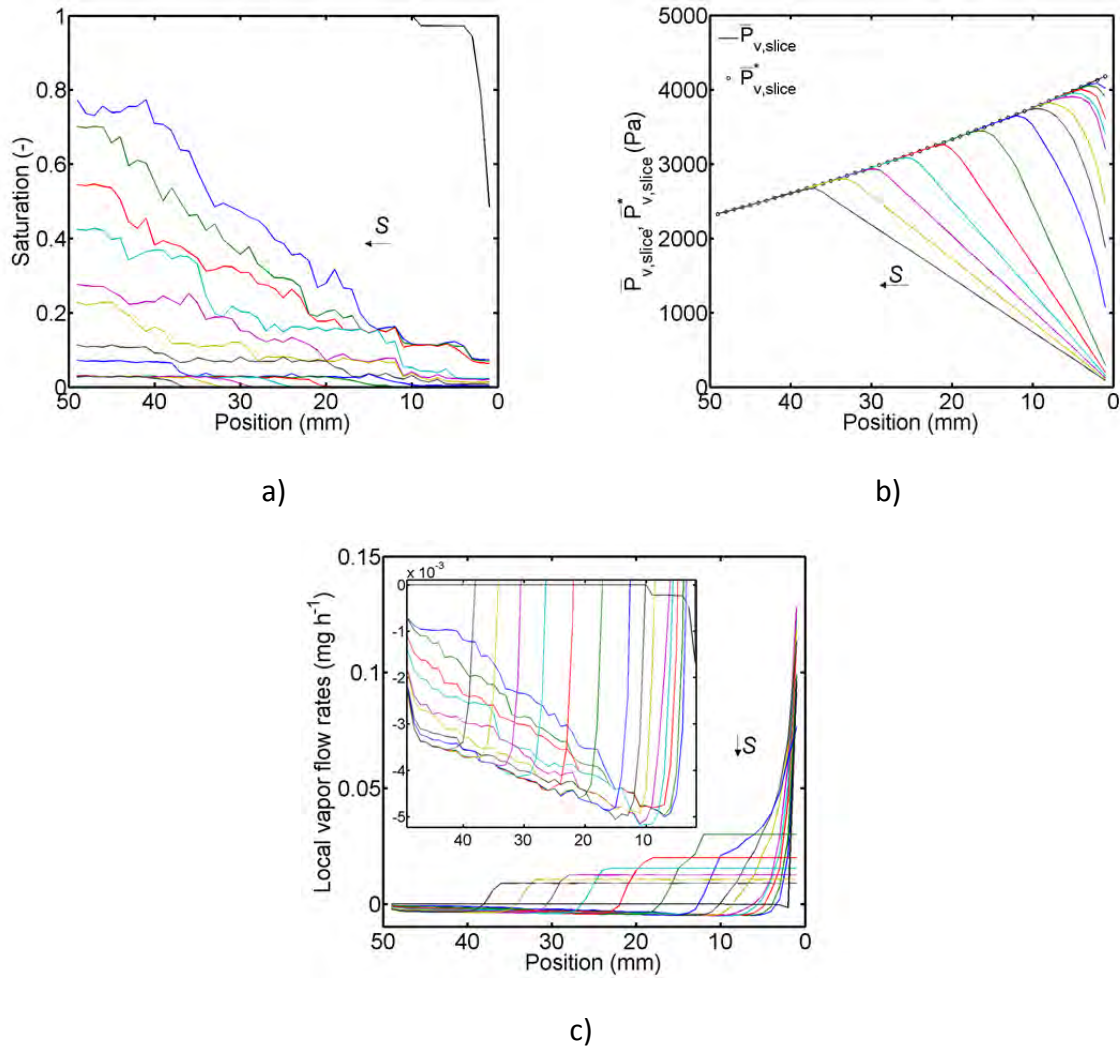
### 6.3.2 The heat pipe effect

Schluender (2004) hypothesized that moisture circulates macroscopically in the partially saturated zone of a drying front, like in a heat pipe, if a temperature gradient with high temperature at the surface and lower temperature in the core of the porous medium is applied. This assumption is based on the observation of liquid migration and vapor diffusion: while vapor *partially* travels towards the colder core and condenses, liquid is pumped to the

surface and evaporates. Consequently, a watershed is found where the vapor pressure exhibits a maximum value (Fig. 5 in Schluender 2004). This watershed must not necessarily be located at the drying front tip; its position rather depends on the interaction of capillarity, vapor diffusivity and hygroscopicity. Moreover, this effect could explain why the temperature is almost uniform during the falling rate period due to the additional enthalpy back diffusion and condensation. Schluender (2004) concluded that any observed saturation decrease can only be based on capillary pumping from the product center to the surface. This conclusion, however, must be based on the existence of wetting liquid films covering the solid walls and allowing for liquid connectivity to the surface of the porous medium. Due to the theory in Sections 2.3.6 and 2.5.4 liquid pressure is significantly decreased inside the liquid films. Based on this, liquid can be transported against the temperature gradient (Fig. 2-30). The findings discussed below indicate that the edge effect, studied in the previous sections, might be adopted in presence of imposed temperature gradients in order to allow for a longer pinning of the liquid phase (i.e. also at lower overall PN saturations).

The heat pipe phenomenon can be investigated on the pore scale using the developed non-isothermal PNM and a bimodal pore size distribution. In this simplified non-isothermal film model, the liquid films are represented by micro pores/throats with radii that are only 10 % of the radii of the macro pores/throats (which represent the bulk liquid phase). Figure 6-35 summarizes saturation profiles, vapor pressure field as well as the local diffusion flow rates of an example simulation. The profiles are shown in different colors for identical saturation, allowing for a direct comparison of the different plots. Position of the 2-phase zone can be identified from the saturation profiles in the zone with  $0 < S < 1$ . Notice that breakthrough of the gas phase to the PN bottom occurs in the macro throats at a network saturation of  $S = 0.61$  and for  $S \leq 0.22$  the liquid phase is entirely contained in micro throats while the macro throats are completely empty. The average slice saturation of the remaining film zone is  $S \cong 0.035$ . Transition between  $S \cong 0.035$  and  $S = 0$  marks the evolution of the drying front of the film zone. The vapor pressure curves in Fig. 6-35b show the temperature depending decrease of the slice average saturation vapor pressure (circles) as well as the mean vapor pressure in the partially saturated and the dry zone of the PN (lines). Notice that the mean vapor pressure increases inside the partially saturated zone, passes through a maximum value and then decreases inside the dry zone (from bottom at  $z = 49L$  to top at  $z = 0$ ). From this follows that local vapor diffusion can occur in different directions, i.e. towards the open PN side (at higher temperature) *and* also towards the PN bottom (at lower temperature). This is revealed by the change of sign of local diffusion flow rates in Fig. 6-35c. Location of the watershed of vapor diffusion agrees with the location of maximum mean vapor pressure. Comparison of these curves with saturation profiles in Fig. 6-35a indicates that the watershed separates a region of constant saturation, connected to the PN bottom side, and a region of decreasing saturation connected to the PN top side.

Figure 6-36 specifies the phase distributions for selected overall network saturations. The images indicate that the liquid phase initially only recedes in macro throats, while micro throats (mimicking liquid films) remain liquid saturated. Furthermore, Fig. 6-36 indicates that the liquid phase inside micro throats starts to recede while macro throats are still partially liquid saturated. This is in good agreement with theory of film flow. From Fig. 6-36 it can be concluded that the watershed is located in the upper region of the drying front as long as liquid films in micro throats did not detach from the PN surface as also after detachment of liquid films in micro throats. Exemplarily, for  $S = 0.033$  the LAP of the film region in column 38 coincides with the location of the watershed at position  $z = 14L$  to  $z = 20L$  in agreement

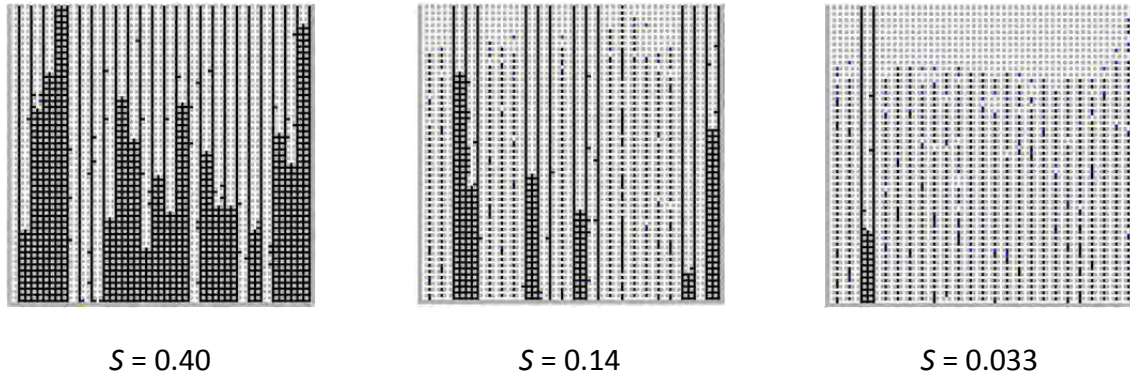


**Figure 6-35** a) Saturation profiles, b) slice average vapor pressure and slice average saturation vapor pressure and c) sum of vapor diffusion rates through PN slices in a drying process with negative thermal gradient ( $\Delta T = 10$  K) and radius distribution as in the reference PN. The liquid films are represented by throats (and pores) with radii that are 10 % of the radii of the throats containing the bulk liquid phase. (For this, the reference throat radii in every second vertical row are multiplied with factor 0.1). The curves are shown for  $S = [0.98, 0.40, 0.33, 0.27, 0.20, 0.14, 0.097, 0.06, 0.033, 0.019, 0.016, 0.013, 0.011, 0.0085, 0.006]$ . Simulation with PNM level 4, CLO2 and  $s_{BL} = 2L$ .

with the peak of the vapor pressure curve in Fig. 6-35b and the position where reversion of the direction of vapor flow rates is observed in Fig. 6-35c (green curves for  $S = 0.033$ ). The critical local slice saturation at which the vapor flow rates can be reversed is high ( $S \cong 0.8$ ) in case of an overall high network saturation (refer to the black curves in Fig. 6-35). While at lower overall PN saturation reversion occurs at significantly lower slice saturation ( $S \leq 0.08$ ). It is expected that the position of the watershed depends on the height of the temperature gradient and the overall evaporation rate if pore size distribution is fixed. A future work might investigate how this interrelates with the width of the drying front.

It could furthermore be argued that the presented results were obtained for a constant imposed temperature gradient, i.e. ignoring the potential temperature equilibration due to

combined evaporation and condensation inside the 2-phase zone. A more detailed simulation could additionally incorporate heat transfer instead of imposing a constant temperature profile. Such kind of simulation could shed light on the dependence of the width of the drying front on the temperature profile and the ratio of vapor flowing countercurrently to the liquid (e.g. Shaw 1987).



**Figure 6-36** Phase distributions from a PN mimicking the film effect by a reduction of the throat size in every second pore column. The image shows that the liquid phase initially recedes inside macro throats before drying of the film region starts. (Note that in the neighborhood of liquid filled macro throats liquid films remain connected to the open PN side). Liquid in black, vapor in white and solid in gray. The related positions of the watershed are  $z \cong [4, 6, 14] \cdot L$ .

### 6.3.3 Pore network drying with destabilizing thermal gradient

In this section drying with imposed temperature gradient similar as in contact drying is discussed. Model parameters (pore size distribution and temperature field) for the simulations are adopted from the respective experiments. BL thickness is the same as previously and the edge effect is incorporated as before (Table 6-4). As in the previous section, the non-isothermal PNM in its different versions is applied but liquid rings are disregarded here. The simulated drying behavior is compared with experimental results discussed in Section 4.4.2. At first phase distributions are compared in Fig. 6-37, then the drying curves and drying rate curves are presented (Fig. 6-38) and discussed in relation to the properties of the travelling 2-phase zone (Figs. 6-39- 6-41).

Table 6-5 summarizes the condensation effect obtained from the different versions of the PNM. It clearly evidences that the condensation effect is more significant in the simulation with positive thermal gradient (compared to drying with negative thermal gradient), independently of the choice of the cluster growth mechanism. From this can be concluded that temperature affected vapor diffusion controls the evolution of liquid distributions (Fig. 6-37) more strongly than in the situation with negative thermal gradient. It is highlighted that the number of invasion steps in the simulation with PNM level 4 and CLO1 is lower than in the simulation with negative thermal gradient where the edge effect was much stronger. In contrast, the positive thermal gradient studied here causes a liquid phase destabilization, leading to breakthrough of the gas phase and initiation of a 2-phase zone travelling towards the open PN side; the edge effect plays a minor role in this situation.

**Table 6-4** Summary of model parameters.  $P$ ,  $P_v^\infty$ ,  $L$ ,  $L_d$ ,  $\cos \theta$  as in Table 6-1.

$T_{BL}$	$T^{min}$	$T^{max}$	$\bar{T}$	$S_{BL}$	$f^{red}$	$z^{pin}$
25°C	23.58°C	50.59°C	37.79°C	500 $\mu\text{m}$	0.85	(5-10) $L$

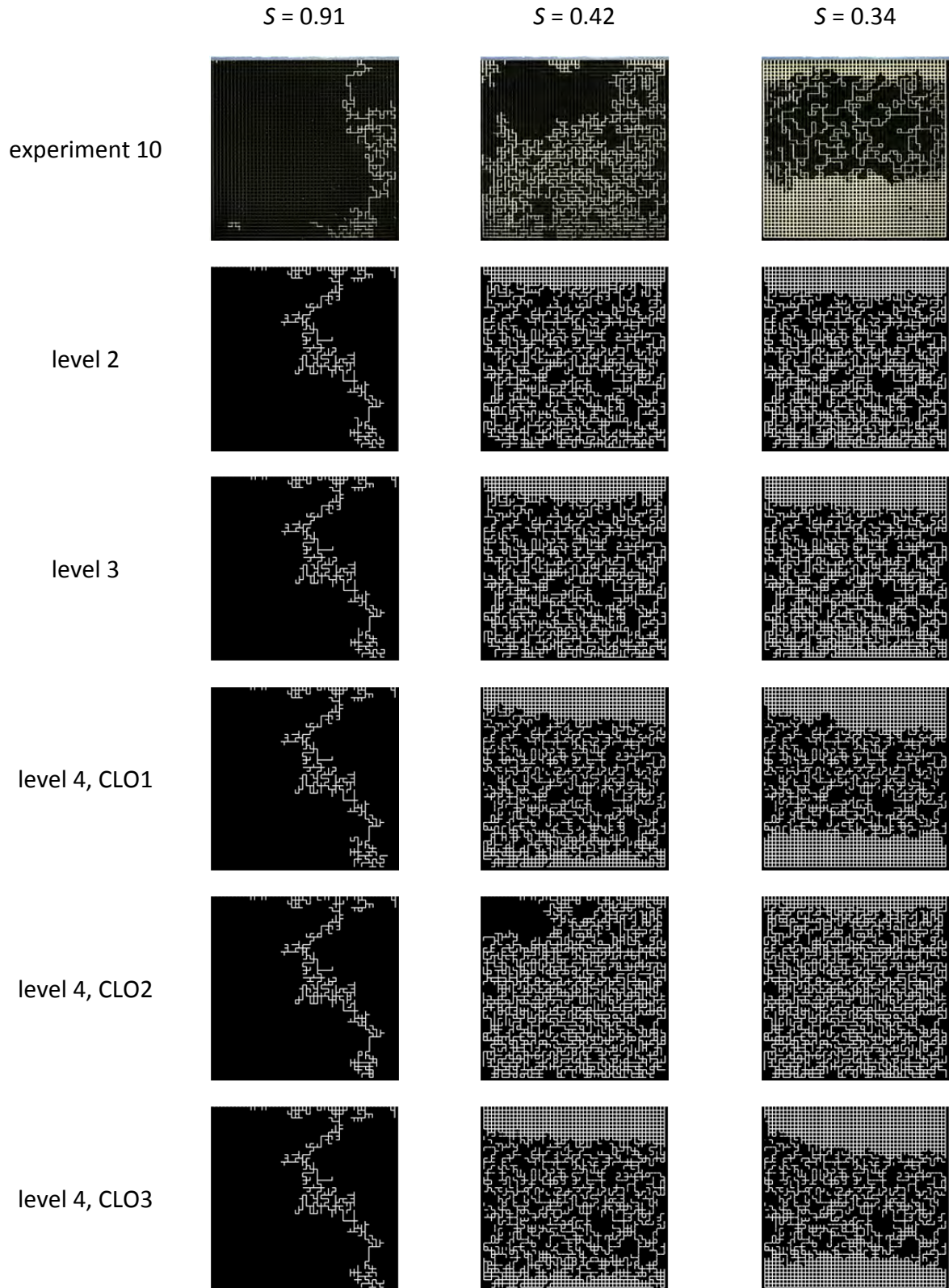
**Table 6-5** Dependence of the condensation effect on the version of the PNM and its impact on the computational effort (Intel i5\_4460, CPU 3.2 GHz, 8 GB RAM, 64 Bit, Matlab R2014a).

Parameter	Level 2	Level 3	Level 4, CLO1	Level 4, CLO2	Level 4, CLO3
$v_c^{+,-}$	0.22 ( $v_c^-$ )	0.30 ( $v_c^-$ )	0.16 ( $v_c^+$ )	0.072 ( $v_c^+$ )	0.18 ( $v_c^+$ )
$N_{steps}$	7301	7563	81557	12705	33607
$t_{comp}$	269 s	283 s	5.7 h	0.96 h	2.94 h

### 6.3.3.1 Phase distributions

In agreement with the experimental findings in Fig. 4-27, the phase distributions summarized in Fig. 6-37 reveal the four different drying periods already distinguished from the experimental images. These are again summarized as follows. In the first drying period, a gas branch breaks through from the upper drying front at the PN surface to the PN bottom side. In the second drying period, the liquid phase is ramified by an invasion front travelling through the partially saturated zone starting from the PN bottom. In the third drying period a second evaporation front occurs at the bottom of the PN when the dry region at the surface of the PN becomes sufficiently large. This front travels upwards, i.e. countercurrently to the upper evaporation front, leading to the shrinkage of the 2-phase zone while the clusters confined in this zone are growing (PNM level 4) or at least not shrinking (PNM level 2, 3). (Notice that this period is not observed in the simulation with PNM level 4 and CLO2). In the fourth period the LAP of the front recedes further and the liquid clusters dry out.

The first and second drying periods are in very good agreement with experiment 10 while differences in the patterns of the different versions of the PNM and experiment occur in the drying period after split up of the liquid phase (third and fourth drying period). These are based on the different treatment of the condensation effect and the different liquid connectivity related to each cluster labeling option. The differences concern the position of the LAP of the drying front, the initiation of the travelling 2-phase zone, and its saturation and structure. The phase distributions in Fig. 6-37 indicate that the PNM level 4, CLO1 and CLO3 well predict position and saturation of the 2-phase zone in the third period of drying while CLO2 (which achieved the best agreement in the study of the negative thermal gradient in the previous section) does not. However, the disagreement is comprehensible in the situation studied here, since the small clusters found in Fig. 6-37 are usually interconnected in the model using CLO2 and thus allow for capillary controlled emptying and refilling of the 2-phase zone (in contrast to the other two model options which allow for

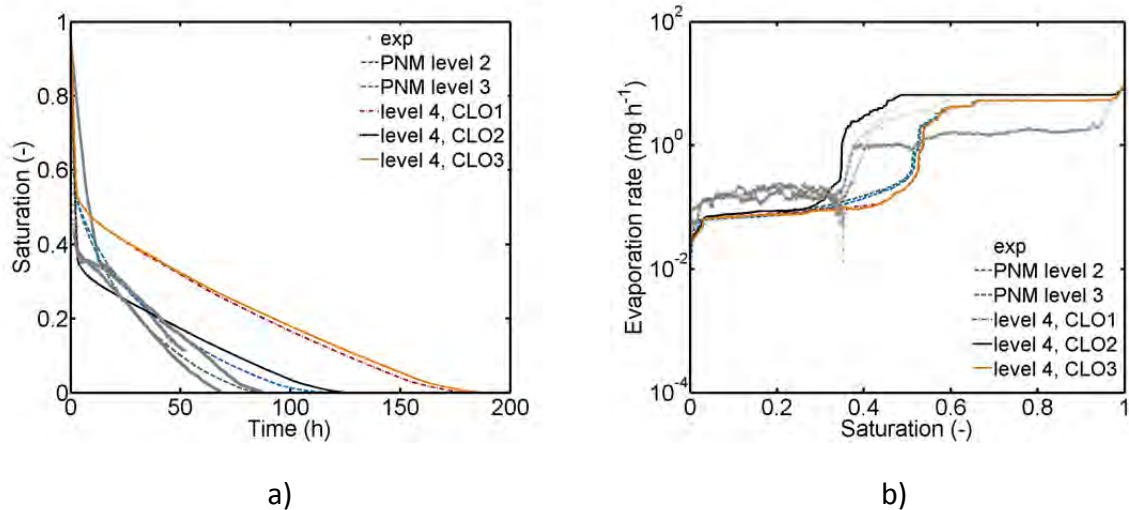


**Figure 6-37** Phase distributions from drying with imposed positive thermal gradient. The pores are shown in black for  $S_p > 0.8$ .

vapor diffusion controlled emptying of the 2-phase zone during the third drying period). Consequently, the interconnected liquid structure is rather controlled by capillary effects in CLO2 than by vapor diffusion and condensation, which are though expected to dominate the invasion process in presence of the positive thermal gradient. This is captured with CLO1 and CLO3. The PNMs level 2 and level 3 in Fig. 6-37 show very similar phase patterns, overestimating the LAP of the front and underestimating the initiation of the traveling 2-phase zone.

### 6.3.3.2 Drying curves and drying rate curves

Drying curves and drying rate curves corresponding to Fig. 6-37 are summarized in Fig. 6-38. Figure 6-38 reveals that the best agreement of simulated and experimental drying time is obtained with PNM level 2, thus with the model completely ignoring refilling of the void space due to condensation. This appears surprising, but it can easily be explained with the counteracting physical phenomena that control drying at the pore level. One of these phenomena is the refilling of the void space with liquid as a consequence of condensation. Precisely, in a drying process with condensation the liquid phase experiences several cycles of evaporation and condensation (also refer to Appendix B.3). This leads to an increase of drying time in the simulations that take the cluster growth mechanism into account (PNM level 3 partly and PNM level 4). In PNM level 2, the negligence of the condensation effect ergo leads to a reduction of drying time, because the liquid phase experiences only one phase change. Exemplarily, PNM level 2 predicts much faster drying than PNM level 4 and CLO3 although the drying rate curves are almost overlapping. More precisely, in contrast to the experimental findings PNM level 2 shows an earlier drop of drying rates. The match of the drying time with PNM level 2 is thus only ascribed to the total amount of liquid volume evaporated from the PN, which is lower than in the other situations. Instead, the best agreement of drying rate curve is found for the PNM level 4 with CLO2. This is in agreement with the results of the study of drying with negative thermal gradient and it is again explained with the ability of cluster labeling to mimick the high interconnection of the liquid phase by liquid films. This can lead to a reduction of drying time since the films allow for a more favorable front position on the one hand and for a reduced condensation effect on the other hand. It is found that this effect is strongly influencing PNM level 4, CLO2, because a longer CRP can be simulated with this version of the PNM compared to the other versions ignoring the higher cluster interconnectivity by liquid films. Nevertheless, drying rates in the fourth period of drying (when the LAP recedes further from the PN surface) are lower than experimentally observed. As in drying with stabilizing thermal gradient, PNM level 4, CLO2 cannot capture the drying period when the liquid phase is split up and vapor diffusion through the partially zone controls the invasion process. This might mainly be explained with the pore scale structure of liquid connectivity (i.e. by liquid rings and wall covering films along the PN side walls in the SiO<sub>2</sub> microfluidic network) which is seemingly overestimated by the adapted cluster labeling. It is thus concluded that the implementation of the high liquid connectivity is important in drying periods in which the invasion is controlled by the capillarity of the PN. In later stages of drying, when vapor diffusion controls invasion, the liquid connectivity becomes less important (CLO2 fails to predict drying after the drop of drying rates, i.e. for  $S \leq 0.38$ ). This shows, although the macroscopic drying behavior is well described, uncertainties about the structural differences in the pore scale liquid distribution remain.



**Figure 6-38** a) Drying curves and b) drying rate curves corresponding to Fig. 6-37. The curves from experiments 10, 11, 18 are shown in gray.

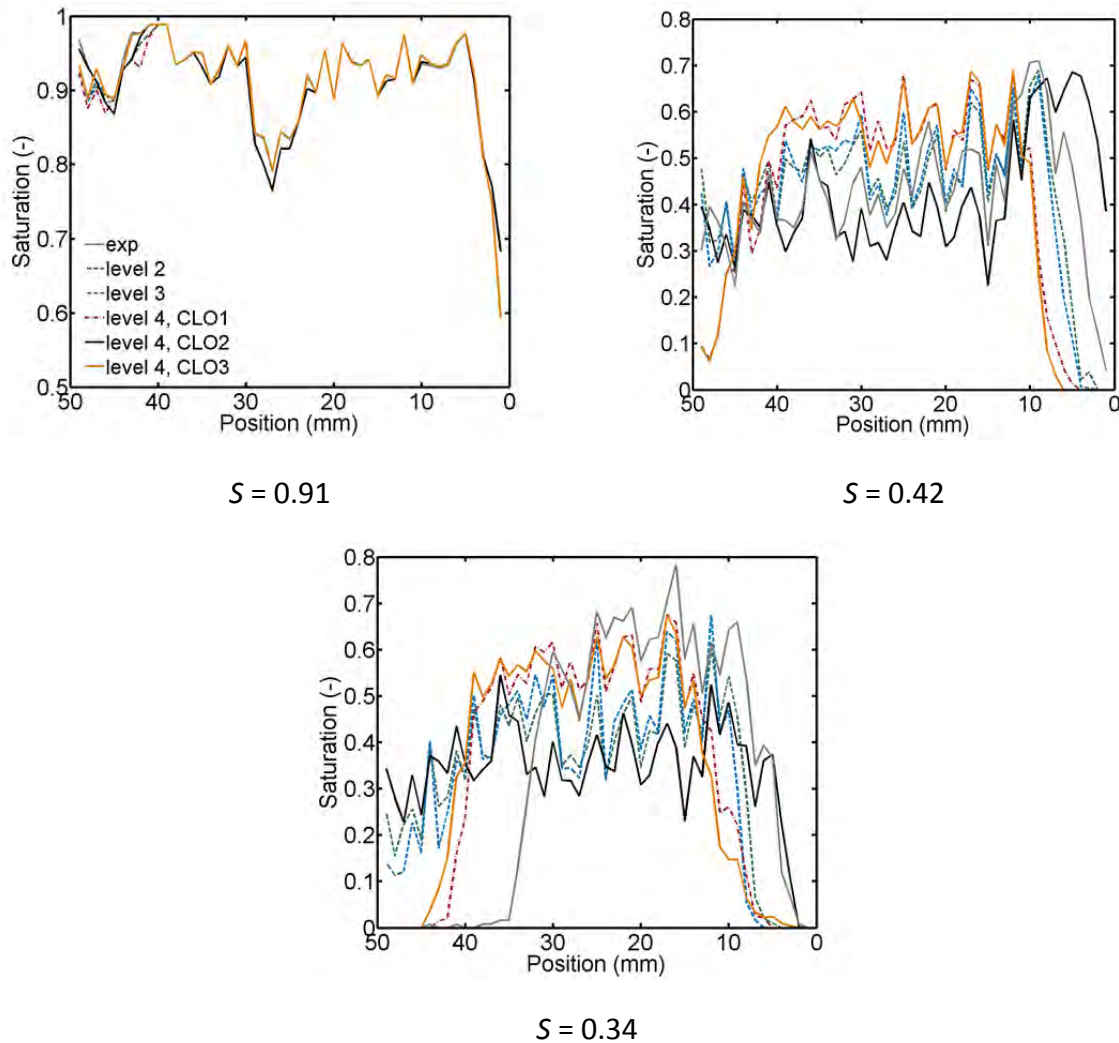
### 6.3.3.3 Structural analysis of pore scale liquid distribution

Saturation profiles in Fig. 6-39 show overall very good agreement of simulated and experimental distribution of liquid for  $S = 0.91$ . However, greater deviations are found at later stages of drying ( $S = 0.42$  and  $S = 0.34$ ). The most striking differences are in the prediction of the LAP of the front (see also Fig. 6-40a) and in the detachment of liquid phase from the PN bottom side. Especially at  $S = 0.34$  the travelling liquid zone appears more dense (with overall higher saturation and smaller expansion) in experiments than in the simulation. It is remarked that the LAP of the travelling 2-phase zone is rather captured by CLO2; but the detachment from the PN bottom side occurs at higher network saturation in experiment than in the simulation with CLO2. This is reflected by Figs. 6-40b and 6-40c, which show the width of the travelling 2-phase zone and its most advanced point (MAP) (associated with initiation of the travelling 2-phase zone). Slightly better agreement of the predicted and measured drying front width as well as of the MAP is found for PNM level 4 with CLO1 and CLO3. Figure 6-40 also reveals that PNM level 2 and level 3 (i.e. neglecting the condensation induced cluster growth) cannot predict the pore scale liquid distribution.

In addition to that, Fig. 6-41 summarizes the structure of the liquid phase by means of the cluster structure. These figures indicate that the number of liquid clusters as well as the maximum size of liquid clusters are rather well predicted by CLO2. Although the maximum number of clusters is overestimated by factor 2 (Fig. 6-41a), the trend of the cluster number as well as the saturation at which the peak is achieved are very well predicted (Fig. 6-41b). Additionally, agreement of experimental and predicted cluster sizes appears very good in Fig. 6-41c, except of the increase in cluster size after the drop at  $S \cong 0.35$ . This is explained with an underestimation of cluster growth as will be discussed in Section 6.3.3.4. The remaining deviations might be explained with uncertainties in the image analysis of experimental data and the simplified representation of liquid connectivity in CLO2 which might lead to an overestimation of liquid connectivity in this situation.

As expected, PNM level 2 and level 3 fail to predict the pore scale liquid structure, emphasizing the importance of condensation induced refilling in presence of a positive thermal gradient. But surprisingly also PNM level 4 with CLO1, CLO3 do not predict these



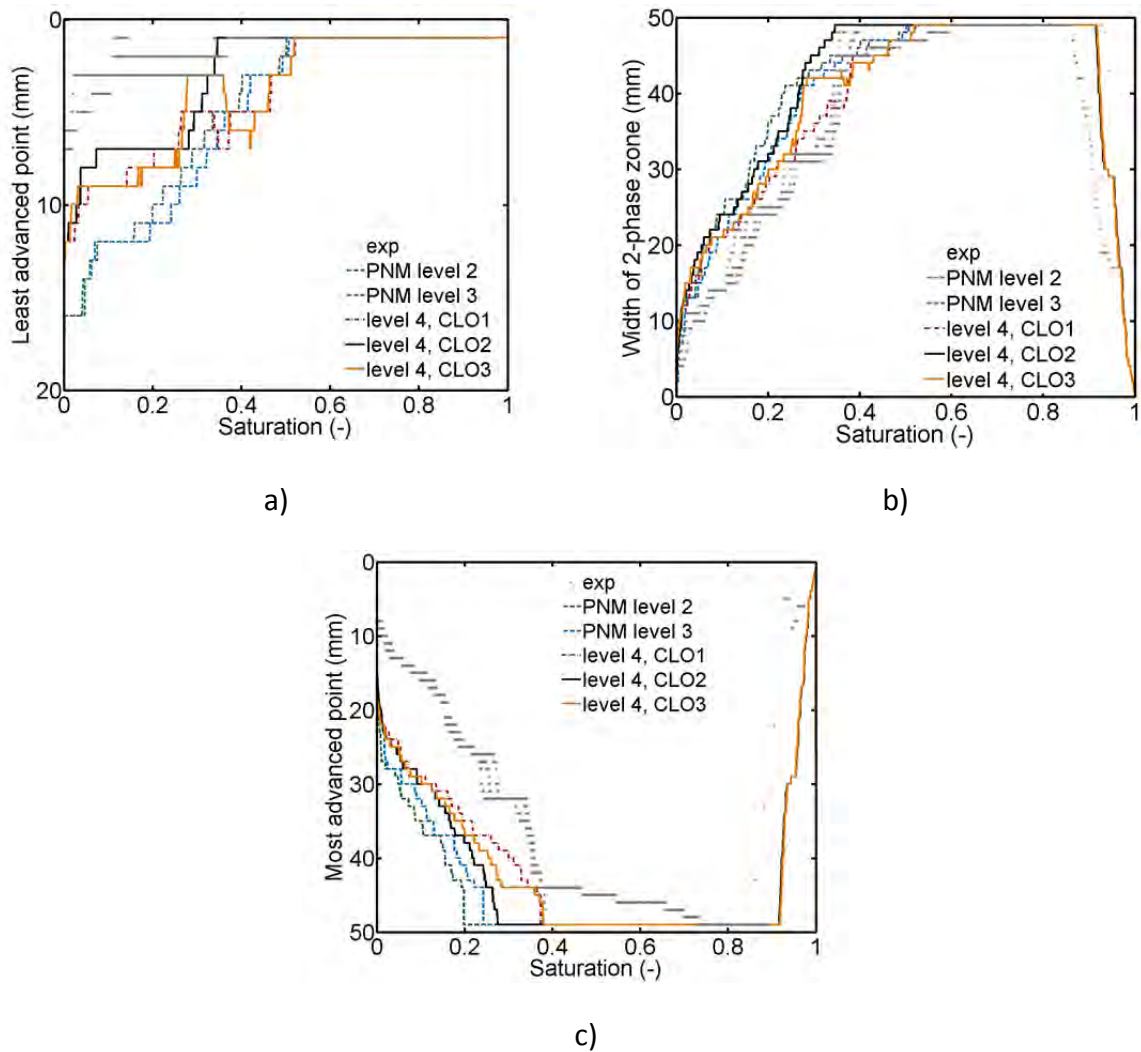


**Figure 6-39** Saturation profiles corresponding to Fig. 6-37 (experiment 10 in gray).

properties of the liquid patterns accurately (Fig. 6-41). PNM level 4 and CLO3 shall therefore be further analyzed in comparison to CLO2 in the following section; CLO1 is disregarded from this comparison as it principally allows for very similar results as CLO3 (the difference between the two versions is basically the treatment of condensing elements connecting two clusters, which are interpreted as non-connecting elements in CLO3 with the result of reduced oscillation of the invasion process).

#### 6.3.3.4 Analysis of the impact of cluster labeling

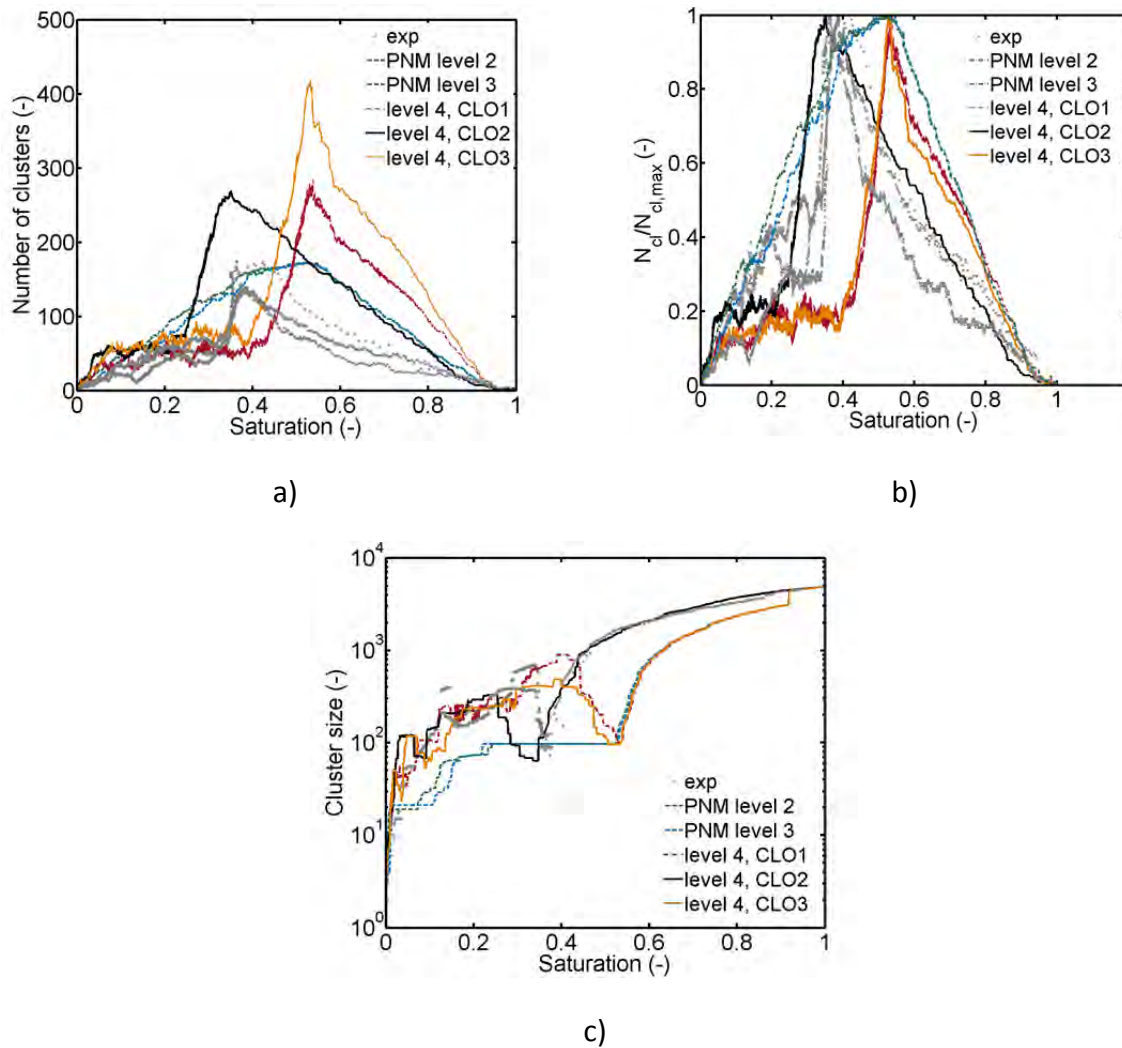
From the above discussion it can be concluded that the two model options PNM level 4 CLO2 and CLO3 might be applied to predict drying of the PN with imposed positive thermal gradient. While with CLO3 the phase distributions in Fig. 6-37 as well as initiation of the travelling 2-phase zone (Figs. 6-39 and 6-40) are well predicted, CLO2 shows very good agreement in terms of drying time (Fig. 6-38a), evaporation rate (Fig. 6-38b) and cluster size and cluster number (Fig. 6-41). Additionally, both model options are advantageous in terms of computational effort. For this reason, those two cluster labeling options shall be compared in more detail in what follows.



**Figure 6-40** Analysis of saturation profiles: a) least advanced point of the drying front, b) width of the 2-phase zone, c) most advanced point of the drying front. Experiments 10, 11, 18 are represented by gray lines.

It is recalled that CLO3 is based on the conventional cluster labeling method due to which cluster boundaries are determined from the boundaries of liquid continuity whereas CLO2 allows for a higher liquid interconnectivity because neighboring liquid elements are assigned to the same cluster also if separated by an empty throat or pore (i.e. in the absence of liquid continuity).

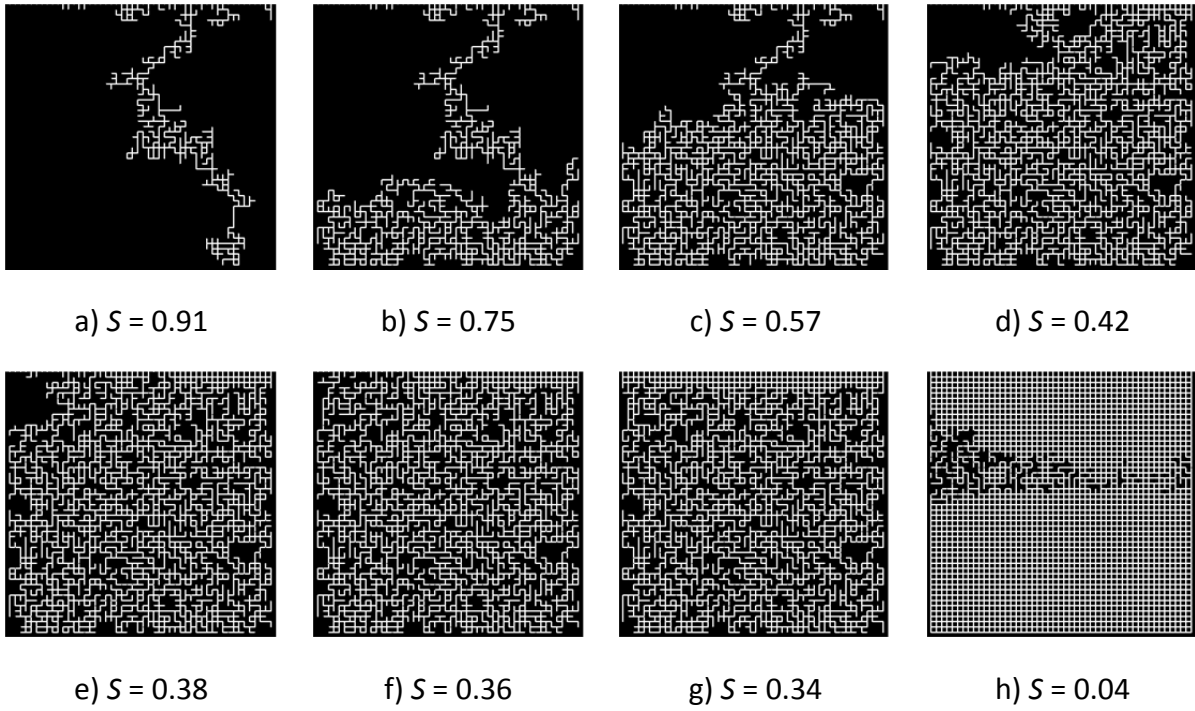
At first, phase distributions are contrasted in more detail in Figs. 6-42 and 6-43. Comparison of these images with Fig. 4-27 clearly reveals the deficits of both models when regarding the drying period after complete disruption of the liquid phase: as discussed before with CLO2 the cluster sizes appear too small and also the width of the 2-phase zone is overestimated; with CLO3 the internal liquid saturation of the 2-phase zone is underestimated and the LAP of the drying front is overestimated (i.e. more advanced). If one further anatomizes the phase distributions in Fig. 6-44 it becomes clear that initiation of the travelling 2-phase zone occurs later in the simulation with CLO2 (because the LAP and the MAP are more stable in this simulation) and also that the temporal increase of saturation of the 2-phase zone is less pronounced.



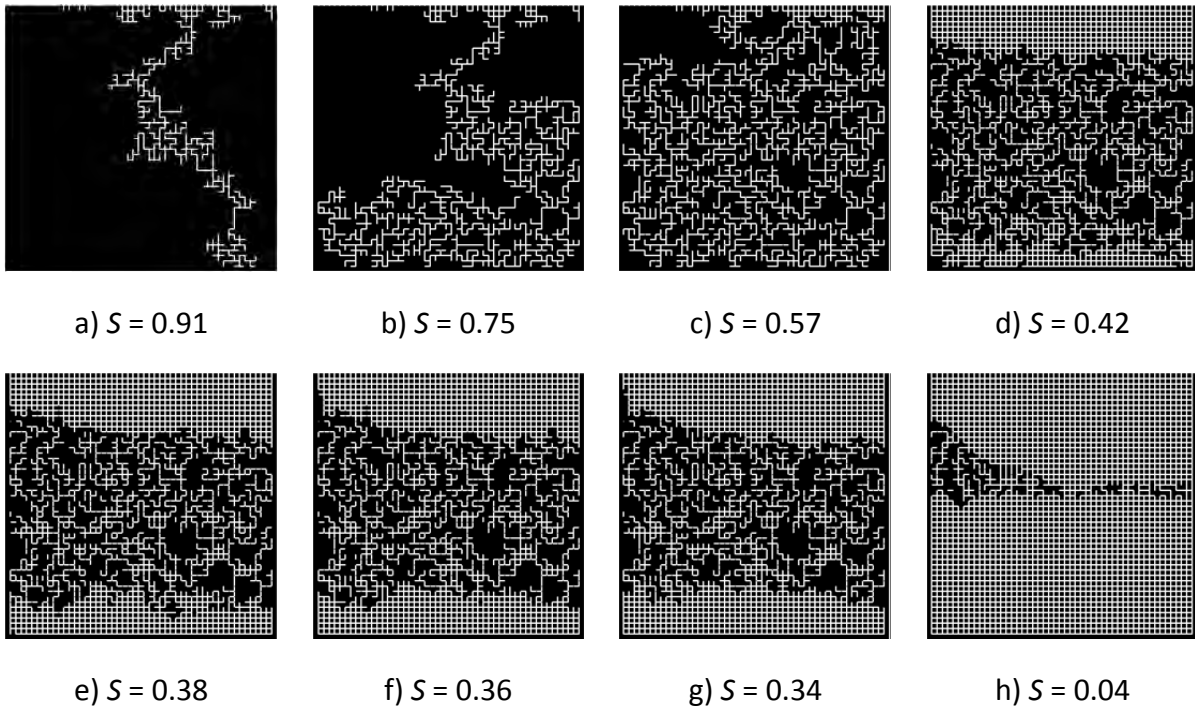
**Figure 6-41** Pore scale structure of the liquid phase: a) number of liquid clusters, b) standardized number of liquid clusters, c) maximum cluster size. Exps. 10, 11, 18 in gray.

Figure 6-44 also reveals that the agreement of the computed condensation effect with experiments is poor when using CLO3. The comparison with experiments in Fig. 6-45a shows a higher increase of liquid saturation within the 2-phase zone in the period after complete disruption of the liquid phase. This might explain the deficits of the computed phase distributions, which reveal a smaller increase of the saturation. Though, the onset of cluster growing, indicated by the decrease in the slope of the saturation curve, coincides very well with experiments.

It is noted that use of other diffusivities, as exemplarily proposed by Krischer and Rohnalter (1940) (see e.g. Appendix B.1) did not yield a significantly better agreement of experimental and simulated phase patterns in terms of a denser liquid structure (Fig. 6-45b). Instead, a greater increase of diffusivity (by a factor of  $> 10$ ) would be required to overcome this discrepancy as this would have a positive effect on vapor condensation in the 2-phase zone; however then the drying time becomes too small ( $t \leq 20$  h). Another option would be the reduction of the overall evaporation rate as this would result in an increase of the total amount of condensed liquid volume (e.g.  $v^+ = 0.2$  using PNM level 4 and CLO3 with edge effect and  $s_{BL} = 5L$ ); however then the drying time is overestimated ( $t \cong 200$  h).

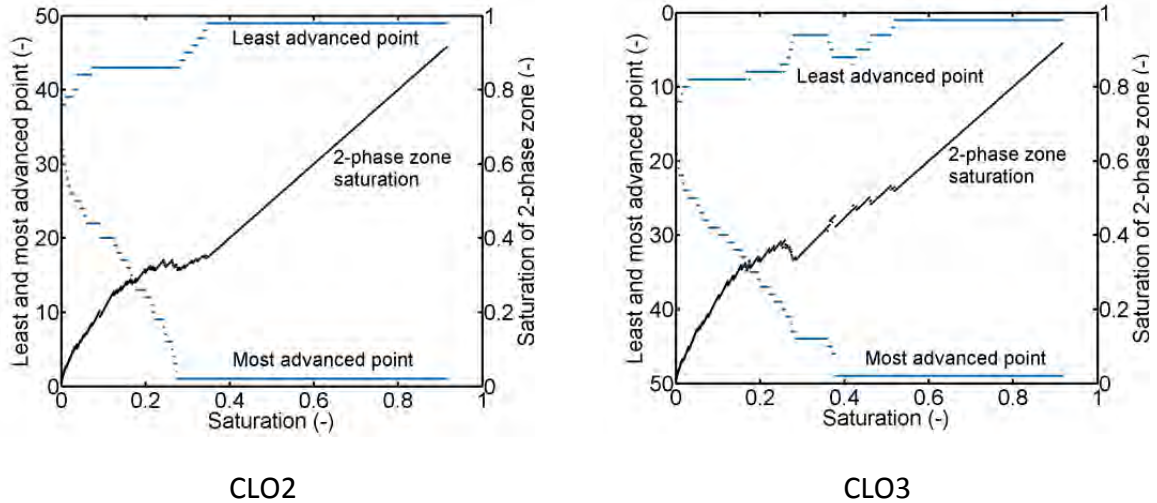


**Figure 6-42** Phase distributions obtained with PNM level 4 and CLO2.

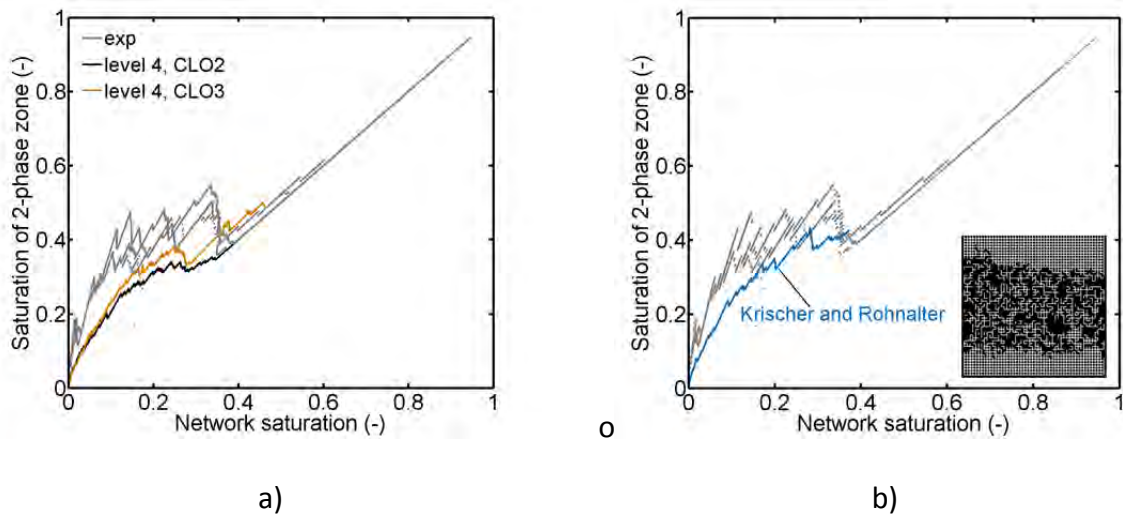


**Figure 6-43** Phase distributions obtained with PNM level 4 and CLO3.

This indicates that in the vapor diffusion dominated drying regime also further information about the internal vapor diffusion processes must be gained. This is shown in Figs. 6-46 and 6-47.

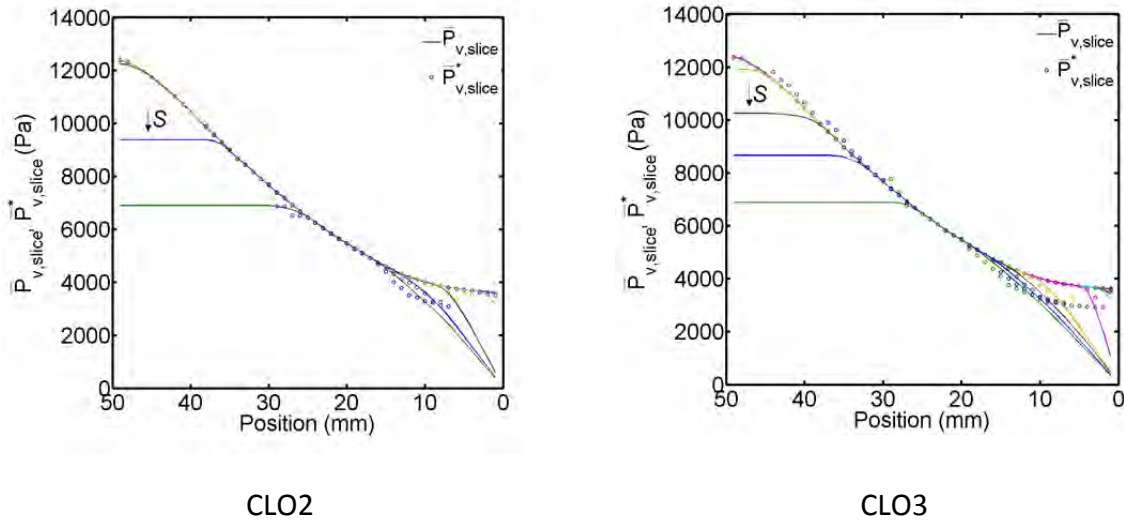


**Figure 6-44** Analysis of the 2-phase zone. The saturation curves have been computed from  $S_{2PZ} = S(\sum V_t + \sum V_p) / V_{Void,2PZ}$ . The curves are shown for the drying period after breakthrough of the gas phase.

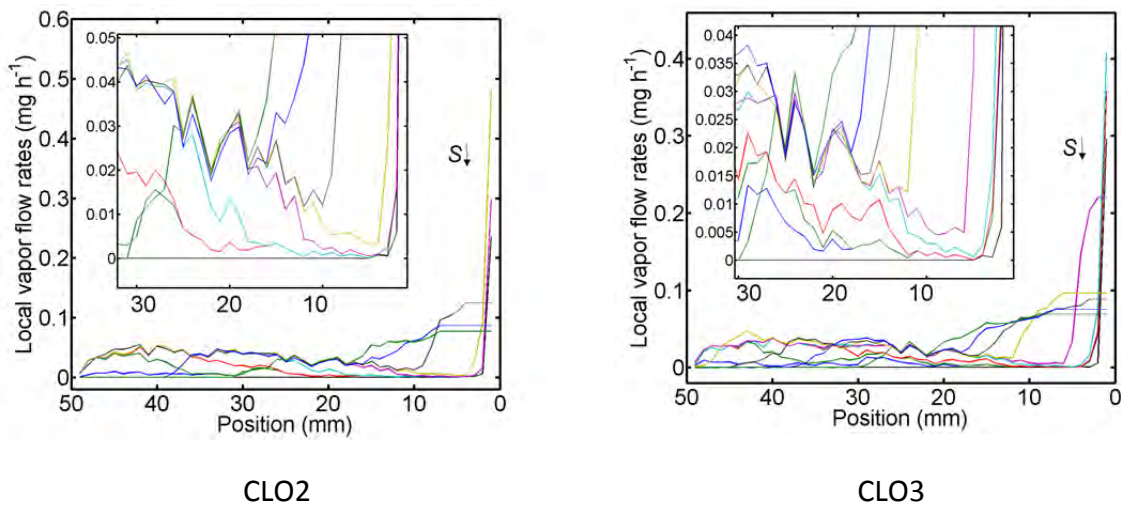


**Figure 6-45** a) Comparison of the computed liquid saturation of the 2-phase zone with experimental data. b) Computation of the saturation curve with diffusion coefficient from Krischer and Rohnalter (1940) and CLO3. The inset of the figure shows the liquid distribution for a PN saturation of  $S = 0.34$ . The phase pattern looks very similar as in Fig. 6-43, computed with the diffusion coefficient from Schirmer (1938).

The vapor pressure curves in Fig. 6-46 show that i) the gradient of the slice average saturation vapor pressure decreases towards the PN surface; ii) the slice average vapor pressure can become greater than the slice average saturation pressure. This is especially observed close to the PN surface, evidencing that vapor accumulates here by condensation. Accordingly, slice average vapor flow rates plotted in Fig. 6-47 become minimal at the evaporation front. This indicates that the highest vapor condensation rates are expected in this region. This phenomenon is observed in both PN simulations and it is very similar to



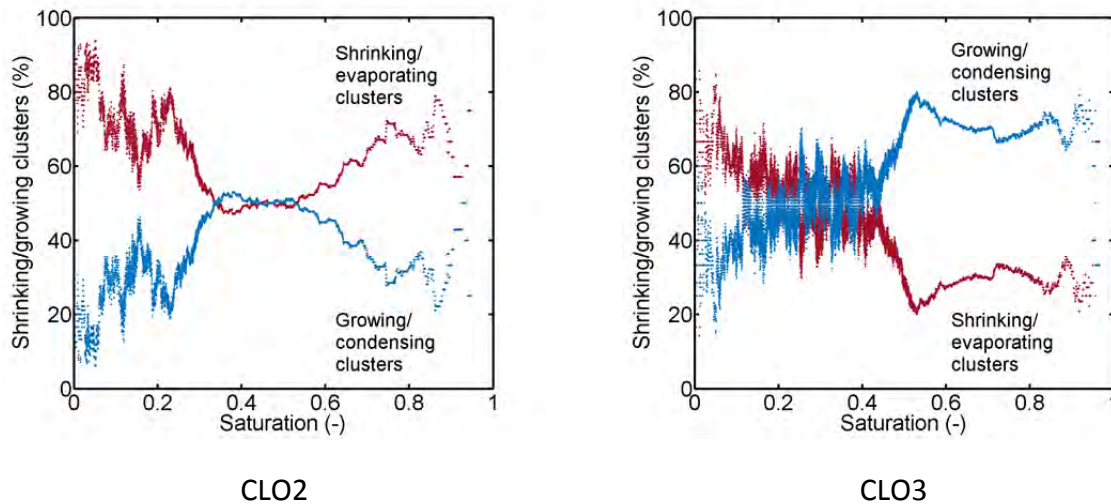
**Figure 6-46** Slice average vapor pressure curves and slice average saturation vapor pressures shown for  $S = [0.1:0.1:0.9, 0.98]$ .



**Figure 6-47** Sum of vapor flow rates through PN slices shown for  $S = [0.1:0.1:0.9, 0.98]$

experimental data in Fig. 4-30, where the local increase in liquid saturation indicates that most of the condensation appears in this region. However, apart from that, it is assumed that the specific structure of the liquid films crucially impacts on the redistribution of liquid, which shall be further analyzed in future.

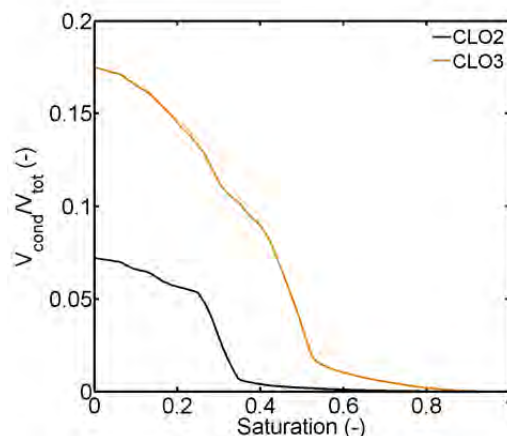
Figure 6-48 compares the percentage ratio of evaporating and condensing clusters in the 2-phase zone. This information is recorded in each invasion step, thus in contrast to the plots given in Fig. 4-34, where the information is obtained from analysis of two consecutive images (recorded at discrete time steps). Nevertheless, general trends given in Fig. 6-48 are comparable to the experimental data of Fig. 4-34. It is found that CLO2 yields a significantly better agreement with experimental observation: initially individual liquid clusters experience a period of dominating evaporation; this period is followed by a transient period dominated by condensation (occurring during the third drying period), while at the end of



**Figure 6-48** Comparison of the percentage ratio of condensing (blue) and evaporating (red) clusters for simulation with PNM level 4, CLO2 and CLO3.

the drying process evaporation is again dominant. Simulation with CLO3 instead reveals dominance of condensation already at the start of drying, while evaporation plays a major role at the end of the drying process. This shows the relevance of the interconnectivity of the liquid phase (by liquid films) for condensation. It clearly reveals that the condensation effect is less pronounced in simulation with CLO2. Again, this is explained with the cluster interconnectivity. In PNM level 4, CLO2 the liquid phase is interconnected over a wide range of the 2-phase zone. The condensation rates of clusters beneath the upper evaporation front can be compensated by the evaporation rate of clusters located at this front. Consequently, the clusters grow slower than in the simulation with CLO3, where the clusters are separated.

In agreement with the trends in Fig. 6-44 and Fig. 6-48 as well as with Table 6-5, Fig. 6-49 emphasizes that more liquid is indeed condensed in the model with CLO3. Experimental data is not available, but it is expected that the ratio is still higher in drying experiments.



**Figure 6-49** Computed ratio of condensed liquid volume (related to the initial total liquid volume contained inside the PN at the start of drying).

### **6.3.3.5 Summary**

It could be shown that the proposed non-isothermal PNM with implemented cluster growth mechanism can very well predict experimental drying if the high interconnectivity related to liquid films is incorporated simply by the cluster labeling option. This is revealed by simulations with CLO2. The remaining differences mainly concern underestimation of the saturation of the 2-phase zone which must be associated with underestimation of the condensation effect. This might be a consequence of the higher liquid interconnectivity achieved with this model; however, clearly more details about this phenomenon must be gained in future experimental work. Although PNM level 4 with CLO3 better predicted the condensation effect, results presented above indicate that interconnectivity of liquid phase is not accurately captured with this model. A better agreement might be obtained if the particular structure of liquid films would be incorporated. Exemplarily, isothermal simulation has shown that more liquid can remain inside the 2-phase zone if liquid rings are present. Following this, it may be deduced that implementation of liquid rings in the non-isothermal PNM with cluster growth can contribute to a higher saturation of the 2-phase zone without overestimating the liquid interconnectivity (as partly achieved with CLO2). A modified PNM should therefore take the cluster growth mechanism *and* the specific structure of the liquid films into account. However, this will certainly increase the computational effort. In this sense, more clarity must also be achieved in the mechanisms dominating the invasion process. Experiments indicate that piston type invasion controlled non-isothermal drying even in presence of liquid films; consequently invasion was simulated as piston like in the proposed model. However, the time scale of image recording might have been too short to distinguish piston type and snap-off invasion. Accordingly, a detailed study of the invasion process may be essential in future. Another aspect, not yet considered in the proposed model, is the sudden liquid redistribution due to Haines jumps. It is expected that this effect partly controls phase distributions in experiments, so that its implementation in the PNM might partly lead to a better agreement. In this sense, it shall also be mentioned that the impact of the computation of partially saturated pores and throats (which are essentially contradictory to the basic assumptions of quasi-steady invasion) should also be taken into account in future work. It might also be argued that the pore structure of the microfluidic PN was simplified by Eqs. 5-3 and 5-7. The total void volume inside the microfluidic PN actually might have been smaller than theoretically assumed, which might have had a positive impact on the phase patterns. However, simulation with a PN of reduced liquid volume by around 50 % did not reveal any positive impact on the condensation effect or the cluster structure.

In addition to that, the study presented in Appendix B.3 evidences interrelation of the height of the temperature gradient, evaporation rate and condensation effect (for a given pore size distribution). It is shown that condensation is positively affected by higher temperature gradients and lower drying rates. It is also shown that the drying time can be reduced even in presence of strong condensation effects, because the LAP of the front can be located at a favorable position very close or at the PN surface. From this study it might be concluded that a higher temperature gradient or decrease in the overall evaporation rate might give a better agreement of experimental and simulated data. This is partly revealed by the comparison of drying curves and drying rate curves in Fig. 4-37: due to a lower saturation of the pore network surface from the start of drying in experiment 18, the initial level of the evaporation rate is lower than compared to experiments 10 and 11. Nevertheless, drying appears faster in the third period of drying which is associated with a more pronounced

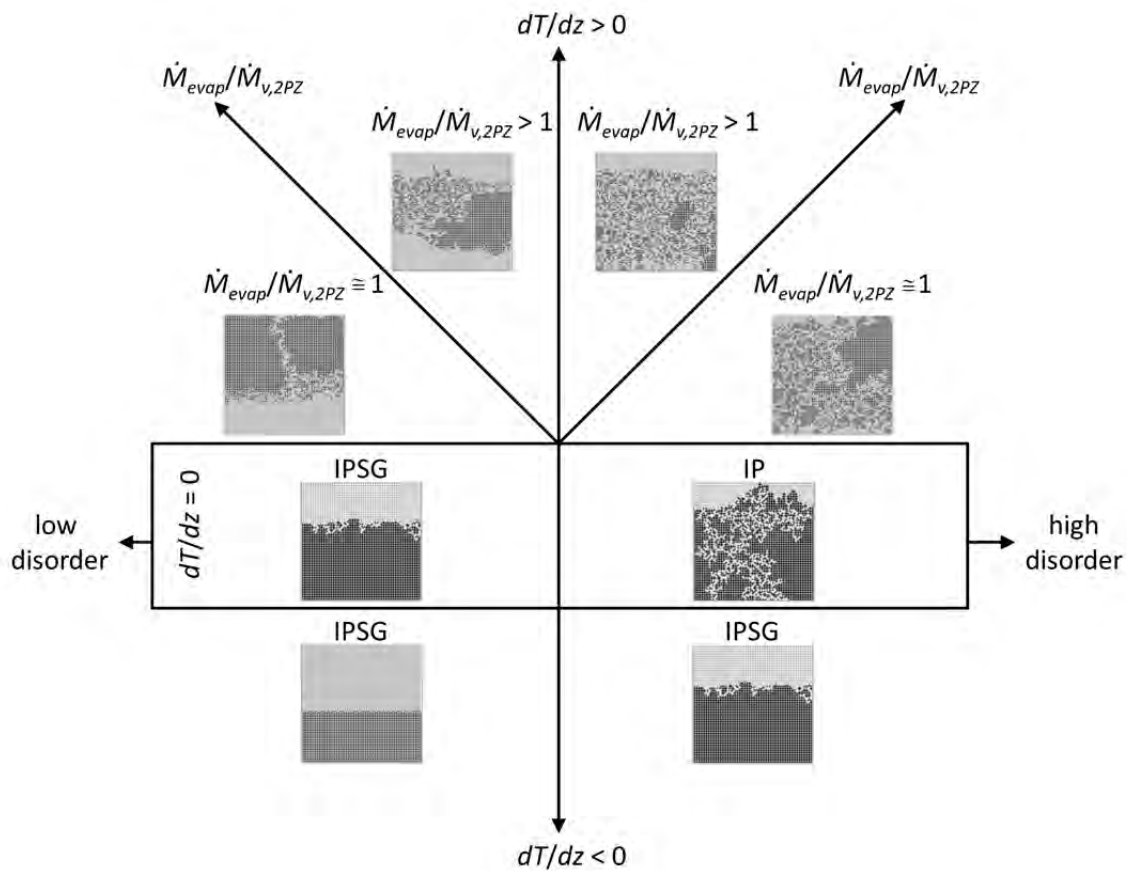


condensation effect in this experiment and the related favorable position of the upper drying front (Fig. 4-32). This indicates, that variation of  $P_v^\infty$  might positively affect the condensation rates.

Another, rather marginal, aspect which shall be mentioned here is the temporal drop of temperature of the thermal baths during refilling in microfluidic experiments (Appendix A). The very short drop of temperature might have induced a stronger condensation effect than simulated. However, very similar condensation behavior was observed in each experiment with positive thermal gradient although the temperature drops were very random and also not correlated with the distinct drying periods. Also the data analysis in Chapter 4 does not reveal any correlation of the condensation effect with the refill of thermal baths. Instead the condensation effect is very well associated with the different periods of drying.

#### 6.4 Phase diagram of thermally affected drying

Following the concepts of Plourde and Prat (2003) (Fig. 2-7) a different phase diagram is proposed for thermally affected drying taking into account the vapor diffusion through the partially saturated zone and the resulting condensation flow rates (Fig. 6-50). In contrast to Fig. 2-7, the proposed phase diagram contains a third dimension, thus accounting for the disorder of the PN, the temperature gradient and the ratio of vapor flow rates through the partially saturated zone and overall drying rate.



**Figure 6-50** Phase diagram of thermally affected drying. In the upper region of the diagram the phase patterns are controlled by capillarity *and* vapor diffusion.

In agreement with Plourde and Prat (2003), invasion patterns of the kind ‘invasion percolation with progressive evaporation of liquid clusters’ (IP) are obtained in an isothermal PN of sufficient disorder whereas invasion patterns of the kind ‘invasion percolation in a stabilizing gradient’ (IPSG) are obtained in a PN with low disorder and in a PN with imposed negative temperature gradient. The phase patterns for the positive thermal gradient, instead, are further distinguished based on the above results. The basic difference in contrast to the concept of Plourde and Prat (2003) concerns the dependence of the invasion process on both, capillarity and vapor diffusion as well. As found in Fig. 6-40, this affects the location and the structure of the 2-phase zone after breakthrough of the gas branch to the PN bottom. Similar phase patterns as anticipated by Plourde and Prat (2003) are found if the vapor flow rates through the 2-phase zone are low compared to the overall drying rate over most of the drying process. Then, the drying periods as described above, with breakthrough of the gas phase, ramification of the liquid phase and afterwards initiation of the travelling 2-phase zone can be observed. The ramification of the liquid phase during the third period of drying is higher, if the disorder is higher (upper images in Fig. 6-50). If contrary the evaporation rate is low compared to the vapor diffusion rates through the 2-phase zone (i.e.  $\dot{M}_{evap}/\dot{M}_{v,2PZ} \cong 1$ ) and the disorder of the PN is small, second, third and fourth drying period are not observed. Instead the PN dries out from the bottom side while the liquid phase mainly remains connected in a liquid cluster covering the 2-phase zone. (Similar phase patterns are expected for  $\dot{M}_{evap}/\dot{M}_{v,2PZ} > 1$  but very low disorder). In the situation of high disorder, however, the liquid phase can partly be ramified while the LAP can remain at a favorable position close to the PN surface.

This reveals that the pore scale liquid distribution during drying might be controlled by the pore size distribution (or disorder), the temperature profile along the PN and the evaporation rate as well. Further analysis of this context can be found in Appendix B.3.

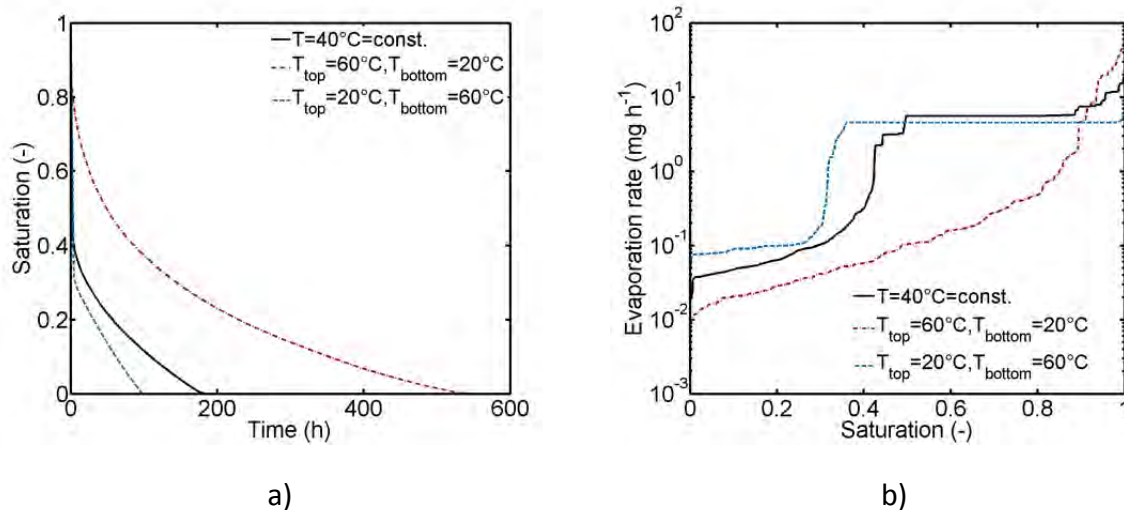
## **6.5 Comparison of PN drying with different heating modes**

From interpretation of findings above as well as the study of thermally affected drying in Appendix B.3 the question arises how drying processes might be positively affected, i.e. in terms of control of the evolution of phase distributions as well as efficiency, by adjustment of temperature profiles. As explained in detail in this thesis, drying can be fast if the evaporation front remains connected to the surface as long as possible. This is usually achieved in presence of liquid films, as shown in Section 6.2.5. Thus, if liquid films are present in a PN (or a porous medium) liquid can be efficiently transferred by capillary film flow. In addition to that, simulation results presented in Section 6.3 elucidate that drying with imposed positive thermal gradient can profit from the favorable invasion of the PN bottom at the start of drying, while the evaporation front remains connected to the surface. As revealed in Fig. 6-51, drying with imposed positive thermal gradient can be much faster than isothermal drying although the initial evaporation rate is lower related to the lower network temperature at the surface. Contrarily, drying with negative thermal gradient appears rather unfavorable because liquid from the bottom of the PN is removed at significantly lower temperature (and thus reduced driving force) than in the other two drying processes. However, the situation might be different when regarding 3-dimensional porous media in real drying processes. With increasing distance of the travelling 2-phase zone from

the heat source, heat transfer resistances usually increase which leads to a drop of drying rates at the second evaporation front. This effect can drastically diminish the efficiency of drying performance.

Despite of this, an application of drying with travelling 2-phase zone initiated by an imposed thermal gradient is the microwave drying of porous media (e.g. Turner and Jolly 1991). Here, energy of the penetrating electromagnetic waves is dissipated by liquid contained inside the core of the wet product. This leads to temperature profiles as in PN drying with imposed positive thermal gradient. The proposed PNM might be applied in this context to study dominating pore scale effects and their impact on the overall drying behavior in this and related processes.

Another application, where the impact of imposed temperature gradients could be exploited, is the distribution of colloidal particles (e.g. catalyst particles inside a solid matrix) after drying. As shown above, the pore scale evolution of the liquid phase can be controlled by the temperature gradient. Thus the distribution of the particles might positively be affected by playing with the temperature profile along the porous medium during drying, e.g. by application of a periodic variation of temperature. This would force the liquid to change its direction of migration periodically, leading to a rather homogenous saturation profile along the porous medium and higher connectivity of the liquid phase.



**Figure 6-51** Comparison of the convective heating mode, contact heating mode and isothermal drying (at  $T = 40^{\circ}\text{C} = \text{const.}$ ). a) Drying curves, b) drying rate curves. The curves indicate that drying by contact heating ( $T_{\text{top}} = 20^{\circ}\text{C}$ ,  $T_{\text{bottom}} = 60^{\circ}\text{C}$ ) can be faster than drying by convective heating ( $T_{\text{top}} = 60^{\circ}\text{C}$ ,  $T_{\text{bottom}} = 20^{\circ}\text{C}$ ) because of higher drying rates over the longest period of the drying process (although the percentage ratio of condensed liquid volume is greater in the contact heating mode,  $v^+ \cong 0.09$ , than in the convective heating mode, where  $v^+ \cong 0.02$ .)

It is remarked that the findings derived from Fig. 6-51 seem to be in contrast with experimental findings presented in Chapter 4. There, drying time was approximately 47 h in the quasi-isothermal experiment and 24 h in drying with imposed negative thermal gradient and furthermore 70 h – 90 h in drying with imposed positive thermal gradient. This opposed behavior can be explained with the mean temperature achieved in each drying experiment:

precisely,  $\bar{T} \cong 36^\circ\text{C}$  in experiment with positive thermal gradient and thus significantly lower than in the other two experiments where the mean temperature was  $\bar{T} \cong 63^\circ\text{C}$  (quasi-isothermal drying) and  $\bar{T} \cong 64^\circ\text{C}$  (drying with negative thermal gradient). Additionally, residual moisture content inside the PN at the end of the drying process was significantly different (compare Figs. 4-16, 4-24 and 4-37).

## 6.6 Summary and discussion

In this chapter, simulation results from drying of a 2D PN, identical to the microfluidic network studied in Chapter 4, were presented and discussed in relation to experimental results with the aim to validate the proposed non-isothermal PNM with secondary capillary effects and cluster growth. The evaluation of the PNM was based on a precise structural analysis of the pore scale liquid distribution in the microfluidic PN; such a study has not been presented in literature before. It was found that the PNM can very well predict peculiarities of drying under different thermal conditions. These were the progressive invasion of the liquid saturated PN with formation of capillary liquid rings in quasi-isothermal drying, stabilization of drying front in presence of an imposed negative thermal gradient and breakthrough of the gas phase with initiation of a travelling 2-phase zone in presence of a positive thermal gradient. These findings can be instrumental for control of the pore level mass transfer during drying. In detail, it was shown that drying with positive thermal gradient can be faster than drying with identical negative thermal gradient (Fig. 6-51). This was explained with the higher evaporation rates associated with the more favorable drying front position over a longer time period in case of the positive thermal gradient.

### *Drying under quasi-isothermal conditions*

In detail, morphology of the 2-phase zone as well as drying rate and drying time can be controlled by thick wetting liquid films forming around the solid islands of the PN. Structure of this film zone, namely limited extension over only a few pore rows, could be well predicted with the PNM accounting for liquid film rings; contrarily a wide and continuous film region was simulated with the film model proposed by Prat (2007). The film rings were implemented with width  $L_r = 21.4 \mu\text{m}$  and with an effective evaporation area of  $\alpha = 2$ . With this, higher interconnectivity of the liquid phase was obtained when the labeling option RLO2 was applied. It was also shown that the liquid covered side walls of the PN had a strong impact in this heating mode, because they allowed for a favorable drying front position over the longest drying time. This was captured by the implementation of the edge effect with increased invasion pressure thresholds inside one lateral column of vertical and horizontal throats ( $f^{red} = 0.85$  and  $z^{pin} = (5-49)L$ ). It was found that the position of the pinning of the liquid phase at the side walls could also be predicted with the film model proposed by Prat (2007). However, this model could not predict the accurate structure of the liquid phase in the center of the PN. Anyway, with both approaches (edge effect, continuous film model) the drying time could be significantly decreased. This revealed the strong impact of secondary invasion. In general, the occurrence of wetting liquid films plays a major role in drying processes if the porous medium is wettable (Shaw 1987, Tsimpanogiannis et al. 1999, Lenormand et al. 1983, Segura 2007). Comparison of experiments and simulation results reveals that liquid films impact on the drying process especially in the RFP, when the bulk

liquid phase is disconnected and when the drying front has detached from the surface. Exemplarily, they interconnect the bulk liquid phase and thus allow for a different order of invasion. More clearly, the MAP of the drying front can advance while the evolving clusters confined inside the film region are supplied with liquid via continuous liquid films. This can lead to a more advanced position of the drying front and higher drying rates. These outcomes are also relevant for drying of solutions of suspended particles or dissolved salt (e.g. Boernhorst et al. 2016), as the interconnectivity of the liquid phase is modified in presence of liquid films. Though, it is emphasized that the ring structure of films is specific to 2D networks and glass bead packings (Wang et al. 2013). In more realistic porous structures, a combination of both film morphologies is rather expected (Geistlinger et al. 2016). In more detail, the wall covering liquid films (simulated with the approach of Prat 2007) can sustain liquid connectivity of liquid rings in such a situation.

Apart from that, optimal agreement of quasi-isothermal experiments and simulations (concerning prediction of drying time, distribution of gas and liquid phase during drying as well as the trend of the drying rate curve) was obtained by incorporation of the local temperature variation (as observed in drying experiments with the microfluidic SiO<sub>2</sub> PN), because then the temporal stabilization of the drying front could be captured. This resulted in a more accurate prediction of the breakthrough of the gas phase to the bottom of the PN. Especially, the simulated structure of the main liquid cluster was very similar to the experimentally observed structure. A similar stabilization was obtained by implementation of pore volumes and liquid pumping (due to viscous effects). However, it was shown that the effect of temperature on capillary invasion dominated over the other two stabilization effects (in the given PN structure and temperature field).

#### *Drying with imposed thermal gradients*

The study of drying with imposed thermal gradients revealed significantly different drying behavior depending on the direction of the temperature gradient. While drying in the stabilizing regime was mainly controlled by secondary capillary effects (precisely the lateral pinning of the liquid phase), drying performance in the destabilizing regime was controlled by the interaction of secondary effects (mimicked by cluster labeling) and the cluster growth mechanism. The occurrence of the lateral pinning of the liquid phase in drying with stabilizing gradient furthermore revealed the relevance of the diffusion of vapor from the tip of the liquid phase pinned at the side walls (at higher temperature) towards the drying front in the center of the PN (at lower temperature). This allowed for the condensation of vapor at liquid cluster boundaries close to the side walls, whereas clusters located at the axis of the PN evaporated. This effect was referred to as the heat pipe effect. In general, liquid films can pump liquid to the surface of the PN if the capillary pressure associated with the width of the liquid films is high enough (as mimicked by the edge effect). This is observed even if temperature of the films is higher than the temperature in the liquid phase below. At the same time part of the evolving vapor flows countercurrently to the liquid phase and condenses at the colder clusters below the film tip. This can lead to stabilization of the drying front (width) by vapor diffusion induced invasion. Thus, the edge effect, although unfavorable in terms of complexity of the PNM (discussed in Section 3.1), though illuminated the relevance of liquid films for transport processes in presence of thermal gradients, as usually observed in convective drying.

In contrast to that, the edge effect played a minor role in drying with destabilizing thermal gradient because the upper front of the liquid phase essentially remained close to the PN surface. It was found that secondary capillary effects control drying in the capillarity controlled stages. This concerns the first and second period of drying, when a tortuous gas branch penetrates the PN from the upper drying front at constant position at the PN surface towards the PN bottom (first period) and when afterwards the two resulting main clusters are split up by a front moving upwards in the PN until coinciding with the upper evaporation front. In these drying periods, application of PNM level 4 and CLO2 (mimicking increased cluster connectivity by manipulation of the labeling) yields very good agreement of phase patterns and drying rate curve as well. In the consecutive third period of drying, the connectivity of the liquid phase is overestimated by this version of the PNM which is basically revealed by a less pronounced condensation effect (due to the compensation of condensation rates by the overall evaporation rate from the top of the PN which is interconnected with the smaller clusters in this CLO). Then PNM level 4 CLO3 shows a better agreement in terms of phase patterns while the drying rate is underestimated. Underestimation of drying rate with this PNM as well as underestimation of the saturation of the travelling 2-phase zone was explained with a lower condensation effect than experimentally observed. In more detail, smaller clusters and also a more advanced position of the drying front were predicted with CLO3. It was discussed that higher vapor diffusivities might overcome the remaining discrepancy, making worth a more detailed study in future. In this, impact of the peculiar structure of the liquid films and the related connectivity of the liquid phase shall be considered as well as the impact of the computation of partially saturated liquid elements.

Independently of this, it could nicely be demonstrated that the structure of the liquid phase distribution (in the period of drying when the liquid phase is split up) is not only dictated by the interrelation of structural parameters and the height of the thermal gradient (as proposed by Plourde and Prat (2003)), thus the thermally affected capillarity of the PN, but that instead interrelation of vapor diffusion through the partially saturated zone, induced by the temperature gradient, and the overall evaporation rate must additionally be considered. Consequently, morphology of the travelling 2-phase zone is a function of the overall drying rate and height of the thermal gradient imposed on the PN in the third period of drying. This is studied in more detail in Appendix B.3.

In purpose of a PNM that might be applied to drying of 3D porous structures of greater dimension than studied here, it is proposed to incorporate the limitation of liquid pumping due to viscous friction forces in the non-isothermal PNM with cluster growth. While it is assumed that liquid flow stabilization due to viscous forces can be neglected in the PN studied here, viscosity plays a major role in the secondary capillary transport, especially in wall covering liquid films over long distances. Furthermore, viscous stabilization is expected to become increasingly important in larger PNs. Exemplarily, Shaw (1987) has shown that a fractal structure of the drying front can be found on the microscale whereas a stabilized front is observed on the macroscale. He assumed that viscous friction forces play a greater role in a larger system (Shaw 1987, Schluender 2004, Tsimpanogiannis et al. 1999). At the same time, also gravity forces might be included in PNMs for greater 3D systems.

„Ideen an sich haben keinen Wert, wenn man nicht anwendungsorientiert arbeitet.“

Werner von Siemens

\* December 13, 1816 in Lenthe, Germany

† December 6, 1892 in Berlin, Germany

## Chapter 7

# Summary and Outlook

### 7.1 Summary

In this thesis, development of a non-isothermal PN drying model based on an experimental study of drying in a microfluidic 2D SiO<sub>2</sub> PN was presented and discussed. Base of the thesis was the lack of experimental validation of existing isothermal and non-isothermal pore network models (PNMs) as well as a lack of knowledge of the leading pore scale effects that control the macroscopic drying behavior under both, isothermal and non-isothermal conditions. Both gaps could be filled with this work supported by a precise analysis of the pore scale liquid distribution evolving in the microfluidic PN. The proposed PNMs are very efficient and can be seen as a step towards more realistic drying models of porous media with a strong physical base.

#### *Secondary capillary effects*

At first it could be shown that, as a priori expected, wetting liquid films control drying rate and drying time of the microfluidic PN with good wettability and structural peculiarities that favor their formation. Moreover it was revealed that the structure of liquid films must be distinguished between the liquid films that continuously cover the (rough) walls of the PN over a growing distance when the drying front recedes and discrete liquid rings forming inside the narrow wedges of solid islands covering the microfluidic PN usually only inside the 2-phase zone or 1 or 2 pore rows upstream of the drying front. Such a study of the detailed morphology of liquid films in 2D PNs, its interrelation and the impact on drying has not been presented before.

The wall covering liquid films were observed along the straight side walls of the microfluidic PN. They usually extended over several pore rows, thus connecting the drying front in the center of the PN with liquid pinned to a position only a few pore rows below the PN open surface. This was also referred to as the edge effect. It could be shown that this effect could

increase the overall drying rates in the microfluidic PN. The liquid rings could be detected by Confocal Laser Scanning Microscopy. The microscopy measurements revealed that the liquid rings, remaining around the solid islands in the center of the 2D PN, are discrete liquid elements as it could be demonstrated that drying of these rings occurs independently of each other. It was thus assumed that drying of liquid rings can be associated with discrete invasion events. Both observations, i.e. the continuous liquid films as well as the liquid rings, are in very good agreement with literature observations (referred to 2D PNs and glass bead packings).

Based on these findings, a new PNM was proposed and compared to the classical continuous film model proposed by Prat (2007). With the continuous film model, drying time can be very well predicted if wettability of the PN with water is well adapted. (Alternatively, the roundness of the corners can be adapted). However, comparison of the gas-liquid phase distribution simulated with this model with own experiments revealed that the specific pore level phenomena could not be captured because neither the computed structure of the bulk liquid phase nor the position of the cluster front in the center of the PN agreed with experimental observations. Instead, the good agreement of the computed drying time using the continuous film model was explained by the lateral pinning of the liquid phase. It could be shown that the position of lateral pinning along the side walls of the microfluidic PN was in very good agreement with the least advanced point of the film region in the drying simulation. From this follows, that the continuous film model can capture the lateral pinning (which is essentially a result of wall covering films along the side walls), but due to the continuity of the film region, position of the drying front in the center of the PN is overestimated. Consequently, a novel film model was proposed in which discrete liquid rings were implemented as additional liquid elements in the PNM. Contrary to the continuous film PNM, presence and width of the liquid film rings was implemented independently of the capillary number. Instead it was shown that the impact of the liquid film rings can be adjusted by adaption of ring width as well as the cluster interconnectivity achieved by these liquid elements. It could be shown that the improved representation of the film structure by discrete liquid rings together with a simplified representation of the edge effect (by manipulation of the entry pressure thresholds of the throats along the sides of the PN) could improve predictability of the PNM.

In summary, it was shown that implementation of different specific morphologies of wetting liquid films affects the simulated drying behavior significantly. Implementation of the continuous liquid films can lead to a broad film region that can cover most of the PN for a long time. In contrast, the liquid rings are usually confined in the 2-phase zone, i.e. within the limits of the least and most advanced point of the cluster front. It was shown that the different structures of the liquid films affect drying rate and drying time. While the continuous films can lead to a period of constant drying rate, which duration depends on the expansion of the films to the PN surface, the same is not achieved by liquid rings. However, the latter can interconnect single menisci and single clusters and thus increase the interconnectivity of the liquid phase within the 2-phase zone. It is strongly expected that a combination of the two different morphologies of wetting liquid films is likely to occur in 3-dimensional porous media with realistic pore structure. The liquid rings would then represent the liquid bridges forming inside the throats and pores of a 3D porous matrix and the pendular rings at the contact points of spherical particles in a 3D particle packing. Thus, it is worth to further investigate the particular impact as well as the interplay of the two different pore scale film effects in future work.



*Drying with imposed thermal gradients*

Another focus of the thesis was on drying experiments with imposed thermal gradients aiming at the validation of governing mass transfer phenomena in thermally affected PNs. Experiments with imposed negative and positive thermal gradients nicely agreed with the existing theory about thermal stabilization and destabilization of the drying front. It could be verified that a temperature gradient with maximum temperature at the PN surface and minimum temperature at the PN bottom can lead to stabilization of the drying front if the variation of capillary pressure due to the temperature dependency of surface tension dominates over the variation of capillary pressure due to pore size distribution. Such kind of a temperature gradient is also expected in processes of convective drying of porous media. However, in contrast to a priori assumptions, the liquid phase could not be perfectly stabilized in the microfluidic experiments as again the edge effect resulted in a more favorable position of the evaporation front at the side walls of the PN. From this observation basically three effects could be derived. At first, the position of the evaporation front close to the PN surface increased the overall drying rate as also observed in isothermal drying. At second, this revealed that liquid connectivity can be sustained over a temperature gradient if the difference of invasion pressure thresholds is sufficiently large. This was achieved by the reduction of the width of the pores and throats along the PN lateral side walls (mimicking the ledge effect in microfluidic experiments). At third, it could be shown that in this situation vapor can diffuse from the film tips towards the clusters confined in the region of lower temperature. This leads to a heat pipe effect within the drying front and has never been studied before by PN simulation.

A gradient with maximum temperature at the bottom of the PN and minimum temperature at the surface is expected to evolve in contact drying of porous media. The specific pore level events associated with such a temperature gradient are significantly different from those observed in isothermal drying or thermally affected drying with negative gradient. These are namely the early breakthrough of the gas phase to the bottom of the PN, the split up of the liquid phase starting from the PN bottom, the initiation of a second evaporation front and a 2-phase zone travelling from the bottom of the PN towards the PN surface. (Obviously, the edge effect plays a minor role here). These effects are associated with the different periods of drying. Invasion of the PN during the first and second period of drying (i.e. when the liquid phase is interconnected to the PN surface) is controlled by the thermally affected capillarity. Precisely, the capillary pressure gradient induced by the thermal gradient between the surface and the bottom of the PN allows for the breakthrough of a single gas branch to the hot bottom at the start of drying and the complete split up of the two liquid clusters resulting from the breakthrough. Capillary invasion stops with the complete split up of the liquid phase into separated single clusters, which are significantly smaller than the original liquid cluster spanning the PN at the start of drying. In these drying periods, interconnectivity of the liquid clusters by liquid films plays a major role. Then, in the third and fourth period of drying, vapor diffusion governs moisture migration. Basically, more liquid is evaporated at the bottom of the PN where the temperature is higher. This leads to the initiation of a second invasion front. The vapor travels through the 2-phase zone due to the temperature gradient. However, if the vapor pressure exceeds the saturation vapor pressure at a cluster boundary with lower temperature, vapor condenses and the condensed liquid invades the already dried void space. This leads to growing and merging of liquid clusters, nicely demonstrated by PN drying experiments. As a result, extension of the 2-phase zone decreases while the liquid phase becomes apparently more dense. At the end

of the third drying period, a compact liquid cluster with an apparently greater size than the single clusters present at the end of the second drying period is found close to the PN open surface. The liquid distribution inside the 2-phase zone as well as the position of the 2-phase zone at the transition of this drying period towards the fourth drying period (i.e. when the clusters finally dry out) is dictated by the interaction of vapor diffusion, height of the temperature gradient and overall drying rate. Thus, experiments with imposed positive thermal gradient demonstrated that the diffusion and condensation of vapor controls the evolution of the 2-phase zone in the period of drying when the liquid phase is split up into separate clusters. In contrast to the capillarity controlled liquid distribution in the first and second period of drying, in this drying period the liquid interconnectivity by liquid films played a minor role in the investigated microfluidic PN. However, due to the merging of formerly separated liquid clusters, capillary connectivity can be reactivated in the non-isothermal PN during the third period of drying.

From this can be concluded that drying with positive thermal gradient can be more efficient because i) the drying front does not recede significantly from the PN surface and ii) capillary liquid connectivity to the surface is sustained or reactivated due to the condensation of vapor. Based on this finding, a novel PNM was proposed that takes the simultaneous evaporation and condensation of liquid and vapor into account by a cluster growth mechanism. It was shown, that this model can very well predict the experimental drying behavior if the high interconnectivity of the liquid phase by liquid films in the first and second drying period is carefully adapted. Simulations revealed that position of the least advanced point of the travelling 2-phase zone, its extent and local saturation at the end of the third drying period strongly depend on the combination of the height of the temperature gradient and overall evaporation rates (for a given pore size distribution). Accordingly, temperature gradients can be instrumental for control of the overall efficiency of drying processes: drying with positive thermal gradient can be faster than drying with negative thermal gradient if the mean temperature is similar; however, the predicted drying time strongly depends on the amount of condensed liquid volume. Additionally, the liquid distribution during drying can be controlled by the thermal gradient. This can be instrumental for product quality, if one thinks of catalysts, proton exchange membranes etc.

Finally, it is concluded that development and control of modern drying processes should consider the pore level liquid distribution during drying, because choice of an appropriate drying method controls product quality after drying (such as the distribution of dissolved species or also shrinkage of the product) on the one hand, and overall drying time on the other hand. Some examples are discussed in the outlook below together with the requirements to PNMs and microfluidic experiments necessary for a reliable prediction.

### 7.2 Outlook

The experimentally validated non-isothermal PNM with secondary capillary invasion might be used to study mass transfer processes in presence of imposed thermal gradients with the purpose to exploit temperature control as a perspective for the formulation of industrial and natural products by drying. Such processes are e.g. the microwave drying of porous wet clay, i.e. where the temperature field evolves from the dissipation of electromagnetic energy. Also temperature fields imposed on thin porous media (such as membranes or thin films for

organic electronics or also gas diffusion layers or porous transport layers) in the through-plane direction are examples, where the proposed PNM might illuminate the phenomena of thermally affected mass transfer through porous media. It has been shown in preliminary work that the temperature profile can be implemented by empirical functions of temperature in space and time. This is especially relevant in regard of the computational time, which can be reduced if heat transfer must not be computed. Drying processes controlled by transient heat transfer, however, might rather be studied based on the approach given in Surasani (2009), though adjusted by the findings of this work. This regards the incorporation of liquid films *and* cluster growth as well, since it was shown that both effects crucially impact on the drying process depending on the direction of the temperature gradient and vapor diffusion.

In this context, it is highlighted that different film morphologies were explored in this work. It was shown that different invasion mechanisms are associated with these structures, making worth a more detailed experimental and PNM study in future. This can be seen as a step towards a more realistic PNM for drying of real porous media, where both, continuous wall covering liquid films and discrete films are expected. One first step is the implementation of continuous liquid films by virtual layers connected to the PN. In this approach, a continuous film region can be achieved, the extent of which is controlled by the modification of the interconnection of the virtual layers with the PN (i.e. by cluster labeling) as well as by the pore size distribution in the film layers. A very good agreement could already be shown, if the viscous effects in the liquid phase are taken into account in this model (i.e. by computing the dynamic invasion of pores and throats). This version of the PNM allows to link the continuous film layer with the liquid rings as well as liquid clusters with the aim to enable intercluster liquid transfer by the continuous film region.

In the same spirit, the microfluidic PN might be revised to a technically feasible extent. This mainly concerns the edge effect, which might be avoidable in a PN with greater width of the vertical throats along the PN sides or by providing barriers (such as the solid islands in the center of the PN) that interrupt film flow. The existing microfluidic PN (presented in this thesis) can instead be used to investigate the aforementioned coupling of the different film effects. Furthermore, analysis of the experimental data shows that more accuracy is needed concerning the experimental procedure at the start of experiments as well as estimation of liquid films and pore scale invasion. So far, only the fully saturated and the totally dry elements were considered for the validation of the PNM; the liquid films as well as liquid bridges (or partially saturated elements) were not numerically analyzed. It is also not yet clear how these films impact on the pore scale invasion of pores and throats, i.e. by snap-off or by piston type advance, and how this affects the re-saturation of the partially saturated zone in drying with cluster growth induced by a positive thermal gradient. More insights about the different pore scale invasion mechanisms are thus another issue of future work.

Independent of this, the results presented in this thesis might be a step towards control of product quality and drying time by careful adjustment of drying conditions. Exemplarily, mechanically stressed media might be preferably dried in a heating mode that avoids formation of liquid pressure gradients, while the distribution of suspended particles or salt crystals might be positively affected by positive temperature gradients. Moreover, the observed heat pipe effect with condensation of liquid and refilling of desaturated pores and pore throats might be exploited to control temporal evolution of phase distributions, product quality and drying time.

## References

1. Ackermann, G. (1934) Theorie der Verdunstungskühlung, Ing.-Archiv Bd. 5, p. 124
2. Al-Futaisi, A. and Patzek, T.W. (2003) Extension of Hoshen–Kopelman algorithm to non-lattice environments, *Journal of Physics A* 321, 665-678
3. Amyot, O.; Flukiger, F.; Geoffroy, S.; Plouraboué, F.; Prat, M. (2007) Critical point network for drainage between rough surfaces, *Transport in Porous Media* 70, 257-277
4. Arnold, J.; Dasbach, U.; Ehrfeld, W.; Hesch, K.; Löwe, H. (1995) Combination of excimer laser micromachining and replication processes suited for large scale production, *Applied Surface Science* 86, 251-258
5. Baesch, S.; Scharfer, P.; Schabel, W.; Francis, L. (2017) Influence of the drying conditions on the particle distribution in particle-filled polymer films: Predictive simulation of the particle distribution during drying, *Journal of Composite Materials*, DOI:10.1177/0021998316687144
6. Berg, S.; Ott, H.; Klapp, S.A.; Schwing, A.; Neitelr, R.; Brussee, N.; Makurat, A.; Leu, L.; Enzmann, F.; Schwarz, J.-O.; Kersten, M.; Irvine, S.; Stampanoni, M. (2012) Real-time imaging of Haines jumps in porous media flow, *PNAS* 110 (10), 3755-3759
7. Berkowitz, B. and Ewing, R.P. (1998) Percolation theory and network modeling applications in soil physics, *Surveys in Geophysics* 19, 23-72
8. Beyhaghi, S.; Geoffroy, S.; Prat, M.; Pillai, K.M. (2014) Wicking and evaporation of liquids in porous wicks: A simple analytical approach to optimization of wick design, *AIChE Journal* 60 (5), 1930-1940
9. Bird, B.; Stewart, W.E.; Lightfoot, E.N. (1960) *Transport Phenomena*, John Wiley and Sons, New York, USA

10. Blunt, M.J.; Jackson, M.D.; Piri, M.; Valvatne, P.H. (2002) Detailed physics, predictive capabilities and macroscopic consequences for pore-network models of multiphase flow, *Advances in Water Resources* 25, 1069-1089
11. Bonnet, J. and Lenormand, R. (1977) Réalisation de micromodèles pour l'étude des écoulements polyphasiques en milieu poreux, Note technique dans *Revue de L'Institut Français du Pétrole* 42 (3), 477-480
12. Bories, S.A. (1991) Fundamentals of drying of porous media, In: S. Kakac et al. (Eds.) *Convective Heat and Mass Transfer in Porous Media*, Kluwer Academic Publishers, 391-434, Dordrecht, Netherlands
13. Boernhorst, M.; Walzel, P.; Rahimi, A.; Kharaghani, A.; Tsotsas, E.; Nestle, N.; Besser, A.; Kleine Jäger, F.; Metzger, T. (2016) Influence of pore structure and impregnation: drying conditions on the solid distribution in porous support materials, *Drying Technology* 34 (16), 1964-1978
14. Buckley, J.S. (1991) Multiphase displacements in micromodels, In: N.R. Morrow (Ed.) *Interfacial Phenomena in Petroleum Recovery*, Dekker, New York, USA
15. Bustos, C.I. and Toledo, P.G. (2003) Pore-level modeling of gas and condensate flow in two- and three-dimensional pore networks: Pore size distribution effects on the relative permeability of gas and condensate, *Transport in Porous Media* 53, 281-315
16. Celia, M.A.; Reeves, P.C.; Ferrand, L.A. (1995) Recent advances in pore scale models for multiphase flow in porous media, *Reviews of Geophysics Supplement* 33 (2), 1049-1057
17. Chapuis, O. (2006) Influence des conditions de mouillage sur les déplacements quasi-statiques eau-air et l'évaporation en milieux poreux modèles: Application à la gestion de l'eau dans les piles à combustibles de type PEMFC, PhD Thesis, L'Institut National Polytechnique de Toulouse, Toulouse, France
18. Chapuis, O. and Prat, M. (2007) Influence of wettability conditions on slow evaporation in two-dimensional porous media, *Physical Review E* 75, 046311
19. Chatzis, I. and Dullien, F.A.L. (1983) Dynamic immiscible displacement mechanisms in pore doublets: Theory versus experiment, *Journal of Colloid and Interface Science* 91 (1), 199-222
20. Chatzis, I.; Morrow, N.R.; Lim H.T. (1983) Magnitude and detailed structure of residual oil saturation, *Society of Petroleum Engineers of AIME* 23, 311-326
21. Chauvet, F.; Duru, P.; Geoffroy, S.; Prat, M. (2009) Three periods of drying of a single square capillary tube, *Physical Review Letters* 103, 124502
22. Chauvet, F.; Duru, P.; Prat, M. (2010) Depinning of evaporating liquid films in square capillary tubes: Influence of corners' roundedness, *Physics of Fluids* 22, 112113
23. Crausse, P. (1983) Étude fondamentale des transferts couples de chaleur et d'humidité en milieu poreux non-saturé, PhD Thesis, L'Institut National Polytechnique de Toulouse, Toulouse, France
24. Daian, J.-F. and Saliba, J. (1991) Détermination d'un réseau aléatoire de pores pour modéliser la sorption et la migration d'humidité dans un mortier de ciment, *International Journal of Heat and Mass Transfer* 34 (8), 2081-2096

25. de Boer, R. (1988) A historical review of the formulation of porous media theories, *Acta Mechanica* 74, 1-8
26. Defraeye, T.; Radu, A.; Derome, D. (2016) Recent advances in drying at interfaces of biomaterials, *Drying Technology* 34 (16), 1904-1925
27. de Gennes, P.-G. (2004) *Capillarity and wetting phenomena: Drops, bubbles, pearls, waves*, Springer, New York, USA
28. Diaz, R.E.; Acuna, S.M.; Segura, L.A. (2011) Construction of 2D transparent micromodels in polyester resin with porosity similar to carrots, *Ciência e Tecnologia de Alimentos* 31(4), 960-966
29. Dullien, F.A.L. (2012) *Porous media: Fluid transport and pore Structure*, In: Hacourt et al. (Eds.) Academic Press, San Diego, USA
30. Fatt, I. (1956a) The network model of porous media, Part 1: Capillary pressure characteristics, *AIME Petroleum Transactions* 207, 144-159
31. Fatt, I. (1956b) The network model of porous media, Part 2: Dynamic properties of a single size tube network, *AIME Petroleum Transactions* 207, 160-163
32. Fatt, I. (1956c) The network model of porous media, Part 3: Dynamic properties of networks with tube radius distribution, *AIME Petroleum Transactions* 207, 164-181
33. Fenwick, D.H. and Blunt, M. (1998) Three-dimensional modeling of three phase imbibition and drainage, *Advances in Water Resources* 21 (2), 121-143
34. Fuller E.N.; Ensley K., Giddings J.C. (1969) Diffusion of halogenated hydrocarbons in helium, *Journal of Physical Chemistry* 73 (11), 3679-3685
35. Geistlinger, H.; Ataei-Dadavi, I.; Vogel, H.-J. (2016) Impact of surface roughness on capillary trapping using 2D-micromodel visualization experiments, *Transport in Porous Media* 112, 207-227
36. Geoffroy, S. and Prat, M. (2014) A review of drying theory and modelling approaches, In: J.M.P.Q. Delgado (Ed.) *Drying and Wetting of Building Materials and Components (Building Pathology and Rehabilitation Vol. 4)*, Springer International Publishing, Switzerland, DOI: 10.1007/978-3-319-04531-3\_7
37. Gu, L.; Ho, C.K.; Plumb, O.A.; Webb, S.W. (1998) Diffusion with condensation and evaporation in porous media, In: *Proceedings of 7th AIAA/ASME Joint Thermophysics and Heat Transfer Conference*, Albuquerque, USA, June 15-18, 1998
38. Gueven, A. and Hicsasmaz, Z. (2013) *Pore structure in food: Simulation, measurement and applications*, Springer Briefs in Food, Health, and Nutrition, Springer, New York, USA
39. Haines, W.B. (1930) Studies in the physical properties of soil, Part 5: The hysteresis effect in capillary properties, and the modes of moisture distribution associated therewith, *Journal of Agricultural Science* 20 (1), 97-116
40. Huang, C.L.D. (1979) Multi-phase moisture transfer in porous media subjected to temperature gradient, *International Journal of Heat and Mass Transfer* 22, 1295-1307
41. Huang, X.; Qi, T.; Wang, Z.; Yang, D.; Liu, X. (2014) A moisture transmembrane transfer model for pore network simulation of plant materials drying, *Drying Technology* 30 (15), 1742-1749

42. Huinink, H.P.; Pel, L.; Michels, M.A.J.; Prat, M. (2002) Drying processes in the presence of temperature gradients: Pore-scale modelling, *European Physical Journal E* 9, 487-498
43. Idakiev, V.V.; Lazarova, P.V; Bueck, A.; Tsotsas, E.; Moerl, L. (2017) Inductive heating of fluidized beds: Drying of particulate solids, *Powder Technology* 306, 26-33
44. Iliescu, C.; Jing, J.; Tay, F.E.H.; Miao, J.; Sun, T. (2005) Characterization of masking layers for deep wet etching of glass in an improved HF/HCl solution, *Surface and Coatings Technology* 198, 314-318
45. Irawan, A.; Metzger, T.; Tsotsas, E. (2005) Pore network modelling of drying: Combination with a boundary layer model to capture the first drying period. In: *Proceedings of 7th World Congress of Chemical Engineering, Glasgow, Scotland, July 10–14, 2005*
46. Irawan, A. (2006) Isothermal drying of pore networks: Influence of pore structure on drying kinetics, PhD thesis, Otto von Guericke University, Magdeburg, Germany
47. Kainourgiakis, M.W.; Stubos, A.K.; Konstantinou, N.D.; Kanellopoulos, N.K.; Milisic, V. (1996) A network model for the permeability of condensable vapours through mesoporous media, *Journal of Membrane Science* 114, 215-225
48. Kowalski, S.J. (2007) *Drying of Porous Materials*, Springer, Dordrecht, Netherlands
49. Krischer, O. and Rohnlalter, H. (1940) Wärmeleitung und Dampfdiffusion in feuchten Gütern, *Verein Deutscher Ingenieure, Forschungsheft* 402
50. Krischer, O. and Kast, W. (1992) *Trocknungstechnik. 1. Band: Die wissenschaftlichen Grundlagen der Trocknungstechnik, Dritte Auflage*, Springer Verlag, Germany
51. Laurindo, J.B. and Prat, M. (1996) Numerical and experimental network study of evaporation in capillary porous media: Phase distributions, *Chemical Engineering Science* 51 (23), 5171-5185
52. Laurindo, J.B. and Prat, M. (1998) Numerical and experimental network study of evaporation in capillary porous media: Drying rates, *Chemical Engineering Science* 53 (12), 2257-2269
53. Lenormand, R.; Zarcone, C.; Sarr, A. (1983) Mechanisms of the displacement of one fluid by another in a network of capillary ducts, *Journal of Fluid Mechanics* 135, 337-353
54. Lenormand, R. and Zarcone, C. (1984) Role of roughness and edges during imbibition in square capillaries, In: *Proceedings of the SPE Annual Technical Conference and Exhibition, SPE 13264, Houston, Texas, September 16-19, 1984,*
55. Lenormand, R.; Touboul, E.; Zarcone, C. (1988) Numerical models and experiments on immiscible displacements in porous media, *Journal of Fluid Mechanics* 189, 165-187
56. Lenormand, R. (1989) Flow through porous media: Limits of fractal patterns, *Proceedings of the Royal Society London A* 423, 159-168
57. Lenormand, R. (1990) Liquids in porous media, *Journal of Physics: Condensed Matter* 2, SA79-SA88
58. Li, Y. and Wardlaw, N.C. (1986a) Mechanisms of nonwetting phase trapping during imbibition at slow rates, *Journal of Colloid and Interface Science* 109 (2), 473-486

59. Li, Y. and Wardlaw, N.C. (1986b) The influence of wettability and critical pore-throat size ratio on snap-off, *Journal of Colloid and Interface Science* 109 (2), 461-472
60. Li, X. and Yortsos, Y.C. (1995) Visualization and simulation of bubble growth in pore networks, *AIChE Journal* 41, 214-222
61. Liu, H.-C.; Lin, Y.-H.; Hsu W. (2003) Sidewall roughness control in advanced silicon etch process, *Microsystem Technologies* 10, 29-34
62. Lucas, R. (1918) Über das Zeitgesetz des kapillaren Aufstiegs von Flüssigkeiten, *Kolloid Z.* 23, 15-22
63. Luikov, A.V. (1958) Transporterscheinungen in kapillarporösen Körpern, In: K. Steffens (Ed.) Akademie Verlag, Berlin, Germany
64. Luikov, A.V. (1966) Heat and mass transfer in capillary-porous bodies, Pergamon Press, Oxford, UK
65. Mache, H. (1910) Wiener Berichte Abt. Ila, Bd 119, p. 1399
66. Masoodi, R. and Pillai, K.M. (2012) Wicking in porous media, Traditional and modern modeling approaches, CRC Press, Taylor and Francis Group, Boca Raton, USA
67. Metzger, T.; Irawan, A.; Tsotsas, E. (2003) Remarks on the paper "Extension of Hoshen-Kopelman algorithm to non-lattice environments" by Al-Futaisi, A., Patzek, T.W.: *Phys. A* 321 665-678 (2003), *Phys. A* 363, 558-560
68. Metzger, T. and Tsotsas, E. (2005a) Influence of pore size distribution on drying kinetics: A simple capillary model, *Drying Technology* 23, 1797-1809
69. Metzger, T.; Irawan, A.; Tsotsas, E. (2005b) Discrete modelling of drying kinetics of porous media, In: T.M. Eikevik et al. (Eds.) Proceedings of the 3rd Nordic Drying Conference (NDC 2005), Karlstad, Sweden, June 15-17, 2005
70. Metzger, T.; Irawan, A.; Tsotsas, E. (2007a) Isothermal drying of pore networks: Influence of friction for different pore structures, *Drying Technology* 25, 49-57
71. Metzger, T.; Tsotsas, E.; Prat, M. (2007b) Pore-network models: A powerful tool to study drying at the pore level and understand the influence of structure on drying kinetics, In: E. Tsotsas, A.S. Mujumdar (Eds.) *Modern Drying Technology, Vol. 1: Computational Tools at Different Scales*, Wiley-VCH: Weinheim, 57-102
72. Metzger, T.; Irawan, A.; Tsotsas, E. (2007c) Influence of pore structure on drying kinetics: A pore network study, *AIChE Journal* 53 (12), 3029-3041
73. Metzger, T. and Tsotsas, E. (2008) Viscous stabilization of drying front: Three-dimensional pore network simulations, *Chemical Engineering Research and Design* 86, 739-744
74. Moebius, F. and Or, D. (2012) Interfacial jumps and pressure bursts during fluid displacement in interacting irregular capillaries, *Journal of Colloid and Interface Science* 377, 406-415
75. Mogensen, K. and Stenby, E.H. (1998) A dynamic two-phase pore-scale model of imbibition, *Transport of Porous Media* 32, 299-327



76. Moghaddam, A.A.; Kharaghani, A.; Tsotsas, E.; Prat, M. (2017) Kinematics in a slowly drying porous medium: Reconciliation of pore network simulations and continuum modeling, *Physics of Fluids* 29, 022102
77. Mohanty, K.K.; Davis, H.K.; Scriven L.E. (1980) Physics of oil entrapment in water-wet rock, *Reservoir Engineering in Society of Petroleum Engineers* 2 (1), DOI: <https://doi.org/10.2118/9406-PA>
78. Mani, V. and Mohanty, K.K. (1999) Effect of pore-space spatial correlations on two-phase flow in porous media, *Journal of Petroleum Science and Engineering* 23, 173-188
79. Morrow, N.R. (1970) Physics and thermodynamics of capillary action in porous media, *Industrial and Engineering Chemistry* 62 (6), 32-56
80. Mujumdar, A. S. (2015) *Handbook of Industrial Drying*, 4th Edition, CRC Press, Boca Raton, USA
81. Nowicki, S.C.; Davis, H.T.; Scriven, L.E. (1992) Microscopic determination of transport parameters in drying porous media, *Drying Technology* 10 (4), 923-946
82. Okada, Y. and Tokumaru, Y. (1984) Precise determination of lattice parameter and thermal expansion coefficient of silicon between 300 and 1500 K, *Journal of Applied Physics* 56, 314
83. Oyarzun, C.A. and Segura, L.A. (2009) Design and construction of glass micromodels for the study of moisture transport in softwoods, *Drying Technology* 27 (1), 14-29
84. Palzer, S.; Hiebl, C.; Sommer, K.; Lechner, H. (2001) Einfluss der Rauigkeit einer Feststoffoberfläche auf den Kontaktwinkel, *Chemie Ingenieur Technik* 73 (8), 1032-1038
85. Patzek, T.W. (2000) Verification of a complete network simulator of drainage and imbibition, *SPE Journal*, SPE 71310
86. Peron, H.; Delenne, J.Y.; Laloui, L.; El Youssoufi, M.S. (2009) Discrete element modelling of drying shrinkage and cracking of soils, *Computers and Geotechnics* 36, 61-69
87. Perré, P. and Turner, I.W. (1999) Transpore: A generic heat and mass transfer computational model for understanding and visualizing the drying of porous media, *Drying Technology* 17, 1273-1289
88. Perry, R.H. and Green, D.W. (1997) *Perry's Chemical Engineers' Handbook*, 7th Edition, McGraw Hill, USA
89. Phillip, J.R. and de Vries, D.A. (1957) Moisture movement in porous materials under temperature gradients, *Transactions of the American Geophysical Union* 38 (2), 222-232
90. Plourde, F. and Prat, M. (2003) Pore network simulations of drying of capillary porous media: Influence of thermal gradients, *International Journal of Heat and Mass Transfer* 46, 1293-1307
91. Plumb, O.A. (2000) Transport phenomena in porous media: Modeling the drying process, In: K. Vafai (Ed.) *Handbook of Porous Media*, Marcel Dekker, 755-785, New York, USA,

92. Prandtl, L. (1904) Über Flüssigkeitsbewegungen bei sehr kleiner Reibung. Internationaler Mathematischer Kongress, Heidelberg, Germany
93. Prat, M. (1993) Percolation model of drying under isothermal conditions in porous media, *International Journal of Multiphase Flow* 19 (4), 691-704
94. Prat, M. and Bouleux, F. (1999) Drying of capillary porous media with a stabilized front in two dimensions, *Physical Review E* 60, 5647-5656
95. Prat, M. (2002) Recent advances in pore scale models of porous media, *Chemical Engineering Journal* 86, 153-164
96. Prat, M. (2007) On the influence of pore shape, contact angle and film flows on drying of capillary porous media, *International Journal of Heat and Mass Transfer* 50, 1455-1468
97. Prat, M. (2011) Pore network models of drying, contact angle, and film flows, *Chemical Engineering Technology* 34 (7), 1029-138
98. Prat, M. and Agaesse, T. (2015) Thin porous media, In: K. Vafai (Ed.) *Handbook of Porous Media*, 3rd Edition, CRC Press, 89-112, Boca Raton, USA,
99. Quino, J.; Ruehl, M.; Klima, T.; Ruiz, F.; Will, S.; Braeuer, A. (2016) Supercritical drying of aerogel: In situ analysis of concentration profiles inside the gel and derivation of the effective binary diffusion coefficient using Raman spectroscopy, *Journal of Supercritical Fluids* 108, 1-12
100. Rahimi, A.; Metzger, T.; Kharaghani, A.; Tsotsas, E. (2016) Interaction of droplets with porous structures: Pore network simulation of wetting and drying, *Drying Technology* 34, 1129-1140
101. Ransohoff, T.C. and Radke, C.J. (1988) Laminar flow of a wetting liquid along the corners of a predominantly gas-occupied noncircular pore, *Journal of Colloid and Interface Science* 121, 392-401
102. Sahimi, M. (1995) *Flow and Transport in Porous Media and Fractured Rock: From Classical Methods to Modern Approaches*, VCH, Weinheim, Germany
103. Scherer, G.W. (1990) Theory of drying, *Journal of the American Ceramic Society* 73 (1), 3-14
104. Schirmer, R. (1938) Die Diffusionszahl von Wasserdampf-Luft-Gemischen und die Verdampfungsgeschwindigkeit, PhD Thesis, Technische Hochschule München, Munich, Germany
105. Schlichting, H. (1942) Lecture Series "Boundary layer theory", National Advisory Committee for Aeronautics, Technical Memorandum 1217
106. Schluender, E.-U. (2004) Drying of porous material during the constant and the falling rate period: A critical review of existing hypotheses, *Drying Technology* 22 (6), 1517-1532
107. Schmidt, M.-P.; Hirsch, S.; Schmidt, B. (2011) Nasschemische Strukturierung von Glassubstraten für Mikrofluidische Anwendungen, In: *Proceedings of the 10th Magdeburger Maschinenbau-Tage*, Magdeburg, Germany, September 27-29, 2011

108. Segura, L.A. and Toledo, P.G. (2005) Pore-level modeling of isothermal drying of pore networks accounting for evaporation, viscous flow, and shrinking, *Drying Technology* 23 (9), 2007-2019
109. Segura, L. A. (2007), Modeling at pore-scale isothermal drying of porous materials: liquid and vapor diffusivity, *Drying Technology* 25 (10), 1677-1686
110. Segura, L. A.; Garrido, D.L.; Villagra, F.V.; Badillo, G.M. (2014) The effect of capillary pressure on shrinkage during drying: Experiments using 2D deformable micromodels, In: *Proceedings of the 19th International Drying Symposium (IDS 2014)*, Lyon, France, August 24-27, 2014
111. Selyakov, V.I. and Kadet, V.V. (1996) *Percolation models for transport in porous media, with applications to reservoir engineering*, Kluwer Academic Publishers, Dordrecht, Netherlands
112. Sghaier, N., Prat, M., Ben Nasrallah, S. (2006) On the influence of sodium chloride concentration on equilibrium contact angle, *Chemical Engineering Journal* 122, 47-53
113. Shaw, T.M (1987) Drying as an immiscible displacement process with fluid counterflow, *Physical Review Letters* 59 (15), 1671-1675
114. Smiles, S. (1914) *Chemische Konstitution und physikalische Eigenschaften*, In: R.O Herzog (Ed.) Springer Verlag, Heidelberg, Germany
115. Stauffer, D. and Aharony, A. (1994) *Introduction to percolation theory*, Taylor and Francis, London, UK
116. Stefan, J. (1889) Über die Verdampfung und die Auflösung als Vorgänge der Diffusion, *Sitzungsberichte der kaiserlichen Academie der Wissenschaften in Wien, math.-naturw. Cl., Bd. 98. Abth. IIa.*
117. Sukop, M.C. and Or, D. (2004) Lattice Boltzmann method for modeling liquid-vapor interface configurations in porous media, *Water Resources Research* 40 (1)
118. Sun, Y. (2014) *Liquid imbibition in porous media investigated by pore network models and pore-scale experiments*, PhD Thesis, Otto von Guericke University, Magdeburg, Germany
119. Surasani, V.; Metzger, T.; Tsotsas, E. (2008a) Influence of heating mode on drying behavior of capillary porous media: Pore scale modeling, *Chemical Engineering Science* 63, 5218-5228
120. Surasani, V.; Metzger, T.; Tsotsas, E. (2008b) Consideration of heat transfer in pore network modelling of convective drying, *International Journal of Heat and Mass Transfer* 51 (9–10), 2506-2518
121. Surasani, V. (2009) *A non-isothermal pore network drying model*, PhD Thesis, Otto von Guericke University, docupoint Verlag, Magdeburg, Germany
122. Surasani, V.; Metzger, T.; Tsotsas, E. (2010) Drying simulations of various 3D pore structures by a nonisothermal pore network model, *Drying Technology* 28 (5), 615-623
123. Suzuki, M. and Maeda, S. (1967) On the mechanism of drying of granular beds, *Journal of Chemical Engineering of Japan* 1 (1), 26-31

124. Talbi, M. and Prat, M. (2019) About Schlünder's model: A numerical study of evaporation from partially wet surfaces, to appear in *Drying Technology*
125. Tran, Q.T. (2010) *Trocknungsexperimente mit Porennetzwerken: Bildanalytische Auswertung und Einfluss von Temperaturgradienten*, Pre-diploma thesis, Otto von Guericke University Magdeburg
126. Tsakiroglou, C.D. and Avraam, D.G. (2002) Fabrication of a new class of porous media models for visualization studies of multiphase flow processes, *Journal of Materials Science* 37, 353-363
127. Tsimpanogiannis, I.N.; Yortsos, Y.C.; Poulou, S.; Kanellopoulos, N.; Stubos, A.K. (1999) Scaling theory of drying in porous media, *Physical Review E* 59 (4), 4353-4365
128. Tsotsas, E.; Metzger, T.; Gnielinski, V.; Schluender, E.-U. (2012) Drying of solid materials, In: *Ullmann's Encyclopedia of Industrial Chemistry*, Wiley-VCH, Weinheim, Germany
129. Turner, I.W. and Jolly, P.C. (1991) Combined microwave and convective drying of a porous material, *Drying Technology* 9 (5), 1209-1269
130. Udell, K.S. (1985) Heat transfer in porous media considering phase change and capillarity: The heat pipe effect, *International Journal of Heat and Mass Transfer* 28 (2), 485-495
131. van Brakel, J. (1975) *Capillary liquid transport in porous media*, PhD thesis, TU Delft, Delft, Netherlands
132. Veran-Tissoires, S. and Prat, M. (2014) Evaporation of a sodium chloride solution from a saturated porous medium with efflorescence formation, *Journal of Fluid Mechanics* 749, 701-749
133. *VDI Heat Atlas, 2nd Edition (2010)* Verein Deutscher Ingenieure VDI-Gesellschaft Verfahrenstechnik und Chemieingenieurwesen (GVC), Springer Verlag, Düsseldorf, Germany
134. Vidakovic-Koch, T. (2016) Electrochemical processing, In: E. Drioli, L. Giorno (Eds.) *Encyclopedia of Membranes*, Springer, Berlin, Germany
135. Vorhauer, N.; Metzger, T.; Tsotsas, E. (2010) Empirical macroscopic model for drying of porous media based on pore networks and scaling theory, *Drying Technology* 28, 991-1000
136. Vorhauer, N.; Tran, Q.T.; Metzger, T.; Tsotsas, E.; Prat, M. (2013) Experimental investigation of drying in a model porous medium: Influence of thermal gradients, *Drying Technology* 31, 920-929
137. Vorhauer, N.; Tsotsas, E.; Prat, M. (2014) Isothermal drying in the presence of capillary liquid films: Comparison of experiments with pore network simulations in a model system, In: *Proceedings (CD) of the 19th International Drying Symposium (IDS 2014)*, Lyon, France, August 24-27, 2014
138. Vorhauer, N.; Wang, Y.J.; Kharaghani, A.; Tsotsas E.; Prat, M. (2015) Drying with formation of capillary rings in a model porous medium, *Transport in Porous Media* 110, 197-223

139. Vu, T.H. (2006) Influence of pore size distribution on drying behavior of porous media by a continuous model, PhD thesis, Otto von Guericke University, Magdeburg, Germany
140. Wang, Y.J.; Kharaghani, A.; Tsotsas, E. (2013) Pore-scale visualization and simulation of liquid films for drying particle packing, In: Proceedings of EuroDrying 2013, Paris, France, October 2-4, 2013
141. Washburn, E.W. (1921) The dynamics of capillary flow, *Physical Review* 17, 273
142. Westphal, W.H. (1970) *Physik: Ein Lehrbuch*, Springer Verlag, Heidelberg, Germany
143. Whitaker, S. (1977) *Fundamental Principles of Heat Transfer*, Pergamon Press, Oxford, UK
144. Wilkinson, D. and Willemsen, J.F. (1983) Invasion percolation: A new form of percolation theory, *Journal of Physics A: Mathematical and General* 16 (1983), 3365-3376.
145. Wilkinson, D. (1986) Percolation effects in immiscible displacement, *Physical Review A* 34 (2), 1380-1391
146. Winkelmann, A. (1889) *Annalen der Physik* 36, 93
147. Wu, R.; Kharaghani, R.; Tsotas, E. (2016) Capillary valve effect during slow drying of porous media, *International Journal of Heat and Mass Transfer* 94, 81-86
148. Xu, B.; Yortsos, Y.C.; Salin, D. (1998) Invasion percolation with viscous forces, *Physical Review E* 57 (1), 739-751
149. Xu, L.; Davies, S.; Schofield, A.B.; Weitz, D.A. (2008) Dynamics of drying in 3D porous media, *Physical Review Letters* 101, 094502
150. Yiotis, A.G.; Boudouvis, A.G.; Stubos, A.K. ; Tsimpanogiannis, I.N.; Yortsos, Y.C. (2004) Effect of liquid films on the drying of porous media, *AIChE Journal* 50 (11), 2721-2737
151. Yiotis, A.G.; Stubos, A.K.; Boudouvis, A.G.; Tsimpanogiannis, I.N.; Yortsos, Y.C. (2005) Pore-network modeling of isothermal drying in porous media, *Transport in Porous Media* 58, 63-86
152. Yiotis, A.G.; Psihogios, J.; Kainourgiakis, M.E.; Papaioannou, A.; Stubos, A.K. (2007) A lattice Boltzmann study of viscous coupling effects in immiscible two-phase flow in porous media, *Colloids and Surfaces A* 300, 35-49
153. Yiotis, A.G.; Salin, G.; Tajer, E.S.; Yortsos, Y.C. (2012a) Analytical solutions of drying in porous media for gravity-stabilized fronts, *Physical Review E* 85, 046308
154. Yiotis, A.G.; Salin, G.; Tajer, E.S.; Yortsos, Y.C. (2012b) Drying in porous media with gravity-stabilized fronts: Experimental results, *Physical Review E* 86, 046308
155. Zhou, D.; Blunt, M.J.; Orr, F.M. Jr. (1997) Hydrocarbon drainage along corners of noncircular capillaries, *Journal of Colloid and Interface Science* 187, 11-21

## Appendix A

# Experimental data

### A.1 Equipment

**Table A-1** Experimental equipment used in microfluidic drying experiments.

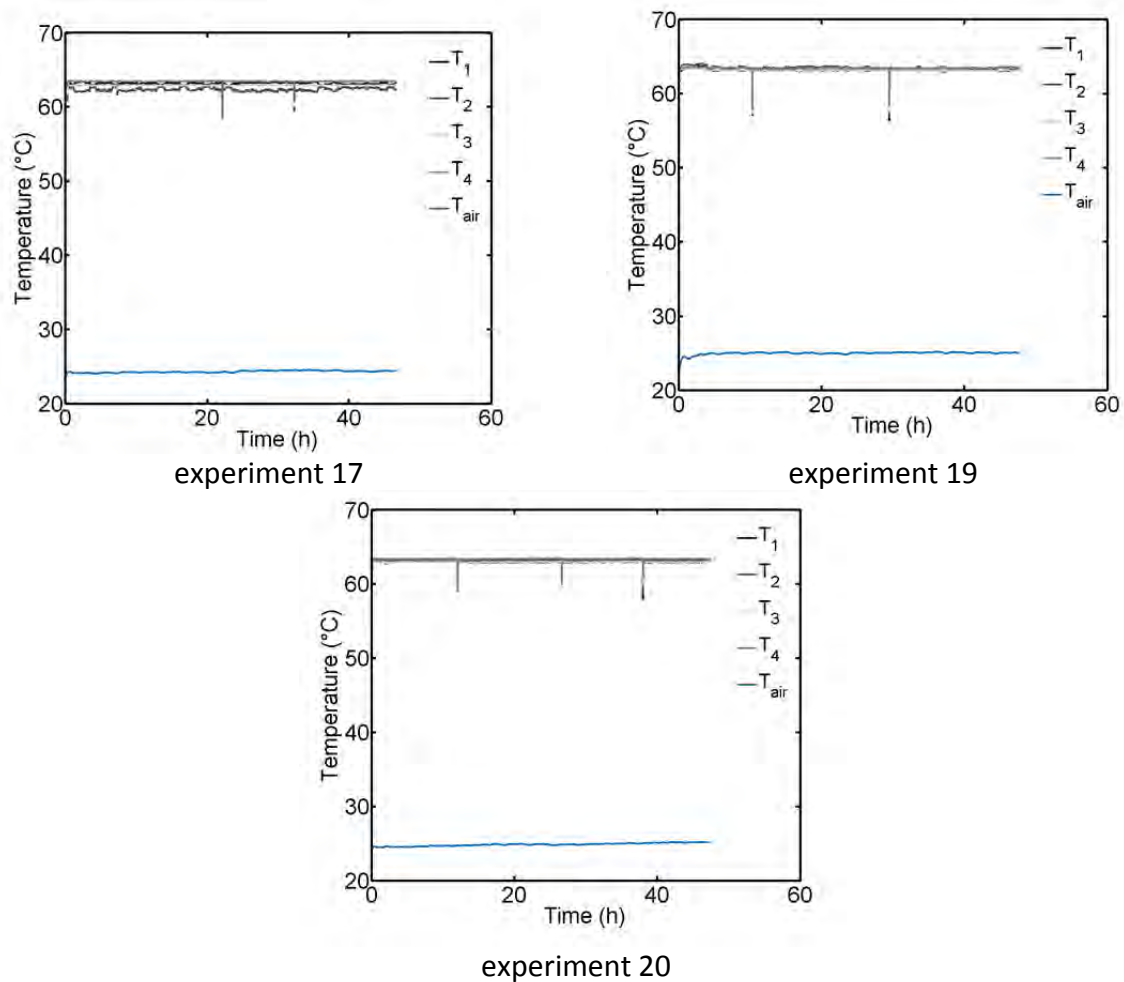
Device	Details
Vacuum pump	BOC Edwards UK, XDS5, $P^{min} = 0.03$ bar
Heat exchanger	Haake K10 circulating bath ( $V = 3$ l), circulator Haake DC30 ( $P = 2$ kW)
CCD camera	Panasonic AG-HVX 200E
LED lights	Type E27 PAR20, 105 diodes (x 4), 6.5 W, 230 V
thermocouples	Type K, $\varnothing$ 1 mm, precision: 1 K (x 4)
IR camera	Infratec IR8300, precision: 0.025 K, software IRBIS 3 professional
Data acquisition	Daisy-Lab 10.00.01
Image capturing	IC-Capture 2.2.174.793, $\Delta t = 0.5 \dots 10$ min
Tripod	Kaiser Reprosystem (420x320 mm)

Experiments were conducted using dry air with volume flow rate  $\dot{V}_{air} = 20$  l min<sup>-1</sup> and dew point temperature  $T_{dew} = -15^\circ\text{C}$ . Some experiments did not yield useable data, because e.g. the image recording, air flow or heat supply were interrupted or because the image data was not good enough (in most cases unstable position of the PN). Also, at the start of this study a different microfluidic PN was used, which revealed undesired properties during the experiments. Experiments of insufficient quality are not discussed further. The others are summarized in the following sub-sections.

## A.2 Experiments with quasi-constant temperature in time and space

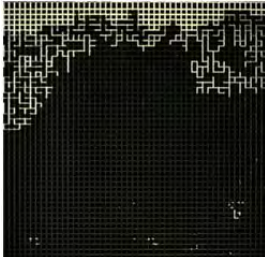
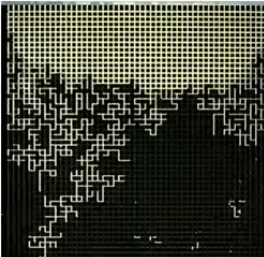

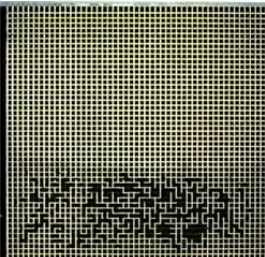
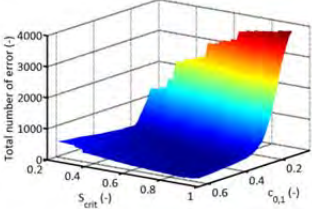
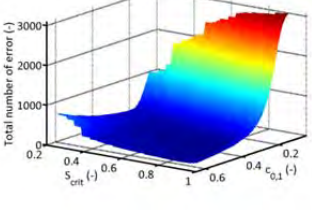
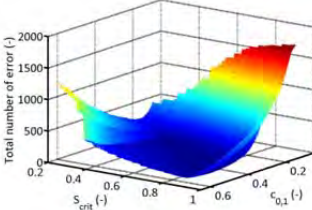
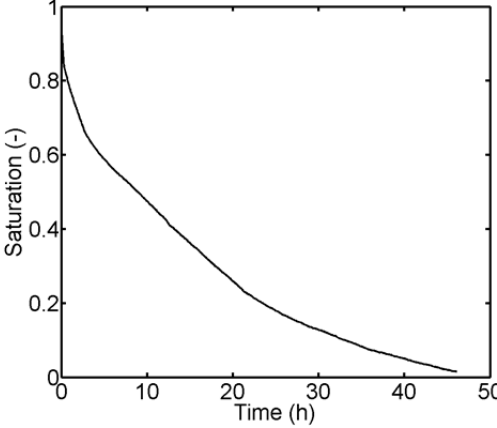
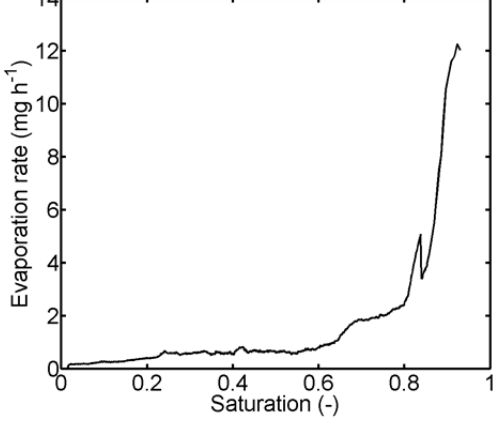
**Table A-2** Summary of experiments with quasi-constant temperature in time and space.

Experiment number	Date of experiment	Air temperature	Temperature thermostat 1	Temperature thermostat 2	Temperatures metal plate
17	01.08.2011	$T_{air} \cong 24^\circ\text{C}$	$T_{L,1,in} \cong 64^\circ\text{C}$	$T_{L,2,in} \cong 65^\circ\text{C}$	$T_{1-4} \cong 63^\circ\text{C}$
19	16.08.2011	$T_{air} \cong 25^\circ\text{C}$	$T_{L,1,in} \cong 65^\circ\text{C}$	$T_{L,2,in} \cong 64^\circ\text{C}$	$T_{1-4} \cong 63^\circ\text{C}$
20	22.08.2011	$T_{air} \cong 25^\circ\text{C}$	$T_{L,1,in} \cong 65^\circ\text{C}$	$T_{L,2,in} \cong 64^\circ\text{C}$	$T_{1-4} \cong 63^\circ\text{C}$

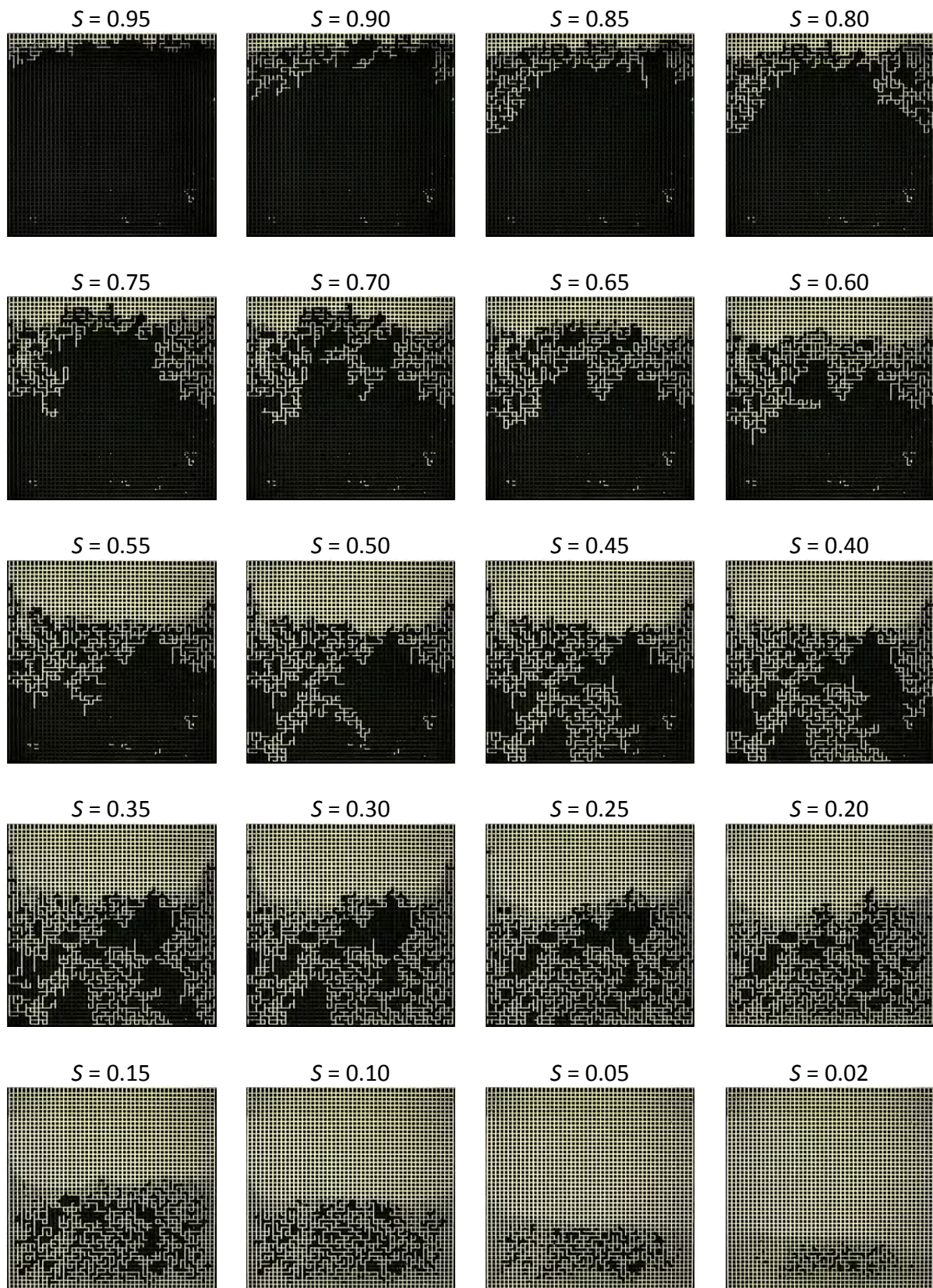


**Figure A-1** Temperature profiles from thermocouples. The peaks are explained with the refilling of the heat exchanger (water thermostat) with water at room temperature.

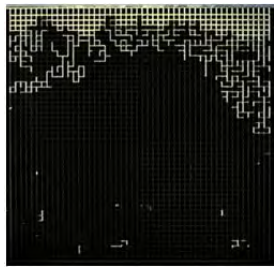
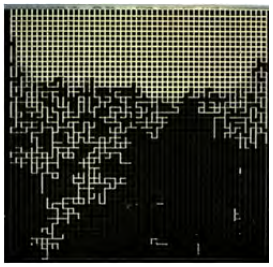
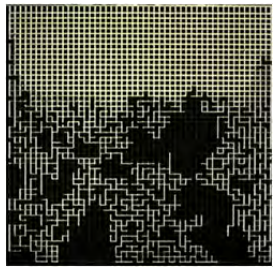
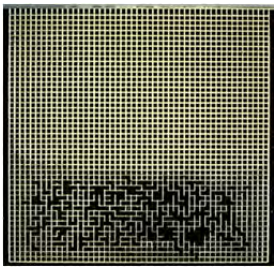
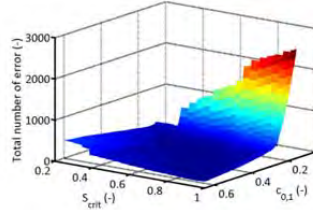
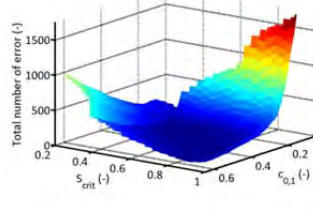
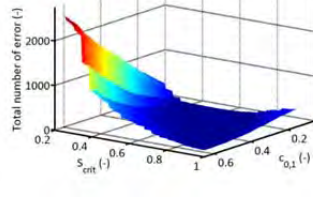
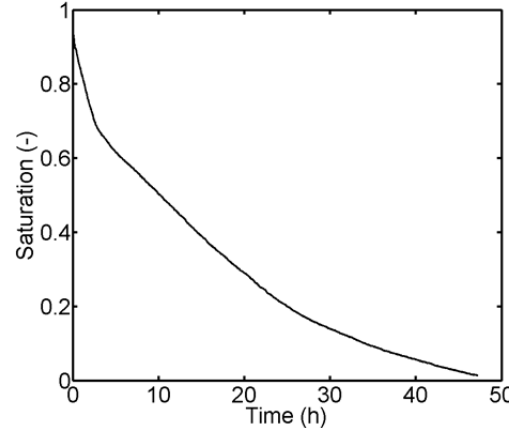
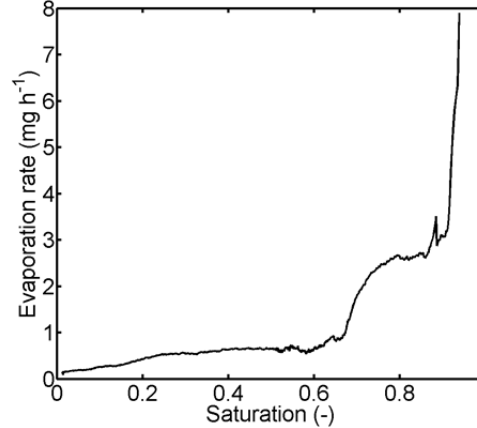
**Table A-3** Specific details of experiment 17.

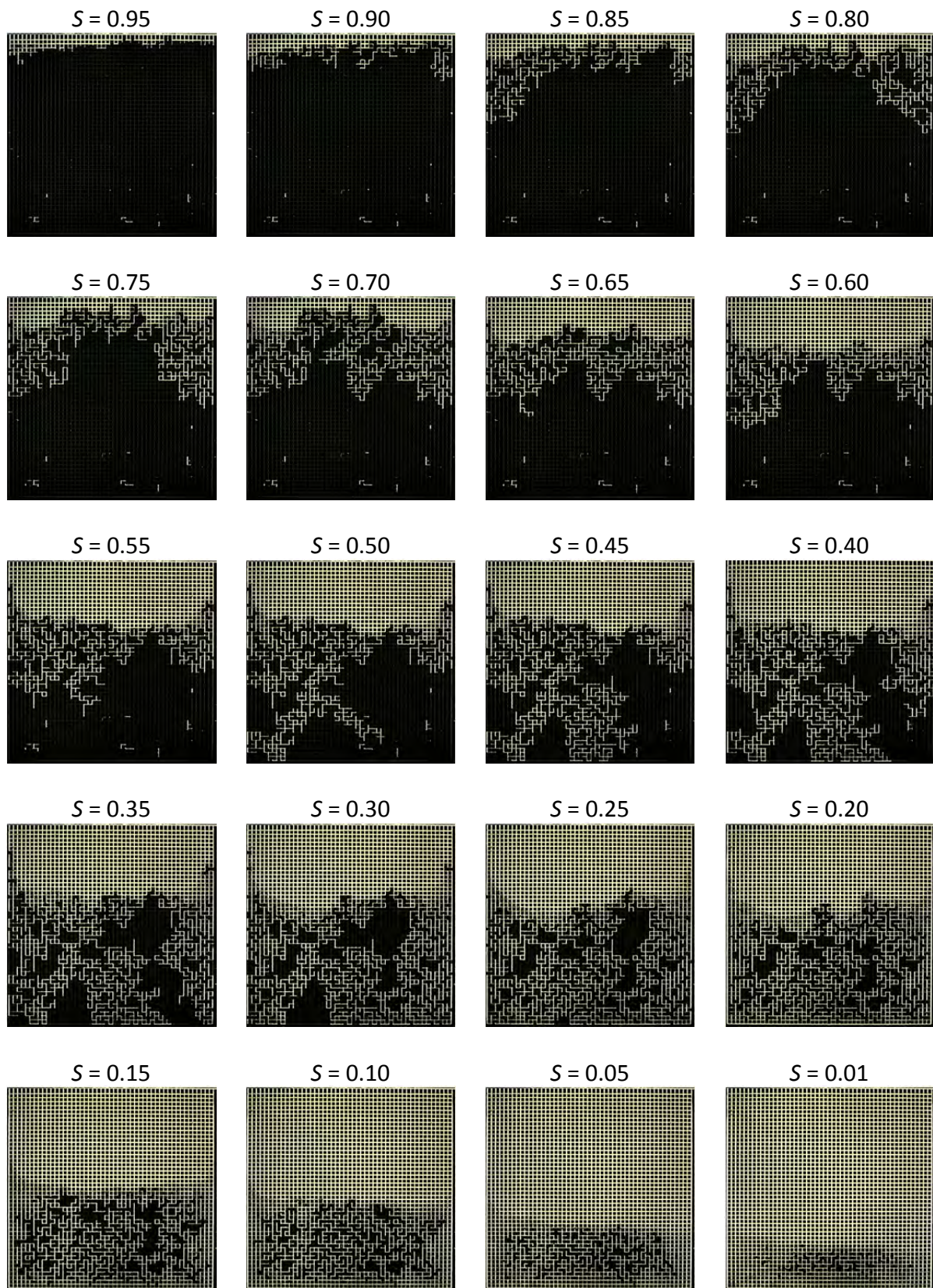
$S = 0.81$	$S = 0.53$	$S = 0.33$	$S = 0.06$
			
<p><b><u>Image processing parameters</u></b></p> <p><b>Binarization</b>  <math>c_{0,1} = 0.38</math></p> <p><b>Network size</b>            left bound  <math>lb = 111</math>            width  <math>w = 539.2</math>            upper bound  <math>ub = 19</math>            height  <math>h = 524.8</math></p> <p><b>Scaling</b>  <math>c_{w,h} = 10950</math>  <math>c_h = 0.97</math></p> <p><b>Critical saturation</b>  <math>S_{crit} = 0.8</math></p>	<p><b><u>Error quantification</u></b></p> <p><math>t = 25 \text{ min}</math></p>  <p><math>t = 205 \text{ min}</math></p>  <p><math>t = 999 \text{ min}</math></p> 	<p><b><u>Drying curve parameter</u></b></p> <ul style="list-style-type: none"> <li>- CMA Filter</li> <li>- <math>n = 51</math></li> </ul> <p><b><u>Drying curve</u></b></p>  <p><b><u>Drying rate</u></b></p>  <p>Duration of experiment: 46 h 49 min.</p>	



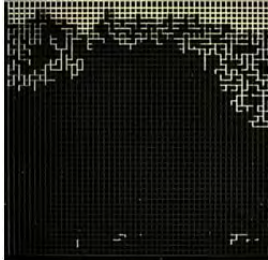
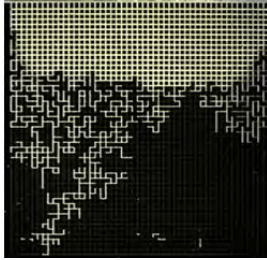
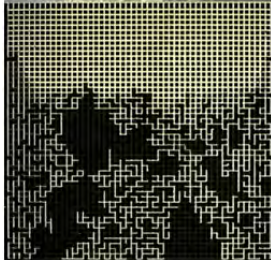
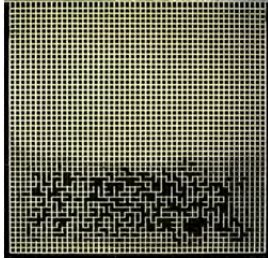
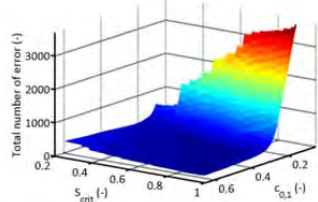
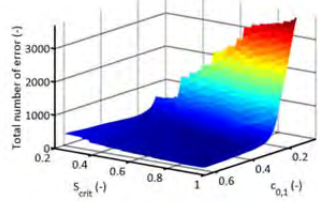
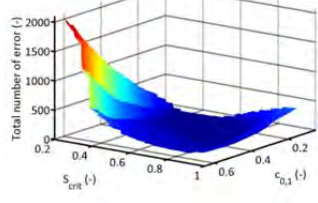
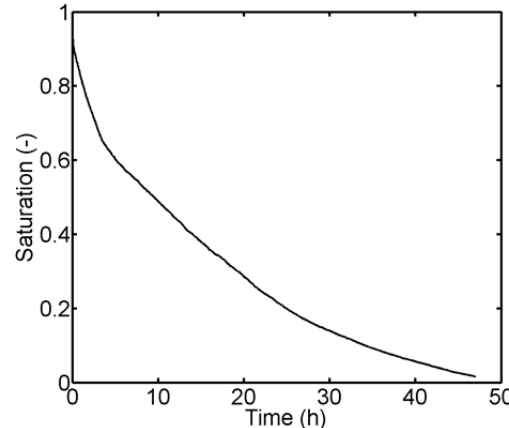
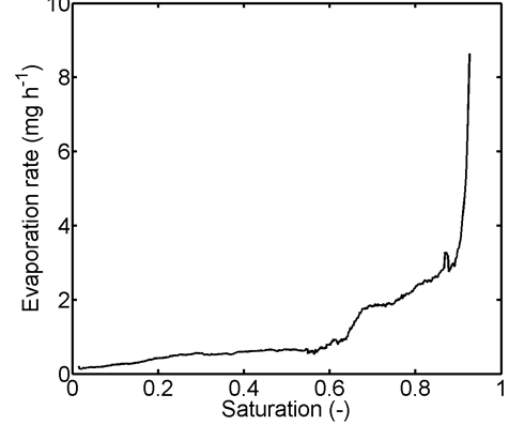
**Table A-4** Summary of image data of experiment 17.

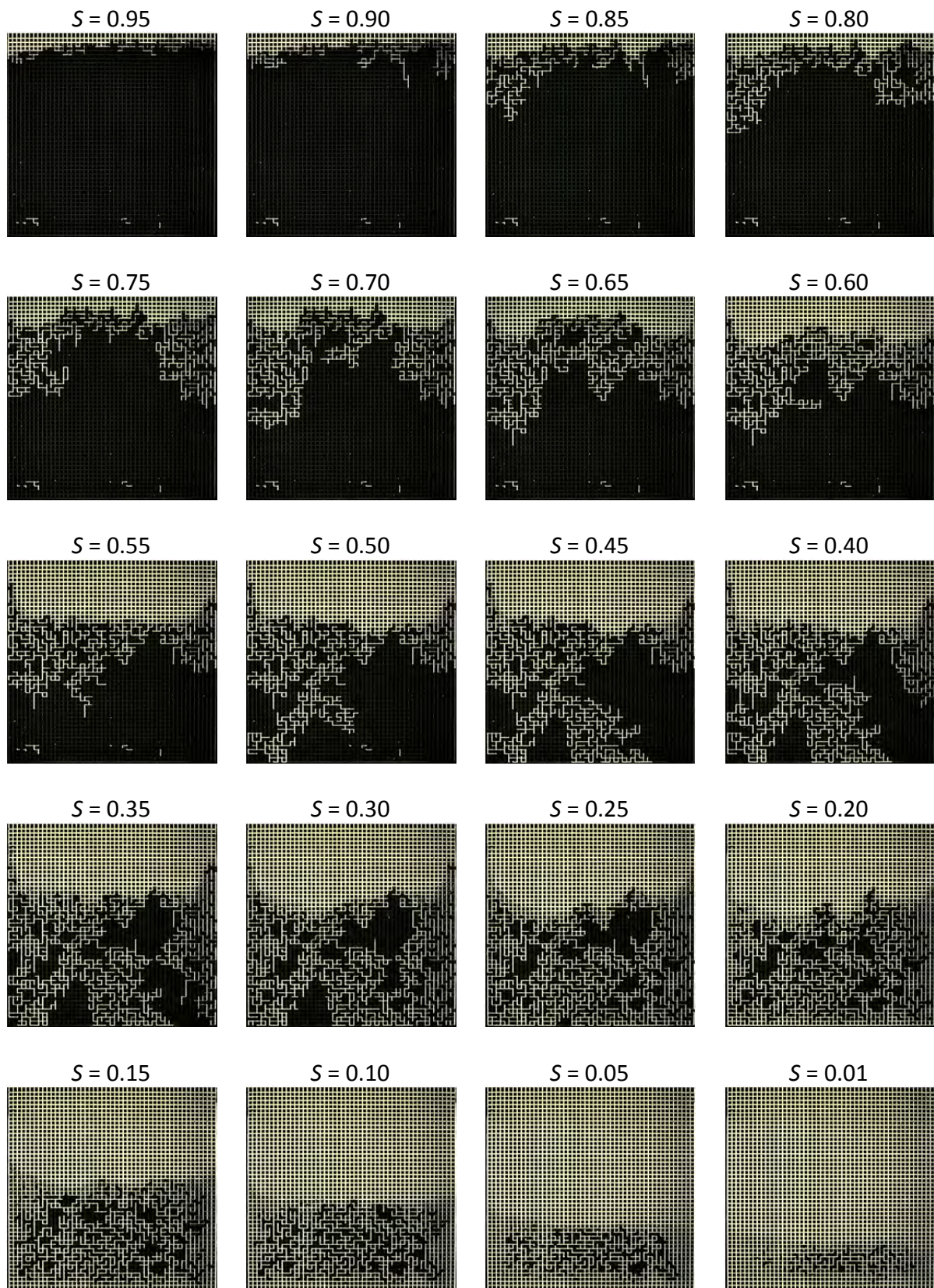
**Table A-5** Specific details of experiment 19.

$S = 0.81$	$S = 0.53$	$S = 0.33$	$S = 0.07$
			
<p><b><u>Image processing parameters</u></b></p> <p><b>Binarization</b>  <math>c_{0,1} = 0.42</math></p> <p><b>Network size</b>  left bound  <math>lb = 117.5</math>  width  <math>w = 542</math>  upper bound  <math>ub = 27</math>  height  <math>h = 525</math></p> <p><b>Scaling</b>  <math>c_{w,h} = 11000</math>  <math>c_h = 0.97</math></p> <p><b>Critical saturation</b>  <math>S_{crit} = 0.8</math></p>	<p><b><u>Error quantification</u></b></p> <p><math>t = 30</math> min</p>  <p><math>t = 300</math> min</p>  <p><math>t = 2341</math> min</p> 	<p><b><u>Drying curve parameter</u></b></p> <ul style="list-style-type: none"> <li>- CMA Filter</li> <li>- <math>n = 51</math></li> </ul> <p><b><u>Drying curve</u></b></p>  <p><b><u>Drying rate</u></b></p>  <p>Duration of experiment: 47 h 16 min.</p>	

**Table A-6** Summary of image data of experiment 19.

**Table A-7** Specific details of experiment 20.

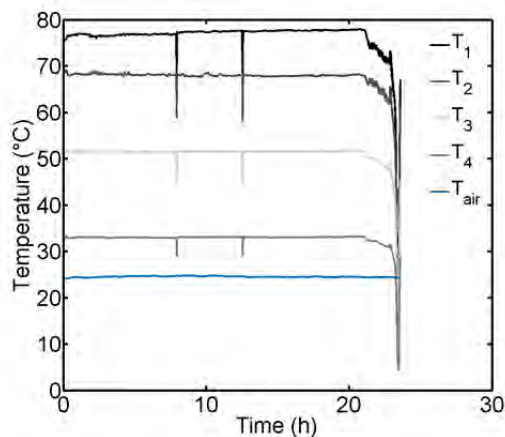
$S = 0.81$	$S = 0.53$	$S = 0.33$	$S = 0.07$
			
<p><b><u>Image processing parameters</u></b></p> <p><b>Binarization</b>  <math>c_{0,1} = 0.265</math></p> <p><b>Network size</b>  left bound  <math>lb = 133.5</math>  width  <math>w = 535.25</math>  upper bound  <math>ub = 22.5</math>  height  <math>h = 520.5</math></p> <p><b>Scaling</b>  <math>c_{w,h} = 10925</math>  <math>c_h = 0.969</math></p> <p><b>Critical saturation</b>  <math>S_{crit} = 0.7</math></p>	<p><b><u>Error quantification</u></b></p> <p><math>t = 20</math> min</p>  <p><math>t = 420</math> min</p>  <p><math>t = 2245</math> min</p> 	<p><b><u>Drying curve parameter</u></b></p> <ul style="list-style-type: none"> <li>- CMA Filter</li> <li>- <math>n = 51</math></li> </ul> <p><b><u>Drying curve</u></b></p>  <p><b><u>Drying rate</u></b></p>  <p>Duration of experiment: 47 h 5 min.</p>	

**Table A-8** Summary of image data of experiment 20.

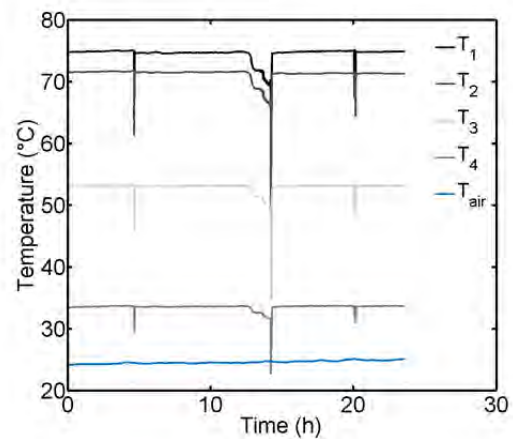
### A.3 Experiments with a negative temperature gradient

**Table A-9** Summary of non-isothermal experiments with negative temperature gradient.

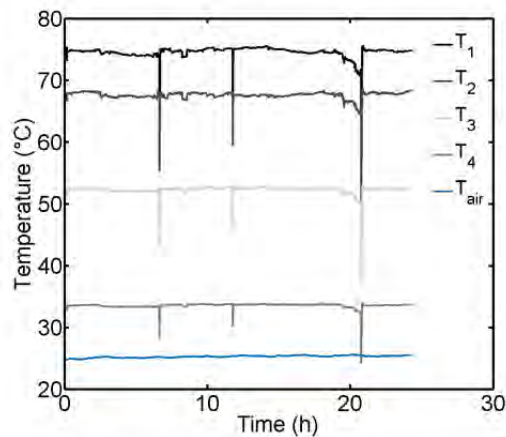
Exp. number	Date of experiment	Air temperature	Temperature thermostat 1	Temperature thermostat 2	Temperatures metal plate
8	27.04.2011	$T_{air} \cong 25^{\circ}\text{C}$	$T_{L,1,in} \cong 88^{\circ}\text{C}$	$T_{L,2,in} \cong 2^{\circ}\text{C}$	$T_1 \cong 76^{\circ}\text{C}, T_2 \cong 67^{\circ}\text{C}$ $T_3 \cong 51^{\circ}\text{C}, T_4 \cong 33^{\circ}\text{C}$
13	27.06.2011	$T_{air} \cong 25^{\circ}\text{C}$	$T_{L,1,in} \cong 88^{\circ}\text{C}$	$T_{L,2,in} \cong 1.5^{\circ}\text{C}$	$T_1 \cong 75^{\circ}\text{C}, T_2 \cong 71^{\circ}\text{C}$ $T_3 \cong 53^{\circ}\text{C}, T_4 \cong 34^{\circ}\text{C}$
15	19.07.2011	$T_{air} \cong 25^{\circ}\text{C}$	$T_{L,1,in} \cong 87^{\circ}\text{C}$	$T_{L,2,in} \cong 3^{\circ}\text{C}$	$T_1 \cong 75^{\circ}\text{C}, T_2 \cong 68^{\circ}\text{C}$ $T_3 \cong 52^{\circ}\text{C}, T_4 \cong 34^{\circ}\text{C}$



experiment 8



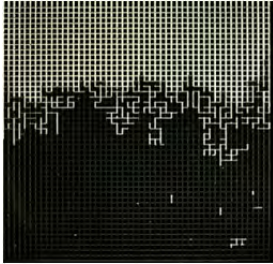
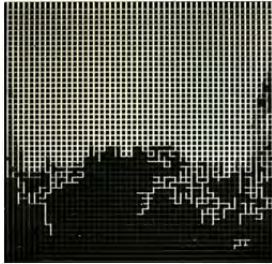
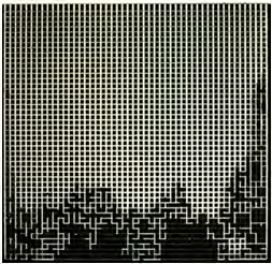
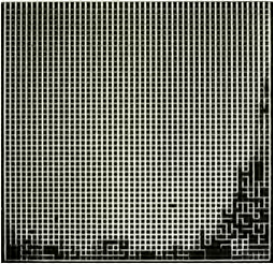
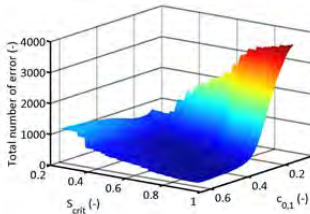
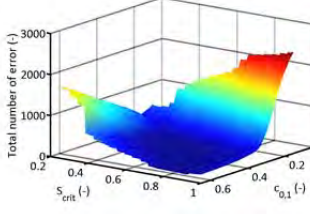
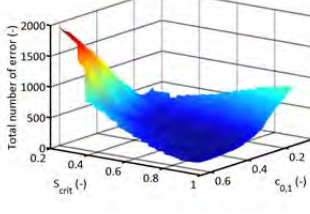
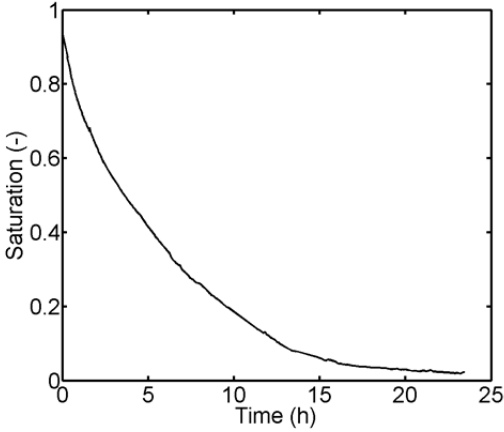
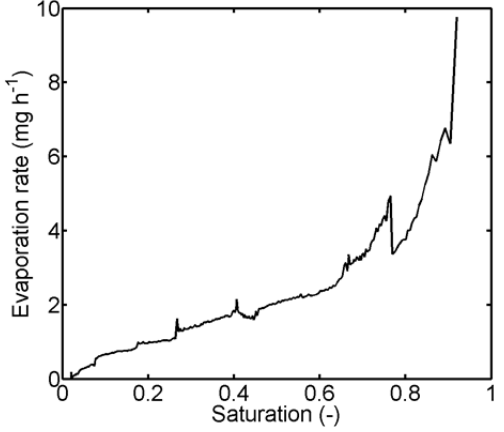
experiment 13



experiment 15

**Figure A-2** Temperature profiles from thermocouples. The peaks are explained with the refilling of the heat exchanger (water thermostat) with water at room temperature.

Table A-10 Specific details of experiment 8.



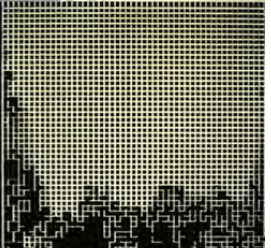
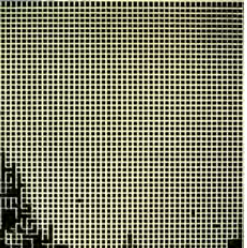
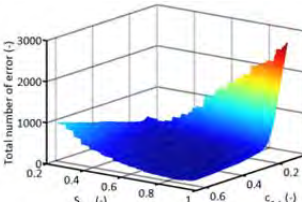
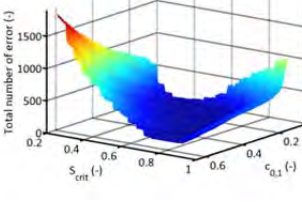
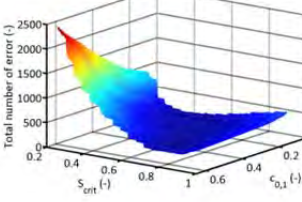
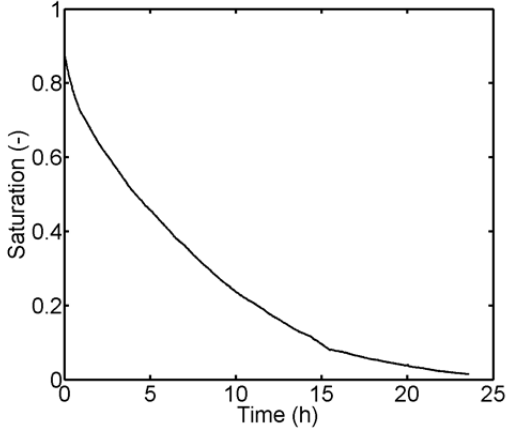
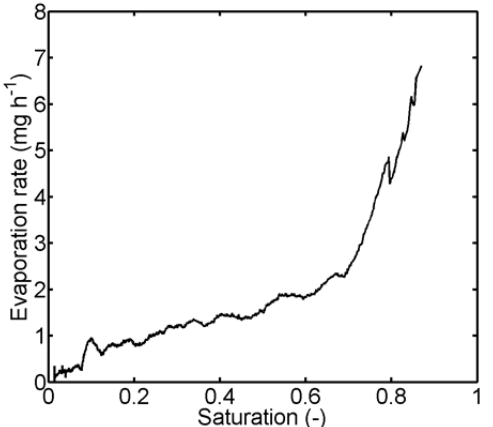
$S = 0.57$	$S = 0.32$	$S = 0.14$	$S = 0.05$
			
<p><b><u>Image processing parameters</u></b></p> <p><b>Binarization</b>  <math>c_{0,1} = 0.42</math></p> <p><b>Network size</b>  left bound  <math>lb = 96.5</math>  width  <math>w = 543</math>  upper bound  <math>ub = 18</math>  height  <math>h = 530</math></p> <p><b>Scaling</b>  <math>c_{w,h} = 11000</math>  <math>c_h = 0.972</math></p> <p><b>Critical saturation</b>  <math>S_{crit} = 0.8</math></p>	<p><b><u>Error quantification</u></b></p> <p><math>t = 55 \text{ min}</math></p>  <p><math>t = 221 \text{ min}</math></p>  <p><math>t = 582 \text{ min}</math></p> 	<p><b><u>Drying curve parameter</u></b></p> <ul style="list-style-type: none"> <li>- CMA Filter</li> <li>- <math>n = 51</math></li> </ul> <p><b><u>Drying curve</u></b></p>  <p><b><u>Drying rate</u></b></p>  <p>Duration of experiment: 23 h 27 min.</p>	

**Table A-11** Summary of image data of experiment 8.





**Table A-12** Specific details of experiment 13.

$S = 0.57$	$S = 0.32$	$S = 0.14$	$S = 0.05$
			
<p><b><u>Image processing parameters</u></b></p> <p><b>Binarization</b>  <math>c_{0,1} = 0.391</math></p> <p><b>Network size</b>            left bound  <math>lb = 141.5</math>            width  <math>w = 541</math>            upper bound  <math>ub = 12</math>            height  <math>h = 524.5</math></p> <p><b>Scaling</b>  <math>c_{w,h} = 10985</math>  <math>c_h = 0.973</math></p> <p><b>Critical saturation</b>  <math>S_{crit} = 0.7</math></p>	<p><b><u>Error quantification</u></b></p> <p><math>t = 52</math> min</p>  <p><math>t = 552</math> min</p>  <p><math>t = 852</math> min</p> 	<p><b><u>Drying curve parameter</u></b></p> <ul style="list-style-type: none"> <li>- CMA Filter</li> <li>- <math>n = 51</math></li> </ul> <p><b><u>Drying curve</u></b></p>  <p><b><u>Drying rate</u></b></p>  <p>Duration of experiment: 23 h 35 min.</p>	

**Table A-13** Summary of image data of experiment 13.

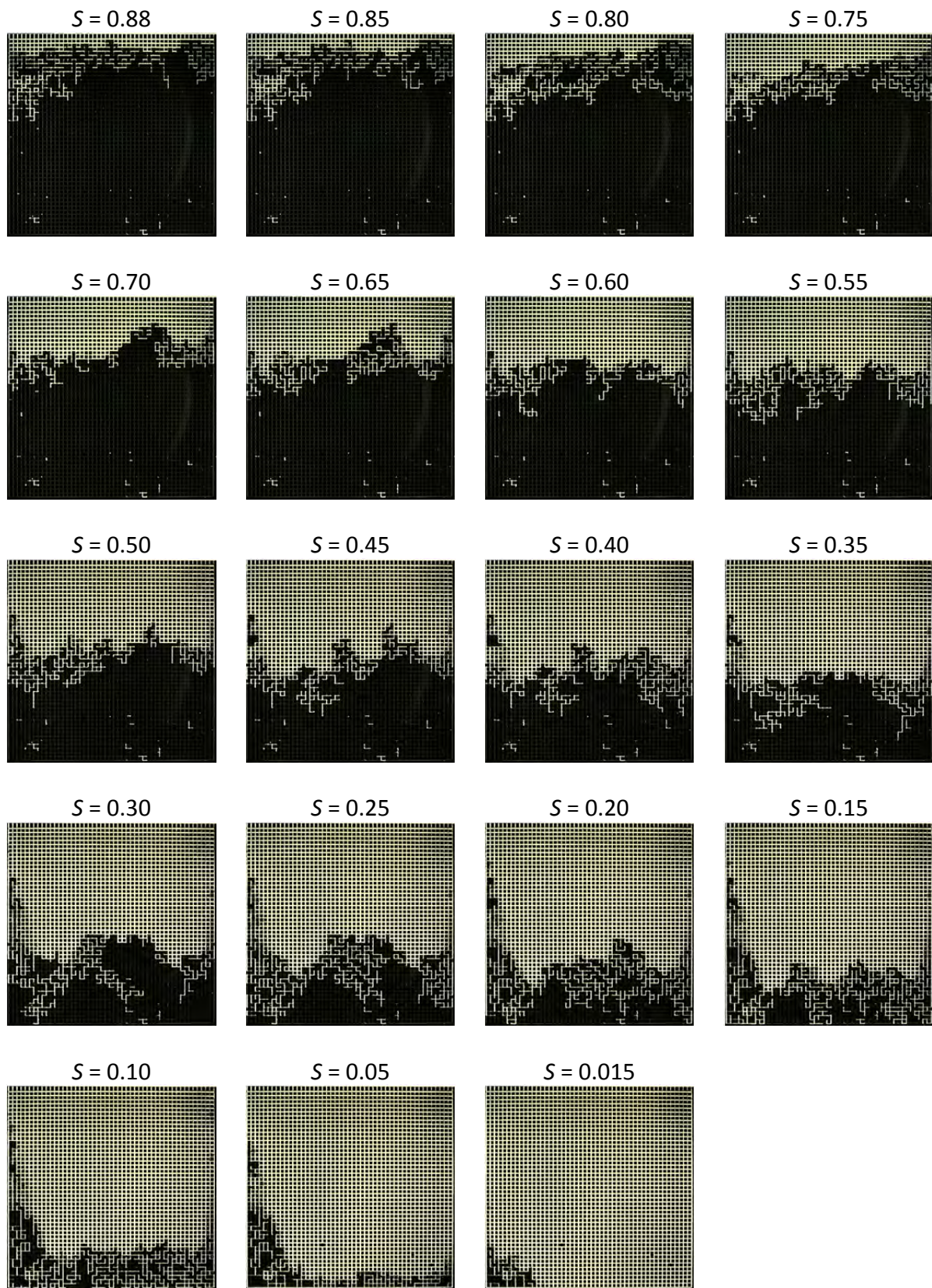


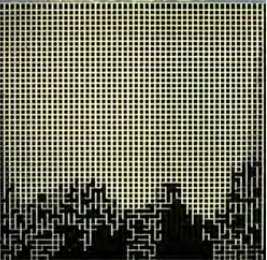
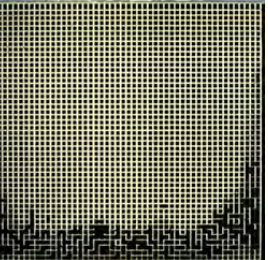
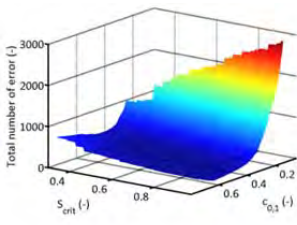
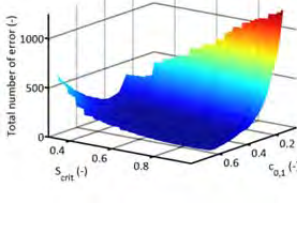
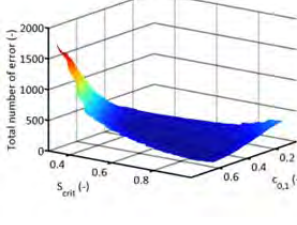
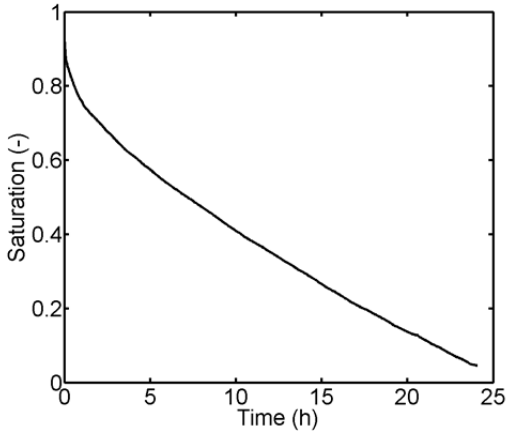
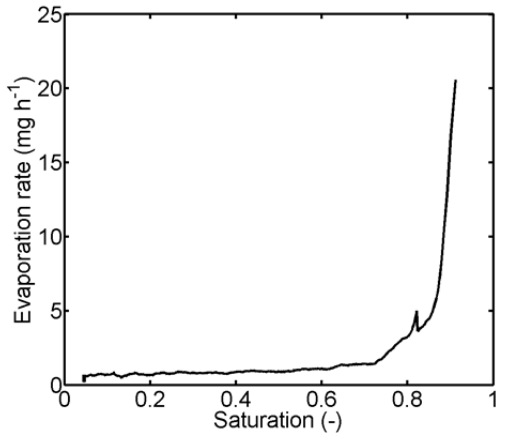
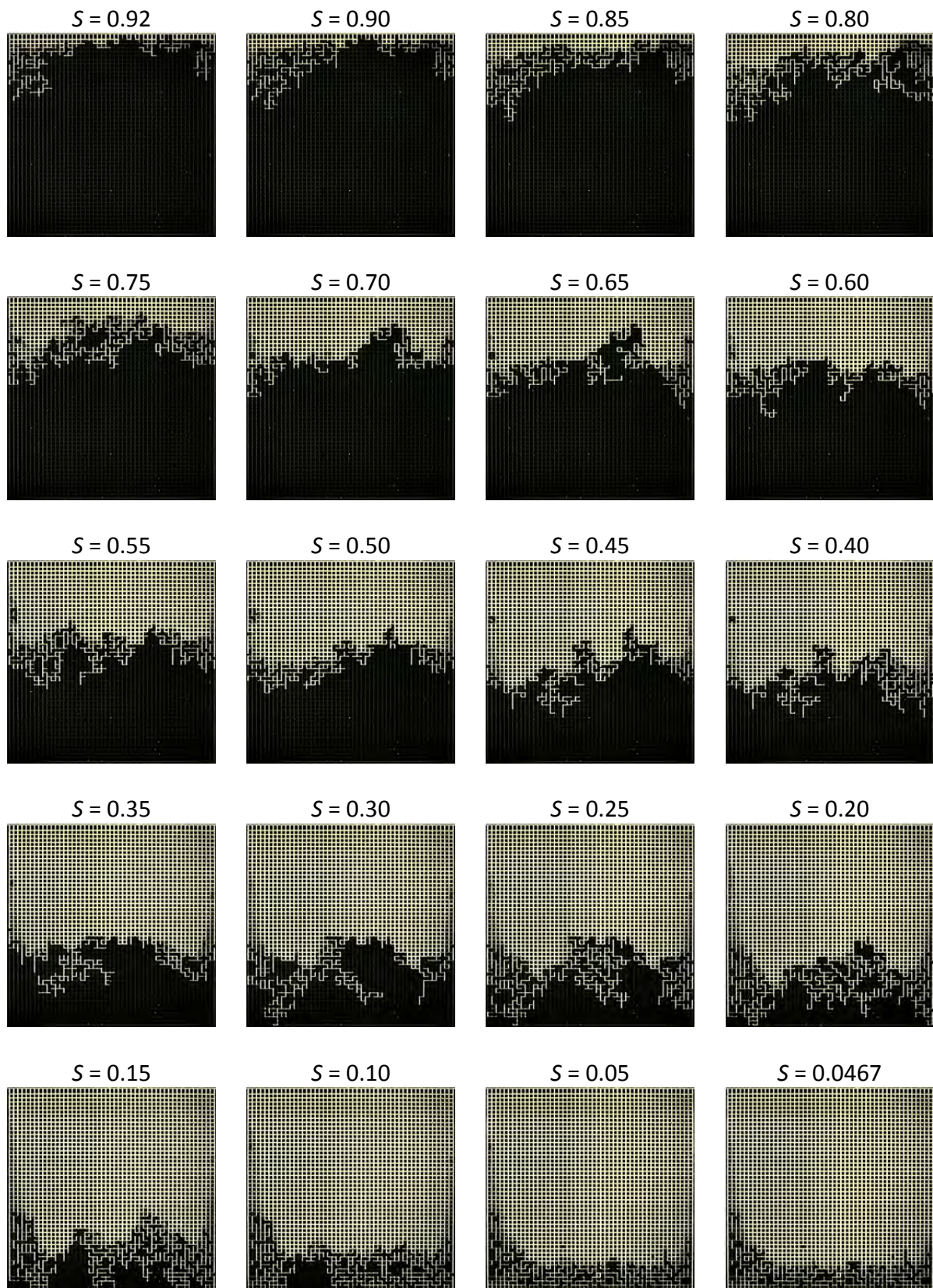


Table A-14 Specific details of experiment 15.

$S = 0.57$	$S = 0.32$	$S = 0.14$	$S = 0.05$
			
<p><b><u>Image processing parameters</u></b></p> <p><b>Binarization</b>  <math>c_{0,1} = 0.4</math></p> <p><b>Network size</b>  left bound  <math>lb = 116</math>  width  <math>w = 539.2</math>  upper bound  <math>ub = 27</math>  height  <math>h = 523.8</math></p> <p><b>Scaling</b>  <math>c_{w,h} = 10940</math>  <math>c_h = 0.97</math></p> <p><b>Critical saturation</b>  <math>S_{crit} = 0.8</math></p>	<p><b><u>Error quantification</u></b></p> <p><math>t = 25</math> min</p>  <p><math>t = 561</math> min</p>  <p><math>t = 1381</math> min</p> 	<p><b><u>Drying curve parameter</u></b></p> <ul style="list-style-type: none"> <li>- CMA Filter</li> <li>- <math>n = 51</math></li> </ul> <p><b><u>Drying curve</u></b></p>  <p><b><u>Drying rate</u></b></p>  <p>Duration of experiment: 24 h 4 min.</p>	

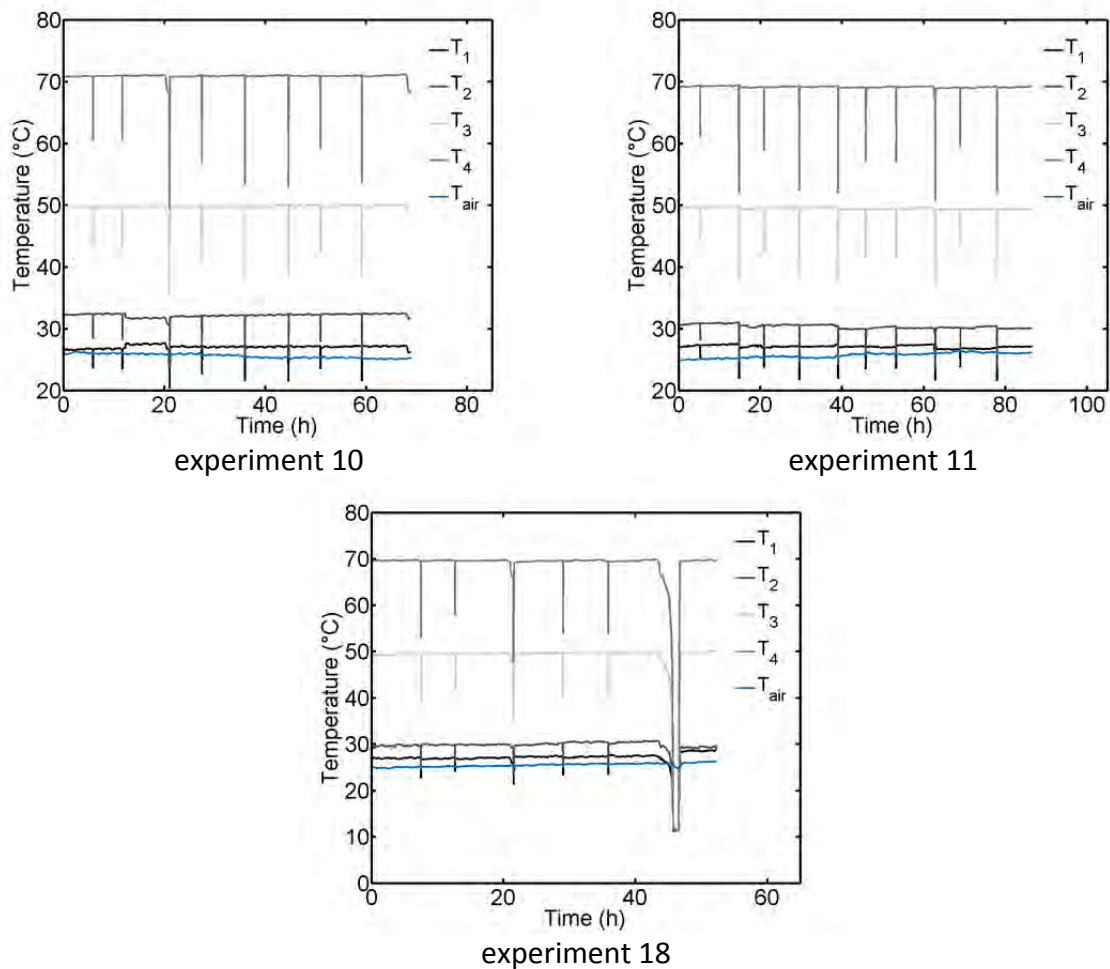
**Table A-15** Summary of image data of experiment 15.



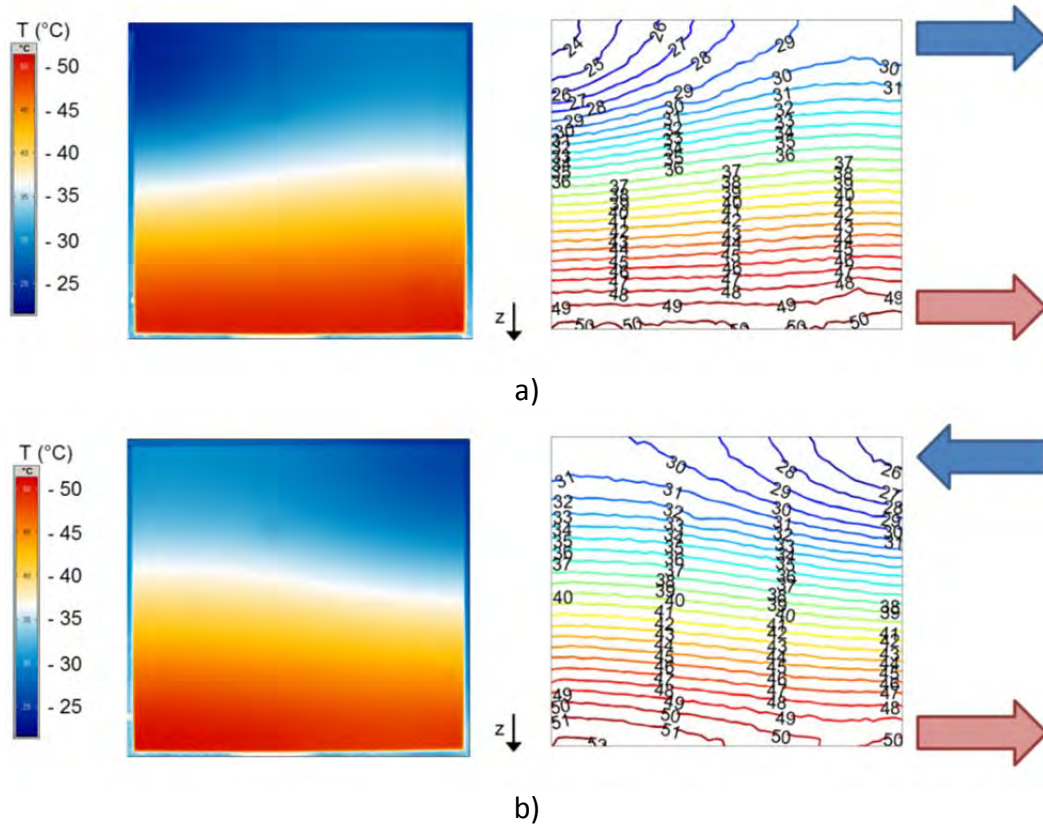
## A.4 Experiments with a positive temperature gradient

**Table A-16** Summary of non-isothermal experiments with positive temperature gradient.

Exp. number	Date of experiment	Air temperature	Temperature thermostat 1	Temperature thermostat 2	Temperatures metal plate
10	10.06.2011	$T_{air} \cong 26^\circ\text{C}$	$T_{L,1,in} \cong 1.5^\circ\text{C}$	$T_{L,2,in} \cong 88^\circ\text{C}$	$T_1 \cong 27^\circ\text{C}, T_2 \cong 32^\circ\text{C}$ $T_3 \cong 50^\circ\text{C}, T_4 \cong 71^\circ\text{C}$
11	19.06.2011	$T_{air} \cong 26^\circ\text{C}$	$T_{L,1,in} \cong 5^\circ\text{C}$	$T_{L,2,in} \cong 87^\circ\text{C}$	$T_1 \cong 27^\circ\text{C}, T_2 \cong 30^\circ\text{C}$ $T_3 \cong 49^\circ\text{C}, T_4 \cong 69^\circ\text{C}$
18	12.08.2011	$T_{air} \cong 25^\circ\text{C}$	$T_{L,1,in} \cong 10^\circ\text{C}$	$T_{L,2,in} \cong 88^\circ\text{C}$	$T_1 \cong 27^\circ\text{C}, T_2 \cong 29^\circ\text{C}$ $T_3 \cong 49^\circ\text{C}, T_4 \cong 68^\circ\text{C}$

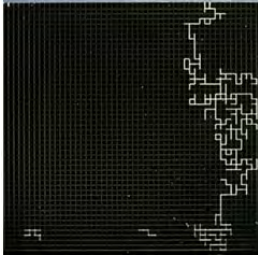
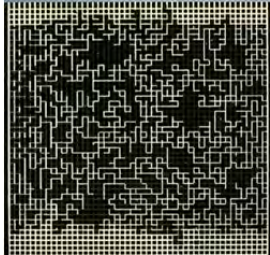
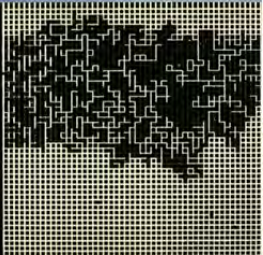

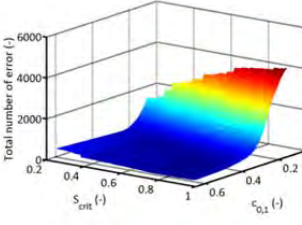
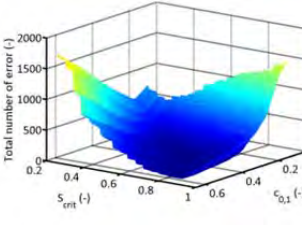
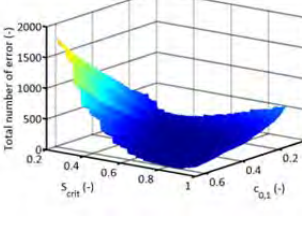
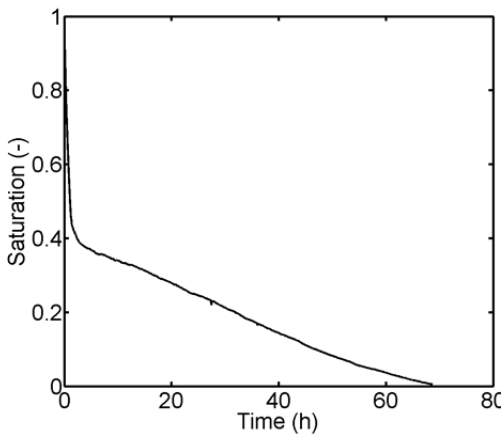
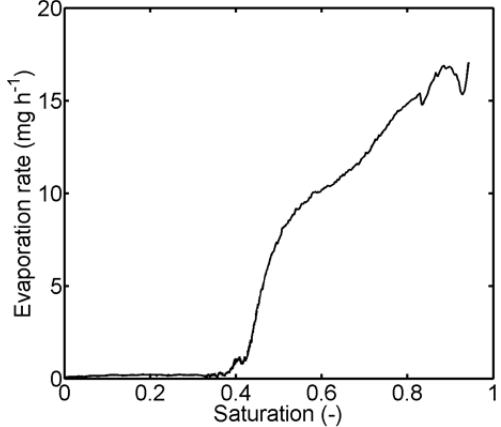


**Figure A-3** Temperature profiles from thermocouples. The peaks are explained with the refilling of the heat exchanger (water thermostat) with water at room temperature.



**Figure A-4** Thermographic images of temperature fields as imposed in experiments: a) 10 and b) 11, 18 and according isotherms. The arrows indicate the direction of the heating flows from the thermostats (also refer to Figs. 3-6 and 3-7).

Table A-17 Specific details of experiment 10.

$S = 0.93$	$S = 0.39$	$S = 0.28$	$S = 0.16$
			
<p><b><u>Image processing parameters</u></b></p> <p><b>Binarization</b>  <math>c_{0,1} = 0.45</math></p> <p><b>Network size</b>  left bound  <math>lb = 155</math>  width  <math>w = 538.2</math>  upper bound  <math>ub = 45</math>  height  <math>h = 520.8</math></p> <p><b>Scaling</b>  <math>c_{w,h} = 10930</math>  <math>c_h = 0.969</math></p> <p><b>Critical saturation</b>  <math>S_{crit} = 0.8</math></p>	<p><b><u>Error quantification</u></b></p> <p><math>t = 7.5</math> min</p>  <p><math>t = 602</math> min</p>  <p><math>t = 2547</math> min</p> 	<p><b><u>Drying curve parameter</u></b></p> <ul style="list-style-type: none"> <li>- CMA Filter</li> <li>- <math>n = 51</math></li> </ul> <p><b><u>Drying curve</u></b></p>  <p><b><u>Drying rate</u></b></p>  <p>Duration of experiment: 68 h 41 min.</p>	

**Table A-18** Summary of image data of experiment 10.

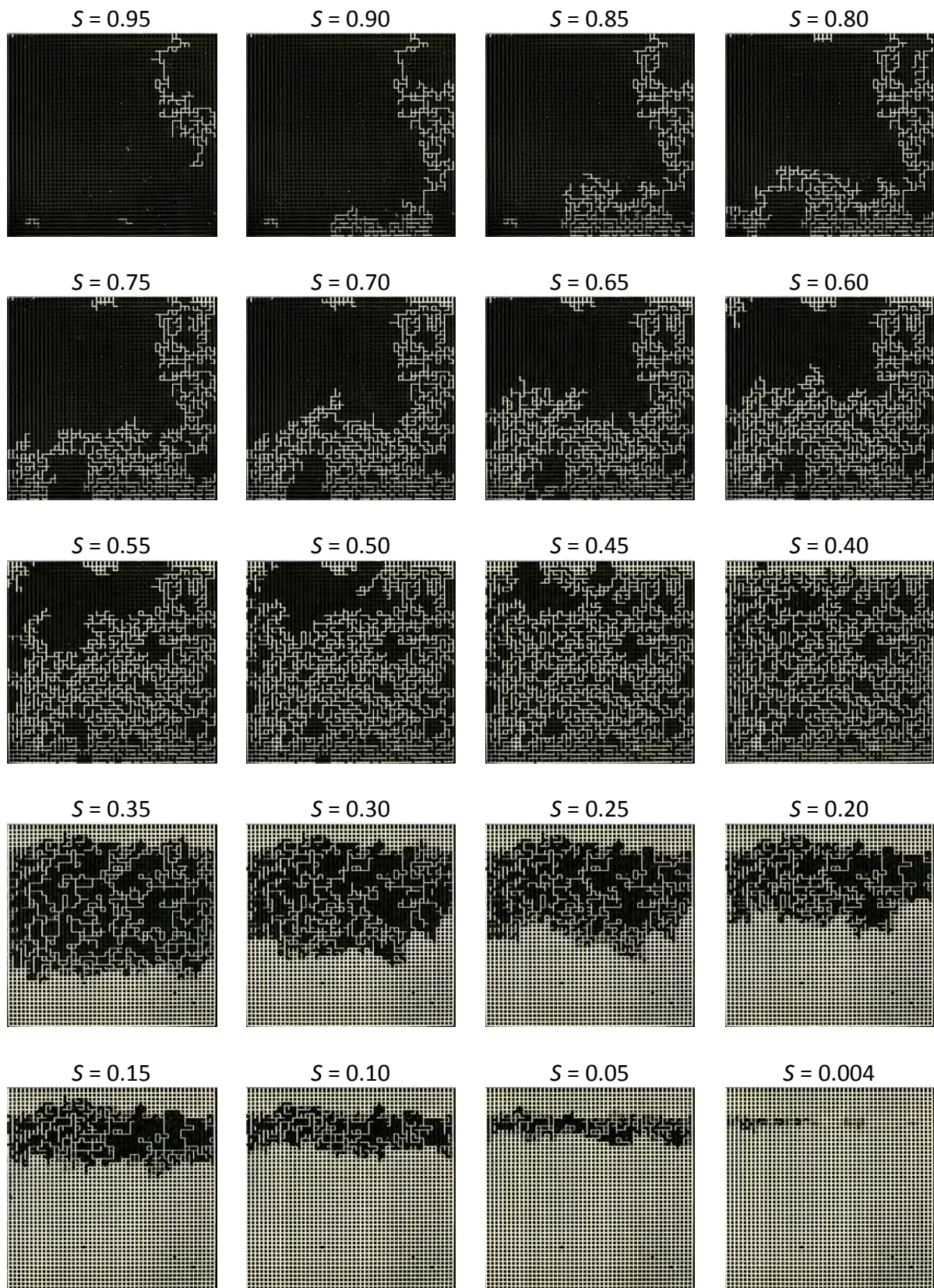
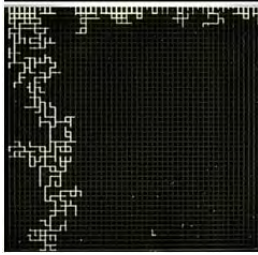
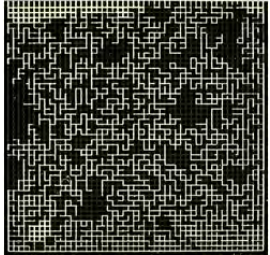
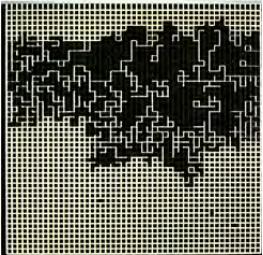
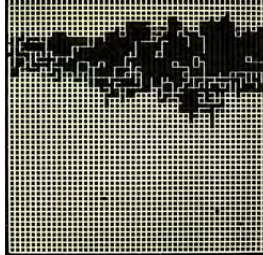
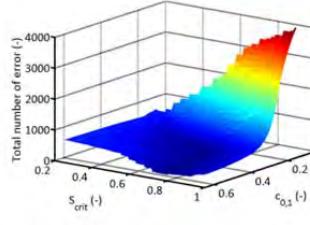
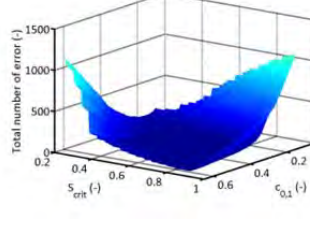
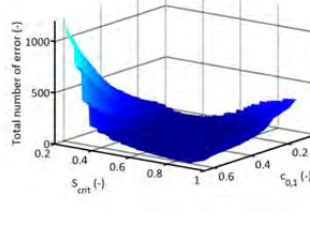
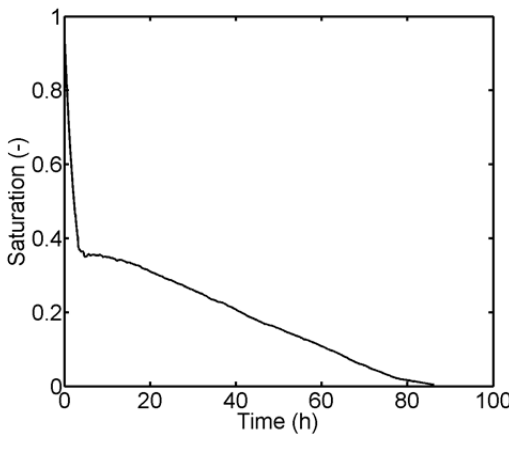
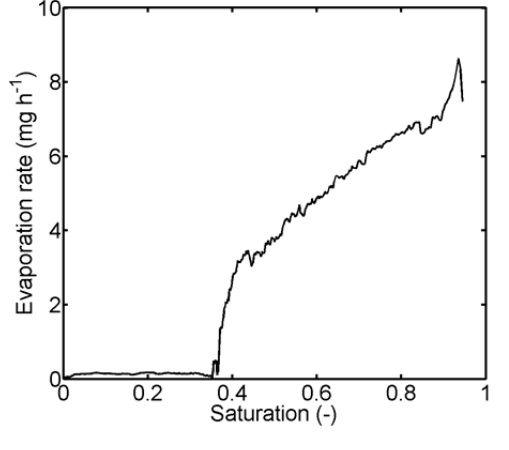




Table A-19 Specific details of experiment 11.

$S = 0.87$	$S = 0.39$	$S = 0.28$	$S = 0.16$
			
<p><b><u>Image processing parameters</u></b></p> <p><b>Binarization</b>  <math>c_{0,1} = 0.52</math></p> <p><b>Network size</b>  left bound  <math>lb = 165</math>  width  <math>w = 535.2</math>  upper bound  <math>ub = 20</math>  height  <math>h = 520.8</math></p> <p><b>Scaling</b>  <math>c_{w,h} = 10945</math>  <math>c_h = 0.972</math></p> <p><b>Critical saturation</b>  <math>S_{crit} = 0.85</math></p>	<p><b><u>Error quantification</u></b></p> <p><math>t = 26</math> min</p>  <p><math>t = 2061</math> min</p>  <p><math>t = 3981</math> min</p> 	<p><b><u>Drying curve parameter</u></b></p> <ul style="list-style-type: none"> <li>- CMA Filter</li> <li>- <math>n = 51</math></li> </ul> <p><b><u>Drying curve</u></b></p>  <p><b><u>Drying rate</u></b></p>  <p>Duration of experiment: 86 h 11 min.</p>	

**Table A-20** Summary of image data of experiment 11.

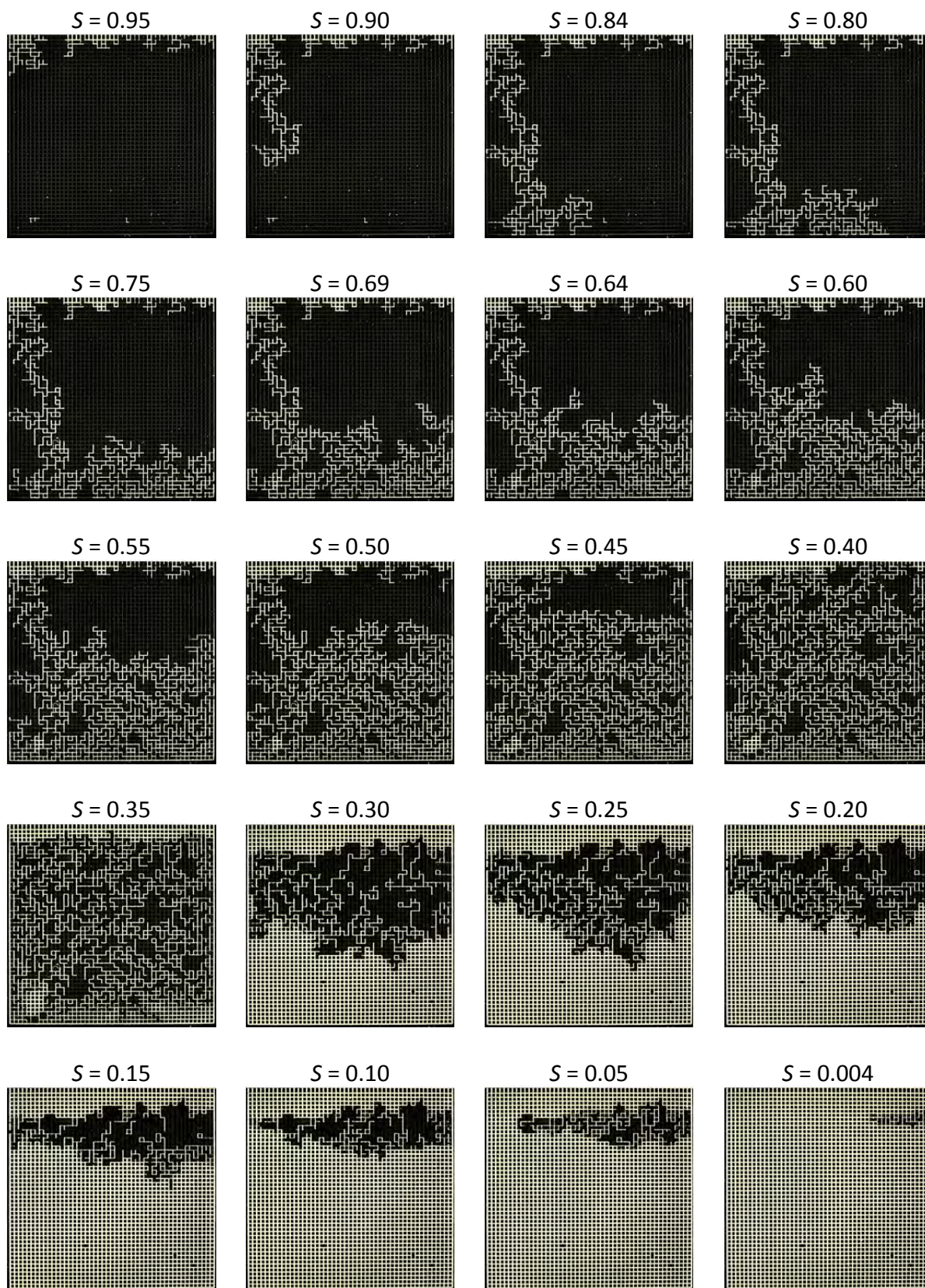
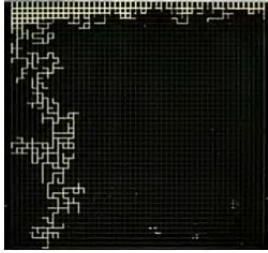
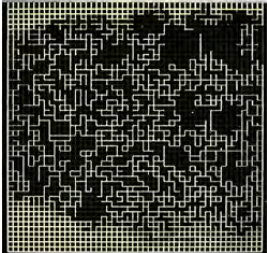

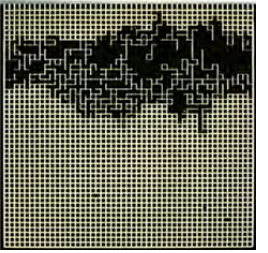
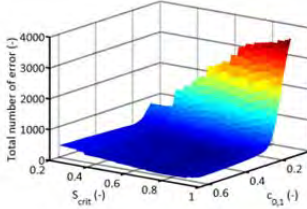
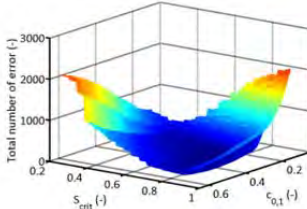
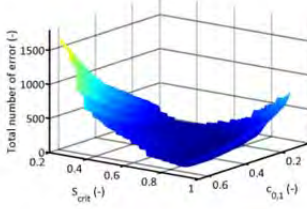
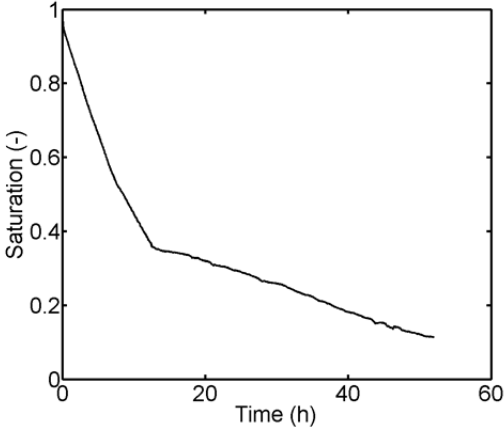
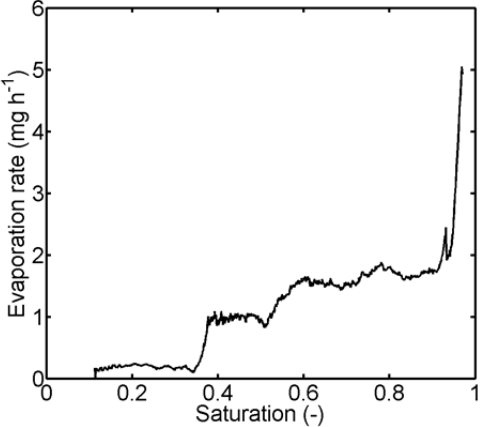
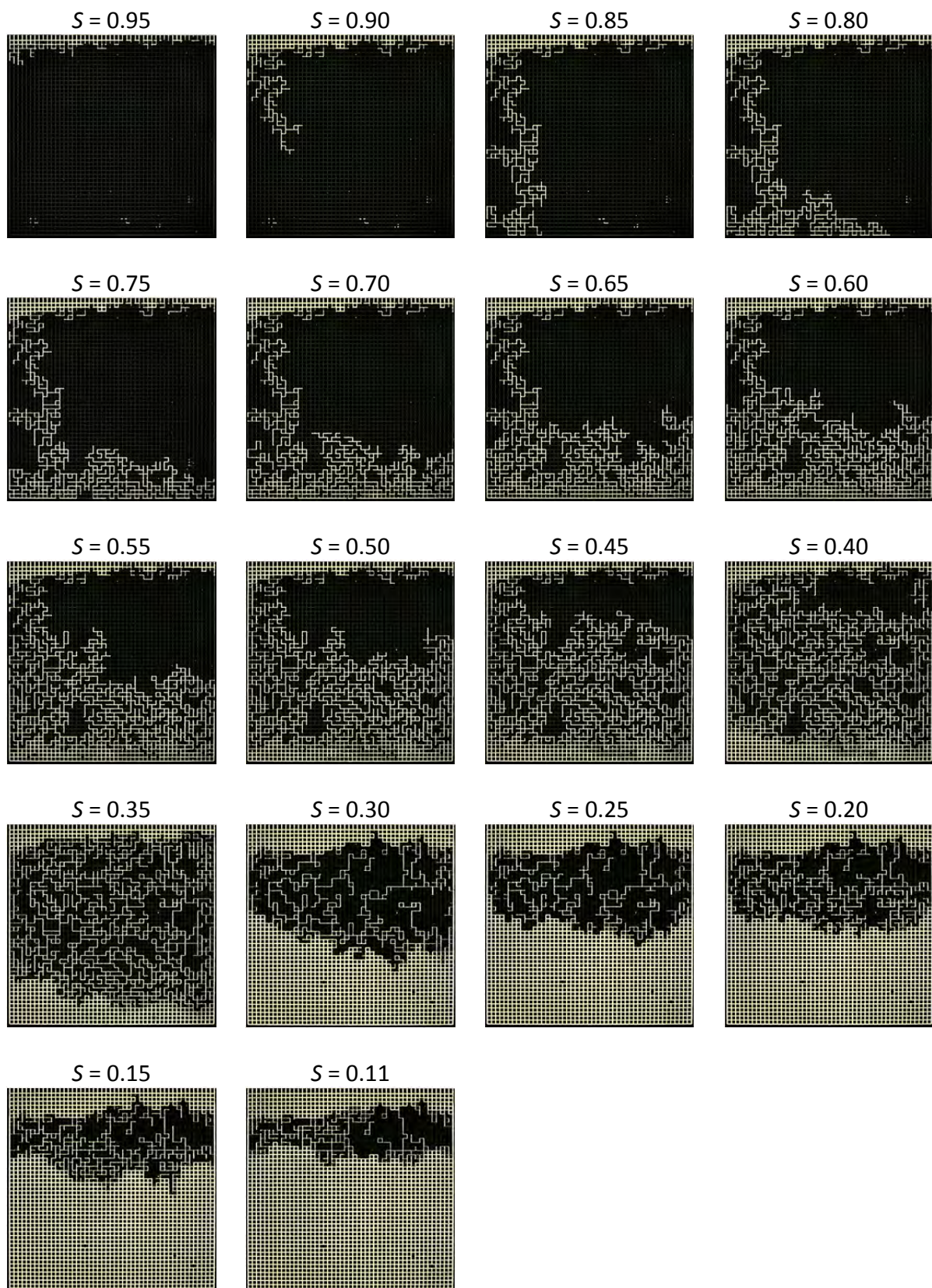


Table A-21 Specific details of experiment 18.

$S = 0.87$	$S = 0.38$	$S = 0.28$	$S = 0.16$
			
<p><b><u>Image processing parameters</u></b></p> <p><b>Binarization</b>  <math>c_{0,1} = 0.33</math></p> <p><b>Network size</b>  left bound  <math>lb = 126.5</math>  width  <math>w = 541</math>  upper bound  <math>ub = 28</math>  height  <math>h = 524.5</math></p> <p><b>Scaling</b>  <math>c_{w,h} = 10980</math>  <math>c_h = 0.9755</math></p> <p><b>Critical saturation</b>  <math>S_{crit} = 0.85</math></p>	<p><b><u>Error quantification</u></b></p> <p><math>t = 80</math> min</p>  <p><math>t = 630</math> min</p>  <p><math>t = 2158</math> min</p> 	<p><b><u>Drying curve parameter</u></b></p> <ul style="list-style-type: none"> <li>- CMA Filter</li> <li>- <math>n = 51</math></li> </ul> <p><b><u>Drying curve</u></b></p>  <p><b><u>Drying rate</u></b></p>  <p>Duration of experiment: 52 h 8 min.</p>	

**Table A-22** Summary of image data of experiment 18.



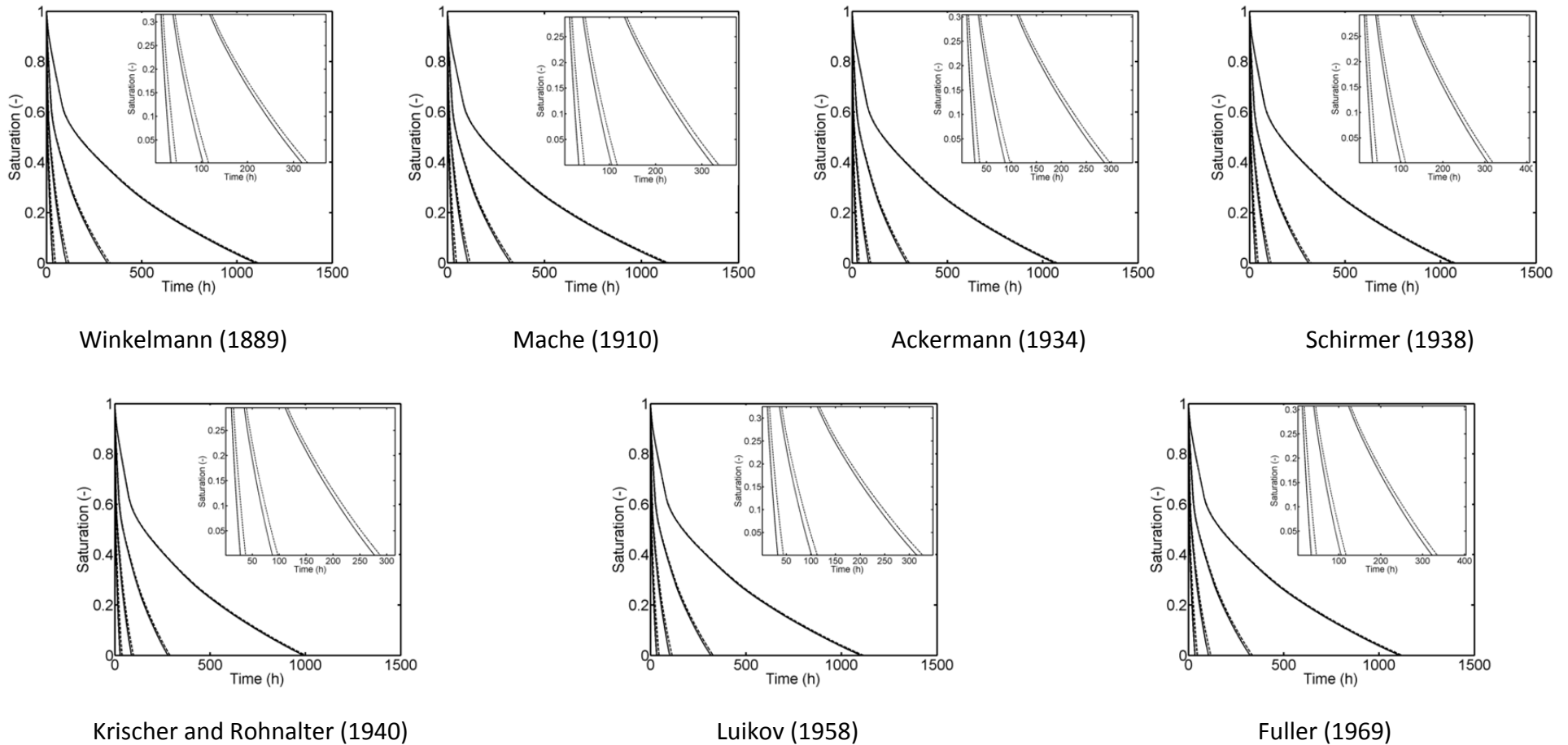
## Appendix B

### PN simulations

#### B.1 Study of the vapor transport equation and diffusion coefficient

The gas side moisture transfer is basically either described by linear vapor diffusion or non-linear vapor diffusion, depending on the temperature (refer to Section 2.3.2). Additionally different temperature dependent diffusion coefficients are given in Section 2.4.1.2. In this thesis, the non-linear diffusion equation (Eq. 2-15) with the temperature dependent diffusion coefficient proposed by Schirmer (1938) are applied in most situations following the proposal of Surasani (2009). Besides this, the correlation of Krischer and Rohralter (1940) is used in non-isothermal PN drying simulations with significant condensation of vapor in order to study the impact of vapor diffusion on the phase patterns. As shown in Fig. B-1 the PN drying simulation is almost unaffected by the choice of the diffusion coefficient, whereas different simulation results are obtained for the two different diffusion approaches. The drying curves shown in Fig. B-1 are obtained from the PNM proposed by Metzger et al. (2007c) (Table C-21).

In detail, the results presented in Fig. B-1 reveal, as expected from the correlations given in Fig. 2-23, that the temperature dependent diffusivities  $D$  computed with the correlations of Ackermann (1934), Krischer and Rohralter (1940) as well as Schirmer (1938) yield very similar drying times. More precisely, Ackermann (1934) and Krischer and Rohralter (1940) predict overall slightly shorter drying times for  $T > 20^{\circ}\text{C}$ . The correlation estimated by Krischer and Rohralter (1940) generally yields the shortest drying times over the whole temperature range (except of that given by Ackermann for  $T > 58^{\circ}\text{C}$ ). The correlations from Winkelmann (1889), Luikov (1958) and Fuller (1969) predict very similar drying times with negligible deviation. Mache (1910) yields slightly longer drying times for  $T \leq 40^{\circ}\text{C}$ . In summary, the predicted drying times lie in the range of  $t \cong 995 - 1138$  h (for  $T = 20^{\circ}\text{C}$ ),  $t \cong 280 - 335$  h (for  $T = 40^{\circ}\text{C}$ ),  $t \cong 87 - 166$  h (for  $T = 60^{\circ}\text{C}$ ),  $t \cong 27 - 46$ h (for  $T = 80^{\circ}\text{C}$ ).

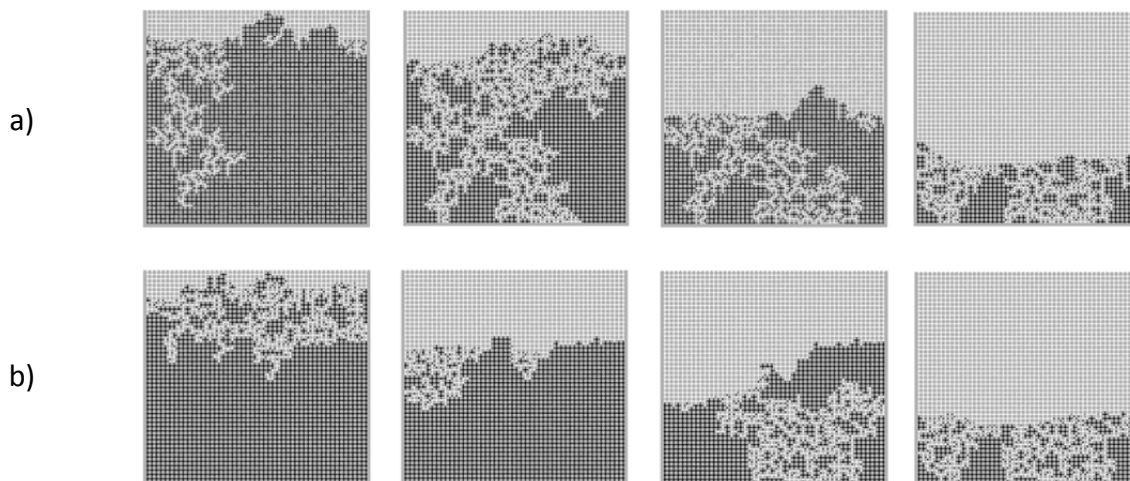


**Figure B-1** PN drying simulations with linear diffusion (dotted lines) (Eq. 2-10) and non-linear diffusion (solid lines) (Eq. 2-15). Shown are the results for application of  $D$  from the different correlations summarized in Table 2-1 and  $T = [20, 40, 60, 80]^{\circ}\text{C}$  (corresponding to curves from right to left). Simulations with the isothermal PNM of Metzger et al. (2007c) (Table C-21).

Apart from that, the deviation between the linear diffusion equation (dotted lines in Fig. B-1) and the non-linear diffusion equation (solid lines) indicates that different drying times can be computed with both approaches. Exemplarily, for the simulation with  $D$  from Schirmer (1938) deviations of around 1% at 40°C, 8% at 55°C, 10% at 60°C and around 26% at 80°C (compared to the simulation at  $T = 20^\circ\text{C}$ ) are found. This indicates that the impact of the vapor pressure dependency becomes significant for temperatures higher than approximately 40°C and must be considered in the PN drying simulations where  $T \geq 40^\circ\text{C}$  in frequent situations.

## B.2 Study of the effect of capillary pore invasion during drying

Invasion of the PN with the gas phase alters if the connecting elements between the throats, namely the nodes or pores, are assigned with a volume and capillary invasion pressure threshold. This is indicated by Fig. B-2 where a PN simulation neglecting the capillarity of pores (Fig. B-2a) is compared with a PN simulation that takes the capillarity into account (Fig. B-2b).

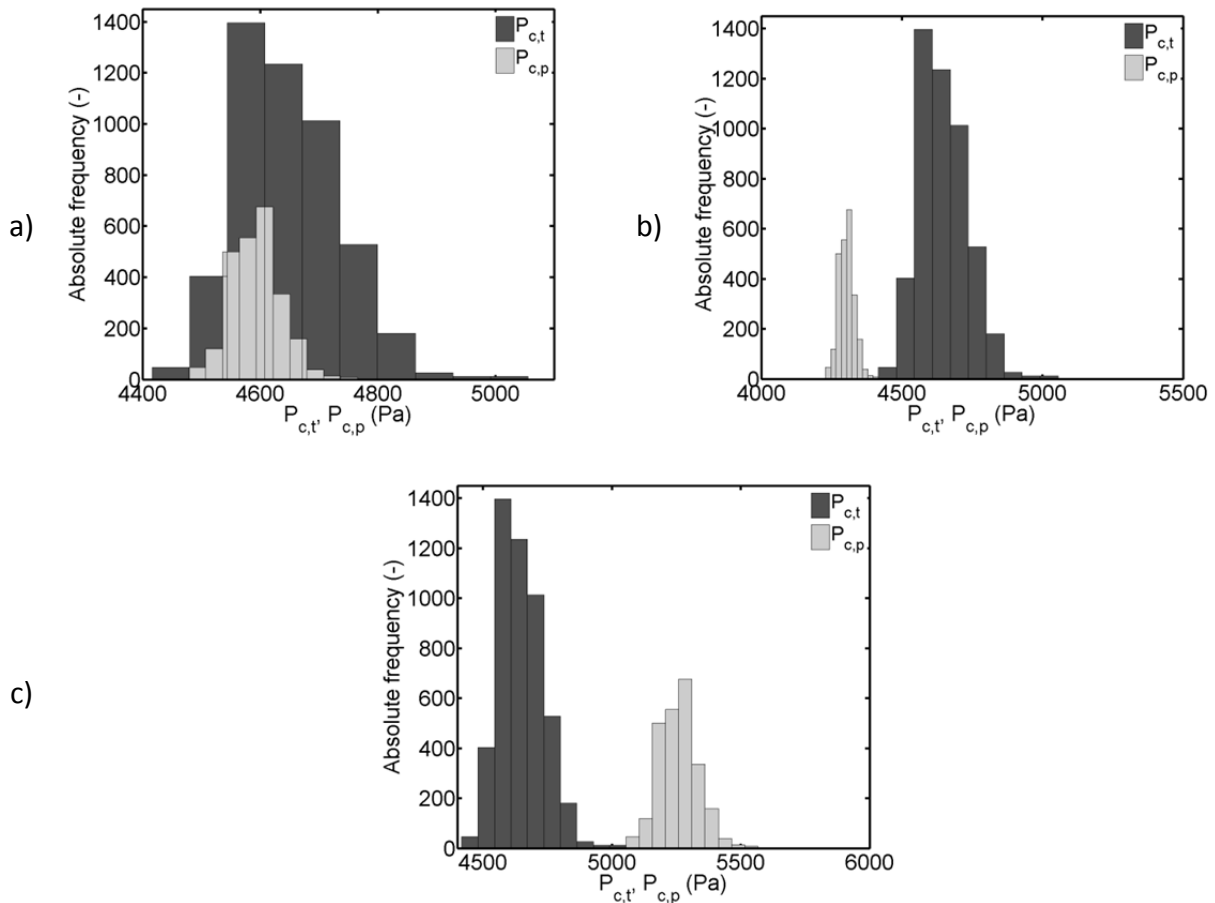


**Figure B-2** Comparison of PN simulations that ignore capillarity of single liquid pores (benchmark model) (a) with simulations that take into account capillarity of pores (PNM level 1) (b) with else identical parameter setting. In the PNM ignoring capillarity of pores the liquid volume of the pores is added to the volume of the largest throat neighbor. This allows for identical total liquid volume in both networks ( $V_{tot} = 28.486 \mu\text{l}$ ). Phase distributions are shown for  $S = [0.8, 0.6, 0.4, 0.2]$ . Liquid in black, empty pores and throats in white and solid in gray. The PN is open at the top edge. Simulation with the parameter setting given in Table 6.1 but  $T = T_{BL} = 20^\circ\text{C} = \text{const.}$  and  $s_{BL} = 2L$  (liquid film effect ignored).

The implementation of pore volumes basically leads to two limits regarding the competition of pores and throats in capillary invasion (Fig. B-3). In the first limit, pores are assigned with radii that are larger than the throat radii, i.e.  $r_p^{min} > r_t^{max}$ . This refers to a situation with overall lower entry pressure thresholds associated with the pores. In this case, the order of throat invasion is not affected as capillary invasion pressures of pores are generally lower than the throat invasion pressures (Fig. B-3b) and the PN dries as a PN ignoring the capillarity

of liquid pores. In more detail, the pores are invaded right after the invasion of one of their throat neighbors. In the second limit,  $r_p^{max} < r_t^{min}$ , pores generally produce higher capillary invasion pressures than their throat neighbors affecting the order of invasion (Fig. B-3c). In this case, liquid filled pores can be entirely surrounded by empty throats.

Using the PN presented in Chapter 5 (PNM level 1), it is investigated how the capillary invasion pressure associated with the liquid filled pores influences the macroscopic drying behavior. For this, the pore radii given in Table 3-4 were either multiplied with factor  $f = 0.56$  (pore size reduction) or with  $f = 1.52$  (pore size increase) (and other values of  $f$  as will be discussed below). The effect of this variation on the drying curves and normalized drying rate is shown in Figs. B-4a,b and compared with the result obtained for  $f = 1$  (effective pore size of the investigated PN derived from the arrangement of neighbor throats as discussed in Section 5.2.1). It is noted that the pore volumes are artificially adapted without adaption of throat volumes. This leads to an overall greater pore volume in case of  $f = 1.52$ , which might be withdrawn from the largest throat neighbor in a more precise investigation. In the other situation, with  $f = 0.56$ , less liquid is contained in the pores. In the same spirit, the excess

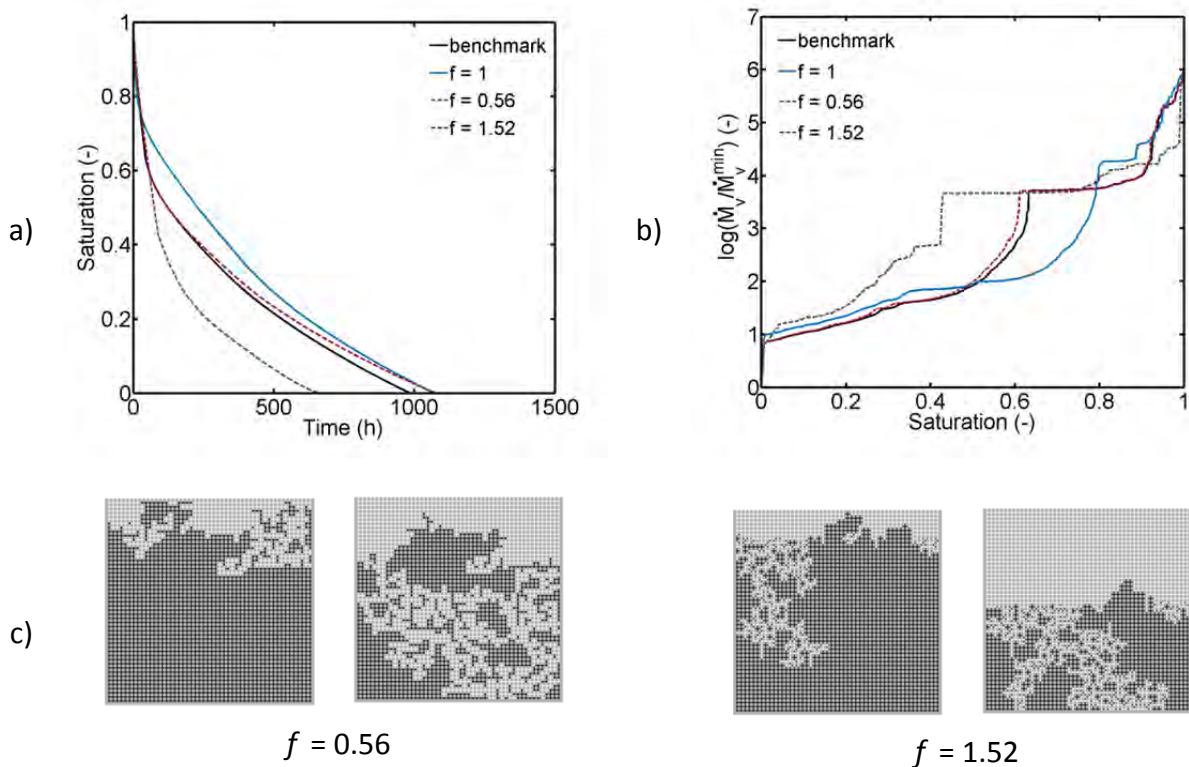


**Figure B-3** Distribution of capillary pressures in throats ( $P_{c,t}$ ) and pores ( $P_{c,t}$ ) for different overall pore volumes ( $T = 20^\circ\text{C}$ ). Throat volumes are unaffected. a) Overlapping of capillary pressures in the investigated PN ( $f = 1$ ). b) Capillary pressure distribution for  $r_p^{min} \geq r_t^{max}$  ( $f = 1.52$ ) which can lead to the same drying behavior as in a PNM neglecting the capillarity of pores. c) Capillary pressures in pores are invariably higher than throat capillary pressures for  $r_p^{max} \leq r_t^{min}$  ( $f = 0.56$ ), leading to single liquid pores totally surrounded by empty throats.



volume might be added to the largest throat neighbor. However, the difference of total liquid volumes is small between the PNs with  $f = 1.52$  and with  $f = 0.56$ , namely  $\Delta V = 0.55 \mu\text{l}$  and thus  $\cong 2\%$  of the total liquid volume contained in the original PN. For this reason, the throat liquid volume was not adapted for this investigation.

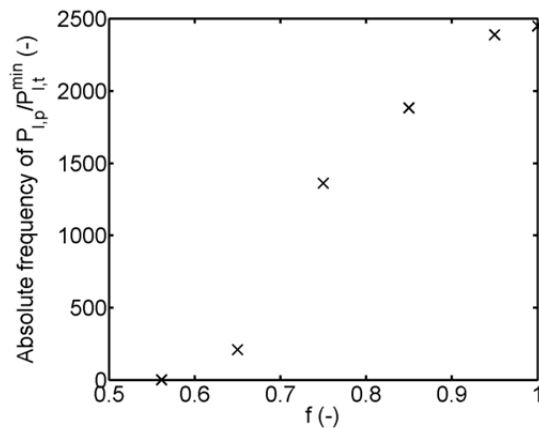
Comparison of the normalized drying rate curves in Fig. B-4b evidences, as expected, that the PNM ignoring the capillarity of pores and the PN with  $f = 1.52$  give very similar results (the drying rate curves are almost overlapping; the small shift is caused by the different total liquid volumes). Furthermore, comparison of the phase distributions in Fig. B-2a with the phase distributions in Fig. B-4c shows that the pore scale invasion is almost identical. Contrarily, the pore size reduction ( $f = 0.56$ ) obviously results in a longer period of high drying rates (drying rates drop at  $S = 0.4$ ), which is a result of the more favorable drying front position over the longest period of drying (i.e. close to the PN open side) and higher liquid connectivity (Fig. B-4c). Interestingly, the drying rate curve for  $f = 1$  is found outside of these limits (Fig. B-4b), thus making worth a detailed investigation of pore invasion in the following.



**Figure B-4** a) Drying curves from simulations with a PNM that assigns the pore volume to the largest liquid filled throat neighbor (benchmark) and a PNM that accounts for separate invasion of liquid pores with  $f = [0.56, 1, 1.52]$ . (Notice that the long duration of the drying process is a result of the very low temperature of  $T = T_{BL} = 20^\circ\text{C} = \text{const.}$ ). b) Corresponding normalized drying rate curves for a BL thickness of  $s_{BL} = 2L$ . c) Phase distributions for overall network saturation  $S = [0.8, 0.4]$ .

Figure B-5 shows the trend of the computed ratio between the liquid pressure imposed on a liquid cluster to which the invading pore belongs to (maximum cluster liquid pressure) and the minimum liquid pressure that would be produced by invading meniscus throats at the same cluster boundary. The curve is computed from PN simulations as given in Fig. B-2b and

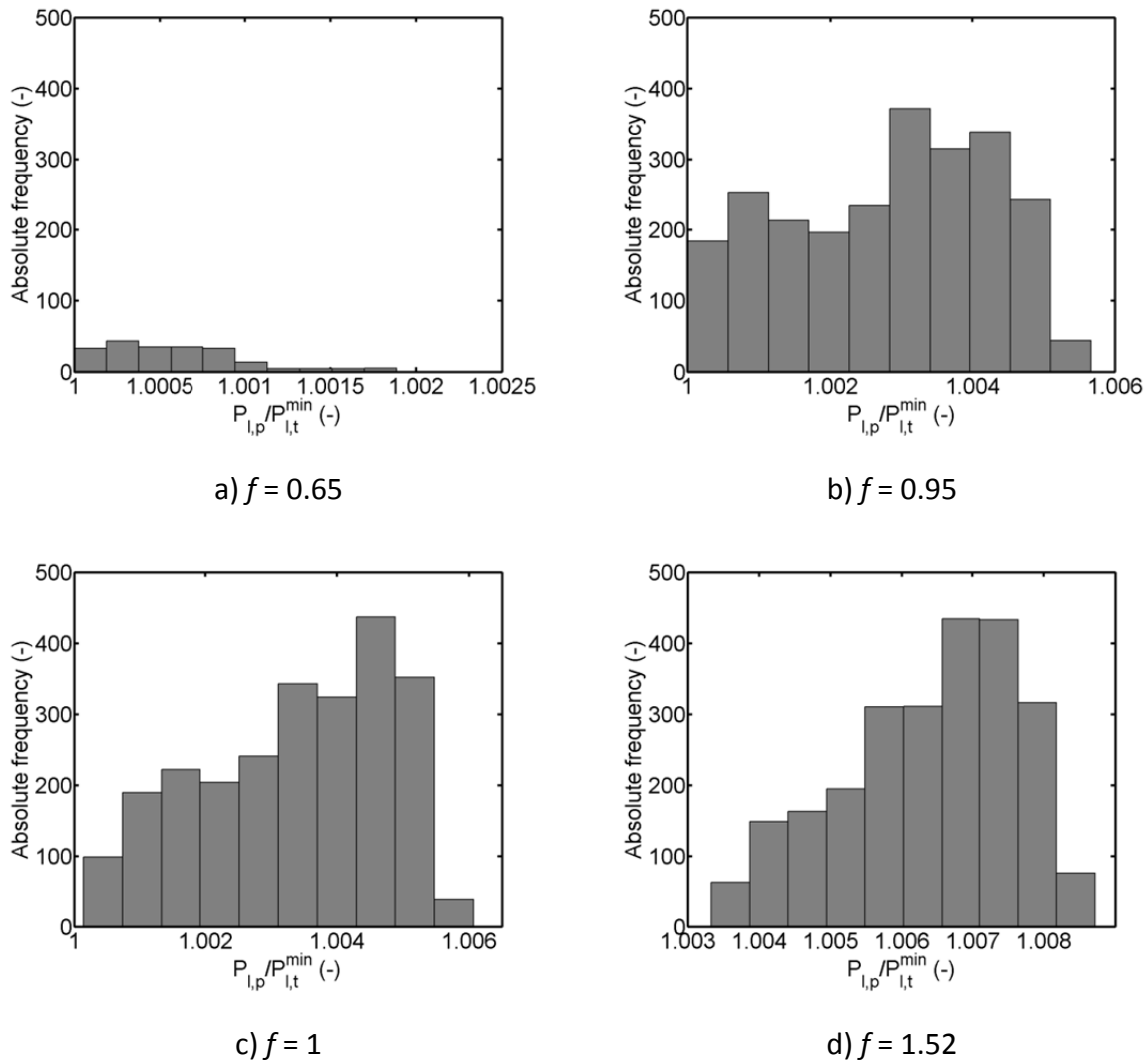
factor  $f$  varying between 0.56 and 1.52. As long as  $f \geq 1$  the order of invasion is not shifted in the favor of pores (because then the invasion pressure threshold of the pores is lower than the invasion pressure threshold of the throats and thus the liquid pressure associated with the pore invasion is always  $P_{l,p} > P_{l,t}^{min}$  and thus higher than the liquid pressure that would be associated with the invasion of the smallest throat at the cluster boundary). This occurs more frequently if the pre-factor  $f$  is higher. Contrarily, if  $f = 0.56$  the minimum liquid pressure imposed on the cluster by the invading throats ( $P_{l,t}^{min}$ ) is always greater than the liquid pressure that would be associated with invading meniscus pores; thus  $P_{l,p}/P_{l,t}^{min} = 0$  reflects the case when the cluster boundary is completely occupied by pores.



**Figure B-5** Absolute frequency of  $P_{l,p}/P_{l,t}^{min}$  computed for invading clusters. For  $f = 1$  all inner network pores (2450) empty in presence of at least one cluster boundary meniscus throat. For  $f = 0.56$  such cluster boundary meniscus throats do not exist, wherefore  $P_{l,p}/P_{l,t}^{min} = 0$ .

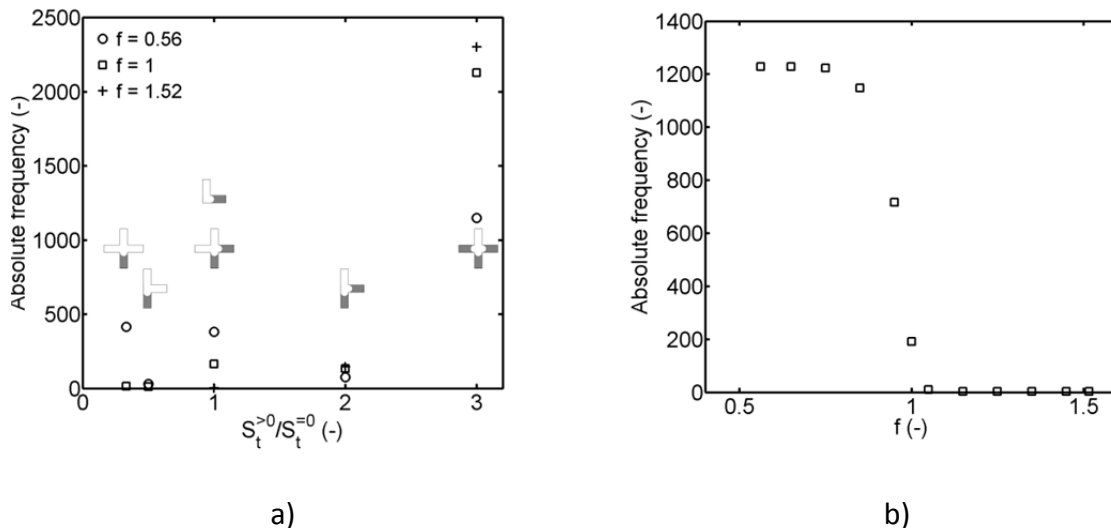
This is also confirmed by Fig. B-6, where the number of pores invading in the presence of meniscus throats located at the cluster boundary increases with increasing  $P_{l,p}/P_{l,t}^{min}$ . This is always found for  $f = 0.56$ , while increasing  $f$  allows more often for a competition of pore and throat invasion. The peak of the distribution moves to higher ratios, indicating that (in contrast to the simulation ignoring capillarity of liquid pores) the influence of the separate pore invasion on the drying process decreases with increasing pore width.

The liquid configuration in the vicinity of an emptying pore is detailed in Fig. B-7a for  $f = [0.56, 1, 1.52]$ . For  $f = 1.52$  liquid configurations are generally as obtained with the PNM ignoring the separate invasion of liquid pores. In the reference network (with  $f = 1$ ) it occurs more often that the invading pore has more than one dried throat neighbor, i.e. the number of throat neighbors with  $S_t > 0$  is equal or smaller than the number of throats with  $S_t = 0$ . If the multiplier is furthermore decreased to  $f = 0.56$  the liquid configuration is shifted to smaller values of  $S_t^{>0} > S_t^{=0}$ . Figure B-7b summarizes how often the sequence of invasion is changed (compared to the benchmark PNM) when  $f$  decreases.



**Figure B-6** Ratio of liquid pressure imposed on liquid clusters by invading pores over the minimum liquid pressure theoretically associated with invading meniscus throats. This ratio cannot be computed for  $f = 0.56$ , as in this case all cluster meniscus throats dry out before the cluster meniscus pores.

From these results the following can be concluded. In the investigated network structure (Table 3-4, with  $f = 1$ ) the competition of pore and throat invasion seems to be negligible in isothermal drying with  $T = 20^\circ\text{C} = \text{const.}$  as the order of emptying is rarely affected by the presence of capillary liquid pores (Fig. B-7). Only around 200 pores are emptied in presence of two empty throat neighbors in this case. However, it is remarked that temperature gradients affect liquid pressures and thus the sequence of pore and throat emptying. Additionally, temperature gradients allow for condensation and re-invasion of empty pores by the gas phase. Consequently, the situation is more complex allowing for different liquid configurations than studied here. This was discussed in Section 6.2.3 where it was shown that the competitive invasion of pores and throats can temporally stabilize the drying front.



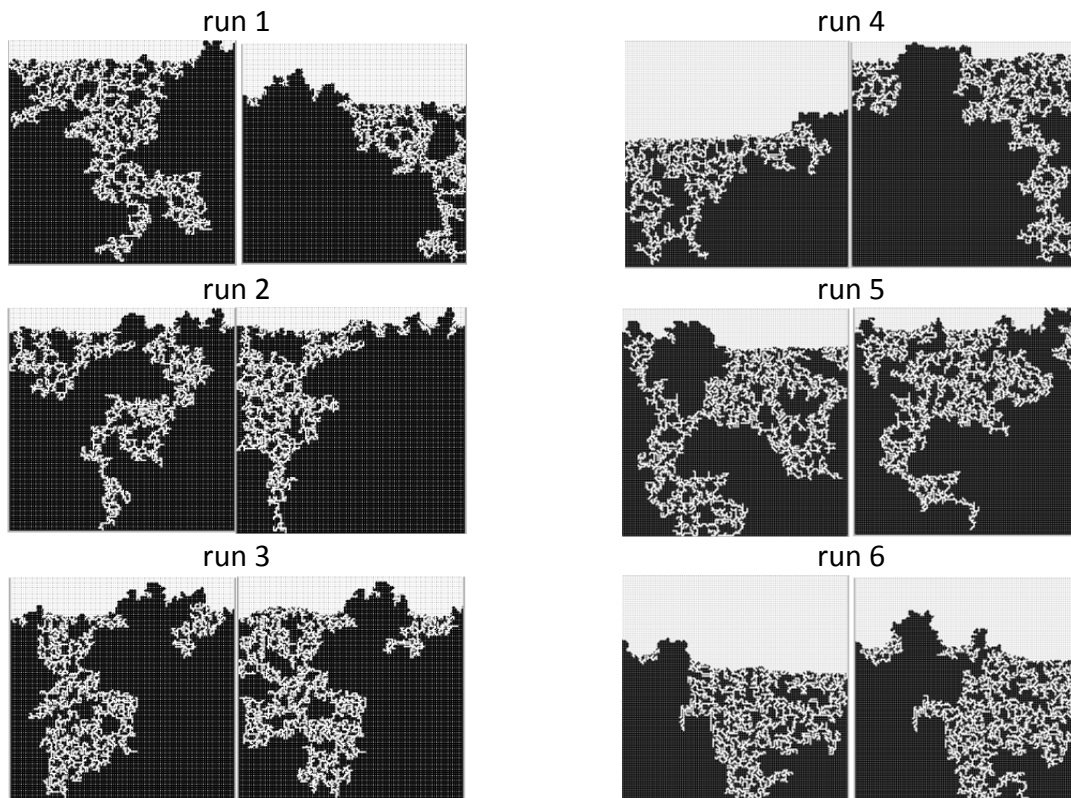
**Figure B-7** a) Absolute frequency of liquid configurations. b) Absolute frequency of altered order of invasion due to the existence of pores compared to the benchmark PNM neglecting pore invasion. Interpretation is as follows: if the multiplier  $f$  is smaller than 1, up to almost half of the total number of pores (namely 1228) can remain liquid saturated in the vicinity of more than one empty throat neighbor. (Note that each throat is connected to two neighbor pores).

Monte Carlo simulations using a PN of size 100x100 pores and identical radii distribution for the simulations ignoring the capillarity of pores (pore volumes assigned to their largest throat neighbors) and simulations allowing for discrete pore emptying indicate that the order of invasion is altered in presence of capillary liquid pores (Fig. B-8). However, although the phase distributions partly reveal significant differences, the drying curves are almost identical (especially in the period of drying when the drying front has receded into the PN). The differences in the phase distributions are explained with the altered order of invasion and the alteration of the time steps associated with the invasion of liquid elements. In detail, the separate pore invasion allows for very short time steps which can also affect the order of throat invasion.

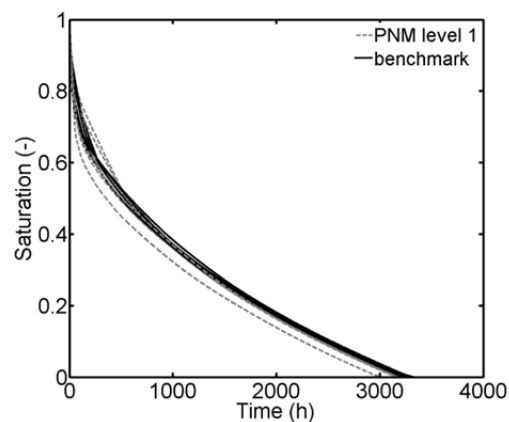
### B.3 Study of the condensation effect in a pore network with positive thermal gradient

#### *Pore scale analysis of mass transfer through the 2-phase zone*

The condensation induced refilling of the PN can be very well illustrated by simulating a partially saturated PN with arbitrary liquid configuration under the impact of a positive temperature gradient ( $T_{top} = 20^\circ\text{C}$ ,  $T_{bottom} = 70^\circ\text{C}$ ). If not other mentioned, simulation is with PNM level 4, CLO3, the PSD from the microfluidic PN and the setting given in Table 6.1 (with adjusted temperature and BL).



a)

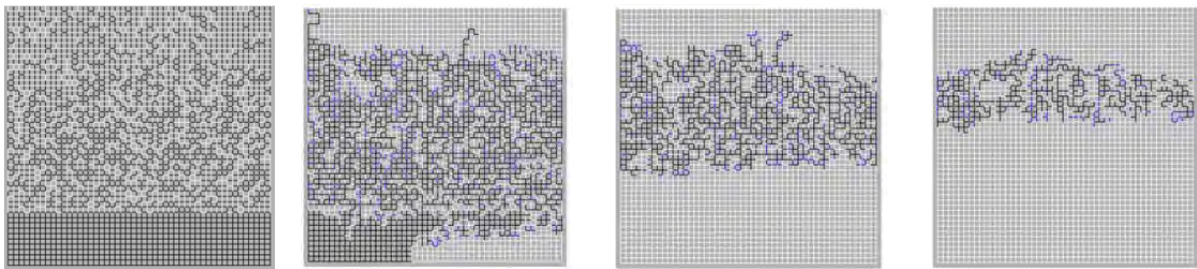


b)

**Figure B-8** a) Comparison of the breakthrough phase distributions from 6 different simulations using a PN of size 100x100 pores (Table C-23). The ratio of the total pore volume to the total throat volume is around 0.75. Left images: simulation without single pores ( $S = [0.79, 0.83, 0.78, 0.51, 0.73, 0.50]$ ). Right images: PN simulation with discrete pore invasion ( $S = [0.70, 0.83, 0.74, 0.83, 0.78, 0.58]$ ). b) Drying curves of the various PN realizations. Note that the total void volume is constant. The long drying time results from the small temperature of the PN.

The PN in Fig. B-9 is initially saturated with liquid at its bottom (pore rows  $z = (41-50)L$ ). Additionally, single throats are randomly saturated with liquid in the (dry) zone above the liquid level. When drying proceeds, moisture migrates from the hot and wet region at the PN

bottom towards the cold open network side. Since the liquid filled throats in the partially saturated zone are initially not interconnected over a wide range and thus liquid communication is interrupted here, growing and merging of clusters in this zone is explained with vapor diffusion and condensation at the gas-liquid interface of menisci inside the partially saturated zone. Thus, it appears that liquid clusters connected to the PN bottom (from the start of drying) can migrate through the 2-phase zone due to the condensation effect. At the later stage of drying, when the compact cluster at the bottom is penetrated by the gas phase, condensation can also occur at the least advanced point (LAP) of this cluster because of the lower temperature. Then, this cluster merges with its neighboring clusters ahead of the initial cluster front. Figure B-9 also reveals that larger clusters develop in the center of the PN, while the single throats at the network open side evaporate and disappear already at the start of drying. This is associated with the interrelation of temperature gradient, pore size distribution and overall drying rates as will be discussed below. In general, the observation of moisture migration during drying is in agreement with the studies of e.g. Schluender (2004) who found that drying front stabilization is a result of the temperature gradient between the most and the least advanced point of the front, resulting in vapor diffusion from the hot tip towards the colder base of the front (in drying with a temperature gradient as in a convective drying process, i.e. contrary to the temperature field discussed here).



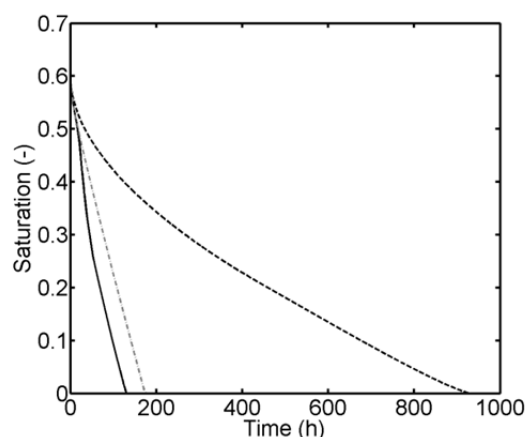
**Figure B-9** Refilling effect in a partially saturated PN with arbitrary initial liquid configuration ( $S = [0.61, 0.5, 0.25, 0.1]$ ). Moisture migrates from the compact cluster connected to the PN bottom towards the open side at the top as a result of combined evaporation, vapor diffusion and condensation as well as capillary invasion inside the developing continuous liquid zone close to the network top. Simulation with  $T_{top} = 20^\circ\text{C}$ ,  $T_{bottom} = 70^\circ\text{C}$ ,  $T_{BL} = 20^\circ\text{C}$ ,  $s_{BL} = 2L$  ( $\dot{M}_{evap,0} = 1.47 \text{ mg h}^{-1}$ ). Solid in gray, liquid phase in black, empty pores and throats in white and partially saturated elements in blue. Only the pores with  $S \geq 0.5$  are shown.

The drying curve in Fig. B-10 shows that the liquid saturation of the PN is constantly decreasing, proving that even in presence of condensation and refilling of the PN with liquid the dominating process is still drying (not imbibition). Notice that the curve in Fig. B-10 is compared to drying simulations partially neglecting the temperature dependency of physical parameters as will be discussed below.

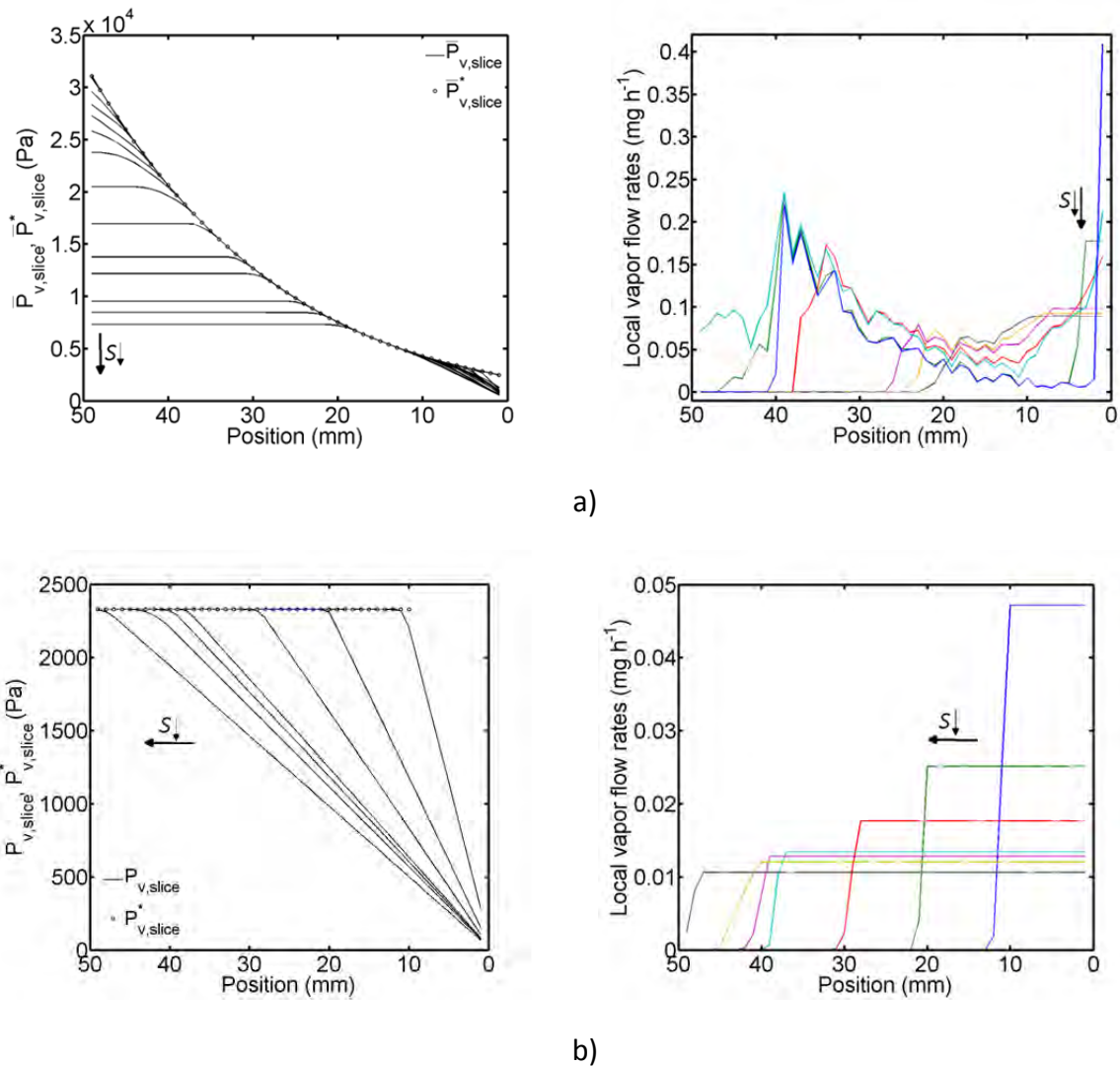
The pore level vapor diffusion affecting cluster growth and shrinkage is illustrated in Fig. B-11, where the vapor pressure field of the example shown in Fig. B-9 is plotted together with the slice accumulated through-plane diffusion flow rates (based on Eq. 5-44). The curves of the non-isothermal simulation are compared with isothermal drying. The curves reveal a significant difference between the two cases. While a linear gradient of the slice average vapor pressure evolves between the drying front and the PN open side in the

isothermal case, the situation appears more complex in drying with a positive temperature gradient, where the mean partial vapor pressure is uniform in the *dry zone* below the 2-phase-zone (at lower overall PN saturations), decreases inside the 2-phase-zone and further decreases in the dry zone connected to the PN surface. Consequently, the plots of the slice accumulated diffusion rates in Fig. B-11 reveal significant differences in the vapor transfer regimes in isothermal and non-isothermal drying. In the non-isothermal situation vapor can also flow through the 2-phase zone with overall positive vapor flow rates over the whole PN length. However, once the 2-phase zone is disconnected from the PN bottom, it screens the totally dry zone (connected to the PN bottom) disrupting vapor diffusion in this region. It can also be seen that the vapor diffusion rates overall decrease with increasing distance from the PN bottom and thus with decreasing temperature, followed by a significant increase of vapor diffusion rates in the dry zone at the PN surface (where the vapor flow rates are constant). This is in contrast to the isothermal case, where the vapor flow rates are zero inside the 2-phase zone, constant in the dry zone and gradually decreasing with decreasing network saturation.

It can be shown that moisture migration inside the PN is affected by vapor transport mechanisms and the effect of vapor condensation in presence of imposed positive temperature gradients. For this, temperature dependency of capillary invasion and temperature dependency of the vapor transport are simulated separately. In principle,  $P_v^*(T) = \text{const.}$  and  $D(T) = \text{const.}$  are assumed in the simulation neglecting the temperature dependency of vapor transport and  $\sigma(T) = \text{const.}$  is assumed in the simulation neglecting the temperature dependency of capillary invasion. As indicated by Figs. B-12 and B-13, peculiarities of the phase distributions shown in Fig. B-9 are dominated by the temperature dependent vapor diffusion because rather similar phase distributions are obtained in the simulation neglecting the temperature dependency of capillary invasion whereas phase distributions similar to isothermal drying are obtained when neglecting the temperature dependency of saturation vapor pressure and diffusivity. Furthermore also the vapor pressure curves and local vapor diffusion rates are as in the isothermal drying process if  $P_v^*(T) = \text{const.}$  and  $D(T) = \text{const.}$  (Figs. B-11b, B-13a).



**Figure B-10** Drying curve of the partially saturated PN with imposed thermal gradient (solid line corresponding to Fig. B-9), comparison to simulation neglecting the temperature dependency of vapor transport (dashed black line) and simulation neglecting the temperature dependency of liquid transport (dashed gray line).



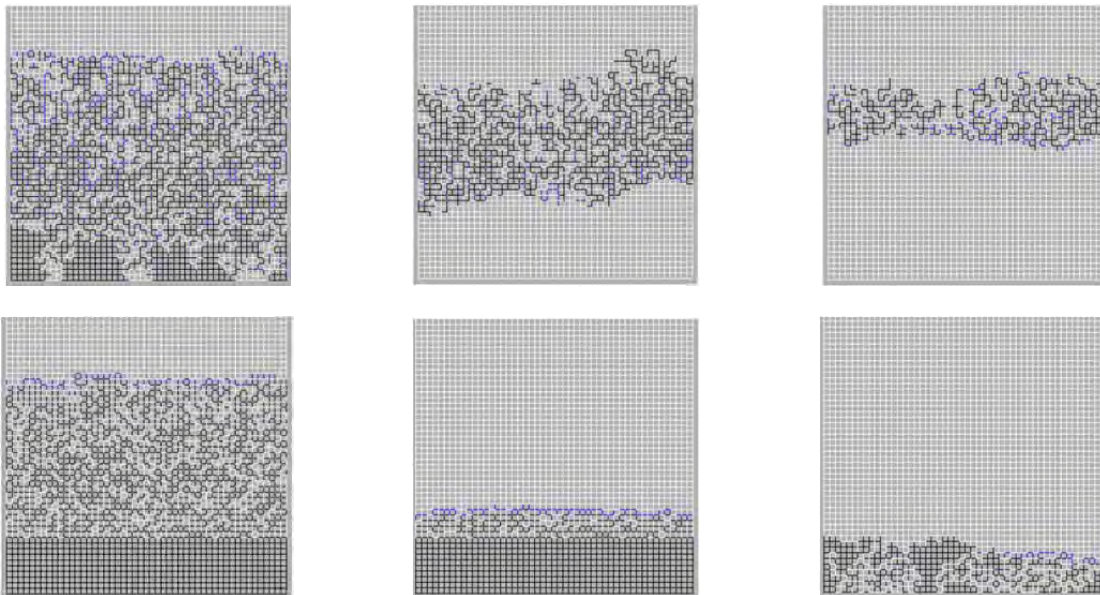
**Figure B-11** a) Slice average partial vapor pressure and slice average saturation vapor pressure profiles as well as total through plane diffusion rates corresponding to Fig. B-9. b) Isothermal PN drying ( $T = 20^\circ\text{C}$ ) with else identical parameter setting.

In agreement with that, much longer drying times are simulated with the model neglecting the temperature dependency of vapor transport (Fig. B-10). This indicates that the liquid distribution in a non-isothermal drying process (with imposed positive temperature gradient) accompanied by strong condensation effects is dictated by the vapor transport kinetics while the capillarity of the PN plays a minor role (as long as the liquid phase is disconnected during the RFP).

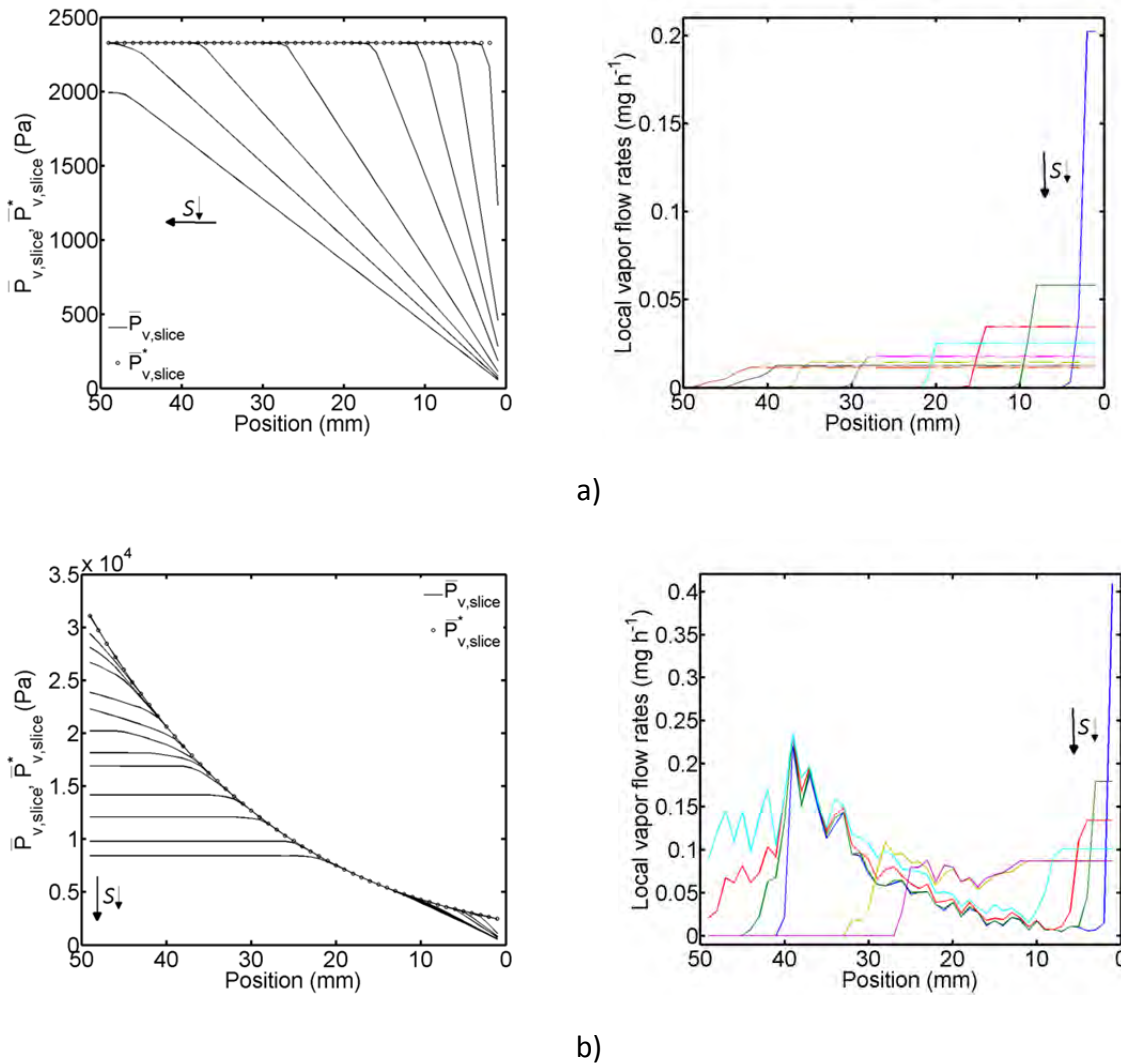
It is remarked that the computational effort increases with each PN element that is refilled with liquid. In certain situations, a liquid element can be invaded several times. Thus, it might be assumed that the computational time increases with the total volume of condensed liquid. As shown in Fig. B-14 the condensation effect indeed increases with increasing temperature gradient ( $T_{top} = 20^\circ\text{C}$  and  $T_{bottom} = [20:10:90, 99]^\circ\text{C}$ ), but the number of invasions and so the computational time stagnates for temperature gradients equal or greater than  $dT/dz = 1.23 \text{ K mm}^{-1}$  (with all other parameters kept constant). This rather counterintuitive observation is related to the individual transient saturation of liquid



elements after invasion with liquid. According to Eqs. 5-71, 5-72 or 5-77 (computation of the time step of an invasion event) and Eqs. 5-73 or 5-78 (computation of the transient throat and pore saturation) the time required to fully invade a throat or pore depends on the current saturation of the throat/pore and the local evaporation or condensation rate. Consequently, the ratio of re-saturation of individual pores and throats due to condensation affects the number of computation cycles (including update of the vapor pressure field and cluster labeling). In detail, overall lower throat and pore saturations are obtained for lower temperature gradients with high oscillation of emptying/refilling cycles, increasing the number of computation cycles accordingly. Contrarily, a more stable invasion of pores and throats can lead to higher individual saturations and obviously to a reduction of computation cycles and overall computational time. From Fig. B-14 it is assumed that the individual transient saturation of liquid pores and throats is higher if  $T_{bottom} \geq 80$  °C. In this situation more pores and throats can be re-saturated to  $S_{t,p} = 1$  than comparably in the situation with  $T_{bottom} < 80$  °C (for the given network structure and the initial saturation given in Fig. B-9). Consequently, also the appearance of the 2-phase zone is expected to be more compact with increasing  $\Delta T$ . This example reveals the impact of the computation of pore and throat saturation. A more precise approach (in the frame of quasi-steady invasion) might consider the role of partially saturated liquid elements (which are essentially contradictory to the basic assumptions of quasi-steady invasion). As will be discussed in the following (Figs. B-15 to B-19), the computational effort can partly be controlled by means of the cluster labeling option as this has a crucial impact on the cluster growth mechanism and the dynamics of the invasion process (Section 5.4.4.3). In this context it shall again be remarked that every single liquid pore is treated as a cluster in the presented CLOs and thus is always assigned a label greater than 0.

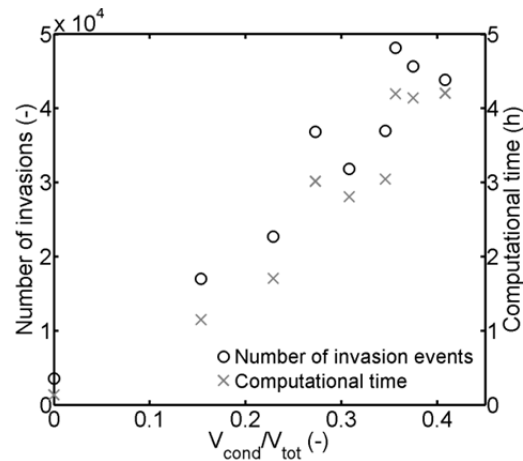


**Figure B-12** Phase distributions of non-isothermal drying neglecting the temperature dependency of capillary pressure (upper row) and neglecting the temperature dependency of vapor transport (bottom row) ( $S = [0.5, 0.25, 0.1]$ ). Detachment of the 2-phase zone and receding of the drying front from the PN bottom side is only found in the case when temperature dependency of capillary pressure is neglected (upper row). Contrarily, neglecting the temperature dependency of the vapor transport results in phase distributions as found in isothermal PN drying (bottom row). Parameter setting as in Fig. B-9.



**Figure B-13** Slice average partial vapor pressure and slice average saturation vapor pressure profiles and total through plane diffusion rates corresponding to Fig. B-12. a) Non-isothermal drying neglecting the temperature dependency of vapor transport, b) non-isothermal drying neglecting the temperature dependency of capillary pressure.

Figure B-15 shows the total number of shrinking (evaporating) clusters in comparison to the total number of growing (condensing) clusters. While the number of growing clusters is constantly decreasing in CLO1 and CLO3, the situation is different in CLO2 due to the increased connectivity of the liquid phase (Fig. 5-15b). Here the number of growing clusters is initially increasing before a maximum of  $N_{cl,cond}^{max} = 93$  is reached (Fig. B-16a). Interestingly,  $N_{cl,cond}^{max}$  is much lower in CLO2 than comparably in CLO1 ( $N_{cl,cond}^{max} = 377$ ) and CLO3 ( $N_{cl,cond}^{max} = 506$ ) (Fig. B-16a) although this labeling option is based on the state of the throat saturation and thus also single throats and additionally also the single pores are identified as a cluster. (The high number obtained for CLO3 is explained with the separation of clusters by condensing partially saturated elements which are partly assigned to identical clusters with CLO1). As a consequence, the size of clusters is greater at the start of drying when using CLO2 (Fig. B-16b). The situation is different in CLO1 and CLO3, where the maximum cluster

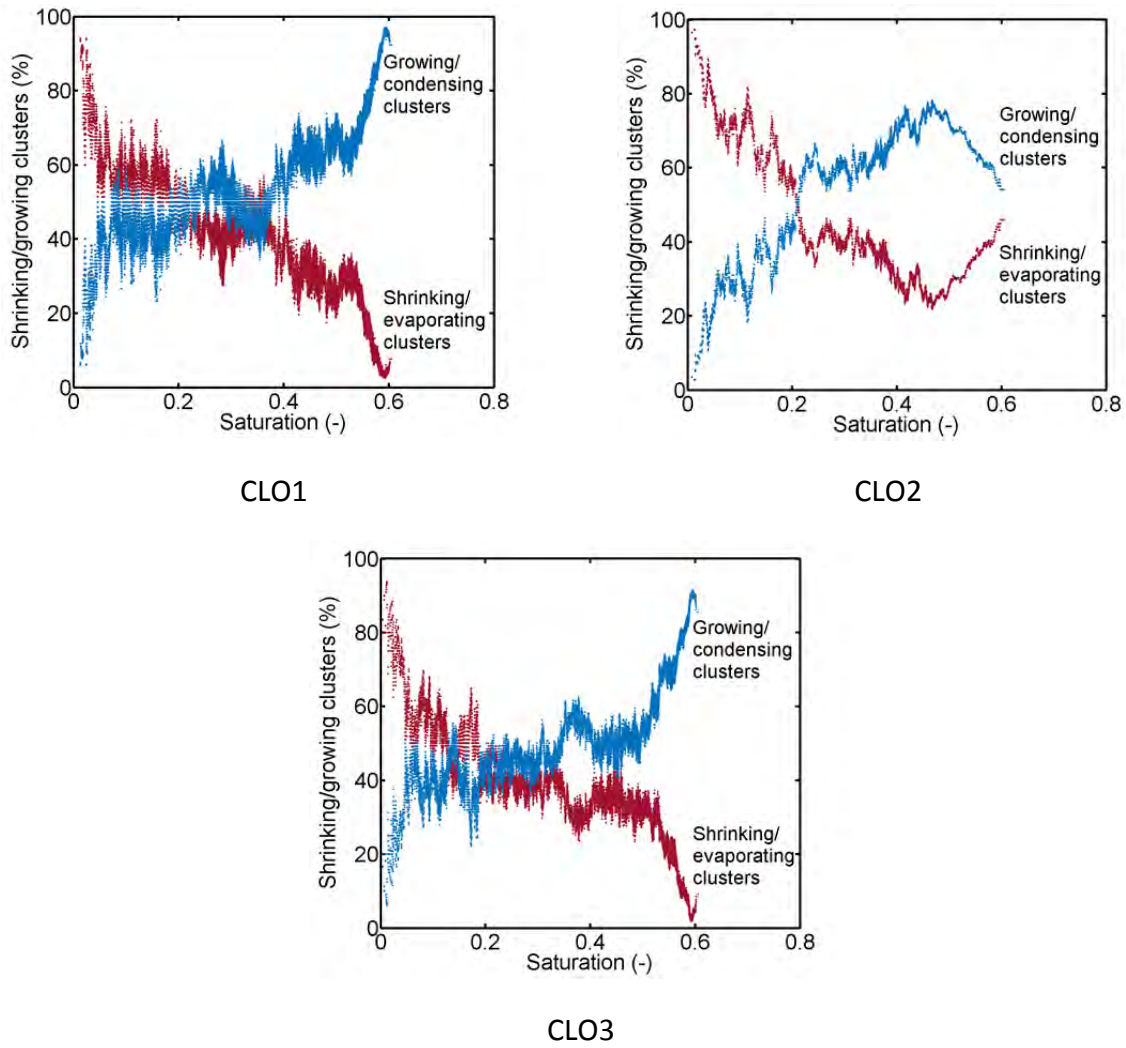


**Figure B-14** Number of invasion events and computational time against ratio of condensed liquid volume corresponding to the situation given in Fig. B-9 and  $T_{bottom} = [20:10:90, 99]^{\circ}\text{C}$ . Note that the ratio  $V_{cond}/V_{tot}$  increases with increasing  $\Delta T$ .

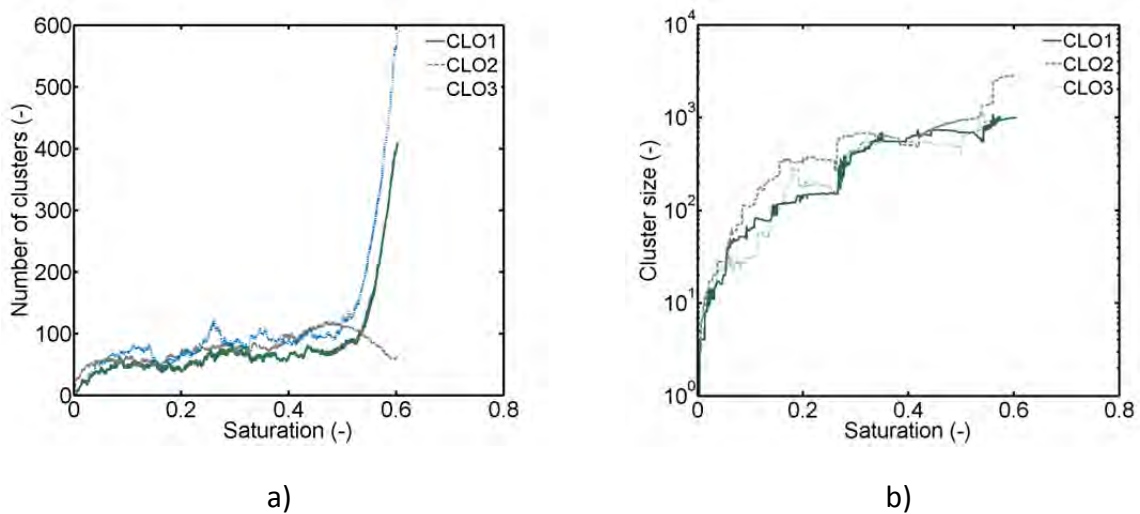
number is found at the start of drying and where furthermore the cluster size is initially almost constant (or slightly increasing). Furthermore, CLO1 indicates a greater fluctuation in the size of clusters (Fig. B-16b) which is referred to the higher oscillation of emptying/refilling of throats. Stabilization of the cluster dynamics is instead achieved with CLO3.

The profiles in Fig. B-17, which show the internal saturation of the 2-phase zone, reflect the cluster dynamics. The condensation effect, which leads to the growing and merging of clusters, is associated with a noticeable increase of the saturation of the 2-phase zone in the simulation with CLO1 and CLO3 (at  $S = 0.2 - 0.25$ ). As expected from the discussions above, this effect does not occur (with comparable significance) in CLO2. This leads to a longer duration of the liquid phase interconnectivity to the PN open side (revealed by the later advance of the LAP in the simulation with CLO2). In this case, the structure of the 2-phase is rather controlled by capillary invasion than by vapor diffusion as long as the 2-phase is connected to the PN surface.

Table B-1 indicates that the relative amount of condensed liquid volume (Eq. 5-80) depends on the choice of the CLO. Interestingly, the computational time does not vary accordingly. Instead, the computational time and the total number of invasion events are much greater in CLO1 than in the other two CLOs. This is explained with the temporal oscillation of (re-)invasion of condensing pores and throats, as already explained above. In summary, the following can be concluded. Although overall less liquid is condensed when applying CLO1 (than compared to CLO3), saturation of single elements changes more frequently in CLO1. This means, that overall more partially saturated single pores and throats (with low liquid saturation) develop and disappear in case of CLO1 (according to discussions in Section 5.4.3). As mentioned before, update of the saturation vapor pressure field as well as of the cluster labeling is necessary after each invasion event, leading to the conclusion that the computational effort dramatically increases with each invasion event. From Table B-1 it is concluded that the situation is rather stabilized in CLO2, where connectivity of the liquid phase is increased and the number of cluster boundaries available for invasion is decreased. Thus, here the condensed liquid volume is accumulated in less pores and throats than comparably in CLO1 and CLO3. In the drying simulation with CLO3 more invasions occur than in the simulation with CLO2. However, stabilization of the cluster dynamics is dramatically



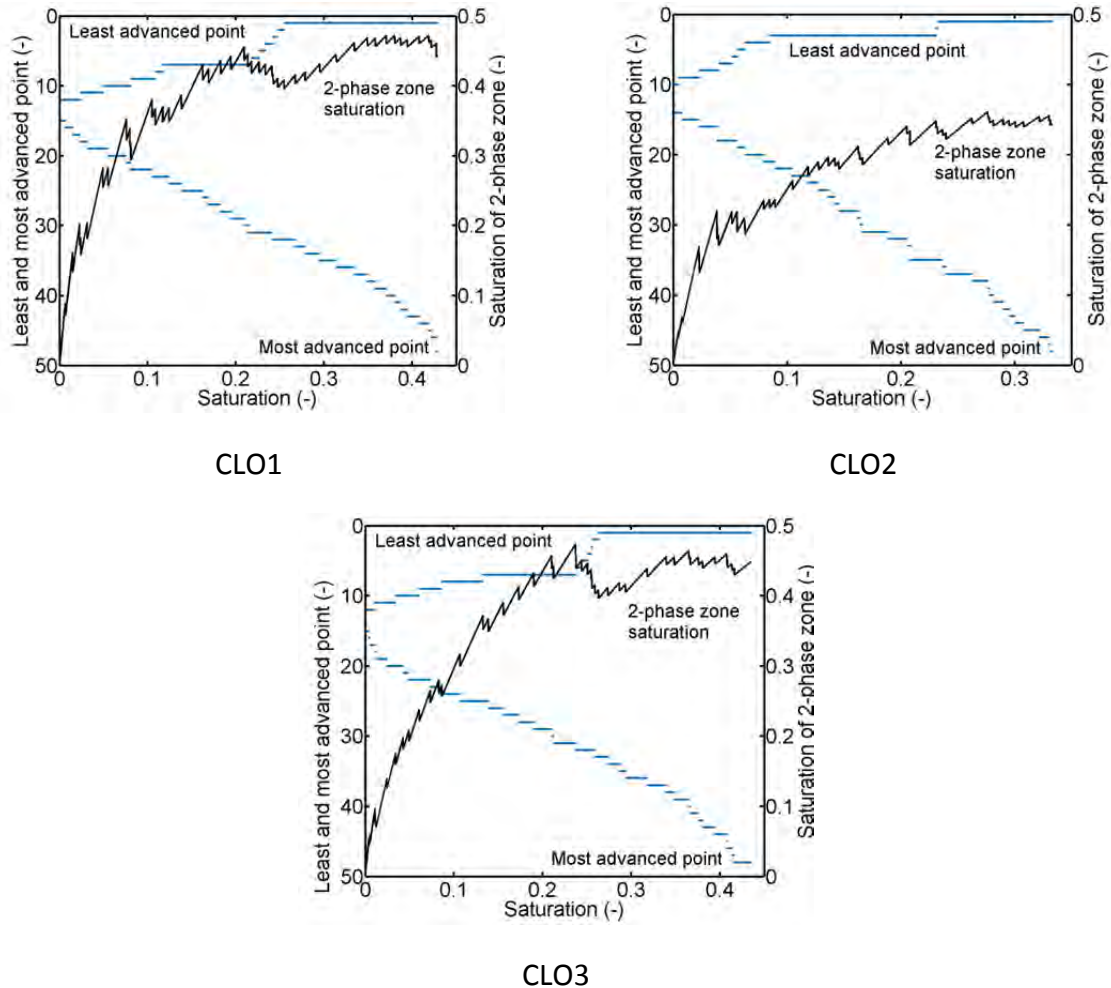
**Figure B-15** Comparison of the number of growing (in blue) and shrinking (in red) clusters for the three CLOs. (Corresponding to Fig. B-9).



**Figure B-16** Comparison of a) overall cluster number and b) maximum cluster size (derived from the total number of throats connected within a cluster). (Corresponding to Fig. B-9).

improved compared to CLO1 (indicated by a lower number of invasion steps and reduced computational time in Table B-1).

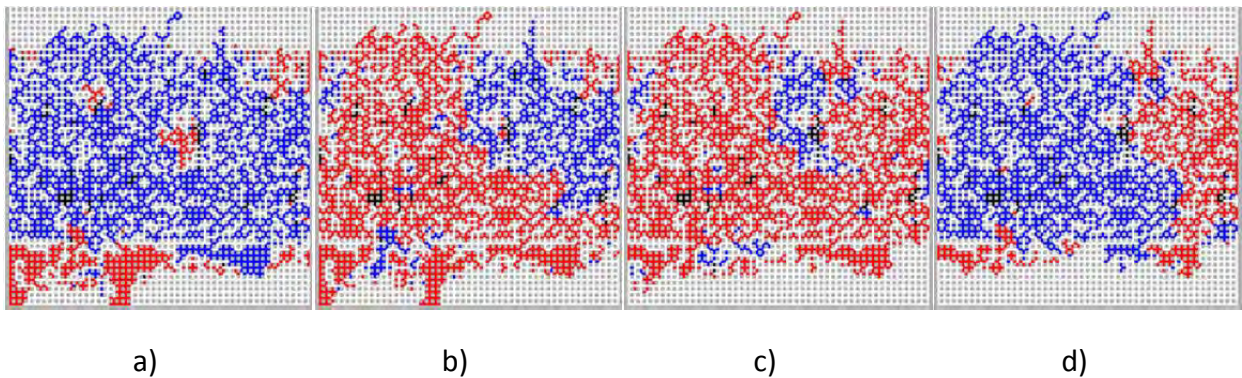
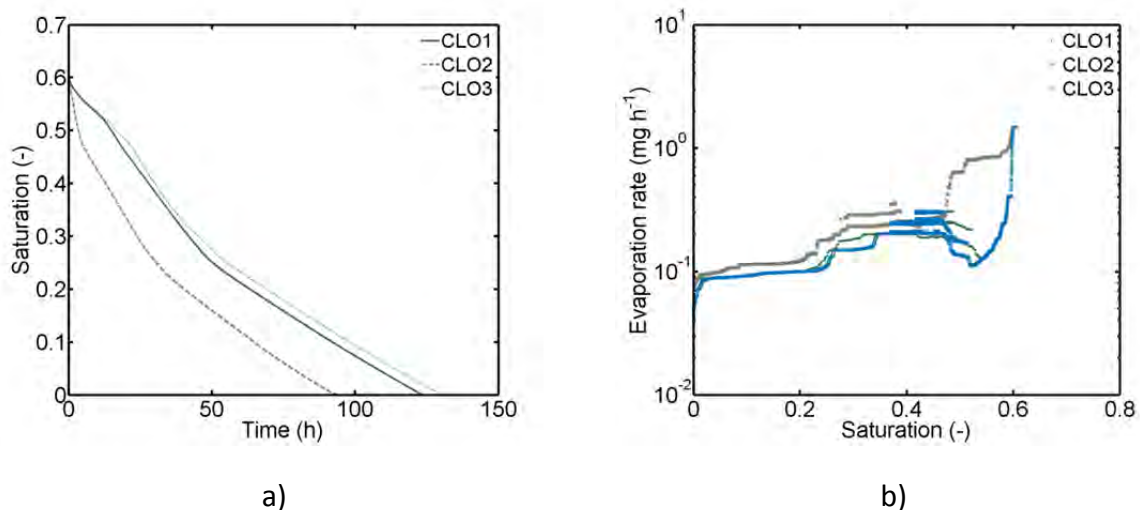
Figure B-18 shows that the dynamic of clusters can suddenly change from shrinking (i.e. evaporating) to growing (i.e. condensing) and vice versa. This behavior was partly also observed in microfluidic experiments with positive thermal gradient. But there usually only the smaller clusters were affected. Simulations with CLO1, CLO2 and CLO3 show overall very similar behavior (as in Fig. B-18), but the fluctuation appears less pronounced in the simulation with CLO2. Finally, the effect of condensation on the overall drying behavior is shown in Fig. B-19. It is found that the drying time is significantly shorter when using CLO2, while very similar drying times are found for CLO1 and CLO3 (Fig. B-19a), although the ratio  $v_c^+$  is 22 % higher in CLO3 compared to CLO1. The short drying time obtained with CLO2 is explained with the higher drying rates (Fig. B-19b) which is again based on the longer period of connection of the liquid phase to the PN surface (indicated by the position of the LAP in Fig. B-17). With CLO2, high interconnectivity of the liquid phase allows for long range capillary invasion (from top to bottom). This is also reflected by the later detachment of the 2-phase zone from the bottom of the PN in Fig. B-17. This leads to shorter drying times.



**Figure B-17** Analysis of liquid distribution simulated with the different CLOs (least and most advanced point and internal saturation of the 2-phase zone computed from  $S_{2PZ} = S(\sum V_t + \sum V_p) / V_{void,2PZ}$ ). The curves are shown for the drying period after disconnection of the liquid phase from the PN bottom.

**Table B-1** Overview of the condensation effect for simulations with PNM level 4.

	CLO1	CLO2	CLO3
$v_c^+$	0.2827	0.1125	0.3458
$N_{steps}$	80915	10356	36952
$t_{comp}$	7.15 h	0.5 h	3.1 h

**Figure B-18** Visualization of evaporating (in red) and condensing (in blue) clusters reveals a fluctuation of cluster dynamics. Stationary clusters are shown in black. The large condensing region in a) suddenly splits up into a large evaporating region and a smaller condensing region in b). c) and d) reveal consistency of this phenomenon. (Example from Fig. B-9 with CLO3).**Figure B-19** Macroscopic drying behavior simulated with PNMs using different options of cluster labeling: a) drying curves, b) drying rates. The fluctuations of the drying rate curves are explained with the fluctuations of the position of the LAP. The curves correspond to Fig. B-9 (with CLO1, CLO2 and CLO3).

*Pore scale analysis of the cooperative impact of capillarity, temperature gradient and evaporation rate on drying with positive thermal gradient*

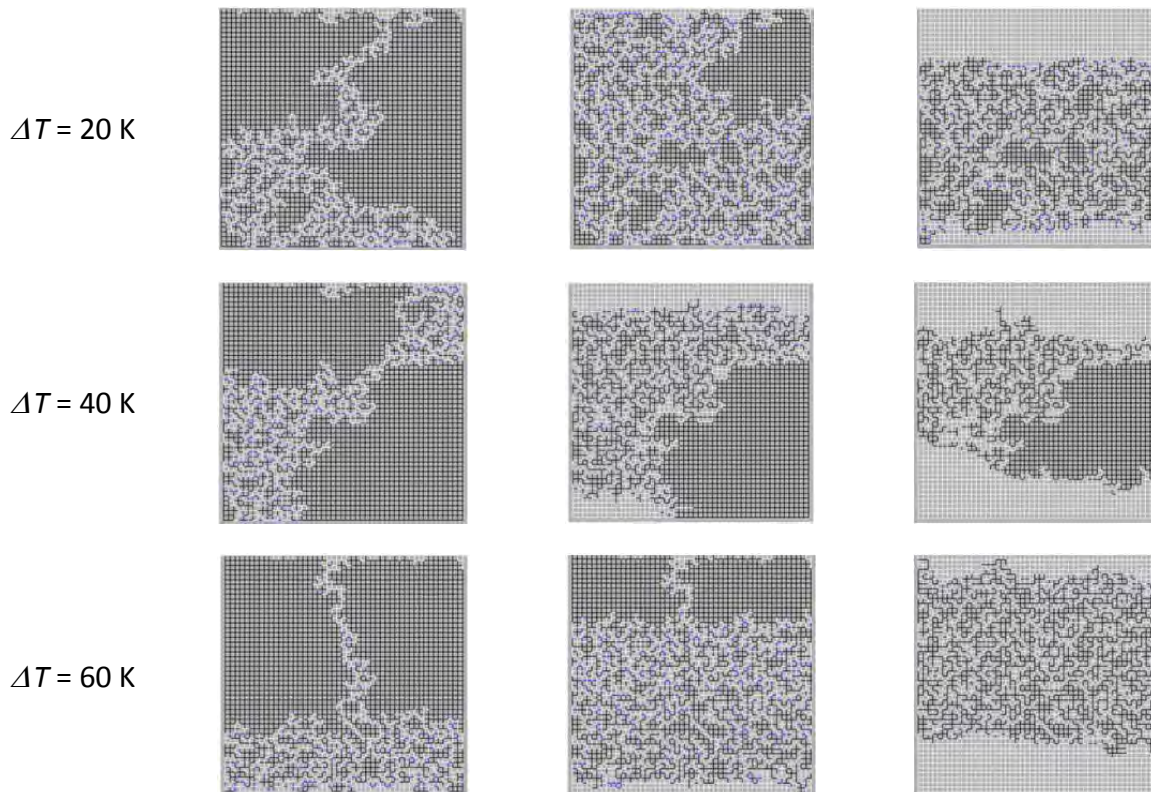
The dependence of the condensation effect on the interrelation of the height of the thermal gradient and the overall evaporation rate is illustrated in Figs. B-20 to B-27 for a given pore size distribution (adopted from the microfluidic PN). If not other mentioned simulation is with PNM level 4, CLO3 and the setting given in Table 6.1 (with adjusted temperature and BL) (Table C-27). The simulation results are shown for varying ratios of the overall drying rate from the fully saturated PN surface and the vapor diffusion rate along a thermal gradient over distance  $L(m-1)$ . This is denoted by  $\dot{M}_v(\Delta T)/\dot{M}_{evap}^0(\beta_{BL})$ , with

$$\dot{M}_{evap}^0 = A\beta_{BL} \frac{P\tilde{M}_v}{\tilde{R}\bar{T}} \ln\left(\frac{P}{P - P_v^*(T_{top})}\right), \quad (B-1)$$

( $\beta_{BL} = D/s_{BL}$ ,  $A = (n-1)L_dL$  with number of PN surface throats  $n = 50$ ) and

$$\dot{M}_v(\Delta T) = A\beta_{PN} \frac{P\tilde{M}_v}{\tilde{R}\bar{T}} \ln\left(\frac{P - P_v^*(T_{top})}{P - P_v^*(T_{bottom})}\right), \quad (B-2)$$

( $\beta_{PN} = D/(L(m-1))$ ,  $A = n\pi\bar{r}^2$  with number of PN columns  $n = 50$  and number of PN rows  $m = 50$ ). In this,  $\beta_{BL}$  and  $\beta_{PN}$  denote the vapor diffusion coefficients over distance  $s_{BL}$  and  $L(m-1)$ , thus spanning the discretized BL and the PN. Notice that the top temperature  $T_{top}$  is kept constant here ( $T_{top} = T_{BL} = 20^\circ\text{C}$ ) and  $\bar{T}$  is the average temperature over the diffusion distance.

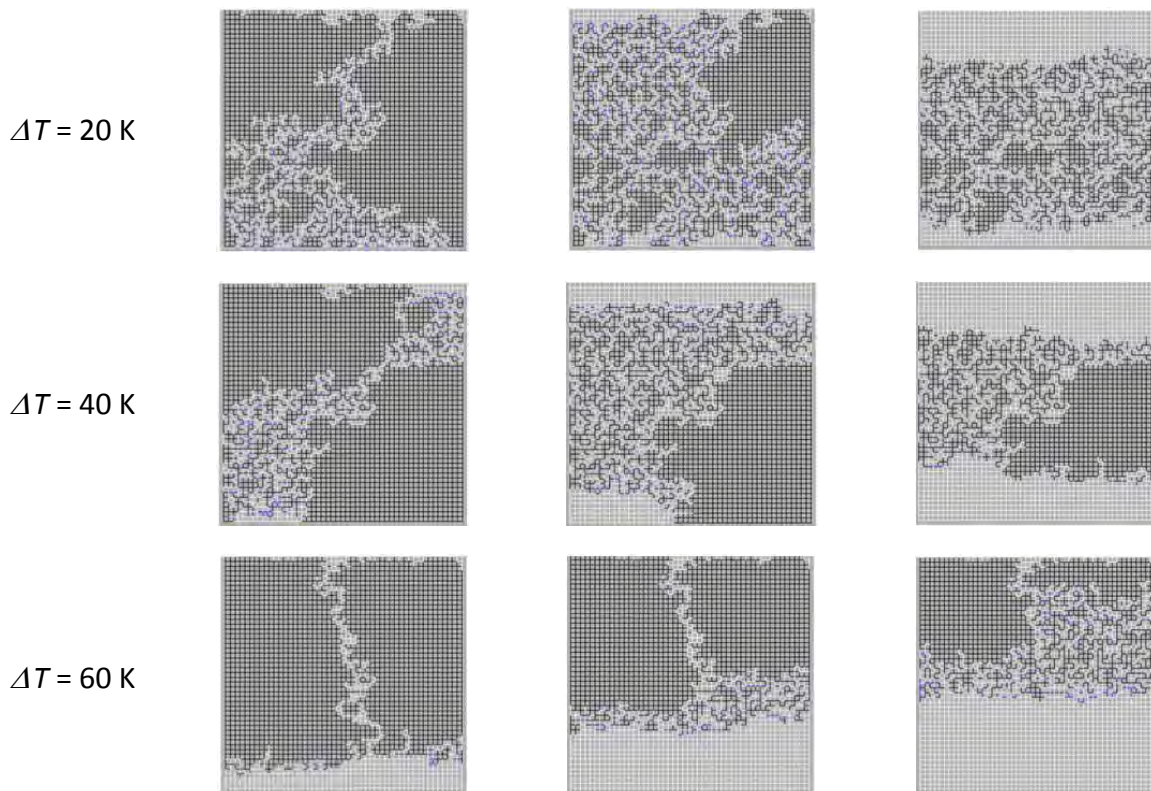


**Figure B-20** Phase patterns obtained from drying with  $s_{BL} = 200 \mu\text{m}$  and different imposed thermal gradients with else identical parameter setting.  $S = [0.8, 0.6, 0.4]$ .

Figures B-19 and B-20 compare the phase patterns obtained for different ratios of  $\dot{M}_v(\Delta T)/\dot{M}_{evap}^0(\beta_{BL})$ . These figures indicate that significantly different phase patterns must be expected for different temperature gradients due to the impact of vapor transfer through the 2-phase zone. In drying with the smallest temperature gradient ( $\Delta T = 20$  K) the liquid phase is completely ramified at high saturation independently of the overall evaporation rate (which is controlled by  $\beta_{BL}(s_{BL})$ ). Detachment from the PN bottom occurs later than in simulations with higher temperature gradient, while position of the drying front is much more advanced at low saturations. Interestingly, the liquid phase appears more dense in drying with the highest temperature gradient ( $\Delta T = 60$  K). Here, after breakthrough of a gas branch to the bottom of the PN, the hot pores and throats close to the bottom are preferentially invaded.

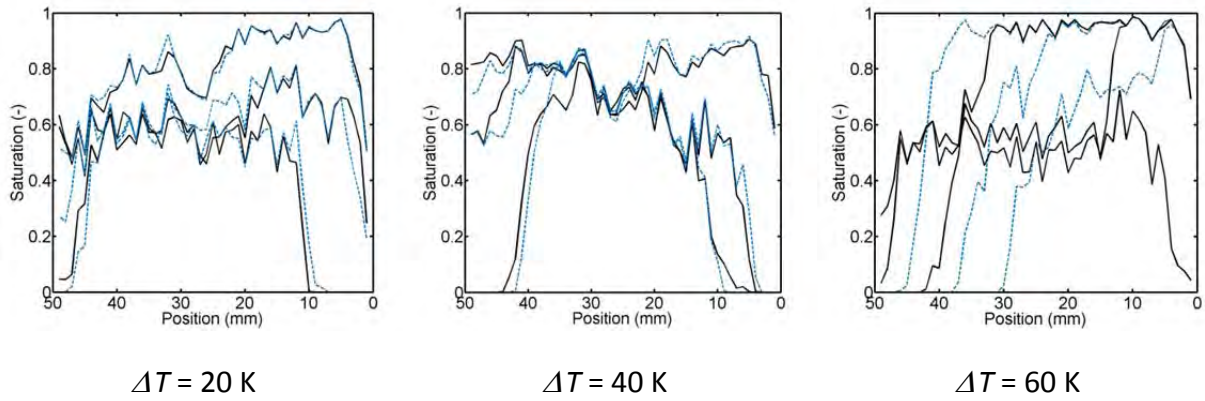
Significant differences can be seen in the patterns corresponding to  $s_{BL} = 200 \mu\text{m}$  and  $s_{BL} = 4000 \mu\text{m}$  and  $\Delta T = 60$  K. In drying with higher overall evaporation rate ( $s_{BL} = 200 \mu\text{m}$ ), ramification of the liquid phase occurs with increasing distance between the PN bottom and the lower boundary of the 2-phase zone resulting in a complete destabilization of the liquid phase. In contrast to that, the initiated second front appears more stabilized when drying with lower evaporation rate ( $s_{BL} = 4000 \mu\text{m}$ ). The liquid phase is less ramified in this situation and the LAP of the travelling 2-phase zone remains connected to PN surface for a significantly longer period.

This is reflected by the saturation profiles in Fig. B-22 which show that the extent of the travelling 2-phase zone is almost not affected by the BL thickness, if the temperature gradient is lower than  $\Delta T = 60$  K.

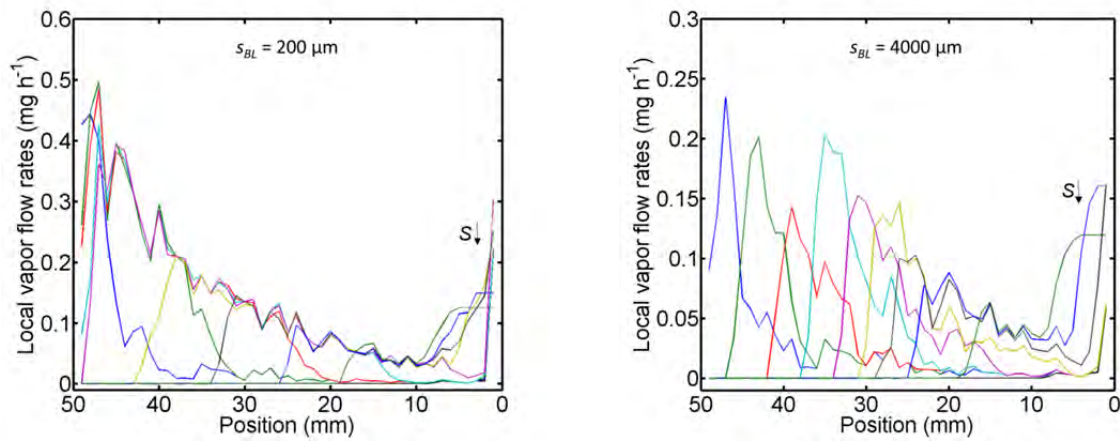


**Figure B-21** Same as Fig. B-20 but with  $s_{BL} = 4000 \mu\text{m}$ .  $S = [0.8, 0.6, 0.4]$ .

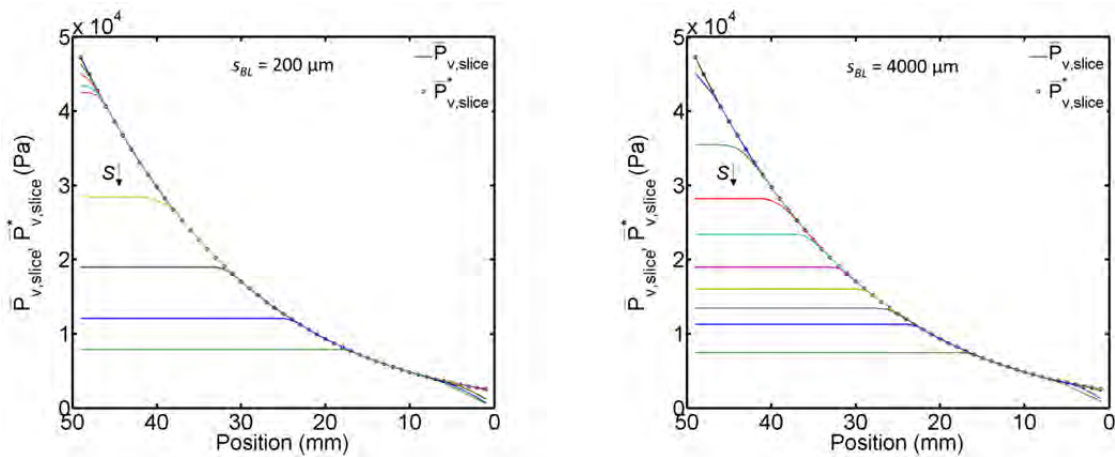




**Figure B-22** Saturation profiles from drying with different temperature gradients. Shown are the profiles for  $s_{BL} = 200 \mu\text{m}$  (solid black lines) and  $s_{BL} = 4000 \mu\text{m}$  (dashed blue lines) and  $S = [0.8, 0.5, 0.2]$ .



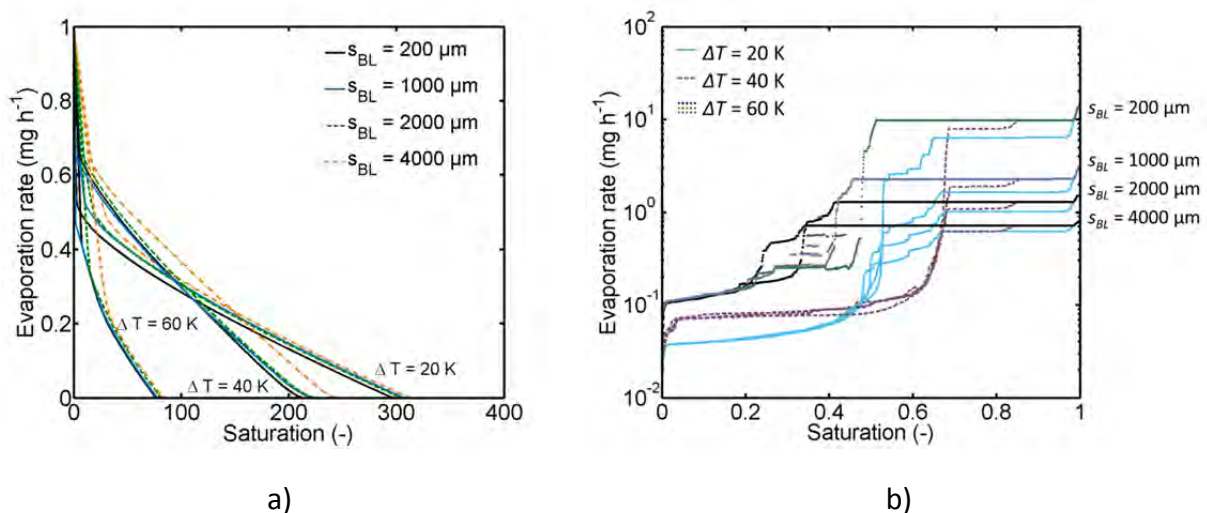
a)



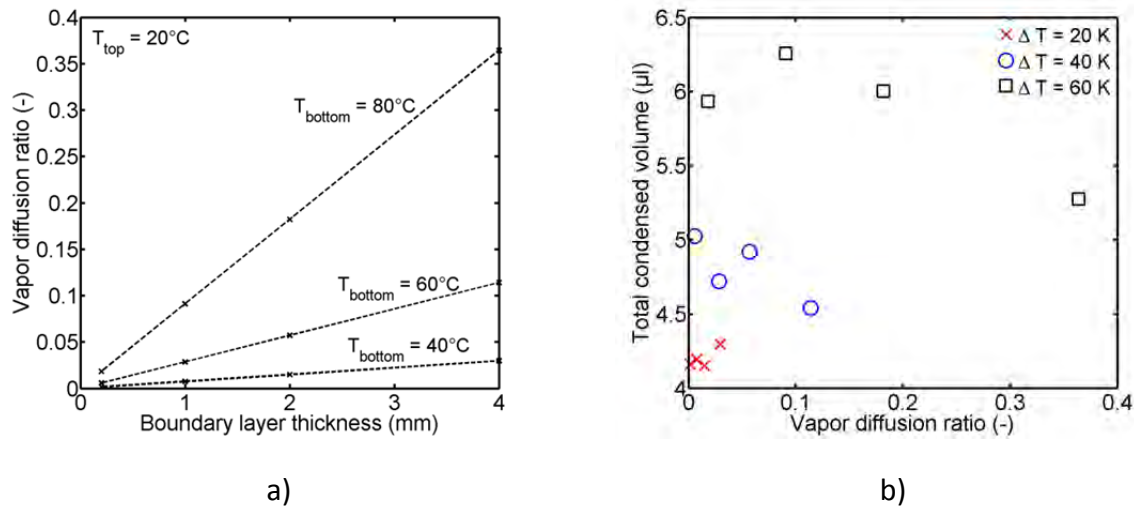
b)

**Figure B-23** a) Comparison of the total vapor flow rates through network slices for simulation with  $\Delta T = 60 \text{ K}$ . b) Slice average vapor pressure gradients. Shown are the profiles for  $S = [0.985, 0.9, 0.8, 0.7, 0.6, 0.5, 0.4, 0.3, 0.2, 0.1]$ .

The LAP of the 2-phase zone is almost independent of  $s_{BL}$  for lower temperature gradients. In case of  $\Delta T = 60$  K, the LAP is significantly affected by  $s_{BL}$ . Also, the saturation profiles corresponding to  $\Delta T = 60$  K in Fig. B-22 reveal that the temporal saturation of the 2-phase zone is overall higher if drying is slow (i.e. in case of  $s_{BL} = 4000 \mu\text{m}$ ). The 2-phase zone appears more dense because its width is smaller (the lower limit is generally found at comparably lower position  $z$  after detachment from the bottom). In addition to that, it is observed that the LAP of the 2-phase zone is generally closer to the network surface in case of a higher temperature gradient. A similar drying behavior (denser liquid phase at the PN surface) was also experimentally observed and is shown in Fig. 4-36. This observation might be explained with the slice average vapor pressure field and the slice average vapor flow rates in Fig. B-23. Obviously, overall higher vapor flow rates are obtained in the simulation with  $s_{BL} = 200 \mu\text{m}$ . However, the gradient of the vapor flow rates, decreasing with decreasing  $z$ , is apparently higher in the simulation with  $s_{BL} = 4000 \mu\text{m}$ . Additionally, the initial overall evaporation rate is about factor 12-18 higher than the vapor flow rates in the simulation with  $s_{BL} = 200 \mu\text{m}$ , while in the simulation with  $s_{BL} = 4000 \mu\text{m}$  the initial overall evaporation rate is roughly in the range of the vapor diffusion rates at the bottom of the PN (Figs. B-23 and B-24b). Thus, it might be concluded that the rate of emptying of pores and throats induced by the evaporation rate is of the same order as the rate of re-invasion by condensation in the latter case. Following this idea, convergence of evaporation rate (at the top of the 2-phase zone) and condensation rate (at the bottom of the 2-phase zone) in the simulation with  $s_{BL} = 4000 \mu\text{m}$  can lead to a stabilization of the liquid phase while the structure of the drying front in the simulation with  $s_{BL} = 200 \mu\text{m}$  is additionally controlled by the thermally affected capillary invasion (at the start of drying when the main liquid cluster is initially invaded). More clearly, in the simulation with  $s_{BL} = 200 \mu\text{m}$  invasion of the small clusters emerging at the bottom of the PN is significantly slower than invasion of the main cluster connected to the PN surface. The different time constants of the invasion processes lead to the survival of the smaller clusters while the structure of the main cluster is controlled by the thermally affected capillarity. Additionally to that, the emerging small



**Figure B-24** a) Drying curves and b) drying rate curves for drying with different thermal gradients ( $\Delta T = [20, 40, 60]$  K) and BL thicknesses ( $s_{BL} = [200, 1000, 2000, 4000]$   $\mu\text{m}$ ). Notice that the drying rate curves for  $s_{BL} = 100 \mu\text{m}$  and  $s_{BL} = 500 \mu\text{m}$  show a fluctuation, which can be explained with a fluctuation of the drying front position due to simultaneous condensation and evaporation.



**Figure B-25** Impact of BL thickness and height of the thermal gradient on moisture migration. a) Ratio  $\dot{M}_v(\Delta T)/\dot{M}_{\text{evap}}^0(\beta_{BL})$  corresponding to the computations discussed above, b) dependence of the total amount of condensed liquid volume on  $\dot{M}_v(\Delta T)/\dot{M}_{\text{evap}}^0(\beta_{BL})$ .

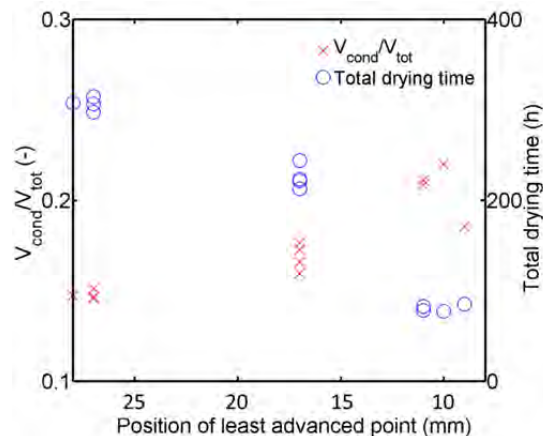
clusters and single throats have a smaller potential to equilibrate condensation rates which leads more often to growth of these clusters (and comparably higher  $v_c^+$  as discussed below). Interestingly, the drying time is almost not affected by the condensation effect (Fig. B-24a).

Figure B-25 shows that in total more liquid is condensed if the temperature gradient is higher (which is in agreement with the results of drying of the initially partially saturated PN presented above). However, in case of  $\Delta T = [40, 60]\text{ K}$  less vapor is condensed if the BL is thicker and thus drying is overall slower. As already explained above, in the simulation with  $s_{BL} = 4000\ \mu\text{m}$  evaporation of the small clusters at the second drying front is faster or similar as evaporation of the main cluster at the top of the PN (Fig. B-21). The evolving vapor is then condensed at the lower boundary of the main cluster (which is also connected to the top of the PN) with a condensation rate which is almost equal to the evaporation at the top of the PN. This leads to a reduction of the overall evaporation rate according to Eq. 5-56, but not necessarily to the refilling of the void space. In contrast, the condensation rates are not compensated by the small clusters evolving at the second drying front wherefore the condensation rate is higher if BL is smaller. More clearly, if the BL thickness is related to the air velocity of the drying air (Eq. 2-18), the air flow rate could be reduced without loss of drying time (Fig. B-24a and Fig. B-26); the drying time is almost identical independently of  $\dot{M}_{\text{evap}}^0(\beta_{BL})$  if  $\Delta T = 60\text{ K}$  although duration of the constant drying period increases with increasing BL thickness (Fig. B-24b); the drying rates obtained for greater BL thickness can temporally become greater than the drying rates simulated with lower BL thickness because of the favorable drying front position. At the same time, condensation of liquid with refilling of the void space is reduced with increasing  $s_{BL}$ . These two effects can compensate drying time in the face of the different levels of the initial constant drying rates for varying  $s_{BL}$  (Fig. B-24 and Fig. B-26). This is partly also found for  $\Delta T = 20\text{ K}$ , but here duration of the

constant rate period is almost unaffected and also very similar amount of liquid is condensed. However, for  $\Delta T = 40$  K the effect is less pronounced (Fig. B-24a).

It could also be argued that the mean temperature is overall increased in a PN with greater  $\Delta T$  and thus vapor flow rates are generally higher. However since the drying front position is less (or not) advanced for higher  $\Delta T$ , this effect is expected to vanish (because essentially then drying rate is controlled by vapor diffusion through the BL). In summary, simulation with  $\Delta T = 20$  K results in an overall drying time of around 300 h,  $\Delta T = 40$  K yields a drying time of 200-250 h and  $\Delta T = 60$  K a drying time of around 80 h (Fig. B-24a).

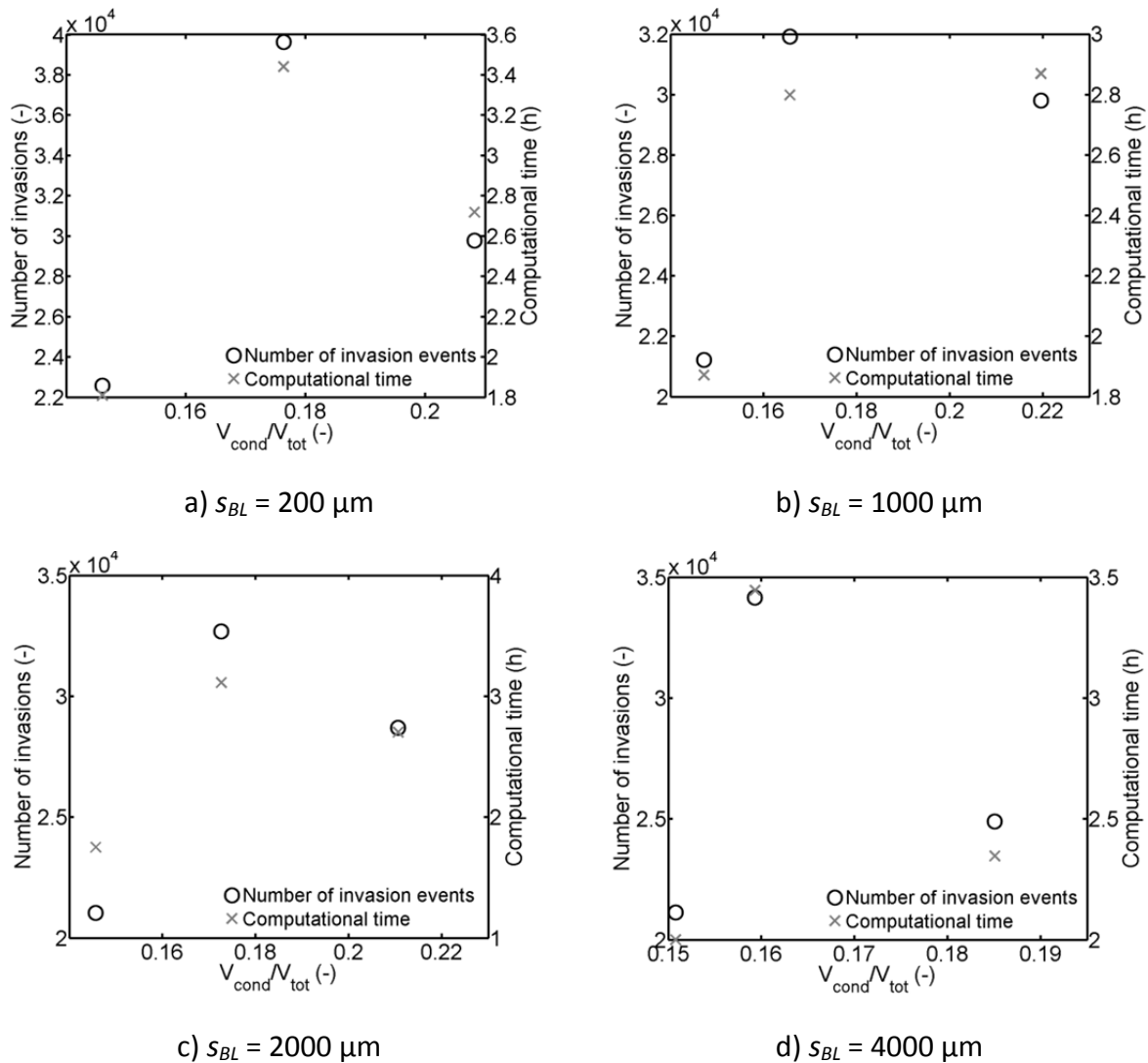
Figure B-27 summarizes the impact of the condensation effect by means of the ratio of the condensed liquid volume on both, the number of invasion events and the overall computational time. The highest number of invasion events and accordingly the highest computational effort is found for  $s_{BL} = 200$   $\mu\text{m}$  (and  $\Delta T = 40$  K). This is surprising in the face of the ratio of the condensed liquid volume which is in the same range as in the other simulations with higher BL thickness. Obviously, following discussions above, more oscillation of emptying/refilling cycles must be anticipated in case of the central value. This is usually expected if throats and pores at the cluster boundaries are only marginally saturated during the refilling cycle (refer to Section 5.4.3). In the same sense, higher saturation of throats and pores can reduce the computational time, even if the condensation effect is higher. This is especially indicated by Fig. B-27d where the computational time is significantly lower for a higher ratio of condensed liquid volume ( $V_{cond}/V_{tot} > 0.18$ ).



**Figure B-26** Drying time and the ratio of condensed liquid volume related to the position of the maximum LAP of the 2-phase zone during drying. The point clouds refer to the different temperatures studied here. From left to right:  $\Delta T = 20$  K,  $\Delta T = 40$  K,  $\Delta T = 60$  K.

### Summary

In this section the condensation effect was studied by simulations with i) an initially partially saturated PN and ii) an initially fully saturated PN drying under different thermal and external mass transfer conditions. Moreover, it was demonstrated how the computation with different cluster labeling options (CLOs) influences the simulation result (pore scale liquid distribution and macroscopic drying rate and drying time) as well as the computational effort.



**Figure B-27** Dependence of the computational time on the number of invasion events and the total amount of condensed liquid volume.

Simulation with the partially saturated PN clearly revealed that the feasibility of vapor transfer through the partially saturated region in presence of a positive thermal gradient can control the pore scale liquid distribution in such a case (which is exemplarily expected in the period of drying when the liquid phase is split up and liquid interconnectivity is interrupted). It was shown that for higher temperature gradients imposed on the PN (with fixed pore size distribution and overall evaporation rate) a higher ratio of condensed liquid volume can be anticipated. In addition to that it was also observed that the ratio of condensed liquid volume can be reduced if the initial level of the overall evaporation rate of the PN is reduced in simulations with temperature gradients  $\Delta T > 20$  K. Only small impact was seen in case of  $\Delta T = 20$  K; almost identical total amount of condensed liquid was found independently of the BL thickness. But in case of  $\Delta T = 60$  K, increase of the BL thickness and thus reduction of the initial level of the constant drying rate led to a decrease in the total amount of condensed liquid. This observation was explained with the partial compensation of condensation rates by the overall evaporation rate found in situations of long term connectivity of the main liquid cluster to the PN surface. From this was concluded that

efficiency of the drying process might be positively affected by optimization of the temperature gradient and convective air flow rate for a given porous structure.

Furthermore, stagnation or rather decrease of the number of invasion events -while the total amount of condensed liquid volume increased- was linked to the distinct pore and throat saturation achieved in a given temperature setting. It was argued that higher transient pore and throat saturations are obtained for greater  $\Delta T$ . This allows for a more compact appearance of the liquid phase in case of higher thermal gradients. It is suggested to investigate in future work whether this phenomenon depends mainly on the characteristics of the PNM (mainly the tolerance of partially saturated pores and throats) or if this could also be validated in drying experiments with the microfluidic PN. Following up on this, incorporation of liquid film effects by adaption of the CLO revealed higher interconnectivity of the liquid phase (CLO2). With this, the number of invasion events could be reduced. This also showed that the effect of liquid films can partly be implemented in the non-isothermal PNM without increasing the complexity and computational effort of this model. In addition to that, it was shown that CLO3 can reduce the computational effort without affecting the overall drying behavior. However, less impact is expected if the limitation of liquid pumping due to viscous forces would be taken into account. The impact of cluster labeling should almost vanish in this situation and cluster dynamics are expected to be more stabilized, i.e. with less fluctuation in cluster evaporation/condensation.

## **B.4 Details of the continuous film pore network model with remarks on the implementation**

The PNM with continuous liquid films proposed by Prat (2007) incorporates the film effect by empirical functions based on the theory of Ransohoff and Radke (1988). In this, liquid films are expected to form a continuous region spanning the 2-phase zone as well as part of the dry zone upstream of the drying front (see e.g. Fig. 6-17). As a result, drying rates can be sustained at a high (and over long period constant) level due to the relocation of the evaporation front closer to the surface of the PN. In the following, at first the general model assumptions are summarized. Then the parameters of the film PNM, as implemented for the drying simulation presented in Section 6.2.5.2, are given. Afterwards, the structure of the model and the drying algorithm are briefly discussed.

### *Model assumptions*

1. Capillarity of single liquid pores is ignored; the liquid volume in pores is assigned to the largest throat neighbors.
2. Throats obey the PSD of the microfluidic PN.
3. Throats and pores have rectangular cross section with  $r_m$  from Eq. 2-24.
4. The edge effect is implemented in the film PNM from Eq. 5-17 with  $f^{red} = 0.85$ ,  $z^{pin} = 5L$ .
5. Invasion of the bulk liquid phase is capillarity controlled and viscous forces are only considered for the film flow.
6. Films are always connected to the throat entrance (i.e. films do not recede inside the throats) and the evaporation rate is computed independently of the liquid curvature.

7. Throats that are either wetted by the bulk liquid phase or liquid films are assigned with saturation vapor pressure.
8. Empty throats are assigned with constant radius  $\bar{r}_t$ .
9. Vapor diffusion in dry throats and in the BL is computed from Eq. 2-10.
10. The BL is not discretized.
11. The current network saturation is computed from the sum of liquid in pores and throats. Liquid volume contained in films is neglected.

Concerning assumption 6 it must be remarked that naturally  $dr_{film}/dz = f(Ca)$  (Fig. 2-20). The radius of curvature is thus a function of position  $z$  of the film inside the throat. Since the evaporation rate naturally depends on the evaporation interface, a gradual decrease would be associated with receding of the film tip as the curvature decreases with  $z$ . However, in this model it is assumed that  $r_{film} = const.$  and  $\dot{M}_{evap,t} = const.$  as the film recedes inside a throat.

### Parameter definition

The physical parameters are summarized in Table B-2. The geometrical parameters are as in the other simulations studied in this thesis, except of the thickness of the non-discretized BL, which is  $s_{BL} = 225 \mu\text{m}$ . Further specific parameters of the film model are summarized in Table B-3. In this, notation is following the reference publication (Prat 2007).

It is remarked that due to the assumption of constant temperature inside the PN and the non-discretized diffusive BL ( $T = 63^\circ\text{C}$ ) higher vapor diffusion rates can be computed in the BL based on Eqs. 2-10 and 2-51. (Compared to the PNMs with  $T_{BL} = T_{air}^{exp}$  which was usually  $T = 24\text{-}26^\circ\text{C}$ ). The temperature increase has an impact on the BL thickness. If a constant drying rate is anticipated, increase of the temperature must result in an increase of the BL thickness, as already discussed before. However, comparing the different simulation results and drying experiments,  $s_{BL}$  is much smaller in the PNM with continuous liquid films. This is related to the different cross sections of BL throats in the film model and the PNM ignoring continuous liquid films. The cross section is significantly larger in the PNM ignoring the film, namely  $A_{BL} = L_d L_{BL}$  (Fig. 5-6), while  $A_{BL} = A_f^* \bar{r}_t^2$  in the film PNM. This can explain the decrease of the BL thickness in the film PNM.

The dimensionless resistance factor  $B$  in Table B-3 accounts for the reduced liquid conductivity of the wetting film attached to the solid (Mogensen and Stenby 1998, Bustos and Toledo 2003, Yiotis et al. 2005). In this formulation a no-slip boundary condition for the solid/wetting interface and a no-stress boundary condition at the liquid/air interface is anticipated. The dimensionless factor  $A_f^*$  is based on a geometrical analysis of the wetting films forming in a throat of non-cylindrical cross section. It is a function of the cross sectional area of dry throats;  $A_f^* = 4$  in a square capillary,  $A_f^* = 2$  in a triangular cross section and  $A_f^* = 2L_d/\bar{r}_t$  in a rectangular cross section. The latter is derived from

$$A_f^* = 2\bar{r}_t L_d / \bar{R}^2 \cong 2\bar{r}_t L_d / \bar{r}_t^2. \quad (\text{B-3})$$

**Table B-2** Physical parameters.

Parameter	Symbol	Value
Temperature in PN and BL	$T$	63°C
Total pressure	$P$	$1 \cdot 10^5$ Pa
Vapor pressure in the bulk air phase	$p^\infty$	0
Equilibrium vapor pressure (Eq. 2-5)	$P_v^*$	$2.3 \cdot 10^4$ Pa
Equilibrium mass fraction of vapor	$c_{eq}$	0.1552
Mass fraction of vapor in bulk air	$c^\infty$	0
Diffusion coefficient (Eq. 2-51) with the constants of Schirmer (1938)	$D$	$3.291 \cdot 10^{-5}$ m <sup>2</sup> s <sup>-1</sup>
Surface tension (Eq. 2-53)	$\sigma$	0.0656 N m <sup>-1</sup>
Dynamic liquid viscosity (Eq. 2-54)	$\eta$	$466.59 \cdot 10^{-6}$ Pa s <sup>-1</sup>
Mass transfer coefficient in BL	$\beta = D/L \cdot \tilde{M}_v / \tilde{R}T$	$9.43 \cdot 10^{-7}$ s m <sup>-1</sup>

**Table B-3** Specific parameters of the film model (symbols according to Prat (2007)).

Parameter	Symbol and equation	Value(s)
Radius of the largest inscribed sphere at start of film tip receding	$R^0 \cong \bar{r}_t = \bar{w}_t/2$	81.8 μm
Corner radius	$r_0$	0
Dimensionless radius of the corner	$r_f = \frac{r_0}{r_m}$	0
Dimensionless curvature	$R^{0*} \cong \frac{\bar{r}_t}{R^0}$	1
Number of throat corners	$N$	4
Half angle of the corner ( $N = 4$ )	$\alpha$	$\pi/4$
Parameter adjusting vapor diffusion	$k$	0.9
Contact angle	$\theta$	0.7465, 0.7495, 0.76, 0.7653 (rad)



Table B-3 Continued.

Parameter	Symbol and equation	Value(s)
Critical contact angle	$\theta^* = \frac{\pi}{N}$	0.7854 rad
Cross sectional area of dry throats ( $N = 4$ , rectangular)	$A_f^* = 2 \frac{L_d}{\bar{r}_t}$	1.0591
Dimensionless curvature (at maximum film thickness)	$\chi = \cos\theta + \sqrt{\theta^* - \theta + \frac{\sin\theta \cdot \cos\theta}{\tan\theta^*}}$	-
Numerical factor	$B = (\pi/2 - \alpha) \tan\alpha$	0.7854 rad
Numerical factor	$\psi_1 = (1 + \cos(2(\alpha + \theta))) / (2 + \cos(\alpha + \theta) \sin(\alpha + \theta) \tan(\alpha))$	-
Numerical factor	$\psi_2 = 1 - \frac{\theta}{\pi/2 - \alpha}$	-
Numerical factor	$\psi_3 = \frac{\cos(\alpha + \theta)}{\cos\alpha}$	-
Numerical factor	$\psi_4 = \frac{\cos\theta}{\sin\alpha} \cos(\alpha + \theta) - \pi/2 + \alpha + \theta$	-
Dimensionless resistance factor	$B = \frac{6(1 - \cos(2\alpha))(1 - B)^2 (\psi_1 - B\psi_2)(\psi_3 - (1 - B)r_f)^2}{(1 - \sin\alpha)^2 B^2 (\psi_1 - B\psi_2 - (1 - B)r_f^2)^3}$	-
Dimensionless parameter	$\kappa = \frac{\psi_4}{B}$	-
Capillary number	$Ca = 3 \frac{\eta D c_{eq}}{\sigma \bar{r}_t} \frac{\rho_v}{\rho_l}$	$9.1 \cdot 10^{-7}$
Dimensionless factor	$f = \frac{A_f^*}{N\kappa}$	-

In this,  $\bar{R}$  denotes the mean curvature of the gas liquid interface in the cross section of the non-cylindrical throat. It is assumed that roughly  $\bar{R} = \bar{r}_t$  with  $\bar{r}_t = \bar{w}_t/2$ . In principle,  $R$  is variable with  $z$  and it is thus unknown in the film region. At the film base it is  $R = R^0/\chi$ , with

radius of the largest inscribed sphere  $R^0$ . With this, the radius of the film curvature is overestimated if  $L_d \ll \bar{r}_t$ . This might result in an underestimation of the film transport compared to a PNM that would implement a more exact value of  $\bar{R}$ .

### Model construction

#### Capillary invasion of the bulk menisci

The order of emptying is computed based on the Young-Laplace equation (Eq. 5-60), following the concept of quasi-steady invasion. The order of emptying is thus based on the disorder of throat width in the wet zone of the PN. The time required to remove enough liquid to fully invade a throat is linked to the overall evaporation rate at the cluster boundary (or at the interfacial area of single liquid menisci) (see Section 5.4.3.1 for further details). It is highlighted that the same order of invasion is computed with the film PNM as with the PNM ignoring liquid films. This is based on the separation of liquid transport in films and capillary invasion. More clearly, in the continuous film PNM liquid cannot be pumped from the bulk liquid menisci to the films. From this follows that intercluster liquid transfer is not possible. Basically, the cluster boundary conditions are constant in this model.

#### Vapor transport

As in the PNM ignoring film flow, mass balances are set up and solved for each computational node located in pore centers applying the conditions given in Section 5.3.2. Following the proposal of Prat (2007), linear vapor diffusion (Eq. 2-10) is assumed in this model. Additionally, constant half width of throats  $\bar{r}_t = \bar{w}_t/2$  is assumed in the dry zone of the PN. This results in overall higher vapor flow rates than presented in the PNM ignoring the film effect. But, for reasons of comparability the mean radius of throats in the dry zone is multiplied with factor  $k = 0.9$  in order to allow identical effective vapor diffusion through the dry zones in the PNM with continuous liquid films and the PNM ignoring continuous liquid films (Vorhauer et al. 2014).

#### Film transport inside the PN

Based on the proposal of Prat (2007) a dimensionless composite variable is introduced to describe vapor diffusion and film transport in the dry zone of the PN:

$$\phi = \frac{(R^{0*})^3}{\chi^3} + fCac^*, \quad (B-4)$$

with

$$c^* = \frac{c - c^\infty}{c_{eq} - c^\infty} \quad (B-5)$$

As can be seen, this variable depends on the geometrical parameters of the throat and the film confined in the throats as well as capillary number (Table B-3). The boundary conditions are specified as follows. It is

$$\phi = \phi^* = \frac{1}{\chi^3} + fCa = \text{const.} \quad (\text{B-6})$$

at the boundaries of liquid clusters with  $c = c_{eq}$  and  $R^{0*} \cong 1$ . Furthermore, it is

$$\phi = \phi^\infty = \frac{1}{\chi^3} \quad (\text{B-7})$$

in the bulk air phase, assuming  $c^\infty = 0$ .

Following the details in Section 5.3.1, a vector of boundary conditions (analog to Eq. 5-40) and a matrix of vapor conductances (analog to Eq. 5-39) can be defined using the dimensionless composite variable from Prat (2007). Consequently, basically

$$\mathbf{A}\phi = \mathbf{b}. \quad (\text{B-8})$$

Table B-4 summarizes the neighbor relations stored in matrix  $\mathbf{A}$  as well as the boundary conditions stored in vector  $\mathbf{b}$  in dependence of the saturation state of the pores. Distinction is between pores at saturation vapor pressure (or  $\phi = \phi^*$ ), which denote the liquid filled pores in the PN and the pores located at the gas-liquid interface as well as the film pores and empty pores at unknown vapor pressure. Furthermore, pores inside the PN are distinguished from the pores at the PN open surface. In Table B-4  $N_i$  denotes the sum of pore neighbors.

**Table B-4** Definition of matrix  $\mathbf{A}$  and vector  $\mathbf{b}$  of pores  $i$  and their pore neighbors. (Analog to Sections 5.2.4 and 5.3.1).

Liquid pore ( $S_i = 1$ ) or interface pore	Film in surface pore ( $S_i = 0$ )	Empty surface pore ( $S_i = 0$ )	Film in network pore ( $S_i = 0$ )	Empty network pore ( $S_i = 0$ )
$\mathbf{A}(i,i) = 1$	$\mathbf{A}(i,i) = 1$	$\mathbf{A}(i,i) = 1 + L/s_{BL}$	$\mathbf{A}(i,i) = N_i$	$\mathbf{A}(i,i) = N_i$
-	$\mathbf{A}(i, pnp(i)) = -1$	$\mathbf{A}(i, pnp(i)) = -1$	$\mathbf{A}(i, pnp(i)) = -1$	$\mathbf{A}(i, pnp(i)) = -1$
$\mathbf{b}(i) = \phi^*$	$\mathbf{b}(i) = -\frac{fCa}{s_{BL}/L}$	$\mathbf{b}(i) = 0$	$\mathbf{b}(i) = \phi^*$	$\mathbf{b}(i) = 0$

It is remarked that mass transfer through throats containing liquid films is computed as mass transfer through dry throats.

It is

$$\dot{M}_{v,ij} = \frac{A_f^* (\phi_i - \phi_j)}{fCa \ L/(k\bar{r}_t)} \quad (\text{B-9})$$

the vapor diffusion flow rate through throats  $ij$  with neighbor pores  $i$  and  $j$ . The evaporation rate at liquid menisci is computed analog to Eq. 5-52:

$$\dot{M}_{evap,ij} = \sum_{i=1}^2 \left( \frac{A_{ij}}{\sum_{ij} A_{ij}} \sum_{ij} \dot{M}_{v,ij} \right). \quad (B-10)$$

### Drying algorithm

Initially, liquid pressure of throats containing liquid menisci is computed from Eq. 5-60. Then, saturation vapor pressure is defined for liquid saturated pores and pores located at the gas-liquid interface, i.e.  $\phi = \phi^*$ . The  $\phi$ -field is then computed from Eq. B-8. Solving this equation is an iterative problem as boundary conditions depend on the state of individual empty pores. Precisely, it is a priori not defined if pores either contain liquid films, thus  $S = 0$  and  $\phi = \phi^*$ , or if they are totally dry, thus  $S = 0$  and  $\phi \neq \phi^*$ . Starting the iteration from the  $\phi$ -field of the previous invasion step, the solution is obtained already after one iteration. As a result, the location of pores containing liquid films can then be determined from  $\phi > fCa$ , whereas completely dry pores fulfil the condition  $\phi \leq fCa$ .

Evaporation rates from meniscus throats (also from those connected to liquid films) are computed from Eq. B-10. The dimension of the vapor flow rates is converted into  $\text{kg s}^{-1}$  by multiplication with

$$E^{ref} = \rho_g D (c_{eq} - c^\infty) k \bar{r}_t, \quad (B-11)$$

according to Prat (2007).

The overall evaporation rate to the bulk air phase is given by:

$$\dot{M}_{evap} = \beta A_f^* k \bar{r}_t^2 \sum (|P_{v,p} - P_v^\infty|), \quad (B-12)$$

with  $\beta$  from Table B-2. Satisfying the mass balance at the gas-liquid interface, any liquid cluster or single meniscus throat is invaded at the current overall cluster evaporation rate. Following Eq. 5-56 it is

$$\dot{M}_{evap,cl} = \sum \dot{M}_{evap,t}. \quad (B-13)$$

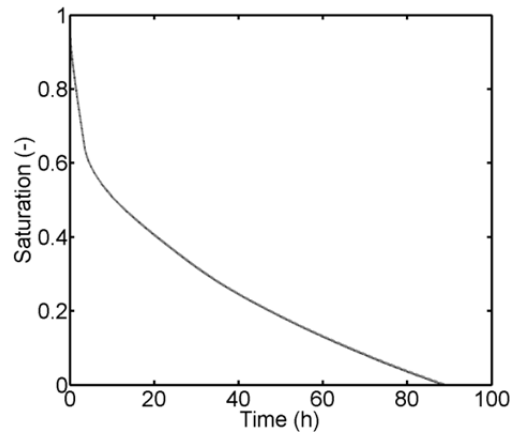
Since invasion is computed in the order of decreasing throat radii, in each cluster the largest throat containing a meniscus is invaded by the gas phase. The time required to remove enough liquid from the cluster to fully invade the throat is computed from:

$$\Delta t = \frac{S_t V_t \rho_l}{\dot{M}_{evap,cl}}. \quad (B-14)$$

After invasion of the throat parameters are updated following the concepts of Chapter 5 and the basics of the algorithm given in Section 5.5 (except that liquid rings are not considered here).

### Simulation results

This model is verified by comparison of the simulation results to the benchmark PNM from Metzger et al. (2007c) ignoring liquid films in the limit of  $\theta = \theta^* = 45^\circ$ , i.e. in the limit of no film occurrence. In this limit, the BL thickness and the half width of the gas throats  $k\bar{r}_t$  can be fitted so as to allow identical initial evaporation rates. It is found that for  $k = 0.9$  drying curves of both models overlap for  $\theta = \theta^*$  (Fig. B-28).



**Figure B-28** Comparison of PN simulations obtained from the benchmark PNM (Metzger et al. 2007c) and the continuous film PNM (Prat 2007) in the limit of  $\theta = \theta^*$ . The curves are overlapping for  $k = 0.9$  as well as  $s_{BL} = 150 \mu\text{m}$  in the film PNM and  $s_{BL} = 1600 \mu\text{m}$  in the benchmark PNM (Vorhauer et al. 2014).

## Appendix C

### Summary of simulations

In this section, the parameters of the simulations presented in this thesis are summarized. If not other mentioned, the following parameters were kept constant:  $n = 50$  (number of pore columns),  $m = 50$  (number of pore rows),  $P = 1$  bar (atmospheric pressure),  $P_v^\infty = 0$  (partial vapor pressure in the bulk air phase),  $L = 1000 \mu\text{m}$  (lattice spacing),  $L_d = 39 \mu\text{m}$  (PN depth),  $N_{BL} = 1$  (number of layers of the discretized BL),  $S_0 = 1$  (initial saturation of the PN),  $\cos\theta = 1$ . Additionally,  $\sigma(T)$  was computed from Eq. 2-53,  $D(T)$  from Eq. 2-51 with the constants from Schirmer (1938),  $P_v^*(T)$  from Eq. 2-5 and  $\rho_l(T)$  from Eq. 2-55. If not other mentioned the PSD and the temperature fields from the experiments were applied.

#### *Simulations in Section 6*

**Table C-1** Simulation in Figs. 6-1b and 6-2.

---

Benchmark PNM from Metzger et al. (2007c)

---

Number of simulations	1
$T_{BL}$	24.3°C
$T_{PN}$	63°C = <i>const.</i>
$S_{BL}$	2L

---

Note that pores are invaded together with the largest throat neighbor.

**Table C-2** Simulations in Fig. 6-3.

Vapor diffusion through diffusive BL	
Number of simulations	2 (one with variation of $N_{BL}$ and one with variation of $L_{BL}$ )
$n$	50
$m$	1
$T_{BL}$	25°C
$T_{PN}$	63°C
$N_{BL}$	[1:1:100]
$L_{BL}$	[1:1:100] · 0.05 $L$

**Table C-3** Simulations in Fig. 6-4.

PNM level 1 (separate pore invasion) and temperature field from experiment	
Number of simulations	3
$T_{BL}$	24.3°C
$T^{min}$	62.58°C
$T^{max}$	64.09°C
$\bar{T}$	63.5°C
$N_{BL}$	1
$S_{BL}$	300 $\mu\text{m}$ , 1600 $\mu\text{m}$ , 3000 $\mu\text{m}$

The temperature field corresponding to experiment 17 is applied here (Fig. 3-8a).

**Table C-4** Simulation in Figs. 6-5 and 6-6 (dotted lines).

PNM from Metzger et al. (2007a) (dynamic invasion of the PN)	
Number of simulations	1
$T_{BL}$	24.3°C
$T_{PN}$	63°C = <i>const.</i>
$S_{BL}$	1600 $\mu\text{m}$
$\eta$	466.59 · 10 <sup>-6</sup> Pa s

Note that pores are invaded together with the largest throat neighbor.

**Table C-5** Simulations in Figs. 6-7 and 6-8.

PNM with temperature field from experiment (comparison of Metzger et al. 2007a with benchmark PNM)	
Number of simulations	2
$T_{BL}$	24.3°C
$T^{min}$	62.58°C
$T^{max}$	64.09°C
$\bar{T}$	63.5°C
$S_{BL}$	1600 $\mu\text{m}$
$\eta$	466.59 · 10 <sup>-6</sup> Pa s (in the PNM with dynamic invasion)

Note that pores are invaded together with the largest throat neighbor.

**Table C-6** Simulation in Figs. 6-9 and 6-10 (dotted lines).

PNM level 1 (separate invasion of liquid pores)	
Number of simulations	1
$T_{BL}$	24.3°C
$T_{PN}$	63°C = <i>const.</i>
$S_{BL}$	1600 $\mu\text{m}$

**Table C-7** Simulations in Figs. 6-11 and 6-12.

PNM level 1 with $\sigma(T)$ , PNM level 2, level 3, level 4 with CLO3	
Number of simulations	4
$T_{BL}$	24.3°C
$T^{min}$	62.58°C
$T^{max}$	64.09°C
$\bar{T}$	63.5°C
$S_{BL}$	1600 $\mu\text{m}$

Note that the pores are separately invaded in these models. The temperature field corresponding to experiment 17 is applied here (Fig. 3-8a).

**Table C-8** Simulation in Fig. 6-14 (dotted line) and Fig. 6-15.

Benchmark PNM from Metzger et al. (2007c) adapted by edge effect	
Number of simulations	1
$T_{BL}$	24.3°C
$T_{PN}$	63°C = <i>const.</i>
$S_{BL}$	1600 $\mu\text{m}$
$f^{red}$	0.85
$z^{pin}$	(5-49)L

Note that pores are invaded together with the largest throat neighbor.

**Table C-9** Simulation in Figs. 6-16 and 6-17.

Continuous film PNM	
Number of simulations	1
$T_{BL}$	24.3°C
$T_{PN}$	63°C = <i>const.</i>
$S_{BL}$	225 $\mu\text{m}$
$\theta$	42.77°
$r_0$	0
$N$	4
$k$	0.9

Note that pores are invaded together with the largest throat neighbor.



**Table C-10** Simulation in Figs. 6-18 and 6-19 (solid red line).

Continuous film PNM adapted by edge effect	
Number of simulations	1
$T_{BL}$	24.3°C
$T_{PN}$	63°C = <i>const.</i>
$S_{BL}$	225 $\mu\text{m}$
$\theta$	43.85°
$r_0$	0
$N$	4
$k$	0.9
$f^{red}$	0.85
$z^{pin}$	(5-49) $L$

Note that pores are invaded together with the largest throat neighbor.

**Table C-11** Simulations in Fig. 6-20.

Continuous film PNM adapted by edge effect	
Number of simulations	4
$T_{BL}$	24.3°C
$T_{PN}$	63°C = <i>const.</i>
$S_{BL}$	225 $\mu\text{m}$
$\theta$	[42.77, 42.97, 43.55, 43.85]°
$r_0$	0
$N$	4
$k$	0.9
$f^{red}$	0.85
$z^{pin}$	(5-49) $L$

Note that pores are invaded together with the largest throat neighbor.

**Table C-12** Simulations in Fig. 6-21.

Capillary ring PNM	
Number of simulations	9
$T_{BL}$	24.3°C
$T_{PN}$	63°C = <i>const.</i>
$S_{BL}$	3 $L$
$w_r$	[10, 21.4, 31.5] $\mu\text{m}$
$\alpha$	[0.1, 2, 4]

Note that pores are invaded together with the largest throat neighbor. The edge effect is ignored here.

**Table C-13** Simulations in Fig. 6-23.

Capillary ring PNM

Number of simulations	3
$T_{BL}$	24.3°C
$T_{PN}$	63°C = <i>const.</i>
$S_{BL}$	[1.6, 3, 15] · $L$
$w_r$	21.4 μm
$\alpha$	2

Note that pores are invaded together with the largest throat neighbor. The edge effect is ignored here.

**Table C-14** Simulations in Section 6.2.6.

Capillary ring PNM with edge effect and temperature field from experiment

Number of simulations	2
$S_0$	[0.94, 1]
$T_{BL}$	24.3°C
$T^{min}$	62.58°C
$T^{max}$	64.09°C
$\bar{T}$	63.5°C
$S_{BL}$	4.82 $L$
$w_r$	21.4 μm
$\alpha$	2
$f^{red}$	0.85
$z^{pin}$	(5-49) $L$

Note that pores are invaded together with the largest throat neighbor.

**Table C-15** Simulations in Figs. 6-29, 6-31 and 6-33.

PNM level 2 with implemented edge effect

Number of simulations	3
$T_{BL}$	25.2°C
$T^{min}$	51.64°C
$T^{max}$	74.76°C
$\bar{T}$	64.22°C
$S_{BL}$	[0.5, 3, 4.82] · $L$
$f^{red}$	0.85
$z^{pin}$	(5-49) $L$

Note that liquid rings are ignored in the simulation with  $S_{BL} = 0.5L$ . In the other two simulations  $w_r = 21.4 \mu\text{m}$  and  $\alpha = 2$ . The temperature field corresponding to experiment 15 is applied here (Fig. 3-8b).

**Table C-16** Simulations in Figs. 6-30, 6-32 and 6-33.

PNM level 3, level 4 and CLO1, CLO2, CLO3 with implemented edge effect	
Number of simulations	4
$T_{BL}$	25.2°C
$T^{min}$	51.64°C
$T^{max}$	74.76°C
$\bar{T}$	64.22°C
$S_{BL}$	0.5 L
$f^{red}$	0.85
$z^{pin}$	(5-49) L

Note that liquid rings are ignored here.

**Table C-17** Simulation in Section 6.3.2.

PNM level 4 and CLO2	
Number of simulations	1
$T_{BL}$	20°C
$T^{min} = T_{bottom}$	20°C
$T^{max} = T_{top}$	30°C
$S_{BL}$	2 L

Note that liquid rings are ignored here.

**Table C18** Simulations in Section 6.3.3.

PNM level 2, level 3, level 4 and CLO1, CLO2, CLO3 with implemented edge effect	
Number of simulations	5
$T_{BL}$	25°C
$T^{min}$	23.58°C
$T^{max}$	50.59°C
$\bar{T}$	37.79°C
$S_{BL}$	0.5 L
$f^{red}$	0.85
$z^{pin}$	(5-10) L

Note that liquid rings are ignored. The temperature field corresponding to experiment 10 is applied here (Fig. 3-8c).

**Table C-19** Simulation in Fig. 6-45b.

PNM level 4 and CLO3 with implemented edge effect	
Number of simulations	1
$T_{BL}$	25°C
$T^{min}$	23.58°C
$T^{max}$	50.59°C
$\bar{T}$	37.79°C
$S_{BL}$	0.5 L
$f^{red}$	0.85
$z^{pin}$	(5-10) L
$D(T)$	from the correlation of Krischer and Rohalter (1940) (Table 2-1)

Note that liquid rings are ignored here.

**Table C-20** Simulation in Fig. 6-51.

PNM level 4 and CLO2 applied for the three different heating modes	
Number of simulations	3
$T_{BL}$	20°C
$T_{bottom}$	[20, 40, 60]°C
$T_{top}$	[60, 40, 20]°C
$\bar{T}$	40°C
$S_{BL}$	0.5 L

Note that liquid rings are ignored here.

*Simulations in Appendix B*

**Table C-21** Simulations in Section B-1.

Benchmark PNM from Metzger et al. (2007c)	
Number of simulations	56
$T_{PN} = T_{BL} = const.$	[20, 40, 60, 80]°C
$S_{BL}$	4 L
Simulation with constant temperature and the different diffusivities from Table 2-1.	

**Table C-22** Simulations in Section B.2 (Figs. B-2 to B-7).

PNM with liquid pore volumes	
Number of simulations	8
$T = T_{BL}$	20°C
$S_{BL}$	2 L
Simulation with separate invasion of pores ( $f = [0.56, 1, 1.52$ and $0.65, 0.75, 0.85, 0.95]$ ) and with pores invaded together with the largest throat neighbor (benchmark simulation).	

Note that the edge effect and liquid film rings are ignored in this simulation.

**Table C-23** Simulations in Fig. B-8.

MC simulation with PN of size 100x100	
Number of simulations	12
$T = T_{BL}$	25°C
$S_{BL}$	4 L
$\bar{r}_t$	65 $\mu\text{m}$
$r_t^{std}$	0.5 $\mu\text{m}$
Monte Carlo simulation with separate pore invasion ( $f = 1$ ) and with benchmark PNM.	

**Table C-24** Simulations in Figs. B-9 to B-13.

Non-isothermal PNM, initially partially saturated	
Number of simulations	4
$S_0$	0.61
$T_{BL}$	20°C
$T_{bottom}$	70°C
$T_{top}$	20°C
$S_{BL}$	2 L

Comparison to PN simulation either neglecting the temperature dependency of vapor transport or the temperature dependency of liquid curvature. Simulation with CLO3. Comparison to isothermal drying with  $T = 20^\circ\text{C} = \text{const.}$

Note that the edge effect and liquid film rings are ignored in this simulation. Pore volumes are implemented as single liquid elements.

**Table C-25** Simulations in Fig. B-14.

Non-isothermal PNM, initially partially saturated	
Number of simulations	9
$S_0$	0.61
$T_{BL}$	20°C
$T_{bottom}$	[20:10:90]°C and 99°C
$T_{top}$	20°C
$S_{BL}$	2 L
Simulation with CLO3.	

Note that the edge effect and liquid film rings are ignored in this simulation. Pore volumes are implemented as single liquid elements.

**Table C-26** Simulations in Figs. B-15 to B-19.

Non-isothermal PNM, initially partially saturated

Number of simulations	3
$S_0$	0.61
$T_{BL}$	20°C
$T_{bottom}$	70°C
$T_{top}$	20°C
$S_{BL}$	2L

Simulation with CLO1, CLO2, CLO3.

Note that the edge effect and liquid film rings are ignored in this simulation. Pore volumes are implemented as single liquid elements.

**Table C-27** Simulations in Figs. B-20 to B-27.

Non-isothermal PNM, initially fully saturated

Number of simulations	12
$T_{BL}$	20°C
$T_{bottom}$	40°C, 60°C, 80°C
$T_{top}$	20°C
$S_{BL}$	200 $\mu\text{m}$ , 1000 $\mu\text{m}$ , 2000 $\mu\text{m}$ , 4000 $\mu\text{m}$

Simulation with CLO3.

Note that the edge effect and liquid film rings are ignored in this simulation. Pore volumes are implemented as single liquid elements.

**Table C-28** Simulation shown in Appendix B.4 (Fig. B-28).

Continuous films PNM (Prat 2007), comparison to benchmark PNM (Metzger et al. 2007c)

Number of simulations	2
$T_{BL}$	63°C (film PNM), 24.3°C (benchmark)
$T_{PN}$	63°C = <i>const.</i>
$S_{BL}$	150 $\mu\text{m}$ (film PNM), 1600 $\mu\text{m}$ (benchmark)
$\theta = \theta^*$	45° (film PNM)
$k$	0.9 (film PNM)

Liquid rings and the edge effect are ignored. Pore volumes are distributed among the (largest) throat neighbors. Parameters of the film model as specified in Appendix B.4.

# Student theses

## with relevance to this PhD

1. Tran, Q.T. (2010) Trocknungsexperimente mit Porennetzwerken: Bildanalytische Auswertung und Einfluss von Temperaturgradienten, Pre-diploma thesis, Otto von Guericke University Magdeburg
2. Duong, N. X (2011) Experimental evaluation of a non-isothermal pore network model of drying, Master thesis, Otto von Guericke University Magdeburg
3. Tran, Q. T. (2011) Optische Experimente an Porennetzwerken zur Bewertung moderner Trocknungsmodelle, Diploma thesis, Otto von Guericke University Magdeburg
4. Trayanov, Y. (2011) Messung von Feuchteprofilen in porösen Medien, Master thesis, Otto von Guericke University Magdeburg
5. Benecke, J. (2012) Experimentelle Untersuchung von Flüssigkeitsfilmen bei der nicht-isothermen Trocknung in Porennetzwerken, Bachelor thesis, Otto von Guericke University Magdeburg
6. Yue, P. (2016) Pore network drying in the presence of liquid films: Mimicking of the film effect using a simple bimodal pore network model, Master thesis (not finished), Otto von Guericke University Magdeburg
7. Yue, P. (2016) Capturing secondary mass transfer in porous media by a secondary pore network, Master thesis, Otto von Guericke University Magdeburg
8. Zulfiqar, B. (2017) A pore network model for mass transfer through the porous transport layer at the anode side of an electrolyser, Master thesis, Otto von Guericke University Magdeburg
9. Ahmad, F. (2017) Pore network study of drying in presence of thermal gradients, Master thesis, Otto von Guericke University Magdeburg

# List of publications

## with relevance to this PhD

### *Peer-reviewed journal papers*

1. Vorhauer, N.; Metzger, T.; Tsotsas, E. (2009) Empirical macroscopic model for drying of porous media based on pore networks and scaling theory, *Drying Technology* 28, 991-1000
2. Prat, M.; Veran-Tissoires, S.; Vorhauer, N.; Metzger, T.; Tsotsas, E. (2012) Fractal phase distribution and drying: Impact on two-phase zone scaling and drying time dependence, *Drying Technology* 30 (11-12), 1129-1135
3. Vorhauer, N.; Tran, Q.T.; Metzger, T.; Tsotsas, E.; Prat, M. (2013) Experimental investigation of drying in a model porous medium: Influence of thermal gradients, *Drying Technology* 31, 920-929
4. Vorhauer, N.; Wang, Y.; Kharaghani, A.; Tsotsas, E.; Prat, M. (2015) Drying with formation of capillary rings in a model porous medium, *Transport in Porous Media* 110, 197-223
5. Vorhauer, N.; Tsotsas, E.; Prat, M. (2017) Drying of thin porous disks from pore network simulations, *Drying Technology*, DOI: 10.1080/07373937.2017.1319853
6. Vorhauer, N.; Tsotsas, E.; Prat, M. (2018) Temperature gradient induced double-stabilization of the evaporation front within a drying porous medium, *Phys Rev Fluids* (accepted)



### *Conference proceedings*

1. Metzger, T.; Vorhauer, N.; Tsotsas, E. (2008) Use of pore networks for macroscopic modelling of drying, Proceedings of the 16th International Drying Symposium (IDS 2008), Drying 2008, Vol. A, 242-249, Hyderabad, India
2. Vorhauer, N.; Metzger, T.; Tsotsas, E. (2010) Drying of porous media: A comparison of discrete and continuous models, Proceedings of the 3rd International Conference on Porous Media and its Applications in Science, Engineering and Industry 2010, Montecatini, Italy
3. Vorhauer, N.; Metzger, T.; Tsotsas, E. (2010) Extraction of effective parameters for continuous drying model from discrete pore network model, Proceedings of the 17th International Drying Symposium (IDS 2010), Drying 2010, Vol. A, 415-422, Magdeburg, Germany
4. Vorhauer, N.; Metzger, T.; Tsotsas, E. (2011) On the influence of temperature gradients on drying of pore networks, Proceedings of the European Drying Conference (EuroDrying 2011), Palma, Spain
5. Vorhauer, N.; Metzger, T.; Tsotsas, E.; Prat, M. (2012) Experimental investigation of drying by pore networks: Influence of pore size distribution and temperature, Proceedings of the 4th International Conference on Porous Media and its Applications in Science, Engineering and Industry 2012, Potsdam, Germany
6. Vorhauer, N.; Tsotsas, E.; Prat, M. (2014) Isothermal drying of pore networks in the presence of capillary liquid films: Comparison of experiments with simulations in a model system, Proceedings of the 19th International Drying Symposium (IDS 2014), Lyon, France
7. Vorhauer, N.; Rahimi, A.; Tsotsas, E.; Prat, M. (2016) Non-isothermal drying of thin porous discs, Proceedings of the 20th International Drying Symposium (IDS 2016), Gifu, Japan
8. Vorhauer, N.; Tretau, A.; Bück, A.; Tsotsas, E.; Prat, M. (2017) Pore scale investigation of drying under periodic temperature variation, Proceedings of the European Drying Conference (EuroDrying 2017), Liège, Belgium
9. Vorhauer, N.; Mirsadraee, N.; Tretau, A.; Bück, A.; Tsotsas, E.; Prat, M. (2017) Combined convective and microwave drying of wet clay, Proceedings of the Nordic Baltic Drying Conference (NBDC 2017), Hamburg, Germany
10. Vorhauer, N.; Först, P.; Schuchmann, H.; Tsotsas, E. (2018) Pore network model of primary freeze drying, Proceedings of the 21st International Drying Symposium (IDS2018), Valencia, Spain, DOI: 10.4995/ids2018.2018

# Curriculum Vitae

<b>Name</b>	Nicole VORHAUER
<b>Date of birth</b>	September 10, 1982
<b>Place of birth</b>	Magdeburg, Germany
<b>Education</b>	
1989-1993	Elementary school, Magdeburg, Germany
1993-1997	Secondary school Europagymnasium Gommern, Biederitz, Germany
1997-2002	Secondary school Gymnasium Burg, Germany
<b>Higher education</b>	
2002-2007	Otto von Guericke University Magdeburg, Germany Diploma thesis: 'Untersuchung des Einflusses von Flüssigkeitsschichten auf das Stoßverhalten elastisch-plastischer Granulate'
<b>Doctoral studies</b>	
2010-2018	Otto von Guericke University Magdeburg, Germany and Institut National Polytechnique de Toulouse/ Université de Toulouse, France Cotutelle de Thèse
<b>Work experience</b>	
2007 till present	Scientific researcher at Otto von Guericke University Magdeburg Parental leave: 11.2009-12.2010 and 10.2012-11.2013